HAL
open science

Combined theoretical and experimental study of the ionic conduction in oxide-carbonate composite materials as electrolytes for solid oxide fuel cells (SOFC)

Chiara Ricca

To cite this version:

Chiara Ricca. Combined theoretical and experimental study of the ionic conduction in oxide-carbonate composite materials as electrolytes for solid oxide fuel cells (SOFC). Chemical Physics [physics.chem-ph]. Université Pierre et Marie Curie - Paris VI, 2016. English. NNT : 2016PA066623 . tel-01638202

HAL Id: tel-01638202

https://theses.hal.science/tel-01638202v1

Submitted on 20 Nov 2017

HAL is a multi-disciplinary open access archive for the deposit and dissemination of scientific research documents, whether they are published or not. The documents may come from teaching and research institutions in France or abroad, or from public or private research centers.

L'archive ouverte pluridisciplinaire **HAL**, est destinée au dépôt et à la diffusion de documents scientifiques de niveau recherche, publiés ou non, émanant des établissements d'enseignement et de recherche français ou étrangers, des laboratoires publics ou privés.

THESE DE DOCTORAT DE
L'UNIVERSITE PIERRE ET MARIE CURIE

Ecole Doctorale De Chimie Analytique et Physique de Paris Centre
(ED 388)

Combined theoretical and experimental study of the ionic conduction in oxide-carbonate composite materials as electrolytes for solid oxide fuel cells (SOFC)

Présentée par

Chiara Ricca

Pour obtenir le grade de

DOCTEUR DE L'UNIVERSITE PIERRE ET MARIE CURIE

Soutenue le 18/11/2016, devant le jury composé par :

M. Philippe D'Arco	*Professeur –UPMC*	Président
M. David Loffreda	*Directeur de Recherche – ENS Lyon*	Rapporteur
M. Antonino Martorana	*Professeur –Università degli Studi di Palermo*	Rapporteur
M. Jean François Halet	*Directeur de Recherche –Université de Rennes 1*	Examinateur
Mme Caroline Pirovano	*Maître de Conférences–ENSC Lille*	Examinatrice
M. Frédéric Labat	*Maître de Conférences –IRCP Chimie Paris-Tech*	Invité
M. Carlo Adamo	*Professeur –IRCP Chimie Paris-Tech*	Directeur de thèse
Mme Armelle Ringuedé	*Chargée de Recherche – IRCP Chimie Paris-Tech*	Co-Directrice de thèse

A Roberto e Sara

Remerciements

En tout premier lieu, je souhaite adresser mes remerciements à mon directeur de thèse, Carlo Adamo, pour m'avoir donné la possibilité de travailler à l'IRCP Chimie Paris-Tech et pour la supervision de mon travail. Je remercie également ma co-directrice, Armelle Ringuedé, pour m'avoir transmis une partie de son expérience et pour sa disponibilité au quotidien.

Je remercie tout particulièrement Frédéric Labat pour avoir encadré la partie théorique de cette thèse, our toutes les connaissances qu'il a su me transmettre, pour le grand l'intérêt porté à mon travail, pour l'aide précieuse qu'il m'a apporté dans toutes les démarches administratives, pour les conseils des plus avisés, ainsi que pour son soutien lors des moments difficiles et particulièrement pendant la dernière année.

Je remercie également Michel Cassir de m'avoir accueillie au sein de l'équipe *Interface, Électrochimie, Énergie* (I2E) et pour avoir pris le temps de partager avec moi de assionnantes discussions sur les sciences, la culture et la politique italiennes. Merci aussi à Ilaria pour l'accueil au sein de l'équipe de *Chimie Théorique et Modélisation* et pour le soutien durant les moments les plus durs de ces trois années et pour ses conseils toujours avisées.

Je tiens de même à remercier Alistar pour l'aide précieuse et ses réponses quant à mes doutes et autres problèmes. Mes remerciements s'adressent également à Andrey et Valérie pour l'aide indispensable qu'ils mont apporté durant mes travaux expérimentaux.

Je souhaite exprimer toute ma reconnaissance envers MM. David Loffreda et Antonino Martorana pour avoir accepté d'être rapporteurs de ce travail, ainsi qu'à M. Philippe D'Arco, M. Jean-François Halet et Mme Caroline Pirovano pour leur participation à mon jury de thèse.

Je tiens à remercier toutes les personnes que j'ai rencontré dans les deux équipes tout au long de ces années: Stefania C., Romain, Valentino, Éric, Vinca, Alexandra, Marika, Domenico, Manel, Arturo, Oumaima, Indira, Luca et en particulier Marta, Liam, Umberto et Marianna pour les discussions et pour tout le temps que nous avons passé ensemble en dehors du laboratoire.

Un remerciement très spécial à Stefania. Son amitié, son aide, ses conseils et son éternel soutien sont inhérent à l'aboutissement de ce projet. Merci surtout de m'avoir toujours encouragée à ne jamais abandonner et pour avoir énorméent contribué à faire en sorte que je puisse me sentir chez moi.

Je suis tout particulièrement reconnaissante envers mes parents, car c'est grâce à eux si aujourd'hui je peux dire avoir vécu cette magnifique expérience parisienne, envers ma soeur pour m'avoir aidée à transformer mon petit studio en un lieu plus confortable, et bien entendu envers mon frère pour ses conseils. Merci à Mario pour avoir tenu bon malgré la distance et toutes les difficultés rencontrées pendant ces trois années.

Enfin, un grand merci à Edda et Andreea qui n'ont jamais cessé de me soutenir malgré les nombreux kilomètres qui nous séparent.

Acknowledgments

First, I would like to thank Prof. Carlo Adamo who has given me the opportunity to work at IRCP Chimie Paris-Tech and for supervising my work. I would also like to thank my co-supervisor Armelle Ringuedé for sharing with me her knowledge in the field of fuel cells and for her kindness.

I would like to particularly acknowledge Frédéric for guiding me through the theoretical part of this thesis, for all the knowledge he has shared with me, the interest he has shown in my work, and the help, advice and support he has provided especially during the most difficult moments in the last year of my PhD.

I would also like to thank Michel Cassir for welcoming me to the I2E team and for the interesting discussions about science or Italian culture and politics, as well as Ilaria for welcoming me to the CTM group and for her advice and support during these three years.

Thanks to Alistar for the help and discussions every time I had doubts or problems and to Andrey and Valérie for helping me with the experimental part of this work.

I would like to acknowledge Mr. David Loffreda, Mr. Antonino Martorana, Mr. Philippe D'Arco, Mr. Jean François Halet and Mrs. Caroline Pirovano for agreeing to be part of my thesis committee.

Thanks to all the people I have met during my PhD in the I2E and CTM groups: Stefania C., Romain, Valentino, Eric, Vinca, Alexandra, Federica, Domenico, Manel, Arturo, Oumaima, Indira, and Luca. In particular, thanks to Marta, Liam, Umberto, and Marianna for the discussions and the time spent together.

I would especially like to thank Stefania for her friendship, help, advice and support. Thanks for having always encouraged me to never give up and for having made it possible for me to feel at home.

Thanks to my parents, since it is thanks to of them that I lived this wonderful experience in Paris, to my sister and brother for their support and advice, and to Mario for holding on despite the distance and all the difficulties.

Finally, thanks to Edda and Andreea for always being there for me despite the distance.

Contents

Abbreviations **xii**

Defect Notation **xiv**

1 General Context and Objectives **1**
1.1 The role of fuel cells in the current energetic context 1
1.2 Fuel Cells 5
1.2.1 Functioning Principles and Classification 5
1.2.2 Fuels for Electrochemical Cells 7
1.2.3 SOFC 8
1.2.4 The problem of lowering SOFC operating temperature 12
1.2.5 MCFCs and SOFCs 14
1.3 Composite Materials 17
1.3.1 Space Charge Layer Theory 18
1.3.2 Carbonate/oxide electrolytes 19
1.3.3 Conduction Mechanisms in oxide-carbonate electrolytes 27
1.4 Research strategy: a combined experimental and theoretical approach . . . 32

2 Theoretical and Experimental Methods **37**
2.1 Introduction 37
2.2 Theoretical Background 37
2.2.1 The Shrödinger Equation 37
2.2.2 The Hartree-Fock (HF) Theory 39
2.2.3 Density Functional Theory (DFT) 43
2.2.4 Modelling of crystalline systems 50
2.2.5 *Ab initio* Molecular Dynamics (MD) 53
2.3 Experimental Background 59
2.3.1 Electrochemical Impedance Spectroscopy (EIS) 59

3 Experimental Results **63**
3.1 Introduction 63
3.2 Preparation of the composite materials 64
3.2.1 Thermal analysis 65
3.2.2 XRD characterization 66
3.2.3 IR and Raman spectroscopy 66

3.3 Electrochemical characterisation 66
3.3.1 EIS experimental details 66
3.3.2 Electrochemical behaviour of oxide-carbonate composites 71
3.4 TGA and DTA analyses 86
3.5 Premilinary XRD characterization 91
3.5.1 YSZ-$(Li,K)_2CO_3$ composite 91
3.5.2 YSZ-$(Li,Na)_2CO_3$ composite 93
3.5.3 TiO_2-$(Li,K)_2CO_3$ composite 93
3.6 IR and Raman characterization 96
3.6.1 Infra-red spectra 96
3.6.2 Raman spectra 99
3.7 Conclusions 102

4 Modeling of the oxide phase: YSZ 103
4.1 Introduction 103
4.2 Computational Details 106
4.3 ZrO_2 bulk 107
4.3.1 Structure 108
4.3.2 Relative Stability 109
4.3.3 Electronic properties 113
4.4 ZrO_2 Surfaces 119
4.4.1 Surface Energetics 120
4.4.2 Surface Geometries 122
4.4.3 Surface Electronic Properties 125
4.5 Reducibility properties of the (111) of *c*-ZrO_2 surface 126
4.5.1 Formation Energy and Structural Rearrangements 128
4.5.2 Electronic structure of oxygen vacancy 131
4.6 Y_2O_3-doped (111) surface 134
4.6.1 Stability and Structural Rearrangements in YSZ-(111) surface . . . 134
4.6.2 Electronic structure of YSZ-(111) surface 137
4.7 Conclusions 139

5 Modeling of the carbonate phase 141
5.1 Introduction 141
5.2 Computational Details 144
5.2.1 DFT Calculations 144
5.2.2 Calculation of the dielectric constant 146
5.2.3 Calculations in presence of an external electric field 147
5.3 $LiNaCO_3$ and $LiKCO_3$ bulk 147
5.3.1 Structure optimization and relative stability 148
5.3.2 IR and Raman Spectra 151
5.3.3 Electronic Properties 153
5.4 $LiNaCO_3$ and $LiKCO_3$ Surfaces 157
5.4.1 Reconstruction of the dipolar (001) $LiNaCO_3$ surface 157

5.4.2 Non polar (110) $LiNaCO_3$ surface 162
5.4.3 (001) and (110) $LiKCO_3$ surfaces 163
5.5 Li transport at the $LiKCO_3$-(001) surface 163
5.5.1 Defect Formation 164
5.5.2 Diffusion mechanism 172
5.6 Conclusions 177

6 DFT simulation of YSZ-$LiKCO_3$ composite 179
6.1 Introduction 179
6.2 Computational Details 181
6.2.1 DFT calculations 181
6.2.2 MD calculations 183
6.3 DFT investigation of the stability and electronic properties of YSZ-$LiKCO_3$ 183
6.3.1 Building the YSZ-$LiKCO_3$ interface model 183
6.3.2 YSZ-$LiKCO_3$ structure and stability 185
6.3.3 IR and Raman Spectra 189
6.3.4 YSZ-$LiKCO_3$ electronic properties 193
6.4 DFT Study of Conduction Mechanisms 196
6.4.1 Li transport 197
6.4.2 Oxygen transport 208
6.4.3 Proton transport 216
6.5 Preliminary Results of the MD Simulations 222
6.6 Conclusions 224

7 DFT simulation of TiO_2-$LiKCO_3$ materials 227
7.1 Introduction 227
7.2 Computational Details and Models 228
7.3 Structure and Stability of the TiO_2-$LiKCO_3$ interface 230
7.4 TiO_2-$LiKCO_3$ Electronic Properties 233
7.5 Li intercalation at the TiO_2-$LiKCO_3$ interface 236
7.6 Conclusions 242

8 Conclusions and Perspectives 245

Bibliography 267

Abbreviations

AFC Alkaline fuel cells

APU Auxiliary Power Unit

BCCF $Ba_xCa_{1-x}Co_yFe_{1-y}O_{3-\delta}$

BSCF $Ba_{0.5}Sr_{0.5}Co_{0.8}Fe_{0.2}O_3$

BSSE Basis set superimposition error

BSY Yttium-doped barium zirconate

CB Conduction band

CHP combined heat and power

COP21 21th Conference of Parties

DFT Density Functional Theory

DTA Differential Thermal Analysis

EELS Electron energy loss spectroscopy

EIS Electrochemical impedance spectroscopy

EU European Union

FC Fuel Cells

GDC Gadolinium Doped Ceria

GGA General gradient approximation

GHG Greenhouse-gas

GTF Gaussian type function

KS Kohn and Sham

HF Hartree Fock

HRTEM High resolution transmission electron microscopy

HT high temperature

IBZ Irreducible Brillouin zone

IT intermediate temperature

LCAO Linear combination of atomic orbitals

LDA Locan density approximation

LSCF $La_xSr_{1-x}Co_yFe_{1-y}O_{3-\delta}$

LSCM $La_{0.75}Sr_{0.25}Cr_{0.5}Mn_{0.5}O_3$

LSGM Lanthanum strontium magnesium gallate

LSM lanthanum strontium manganite

LT low temperature

MCFC Molten carbonate fuel cells

MD Molecular Dynamics

MS Mass Spectrometry

MSE Mean Signed Error

MUE Mean Unsigned Error

NEB Nudget Elastic Band

NVE Microcanonical ensemble

NVT Canonical ensemble

NVP isothermal-isobaric ensemble

ORR Oxygen reduction reaction

PAFC Phosphoric acid fuel cells

PCFC Protonic ceramic fuel cells

PAW Projector Augmented Wave

PEMFC Proton exchange membrane fuel cells

PSZ Partially-stabilized zirconia

PW Plane Wave

SCF Self Consistent Field

SDC Samarium Doped Ceria

ScSZ Scandia-stabilized zirconia

SEM Scanning electron microscopy

SCFC Single Component Fuel Cells

SOFC Solid Oxide Fuel Cells

STF Slater Type Function

TGA Thermogravimetric Analysis

TZP Yttria-doped tetragonal zirconia

VB Valence band

VUV vacuum ultraviolet spectroscopy

XRD X-ray diffraction

YSZ Yttria-stabilized zirconia

ZPE Zero point energy

Defect Notation

V_O^X Neutral O vacancy

$V_O^{\bullet\bullet}$ Doubly positively charged O vacancy

V_{Li}^X Neutral Li vacancy

$V_{Li}^{'}$ Negatively charged Li vacancy

Li_i^X Neutral interstitial Li atom

$Li_i^{\bullet}$ Positively charged interstitial Li ion

Chapter 1

General Context and Objectives

Humanity stands ... before a great problem of finding
new raw materials and new sources of energy
that shall never become exhausted.
In the meantime we must not waste what we have,
but must leave as much as possible for coming generations.
Svante Arrhenius
Chemistry in Modern Life (1925)

1.1 The role of fuel cells in the current energetic context

The 21th Conference of Parties (COP21) held in Paris in December 2015 represented a major milestone in efforts to fight the climate change, one of the most important and difficult challenges that our generation and the next ones have to face. An historical agreement has been indeed signed by 195 countries worlwide. It represents the first-ever universal, legally binding global climate deal, setting out the common intent to limit the global warming well below the 2°C.[1] This 2°C scenario offers a vision of a sustainable energy system of reduced Greenhouse-gas (GHG) and carbon dioxide (CO_2) emissions.[2] The efficient production of energy is then a fundamental of the modern world.

Energy production and use account for about two-thirds of the GHG emissions[3] and are very likely to increase at a rapid rate in the future, because energy is the most valuable resource for human activity, and human progress has always been associated to the growth of the energy demand. For example, since the 1970s, electricity overall share of total energy demand has risen from 9% to over 17%[2] and world's appetite for electricity is expected to increase the demand by more than 40% by 2030[3] and by more than 70% by 2040.[4] Energy-related CO_2 emissions have increased by 75% between 1990 and 2011,[2] with a rate of 2.4% per year since 2000, and are projected to increase to 36.7 Gt in 2040, 16% higher than in 2013.[4] It is consequently clear that, being the largest producer of GHG emissions, the energy sector should play a central role in the challenge to limit climate change.

Up to now, the energy needs have been satisfied mainly through combustion of fossil fuels. Given the continuous consumption of the finite hydrocarbon natural resources and the impact of their use on climate changes, it is of vital importance to first learn how to

use these resources as efficiently as possible and more importantly to introduce conveniently sustainable alternatives. In the 2°C scenario, electricity demand will grow up to 80% by 2050, but CO_2 emissions per unit of electricity must decrease by 90% by the same time.[2] This means that if we want to achieve the 2°C climate goal, huge economic investments and scientific efforts should be addressed to the development of environmental friendly and affordable innovative energy technologies allowing the low-carbon transition.

In this energetic context, renewable energy, that is energy from a source that is not depleted when used (such as wind power, solar power or biomass), represents the key toward the transition. The European Union (EU) has committed to achieve a 20% share of renewable energy in the EU overall energy consumption by 2020, with a further goal to go up to at least 27% by 2030.[5] This target can be reached by increasing the share of energy from all the renewable sources and aims to reduce pollution and GHG emissions together with the renewable production costs and to diversify the energy supply reducing dependence on oil and gas. So far a share of 15.3% of renewable energy has been obtained in 2014. Impressive deployment of renewable technologies is thus beginning to shape a substantially different future in supply. Renewables are already the third largest contributor to global electricity production. They accounted for almost 18% of the electricity production in 2004, after coal (40%) and natural gas (close to 20%), but ahead of nuclear (16%), and oil (7%) and nonrenewable waste.[6] In the 2°C scenario, electricity generated from biomass, wind, solar, geothermal and tide and wavepower will overtake coal reaching 2 872 TWh in 2030, almost eight times higher than now and their share in total generation grows from 2% now to 10% in 2030[4,6] and up to 65% in 2050.[7]

However, fossil energy carriers still accounted, in 2011, for two-thirds of primary fuel in the global electricity mix and covered most of recent demand.[2] In the 2°C scenario, fossil fuel use decreases by 2050, but its share of primary energy supply remains above 40%,[7] reflecting its particularly important role for use in industry, transport and electricity generation. (Figure 1.1).

So far, the principal problem with the diffusion of renewable energy is the cost-effectiveness, because the average price of renewable technologies is still generally not competitive with wholesale electricity and fossil fuel prices. The biggest challenge in this sector is consequently to improve the state-of-the-art so that renewable sources can produce energy with costs that are competitive with the ones of conventional technologies.[6]

Fuel Cells (FC)s are electrochemical devices that allow the direct conversion of the energy stored into a fuel in electricity. They actually represent a promising alternative to conventional technologies to realize the low carbon transition. These devices combine, indeed, high efficiency with low environmental impact. As regards efficiency, from figure 1.2, which shows the typical energy efficiencies of a variety of conventional or sustainable conversion devices, it is in fact evident that FC have one of the highest energy conversion efficiencies among the competing energy conversion devices. In fact, FCs are not limited by Carnot efficiency, as in the case of mechanical devices such as gas turbines, because they produce electricity through isothermal oxidation instead of combustion.[8–10]

Pollutant emissions produced by these devices are related to the fuel in use but are always very low and can drop to zero when hydrogen is used as fuel.[12] Together with these advantages, fuel cells present other important characteristics that strongly contribute to their rising

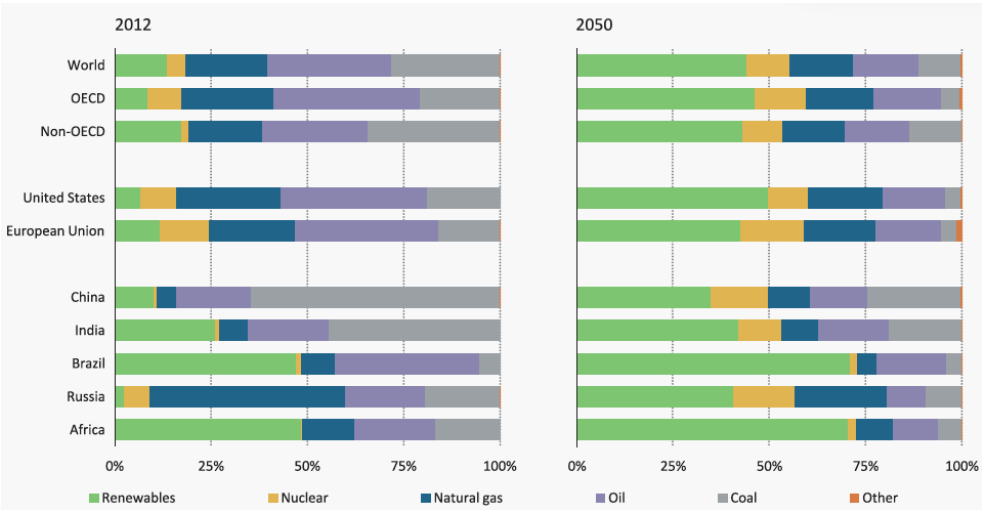

Figure 1.1: Regional primary energy demand profiles in the 2°C scenario. OECD indicates the countries that signed the *Convention on the Organisation for Economic Cooperation and Development*.[7]

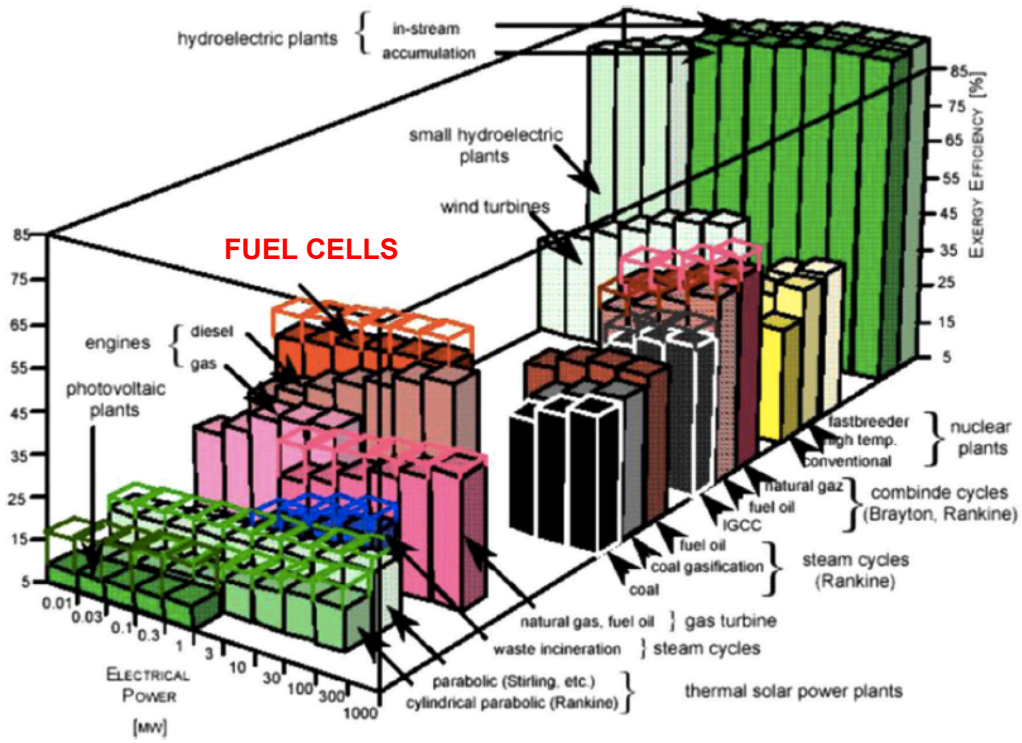

Figure 1.2: Energy efficiencies of the principal types of energy conversion systems. The solid bars represent what currently is possible, while the non-solid extensions depict projected improvements.[9,11]

role in the future clean energy generation: fuel flexibility, production of useful quantity of heat that can can be used in combined heat and power (CHP) applications, flexibility of operation for a wide range of applications, from stationary to portable power supply, continuous energy production provided that the fuel and the oxidant are fed to the cell, and near silent operation.[8–10,12] FCs rapid expansion in the energy conversion sector can be seen in figure 1.3, showing the year on year growth of fuel cell use between 2009 and 2013. In 2012 alone, 125MW of fuel cells for stationary applications were shipped, resulting in a 53% increase compared to 2011.[8] In particular,in Japan there has been a tremendous increase in residential fuel cells with over 33500 units sold since 2009. Initially, 5000 units were sold per year, but today more than 20000 units are being sold annually.[10,13]

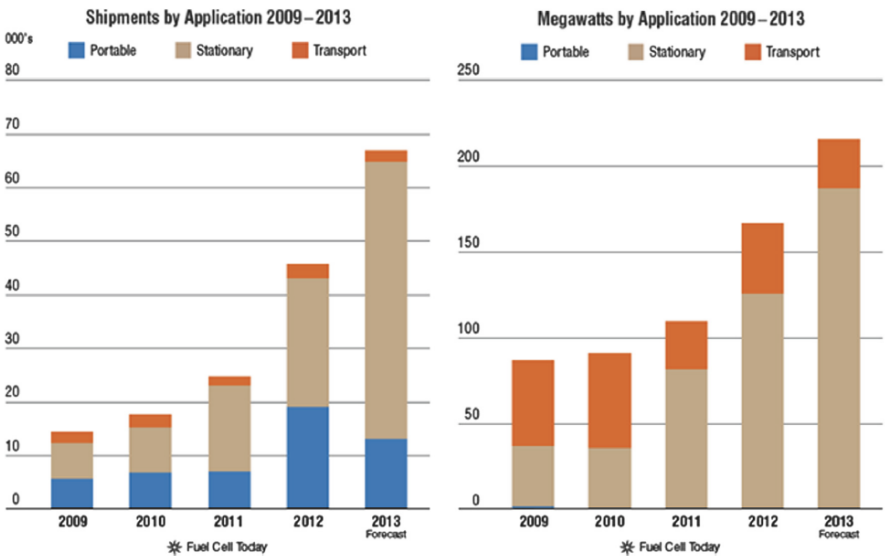

Figure 1.3: Fuel Cell use by application 2009-2013.[8,14]

Among different fuel cell types, Solid Oxide Fuel Cells (SOFC)s can play a critical role in both our current and future energy solutions because they offer additional advantages related to their high operation temperature (typically 600-1000°C).[15] They give the highest potential efficiency for conversion of electricity[13] and the highest overall efficiency since 43% of the energy converted to heat can be more effectively utilized because of its higher quality due to the high operating temperature.[13] They are extremely fuel flexible resulting in a major impact on reducing fossil fuel consumption and GHG emissions: they are capable of operating with high efficiency on hydrogen and on any hydrocarbon fuel, both from conventional sources (natural gas, methanol, jet fuel, hydrocarbons in general, coal, ammonia, diesel, ethanol) and the future alternative biofuels (biomasses).[16,17]. Finally, carbon-containing fuels can be directly reformed in the cell stack eliminating the need of an expensive external reformer.[12]

However, the widespread use of SOFCs has not yet been realized, because of the high cost associated to materials, cell fabrication and maintenance and because of long-term durability issues. In order to increase the economic competitiveness of these devices with respect to the current electric power generation technology from fire power plants, a system cost between 800-400$/kW for devices that are able to guarantee a lifetime of at least 50000h has been

suggested.[15] SOFCs were developed for operating primarily in the high temperature (HT) range 900-1000°C in order to overcome the ohmic losses of a thick layer of Yttria-stabilized zirconia (YSZ), the state-of-the-art electrolyte for these applications. High temperatures are also beneficial for improving the electrode reactions kinetics, but they are also associated with many drawbacks which limit SOFCs commercialization. First of all, they impose restriction on the cell materials, in particular for the expensive ceramic interconnects that dominate the global cost.[13,15] Furthermore, they require large energy input to heat the cell up to the operating temperature, together with long start-up and shut-down cycles. High temperatures also determine unacceptable performance degradation rates due to reactions between component materials, and electrode degradation due to metallic particles coalescence.[10,13,15,16] In order to increase SOFCs competitiveness, it is then necessary to lower the operating temperature down to the intermediate temperature (IT) range (600-800°C) or even the low temperature (LT) (400-600°C) one. These temperatures will allow metallic alloys as interconnect materials and to use less expensive manufacturing methods for seals, manifold and exchangers, thus drastically reducing the manufacturing costs. They also simplify thermal management, help in faster start-up and cool down, and results in less degradation of the cell and stack components because they alleviate solid phase reaction between materials, effectively reducing maintenance and prolonging the lifetime of the fuel cell system.[10,13,15,16] Unfortunately, upon temperature reduction, electrolyte resistivity and electrode polarization will increase. Consequently, there is the urgent need to develop cell components with acceptable low ohmic and polarization losses to maintain sufficiently high electrochemical activity in the targeted range of temperature beween 400 and 600°C. In the last decade, tremendous efforts have been made in these directions, but there is still a lot of work to do in order to effectively use the new materials into practical devices.

In this work, we will illustrate the results of the investigation we performed on composite carbonate-oxide materials, that have been proposed as promising electrolyte for SOFCs applications because of their enhanced conductivity at lower temperatures (close to 0.1 S/cm at 600°C).[18–22] Despite the large number of publications in this field, a deeper understanding on the origins of such improved performances is indeed required and necessary in order to realize their practical commercial application in SOFCs devices working at low temperature with improved reliability.

1.2 Fuel Cells

1.2.1 Functioning Principles and Classification

A fuel cell is a device in which the chemical energy stored into a fuel is directly converted into electricity through an electrochemical process. The cell is composed by an electrolyte in contact with two electrodes (anode and cathode). The fuel cell reaction can be generally represented by two-electrode reactions in which the fuel is oxidized at the anode, while the oxidant is reduced at the cathode. The electrolyte ensures the transport of the species involved in the electrochemical process between the electrodes, but not of the electrons, that travel instead through a wire creating the electric current. The net result of the two reactions is that fuel is consumed, water or carbon dioxide is created, and the generated electric current

can be used to power electrical devices, normally referred to as the load.

The interest for the use of fuel cells in electric generation for practical use started to increase in the late 70s, but fuel cell technology is one of the oldest electrical energy conversion technology, dating back to the 19th century.[23] The scientific foundations are Humphry Davis' researches on electrolysis. The first fuel cell was then designed by Christian Friederich Schoenbein in 1839.[24] In the same year, William Robert Grove realized the first fuel cell (called gas battery back then), through which he proved that the electrochemical reaction between hydrogen and oxygen produces electricity.[25] Fifty years later, in 1889, Ludwig Mond and Charles Langer developped the first operating fuel cell capable to transform hydrogen in electric current obtaining 20 Am^{-2} and introduced the term fuel cell.[26] In 1932, Francis Bacon started to work on a modification of Mond and Langer's cell, patenting in 1959 the first alakine fuel cell which was used in the Apollo spacecraft.[26] In the 50s and 60s, the "space race" promoted the scientific research in this field: alkaline fuel cells were developped by NASA (Nation Administration for Space and Aereonautics) and the Proton exchange membrane fuel cells (PEMFC) developped by *General Electric* were used for the Gemini missions.[27,28]

FC are generally classified according to the electrolyte. It can be solid (ceramic or polymer), liquid (aqueous or molten) and must have high ionic conductivity (O^{2-},OH^-,H^+,or CO_3^{2-},) but neglegible electronic conductivity. Table 1.1 reports the characteristics of the different fuel cell types according to this classification[23,29]:

- **AFCs** (alkaline fuel cells) use an alkaline electrolyte and are fuelled with pure hydrogen and oxygen. The charge carriers are OH^- ions. They work at about 60-90°C. This technology was largely used for space missions in the 60s;

- **PEMFCs** (proton exchange membrane fuel cells) operate at temperature slightly higher than AFC (80-110°C), upon hydrogen but also reformed natural gas from which CO has been removed. The electrolyte is a proton conductor constituted by a water-based acidic polymer membrane. The metal needed at the anode to catalyze the oxidation of the fuel can suffer of poisoning from the CO that can be present in reformed hydrogen used as a fuel;

- **PAFCs** (phosphoric acid fuel cells) use H_3PO_4 immobilised in SiC as electrolyte and are then based on H^+ conduction. They operate at 160-200°C upon reformed hydrogen;

- **MCFCs** (molten carbonate fuel cells) require, as electrolyte, eutectic mixtures of alkali carbonates in the molten state, CO_3^{2-} conductors. They work in the 600-650°C range, where the CO contained in reformed hydrogen can be used as a fuel upon oxidation to CO_2;

- **PCFCs** (protonic ceramic fuel cells) are a relatively new type of fuel cells based on proton conducting oxide electrolytes. They work at about 600-700°C, using hydrocarbons as fuel.

Type	Temperature (°C)	Electrolyte	Cathode	Anode	Primary Fuel	Oxidant	Efficiency (%)	Power Range (W)	Main Applications
AFC	60-90	KOH	Pt/C	Pt/C or carbon	H_2	O_2	35-40	1000	Space transportation
PEMFC	80-110	Polymer	Pt/C	Pt/C	H_2	O_2/air	40-50	1-10000	Portable transportation
PAFC	160-200	H_3PO_4	Pt/C	Pt/C	H_2/reformate	O_2/air	32-42	50000-200000	Stationary
MCFC	600-650	$LiCO_3/K_2CO_3$	NiO	Ni alloy	H_2/CO reformate	CO_2/O_2/air	47-57	200000-300000	Stationary
PCFC[30]	600-700	$Ba(Zr,Ce)O_{3-\delta}$	Pt	Ni cermet	Hydrocarbons	O_2/air	45-60	-	-
SOFC	600-1000	YSZ	LSM	Ni/YSZ	$H_2/CO/CH_4$ reformate	O_2/air	60-65	1000-125000	Stationary

Table 1.1: Types of fuel cells and their characteristics. Adapted from[29] and completed.

- **SOFCs** (solid oxide fuel cells) use solid oxide electrolytes, O^{2-} ion conductors. They require high temperatures (600-1000°C), but allow the use of hydrocarbon fuels together with H_2/CO.

Fuel cells are often classified also upon their working temperature: AFCs, PEMFCs, and PAFCs can be consequently considered low-temperature, while PCFCs, MCFCs and SOFCs are high-temperature fuel cells.

1.2.2 Fuels for Electrochemical Cells

Hydrogen is the most attractive and cleanest fuel for FC as it produces water as the only by-product with zero GHG emissions. Hydrogen is mainly generated from fossil fuel or hydrocarbons, but these methods produce also large amounts of CO or CO_2 that need be cut down to an acceptable level to reduce poisoning issues, especially for FC working at low temperatures. The main challenge for fuel cells working on hydrogen is however related to the green hydrogen high cost and to the safety issues for H_2 storage and transportation.

Liquid fuels like methanol or ethanol can also be applied. Compared to hydrogen, they are cheap, easy to handle and transport and have potentially higher energy density. Their toxicological and ecological hazard should however be taken into account. For example, methanol is highly inflammable and toxic. Their electrochemical oxidation is also hardly complete and harmful by-products can be formed. For example, the electro-oxidation of methanol produces formic acid and formaldehyde, which is highly irritant, corrosive, toxic and carcinogenic.

High temperature fuel cells like SOFCs and MCFCs can also operate with high efficiencies on hydrocarbon fuels. Natural gas is an ideal fuel for its abundance, low cost and distribution infrastructure. Methane can be directly or indirectly (after reforming) used in SOFCs and MCFCs. Finally, these devices can work with very high efficiency on renewable fuels derived from biomass (particularly from non food biomass).[29]

1.2.3 SOFC

The history of SOFC starts in the 30s of the last century, when Baur and Preis started to work with zirconium dioxide (ZrO_2) doped with 15% Y_2O_3, applicating Nernst's idea that this oxide could be an oxide ion conductor.[31] These devices consist in fact of a dense solid oxide electrolyte layer conducting oxide ions and two porous electrodes working in the high temperature range, between 700 and 1000°C. Figure 1.4 schematically shows the operating principles of a SOFC: oxygen molecules introduced at the cathode react with the electrons coming from the external circuit (Oxygen reduction reaction (ORR)), forming oxide ions that migrate through the electrolyte driven by the difference in oxygen chemical potential thus reaching the anode. Here, they are consumed to oxidise the fuel (hydrogen, methane or hydrocarbons) forming H_2O (and/or CO_2). The two-electrode reactions and the overall process, in the case of hydrogen as fuel, are described by equations 1.1, 1.2, and 1.3, respectively.

$$\frac{1}{2}O_2 + 2e^- \longrightarrow O^{2-} \tag{1.1}$$

$$H_2 + O^{2-} \longrightarrow H_2O + 2e^- \tag{1.2}$$

$$H_2 + \frac{1}{2}O_2 \longrightarrow H_2O \tag{1.3}$$

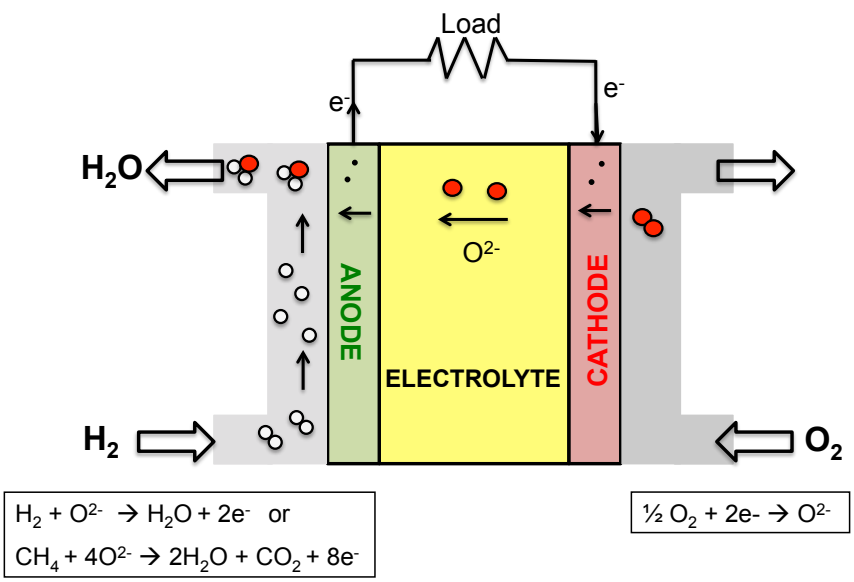

Figure 1.4: Schematic representation of SOFC operating principle.

The interest in SOFCs can be explained considering the peculiar characteristics of these cells compared to the other types:

- As shown in table 1.1, SOFCs provide the highest efficiency (60-65% on average) for conversion of electricity, but the overall efficiency can be higher because of the possibility to efficiently use the heat produced for CHP applications;
- They are very fuel flexible. Because of the high temperature they can work on hydrogen without the need of a previous reforming step, but also the direct use of hydrocarbons is allowed. Hydrocarbons can originate from biofuels or from conventional sources.
- They consequently constitute an environmental-frendly way of producing electricity, since GHG and CO_2 emissions derived from the efficient use of these fuels are very low and they do not contain NOx.
- There is a wide variety of architectures and geometries that can be used for SOFC, like the tubular technology developed by Siemens-Westinghouse or the planar geometry used by Hexis (see figure 1.5).

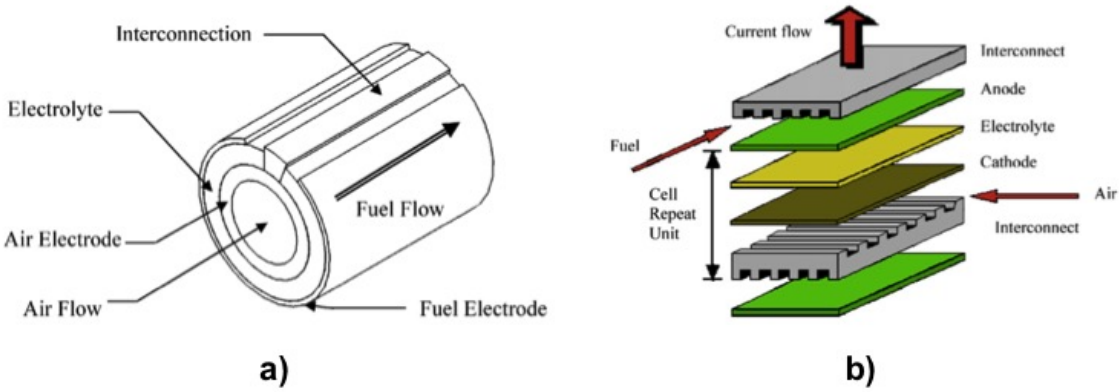

Figure 1.5: Schematic representation of a) tubular and b) planar SOFC geometries.[32]

In the following, we will briefly revise the main properties and characteristics of the materials commonly used for the electrodes and the electrolyte in SOFC applications.

1.2.3.1 Cathode Materials

The cathode material for SOFC application must have high electronic conductivity ($>$ 100 S/cm), high chemical stability in humid air, chemical and mechanical (matching thermal expansion coefficients) compatibility with the electrolyte and the interconnects, and high catalytic activity toward oxygen reduction reaction takeing place at this electrode. Moreover, it is important that the cathode presents a stable porous microstructure, allowing an easy diffusion of gaseous oxygen through the cathode itself to the cathode/electrolyte interface.[10,29,33] The state-of-the-art material is still the lanthanum strontium manganite (LSM), an oxide ceramic material with the formula $La_{1-x}Sr_xMnO_{3-\delta}$. Lanthanum manganite ($LaMnO_3$) is a

perovskite material with intrinsic p-type conductivity, that can be enhanced by substitution of La^{3+} ions with divalent cations like Sr^{2+}. Generally, $0.2 < x < 0.4$ ensures high conductivity while mantaining mechanical and chemical compatibility with the state-of-the-art material for SOFC electrolytes YSZ.[29] LSM has indeed excellent thermal compatibility with YSZ, with a thermal expansion coefficient of 11.3-12.4$\times 10^{-6}$ K^{-1} close to the 10.3$\times 10^{-6}$ K^{-1} of YSZ in the 500-1000°C range.[29,33,34] However, LSM and YSZ can react at high temperature with the formation of a new $La_2Zr_2O_7$ phase, which is way less conducting than zirconia.[35,36] The main disadvantage with LSM use as cathode in SOFCs is though the low oxide ion conductivity (10^{-6} S/cm at 800°C[10]), that is considered the principal factor in the high polarization losses of LSM for the oxygen reduction.[29] The use of composite cathodes, where YSZ or other oxide electrolytes are added to LSM, has shown reduced electrode polarization resistance.[37,38]
Because of the low oxide ion conductivity, LSM is not the ideal canditate for low temperature applications. In this case, lanthanum nickelate perovskites $La_2NiO_{4+\delta}$ have been proposed, but their long-term stability under SOFC operating conditions is generally unproven.[29] Another possibility, already largely exploited, are the mixed ionic-electronic conductors of the $La_xSr_{1-x}Co_yFe_{1-y}O_{3-\delta}$ (LSCF) family, that have higher oxide ion conductivity and faster kinetics for the oxygen reduction reaction.[10] Finally, increment of the electrochemical activity for oxygen reduction was observed by Shao and Haile, by substituting lanthanium in the A-site of LSCF with barium to obtain $Ba_{0.5}Sr_{0.5}Co_{0.8}Fe_{0.2}O_3$ (BSCF). BSCF has very low polarization resistance and high power outputs resulting from the high rate of oxygen diffusion through the material.[39]

1.2.3.2 Anode Materials

The anode material must have high electronic conductivity ($>$ 100 S/cm), high stability in reducing environments and chemical stability toward all the possible fuels for SOFCs (hydrogen, natural gas, CO, methane, etc...), high catalytic activity toward the fuel oxidation reaction, chemical and mechanical (matching thermal expansion coefficients) compatibility with the electrolyte and the interconnects, and, finally, a sufficient porous structure to ensure the diffusion of the gaseous species through it.

The state-of-the-art material is a Ni-YSZ cermet, especially in H_2/H_2O atmosphere.[40] Ni was widely used in the early phases of SOFC development beause of its stability in the reducing conditions and for its high catalytic activity toward the oxidation of the fuel. However, it also possesses a higher thermal expansion coefficient (13.4$\times 10^{-6}$ K^{-1})[10] when compared to YSZ, shows coarsening of microstructure and no ionic conductivity. For these reasons it has been associated to YSZ, allowing to reduce the sintering of Ni metal and adjust the thermal expansion coefficient up to 11.6$\times 10^{-6}$ K^{-1} for a cermet with 30 vol% of Ni.[41] Moreover, mixing Ni with YSZ introduces oxide ion conductivity, provides better adhesion with the electrolyte, and determines the creation of additional reaction sites by extending the three-phase (electrode, electrolyte, gas) boundary where the oxidation reaction takes place.[42] One of the main drawbacks of the Ni-YSZ cermet is the possibility of Ni oxidation with NiO formation. The difference in the lattice structure of this phase can determine mechanical stability issues. This process can happen with thermal cycling or because of carbon deposition

or sulfur poisoning when fuels like methane are used.[43,44] In fact, Ni can catalyze methane reforming, so that it can be used to boost the internal reforming process in SOFCs that operate on methane/water. However, Ni can also catalyze formation of carbon from these fuels. A high steam-to-carbon ratio is thus necessary to reduce carbon deposition. High steam-to-carbon ratio means that the fuel is diluted, consequently reducing the electrical efficiency of the cell.

One possible alternative to reduce carbon deposition is the use of Co-YSZ cermet. Co has high stability in reducing atmosphere, high tolerance to sulfur, does not boost carbon formation from hydrocarbons, but its use implies higher costs. Like Co, also Cu is not an active catalyst for carbon formation and Cu-YSZ or Cu-CeO_2 cermets have also been studied. The use of CeO_2 increases the active catalytic sites for the fuel oxidation. Unfortunately, sintering of copper limits the pratical applications.[10,45]

Finally, oxide-based materials with perovskites structure, like $La_{0.75}Sr_{0.25}Cr_{0.5}Mn_{0.5}O_3$ (LSCM), have been extensively studied as promising alternative anodes for SOFCs.[29,46]

1.2.3.3 Electrolyte Materials

The electrolyte material in SOFCs is responsible for the transport of the oxide ions from the cathode to the anode. It should hence have high ionic conductivity ($>10^{-1}$ S/cm at the working temperature) and an ionic transferance number close to unity. Electronic conductivity should be low to avoid short-circuits. Since it is in contact with both electrodes, it should be chemically stable in both reducing (fuel side) and oxidising (air side) atmospheres, corresponding to a large range of oxygen partial pressure 10^{-20} $<p(O_2)<0.21$ atm. For the same reason, it should be chemically and thermally compatible with the electrode materials. Finally, it must have a dense gas-tight structure which, allowing to separate the gas at the anode and cathode sides, ensures the maximum electrochemical performance.[10,29]

The state-of-the-art electrolyte is YSZ. Yttrium oxide (Y_2O_3) is used to stabilize the cubic fluorite structure of zirconia (ZrO_2), that otherwise would not be stable at temperatures lower than 2376°C. Doping not only stabilizes zirconia, but improves its thermo-mechanical properties and determines the ionic conductivity because of the presence of oxygen vacancies in the doped material. 8-40 mol% Y_2O_3 is necessary to obtain the fully stabilized cubic structure (YSZ). The ionic conductivity, together with the number of vacancies, increases with the dopant concentration reaching a maximum at 8-11 mol% Y_2O_3 and then significantly decreases for higher dopant amount, probably because, at higher yttria content, vacancies are trapped in defect complexes. YSZ shows a conductivity of $>10^{-1}$ S/cm at 1000°C. It however rapidly decreases upon temperature reduction.[47,48] Aging can also lead to a decrease in conductivity. The main drawback of this electrolyte is maybe the possibility of reactivity with the cathode material that can be detrimental for the fuel cell performance. As already stated, LSM and YSZ react at high temperature with the formation of insulating phases like $La_2Zr_2O_7$. Also YSZ and LSCF react in a similar way, but at a lesser extent.[48] Despite the high temperatures necessary to obtain high conductivity and the reactivity issues at the cathode, YSZ is still difficult to substitute because of the chemical and mechanical stability at high temperature and in a large range of oxygen partial pressure.

1.2.3.4 Applications

SOFCs' high efficiency allow power systems based on this technology to be applied in many topics with different power range.

Small power SOFC systems (1-5kW) are widely used in residential applications to supply CHP and for remote distribute generation, as well as military applications. The electrical efficiency of the commercialized devices can go from 30 % and 60% with a total efficiency of over 90% in the case of the CHP units. Futhermore, SOFC devices in these power range are also extensively used in Auxiliary Power Units (APU) in trucks.[10,13]

Adobe Systems, Bank of America, Cox Enterprise, Coca Cola Company, eBay, FedEx, Google, Safeway, Staples, and Walmar are just some of the commercial customers of one of the most successful companies (Bloom energy) that uses SOFC technology in the field of large-scale power generation (>100kW).[10,13]

Finally, SOFC systems are more difficult to integrate in portable devices (from mW to few hundred of W), because of the longer start-up time and heavier weight compared to the PEMFC systems generally preferred for these applications. However, SOFC compared to PEMFC are way more fuel flexible and do not necessarily require hydrogen, consequently being very attractive also for portable devices. Some microtubular SOFC-based portable power units for leisure (off-grid power for camping, climbing, etc...), emergency, and military use or for use with electronic devices, like mobiles and laptops, have thus been recently successfully introduced by some american companies, such as Ultra Electronics AMI or Lilliputian Systems.[10]

1.2.4 The problem of lowering SOFC operating temperature

The lowering of the operation temperature is one of the main interest of the current research in the field of SOFCs. The target is obtaining reasonable power output and durability in the range of intermediate (IT, 600-800°C), and, more interestingly, of low (LT, 400-600°C) temperatures. By lowering the temperature, tremendous benefits can be obtained, such as use of cheap steel materials for the interconnects, easier and more reliable sealing, rapid start-up, improved durability, higher robustness, decrease in thermal stresses due to thermal mismatch of the different materials, and negligible electrode sintering. All these advantages contribute to SOFCs' cost lowering and easier maintenance, that are foundamental for their widespread commercialization, especially in the domain of portable applications. In the last years, some reviews have been devoted to IT- and LT-SOFCs materials, applications and perspectives.[13,15,49–51]

Unfortunately, lowering the operating temperature does not only imply positive effects, but it is also lined to the increase of the electrolyte resistivity and of the electrode polarization, determining a reduction of cell performances.

Concerning the electrodes, the problem is that the processes that take place at the anode and the cathode are thermally activated. Some materials for cathode in LT-SOFCs have been previously described in section 1.2.3.1. Tsipis et al.[52,53] have reviewed in detail the development and performances of SOFC anode materials.

In order to counteract, instead, the increase in the ohmic loss of the electrolyte, two strategies are mainly adopted. The first one is the use of thin films of the usual electrolytes, like

YSZ. The electrolyte resistance is indeed proportional to its thickness.[54,55] There are, however, certain theoretical and practical limitations when reducing the electrolyte thickness.[56] The second way requires the development of new electrolytes with higher ionic conductivity at lower temperatures. The strategies to enhance the ionic conductivities in oxide electrolytes have been reviewed by Hui et al.[57] For example, conductivity can be maximized through composition modification by selecting an appropriate dopant and its optimal concentration. The doping can be either homogeneous to form a solid solution or heterogeneous to form composites. A brief overview of some of the most studied electrolytes for these applications is presented in the following. Figure 1.6, instead, reports a comparison of the oxide ion conductivity of some of these materials.

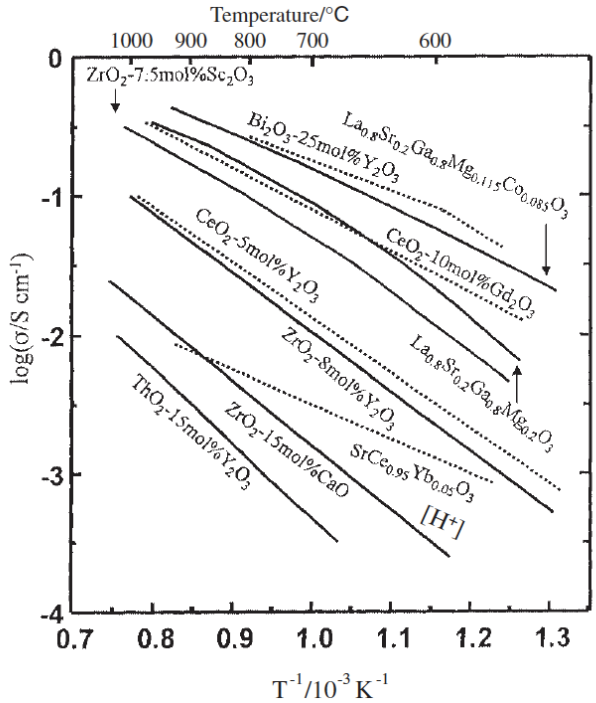

Figure 1.6: Oxide ion conductivity of selected electrolyte materials for SOFC application from[58]

Sc-stabilized zirconia (ScSZ) is an example of the first type of doping. It provides higher conductivities compared to YSZ, attributed to the smaller mismatch in size between Zr and Sc cations. In particular, its conductivity is enough to allow cell operation below 600°C. However, the costs and known aging of ScYZ present challenges for commercial SOFCs.[59,60]

Pure ceria (CeO_2) is not a good oxide ion conductor, but, as zirconia, it can be doped with aliovalent cations in order to increase the ionic conductivity. The highest conductivities are obtained for Gd- and Sm-doped ceria (GDC and SDC, respectively) with a doping concentration of 10-20 mol% Gd_2O_3/ Sm_2O_3. GDC ans SDC have higher conductivity, especially at lower temperatures, compared to YSZ. This makes them good candidates for SOFC operating at about 500-600°C as discussed by Steele.[56,61,62] These materials also have superior compatibility with the cathode materials, like LSM and LSCF, compared to YSZ. They are, in fact, used as interlayers between YSZ and the cathode to prevent the reaction.[10] The main

disadvantage for ceria is its instability in reducing conditions, where it can suffer of partial reduction of Ce^{4+} to Ce^{3+}, introducing electronic conductivity. This can cause internal short circuit current and generate expansion of the lattice that can lead to mechanical failure.[48,49]

Lanthanum strontium magnesium gallate (LSGM) materials are doped $LaGaO_3$ perovskites with good oxide ion conductivities even at lower temperatures (550-800°C). They have good compatibility with a variety of cathode materials and do not have reducible ions like ceria, being thus superior to GDC for use in reducing atmospheres. The main challenge with these electrolytes is the costs of Ga and the mechanical and chemical stability together with problem of volatilization.[10,48]

Doped $BaCO_3$ have also drawn special attention as electrolytes for LT-SOFC because of their high proton conductivity in the 300-1000°C temperature range, even if their chemical instability in atmosphere containing CO_2 and H_2O has limited their practical applications.[49]

Solid electrolytes with apatite structure, like $Ln_{20-x}Si_6O_26$ or $La_{9.33+x/3}Si_{6-x}Al_xO_{26}$ have also been studied since they are low-cost oxides possessing a significant level of oxide ion conductivity. Due to relatively poor sintering, different processing techniques and substantial anisotropy of ionic transport in the apatite lattice, the conductivity values reported in the literature vary broadly even for similar compositions, for example, from 8.4×10^{-5} to 4.3×10^{-3} S/cm at 773 K for $La_{10}Si_6O_{27}$ ceramics.[47]

Cubic δ-Bi_2O_3 has a conductivity that is 10-1000 times higher than that of YSZ, but it also shows various problems, like thermodynamical instability in reducing atmosphere and volatilization of the oxide at intermediate temperatures, that do not allow its direct uses in SOFCs.[63] Doping with V, Y, La, Er, Sr, W, for instance, has provided stabilization of the oxide. In particular, $Bi_2V_{0.9}Cu_{0.1}O_{5.35}$, belonging to the so called BiMeVOx family of ionic conductors, has an ionic conductivity of 0.1 S/cm at 600°C.[50,64]

However, none of these materials, all based on homogeneous doping, reach the critical value of 0.1 S/cm in the target range of LT-SOFCs. In their work on enhancing the ionic conductivities in oxide electrolytes, Hui et al.[57] concluded that there was still absence of well qualified (phase stability and high ionic conductivity) single-phase electrolyte material at low temperature. Therefore, in the same work, they suggested heterogeneous doping with the formation of two-phases composite materials to improve ionic conductivity of single-phase materials. In particular, in the last decade, carbonate-oxide composite materials have showed promising conductivity values at low temperatures (close to 0.1 S/cm in the LT range).[18–22] Since this work is entirely devoted to the study of the conduction properties and mechanisms of these materials, a more detailed bibliographic report of these composites will be presented in section 1.3.

1.2.5 MCFCs and SOFCs

Because the carbonate-oxide composite materials, to which this work is devoted, combine the characteristics of MCFC and SOFC electrolytes, before closing the section on fuel cells, we present a brief overview of MCFC technologies and a simple comparison between MCFCs and SOFCs.

A MCFC is characterized by the use of molten eutectic mixtures of alkali carbonates as the electrolyte. To keep the carbonates in the liquid state, the cell must operate at high

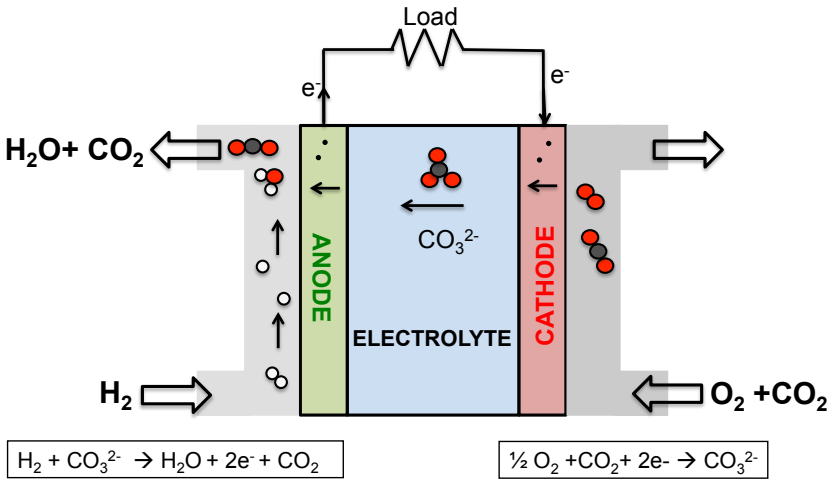

Figure 1.7: Schematic representation of MCFC operating principle.

temperatures of about 650°C. Figure 1.7 schematically shows the operating principles of a MCFC: O_2/CO_2 is fed at the cathode, where reduction takes place leading to carbonate ions (CO_3^{2-}) formation. These ions migrate through the molten carbonate electrolyte, reaching the anode which is fed with the fuel. Here, the fuel is oxidized with formation of water and carbon dioxide. CO_2 formed at the anode can be recycled and consumed at the cathode. The two-electrode reactions and the overall process are described by equations 1.4-1.7.

$$CO_3^{2-} \longrightarrow CO_2 + O^{2-} \tag{1.4}$$

$$\frac{1}{2}O_2 + CO_2 + 2e^- \longrightarrow CO_3^{2-} \tag{1.5}$$

$$H_2 + CO_3^{2-} \longrightarrow H_2O + CO_2 + 2e^- \tag{1.6}$$

$$H_2 + \frac{1}{2}O_2 + CO_2 \longrightarrow H_2O + CO_2 \tag{1.7}$$

As already mentioned, the electrolyte is an eutectic mixture of lithium and potassium ($Li_{0.62}K_{0.38}CO_3$) or lithium and sodium ($Li_{0.52}K_{0.48}CO_3$) carbonates. Li-Na mixtures offer higher ionic conductivity and possibly higher cell performances. Moreover, they also posses lower oxoacidity and lower effective volatility compared to Li-K ones.[65] The carbonate mixture is supported by a porous ceramic matrix. The porosity of the matrix should be enough for its impregnation by the electrolyte, but its should also guarantee the separation of the

fuel and oxidant in the two electrode compartments. The matrix should also be stable in the reducing and oxidasing atmosphere and it should be resistent to the carbonate corrosion. The most used matrix material is a lithium aluminate ($LiAlO_2$) powder.[66]

The most used material for the cathode of MCFCs is NiO. NiO is a p-type semiconductor, in whose lattice alkali cations provided by the electrolyte can be incorporated. The incorporation of these species, lithium in particular, determines the creation of positive holes in the NiO crystal structure enhancing the conductivity. The main drawback associated to the material is NiO dissolution in the electrolyte, leading to the loss of cathode surface area for the oxygen reaction reduction and to possible short circuit. In order to reduce this issue, adjustments of the carbonate acidity (by addition of alkaline earth metal oxides or Ba or Sr carbonates to the elecrolyte) and the use of other cathode materials like $LiCoO_2$ have been proposed. $LiCoO_2$ has higher stability and lower solubility in the carbonate electrolyte, but also higher costs and lower electrical conductivity.[29,65]

Finally, Ni-Cr or Ni-Al alloys are used at the anode. Cr or Al are added to reduce the problem of shrinking and creeping of porous Ni during MCFC operation. However, Cr has the tendency to consume through lithiation by the carbonate, while Ni-Al showed excellent chemical and mechanical stability in a 18000 h field operation.[29,66]

What differenciates SOFCs and MCFCs from the other fuel cell types is their high operating temperature. As previously mentioned, MCFCs' standard operation temperature is about 650°C, while SOFCs work in a larger temperature range between 600-1000°C, depending on the selected electrolyte. Moreover, contrarily to the other fuel cells, SOFCs included, MCFCs require supply of CO_2 at the cathode and are generally equipped with a CO_2 transfer device to recycle the anodic gas to the cathode.

Compared to the other FC types, SOFCs in particular, MCFCs have the steepest polarization curve resulting in the lowest current densities at high power range and high efficiency in the limited range of low current (up to $\sim$ 150 mA/cm^2). Moreover, among hydrogen-oxide fuel cells, they show one of the thickest electrodes-electrolyte assembly (1-3 mm) and the thickest electrolyte to reduce NiO dissolution (0.5-1.5 mm).[67] Performance improvement in MCFCs can be obtained by reducing cathode polarization. In PAFC, PEMFC, and SOFC, the effectiveness of the cathode operation is improved by special techniques of electrode fabrication that are useless in the corrosive environment of the carbonate electrolyte.[67]
MCFC lifespan-limiting phenomena are caused by the corrosive and evaporative electrolyte, the relatively high operating temperatures, and stack pressure. These phenomena include dissolution of the NiO cathode, high-temperature creep and sintering of the porous components, reforming catalyst deactivation, electrolyte losses and electrolyte retention capacity, corrosion of the separator plate, and matrix cracking.[68] Another difficulty of molten carbonates is the lithium alluminate matrix used, which is responsible of about 70% of the ohmic drop in the cell. The nature of the electrolyte consequently creates the main differences with respect to SOFCs. In SOFC technology, the fact that all components, including the electrolyte, are in the solid state can help in prolonging the lifetime and in making industrialization easier compared to MCFC with liquid electrolytes.

However, MCFCs have also some clear advantages compared to SOFCs: (i) their operating temperature is optimal for internal reforming and exploiting of usable heat, while in

SOFC it is generally too high to use cheap, steel elements; (ii) MCFC technology is more established than SOFC, especially for SOFC working in the intermediate or lower temperature range, and (iii) because of the liquid electrolyte, low contact resistance and gas seal are more easily achieved in MCFC than SOFC.[67]

Concerning MCFCs and SOFCs commonalities, it should be mentioned that the high temperatures, common to both fuel cell types, allow to efficiently use the heat produced in the conversion process in heat generations systems, thus improving the overall efficiency of the devices. More importantly, high temperatures make these fuel cells independent of a pure hydrogen infrastructure, since they enable the possibility of hydrocarbon reforming taking place directly inside the cell, since the heat released by the electrochemical oxidation of the fuel can be used for the reforming reaction. Similarities between MCFCs and SOFCs consequently exist, especially on the anode side, where the fuel oxidation takes place with Ni-based catalysts in both cases. Therefore, MCFCs and SOFCs share the same challenges related to the internal reforming process of hydrocarbon fuels at the anodic compartments. Poisoning of the anode because of sulfur contaminants present in the fuel (summed to chemical reactivity of these impurities with the carbonate electrolyte in the case of MCFCs) and carbon deposition issues are common in both applications. Facing these problems can consequently constitute an opportunity for integrated research.[66]
Finally, among the similarities, it must be also considered the fact that both technologies can be applied for carbon dioxide separation from conventional power plant exhaust gasses, which is beneficial in the perspective of exploiting coal as fossil fuel.[67]

1.3 Composite Materials

Composite materials are heterogenous mixtures of two or more phases. Heterogeneous doping requires mixing of phases with limited solubility and determines the creation of interfaces with peculiar properties that are believed to be essential to explain the characteristic features of the final materials. The effect of the heterogenous doping strongly depends on the chemical nature of the components, but also on the morphology of the system. The possibility to optimize the composite properties by varying the type and concentration of the heterogeneous dopant makes this kind of materials extremely interesting for electrochemical applications.[69–71] Composite electrolytes, in particular, are systems consisting of two or more phases mixing different ionic conductivity properties. They generally show enhanced electrochemical features (high conductivity, high transference number, high diffusivity, etc...), that could also be accompanied by improved mechanical properties, such as better shock resistance or higher mechanical strength.[69–71]

Conductivity enhancement in composites was known since the beginning of the early 20th century, when reported by Jander in 1929.[72] However, the interest in this kind of materials started to grow only after the study of Liang in 1973,[73] reporting an increase of the ionic conductivity by a factor 50 with the incorporation of alumina in LiI. Since Liang's work, a large number of composite ionic conductors have been investigated. Agrawal and Gupta[70] have provided an extensive list of the composite electrolyte systems reported in literature.

Composites are generally prepared by milling dry powders pelletised by appliyng a pres-

sure of several kbar. In many works, the pellets are heated, cooled and regrounded before the final pelletizing to ensure a better mixing of the components. X-ray diffraction is the most used structural characterization technique, while scanning electron microscopy is used to observe morphology. Electrochemical impedance spectroscopy (EIS) is by far the most important electrochemical characterization technique, since it allows to separate the contributions of bulk and blocking components (grain boundaries, insulating phases, etc...). Sometimes, ion mobilities are studied through NMR spectroscopy, such as for Li ion conductors considering the high resolution of ^{7}Li-NMR. Differential thermal analysis and calorimetry are also frequently applied to check for the eventual formation of new phases as well as modifications of phase transition temperatures.[71]

1.3.1 Space Charge Layer Theory

The theory of ionic conductor composites explaining the reasons for the conductivity enhancement is rooted in the early works of Gouy,[74] who established the theory of the electrical double layer at the electrode-electrolyte interface in 1903, and of Lehovec, who calculated in 1953 the defect distribution at the surface of ionic crystals and introduced the "*space-charge layer*" theory, based on the idea that the difference between the concentration of lattice defects near the surface and that in the bulk of ionic crystals led to an electrostatic potential between the bulk and the "surface zone" which influences the transport of the ions at the surface.[73] In 1963, Kliewer and Koehler[75] further developed the space charge model in ionic crystals. On these bases, in 1972, Wagner explained the electrical conductivity of semiconductors including another phase using this "*space-charge layer*" concept.[76] Few years later, in 1979, Jow and Wagner[77], in their study on the effect of dispersed alumina particles on the electrical conductivity of cuprous chloride, attempted for the first time to formally introduce the "*space-charge model*" of composite materials. Finally, between the '80s and the early '90s, Maier established the "*space-charge layer*" theory of heterogeneous ionic conductors, giving a quantitative treatment of two-phases systems, made by an ionic conductor and insulator or by two ionic conductors.[78–84] The theoretical concepts on conduction in ionic conductor composites were reviewed by Knauth[71] in 2000 and more recently by Belousov.[85] In the following, we will briefly revise the most important concepts.

The first thing to bear in mind is that the effects responsible for the conductivity enhancement in composites are not simply additive, but rather synergistic, since the whole system is more than the sum of its parts. Interfaces between the two materials are believed to play a major role in the processes determining the improvement of the conductivity, the so called composite effect. First, interfaces themselves are disordered regions and, given their anisotropy, they can act as transport pathways or transport barriers and can affect the charge carrier distribution in the adjacent regions (space charge effect).[71] In fact, different conductivity effects may occur at the interfaces as a consequence of the interaction between the two materials: i) a proper interface mechanism characterized by a novel conductance path; ii) a space charge mechanism which should be mainly characterized by modified defect concentrations as a consequence of the interface interaction.[81] For example, impurities may diffuse from the interface and create mobile defects or act themselves as charge carrier (e.g. protons), dislocations can be formed to compensate lattice misfits, amorphous phases

can be formed at the interfaces or lattice deformations near the interface can enlarge the free volume. All these phenomena generally provide a new conduction mechanism in the zone adjacent to the phase boundary and, therefore, have an activation enthalpy different from the bulk value[69,71,81] and they reveal a very individual transport problem.[81] The space charge mechanism, instead, is of very general nature and is directly related to the thermodynamic describing the equilibrium of the interface interaction.

The space charge model takes an idealized view of interfaces and a major assumption is that the bulk structure is maintained up to the atomic layer in contact with the interface, but it is based on the idea that the mixture of two phases involves formation of defect concentration profiles in the proximity of the interfaces, the deviation from local electrical neutrality (space charges) are hence a consequence of point defect equilibrium at interfaces. The general principle at the base of the space charge theory is the possibility of influencing the defect chemistry in the boundary layers through surface reactions between the two phases. As a result of these reactions, ions can be indeed trapped at the interfaces. The driving force for trapping is the chemical affinity of the second phase for the mobile ions. According to the principle of global electrical neutrality, in order to compensate the accumulation of electronic or ionic charge at the phase boundaries, the formation of space charge regions near the interfaces, where the counter species of the defects are consequently accumulated, should be induced. For example, for a Frenkel-disordered ionic crystal M^+X^-, this process can be written as

$$M_M + V_S \longrightarrow M_S^{\bullet} + V_M^{'} \tag{1.8}$$

whereV_S and $M_S^{\bullet}$ are respectively an empty interface site and metal ion trapped at the interface site. Metal ions are sucked out of the volume of the MX phase and trapped at the interface, while vacancy concentration in the adjacent space charge layer will increase. Space charge effects are pronounced at reduced temperature, due to the low bulk defect concentrations. If the majority charge carriers are accumulated in the space charge regions, a considerable conductivity enhancement may result.

Apart from the space charge layer theory, other models were proposed to explain the enhancement of the ionic conductivity of composites. The percolative model, for example, can be considered complementary to the space charge one. The percolation concept is based on a random distribution between two phases assuming also no interaction between phases and constant grain size.[71,85] Jiang and Wagner[86] suggested a model in which the composite effect was explained in terms of the formation of an amorphous phase at the interface, while Belousov proposed a model in which the conductivity increase is related to the formation of a highly conducting interfacial liquid phase.[85,87]

1.3.2 Carbonate/oxide electrolytes

In 1994, Zhu and Mellander[88] reported for the first time the high ionic conductivity in the composite materials containing one molten phase. After this publication, a series of materials containing one oxide phase, mainly doped CeO_2 oxides like SDC or GDC, mixed

with chlorides, fluorides, sulphates, hydroxides and carbonates have been widely investigated.[89–91] Among them, ceria-carbonates were found to be the most promising ones with high ionic conductivity and excellent fuel cell performances.[18] Conductivities of the order 0.1-1.0 Scm^{-1} were achieved at 400-600°C together with electrochemical power output higher than 800 $mWcm^{-2}$ at 600°C for hydrogen fuel cells.[92] These conductivity values are 10000 higher than those of YSZ and 10-100 higher than that of GDC in the same temperature range (see figure 1.8). After the first work introducing these materials by Zhu[18], more than 100 papers have been published on this subject. The most important features and the performances of these materials have been reviewed in some papers, where detailed information can be found.[51,89,92–96]

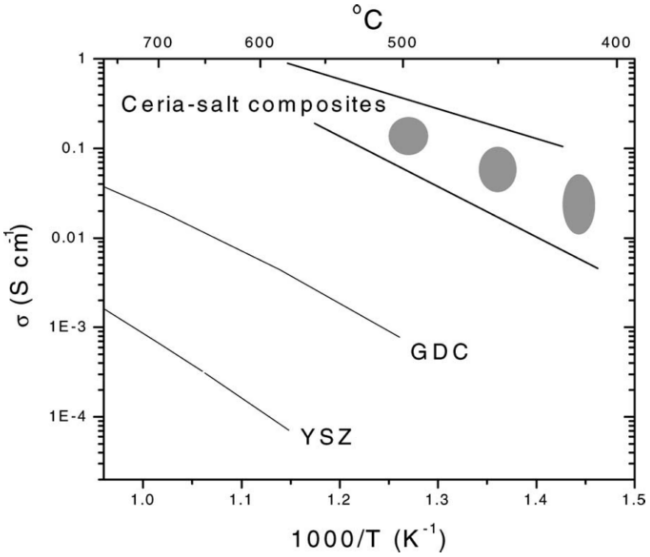

Figure 1.8: Temperature dependence of the conductivity of various ceria-salt composites compared to the conventional SOFC electrolytes, like YSZ and GDC.[18]

These carbonate-oxide composites are multi-phase materials, where the carbonate salt is supported on the solid oxide phase. The two phases are not a simple mixture, since there are some physical interactions between them, but no other compound is to be formed. The conductivity is not limited by the structure, but it is believed to be greatly influenced by composite effects: the oxide provides the conducting path for the oxide ions, while the presence of the carbonate can cause extremely high conductivity due to interfacial effects, without weakening the mechanical strength. On the contrary, the chemical stability and strong mechanical strength of the oxide can benefit the whole system and provide advantages in less corrosion compared to the pure molten carbonate phase. Moreover, a suppression of the electronic conductivity that arises in doped-ceria oxides in anode environment is observed in the composites because of the presence of the carbonate phase. Finally, as we will see in the following, these composites are believed to integrate multi-ion conduction in one system, forming hybrid conductors.[89,97]

The composition of these materials is a mixture of those used in SOFCs and MCFCs, combining the advantages of the two technologies in a new hybrid material. Concerning the

M_2CO_3 (mol %)			Melting temperature	Ref.
Li	Na	K	(°C)	
100			730	[101]
	100		901	[101]
		100	858	[101]
52	48		501	[102]
62		38	488	[102]
42.8		57.2	499	[102]

Table 1.2: Melting points of lithium, sodium, and potassium carbonates and of their eutectic mixtures.

oxide phase, cubic fluorite oxides such as YSZ and doped ceria are still the state-of-the-art material for SOFC. YSZ reaches a conductivity of 0.1 Scm^{-1} at 1000°C, while for doped CeO_2 it varies between 0.01 and 0.10 Scm^{-1} in the temperature range of 500-700 °C, but these oxides can suffer from the reduction of Ce^{4+} to Ce^{4+} under slightly reducing conditions. The majority of the studies in literature reports the use of ceria-based oxides, mainly SDC and GDC for these applications. Only few studies have been devoted to the study of composites with other oxide matrices such as yttria-doped tetragonal zirconia (TPZ),[98] the classical matrix support for molten carbonates in MCFCs $LiAlO_2$,[94] Al_2O_3,[98] and some rare earth-sesquioxides[99] like Y_2O_3, La_2O_3, Gd_2O_3, Yb_2O_3. However, they were not found to be superior to GDC or SDC more commonly used. More studies on the effect of the oxide phase would however help in rationalizing the properties of the composites, maybe allowing at the same time to find new potential candidates for LT-SOFC applications.

As regards the carbonate phase, alkaline carbonates Li_2CO_3, Na_2CO_3 , and K_2CO_3 either separately or as eutectic mixtures are the most widely used carbonates salts in these composites. As reported in table 1.2, single alkali carbonates have melting points of 730, 901, and 858°C respectively for Li_2CO_3, Na_2CO_3, and K_2CO_3. Eutectic mixtures have the advantage of reduced melting temperatures and for this reason are used as MCFC electrolytes. There are two different eutectic compositions for $(Li,K)_2CO_3$ mixtures (62-38 mol% and 42.8-57.2 mol%), but just one for $(Li,Na)_2CO_3$ (52-48 mol%), with melting points of 488, 499, and 501°C, respectively, reported in table 1.2. Tanase et al.[100] showed that the conductivity in the molten state greatly depends on the nature of the alkali cation, with $\sigma_{Li_2CO_3} > \sigma_{Na_2CO_3} > \sigma_{K_2CO_3}$. Consequently, the Li-Na mixture is a better conductor than the Li-K ones and the conductivity of the latter increases with Li amount. For example, conductivity-related activation energy of Li-K mixture with 80-20 mol% composition is lower than that of 62-38 mol% mixture, being 0.16 and 0.26 eV at 900°C, respectively. Moreover, Li-Na eutectics have been suggested to be less corrosive for the electrodes.[94]

XRD patterns of carbonate-oxide composites are dominated by the high intensity oxide peaks, indicating that the oxide maintains its crystalline structure, while the carbonate is mostly in the amorphous form after the grinding and the heat treatment.[49,103] Small contributions of the crystalline carbonates have also been observed.[19,98,99] High resolution transmission electron microscopy (HRTEM)[104,105] and scanning electron microscopy (SEM)[19,98,106,107] images confirmed this feature, showing an homogeneous distribution of both phases with a

core structure constituted by the crystalline oxide surrounded by an amorphous carbonate shell, as can be seen in figure 1.9. At the oxide-carbonate interfaces additional lattice defects or distortion are observed, with cations of the carbonates showing preferential location close to the oxide interface. It is worth noting that in most of the these works, the particle size of the oxide-carbonate composites was found to be in the submicron range and often less than 100 nm.[96] Finally, few infra-red (IR) and Raman spectroscopy studies[49,99] of oxide-carbonate composites can be found in literature, confirming the absence of any newly formed species and reporting peaks that have been attributed to the presence of bidentate carbonate on the surface of the oxide.

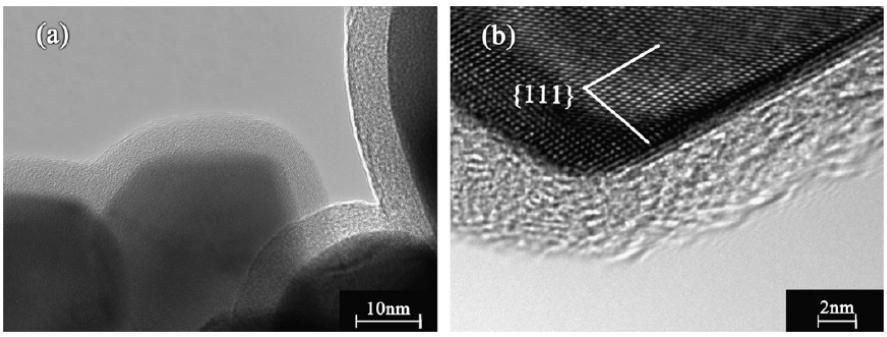

Figure 1.9: (a) TEM image and (b) HRTEM image of a SDC-carbonate composite.[104]

1.3.2.1 Electrochemical Properties

Figure 1.10 reports a schematization of a typical Arrhenius plot of a composite. The key electrochemical feature of carbonate-oxide composites is the elongated Z-shape of this plot, characterized by a sharp-step like increase in electrical conductivity generally observed when approaching the melting temperature of the carbonate phase, firstly reported by Schober.[108] Before and after the temperature at which the discontinuity appears, the Arrhenius plot fits closely to straight lines corresponding to thermally activated process. This result can be explained applying the percolation theory: ionic conduction is dominated by the oxide phase when the composite is all in solid state or by the molten carbonate phase when it is in its solid-liquid state.[109] The activation energies obtained for the low temperature part of the plot are generally found to be slightly higher than the ones of the pure oxide[19] because the oxide ion mobility is partially blocked by solid carbonates. At high temperatures, the activation energies are close but sligthly smaller to the ones of the pure carbonates, again because of the presence of the solid oxide phase partially inhibiting conduction in the carbonate phase. The temperature at which the discontinuity appears is generally 25-50°C below the melting temperature of the carbonate phase.[103] It has been interpreted as a superionic phase transition determined by the interfaces, where, as previously discussed, defects concentration is much higher than in the bulk and can be activated at temperatures lower than the eutectic melting point.[95,108] According to Maier's theory, there could be the formation of a space-charge layer at the interface and when the melting of the carbonate starts in sublattice level at certain temperature caused by the interfacial interaction, the mobility of the defects in

these regions increases greatly leading to enhanced conductivity.[49] The composite system conductivity should thus strongly depends on the coupling between phases. The superionic transition point is considered to be function of the composite composition, in particular of carbonate content, and of the operating conditions, such as temperature raising rate and applied atmosphere.[93,94]

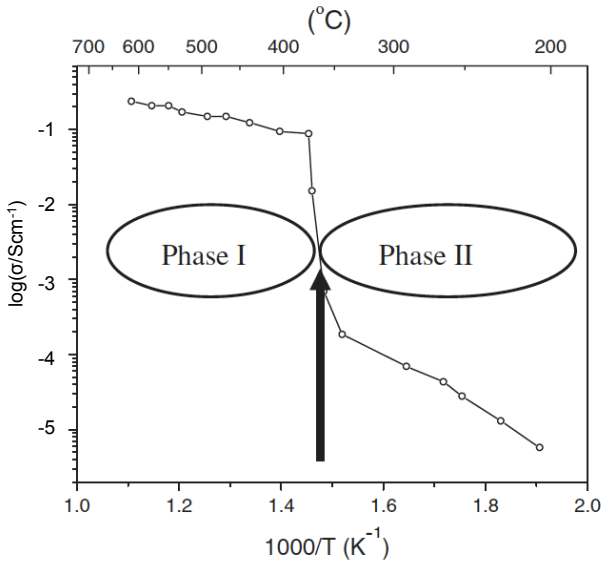

Figure 1.10: Schematic Arrhenius plot for a carbonate-oxide composite material. Adapted from[95]

Table 1.3 reports the conductivities and the fuel cell power density measured for selected carbonate-oxide composite electrolytes in different groups. More comprehensive tables can be found in ref[92,93,96]. Performances of composites show discrepancies from different groups. Naturally, it is necessary to take into account that the composite performances are influenced by the composite composition, microstructure, working atmosphere and so on. Often the thickness of the electrolyte is not mentioned and the effect of different gas atmosphere, electrodes, and preparation methods make the comparison of the composite problematic. However, we must notice that generally electrochemical performances higher than that of SOFC with much thinner doped-ceria electrolytes or MCFC with conventional carbonates mixtures are obtained. In particular, power densities of 1Wcm^{-2} or higher were recorded at temperatures around 600°C: for example, SDC-(Li,Na)$_2$CO$_3$ reached a power density of 1085 mWcm^{-2} using hydrogen as fuel and air as oxidant. Higher performance of 1200 mWcm^{-2} is also achieved when air is replaced with O_2/CO_2 at 600°C.[110]
As regards conductivity, it can be pointed out that the highest conductivity at 650°C of 1.1 Scm^{-1} has been measured for a sample of SDC with the (Li,Na)$_2$CO$_3$ eutectic and a weight ratio of 50:50. It is the only LT-SOFC electrolyte having a conductivity higher than 1 Scm^{-1} at this temperature.[112]
The conductivity of the composite generally increases with carbonate content at high temperature, while the opposite occurs at low temperature.[19] Li et al.[116] found that there is however an optimum value of 80:20 (oxide:carbonate) with higher carbonate content leading to de-

Electrolyte	Gases	Conductivity	T	Power Density	T	Ref.
		S/cm	°C	$mWcm^{-2}$	°C	
SDC-Na_2CO_3	Air	0.1	300	1000	450	[21,104]
SDC-$(Li,Na)_2CO_3$ (80:20 wt%)	Air	0.1	625	1085	600	[111]
SDC-$(Li,Na)_2CO_3$ (80:20 wt%)	H_2	-	-	1200	600	[110]
SDC-$(Li,Na)_2CO_3$ (50:50 wt%)	-	1.1	650	-	-	[112]
SDC-$(Li,Na)_2CO_3$ (50:50 wt%)	-	1.1	650	-	-	[112]
SDC-$(Li,K)_2CO_3$ (80:20 wt%)	Air	0.17	600	410	600	[113]
SDC-$(Li,K)_2CO_3$ (80:20 wt%)	Air	0.17	600	410	600	[113]
TPZ-$(Li,Na)_2CO_3$ (50:50 vol)	Air	0.02	625	-	-	[98]
Al_2O_3-$(Li,K)_2CO_3$ (80:20 wt%)	Air	4.3e-8	625	-	-	[98]
$Ce_{0.8}Gd_{0.05}Y_{0.15}O_{1.9}$	Air	-	-	155	600	[114]
$LiAlO_2$-$(Li,K)_2CO_3$	O_2/CO_2	-	-	159	600	[115]

Table 1.3: Performances of fuel cells based on carbonate-oxide composites together woth the electrolyte conductivity.

crease in conductivity in all temperature range. In any case, the conductivity of the composite was found to be higher that that of the pure oxide even at low temperatures.[110,113,117] However, it should be mentioned that no real consensus has been found on how the ratio between oxide and carbonate affects the melting point of the composite.[19,111,118] The effect of having different carbonate mixtures has been analysed by Benamira et al.[19] and Di et al.[113] and GDC and SDC composites with Li-Na carbonate mixtures always showed the highest conductivities when compared to Li-K or Na-K ones. Concerning the oxides, the highest conductivities were obtained with CeO_2 oxides with respect to TZP or Al-based oxides. Also the size of the oxide particles can influence the conductivity: the smaller the size the higher the surface to volume ratio and the interface properties become more pronounced. Recent works have reported higher conductivities and lower transition temperatures with reducing the grain size.[93]

Carbonate-oxide composites are believed to be multi-ion conductors, depending on the working atmosphere. The conductivity of the oxide ions in the oxide phase does not seem to be largely affected by the atmosphere, at least if no reducing atmosphere (e.g. hydrogen) is used. In hydrogen atmosphere an increase in the conductivity of ceria-based composites and a reduction of the transition temperature is observed[22,96] It was suggested that the composites are also proton conductors because of the observation of water in both gas outlets.[51] Different possible mechanisms for proton conduction have been proposed, including also a combined hybrid H^+/O^{2-} conduction path at the interfaces. More detailed explanations will be provided in section 1.3.3. However, it should be pointed out that there are many contradictory results regarding the contribution of each charge carrier to the overall conduction: it was considered in some earlier reports that oxide ion conduction is predominant over the proton conduction;[119,120] Huang claimed, instead, that SDC carbonate composites are mainly proton conductors by the evidence that almost all water was observed at the cathode side during fuel cell operation.[121] More recently, Di[122] found that the electrolyte is a co-ionic conductor which oxide ion conductivity dominates, while Wang[20] observed that in composites the proton conductivity is 1-2 orders of magnitude higher than oxide ion in the 200-600°C range.

A fuel cell based on oxide-carbonate electrolytes can operate in the same manner as SOFCs or also MCFCs, without additional modifications in system designs and configurations. In MCFC environments, CO_2 is present in the cathode gas. Li's group[110,123–125] found that when CO_2/O_2 is used as oxidant the fuel cell had a much higher power density than when O_2/N_2 gas mixture was used. CO_2 was detected in the anode outlet gas, and water in the outlet gas of both sides. According to the authors, this means that carbonate ion (CO_3^{2-}) conduction from cathode to anode happened and that the material could conduct proton, oxygen and carbonate ions simultaneously. While carbonate ions are blocked when only oxygen is fed at the cathode, in O_2/CO_2 atmospheres carbonate ion (CO_3^{2-}) conduction can indeed take place in the bulk carbonate phase as in a conventional MCFC.

Even if the hybrid H^+/O_2 or $H^+/O_2/CO_3^{2-}$ conduction is well recognized, it is important to remind that the origin of the protonic conduction is still under debate. Nafe[126] observed the only experimental evidence for proton conduction is the occasional, (*i.e.* not reproducible) presence of water in the cathode compartment if the composite is employed under fuel cell conditions and is exposed to hydrogen as fuel and oxygen as oxidant. However, he underlined that oxide will probably not be completely densified considering that the highest temperature the composite material undergoes does not exceed 700°C. As a consequence, due to reduced gas tightness, hydrogen can easily diffuse as neutral molecule from anode to cathode, where it reacts with oxygen to form water. Hence the presence of water would not be related to proton conduction, but to leakage issues. Moreover, the possibility of proton being transported by forming bicarbonate ions (HCO_3^-), that was one of Zhu's proposition for the proton conduction mechanism, is not widely accepted, since there is not such evidence for molten carbonate fuel cells which have more probability to form bicarbonates.[94] Benamira et al.[22] proposed also that the enhancement of the reduction of the transition temperatures in reducing atmosphere is to be ascribed, instead, to the modifcation of the molten phase in a mixture of carbonates and hydroxides which have a lower melting point compared to the carbonates. In their review, also Fan et al.[93], raised several question on proton conduction: how is the extrinsic nature of the proton transport in the composite[127]? It is obviously different situation for protons which do not exists originally in the material compared to intrinsic species like oxygen or carbonate ions. Though the so-called proton conduction with the carbonate by the HCO_3^- intermediate is believed to dominate the whole conductivity, why do MCFCs with similar electrolyte show a much lower performance? How is the dual ionic transport process for the oxygen and proton in one composite materials? Will they meet and produce water inside the composite?

The above discussion underlines that there are still contradictory results, especially about the contributions of the different charge carriers, together with uncertainties on the conducting species and mechanisms. It is thus clear that considerable works are still needed in order to understand the oxide-carbonate composite for future material design for advanced fuel cell applications.

1.3.2.2 Stability of carbonate-oxide composites

The long term stability under operation conditions, in terms of stable ionic conductivity over time, thermal stability, chemical compatibility with the electrodes and long-term fuel

cell operation durability, is a key requirement for a promising electrolyte in order to meet demand for practical applications.

As regards the thermal stability, the main concerns are related to the volatilization or decomposition of the carbonate phase that might happen at operating temperature, resulting in deterioration of fuel cell output. Benamira et al.[19] investigated the thermal stability of the composites after thermal cycling and aging treatment of 168h, observing very low weight losses of both water and CO_2. This is in agreement with results of Ma et al.,[128] who observed that no weight loss happened from 400°C to 800°C under heating process suggesting that there is no volatilization or decomposition reaction in this temperature range, corresponding to the operating temperature range of LT- or HT-SOFCs.

Concerning the compatibility with the electrodes, here, we just recall that the main issues are related to the dissolution of the Ni from the cathode in the carbonate phase, leading to performance degradation. This problem will be adressed more in details in section 1.3.2.3.

In addition, the electrochemical stability against time has been investigated. Benamira et al.[22] measured the conductivity of GDC-carbonate composite over 6000h at 600°C. A high conductivity of about 0.1 S/cm almost stable during the long term stability test was obtained. Zhu et al.[129] studied the performances of SDC-20 wt% carbonates, observing an increase of the power density with working time up to 3 months, followed by a small reduction in the 4th one. Finally, Li and Sun[125] found that the output power density of the fuel cell was constant after operating for more than 200 h at 650°C under simulative MCFC gas atmosphere, where the presence of carbon dioxide at the cathode can help mantaining the stability of the carbonate phase.

The results obtained so far therefore confirm that these materials can be promising electrolytes for practical applcations, even if further investigations are still needed before any commercialization.

1.3.2.3 Electrode Materials

As previously stated, the lowering of the SOFC operating temperature has been limited not only by the reduction of the electrolyte conductivity, but also by the increase in the electrode polarization with temperature reduction. In particular, it was found that at a temperature of about 500 °C, the fuel cell resistance is significantly dominated by the cathode polarization resistance.[130] Despite a lot of work devoted to the study of composite carbonate-oxide materials with enhanced conductivity in the LT range, little attention has been paid to the development of electrode materials, especially cathode, with high catalytic activity at low temperatures which are also compatible with the corrosive carbonate phase of these electrolytes.[94] Recent progresses on anodes and cathodes for carbonate-oxide fuel cells have been reviewed by Fan et al.[93]

The state-of-the-art anode materials for carbonate-oxide composite electrolytes are still Ni-based cermets, since they ensure acceptable electrocatalytic activity toward hydrogen oxidation even at low temperatures.[131] Some efforts to increase Ni activity in the case of fuels like methanol, ethanol, biomass, and glycerol have also been made. Ni-based double- (Ni-Cu, Ni-Zn, Ni-Fe)[90,132,133] or tri- (Ni-Cu-Zn)[131] alloys with power density perfomances between 100 and 600 $mWcm^{-2}$ at 600°C have been proposed for this scope, together with

lithiated transition metal oxides, like LiNiO[134] or LiCuNiZnO,[135,136] with performances of 500-600 mWcm^{-2} at 550-570 °C.

Cathode materials present more serious problems since they are not only responsible of the major polarization losses, but also the lithiated NiO commonly used for carbonate-oxide composites suffers of NiO dissolution in the molten carbonates. LiNiO$_x$ guarantees a power density of 300-800 mWcm^{-2} between 300-800 °C,[18] but exhibits performance degradation in 2 h measurements.[137] Cathode materials for these electrolytes can be divided into three groups: i) noble metals, ii) mixed ionic/electronic perovskites, and iii) lithiated bi- or tri-phase transition metal oxides and their composites.[138]

Noble metals, such as Pt and Ag, are used since the beginning of the composite research, because of their electrocatalytic activity toward oxygen reduction, high electronic conductivity, and high oxygen dissolution and mobility.[49,94] Hu et al. reported a power density of 716 mWcm^{-2} at 590°C for an Ag electrode with ceria composites.[139] However, their use in practical applications is limited by their high costs.

Perovskite oxides are known to be good alternative for cathode in IT-SOFCs, because of their high mixed ionic and electronic conductivity and high catalytic activity for the ORR at these temperatures. BSCF and the less expensive $Ba_xCa_{1-x}Co_yFe_{1-y}O_{3-\delta}$ (BCCF)[140] perovskites have been recently proposed for FC based on composite electrolytes with good performances (326 mWcm^{-2} at 550°C). Pereira et al.[141] tested for the chemical compatibility and electrochemical performances of several provsite based-electrodes in systems based on composite Gd-doped ceria and alkaline carbonate electrolytes.

$LaCoO_3$ and $La_{0.8}Sr_{0.2}Co_{0.2}Fe_{0.8}O_{3-\delta}$ were identified as the most stable cathode materials. Also $Sm_{0.5}Sr_{0.5}Fe_{0.8}Cu_{0.2}O_{3-\delta}$ showed stable performances over 100h continuous/non-stop current density. These materials can be hence stable when coupled to composites electrolytes, but have power density performances that are much lower when compared to lithiated NiO cathodes.

Different lithiated transition metals (Ni, Cu, Zu, Fe, and Co) composite materials with promising catalytic activity for the ORR and chemical compatibility with the carbonate-oxide composites have been proposed by Zhu's group.[138,142,143] These materials show performances similar to the ones of lithiated NiO phases, furthermore the doping of the other oxide reduces the problem of NiO dissolution in the carbonate phase. They can be used as symmetrical electrode applications (both at the cathode and anode side). With these configurations, Jing et al.[144] reached a power density of 1000 mWcm^{-2} at 470°C with a Li-Ni-Cu-Zn oxide. Similar performances (1107 mWcm^{-2} at 500°C) were obtained by Raza et al.[145] with a Zn/NiO/SDC-Na_2CO_3 nanocomposite, used again in a symmetrical fuel cell.

1.3.3 Conduction Mechanisms in oxide-carbonate electrolytes

There is still not a rigorous explanation of the conductivity mechanisms in oxide-carbonate composite materials. Several assumptions have been proposed with time and will be briefly revised in this section.

It is well known that oxide ion conduction can take place in the oxide phase via an oxygen vacancy mechanism.[89] In his first work on carbonate-oxide materials, Bin Zhu[18] indeed suggested that oxide ions are conducted in the oxide phase, but he also suggested

proton conduction in the salt phase (see figure 1.11). However, he underlined that the detailed mechanism of oxide ion and proton conduction as well as the conduction enhancement were not still clear.

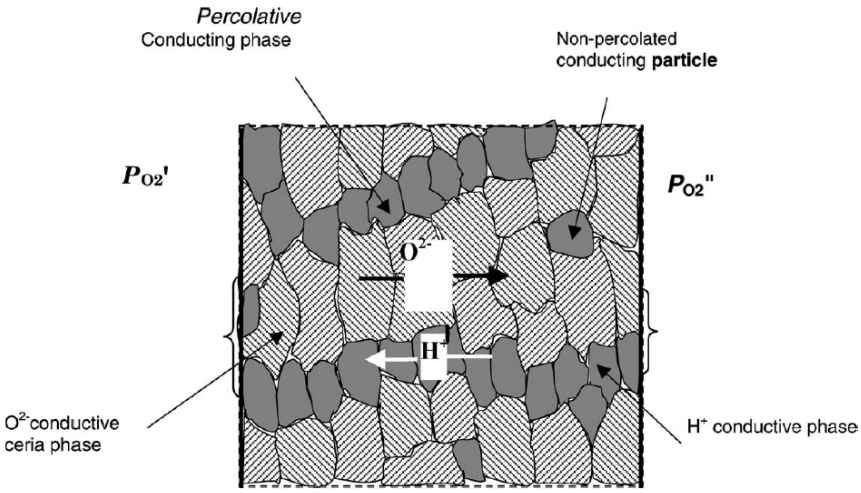

Figure 1.11: Two interpenetrated percolative phases with an oxide ion conducting oxide and a proton conducting carbonate salt according to Zhu et al.[18]

The most common explanation for the claimed superionic conductivity recurs to the Maier's "space charge" layer theory. The carbonate-oxide interface is mainly considered to be responsible of the enhanced electrochemical properties, because a space-charge layer can be formed at the phase boundaries due to the interfacial interaction: for example, oxide ions could accumulate at the interface, where there could also be an enrichment of the cations of the carbonate. The higher concentrations of the defects/ions near the phase boundaries compared with the bulk phase may essentially constitute 'superionic highways' at the boundary between the two phases.
In particular, Zhu et al.[95,146] suggested that there can be different negatively charged oxygen species (O_2^-, O^-, and O^{2-}) covering the surface of the oxide and that special attention should be paid to the interactions between the oxygen ions on the oxide particle and the cations M^+ (Li^+, Na^+, or K^+) of the carbonate phase that establish an electrical field in the interfaces between the two phases (see figure 1.12). They believed that this electric field distribution is a key to realize interfacial ionic conduction, especially oxide ions conduction, allowing ions to move at the interfaces by high conductivity pathways. Also Schober[108], applying the space charge layer theory, believed that the higher concentration of defects in the space charge regions adjacent to the phase boundaries compared to the bulk phases is the origin of the enhanced conduction.

A more systematic explanation of a suggested enhancement mechanism was proposed by Huang et al.[103] using defect chemistry. In this case, according to the authors, high oxide ion conductivity of the oxide can only be realized in the case of consecutive conducting paths formed in the bulk oxide phase and high mobility of oxygen vacancies at elevated temperature. However, in the presence of the carbonate phase, the oxide ion already conducting in the oxide phase via an oxygen vacancy mechanism, may also accumulate on the surface

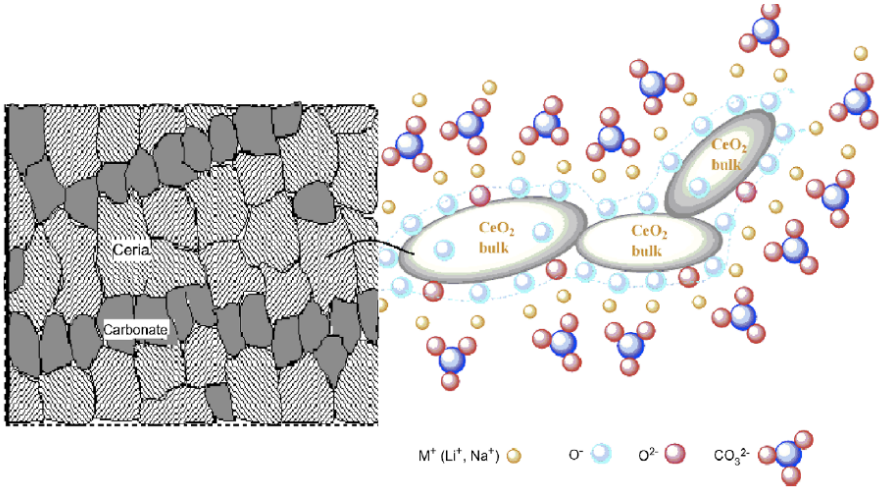

Figure 1.12: Interfacial conduction pathway according to the space charge layer theory according to Zhu et al.[146]

of the oxide particle, resulting in higher oxygen vacancy concentration in the bulk due to interfacial interaction:

$$O_O^X + V_S \longrightarrow V_O^{\bullet\bullet} + O_S^{''} \tag{1.9}$$

where the subscripts S and O indicate a surface and a regular O lattice site, respectively. Also for the carbonate phase (M_2CO_3, M=Li, K, or Na), there could be a surface reaction because of the interaction at the interface, where a space charge layer is formed increasing cation disorder: there is en enrichment of cations at the interface and a consequent increase in cation vacancies in the bulk carbonate phase which gives rise to enhanced conductivity in carbonate-oxide composites in an air atmosphere at temperature below the melting points of the carbonate phase:

$$M_M + V_A \longrightarrow M_A^{\bullet} + V_M^{'} \tag{1.10}$$

where the subscripts A and M indicate an interface and a regular cation lattice site, respectively. Huang et al. underlined also that these defect reactions can be applied to the solid carbonates, but also for carbonates in their molten phase, since, according to the quasi-lattice model, the melt locally maintains the ordered structure and only the distances between the constituent atoms and the cation-anion coordination number decrease.

Great emphasis has been also placed on the supposed multi-ionic nature of these materials[89,92–95]: the composite material is a multi-ion system made by both intrinsic (M^+, CO_3^{2-}, and O^{2-}) and extrinsic (H^+) species. The species involved in the transport vary depending on which fuel cell mode operated or which atmosphere is provided. The multi-ionic conduction can enhance transported ion concentrations/flows resulting in higher fuel cell current/output and may also improve the electrode dynamics/kinetics.[92] In particular, as already

stated, these materials were indeed claimed to be dual or hybrid H^+/O^{2-} or even ternary $H^+/O^{2-}/CO_3^{2-}$ conductors.

Concerning the mechanism for the H^+/O^{2-} binary conduction, the first explanation given by Zhu and Mellander[88] is based on oxide ion conduction in the oxide phase and proton conduction in the carbonate phase through temporal bonding H^+-CO_3^{2-} (HCO_3^-) mechanism. Later, Zhu and Mat[89] suggested that H^+ and O^{2-} transport can be influnced by the composite effect, which concerns ion conduction at interfaces: the interfaces can constitute conduction routes for the hybrid H^+/O^{2-} conduction; here a conduction chain H—O-H, H-O-H, and O-H—O atoms/ions can take place introducing an interfacial conducting path/mechanism that can play a key role in the large conductivity enhancement. (see figure 1.13).

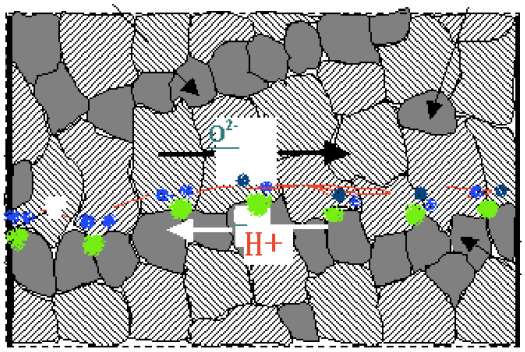

Figure 1.13: A schematic picture of the hybrid H^+/O^{2-} model proposed by Zhu[89] at the interface of the oxide-carbonate materials. Small blue dots represent H^+, while the larger green balls stand for O^{2-}.

Even if the nature of the proton conduction in these materials is still a subject of great debate, a lot of work has been devoted to the identification of proton conduction mechanism since it can be important for LT-SOFC because it can be thermally activated at low temperature much more easily than oxide ion conduction.
For example, Wang et al.[147] proposed an empirical 'Swing Model' to interpret the proton conduction in composites: as shown in figure 1.14, when a proton approaches the electrolyte from the anode it can form metastable hydrogen bonds with O from both the oxide phase or the carbonate anions. When the operating temperature is above the glass transition temperature of the amorphous carbonate phase, the bending and stretching vibrations of C-O bonds are enhanced as well as mobility and rotation of the CO_3^{2-} groups. These enhanced movements facilitate rapid breaking and forming of hydrogen bonds in the interface regions, leading to effective long range proton transport driven by the proton concentration gradient and with carbonate groups that serve as a bridge for the proton to move from one hydrogen bond to the other. The authors started from the premises that hydrogen bond is involved in almost all proton conduction processes and that long range proton transport requires a rapid bond breaking and forming process that can occur in metastable hydrogen-bonded systems. Moreover, they also believed that since the carbonate phase is not known to be a good proton conductor, there should be an important effect of the oxide-carbonate interface in determining a superior proton conduction.

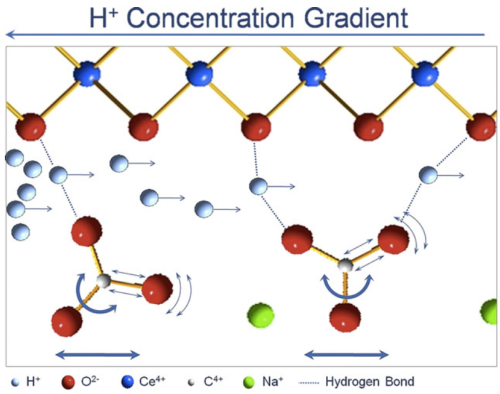

Figure 1.14: A schematic picture of the 'Swing Model' pathway for proton conduction in oxide-carbonate composite according to Wang et al.[147]

Huang et al.[103] used defect chemistry to explain also the proton conduction in composites in hydrogen fuel atmosphere. The proton conduction through temporal bonding of a proton to the carbonate claimed by Zhu[88] can be written as in the following equation:

$$H_i^{\cdot} + X_X^X \longrightarrow HX_X^{\cdot} \tag{1.11}$$

where X indicate a carbonate ion site in the carbonate lattice. However, they believed that at low temperature with low carbonate mobility, it is more reasonable that proton first formed on the surface of the oxygen site in the oxide lattice and then they become interstitial species in the interfacial regions, where they can transport through cation vacancies in the carbonate phase:

$$H_i^{\bullet} + V_M^{'} \longrightarrow H_M^X + V_i^{\cdot} \tag{1.12}$$

Moving to the ternary $H^+/O^{2-}/CO_3^{2-}$ conduction proposed when the composite electrolyte operates with CO_2/O_2 atmosphere at the cathode, Li's group[123,124,148] suggested a mechanism in which oxide ions conduct along the bulk of the oxide like in traditional SOFC electrolytes, proton can be adsorbed by CO_3^{2-} forming HCO_3^- that diffuses in the bulk carbnate phase or at the interface, while CO_3^{2-} transfers in the bulk carbonate phase as in MCFC as described in figure 1.15. When only oxygen is used as the oxidant, carbonate ions are immobile. However, in CO_2/O_2 atmosphere, they believed that the conduction of CO_3^{2-} can take place enhancing O^{2-} transport through O^{2-} exchange with the gas phase CO_2 at the exposed interfaces of the oxide and the molten carbonate phase.

Different possible conduction paths have thus be proposed, many of which underline the important role of the oxide-carbonate interfaces in the conductivity enhancement, however it is still difficult to fully understand the behaviour of this mixed electrolyte. A lot of question related to the multi-ionic conduction and in particular to the proton conduction and also to the role of the interfaces need to be answered. What is the real conduction mechanism and how does it work? A deeper understanding is necessary, but the composite nature of these

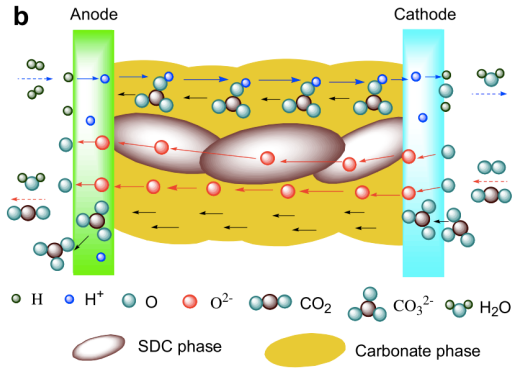

Figure 1.15: A schematic picture of the ternary $H^+/O^{2-}/CO_3^{2-}$ conduction mechanism when CO_2/O_2 is used as the oxidant gases, as proposed by Li's group.[148]

electrolyte constitutes itself a great challenge for their characterization. Zhao[51] and Zhu[149] observed that there is a lack of analytical tools which can investigate the interfacial effects directly. New effective methodologies are consequently urgent to be developed.

1.4 Research strategy: a combined experimental and theoretical approach

Carbonate-oxide composites are promising materials combining the electrolytes of SOFC and MCFC applications, with an enhanced conductivity of the order of 0.1 S/cm at 600°C over 6000h. They could consequently allow SOFC devices to work in the LT range with performances of the order of 1 Wcm^{-2} in terms of power density. Despite the large number of publications in the field of carbonate/oxide composite materials, a deeper understanding on the origins of their improved performances is still necessary. Which are the species that determine the transport in the device: is it the oxide ions, the cations of the salt, the carbonate ions, the protons or several species at the same time? Which are the related conduction mechanisms? Different assumptions have been formulated, but there is still not a rigorous explanation.

Unfortunately, the investigation of the phenomena determining the peculiar properties of these materials is not an easy task. We therefore propose a combined experimental and theoretical approach to study these materials. Experiment and theory can play complementary roles in determining the complex structure of the carbonate-oxide interface, in the characterization of the surface electrochemistry and of the electronic structure of the solid electrolyte, as well as in the understanding of the involved electrochemical processes. In particular, experiments cannot only provide information on the structural, morphological, thermal behavior of the composites, but studies by impedance spectroscopy can also help clarifying electrochemical properties of such new materials. Moreover, experimental measurements can be used to validate and/or calibrate the theoretical model. At the same time, calculations may help experimentalists rationalizing their results; they can be used to make predictions and to enhance our understanding of the electrochemical processes and mechanisms: while

there is a lack of analytical tools which can investigate the interfacial effects directly,[149] theoretical studies can provide a direct picture of the interfaces as well as information on the interfacial effects at the atomic level.

The synthesis protocol for the carbonate-oxide composites involves the preparation of the oxide and carbonate powders separately. The as-prepared carbonate and oxide phases are then mixed in the appropriate weight ratio and grounded, so that they are still in their solid forms. The material is then heated, determining the melting of the carbonate phase. Finally, the composite is quenched at room temperature and grounded (see figure 1.16). The material is then ready to be characterized and used as electrolyte.

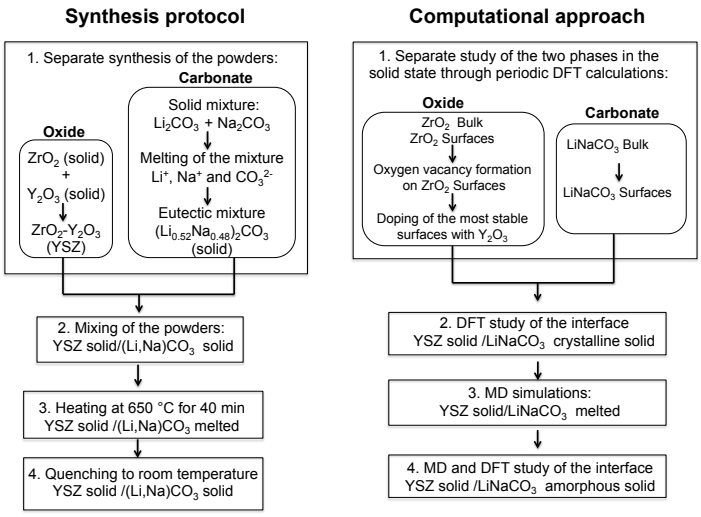

Figure 1.16: Comparison between the experimental protocol for the synthesis of carbonate/oxide composite electrolytes and the proposed computational DFT/MD approach for the modeling of the carbonate/oxide interface at the atomic scale.[150]

Also the proposed computational approach for the modeling of the composite involves the separate study of the oxide and carbonate materials as the first step. The knowledge of the structural and physical properties of each phase is fundamental to improve the understanding of each material and consequently of the processes in which it can be involved as a component of the composite electrolyte in fuel cells. Bulk structures, generally well characterized from the experimental point of view, can be studied through periodic Density Functional Theory (DFT) calculations and the obtained results allow us to select an accurate computational protocol that can then be used to study the surfaces of these materials, providing also information that can be difficult to obtain experimentally. The knowledge of the structural and electronic properties of the surfaces and so of the surface chemistry of the involved material is, indeed, crucial to the understanding of the composite electrolyte, where the phenomena at the interface between the oxide and the carbonate phases are considered to be at the origin of the enhanced conductivity of these materials. A first model of the composite material can thus be constituted by an interface obtained though the combination of the oxide and carbonate most stable surfaces, both in their crystalline state. This model would not simply be a first approximation of the real system, but it can also provide useful information, con-

sidering that the X-ray diffraction (XRD) of the carbonate-oxide composite material showed that small quantities of the carbonate in the crystal phase are present together with the main amorphous carbonate shell that covers the oxide particles [19,98]. Once a suitable starting model of the composite interface is obtained, through Molecular Dynamics (MD) calculations it is possible to melt the carbonate phase by heating the system and subsequently to obtain an amorphous carbonate layer by cooling it down. Hence, transport properties and the proposed conduction mechanisms could be further investigated through MD simulations, with support from the electronic properties that can be obtained through DFT calculations.
A very strict analogy can therefore be envisaged between the steps required by synthesis procedure and the computational approach proposed to simulate the composite material (see Figure 1.16). We believe that this correspondence and the interplay of the theoretical results (microscopic level) and the experimental data (macroscopic level) make the combined approach a very powerful tool for the investigation of the basic operating principles of intermediate-low solid oxide fuel cells with composite materials as electrolytes.

As far as we know, the combination of both approaches has never been reported in the literature for the study of such materials. Moreover, just few works have been dealing with modeling of the interface between an ionic salt and an oxide, including some papers on LiI-Al_2O_2 [151], CsCl-Al_2O_2 [152,153], and CaF_2-BaF_2 [154] composites. However, all these works, published in the early 2000s, rely just on MD simulations of the interface without insights from first principles methods. More recently, a DFT investigation on the proton conductivity in $BaZrYO_3$-carbonate materials appeared in literature. [155] The interface between the two phases has however been created considering simply the adsorption of one carbonate group on the oxide surface.

The work presented in this manuscript is organized in seven chapters.

Chapter 2 presents a brief overview of the fundamentals of the experimental techniques applied and of the theoretical aspects of the computational methods used to study the composites materials. In particular, the basics of electrochemical impedance spectroscopy (EIS), of the density functional theory (DFT) and of molecular dynamics (MD) are revised.

In Chapter 3, the experimental results of the impedance spectroscopy measurements are reviewed. We envisage three different oxide phases: YSZ (ionic conductor), TiO_2 (semiconductor in the working conditions), and doped-CeO_2 oxides (ionic conductor that can suffer of partial reduction in reducing atmosphere at high temperatures). A systematic study of the stability and of the dependence of the conductivity of the carbonate/oxide electrolytes as a function of the oxide phase (ceria-based oxides, YSZ, and TiO_2), but also of the composition of the carbonate phase (eutectic mixture of Li, Na and K carbonates) and of the working atmosphere (reducing or oxidizing environments) has indeed been performed.

Chapter 4 is dedicated to the DFT modeling of the oxide phase, namely YSZ. ZrO_2 bulk structure and electronic properties are investigated, as well as its surface properties. In particular, the reducibility properties of the (111) surface of ZrO_2 cubic phase and its doping with the aliovalent oxide Y_2O_3 to obtain a suitable model for the oxide phase are described in detail.

In Chapter 5, the solid state properties of mixed $LiNaCO_3$ and $LiKCO_3$ carbonates are described. Their bulk geometries and electronic properties are investigated for the first time through DFT methods. Particular attention has then been devoted to the research of the most

stable surfaces of these carbonate materials, also by performing surface reconstruction, when necessary. Li transport on the $LiKCO_3$-(001) most stable surface was subsequently studied.

Chapter 6 is devoted to the simulation of the YSZ-$LiKCO_3$ interface. A first interface model is obtained through the combination of the models of the most stable YSZ and $LiKCO_3$ surfaces previously identified. DFT calculations allowed us to characterize YSZ-$LiKCO_3$ structural and electronic properties, as well as to simulate its IR and Raman spectra and to compare them with the measured experimental data. The role and influence of the interface on the transport properties and on the diffusion mechanisms of different possible charge carriers has also been investigated through both DFT and MD calculations.

In Chapter 7 the same procedure used for YSZ-$LiKCO_3$ is applied to the construction and characterization of the TiO_2-$LiKCO_3$ interface, which alloes getting insights on the oxide role in the interface properties.

Finally, in Chapter 8, we draw up a critical balance sheet on all the work performed so far and we present some possible future developments and perspectives.

Chapter 2

Theoretical and Experimental Methods

Men have become the tools of their tools
Henry David Thoreau

2.1 Introduction

This chapter is devoted to the experimental and theoretical background of the present thesis. In the first section, a general overview concerning the Quantum Mechanics (QM) methods will be presented. After a general introduction, a detailed description of Hartree-Fock (HF) and Density Functional Theory (DFT) will be given, introducing also the peculiarites that arise when treating periodic systems. The basic principles of *ab initio* Molecular Dynamic (MD) will be then proposed. In the second part, the basics of Electrochemical Impedance Spectroscopy (EIS) be reviewed.

2.2 Theoretical Background

2.2.1 The Shrödinger Equation

Ab initio QM methods have been used in this work for the study of the composite electrolytes. These methods are based on the resolution of the Schrödinger equation from *first principles*, without recurring to any empirical parameter derived for reference compounds, as in the case of the second possible type of QM methods, the semi-empirirical ones.

The time-independent and non-relativistic form of the Schrödinger equation can be expressed as:

$$\hat{H}\Psi = E\Psi \tag{2.1}$$

where $\hat{H}$ is the Hamiltonian operator, Ψ the multi-electron wave function describing the quantum state of the system and E is its energy. Solving this equation implies finding the wave function Ψ and the corresponding energy E. For a system with N electrons and M nuclei, the Hamiltonian, in atomic units (the numerical values of the electron mass m_e, of

the reduced Planck's constant $\hbar$ and of the coulomb constant $e^2/4\pi\varepsilon_0$ are all equal to one), can be written as:

$$\hat{H} = \hat{T}_e + \hat{T}_N + \hat{V}_{eN} + \hat{V}_{ee} + \hat{V}_{NN} \tag{2.2}$$

$$\hat{H} = -\frac{1}{2}\sum_{i}^{N}\nabla_i^2 - \frac{1}{2}\sum_{A}^{M}\frac{\nabla_A^2}{M_A} - \sum_{i}^{N}\sum_{A}^{M}\frac{Z_A}{r_{iA}} + \sum_{i}^{N-1}\sum_{i>j}^{N}\frac{1}{r_{ij}} + \sum_{A}^{M-1}\sum_{B>A}^{M}\frac{Z_A Z_B}{R_{AB}} \tag{2.3}$$

where the index i and j are referred to the electrons, while A and B refer to the nuclei, ∇^2 is the Laplacian operator, M_A and Z_A are, respectively, the mass and the charge of the nucleus A, and r and R stands for the interparticle distance. The first two terms represent the kinetic energy of the electrons and nuclei, respectively, while the third stands for electron-nuclei attractive electrostatic interaction ($\hat{V}_{eN}$), the fourth for the electron-electron repulsion ($\hat{V}_{ee}$), and the fifth and last term for the nuclei-nuclei repulsion ($\hat{V}_{NN}$). Unfortunately, this equation cannot be solved exactly when the the electron-electron repulsive term is present (poly-electronic systems), and approximations are therefore necessary in most of the cases.

2.2.1.1 The Born-Oppenheimer Approximation

The first assumption generally introduced is the Born-Oppenheimer approximation[156], that separates the electronic motion from the nuclear motion. The justification for this separation is that since the nuclei are much heavier than the electrons, the electrons move much faster then the nuclei with respect to the center of mass and hence the nuclei can be thought of as seeing only an average electron distribution, whereas the electron can adjust almost instantaneously to any change in the nuclear configuration. In the assumption that the nuclei are stationary, we can consider that the electrons experience a potential generated by a specific fixed nuclei configuration. This implies that, in the Hamiltonian of equations 2.2 and 2.3, we can neglect the term relative to the kinetic energy of the nuclei, while the $\hat{V}_{NN}$ becomes a constant and that the Hamiltonian can now be written as the sum of an operator depending only on the coordinates of the electrons ($\hat{H}_{el}$) and another term depending only on the coordinates of the nuclei ($\hat{H}_{nucl}$):

$$\hat{H} = \hat{H}_{el} + \hat{H}_{nucl} \tag{2.4}$$

with

$$\hat{H}_{el} = -\frac{1}{2}\sum_{i}^{N}\nabla_i^2 - \sum_{i}^{N}\sum_{A}^{M}\frac{Z_A}{r_{iA}} + \sum_{i}^{N-1}\sum_{i>j}^{N}\frac{1}{r_{ij}} \tag{2.5}$$

$$\hat{H}_{nucl} = -\sum_{A}^{M-1}\sum_{B>A}^{M}\frac{Z_A Z_B}{R_{AB}} \tag{2.6}$$

Solving equation 2.1 is now simply reduced to the solution of the electronic part:

$$\hat{H}_{el}\Psi_{el} = E_{el}\Psi_{el} \tag{2.7}$$

with the total wave function of the system given by the product of the electronic wave function Ψ_{el} and of the wave function Ψ_{nucl} describing the nuclear motion:

$$\Psi_{el} = \Psi_{el}\Psi_{nucl} \tag{2.8}$$

and with the total energy of the system given by the sum of the electronic energy E_{el} and nucler repulsion term E_{nucl} :

$$E = E_{el} + E_{nucl} = E_{el} + \sum_{A}^{M-1}\sum_{B>A}^{M}\frac{Z_A Z_B}{R_{AB}} \tag{2.9}$$

The nuclear repulsion term, as well as the terms relative to the kinetic energy of the electrons and to the electron-nuclear interaction can be computed analytically, but the presence of the electron-electron repulsion contribution does not allow to solve exactly equation 2.7 for poly-electronic systems. In these cases, further approximations are thus necessary. Different methods have been developed to solve this equation. They can be divided into two main groups: the methods based on the Hartree-Fock (HF) theory and the Density Functional Theory (DFT).

2.2.2 The Hartree-Fock (HF) Theory

One of the simplest approximate theories for solving the Schrödinger equation is the Hartree-Fock (HF) theory. The essence of the HF approximation is to replace the complex many-electron problem by a one-electron problem in which the electron-electron interaction is treated in an average way. This means that each electron is subject to an average non-local potential arising from the other electrons. Although this approximation can lead to a poor description of the electronic structure, since the correlation among the electrons is neglected, the HF theory represents the starting point for most *ab initio* quantum chemistry methods.

2.2.2.1 Orbitals and Slater Determinants

We define an *orbital* as a wave function for a single electron. A *molecular orbital* is thus a wave function describing an electron in a molecule. In particular, a *spatial orbital* is definable as a function of the position vector ($\mathbf{r}$), that describes the spatial distribution of a given electron so that $|\psi(\mathbf{r})|^2 d\mathbf{r}$ is the probability to find the particle in a volume $d\mathbf{r}$. Spatial orbitals are generally assumed to be orthonormals:

$$\int \psi^*(\mathbf{r})\psi_j(\mathbf{r})d\mathbf{r} = \delta_{ij} \tag{2.10}$$

where δ_{ij} is the Kronecker symbol (δ_{ij}= 1 if $i = j$ and δ_{ij} = 0 if otherwise $i \neq j$).

However, in order to completely describe an electron, the specification of its spin state is also necessary. This condition is obtained through the definition of two orthonormal functions $\alpha(\omega)$ et $\beta(\omega)$ so that the two possible states of spin (spin up and spin down, respectively) are taken into account for each electron. The wave function describing both the spatial and spin distribution for an electron is called *spin-orbital*, $\chi(\mathbf{x})$, where $\mathbf{x}$ indicates both space ($\mathbf{r}$) and spin (ω) coordinates. Consequently, for each spatial orbital, two different spin-orbitals can be defined:

$$\chi(\mathbf{x}) = \begin{cases} \psi(\mathbf{r})\alpha(\omega) \\ \psi(\mathbf{r})\beta(\omega) \end{cases} \tag{2.11}$$

If the spatial wave functions are orthonormal, so are the spin orbitals:

$$\int \chi_i(\mathbf{x})^* \chi_j(\mathbf{x}) d\mathbf{x} = \delta_{ij} \tag{2.12}$$

Having the expression of the wavefunction describing one electron, the approximations used for the multi-electron wave function can be considered. The simplest approximation is the *orbital approximation*. If we neglect the coupling between electrons, the electronic Hamiltonian in equation (2.5) becomes simply a sum of mono-electronic terms ($\hat{h}(i)$), since the interactions between the electrons are null:

$$\hat{H}_{el} = \sum_{i=1}^{N} \hat{h}(i) \tag{2.13}$$

where $\hat{h}(i)$ will have a set of eigenfunctions that can be described through a set of spin orbitals:

$$\hat{h}(i)\chi_i(\mathbf{x}_i) = \varepsilon_i \chi_i(\mathbf{x}_i) \tag{2.14}$$

Consequently, the multi-electron wave function will simply be the product of the spin orbital wave function for each electron (Ψ_{el}^{HP}, the so called Hartree product):

$$\Psi_{el}^{HP} = \chi_1(\mathbf{x}_1)\chi_2(\mathbf{x}_2)...\chi_N(\mathbf{x}_N) \tag{2.15}$$

and the electronic energy will be the sum of the energy of each spin orbital:

$$E_{el} = \sum_{i=1}^{N} \varepsilon_i \tag{2.16}$$

This assumption was proposed by Hartree[157] and the product of the mono electronic wavefunctions is called Hartree product. Nevertheless, according to the Pauli exclusion principle,

the multi-electron wavefunction must change its sign with respect to exchange of the electronic coordinates. This anti-symmetric condition is not satisfied by the Hartree product so that a better description is necessary. The Slater determinant (Ψ_{el}^{SD}, see equation 2.17) is an expression able to describe the multi-electrons wave function including the anti-symmetry requirements. For a N-electron system it is definable as:

$$\Psi_{el}^{SD} = \frac{1}{\sqrt{N!}} \begin{vmatrix} \chi_1(\mathbf{x}_1) & \chi_2(\mathbf{x}_1) & \dots & \chi_N(\mathbf{x}_1) \\ \chi_1(\mathbf{x}_2) & \chi_2(\mathbf{x}_2) & \dots & \chi_N(\mathbf{x}_2) \\ \vdots & \vdots & \ddots & \vdots \\ \chi_1(\mathbf{x}_N) & \chi_2(\mathbf{x}_N) & \dots & \chi_N(\mathbf{x}_N) \end{vmatrix} \tag{2.17}$$

where $\frac{1}{\sqrt{N!}}$ is a normalization constant. In the Ψ_{el}^{SD}, the N electrons occupy the N spin orbitals without specifying which electron is in which orbital. Interchanging the space and spin coordinates of two electrons implies the interchange of two rows of the Slater Determinant, which changes the sign of the determinant, thus meeting the requirement of the anti-symmetric principle. In particular, while the Hartree product is truly an independent-electronic wave function, the Slater determinant, as a consequence of its invariance with respect to the exchange of the electron coordinates, incorporates the so called *exchange correlation*, meaning that the motion of two electrons with parallel spins is correlated. However, since the motion of electron with anti-parallel spin is still not correlated, Slater determinants are referred as an uncorrelated wave function. A single Slater determinant is the simplest antisymmetric wave function that can be used to describe the ground state of an N-electron system and it is used in the HF theory, that is thus referred to as a mono-determinantal method.

2.2.2.2 Hartree-Fock energy

The HF energy can be derived applying the variational principle:

$$E_0^{HF} = \frac{\langle \Psi_0 | \hat{H}_{el} | \Psi_0 \rangle}{\langle \Psi_0 | \Psi_0 \rangle} = \langle \Psi_0 | \hat{H}_{el} | \Psi_0 \rangle \geq E_0^{exact} \tag{2.18}$$

The best wave function is the one which gives the lowest possible energy. This means that, for a given electronic configuration, we can vary the spin orbitals so as to obtain the Slater determinant Ψ_0 providing a minimal energy E_0. The principle is thus applied by minimizing the energy E_0^{HF} as a functional of the spin-orbitals. It can be shown that the obtained energy will be always higher or equal to the exact energy of the ground state (E_0^{exact}).
By minimizing E_0^{HF} with respect of the choice of spin-orbitals, it is possible to derive the *Hartree-Fock equations*, which determine the optimal spin-orbitals. These equations are one electron eigeinvalue equations of the form:

$$\hat{F}(i)\chi_i(\mathbf{x}_i) = \varepsilon_i \chi_i(\mathbf{x}_i) \tag{2.19}$$

Since in the case of the HF approximation, in order to introduce the electron-electron repulsion, each electron is subjected to a mean potential due to the presence of the other N-1

electrons, each spin orbital is function of an effective one-electron operator called *Fock operator* ($\hat{F}$) of the form:

$$\hat{F}(i) = -\frac{1}{2}\nabla_i^2 - \sum_A^M \frac{Z_A}{r_{iA}} + v(i)^{HF} \tag{2.20}$$

$$\hat{F}(i) = \hat{h}_i + v(i)^{HF} \tag{2.21}$$

In other words, the electron-electron interaction $\frac{1}{r_{ij}}$ in the Hamiltonian is substituted by a monoelectronic operator $v(i)^{HF}$ Hartree-Fock potential, representing the average potential experienced by the ith electron due to the presence of the other electrons and given by:

$$v(i)^{HF} = \sum_j^N (\hat{J}_j(\mathbf{x}_i) - \hat{K}_j(\mathbf{x}_i)) \tag{2.22}$$

where $\hat{J}_j$ is the Coulomb operator (2.23) and $\hat{K}_j$ is the exchange operator (2.24):

$$\hat{J}_j(\mathbf{x}_1) = \int \chi_j^*(\mathbf{x}_2)\frac{1}{r_{12}}\chi_j(\mathbf{x}_2)d\mathbf{x}_2 \tag{2.23}$$

$$\hat{K}_j(\mathbf{x}_1)\chi_j^*(\mathbf{x}_1) = \int \chi_j^*(\mathbf{x}_2)\frac{1}{r_{12}}\chi_i(\mathbf{x}_2)\chi_j(\mathbf{x}_1)d\mathbf{x}_2 \tag{2.24}$$

As we can see from the previous equations, $v(i)^{HF}$ depends on the spin orbitals of the other electrons and consequently the Fock operator depends on its eigeinfunctions. The HF equations are thus non linear and have to be solved in an iterative way. The procedure for solving the HF equations is called the Self Consistent Field (SCF) method: starting from an initial trial function for the spin orbitals, the mean field felt by each electron is computed to solve the HF equations (2.19). The obtained new spin orbitals are then used to compute the new mean fields so that an iterative cycle is established. It can be repeated until self-consistency is reached, so that the fields no longer change and the spin orbitals used to construct the Fock operator are the same as its eigeinfunctions. The HF equations are solved by introducing a finite set of spatial basis functions ψ_μ that can be used to expand both the α and β spin orbitals. The larger and more complete is the set of the basis function ψ_μ, the greater the degree of flexibility in the expansion of the spin orbitals and the lower will be the expectation value E_0^{HF}. In the limit of a complete basis set the Hartree-Fock energy reaches a lower limit known as the *Hartree-Fock limit*.

2.2.2.3 Limits of the HF approach

A single determinant, like the one used in the HF formulation, is not able to express the exact wave function since the explicit electron-electron interaction is not taken into account: in the HF method the probability of finding an electron at some location around an atom is determined by the distance from the nucleus but not from the distance to the other electrons so that the correlation due to the coulomb interaction between the electrons (named Coulomb correlation) is completely neglected. Furthermore, although the use of Slater determinants allows to fully account for the correlation between electrons of parallel spin (electron exchange), the correlation between electrons of opposite spins is completely neglected so that the probability of finding two electrons having opposite spins in the same location of space is not equal to zero. The *correlation energy* (E_{corr}) is thus defined as the difference between the exact nonrelativistic energy of the system (E_0^{exact}) and the HF energy (E_0^{HF}) obtained in the limit of a complete basis set:

$$E_{corr} = E_0^{exact} - E_0^{HF} < 0 \tag{2.25}$$

Different methods, like the post-HF methods or the Density Functional Theory (DFT), have been proposed to introduce this correlation energy contribution. In the following section, we will briefly revise the basis of the DFT methods, which have been almost exclusively applied in this work.

2.2.3 Density Functional Theory (DFT)

HF methods are based on a complex mathematical variable, the wave function. Its complexity is due to the dependence of the multi-electron wave function $\Psi(\mathbf{x}_1, \mathbf{x}_2, ..., \mathbf{x}_N)$ from 4N coordinates ($\mathbf{x}$), the three spatial ($\mathbf{r}$) and the spin (ω) coordinates for each of the N electrons of the system (in the Born-Oppenheimer approximation, with nuclei in fixed positions). Futhermore, the wave function does not directly correspond to any physical quantity. The main idea behind DFT consists in describing a system not via its many-body wave function but via its electronic density $\rho(\mathbf{r})$. The electronic density has the advantage of being a physical observable, that just depends from the three spatial coordinates, indipendently from the dimension of the system. $\rho(\mathbf{r})$ is related to the multi-electron wave function by the following expression:

$$\rho(\mathbf{r}) = \int_{\mathbf{r}_2} \cdots \int_{\mathbf{r}_N} \Psi(\mathbf{r}_1, \mathbf{r}_2 \ldots \mathbf{r}_N)^* \Psi(\mathbf{r}_1, \mathbf{r}_2 \ldots \mathbf{r}_N) d\mathbf{r}_N \tag{2.26}$$

The integration of $\rho(\mathbf{r})$ over the all system provides the total number N of electrons:

$$N = \int \rho(\mathbf{r}) d\mathbf{r} \tag{2.27}$$

At the base of DFT, there is the direct dependence of the properties of a system, the energy above all, from the density. The first attempt to use the density to derive the properties

of a system was made by Thomas and Fermi in 1927.[158,159] According to their model, the kinetic energy of a gas of non-interacting electrons depends only from its electronic density. Dirac further completed the model by adding an exchange energy always depending from ρ.[160] However, only after the theorems of Hohenberg e Kohn in 1964, it was mathematically demonstrated that the properties of the ground state of a system are functional of the density. According to these theorems, the energy of the ground state can be expressed as a functional of the density and, in this framework, a variational principle for the minimization of the energy was found.

2.2.3.1 The Hohenberg-Kohn Theorems

The first theorem of Hohenberg and Kohn[161] demonstrates that every observable of a system in its ground state, its energy E_0 in particular, is a unique functional of the electron density:

$$E_0 = E[\rho] \tag{2.28}$$

In the framework of the Born-Oppenheimer approximation, for a multi-electron system system in an external potential v_{ext}, the energy of the system can be written as

$$E[\rho(\mathbf{r})] = T_e[\rho(\mathbf{r})] + V_{ee}[\rho(\mathbf{r})] + \int \rho(\mathbf{r}) v_{ext}(\mathbf{r}) d\mathbf{r} \tag{2.29}$$

where T_e is the kinetic energy of the electrons, V_{ee} is the energy associated to the electron-electron interaction and the last term corresponds to the nuclei-electron interaction V_{Ne}, if no other external potential is applied. Equation 2.29 can be generalized as:

$$E[\rho(\mathbf{r})] = F_{HK}[\rho(\mathbf{r})] + \int \rho(\mathbf{r}) v_{ext}(\mathbf{r}) d\mathbf{r} \tag{2.30}$$

with

$$F_{HK}[\rho] = T[\rho] + V_{ee}[\rho] \tag{2.31}$$

where F_{HK} represents the so-called *universal functional*, since, including just the kinetic and the electron-electron repulsion terms, is independent from the external potential and therefore equivalent in all the multi-electron systems.

According to the *second theorem of Hohenberg and Kohn*[161], the ground state energy can be obtained variationally: the density that minimizes the total energy is the exact real density. It is thus possible to find the value of the energy of the ground state by minimizing the functional starting from a trial density $\tilde{\rho}(\mathbf{r})$. The energy obtained as functional of this approximate electronic density $E[\tilde{\rho}]$ will always be higher or equal to the real energy of the system in the ground state E_0:

$$E[\tilde{\rho}] \geq E_0 \tag{2.32}$$

Hohenberg and Kohn theorems show that the electronic density uniquely defines the Hamiltonian and consequently all the expectation values for the related observables. The electron density is not known *a priori*, but it is possible to apply a variational principle that allows to identify a criterion to determine the electronic density that best reproduces the real one, in a similar fashion to the precedure already applied in HF methods to find the best wave function. Unfortunately, we do not know the exact form of the F_{HK} functional. The electron-electron interaction energy can be divided into terms, one describing the classical coulomb repulsion energy ($J[\rho]$) and one describing the exchange energy that has a quantum origin ($V_q[\rho]$):

$$F_{HK}[\rho] = T[\rho] + V_{ee}[\rho] = T[\rho] + J[\rho] + V_q[\rho] \tag{2.33}$$

while $J[\rho]$ is given by

$$J[\rho] = \int \frac{\rho(\mathbf{r})\rho(\mathbf{r}')}{|\mathbf{r} - \mathbf{r}'|} d\mathbf{r}' \tag{2.34}$$

the form of the kinetic term and of $V_q[\rho]$ is not known. However, knowing the exact form of the universal functional would allow to exactly determine the form of the functional of the energy in the ground state and thus to finally solve the multi-electron problem analytically starting from F_{HK} and from the electronic density.

2.2.3.2 Kohn-Sham method

In order to determine the density and the relative energy of the ground state of a system, in 1965 Kohn and Sham suggested to substitute the real Hamiltonian for a system of N interacting particles with a reference Hamiltonian describing a system of N non-interacting particles, which however has the same density as the real one.[162] We can thus define a monoelectronic Kohn-Sham operator for this reference system without interactions as

$$\hat{H}_{KS} = -\frac{1}{2}\nabla_i^2 + v_{KS}(\mathbf{r}_i) \tag{2.35}$$

where

$$v_{KS}(\mathbf{r}) = J[\rho] + v_{xc}[\rho] + v_{ext}(\mathbf{r}) \tag{2.36}$$

$v_{xc}[\rho]$ is called the *exchange-correlation potential*. It can be described as the one-electron operator for which the expectation value of the corresponding energy is the *exchange-correlation energy* ($E_{xc}[\rho]$):

$$v_{xc}(\mathbf{r}) = \frac{\delta E_{xc}[\rho(\mathbf{r})]}{\delta \rho(\mathbf{r})} \tag{2.37}$$

We can now introduce a set of orbitals ψ_i, named the Kohn-Sham orbitals, that are the eigeinfunctions of the monoelectronic Kohn-Sham (KS) eigeinvalue equations:

$$\hat{H}_{KS}\psi_i = \varepsilon_i\psi_i \tag{2.38}$$

With the same self-consistent procedure applied in the case of HF methods, this Kohn-Sham orbitals allow to minimize the energy of the system

$$E_{tot}^{KS}[\rho] = T_s[\rho] + J[\rho] + E_{xc}[\rho] + \int v_{ext}(\mathbf{r})\rho(\mathbf{r})d\mathbf{r} \tag{2.39}$$

where $T_s[\rho]$ represents the kinetic energy of the non-interacting electrons system, $J[\rho]$ the classical electron-electron repulsion, E_{xc} the exchange correlation energy and $\int v_{ext}(\mathbf{r})(\mathbf{r})d\mathbf{r}$ the interaction energy with the external potential.
According to the Hohenberg-Khon theorems, $E_{tot}^{KS}[\rho]$ should be equal to the total energy of the interacting system, $E_{tot}^{real}[\rho]$:

$$E_{tot}^{real}[\rho] = T[\rho] + J[\rho] + V_q[\rho] + E_{xc}[\rho] + \int v_{ext}(\mathbf{r})\rho(\mathbf{r})d\mathbf{r} \tag{2.40}$$

The exchange-correlation energy can be therefore expressed as:

$$E_{xc}[\rho] = T[\rho] - T_s[\rho] + V_q[\rho] \tag{2.41}$$

including the correction to the kinetic energy due to the interaction between the electrons and the $V_q[\rho]$ term, which contains all the non-classical corrections to the electron-electron repulsion.
Finally, in the Kohn-Sham approach, the electronic density of the system can be written as:

$$\rho(\mathbf{r}) = \sum_{i=1}^{N} |\psi_i(\mathbf{r})|^2 \tag{2.42}$$

The evaluation of this exchange-correlation energy contribution represents the main problem of DFT based methods since the exact exchange and correlation functional is still not known. If this functional was exactly known, the resolution of the KS through the SCF procedure would allow to obtain the exact energy of the ground state of the system. The differences with the Hartree Fock approximation are thus evident. HF is a deliberately approximate theory whose development was motivated by the ability to solve the Schrödinger equation. Kohn-Sham method is, instead, in principle an exact theory, where the KS equations must be solved approximately because a key operator has unknown form. So, significant research effort has gone into finding functionals of the density that may be expected to give reasonable E_{xc} in order to make this method more and more accurate.

2.2.3.3 Exchange-correlation functionals

Different approximations fot the *exchange-correlation functional* (F_{xc}) have been proposed:

$$E_{xc}[\rho(\mathbf{r})] = \int F_{xc}[\rho(\mathbf{r})]d\mathbf{r} \tag{2.43}$$

Here, we just recall that the functional dependence of E_{xc} on the electron density is expressed as an interaction between the electron density and the so-called energy density ϵ_{xc}, which in turn depends on ρ:

$$E_{xc}[\rho(\mathbf{r})] = \int \rho(\mathbf{r})\epsilon_{xc}[\rho(\mathbf{r})]d\mathbf{r} \tag{2.44}$$

Moreover, E_{xc} is generally divided in two separate exchange and correlation contributions:

$$E_{xc}[\rho] = E_x[\rho(\mathbf{r})] + E_c[\rho(\mathbf{r})] \tag{2.45}$$

The different types of approximations to the exchange-correlation energy functional are divided in different families, according to the different degree of complexity of the approximation. The simplest one is the **local density approximation (LDA)**[160], according to which E_{xc} depends only on the electronic density:

$$E_{xc}^{LDA}[\rho] = \int \rho(\mathbf{r})\epsilon_{xc}[\rho(\mathbf{r})]d\mathbf{r} \tag{2.46}$$

The electronic density is assumed locally uniform and the value of the energy density ϵ_{xc} at some position can be computed only from the value of ρ at that position. Because of this assumption, the LDA approximation is appropriate only for systems where the electron density is almost spatially uniform, that is typically not true for most of the molecular systems. The Dirac-Slater (S)[160] exchange and the Vosko, Wilk,and Nusair correlation (VWN)[163], often indicated as LSDA or SVWN, are a typical example of LDA functionals.

It is possible to improve this approximation by introducing a dependency of the functional also on the gradient of the density ($\nabla\rho$) that indicates the degree to which the density is locally changing. The functionals including the gradient correction belong to the **generalized gradient approximation (GGA)** family:

$$E_{xc}^{GGA}[\rho] = \int \epsilon_{xc}[\rho(\mathbf{r}), \nabla\rho(\mathbf{r})]\rho(\mathbf{r})d\mathbf{r} \tag{2.47}$$

The first popular GGA exchange functionals have been developed by Becke and are simply abbreviated with B,[164]. Among the most used GGA correlation functionals there are, instead, the one proposed by Lee, Yang and Parr (LYP)[165] or the Perdew-Wang PWGGA functional[166–169]). Also the Perdew-Burke-Ernzerhof (PBE)[170] exchange and correlation functional, used in this work, belongs to the GGA family.

We also tested the performance of different **global hybrid functionals** (GH). In the functionals belonging to this family, a fraction of the exact Hartree-Fock exchange is introduced in a GGA functional. They consequently use an exchange energy given by the combination of HF and DFT (GGA) contributions. Three hybrid functionals have been used:

- **B3LYP** is based on the GGA exchange of Becke (B[164]) and the LYP[165] functional) correlation functional. It uses three parameters a, b and c to combine the different contributions:

$$E_{xc}^{B3LYP} = (1-a)E_x^{LSDA} + aE_x^{HF} + bE_x^{B} + (1-c)E_c^{VWN} + cE_c^{LYP} \quad (2.48)$$

  The parameters have been determined empirically ($a = 0.20$, $b = 0.72$, $c = 0.81$), so as to reproduce the atomistic energies, ionization potentials and electronic affinities of a range of appropriately selected molecules.[163,171]

- **B3PW** is similar to B3LYP, but uses Perdew-Wang[166–169]) correlation:

$$E_{xc}^{B3LYP} = (1-a)E_x^{LSDA} + aE_x^{HF} + bE_x^{B} + (1-c)E_c^{VWN} + cE_c^{PW} \quad (2.49)$$

- **PBE0** is obtained by combining the GGA functional PBE with a fixed quantity of HF exchange (25%):

$$E_{xc}^{PBE0} = E_{xc}^{PBE} + \frac{1}{4}(E_x^{HF} - E_x^{PBE}) \quad (2.50)$$

  Compared to the previous ones, this last functional is not parameterized: the HF percentage is not derived empirically, but it comes from arguments derived on the base of the perturbation theory.[172,173]

Another type of hybrid functionals, the so called **Range-Separated hybrids** (RSH), has also been developed. In this case, the amount of HF exchange included in the functional depends on the distance between electrons; the Coulomb potential is generally separated into a short- and long-ranged parts and these contributions are treated separately. An example is the HSE[174–176] functional, which partitions the Coulomb potential for exchange into short-range (SR) and long-range (LR) components according to the following expression:

$$\frac{1}{r} = \frac{\text{erfc}(\omega r)}{r} + \frac{\text{erf}(\omega r)}{r} \quad (2.51)$$

where $\text{erfc}(\omega r) = 1 - \text{erf}(\omega r)$ and ω is an adjustable screening parameter defining the separation range. The exchange-correlation energy is then computed as:

$$E_{xc}^{HSE} = aE_x^{HF,SR}(\omega) + (1-a)E_x^{PBE,SR}(\omega) - E_x^{PBE,LR}(\omega) + E_c^{PBE} \tag{2.52}$$

where $E_x^{HF,SR}$ is the short-range HF exchange, $E_x^{PBE,SR}$ and $E_x^{PBE,LR}$ are the short-range and long-range components of the PBE exchange functional and E_c^{PBE} is the PBE correlation energy. The parameter $a = \frac{1}{4}$ is the HF mixing constant derived from perturbation theory. For $\omega = 0$, HSE reduces to PBE0, while for $\omega \to \infty$ becomes identical to PBE. The screening of the Coulomb potential allows to reduce the computational cost associated to the calculation of the exact HF exchange for large molecules and solids, especially for the ones with metallic characteristics.

A general drawback of all conventional GGA and hybrid functionals is that they cannot describe the long-range electron correlations that are responsable for the Van der Waals (vdW, dispersive) forces. However, the vdW interactions between atoms and molecules play an important role in many chemical systems. A simple and efficient method to include long-range dispersion contributions to the computed KS-DFT energy is the semiclassical correction, generally indicated as **DFT-D** or DFT+disp. This approach is based on an atom pairwise additive treatment of dispersion energy. For example, the DFT-D2 scheme, proposed by Grimme and implemented in the CRYSTAL code, calculates a London-type pairwise empirical correction to the energy to introduce long-range dispersion contributions to the computed *ab initio* total energy and gradients. The total energy is then given by:

$$E_{DFT-D} = E_{KS-DFT} + E_{disp} \tag{2.53}$$

where E_{KS-DFT} is the usual self-consistent KS energy obtained from the chosen DFT method and E_{disp} is an empirical correction given by:

$$E_{disp} = -s_6 \sum_{i=1}^{N_{at}-1} \sum_{j=i+1}^{N_{at}} \frac{C_6^{ij}}{R_{ij}^6} f_{dump}(R_{ij}) \tag{2.54}$$

where N_{at} is the number of atoms in the system, C_6^{ij} is the dispersion coefficient for the atom pair ij, s_6 is a global scaling factor used to adjust the correction to the repulsive behaviour of the chosen DFT method, and R_{ij} is the interatomic distance of the ij atom pair. A damping function is used to avoid near-singularities for small interatomic distances:

$$f_{dump}(R_{ij}) = \frac{1}{1 + e^{-d(R_{ij}/R_r - 1)}} \tag{2.55}$$

where R_r is the sum of atomic vdW radii, and d determines the steepness of the damping function. The C_6^{ij} dispersion coefficients are computed by using a geometric mean

$$C_6^{ij} = \sqrt{C_6^i C_6^j} \tag{2.56}$$

from the atomic coefficients reported by Grimme together with the Van der Waals raddii for atoms from H to Xe in ref[177]. These scheme can be applied to all DFT levels; for example, in this work, we used the PBE0 functional corrected according to this scheme and indicated as PBE0-D.

2.2.4 Modelling of crystalline systems

From a theoretical point of view, systems with an infinite periodic structure, obtained by repeating in the space an elementary structure called unit cell, like crystals, can be studied using an Hamiltonian that posseses the same periodicity as the system, imposing some *periodic bounday conditions* (PBC or Born-Von Karman boundary conditions) and by introducing the Bloch functions, monoelectronic crystalline orbitals, at the place of the monoelectronic molecular orbitals used so far in the HF or KS formalism for molecular systems. Indeed, Bloch[178] demonstrated that, in these conditions, the monoelectronic crystalline orbitals can be written as:

$$\psi^{\mathbf{k}}(\mathbf{r}) = e^{i\mathbf{k}\mathbf{r}} u^{\mathbf{k}}(\mathbf{r}) \tag{2.57}$$

$$u^{\mathbf{k}}(\mathbf{r} + \mathbf{T}) = u^{\mathbf{k}}(\mathbf{r}) \tag{2.58}$$

where $\mathbf{k}$ is a vector of the reciprocal lattice of the crystal, $\mathbf{T}$ is a vector of the direct lattice, and $u^{\mathbf{k}}$ is the periodic part of the Bloch function ($\psi^{\mathbf{k}}(\mathbf{r})$). Thanks to the translational properties of the Bloch functions in the reciprocal lattice, the resolution of the HF or KS equations is limited to the first Brillouin zone (the unit cell of the reciprocal lattice) or even at the irreducible Brillouin zone (IBZ, the first Brillouin zone reduced by all of the symmetries in the point group of the lattice). The complete set of $\{\psi^{\mathbf{k}}(\mathbf{r})\}$ is obtained considering a small value of $\mathbf{k}$ points and solving the system indipendently for each of this point. Indeed, the computed properties, such as the total energy, converge with the number of $\mathbf{k}$ vector used. It is thus sufficient to identify the finite number of $\mathbf{k}$ points necessary to ensure convergence.

The monoelectronic wave function $\psi^{\mathbf{k}}(\mathbf{r})$ can be developed in a similar manner to what is generally done for the molecular orbitals $\psi(\mathbf{r})$ in the molecules that are obtained as a linear combination of mathematical functions centered on the atoms according to the *linear combination of atomic orbitals* approximation (LCAO):

$$\psi_n^{\mathbf{k}}(\mathbf{r}) = \sum_{\mu} c_{\mu n}^{\mathbf{k}} \Phi_{\mu}^{\mathbf{k}}(\mathbf{r}) \tag{2.59}$$

where $c_{\mu n}^{\mathbf{k}}$ are the coefficients of the linear combination. Two main different types of Bloch functions are used for the development in equation 2.59: localized basis sets or plane waves.

2.2.4.1 Localised basis sets

Localized basis sets are made by local functions χ_μ centered on the atoms of the primitive cell and replicated in the others so as to obtain the periodic part of the Bloch functions, which are thus given by:

$$\Phi_\mu^{\mathbf{k}}(\mathbf{r}) = \frac{1}{\sqrt{N}} \sum_{\mathbf{T}} e^{i\mathbf{k}\mathbf{T}} \chi_\mu^{\mathbf{T}}(\mathbf{r} - \mathbf{r}_\mu) \tag{2.60}$$

indicating that the local functions χ_μ centered on the atoms of the primitive cell are repeated in all the other cells of the crystal.

From a mathematical point of view, two main type of functions are used to describe the basis functions χ_μ: Slater type (STF) and Gaussian type (GTF) functions.
STFs and GTFs can be expressed, respectively, as:

$$\chi^{STF}(\mathbf{r}) = AY_l^m(\theta, \varphi) r^{n-1} e^{-\zeta r} \tag{2.61}$$

$$\chi^{GTF}(\mathbf{r}) = AY_l^m(\theta, \varphi) x^i y^j z^k e^{-\alpha r^2} \tag{2.62}$$

where ζ and α are the Slater and Gaussian orbital exponents, respectively, $Y_l^m(\theta, \varphi)$ is a spherical harmonic, n, l, m are quantum numbers, and i, j, k are integer numbers. STFs have the advantage of providing a more correct description of the qualitative features of the orbitals, expecially in proximity of the nuclei, with respect to the GTF; the exact solutions of the Schrödinger equations for the hydrogen atom are Slater functions. On the other side, the resolution of the HF or KS equations is much more time consuming with Slater functions compared with GTF, since the product of two GTF is still a gaussian function and this makes the evaluation of the multi-centers integrals involved in the HF or KS formalisms faster. For these reasons, the functions normally used are obtained through the contraction of GTFs in order to reproduce the behaviour of the STFs. The Gaussian functions used in the linear combinations are called primitive functions, while the resulting function is referred to as a contracted Gaussian function (CGTF):

$$\chi^{CGTF} = \sum_\mu d_{\mu r} \chi_\mu^{GTF} \tag{2.63}$$

where $d_{\mu r}$ are the coefficients of the contraction. Following this idea, different set of basis functions (called *basis set*) can thus be produced and used. Naturally, in order to exactly describe the monoelectronic orbitals it would be necessary to use an infinite basis set, which is not possible from a practical point of view. Obviously, larger basis sets approximate more accurately the orbitals, but on the same time make the calculations more time consuming. The selection of a basis set therefore involves a compromise between accuracy and computational cost and represents one of the critical parameters for setting a quantum chemistry calculation.

In same cases, especially for atoms of large atomic number, in order to reduce the cost of the calculations, it is possible to separate the core and valence electrons. Since the core ones are less involved in the chemical bonds, thier exact description is not always necessary to correctly describe the properties of the system. The core electrons can be thus substitued with a pseudopotential operator optimized in order to reproduce the effect of the Coulomb potential of the nuclei and the effects due to the core electrons that are strongly bounded by an ionic potential experienced also by the valence electrons. Relatively to the number of electrons taken into account by this operator, we can distinguish between *small core* or *large core* effective core pseupotentials (ECP).

This approach based on localized functions is the one applied in the periodic CRYSTAL[179,180] code that we used for the majority of the calculations in this work, recurring to both all-electron and ECP basis sets.

2.2.4.2 Plane waves

Plane waves (PW) can also be used to expand the crystalline orbitals. These functions can be written as[181]:

$$\Phi^{\mathbf{k}}_{\mathbf{K}_n}(\mathbf{r}) = \frac{1}{\sqrt{N\Omega_0}} e^{i\mathbf{r}(\mathbf{k}+\mathbf{K}_n)} \tag{2.64}$$

where $\mathbf{K}_n$ is a vector of the reciprocal lattice and $N\Omega_0$ is the total volume of the system. The orbitals are expanded in a finite PW basis set. The number of PWs is computed introducing a kinetic energy cutoff, E_{cut} and using the PWs that fulfill the relationship

$$(\mathbf{K}_n + \mathbf{k})^2 \leq E_{cut} \tag{2.65}$$

where E_{cut} is sufficiently large to assure a good representation of the wave functions.

Generally, the *frozen core* approximation[182] is used in these PWs: only the valence electrons are treated explicitely, while the core one are considered to be frozen with the nuclei and represented by a pseudopotential. Both *norm-conserving*[183,184] or *ultra-soft*[185,186] pseudopotentials have been widely used in periodic calculations in the PW approach. Another possibility is to use the *projected augmented wave method* (PAW) originally proposed by Blöchl[187]. Valence wave functions tend to have rapid oscillations near ion cores due to the requirement that they be orthogonal to core states; this situation is problematic because it requires, for example, a very fine mesh in the case of grid-based methods to describe the wave functions accurately. The PAW approach addresses this issue by transforming these rapidly oscillating wave functions into smooth wave functions which are more computationally convenient, and provides a way to calculate all-electron properties from these smooth wavefunctions. Therefore, contrarily to the pseudopotential approach, the PAW method has been described an all-electron method, since it correctly describes the nodal features of the valence orbitals which are also correctly orthogonalized to the core wave functions. However, we should recall that also the PAW approach is based on the frozen core approximation.

Some calculations realized through the VASP[188–191] code in the PAW approach will also be presented in this work.

2.2.4.3 From bulk to surfaces

Different approaches have been developed to model surfaces. Among them, the model usually adopted is that of the so called slab: a thick slice of material (consisting of several layers), obtained by cleaving the bulk structure along the Miller indices (hkl) that define the surface, and delimited by two free surfaces. In the CRYSTAL code, we use for the majority of the calculations,[179,180] two different schemes based on this two-dimensional (2-D) model are available. By forcing a 3-D periodicity, slabs are periodically repeated along the normal to the surface. On the other hand, by imposing 2-D periodic boundary conditions, the system is really two-dimensional and thus isolated. The majority of the calculations reported in this work have been performed using the latter model. To ensure a faithful description of an ideal surface, sufficiently thick slabs have to be considered, so that the computed surface properties can be considered at convergence with respect to the number of atomic layers. Each time a surface termination was taken into account for one material, slabs built with a different number of layers have been thus relaxed, investigating the convergence of the computed structure, surface energy, and electronic properties with respect to the number of layers, so as to identify a sufficiently thick slab model that corresponds to a good surface model. The other slab scheme (3D) was instead used in the case of the calculations in the presence of an external electric field (cf. 5.5.2.3) or for the MD simulations performed with the VASP code[188–191] (cf. chapter 6). In this case, the lattice parameter in the direction perpendicular to the surface should be carefully chosen in order to ensure the presence of an adequate vacuum layer preventing interaction between succesive slabs.

Furthermore, when studying processes of adsorption or defect formation, the unit cell of the surface can be too small to avoid spurious interactions between the defect or the adsorbate and its periodic image. In these cases, the supercell approach can be applied. For surfaces, creating a supercell corresponds to multiplicating the surface unit cell in the two periodic directions. The dimensions of the supercell should be such as to ensure that the spurious interactions become negligible.

2.2.5 *Ab initio* Molecular Dynamics (MD)

Molecular dynamcs (MD) simulations allow to study the dynamic of the evolution of a system in time by solving Newton's equations of motion[192]. Indeed, by integrating the Newton's lows of motion, successive configurations of the system are generated and the trajectories specifying how the positions and velocities of the particles in the system vary with time is obtained. From these atomic trajectories a variety of properties can be obtained.

At the very heart of any MD simulations is the selection of a good model to represent the interatomic forces acting between the atoms composing the system. This can be done in two obvious ways: i) fitting empirical potentials using the results from experiments or from *ab initio* or semiempirical calculations, ii) generating the forces directly from the electronic structure calculations as the MD trajectory evolves.

The traditional route followed in *classical MD* is to make recourse to empirical force field (FF) based methods. A FF is a mathematical expression describing the dependency of a system on the coordinates of its particles. It consists of an analytical form of the interatomic potential energy and a set of parameters, empirically derived, entering into this form. Molecules

are simply defined as set of atoms with a certain mass held together by simple elastic forces moving in an effective potential field, given by the FF. The motion of these masses is governed by the law of classical mechanics. The main disadvantages of these methods is that the quality of the FF needs to be assessed, thus the reliability of the prediction will depend on whether the FF is sufficiently accurate. Furthermore, if the FF is not defined for the system to which one is interested it should be found and many different atom types included in the model give rise to a steeply rising number of interactions that need to be parametrized. More importantly, changes in the electronic structure are generally not accounted for.

The other possibility is to derive the forces describing the interaction from *first principles*, solving the electronic structure for a particular configuration of the nuclei, and then calculating the resulting forces on each atom. This is the basis of the *ab initio* MD (AIMD) techniques we used in this work. Thus, AIMD is based on Newton's as well as Schrödinger equations. This method not only allows one to tackle chemically complex problems such as those involving breaking and formation of chemical bonds, but also it has a truly predictive power.[193] Despite its obvious advantages, it is evident that a price has to be paid for putting MD on *ab initio* grounds: the correlation lengths and relaxation times that are accessible are much smaller than what is accesible via classical MD. *Ab initio* MD simulations are limited to time scales of a few tens of picoseconds and length scales of a few nanometers, *i.e.* they are limited to systems of hundreds of atoms[194]. There are two main *ab initio* schemes which are in widespread use namely Born-Oppenheimer[156] and Car-Parrinello[195]. In Born-Oppenheimer[156] MD, the electronic structure in MD simulations is included by straightforwardly solving the static electronic structure problem in each MD step given the set of fixed nuclear positions at that instance of time. Thus, the electronic structure part is reduced to solving a time-independent quantum problem, *e.g.* by solving the time-independent Schrödinger equation, concurrently to propagating the nuclei via classical MD. Thus, the time-dependence of the electronic structure is not intrinsic and is a consequence of nuclear motion[194]. A more detailed discussion about Born-Oppenheimer MD will be presented in section 2.2.5.2. The Car-Parrinello[195] method explicitly introduces the electronic degrees of freedom as (fictitious) dynamical variables, obtaining a system of coupled equations of motion for both ions and electrons. In this way, an explicit electronic minimization at each time step, as done in Born-Oppenheimer MD, is not needed: after an initial standard electronic minimization, the fictitious dynamics of the electrons keeps them on the electronic ground state corresponding to each new ionic configuration visited along the dynamics, thus yielding accurate ionic forces. In order to maintain this adiabaticity condition, it is necessary that the fictitious mass of the electrons is chosen small enough to avoid a significant energy transfer from the ionic to the electronic degrees of freedom. But this small fictitious mass in turn requires that the equations of motion are integrated using a smaller time step than the one commonly used in Born-Oppenheimer MD.

2.2.5.1 Basic Principles

In a MD simulation, a trajectory for a system composed of N particles is generated by the solution of the classical Newton's equations of motion:

$$m_i \frac{d^2\mathbf{r}_i}{dt^2} = \mathbf{F}_i \tag{2.66}$$

$$\mathbf{F}_i = -\frac{\partial V(\mathbf{r}_i, \ldots \mathbf{r}_N)}{\partial \mathbf{r}_i} \tag{2.67}$$

where m_i is the mass of the ith particle, $\mathbf{F}_i$ is the force on atom i, $V(\mathbf{r})$ is the potential energy that must be a differentiable function of the atomic coordinates $\mathbf{r}_i$, and time is denoted by t. We thus need a set of initial conditions (positions and velocities of each particle), a model to represent the forces acting between the particles, we need to define the boundary conditions to be employed, and, finally, an accurate and stable algorithm to solve these equations. In case of crystalline systems, the initial positions can be derived from the crystallographic files or from previous calculations and, as previously seen, we can easily apply periodic boundary conditions (PBC). The initial velocities of each particle is attributed randomly from a Maxwellian distribution centered on the desired temperature and then they are adjusted in order to zero the angular momentum and the center of mass velocity of the total system. In the following, we will see how forces are evaluated from electronic structure calculations in the case of Born-Oppenheimer MD (cf. 2.2.5.2) and the most common integration algorithms (cf. 2.2.5.3) used in MD simulations.

Static and dynamic quantities can be obtained by averaging over the thus computed trajectory, which must be of sufficient length to form a representative ensemble of the state of the system (cf. 2.2.5.4).

2.2.5.2 Born-Oppenheimer MD

As already shown in section 2.2.1, the non-relativistic Hamiltonian of a system is given by:

$$\hat{H} = T_N + T_e + V_{ee}(\mathbf{r}) + V_{NN}(\mathbf{R}) + V_{eN}(\mathbf{r}, \mathbf{R}) \tag{2.68}$$

where $\mathbf{r}$ and $\mathbf{R}$ stand, respectively for the positions of the electrons and the nuclei. The resolution of the complete quantum mechanical problem would require the identification of the eigenfunctions and eigenvalues of this Hamiltonian by solving the time-independent Schrödinger equation

$$[T_N + T_e + V_{ee}(\mathbf{r}) + V_{NN}(\mathbf{R}) + V_{eN}(\mathbf{r}, \mathbf{R})]\Psi(\mathbf{x}, \mathbf{R}) = E\Psi(\mathbf{x}, \mathbf{R}) \tag{2.69}$$

where $\Psi(\mathbf{x}, \mathbf{R})$ is the total wave function of the system depending on both the electron ($\mathbf{x}$, spin and position variables) and nuclei coordinates. By applying the Born-Oppenheimer approximation, this function can be written as product of a nuclear wave function ($\Psi_{nucl}(\mathbf{R})$) and an electronic wave function depending on the coordinates of the electrons and parametrically on the nuclear positions ($\Psi_{wl}(\mathbf{x}, \mathbf{R})$):

$$\Psi(\mathbf{x}, \mathbf{R}) = \Psi_{el}(\mathbf{x}, \mathbf{R})\Psi_{nucl}(\mathbf{R}) \tag{2.70}$$

We have also seen how we can thus solve the electronic part of the Schrödinger equation for a fixed nuclei configuration:

$$[T_e + V_{ee}(\mathbf{r}) + V_{eN}(\mathbf{r}, \mathbf{R})]\Psi_{el}(\mathbf{x}, \mathbf{R}) = \varepsilon_n(\mathbf{R})\Psi_{el}(\mathbf{x}, \mathbf{R}) \tag{2.71}$$

Each electronic eigeinvalue $\varepsilon_n(\mathbf{R})$ will give rise to an electronic surface on which the nuclear dynamics is determined by the time-dependent Schrödinger equation for the time-dependent nuclear wave function:

$$[T_N + V_{NN}(\mathbf{R}) + \varepsilon_n(\mathbf{R})]\Psi_{nucl}(\mathbf{R}, t) = i\hbar\frac{\partial}{\partial t}\Psi_{nucl}(\mathbf{R}, t) \tag{2.72}$$

If we assume that non-adiabatic effects can be neglected, the motion on the ground state electronic surface can be thus described as

$$[T_e + V_{ee}(\mathbf{r}) + V_{eN}(\mathbf{r}, \mathbf{R})]\Psi_{0el}(\mathbf{x}, \mathbf{R}) = \varepsilon_0(\mathbf{R})\Psi_{0el}(\mathbf{x}, \mathbf{R}) \tag{2.73}$$

$$[T_N + V_{NN}(\mathbf{R}) + \varepsilon_0(\mathbf{R})]\Psi_{nucl}(\mathbf{R}, t) = i\hbar\frac{\partial}{\partial t}\Psi_{nucl}(\mathbf{R}, t) \tag{2.74}$$

The next step requires to approximate the nuclei as classical point particles. A well-known way to extract classical mechanics from QM starts with rewriting the corresponding wave function in terms of an amplitude factor A and a phase S which are both considered to be real:

$$\Psi_{nucl}(\mathbf{R}, t) = A(\mathbf{R}, t)e^{iS(\mathbf{R},t)/\hbar} \tag{2.75}$$

After transforming the nuclear wave function in equation 2.74 accordingly, separating the real and imaginary parts and neglecting the terms depending on $\hbar$, an approximate equation for $S(\mathbf{R}, t)$ is obtained:

$$\hat{H}_N(\nabla_1 S, \ldots, \nabla_N S, \mathbf{R}_1, \ldots \mathbf{R}_N) + \frac{\partial S}{\partial t} = 0 \tag{2.76}$$

This is the classical Hamilton-Jacobi equation

$$\hat{H}_N(\mathbf{P}_1, \ldots, \mathbf{P}_N, \mathbf{R}_1, \ldots \mathbf{R}_N) = \hat{T}_N + V_{NN}(\mathbf{R}) + \varepsilon_0(\mathbf{R}) \tag{2.77}$$

with the connecting transformation between the momentum $\mathbf{P}_i$ and the phase S_i

$$\mathbf{P}_i \equiv \nabla S_i \tag{2.78}$$

This Hamilton-Jacobi is equivalent to the classical motion on the ground-state surface ($E_0(\mathbf{R}) = \varepsilon_0(\mathbf{R}) + V_{NN}(\mathbf{R})$) given by:

$$M_i \frac{d^2\mathbf{R}_i}{dt^2} = -\nabla_i E_0(\mathbf{R}) \tag{2.79}$$

$$\hat{H}_{el}\Psi_0 = E_0\Psi_0 \tag{2.80}$$

The Born-Oppenheimer MD thus requires an algorithm to solve numerically equation 2.79 with forces obtained from the resolution of the time-independent eletronic Schrödinger equation at each step of the calculation. As we showed in the previous section, this latter step can be achieved recurring, for example, to DFT methods.

Born-Oppenheimer MD simulations, as implemented in the VASP code[188–191], have been performed in this work.

2.2.5.3 Integration Algorithms

Newton's equation of motion (2.66, 2.67, or 2.79) are a system of N coupled second order non linear differential equations that can only be solved numerically. It is thus necessary to discretize the trajectory and use an integration to advance over small time steps (Δt). The integration algorithms should provide good stability even if large time steps are used, good accuracy and conservation of energy and momentum, time reversibility and should not require more than one cycle of force evaluation for time steps, since this is the most expesive part of a MD run.

One of the most used integration techniques is the Verlet algorithm.[196] Positions, as well as velocities and accelerations, can be approximated by Taylor expansions. In the Verlet algoritm, the Taylor expansions for $t + \Delta t$ and $t - \Delta t$ given by

$$\mathbf{r}_i(t_0 + \Delta t) = \mathbf{r}_i(t_0) + \frac{d\mathbf{r}_i(t_0)}{dt}\Delta t + \frac{1}{2}\frac{d^2\mathbf{r}_i(t_0)}{dt}\Delta t^2 + O(\Delta t^3) \tag{2.81}$$

$$\mathbf{r}_i(t_0 - \Delta t) = \mathbf{r}_i(t_0) - \frac{d\mathbf{r}_i(t_0)}{dt}\Delta t + \frac{1}{2}\frac{d^2\mathbf{r}_i(t_0)}{dt}\Delta t^2 - O(\Delta t^3) \tag{2.82}$$

are summed, thus obtaining:

$$\mathbf{r}_i(t_0 + \Delta t) = -\mathbf{r}_i(t_0 - \Delta t) + 2\mathbf{r}_i(t_0) + \frac{d^2\mathbf{r}_i(t_0)}{dt}\Delta t^2 + O(\Delta t^4) \tag{2.83}$$

The intrinsic error of the algorithm is therefore $O(\Delta t^4)$. Note that the velocities do not appear explicitly in the Verlet algorithm, but they can be calculated in various ways, such as

$$\mathbf{v}_i(t_0 + \Delta t) = \frac{\mathbf{r}_i(t_0 + \Delta t) - \mathbf{r}_i(t_0 - \Delta t)}{2\Delta t} \tag{2.84}$$

Other two algorithms, the leap-frog[197] and the velocity-Verlet[198], produce the same trajectories as the Verlet. These three schemes are very simple, yet efficient, stable and reasonably accurate.

Naturally, when applying these algorithm a suitable time step (Δt) has to be chosen. This requires a compromise: small time steps will improve the accuracy but will also require much more steps to obtain a trajectory of the required length; too large Δt will however cause large drifts in the energy possibly making the simulation not stable. As a general rule of thumb, the time step should be approximately one tenth the time of the shortest motion. For instance in flexible molecules the shortest period of motion is given by bond stretches, especially those involving hydrogen atoms for which the vibration has a repeat period of about 10 fs so that a time step of 1 fs is commonly used.

2.2.5.4 Thermodynamic Ensembles

MD simulations produce information at the microscopic level such as atomic positions and velocities. The connection between distribution and motion of the atoms and macroscopic properties such as temperature, pressure and energy is made via statistical mechanics, the mathematical method to compute the thermodynamic properties of a material starting from a molecular description. In statistical mechanics, a small set of parameters, like the temperature T, the pressure P and the number of particles N defines a thermodynamic state. The microscopic state is defined by the atomic positions and momenta that can be seen as coordinates in a multidimensional space called *phase space* with 6N dimensions (where N is the number of the particles of the system). During a MD simulation a sequence of points in the phase space is generated as a function of time. A collection of points in phase space is called *ensemble*. We can distringhuish some particular ensemble satisfying some properties. There most commons are:

- **microcanonical (NVE) ensemble**: the system is closed and isolated, so it is constant in the number of particles (N), volume (V) and total energy (E). A microcanonical MD trajectory can be seen as an exchange of potential and kinetic energy, with total energy being conserved.

- **canonical (NVT) ensemble** is closed but not isolated number of atoms (N), volume (V) and temperature (T) are kept constant through the simulation. The temperature is directly correlated to the kinetic energy of the system, consequently we can change it by modifiyng the velocities of the atoms. The first method proposed to control the temperaure was the velocity scaling: all the velocities are scaled by a $\sqrt{T_B/T(t)}$ factor, where T_B is the desired temperature and $T(t)$ is the instantaneous temperature before the scaling. A more physical way to control temperature is to use a thermostat through

the weak coupling of the system with a heat bath. Different type of thermostats have been proposed (Berendsen,[199] Andersen,[200] and Langevin[201]). However, the most used method is to use the Nosè-Hoover[202–204] thermostat. In this case, the heat bath becomes an integral part of the system by adding an artificial variable with an associated effective mass. The choice of the mass for this variable should be done carefully because if too large the coupling will be too lose and the control of the temperature too slow to reach equilibrium, if too small the control is poor and wild oscillation in temperature will be produced.

- **isothermal-isobaric (NPT) ensemble**: amount of particles (N), pressure (P) and temperature (T) are conserved. In addition to a thermostat, a barostat is needed. The approaches to control the pressure are similar to those employed for the temperature.

2.3 Experimental Background

2.3.1 Electrochemical Impedance Spectroscopy (EIS)

Electrochemical impedance spectroscopy (EIS), or simply impedance measurement, is based on applying to the system an external sinusoidal perturbation with constant amplitude but variable frequency f (and angular frequency $\omega = 2\pi f$) and then measuring its response.[205,206] In theory, the response should be a sinusoidal current whose amplitude and phase shift compared to the voltage depends on the sample properties, *e.g.* charge transfer and conductivity. In practice, electrochemical impedance is normally measured using a small excitation signal. This is done so that the system's response is pseudo-linear. In a linear (or pseudo-linear) system, the current response to a sinusoidal potential will indeed be a sinusoid at the same frequency but shifted in phase. The electrical impedance $Z(\omega)$ of a system is the complex ratio of the applied AC potential that has the form:

$$E(\omega) = E_0 e^{(j\omega t)} \tag{2.85}$$

and the resulting current given by

$$I(\omega) = I_0 e^{j(\omega t + \varphi)} \tag{2.86}$$

In these expressions, E_0 and I_0 are the amplitudes of the potential and current, respectively, ω is the angular frequency, φ is the phase shift of the current compared to the voltage, and j is a complex number defined as $j^2 = -1$. Consequently we can write:

$$Z(\omega) = \frac{E(\omega)}{I(\omega)} = \frac{E_0 e^{(j\omega t)}}{I_0 e^{j(\omega t + \varphi)}} = Z_0 \frac{e^{(j\omega t)}}{e^{j(\omega t + \varphi)}} = Z_0 e^{-j\varphi} \tag{2.87}$$

The impedance is therefore expressed in terms of a magnitude, (Z_0) and a phase shift (φ). $Z(\omega)$ is thus a complex number, that can be written as:

$$Z(\omega) = Z' + jZ'' \tag{2.88}$$

where Z' and Z'' are the real and imaginary components of $Z(\omega)$.

The EIS data is often presented as a Bode plot (figure 2.1a). The impedance is plotted with log frequency on the *x*-axis and both the absolute values of the impedance ($|Z| = Z_0$) and the phase-shift on the *y*-axis. This type of representation is mainly used by physicists.

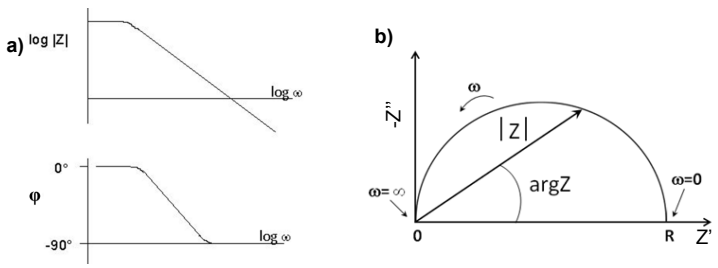

Figure 2.1: Schematic representation of a Bode (a) or Nyquist (b) plot.

In electrochemistry, impedance measurements are mostly shown as a Nyquist plot, where $-Z''$ is plotted as a function of the real Z' component (figure 2.1b). We can note that in this plot the *y*-axis is negative and that each point corresponds to the impedance at one frequency. Futhermore, low frequency data are on the right side of the plot, while higher frequencies are on the left. On the Nyquist plot the impedance can be represented as a vector (arrow) of length $|Z|$. The main drawback of Nyquist plots is that, unlike the Bode plot, when looking at any data point it is not possible to easily tell what frequency was used to record that point.

In a Nyquist plot, the ionic conductivity of an electrolyte and/or the electrode contributions can be determined from the semicircles in the plot (it is worth noting that the diagrams must be normalised with orthogonal axes and same scale on both axes). For this reason, EIS has been used in several works to study the materials, both electrolytes and electrodes, used in solid oxide fuel cells applications and the interfaces between electrolyte and electrodes.[96] According to the range of frequencies conisidered, the plot can be divided in three main regions (see figure 2.2). The identification of the different semicircles can be done by systematic studies using different experimental parameters, like:

- the amplitude of the applied potential;
- the geometric factor of the sample, *i.e* the ratio between the surface area of the electrodes and the thickness of the sample;
- the sample composition, *e.g.* type of the oxide and dopant concentration;
- microsctructure of the sample: single crystal or polycrystalline powder, particle size, etc...

- the nature of the electrodes: metal, semi-conductor, mixed-conductor;
- oxygen partial pressure

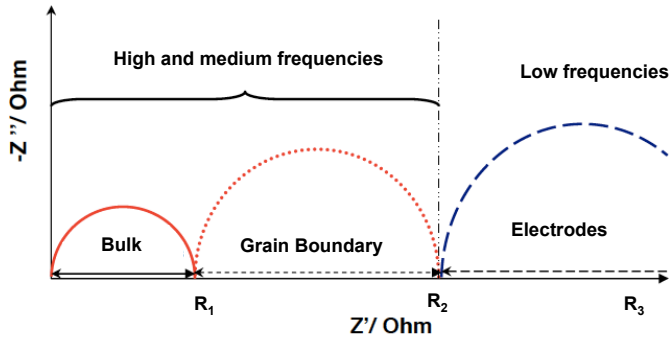

Figure 2.2: Schematic representation of the Nyquist plot of a typical electrolyte-electrode system.

We can thus describe the different contributions as such:

- the high frequency semicircle is attributed to bulk conductivity in the electrolyte. R_1 is thus the intrinsic resistance of the material;
- the medium frequency is due to grain boundary conductivity (or blocking phases from a general point of view). R_2 is the corresponding resistance;
- the low frequency arc, with a resistance R_3, is associated to the electrode contributions (charge transfer at the interface, mass transport...).

In practice, equivalent circuits are used to estimate the contributions of different parts of the sample. For example, the diagram in figure can be decomposed in a series of three electrical circuit each given by a resistor and a capacitor in parallel (see figure 2.3). However, care has to be taken in choosing the correct circuit and fitting algoritm to minimize the analysis errors.

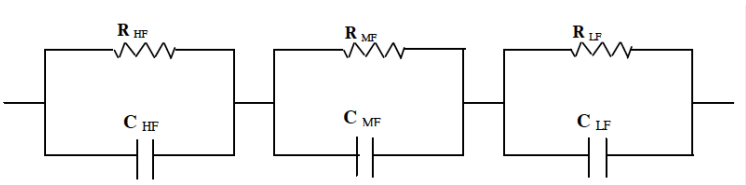

Figure 2.3: Equivalent cicuit corresponding to the Nyquist plot in figure 2.2

In chapter 3, we will describe the main characteristic of the EIS spectra of composite oxide-carbonate electrolytes.

Chapter 3

Experimental Results

I am somewhat exhausted;
I wonder how a battery feels
when it pours electricity into a non-conductor?
Arthur Conan Doyle
The Adventure of the Dying Detective

Contents

3.1 Introduction **63**
3.2 Preparation of the composite materials **64**
3.3 Electrochemical characterisation **66**
3.4 TGA and DTA analyses **86**
3.5 Premilinary XRD characterization **91**
3.6 IR and Raman characterization **96**
3.7 Conclusions **102**

3.1 Introduction

Electrochemical impedance spectroscopy (EIS) is currently the most commonly used method for measuring the conductivity of oxide-carbonate composite electrolytes. The works in which the electrochemical properties of these materials were studied through EIS have been reviewed in a recen paper by Patakangas et al.[96], reporting also the general parameters (amplitude, frequency range and electrode type) that have been used to perform the measurements. While more attention has been paid to the role of the carbonate phase,[19,22] the majority of these studies have been performed on ceria-based composites. Only few studies have been devoted to the study of composites with other oxide matrices such as yttria-doped tetragonal zirconia (TPZ),[98] $LiAlO_2$ which is the classical matrix support for molten carbonates in MCFCs ,[94] Al_2O_3,[98] and some rare earth-sesquioxides[99] like Y_2O_3, La_2O_3, Gd_2O_3,

Yb_2O_3. These composites were not found to be superior to GDC or SDC more commonly used. Nonetheless, more studies on the effect of the oxide phase would however help in rationalizing the properties of the composites, maybe allowing at the same time to find new potential candidates for LT-SOFC applications.
The main objective of the experimental work of this thesis was thus to complete the existing set of data concerning the impact of the oxide and carbonate phases conductivity (type and level) on the composite electrical behavior, as well as the influence of the operating atmosphere on the stability when cycling a minimum of one heating and one cooling stages. Moreover, some structural and microstructural characterisations were carried out, in the contex of the PhD work of Andrey Grishin at Chimie ParisTech, in view of providing additional information for a deeper understanding of the phenomena taking place and for the validation of the theoretical calculations.

For these reasons, in this chapter, we will report the results of a systematic study on the electrochemical behaviour of oxide-carbonate composite electrolytes. We will first describe the various procedures, beginning with the preparation of the composite powders and pellets. We will then discuss the electrical behaviour (electrochemical impedance spectroscopy, EIS) as a function of the oxide or carbonate phase and of the operating atmosphere. Finally, we will complete the description through the physico-chemical characterisations (X-Ray Diffraction, Infra-Red and Raman spectroscopies, Thermal Gravimetry Analysis and Differential Scanning Calorimetry, Gas Chromatography combined to Mass Spectrometry),

3.2 Preparation of the composite materials

The composite materials were prepared by the solid-state method established by M. Benamira during his PhD and reported in the associated papers.[19,22] Even if it could still be optimised, this one has proven that the final product was an accurate mixture of oxides and carbonates. It is worth mentioning that molten carbonates can be transformed into oxides when there is no CO_2 in the operating atmosphere; nevertheless, it has been checked carefully that it was not the case following Benamira's synthesis procedure.

The required steps are the following:

- *Fabrication of the carbonate eutectics*, based on Li_2CO_3-K_2CO_3 (62-38 mol%) or Li_2CO_3-Na_2CO_3 (52-48 mol%) by heating the right proportions in CO_2-air atmosphere (30-70 vol%) up to 650°C (heating rate: 3°Cmin^{-1}) during 1 hour in order to melt the carbonate mixture and form an homogeneous eutectic phase. It is then slowly cooled down.

- *Fabrication of the composite powders* by mixing the grounded solid bulk resulting form the carbonate preparation with the oxide powder respecting the oxide:carbonate ratio 70:30 wt%. This new mixture is heated again up to 650°C for 1 hour in the same conditions than previous ones, and finally air-quenched.

- *Fabrication of the pellets*: 0.9 g of composite powder are first pressed in a stainless steel mold (13 mm of diameter) under 1 ton and relaxed to expel trapped gases, and

then under 4 tons for 5 minutes. The pellets are finally annealed at 600°C for 1 hour, with a 5°Cmin^{-1} heating and cooling rates.

- For electrical measurements by impedance spectroscopy, gold paste is painted on both faces of the pellet, then annealed following the temperature histogram depicted in figure 3.1. Resistance of both electrodes is measured and must be lower than 1 Ω in order to avoid additional contributions in the total system impedance.

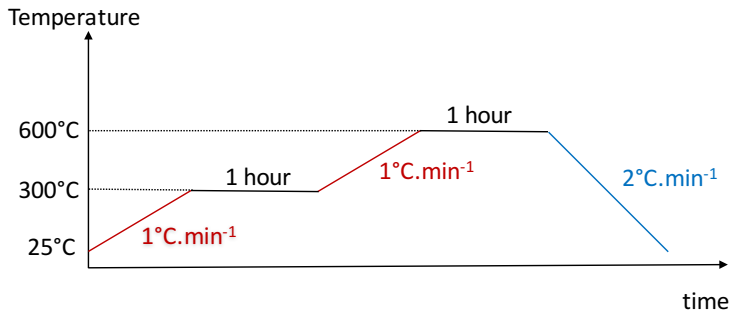

Figure 3.1: Scheme of the temperature program followed to anneal the gold electrodes on the pellets before electrical characterisation.

As already mentioned, sample compositions varied as a function of the oxide phase and carbonate composition. Acronyms, composition and commercial references are given below:

YSZ - Yttria Stabilised Zirconia: $Zr_{0.84}Y_{0.16}O_{2-\delta}$, Tosoh-Zirconia TZ-8Y, Tosoh corporation;

GDC - Gadolinia-doped Ceria: $Ce_{0.9}Gd_{0.1O2-\delta}$, GDC-10-M, Fuel Cell Materials and CGO 90/10 HSA, Anan Kasei Co, LTD;

CeO_2 - CeO_2 Alfa aesar 99.5%;

TiO_2 - TiO_2 99.5% Alfa aesar;

LiK stands for Li_2CO_3-K_2CO_3, 62-38 mol%, made of Carbonate lithium Sigma 99% and Carbonate potassium Sigma 99%;

LiNa stands for Li_2CO_3-Na_2CO_3, 52-48 mol%, made of Carbonate lithium Sigma 99% and Carbonate sodium Sigma aldrich, 99.8%.

3.2.1 Thermal analysis

Thermo-gravimetric analysis-differential thermal analysis (TGA-DTA) were carried out on a *TGA-DTA Setaram SETSYS-1750 CS Evolution* thermal analyzer at a rate of 5°C min^{-1} up to 600 °C on heating and cooling. Al_2O_3 crucibles were used. Experiments were carried in different atmospheres: dry air (O_2/N_2- 20%/80%) or hydrogen (100%). For selected cases, TGA-DTA analysis was coupled with gas chromatography-mass spectrometry (GC-MS) (*Trace 1300 Gas Chromatograph and ISQ QD Single Quadrupole, Thermo Scientific*) to characterize the exhaust gas. In these cases, experiments were carried out in argon at a rate of 10°C min^{-1} up to 800°C on heating.

3.2.2 XRD characterization

X-ray diffraction (XRD) were used to characterise the composite samples. XRD patterns were recorded at room temperature using a *X'Pert PRO ele PANalytical* diffractometer using the Cu K_α radiation (λ=1.54 Å) with 2θ varying from 20 to 80°and a step of 0.04°during 50 minutes.

3.2.3 IR and Raman spectroscopy

Raman spectra of the composite electrolytes were acquired in a *Lab Raman HR-800* (*Horiba-Jobin-Yvon*) spectrometer coupled to an *Olympus* BX41 microscope using a 10X objective lens to focus the laser beam on the sample. Spectra were recorded from 50 to 2000 cm^{-1}, using a diffraction grating of 1800, hole of 300 μ, and a He-Ne laser with a wavelength of 632.81 nm. On the other hand, Infrared (IR) spectra were obtained from the power of the composite materials using a Nicolet 6700 IR spectrometer between 500 and 2000 cm^{-1}.

3.3 Electrochemical characterisation

3.3.1 EIS experimental details

The impact of the oxide phase conductivity and the carbonate phase one is determined by electrochemical impedance spectroscopy (EIS). A usual 'home-made' set-up built by M.C. Steil (*Plateau M2E, Matériaux Electrochimiques pour l'Energie, Saint Martin d'Heres*) was used (photograph in figure 3.2a-b) for most of the impedance spectroscopy analysis. The sample covered by both painted gold electrodes is placed between one gold point electrode and one gold grid as current collectors (3.2c). Platinum wires are used for the current collection and the connection between the gold grid and point electrode and the potentiostat connexion. This configuration corresponds to a symmetric experimental setup, since the two electrodes have the same chemical composition and two parallel surfaces of exactly the same size. In this configuration, it is possible to compute the conductivity from the resistance of the sample, by applying the following equation:

$$\sigma = \frac{1}{R}\frac{l}{S} \tag{3.1}$$

where R is the resistance of the sample obtained from the EIS measurement, and l is the thickness of the pellet, while S is the surface area of the electrodes. Furthermore, the following form of the Arrhenius equation can be applied to represent the dependance of the ionic conductivity of the oxide-carbonate electrolyte on temperature:

$$\sigma = Aexp(-\frac{E_{act}}{k_B T}) \tag{3.2}$$

where σ is the conductivity previously calculated, T the temperature, A is a scaling factor, k_B is Boltzmann constant, and E_{act} the activation energy. If the scaling factor and the energy

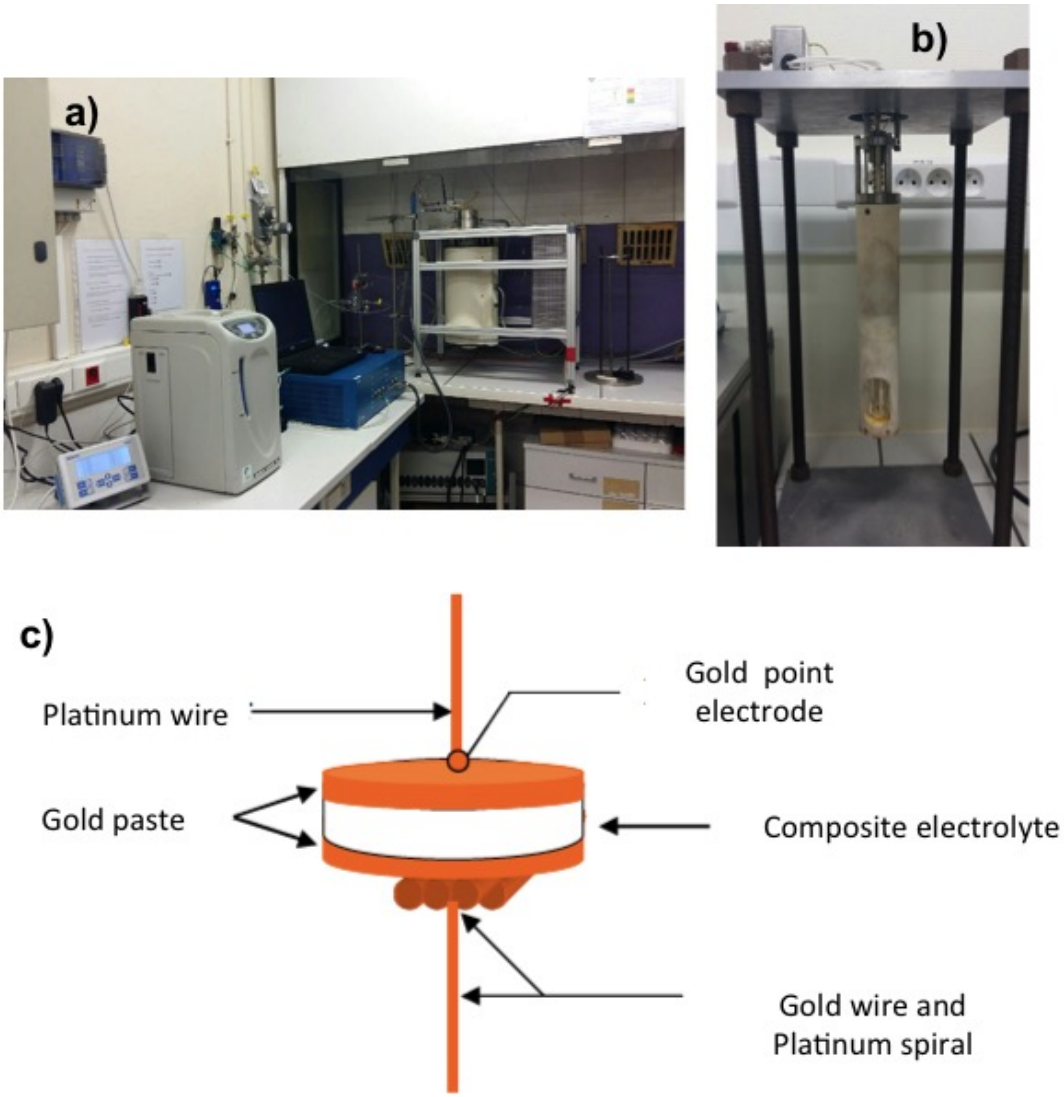

Figure 3.2: a) Photograph of the set-up used for impedance spectroscopy measurements at high temperature in controlled atmosphere. Illustration in the case of the more complete, *i.e.* 'Hydrogen', set-up. b) Photograph of the set-up in which is placed the sample, before being introduced in the furnace. c) Schematic representation of the symmetric configuration used for the EIS measurements.

related to the conduction mechanisms are constant, then $log(\sigma)$ vs. $1/T$ (Arrhenius plot) is a linear function and the activation energy can thus be easily derived from EIS measurements performed at different temperatures.

Resistances were measured by impedance measurements performed in both oxidising (dry air) and reducing (23 % of H_2 diluted in N_2) atmospheres. Dealing with potentiostats, one *Biologic SP-300* was connected to the 'hydrogen' set-up while a *Modulab* was used for the 'oxygen' set-up. Concerning the atmosphere controls, mass flow meters allowed us to fix the flow and control the ratio in the case of H_2-based atmosphere. The total flow was kept constant and equal to 50 mLmin^{-1} for measurements in air and 65 mLmin^{-1} for measurements in H_2. H_2 was produced by water electrolysis through a *PGH2-100* (*DBS*) electrolyser.

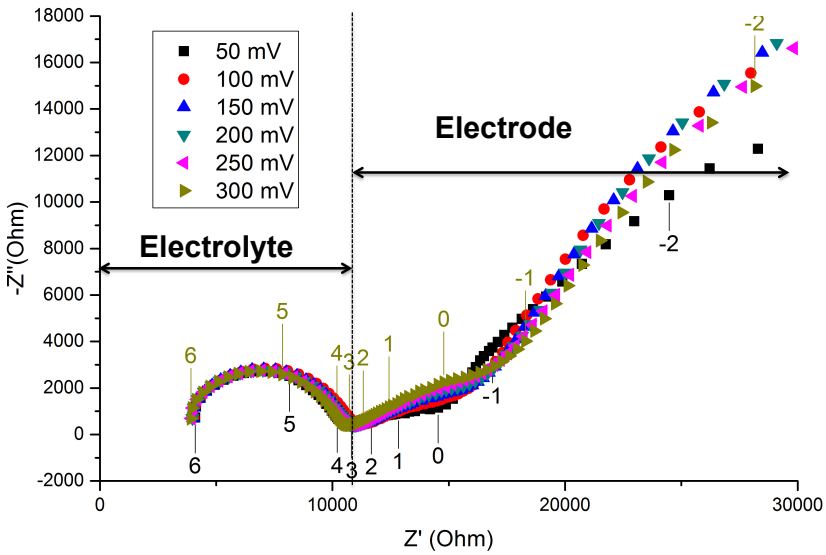

Figure 3.3: Nyquist impedance diagrams measured at 385 °C under ambient air with different signal amplitudes (from 50 to 300 mV) on a YSZ-LiK composite.

Concerning the acquisition parameters, as only two electrodes are necessary for electrical conductivity measurements, no dc polarisation was applied (Open Circuit Voltage OCV=0 because of the symmetry of the configuration). All measurements were performed in the 1 MHz-1 mHz frequency range with 11 points per decade of frequency. 30 minutes were required to reach the system stability after each 5 or 10°C as temperature increment. An ac signal amplitude of 100 mV was used in potentiostatic mode, in respect to the linearity of the system. Figure 3.3 illustrates the impact of the ac signal amplitude on the system response.

This is a way also to identify the electrolyte contribution versus the interfacial electrode behaviour. Electrolyte resistance is read on the left of the impedance diagram when using Nyquist plane. It is worth explaining that the electrolyte is less affected by the variation of the signal amplitude than the electrodes phenomena. Therefore, the unchanged part of the plot in figure 3.3 (at high frequencies, left of the Nyquist plot), where diagrams obtained

applying different amplitudes correspond, can be associated with the electrolyte and used to derive its resistance. The part that changes by varying the signal amplitude (at the lowest frequencies used, right of the Nyquist diagram) is, instead, ascribed to the electrodes.

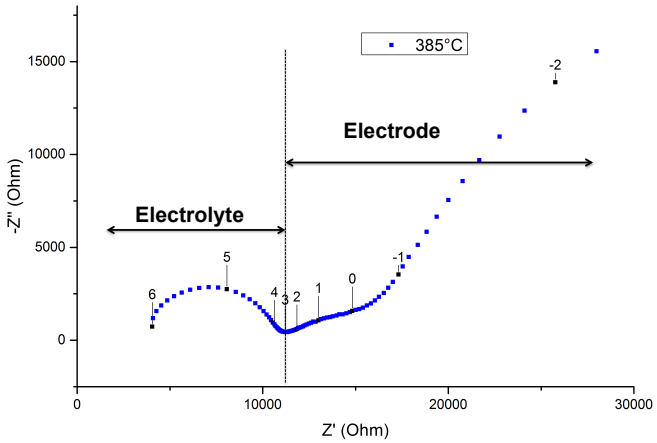

Figure 3.4: Typical impedance diagrams measured at low temperatures for a YSZ-LiK composite.

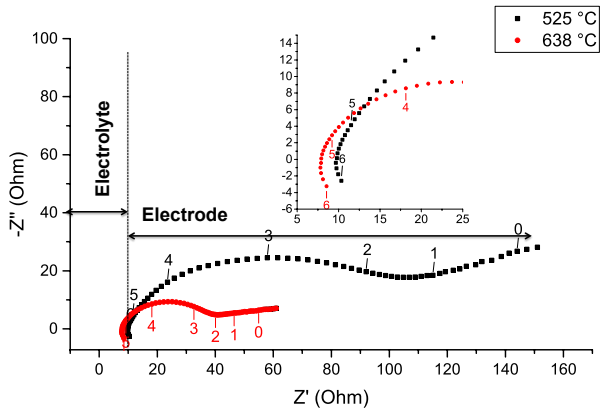

Figure 3.5: Typical impedance diagrams measured at high temperatures for a YSZ-LiK composite.

When the EIS measurements are performed increasing the temperature, not only the electrolyte resistance was modified because of the temperature activation, but we also noted two main kinds of diagram shape, as shown in figure 3.4 and 3.5, at low and high temperature respectively. As described in Benamira's previous works,[19] at low temperatures (figure 3.4), the carbonates are solid and it is quite difficult for ions to migrate through this insulating phase. Oxide ions can still migrate in the solid oxide, but they are partially blocked by

the solid carbonate phase. Therefore, the composite behaviour is assimilated to a dielectric material and the high frequency part corresponds to a semi-circle in Nyquist coordinates, due to resistive and capacitive effects in parallel. At what is called high temperature (figure 3.5), that means at temperatures higher than the carbonate melting temperature, the electrolyte impedance is reduced to a pure resistance because of an easier conductivity through the molten phase. The oxide phase in that temperature range just acts as a blocking phase towards the ion displacement. Thus the associated resistance corresponds to the intercept of the diagram with the x-axis. Furthermore, at high temperatures, we can observe the presence negatively aligned points visible in figure 3.5. They are due to the connexion contributions introducing an inductive component which can be subtracted for a higher accuracy of the resistance value.

3.3.2 Electrochemical behaviour of oxide-carbonate composites

Table 3.1 reports the main parameters describing the electrochemical behaviour of GDC-, YSZ-, and TiO_2-based composites with LiK or LiNa eutectic mixtures. In the following we will discuss data and compare in detail the performances of the different materials, trying to understand the effect of the oxide and carbonate phases and of the operating atmosphere on the properties of the composite electrolytes.

		Air				H_2			
Composite	Cycle	E_{act}^{LT}	E_{act}^{HT}	T_t	T_m/T_c	E_{act}^{LT}	E_{act}^{HT}	T_t	T_m/T_c
GDC-LiK	H	1.20[a]	0.40[a]	485[a]	485[a]	1.24	0.52	467	-
GDC-LiK	C	-	-	-	440	1.50	0.32	412-427	-
								311-350	-
GDC-LiNa	H	1.40	0.26	508	501[a]	1.30	0.18	466	-
GDC-LiNa	C	-	-	-	-	1.10	0.03	415-450	-
								320-345	-
YSZ-LiK	H	1.61	0.13	493	484	1.70	0.28	466-496	479-494
		1.41	*0.08*	*502*					
YSZ-LiK	C	1.74	0.89	409	437	1.28		-	417
		1.08		-					
YSZ-LiNa	H	1.50	0.25	505	476-494	1.42	0.26	474	473-493
YSZ-LiNa	C	1.41	0.59	440	461	1.08		-	442
TiO_2-LiK	H	0.84	1.21	500	486-492	0.98	1.69	321, 405	486, 475
						0.81			
TiO_2-LiK	C	0.87	-	-	-	0.34	0.74	418	-

[a] See ref. [19]

Table 3.1: Selected characteristic features of different oxide-carbonate composite electrolytes measured either in oxidising (air) or reducing (H_2) atmosphere during heating (H) or cooling (C) cycles: low (E_{act}^{LT}, in eV) and high (E_{act}^{HT}, in eV) temperature activation energies, transition temperature observed in the Arrhenius diagram (T_t, in °C), compared with the melting (T_m, in °C) or recrystallization (T_c, in °C) temperatures of the carbonate phase as measured through TGA-DTA experiments performed on the composites. Italic values for YSZ-LiK are referred to the measures made on the automated setup (see the text for details).

3.3.2.1 GDC-based composites

The main features of GDC-based materials have been described in a previous work performed in our group on GDC-LiK materials.[22] Here we use the Arrhenius plot of a GDC-LiNa composite, obtained by measuring its conductivity in air (figure 3.6), to describe the electrochemical behaviour of these electrolytes. The key electrochemical feature of carbonate-oxide composites is the elongated Z-shape of the Arrhenius conductivity diagram, which can be separated in a low temperature and a high-temperature region, separated by a discontinuity:

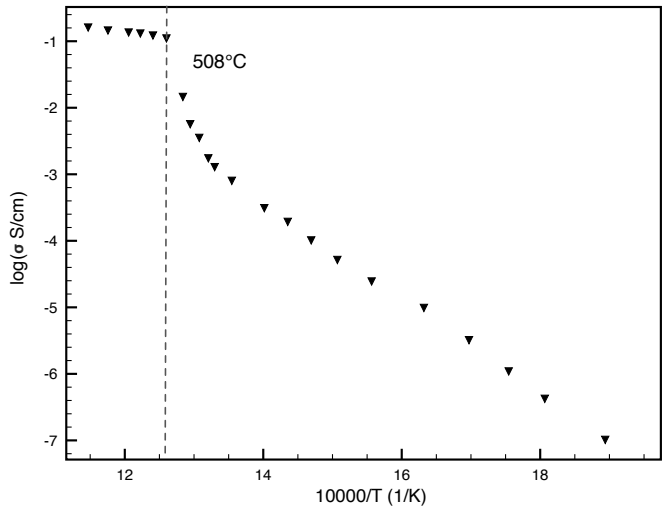

Figure 3.6: GDC-LiNa composite conductivity under oxidising conditions (dry air) during heating.

- At temperatures lower than the melting point of the mixed carbonate, the total conductivity of the oxide-carbonate composite is generally relatively close to the bulk conductivity of the pure oxide. The low temperature activation energies generally exceeds the typical values measured for the pure oxide. For example, in the case of figure 3.6, the low temperature activation energy of 1.40 eV is higher than the one of pure GDC (1.00 eV).[19] We can thus assume that, below the melting temperature of the carbonate phase, the ionic conductivity is mainly controlled by oxide ions, partially inhibited by the presence of solid carbonates.

- The change of slope in figure 3.6 is observed at a transition temperature of about 508°C, that nicely corresponds to the Li-Na carbonate mixture melting point (501°C[19]). We can thus observe that at temperatures around the melting point of the mixed carbonate phase, the conductivity increases drastically by about 2 orders of magnitude. Carbonates are partially molten in this domain and another conductivity pathway is surely favoured by the presence of the molten phase. Considering the studies of J. Maier[78–84] on the ionic conduction in boundary regions, one may attribute this rise in conductivity to the effect of a superionic pathway at the interface between carbonates

and oxide, with the formation of a space charge zone with an excess of microstructural defects allowing a faster movement of ions compared to in the single phases. It is difficult to judge the importance of this phenomenon; nevertheless, the partial transformation of solid to molten carbonates has surely an important influence.

- At higher temperatures, values of conductivity close to 0.1 S/cm are generally obtained for GDC-materials. Transport is mainly due to the conduction of ions in the molten phase, partially inhibited with respect to the pure molten carbonate phase because of the solid oxide environment, as indicated by the high temperatures activation energies that are close, but generally lower than the one of the pure carbonate phase. In the case of GDC-LiNa materials, for example, we obtained a value of 0.26 eV, close to the one of the pure Li-Na eutectic mixture.[100]

3.3.2.2 YSZ-based composite

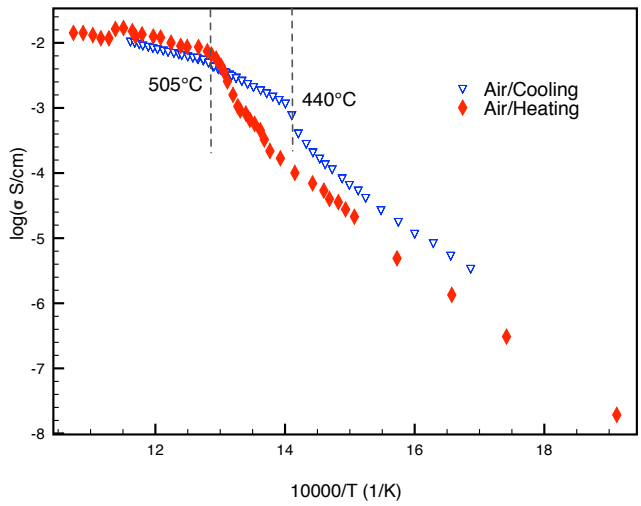

Figure 3.7: YSZ-LiNa composite conductivity under oxidising conditions (dry air) .

The behaviour of YSZ-based composite is shown in figures 3.7 and 3.8 for LiNa or LiK materials, respectively. At a first look, the Arrenius plots show the same features previously described for GDC-composites. During the heating cycle and before the carbonate melting, the electrical behavior of the composite is close to pure YSZ one, considering that oxide ions are the main species moving in the material, even if partially blocked by carbonate solid phase yielding to higher activation energy than for pure YSZ (1.5 and 1.61 eV for YSZ-LiNa and YSZ-LiK, respectively, instead of 1.1 eV for YSZ). At temperatures higher than 500°C, after the carbonate being fully molten, the activation energy is rather low (0.25 eV in the case YSZ-LiNa and 0.13 eV for YSZ-LiK), close to the one of the pure carbonate phase.[207] Conductivity increases again of about 2 orders of magnitude in correspondance of the discontinuity of the Arrhenius plot observed in both case at temperatures around the melting point of the carbonate phase, as confirmed by the TGA-DTA analysis of the samples we will discuss in section 3.4 . Finally, it reaches a maximum value of about 0.01 S/cm

at high temperatures, which is lower compared to the conductivity reached by GDC-based electrolytes in the same temperature range.

Moreover, these YSZ-based materials show another important difference compared to GDC ones. In order to discuss this point, here it is important to note that the measures were performed with a manual setup. It is to say that we performed the experiments during the day, having care to respect the time between two subsequent measurements and to check the stability of the temperature and of the diagrams. In the case of YSZ-LiNa, we can observe that the conductivity continues to increase almost linearly after 500°C, but there is a small drop after about 610°C. In this case, we were able to start performing the cooling cycle right after the end of the heating one and we observed that the conductivity decreased linearly with an actvation energy of about 0.59 eV at high temperatures and of 1.41 eV at low temperatures where it almost reaches the same level obtained during the heating. A discontinuity is observed at 440°C, which can correspond to the recrystallization of the carbonate phase. In the case of the YSZ-LiK materials, after the system was kept at 620°C during the night, the Arrhenius diagram for the cooling cycle showed a sligthly different beaviour: the conducitivity dropped drastically overnight and then it started to decrease linearly with an activation energy of 0.89 eV obtained at temperatures higher than 409°C , where a discontinuity is observed. After this temperature, the Arrhenius plot can almost be superposed to the one obtained at low temperatures during the heating cycle. In order to verify the reproducibility of these observations, the measure was repeated on the YSZ-LiK sample with higher accuracy and an automated setup (cf. figure 3.9): the system was heated at about 620°C, kept at this temperature during several days until we did observe any variation in the measured resistance. Finally, it was cooled down obtaining the Arrhenius plot in figure 3.9. As we can see, the results of the heating phase are in excellent agreement with the ones already discussed. However, the cooling cycle in this case shows a linear variation of the conductivity over the whole temperature range with an activation energy of 1.08 eV and a behaviour extremely close to the one of the pure YSZ phase.

All these observations suggest that in the case of the YSZ-carbonate materials, at about 610-620°C, there is some reactivity taking place between this oxide and the carbonate phase, probably with the formation of zirconate phases and the release of CO_2. Zirconates have much lower conductivities values compared to the composite or to YSZ and the conductivity level is thus determined by the conduction of oxide ions in the YSZ oxide phase. As we will see in the section dedicated to the thermal analysis, TGA-DTA analyses, especially if coupled with mass-spectrometry to analyse the exhaust gas, can help us elucidating the process taking place.

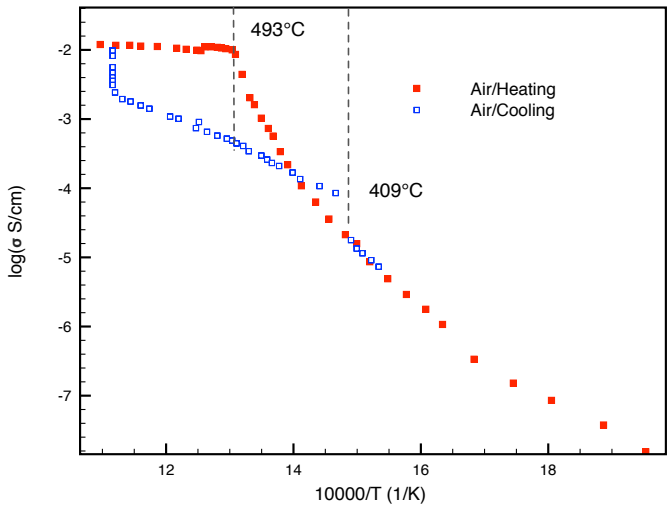

Figure 3.8: Arrehenius plot of the YSZ-LiK composite conductivity measured under oxidising conditions (dry air).

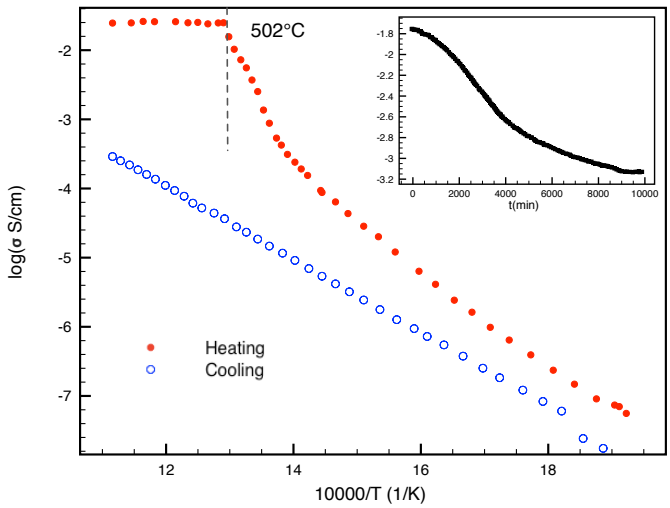

Figure 3.9: Arrehenius plot of the YSZ-LiK composite conductivity measured under oxidising conditions using an automated setup. The inset shows the variation of the conductivity over time when the sample is left in air atmosphere at 620°C.

3.3.2.3 TiO_2-$(Li,K)_2CO_3$ composite

Figure 3.10 shows the electrochemical behaviour of the material synthetized by mixing TiO_2 and $(Li,K)_2CO_3$ in dry air. Starting by the data relative to the heating cycle in air, we can observe that the conductivity increases almost linearly while increasing the temperature. The sigmoidal profile characteristic of GDC- or YSZ-based composites is thus not observed in this case, even at temperature definitely higher than the melting point of the eutectic used (488°C). The samples were heated up to 800-900°C in order to verify if any strong variation of the conductivity could be observed at temperatures higher than 600°C, which was the highest temperature reached in the case of all the other composites investigated. An eventual variation of the eutectic mixture composition, for example a reduction of the Li content after the eventual Li intercalation in the oxide lattice, can indeed determine a variation of the melting point of the eutectic mixture. However, all we were able to observe was that the conductivity continued to increase almost linearly until about 800°C, when it started to drastically drop down. Some conductivity jumps can be observed, but they are mainly related to kinetic effects due to the interruption of the measurements overnight. In particular, the first small jump is observed at about 500°C, close to the melting temperature of the carbonate phase. This jump also separates two areas in which the conductivity varies linearly, but with an activation energy of 0.84 eV and 1.21 eV at lower and higher temperatures, respectively. The subsequent cooling cycle is characterized again by a linear variation of the conductivity, that, at low temperatures, catches up with the values obtained for the heating process. This behaviour of the Arrhenius plot and the low conductivity values (0.0003 S/cm at 740°C) clearly suggest the possibility of a strong reactivity between TiO_2 and the carbonate phase taking place already at temperatures close to the melting point of the carbonate phase and possibly leading to formation of titanate phases like Li_xTiO_2, but also $Li_xK_xTiO_2$ or Li_xTiO_2, that are not good ionic conductors. Again, TGA-DTA analyses can help us further elucidating this point.

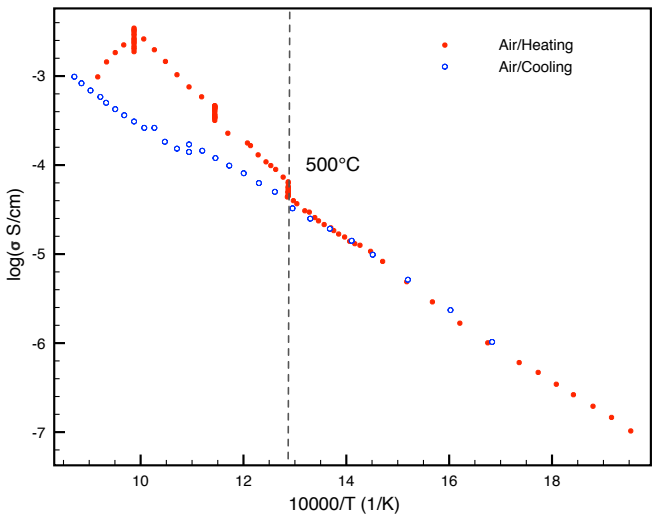

Figure 3.10: Evolution of the conductivity of TiO_2-$(Li,K)_2CO_3$ composite as a function of temperature in dry air.

Now that we have discussed the general electrochemical behaviour of these materials, we can analyse in more details the effect of different parameters on their conductivity.

3.3.2.4 Effect of the carbonate phase

Figure 3.11 illustrates the interest of adding an eutectic mixture of carbonates to an oxide phases such as YSZ. Firstly, as already discussed, the comparison of YSZ based composite to pure YSZ shows a different behavior of the composite as a function of the operating temperature: the variations of YSZ conductivity are linear as expected for such well-known material, while the composite shows like a sigmoïde shape. Furthermore, the composite shows higher conductivities values over all the temperature range, even before the transition temperature, when the carbonate is still in the solid state.

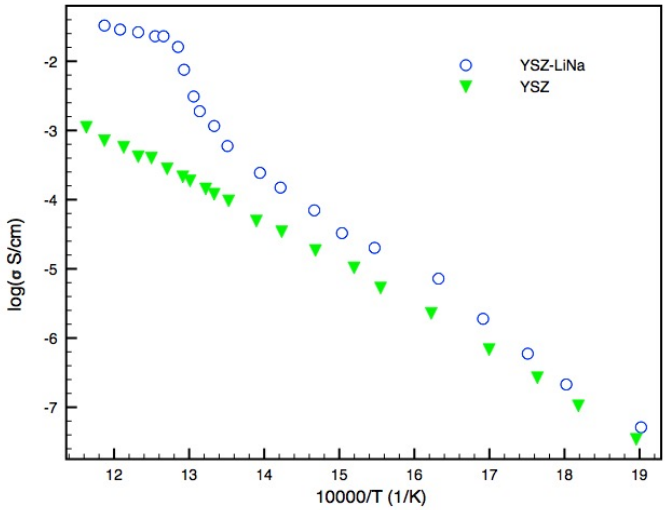

Figure 3.11: Arrhenius plot of pellets made of the YSZ-LiNa composite compared to the one of the pure oxide phase. Measurements performed in air.

The effect of different carbonate phases on the composite electrochemical properties is illustrated in Figure 3.12, comparing YSZ-LiK and YSZ-LiNa conductivities. Kojima et al.[207] reported conductivity values, for $(Li,K)CO_3$ and $(Li,Na)CO_3$ eutectics, of 1.3 S/cm and 2.2 S/cm at 650°C, respectively. When mixed with YSZ in the composite materials, YSZ-LiK is less conductive than YSZ-LiNa, (0.002 S/cm and 0.014 S/cm at 600°C respectively), in agreement with the order of the pure carbonate conductivities. Furthermore, we can observe that, at the highest temperature considered in this study, the composite conductivity is lower than the one of the pure carbonate molten phase. Nevertheless, in MCFCs carbonates are included in a non-conductive Li aluminate matrix that does not allow to reach such high conductivity levels, thus confirming that the present results are still promising.

A more detailed analysis of the effect of the composition of the carbonate mixture has consequently been performed by modifying the $(Li,K)_2CO_3$ eutectic by adding Li, Rb, Cs or La carbonates (5 mol%). The electrical conductivities of GDC composites associated to these modified carbonate phases are reported in figure 3.13 in Arrhenius coordinates (Fig. 3.13a)

and linear coordinates (Fig. 3.13b) in order to focus on the composite electrical behaviour in the highest temperature range, after reaching the (Li,K)CO_3 eutectic melting temperature (T>480°C). As shown in these figures, and according to previous results reported by Lair et al.[208] on the conductivity of the same carbonate phases, composite materials conductivities follow the same trend than the pure carbonate phases: at 550°C, the highest conductivity is measured for an excess of Li ions, while the lowest for La addition. This observation is in line the previous studies of Ferreira et al.[127] dealing with the Li:Na ratio and its impact on the composite conductivity. They observed that the higher the Li^+ concentration in the carbonate mixture the higher the composite conductivity (from 0.079 S/cm to 0.11 S/cm at 566°C when Li:Na goes from 1:2 to 2:1).

We can consequently conclude that the carbonate conductivity directly impacts the composite conductivity in a simple way: the higher the conductivity of the pure carbonate phase the higher the conductivity of the final composite material.

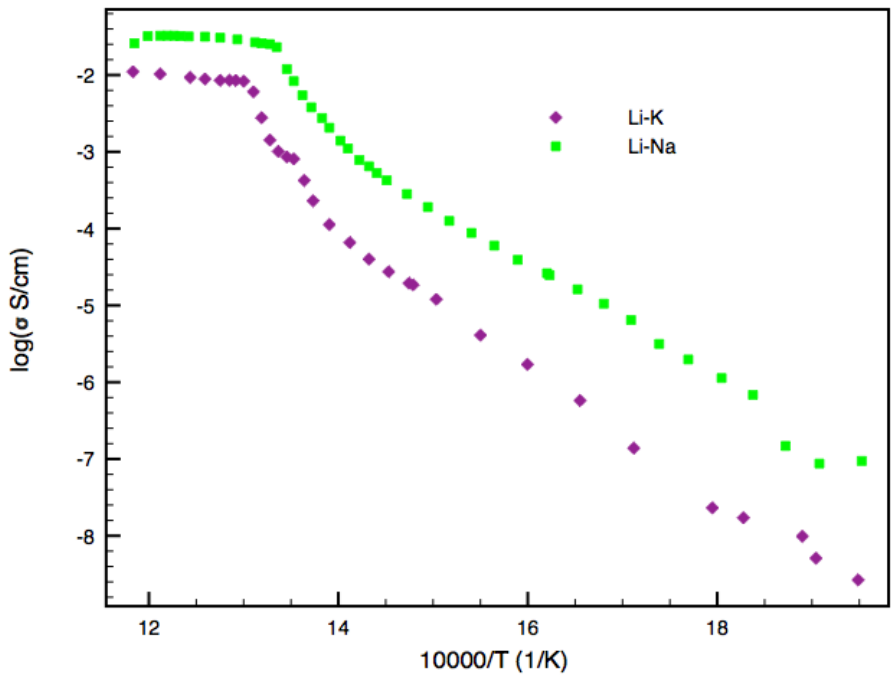

Figure 3.12: Arrhenius plots showing the impact of different carbonate phases on the YSZ-based composite conductivity. Measurements performed in air.

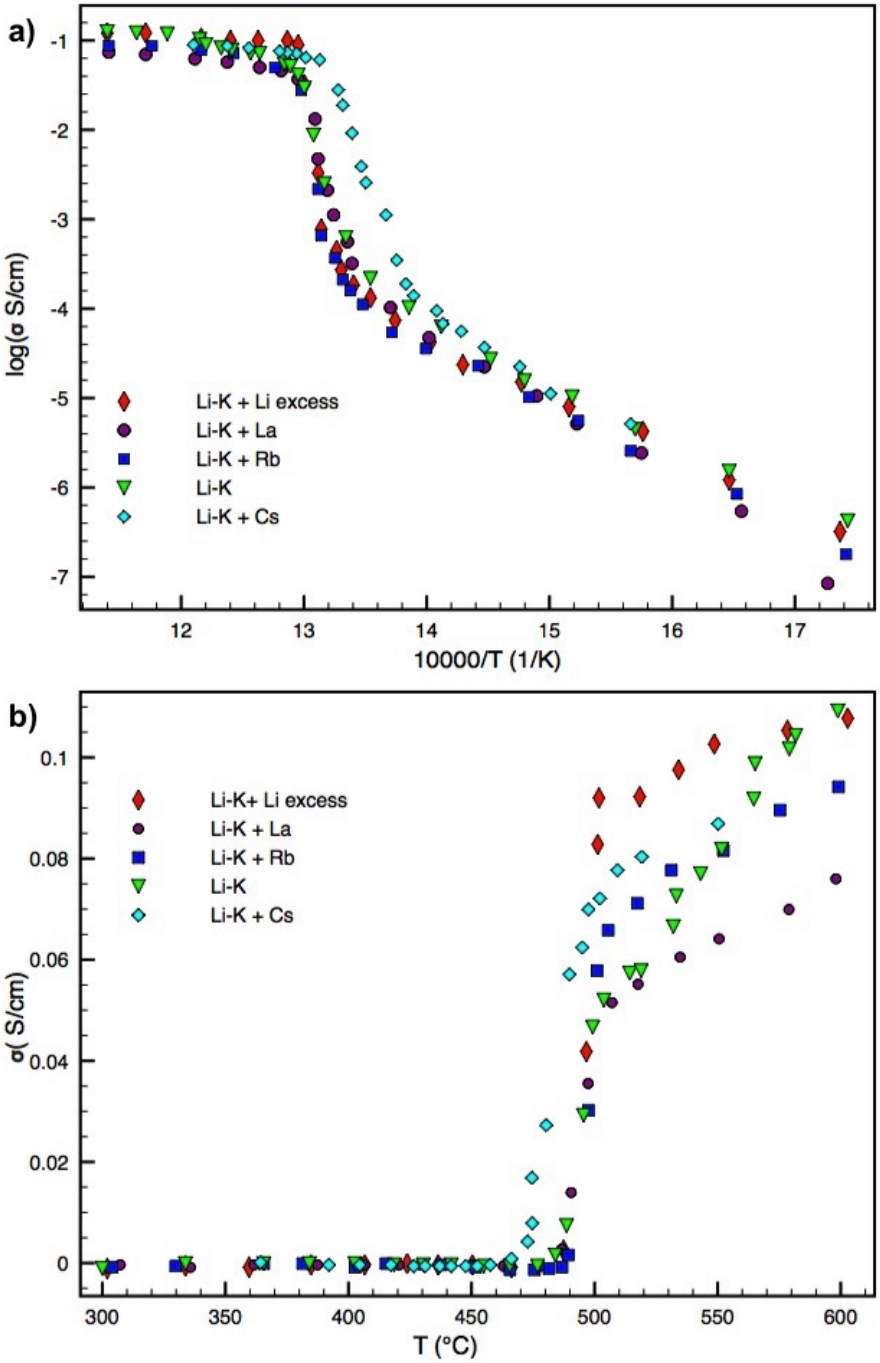

Figure 3.13: Conductivity measurements of GDC-LiK composites, modified by Li, Rb, Cs or La carbonate addition (5 mol%), as a function of temperature. Ambient air is used as gas operating atmosphere. a) Variation reported in Arrhenius coordinates and b) variation reported in linear coordinates.

3.3.2.5 Effect of the oxide phase

Figure 3.14 compares the conductivity in air atmosphere of composites sharing the same carbonate phase, the LiNa carbonate, but with different oxide phases, namely GDC, CeO_2 and YSZ. When looking at GDC- and YSZ-based composites, we can observe that the conductivity of the material with GDC as oxide phase is higher the one based on YSZ. After the transition above the melting temperature of the carbonates, a factor of 4 is gained in favor of GDC compared to YSZ (0.12 S/cm vs 0.03 S/cm respectively), allowing GDC-composites to reach a conductivity higher than 0.1 S/cm at 550°C. It is well-known that GDC pure oxide is more conductive than YSZ in this temperature range and this could have a positive impact determining the higher ionic conductivity of the composite made with the first oxide phase. However, figure 3.14 also shows that composites based on CeO_2 (10000 times less condutor than GDC) have total conductivities values close to the ones of GDC-based materials, and consequently higher also than the ones of YSZ-carbonate materials. These results clearly indicate that the effect of the oxide phase is not straightforward as one could imagine and that it is difficult to explain without taking into account the role of the interfaces.

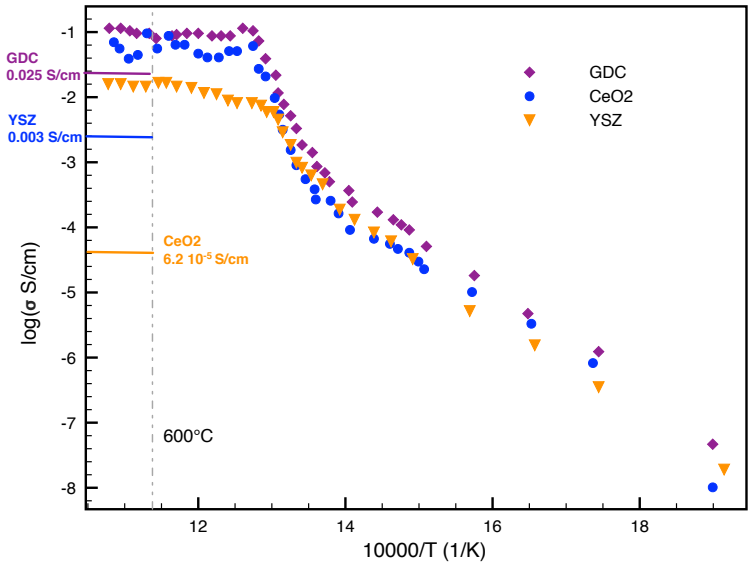

Figure 3.14: Arrhenius plot of oxide-LiNa composites as a function of the oxide phase (YSZ, GDC, CeO_2). Measurements performed in air. The behaviour of the composites is compared to the conductivity level of the pure oxide phases at 600°C indicated by the orizontal lines.[61,209,210]

3.3.2.6 Effect of the working atmosphere

Results shown so far are mainly related to the composite behaviour in air atmosphere. In the following, we will briefly describe the impact of a reducing environment on the electrochemical properties of the different composites we took into account.

GDC-based composites

As reported already in a previous work performed in our group,[22] the electrical behavior of GDC-LiNa in air and in anode gas (H_2/CO_2) is slightly different in terms of transition temperature, occurring at lower temperatures in reducing atmosphere (480°C) than in oxidizing one (510°C). This difference has been reproduced in the conditions of this thesis work (H_2/N_2 mixture, 23% of H_2) as can be seen for both GDC-LiNa and GDC-LiK composites in figure 3.15a-b. Moreover, the conductivity in all the temperature range is slightly higher compared to measurements performed in air (see figure 3.15a).

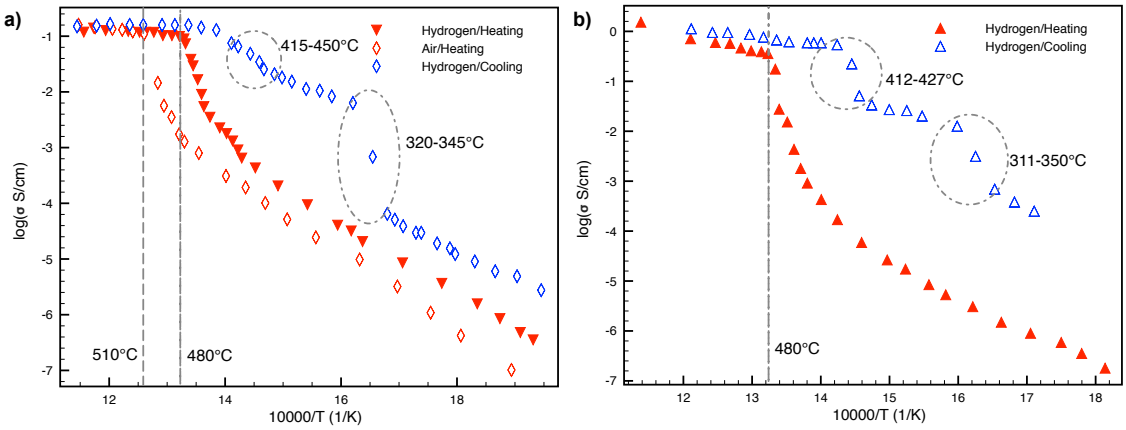

Figure 3.15: a) GDC-LiNa or b) GDC-LiK composite conductivity under reducing conditions (23%H_2 in N_2) during one heating/cooling cycle.

Furthermore, the composites behavior in reducing atmospheres is quite surprising. As reported in figure 3.15, heating and cooling processes are quite different: one jump in conductivity at the melting temperature of the carbonate phase is observed during heating, while during cooling, two drops in conductivity are recorded at around 420°C and 330°C, respectively. Furthermore, a gain of about 1-2 orders of magnitude in conductivity between initial and final stages is observed. Both temperature drops during cooling take place at temperatures lower than the melting one. It is first assumed that the first drop during the cooling process could correspond to the re-crystallisation of the carbonate mixture, even if the difference between melting and recrystallization temperatures represents 50 to 60°C, which is quite large. This assumption has been confirmed by the TGA-DTA measurements previously performed.[19] Concerning the second jump, the only explanation found at this stage is a partial modification of carbonates into hydroxides, whose melting temperature is lower than that of carbonates, thus determining a second conductivity drop at lower temperatures. Hydroxides have, indeed, lower melting points compared to carbonates (LiOH, 471°C and KOH 360°C)[211,212]. This assumption is reinforced when modifying H_2 content in the H_2/N_2 atmosphere. By increasing the amount of H_2, the amplitude of the conductivity drop increases as well (Fig. 3.16), without modifying the behaviour at the lower temperatures. Before and after the two conductivity drops, there is no clear effect of the H_2 amount during cooling. Therefore, these observations can confirm that increasing H_2 amount provokes an accelerated transformation of carbonates into hydroxides. This most probably corresponds

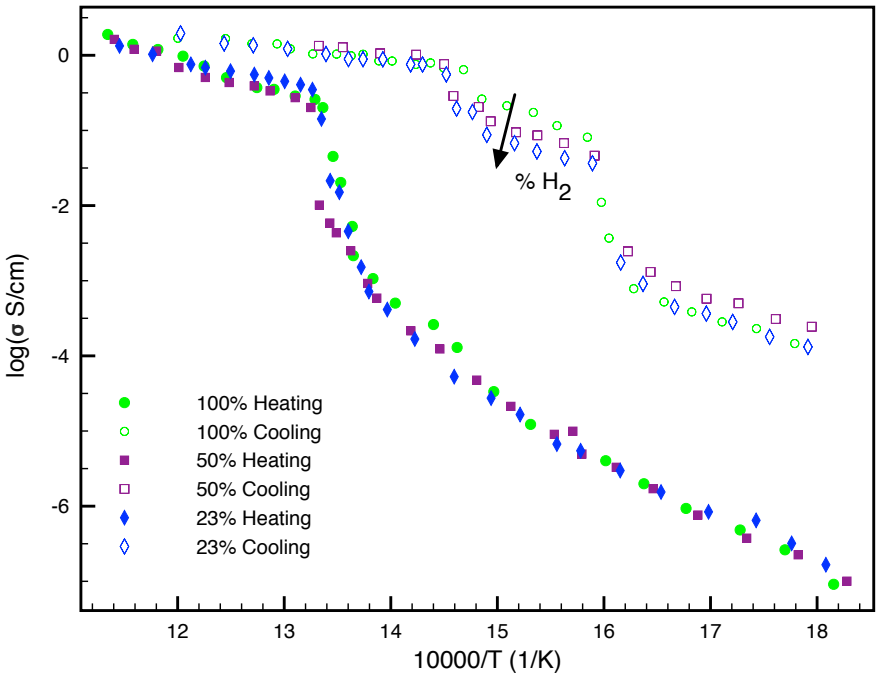

Figure 3.16: Electrical conductivity variations of GDC-LiK during cycling, as a function of the H_2 amount (x) in N_2: x=23%, 50%, and 100%.

to an enhanced reducing effect because of the lower oxygen partial pressure. Electrons are, indeed, required in the mechanism of the hydroxide formation. The origin of the electrons formation and its localisation in the materials to undergo such modification are quite difficult to determine. Zhu attributed the high conductivity levels in reducing environment to the reduction of ceria, which may induce electronic conduction.[146] Anwar et al.[213], in a recent paper, mentioned, instead, that the electronic conductivity of ceria was suppressed by the presence of carbonates. This is also reported by Kim et al.,[214] adding that carbonates are acting as electrical insulators, blocking electronic conduction. According to Rondao et al.[215], there is no direct role of electronic conductivity in H_2 atmosphere when carbonates are associated to ceria. Nevertheless, they suggested the enhancement of redox properties of the oxide surfaces with possible formation of new species. In effect, according to the mechanism previously suggested in our group by Benamira[22], in presence of hydrogen the following reaction can partially occur:

$$H_2 + O^{2-} + 2Ce^{4+} \longrightarrow H_2O + 2Ce^{3+} \tag{3.3}$$

followed by hydroxide formation

$$H_2O + O^{2-} \longrightarrow 2OH^- \tag{3.4}$$

The melting of the hydroxides at lower temperatures will then allow a higher mobility of the

ions involved in the conduction mechanism, which will, in turn, increase conductivity.

YSZ-based composites

Figures 3.18 and 3.17 report the Arrhenius diagrams measured under H_2 environment for YSZ-LiNa and YSZ-LiK, respectively. Similarly to the case of GDC-based materials, during the heating cycle, a decay of about 30 degrees in transition temperature is observed. For YSZ-LiNa, we can see just one transition at about 474°C, while for YSZ-LiK we observed two transtions, the first one at 466°C and the other at 496°C. The main surprising behaviour in this atmosphere is observed at high temperatures. YSZ is the state of the art electrolyte material for high temperature electrochemical applications such as SOFC because of its high stability in reducing and oxidising atmospheres at high temperature. However, at about 520-530°C, the conductivity falls down of about 1 order of magnitude. During the subsequent cooling process, no conductivity drop is observed, the variations are quite linear and the material conductivity obeys a classical Arrhenius law, with activation energy of 1.08 eV for YSZ-LiNa and 1.28 for YSZ-LiK, quite similar to YSZ behaviour without carbonates. This unexpected behavior was reproducible. We already observed some instability at about 600°C for YSZ-carbonate materials in air, that can be attributed to the reactivity between this oxide and the salt. In reducing environment, this reactivity issues thus seems to intervene even at lower temperatures.

Some researches have been carried out to investigate the stability of YSZ in molten carbonates, but the conclusions of these studies are inconsistent. For example, Suski et al.[216] found that YSZ could resist the corrosion in the molten LiNa carbonate eutectics for approximately 1000 hours by monitoring the open-circuit potential values. Irvine et al.[217] showed that a thin YSZ electrolyte is only able to resist the corrosion in the molten Li-K carbonate eutectics under reducing conditions afer investigating the YSZ corrosion by the molten carbonate eutectics in the air, Ar and H_2 atmosphere, respectively. Xu et al. also observed that YSZ corrosion can be retarded in reducing atmospheres.[218]. The majority seems thus to suggest that, when exposed to carbonates, YSZ is likely to be more stable under reducing environments. Our observations are in desagreement with this conlcusion, making the overall results of these stability studies even more controversial. However, the behaviour we observed was found to be reproducible and in agreement with the TGA-DTA analysis we will shortly provide.

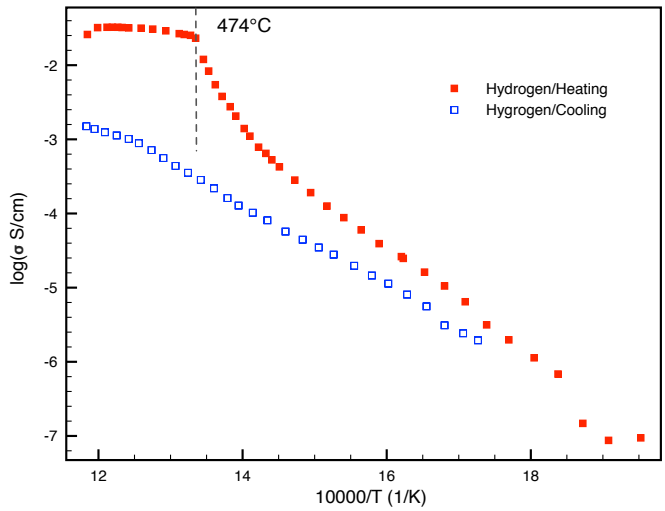

Figure 3.17: Conductivity measurements of YSZ-LiNa composite, during cycling in 23% H_2/N_2.

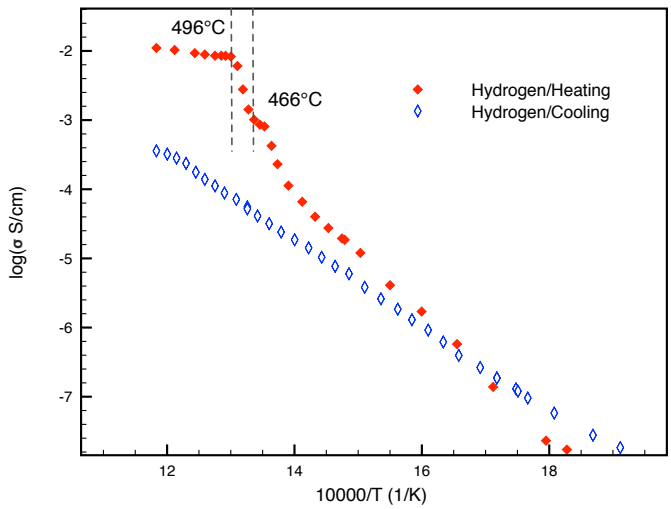

Figure 3.18: Conductivity measurements of YSZ-LiK composite, during cycling in 23% H_2/N_2.

TiO_2-based composites

Results obtained for TiO_2-based composites in reducing atmosphere are even more difficult to rationalize than the ones previously described for the measurements performed in air: at the beginning of the heating cycle the conductivity increases linearly and the profile is almost superimposable with the one obtained in air (cf. figure 3.20); however, at about 321°C, the conductivity starts to increase acting strangely, before decreasing and joining again almost the same values of the curve measured in dry air, at about 475°C (cf. figure 3.20). Three regions with an almost linear variation of the conductivity can thus be observed: the corresponding activation energies are of about 0.98 eV between room temperature and 321°C, 0.81 eV between 321 and 475°C, and of about 1.69 at higher temperatures. Furthermore, during the cooling cycle, the Arrhenius plot does not allow to evidence a clear jump in conductivity, but there is a change in the slop of the Arrhenius curve at about 418°C, with activation energies of 0.74 and 0.34 eV for the linear segments observed, respectively, at temperaratures higher or lower than this point. These observations clearly indicate that there are some chemical processes taking place, in particular associated with the reduction of the sample, as suggested by the conductivity increase, of about 5 order of magnitudes, at the end of the cooling cycle, which can be explained by the introduction of electronic conductivity as in the case of GDC-materials. The reduction of the oxide and also the formation of titanates can also explain the intense blue color assumed by the pellets after these measurements.

Naturally, further structural investigation through XRD and IR/Raman spectroscopy and thermal analysis through TGA-TDA measurements are necessary to better understand the process taking place in these materials and to verify the suggested explanations.

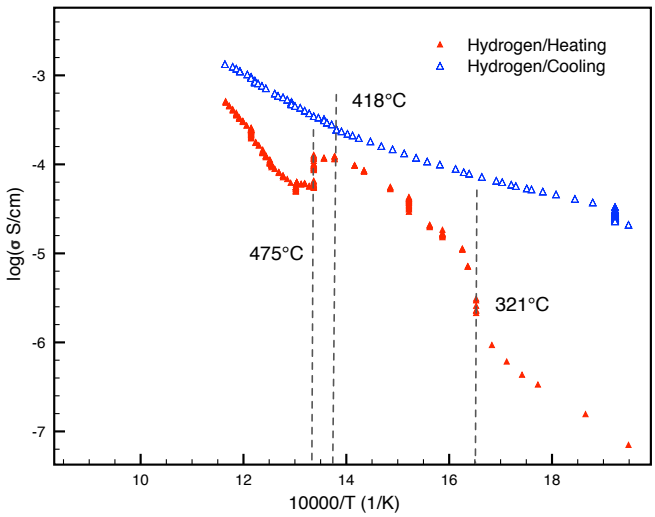

Figure 3.19: Evolution of the conductivity of TiO_2-$(Li,K)_2CO_3$ composite as a function of temperature under reducing (H_2) atmosphere.

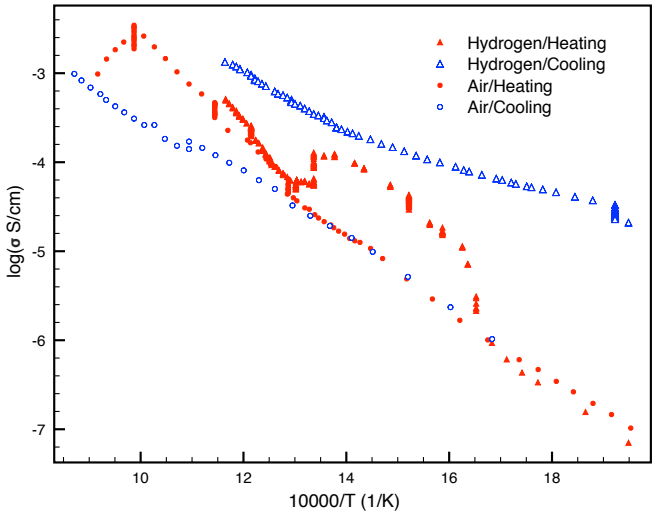

Figure 3.20: Comparison of the Arrhenius plots of TiO_2-$(Li,K)_2CO_3$ materials obtained in air or reducing atmosphere.

3.4 TGA and DTA analyses

TGA and DTA analyses have been performed on the composites in order to determine the chemical and/or physical transformations taking place during the thermal cyles, in order to characterize the transition temperatures observed during the EIS measurements, and to investigate the stability or the possible reactivity issues of these materials.
In a previous work perfomed in our group,[19] the thermal properties of the eutectic carbonate mixtures and of GDC composites with LiK or LiNa carbonates have been already investigated. During heating, these composites showed an endothermic peak detected at high temperatures (485°C and 501°C for samples with the LiK or LiNa eutectic, respectively) that corresponds well to the melting point of the carbonate mixture. It was also observed that the intensity of this peak increased with content of carbonates in the composite.

In order to complete the thermal analysis of the studied composites and to complement the EIS observations, in the following we discuss the TGA-DTA diagrams obtained for YSZ- and TiO_2-based materials in air or H_2 atmosphere.

3.4.0.7 YSZ-$(Li,K)_2CO_3$ composite

Figure 3.21 shows the TGA-DTA spectra measured for YSZ-$(Li,K)_2CO_3$ in air (figure 3.21a-b) or hydrogen (figure 3.21c-d) atmosphere. During the heating cycle (figure 3.21a) an intense peak is observed at about 484°C, in good agreement with the melting temperature of the $(Li_{0.62}K_{0.38})_2CO_3$ eutectic reported in literature (488°C) and close to the transition temperature observed in figure 3.8.[102] Analogously, during the cooling process (figure 3.21b), one exotermic peak at 437°C, can be attributed to the crystallization of the carbonate mixture. Because the instability issues were observed during the EIS measurements in air at temperatures of about 570-600°C, TGA-DTA analysis coupled to mass spectrometry was also performed for this composite. Figure 3.22 shows a broad peak between 570°C and

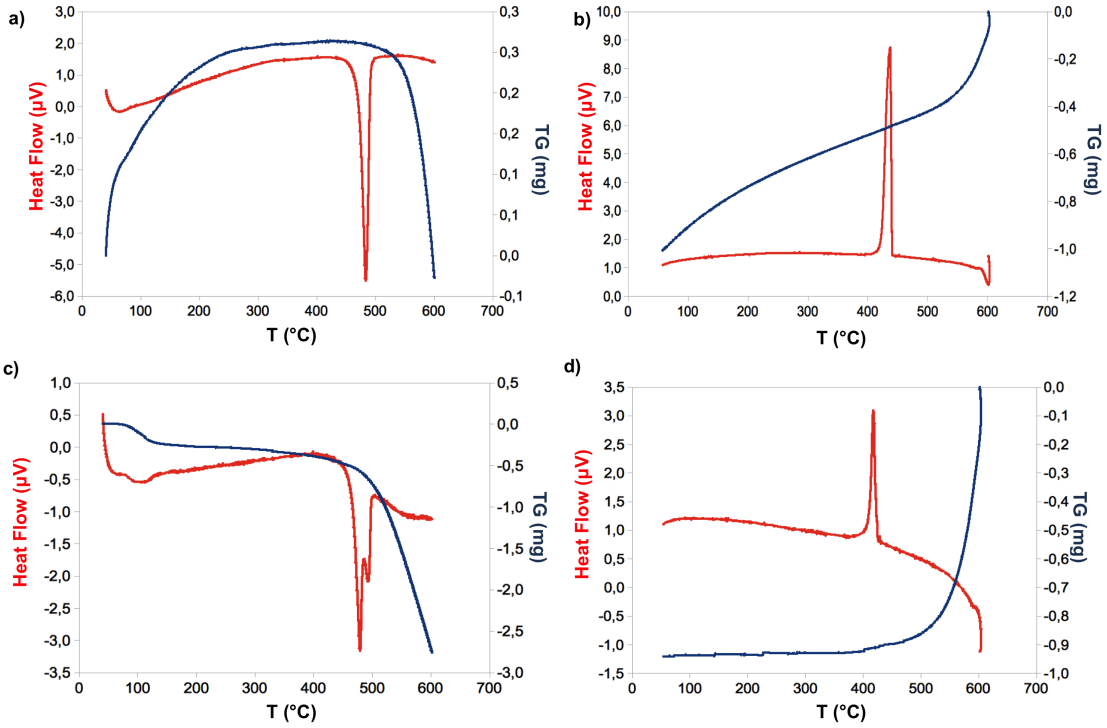

Figure 3.21: TGA and DTA spectra of the YSZ-LiK composite obtained during heating (a and c) or cooling (b and d) in air (a and b) or hydrogen atmosphere (c and d).

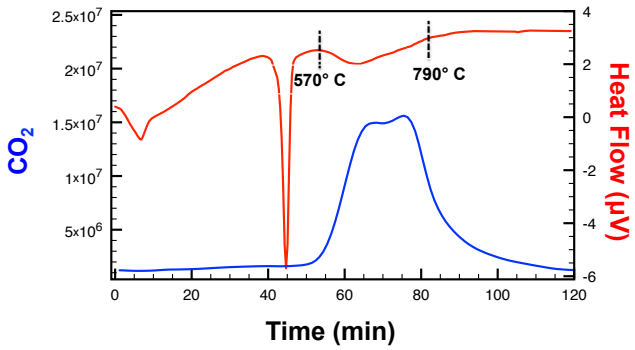

Figure 3.22: DTA and MS spectra of the YSZ-LiK composite obtained during heating.

790°C corresponding to a strong mass loss and associated in the mass spectrum to an intense signal corresponding to mass 44 (CO_2). These observations consequently indicate a process of decarbonation of the composite that can be related to the reactivity between zirconia and the carbonates:

$$M_2CO_3 + ZrO_2 \rightarrow M_2ZrO_3 + CO_2 \tag{3.5}$$

This reaction leads to the formation of zirconates and to the release of CO_2 and generally takes place at temperatures higher than 600°C.[219–221] According to literature, the carbonate decomposition starts at higher temperatures.[221]

Figure 3.21c-d reports the thermal analysis of the same composite in H_2 atmosphere. The behaviour is similar to the one observed in air, but some differences should be discussed. During heating, at about 110°C a small mass loss that can be attributed to water is observed, but more importantly two endothermic peaks are obtained at 479°C and 494°C, in correspondence of the melting of the carbonate phase. This corresponds nicely with the shape of the Arrhenius plot of YSZ-LiK in H_2 environment, where two discontinuities were observed (cf. figure 3.18) At higher temperatures, a broad peak associated to a mass loss is obtained also in this case, but it appears at sligthly lower temperatures (between about 500 and 600°C) compared what observed in air. This can again be attributed to the reactivity between the two phases and is in line with what observed during the EIS measurements in reducing environment, where the instabilities and drop in the conductivity were obsterved at lower temperatures compared to EIS experiments in air. Finally, during the cooling cycle (3.21d), the crystallization of the carbonate phase was observed at 417°C.

3.4.0.8 YSZ-(Li,Na)$_2$CO$_3$ composite

The thermal behaviour depicted in figure 3.23 for YSZ-LiNa is similar to the one just discussed for YSZ-LiK. Here we just underline that the melting of the carbonate phase is observed at 476 and 494°C in air and 473 and 493°C in reducing atmosphere. These temperatures are slightly lower than the melting temperature of 501°C reported in literature for the $(Li_{0.52}K_{0.48})_2CO_3$ eutectic.[102] Crystallization takes, instead, place at 461°C in air and 442°C in H_2 environment. Again the carbonate melting is observed at temperatures close to the transition temperature in the Arrhenius plots in figures 3.7 and 3.17.

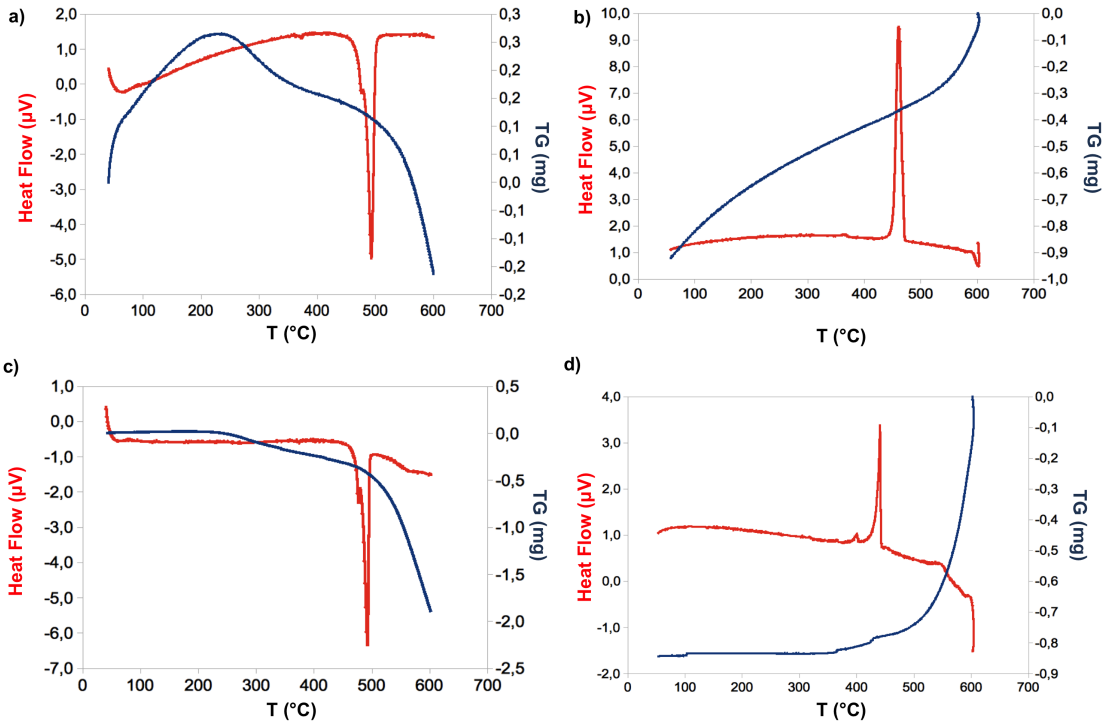

Figure 3.23: TGA and DTA spectra of the YSZ-LiNa composite obtained during heating (a and c) or cooling (b and d) in air (a and b) or hydrogen atmosphere (c and d).

3.4.0.9 TiO$_2$-(Li,K)$_2$CO$_3$ composite

Figure 3.24 reports the TGA-DTA spectra measured for TiO$_2$-LiK in air (figure 3.24a-b) or hydrogen (figure 3.24c-d) atmosphere. The behaviour is definitely different from the one discussed for the YSZ-based composites. During heating cycle in air (3.24a), a first broad peak corresponding to water losses is observed in the DTA plot around 90°C followed by intense endothermic peaks at 486 and 492°C. Again these peaks can be related to the carbonate melting point. However, the TGA shows that this peak is also associated to a consistent mass loss. The same feature characterises the TGA-DTA plot obtained in H_2 atmosphere (figure 3.24c) with endothermic peaks at 456 and 495°C. This process can be

ascribed to the reaction between TiO_2 and the carbonate leading to the formation of titanates, like Li_2TiO_3, and CO_2 following the reaction:

$$M_2CO_3 + TiO_2 \rightarrow M_2TiO_3 + CO_2 \tag{3.6}$$

After this reaction takes place, either in air (figure 3.24b) or reducing (figure 3.24d) atmosphere, the crystallization of the carbonate phase is not observed in the DTA plot and the TGA plot shows low signal corresponding to low weigth losses, evidencing the overall stability of the system. This observation agrees nicely with the fact that in the EIS spectra no conductivity jump is observed during the cooling cycle.

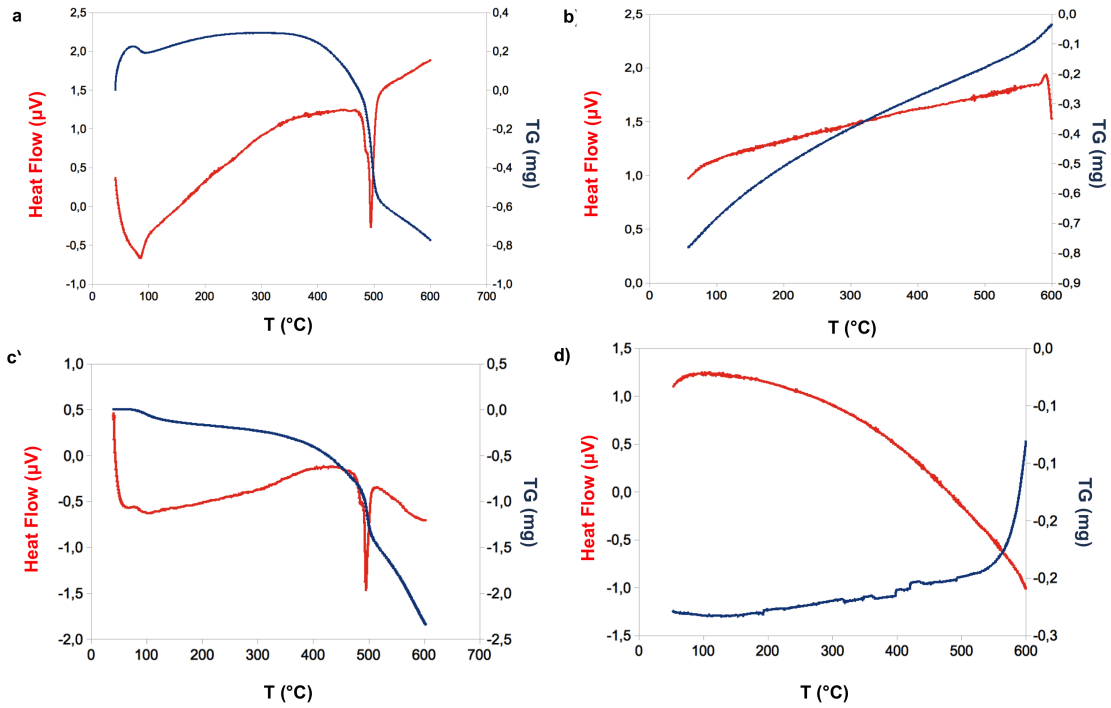

Figure 3.24: TGA and DTA spectra of the TiO_2-LiK composite obtained during heating (a and c) or cooling (b and d) in air (a and b) or hydrogen atmosphere (c and d).

3.5 Premilinary XRD characterization

In order to better undestand the structural properties of the composistes and to identify the products of the eventual reactivity between the oxide and the carbonate, we performed a XRD characterization by analysing the powders obtained after the synthesis and the pellets after the EIS measurement in air or hydrogen atmosphere.

GDC-LiK materials have been studied through XRD in a previous work performed in our group.[19] The results indicated that only the GDC peaks were clearly visible, while the peaks related to Li_2CO_3 and $(Li_{0.50},K_{0.50})_2CO_3$, in good agreement with the expected carbonate melt composition, can be detected as small peaks in the background.

In the following, we will discuss the main results obtained from a preliminary XRD analysis of YSZ- and TiO_2-based materials.

3.5.1 YSZ-$(Li,K)_2CO_3$ composite

In Figure 3.25, the XRD patterns of the YSZ-LiK materials after synthesis and treatment in air or H_2 is compared to the one of the pure YSZ oxide. In all the considered cases, the peaks corresponding to YSZ are the most intense ones. After the synthesis (red pattern in figure 3.25), as in the case of GDC-materials, the major peaks of the oxide are accompanied by low intensity peaks in the background that were identified as Li_2CO_3 (PDF: 04-010-0831) and $Li(_{0.50}K_{0.50})_2CO_3$ (PDF: 00-034-1148), in good agreement with the composition of the eutectic mixture. This indicates the presence of weak traces of crystalline carbonates together with the main amorphous carbonate shell that covers the oxide particles as already described in previous works.[19,49,98,99,103–107]

When the measure is repeated on the material treated in air atmosphere during the EIS measurements (blue pattern in figure 3.25), we can observe the appearance of another pattern with low intensity corresponding to Li_2ZrO_3 (PDF: 00-020-0647). This confirms that the drop in conductivity observed at high temperatures and the mass loss associated to the departure of CO_2 observed in the TGA at 570-790°C in air atmosphere is due do the reactivity between YSZ and the carbonate leading to zirconate formation. The peaks corresponding to this phase are even more intense in the XRD pattern obtained for samples heated in H_2 atmosphere (green pattern in figure 3.25), where they are associated with the appearence of the peaks of K_2CO_3 (PDF: 00-056-0556). It is worth to remind that, in reducing conditions, this kind of reactivity was indeed found to start even at lower temperatures.

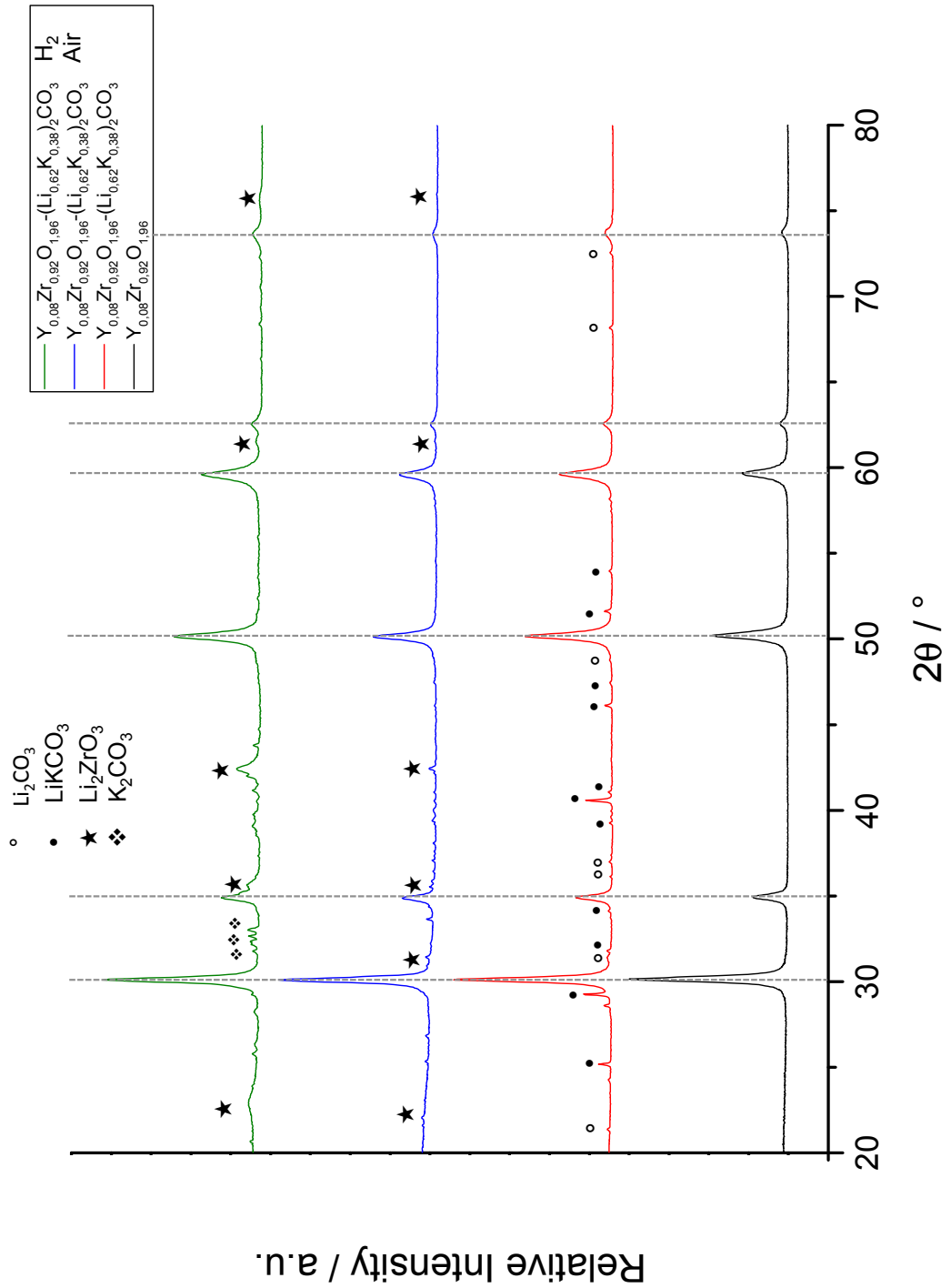

Figure 3.25: XRD patterns for the YSZ-$(Li,K)_2CO_3$ composite obtained after the synthesis and the treatment in air or hydrogen atmosphere. The XRD pattern of the pure YSZ oxide is also reported for comparison.

3.5.2 YSZ-(Li,Na)$_2$CO$_3$ composite

The patterns obtained for the YSZ-(Li,Na)$_2$CO$_3$ composite in figure 3.26 show a more complex appearance and a different behaviour. Already after synthesis (red pattern in figure 3.26), the monoclinic ZrO_2 phase (PDF: 04-007-2132) is clearly present togeter with very weak traces of $Li(_{0.50}Na_{0.50})_2CO_3$ (PDF: 04-011-4058). The formation of Li_2ZrO_3 together with the appearance of Na_2CO_3 pattern (PDF: 04-009-8623) distinguishes the samples treated in air atmosphere during the electrochemical characterization (blue pattern in figure 3.26), as a consequence of the reaction between lithium carbonate and the oxide. This analysis corresponds well with the description of the XRD pattern of composites prepared from the Li-Na eutectic and Yttria-doped tetragonal zirconia (TPZ), where the authors also observed the presence of non-negligible quantities of Li_2ZrO_3.[98] In this context, it is worth to mention the presence in the spectrum of two peaks of relative high intensity indicated with (?) in figure 3.26. The most intense one (at about 38°) was obseved also by Ferreira et al.[98], who explained how this peak could be indexed only to Na_2C_2. However, as also the authors observe, a reducing environment is necessary for the formation of this compound, and this peak is not observed in the XRD of the samples treated in H_2 atmosphere also shown in 3.26 (green pattern). In this last case, we can observe again the monoclinic ZrO_2 phase together with the presence of Li_2ZrO_3 and $(Li_{0.50}Na_{0.50})_2CO_3$.

3.5.3 TiO$_2$-(Li,K)$_2$CO$_3$ composite

Figure 3.27 reports the XRD analysis of the composite materials based on TiO_2. In this case, the patterns are in this case much more complex, expecially for the measurments on samples previously treated in air or hydrogen atmosphere, where we can observe a moltitude of peaks with very low intensity that we were not always able to index. The comparison between the XRD spectra of the pure TiO_2 (black line in figure 3.27) and the TiO_2-(Li,K)$_2$CO$_3$ material after synthesis (red line in figure 3.27) shows that TiO_2 is still present, but some titanate phases, like Li_2TiO_3 (PDF: 00-033-0831) and $K_{0.40}Li_{0.13}Ti_{0.89}O_2$ (PDF: 04-011-447), resulting from the reaction between this oxide and the carbonate mixture, are already formed. The pattern obtained after treatment in air (blu line in figure 3.27) is very complex with several small and also relative high intensity peaks that appears. TiO_2 is not present anymore and Li_2TiO_3 seems to be the more abundant phase accompanied by K_2TiO_3 (PDF: 04-017-3550) and other titanate phases with higher oxygen content, like $K_2Ti_6O_{13}$ (PDF: 00-040-0403) or $Li_2Ti_4O_9$ (PDF: 00-033-0832). It is worth reminding that this samples have been heated up to 800°C during the EIS measurements which could partially explain the extent of the observed reactivity. This reactivity could thus explain why we were not able to observe any discontinuity in the Arrhenius plot measured in air. Finally, the spectrum of the samples treated in reducing atmosphere show the presence of small quantities of TiO_2 and higher amounts of Li_2TiO_3 and $K_{0.40}Li_{0.13}Ti_{0.89}O_2$ already present in the pellets obtined after the synthesis. $KTi_{0.8}O_{16.5}$ is also present in non negligible quantities. This phase was already observed to form when TiO_2 samples exposed to molten carbonates are heated in reducing environments.[222]

To conclude, the obtained patterns are generally extremely complex, expecially for the samples exposed to air or hydrogen, showing a multitude of peaks, sometimes difficult to

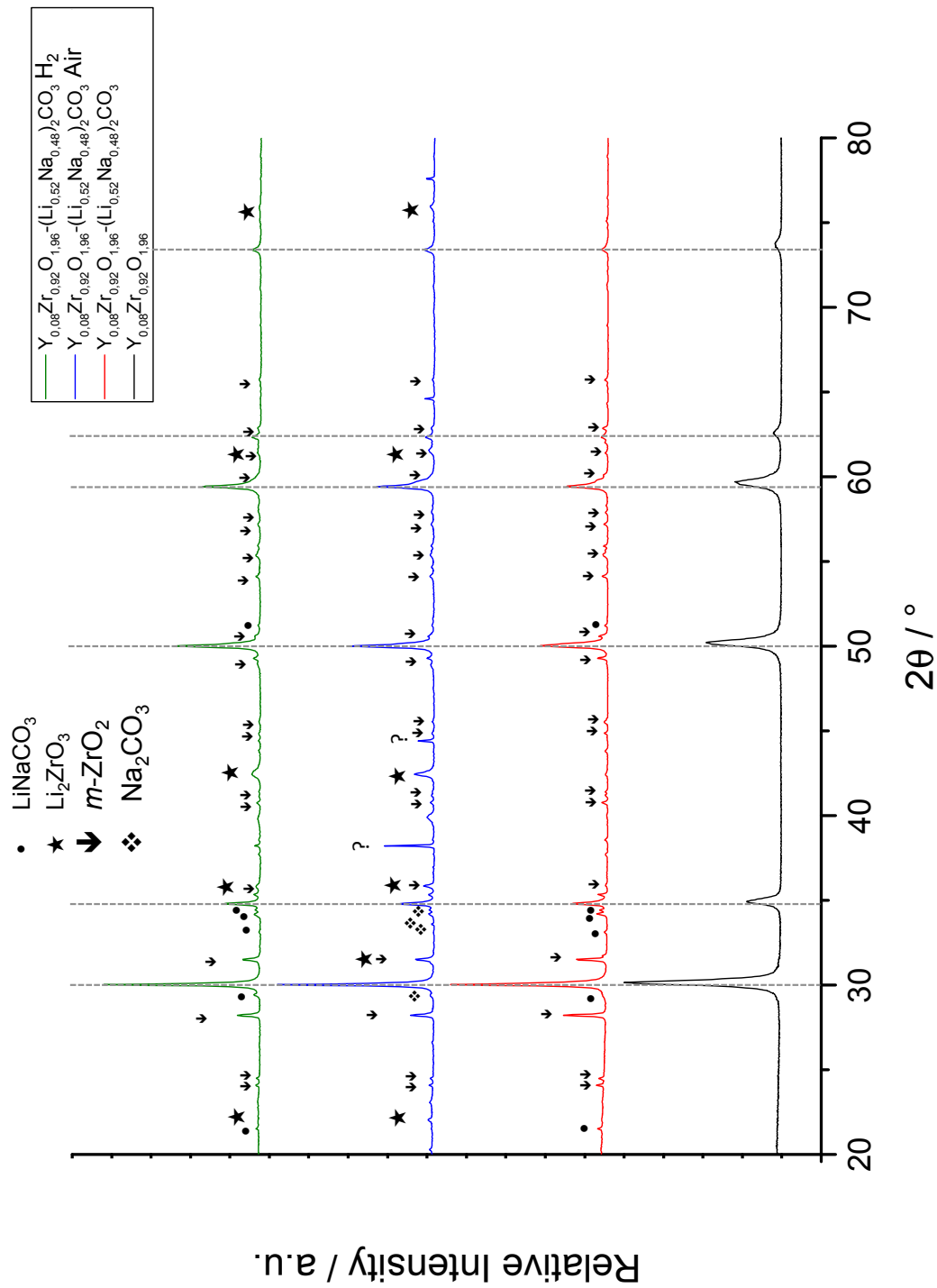

Figure 3.26: XRD patterns for the YSZ-LiNa composite obtained after the synthesis and the treatment in air or hydrogen atmosphere. The XRD pattern of the pure YSZ oxide is also reported for comparison.

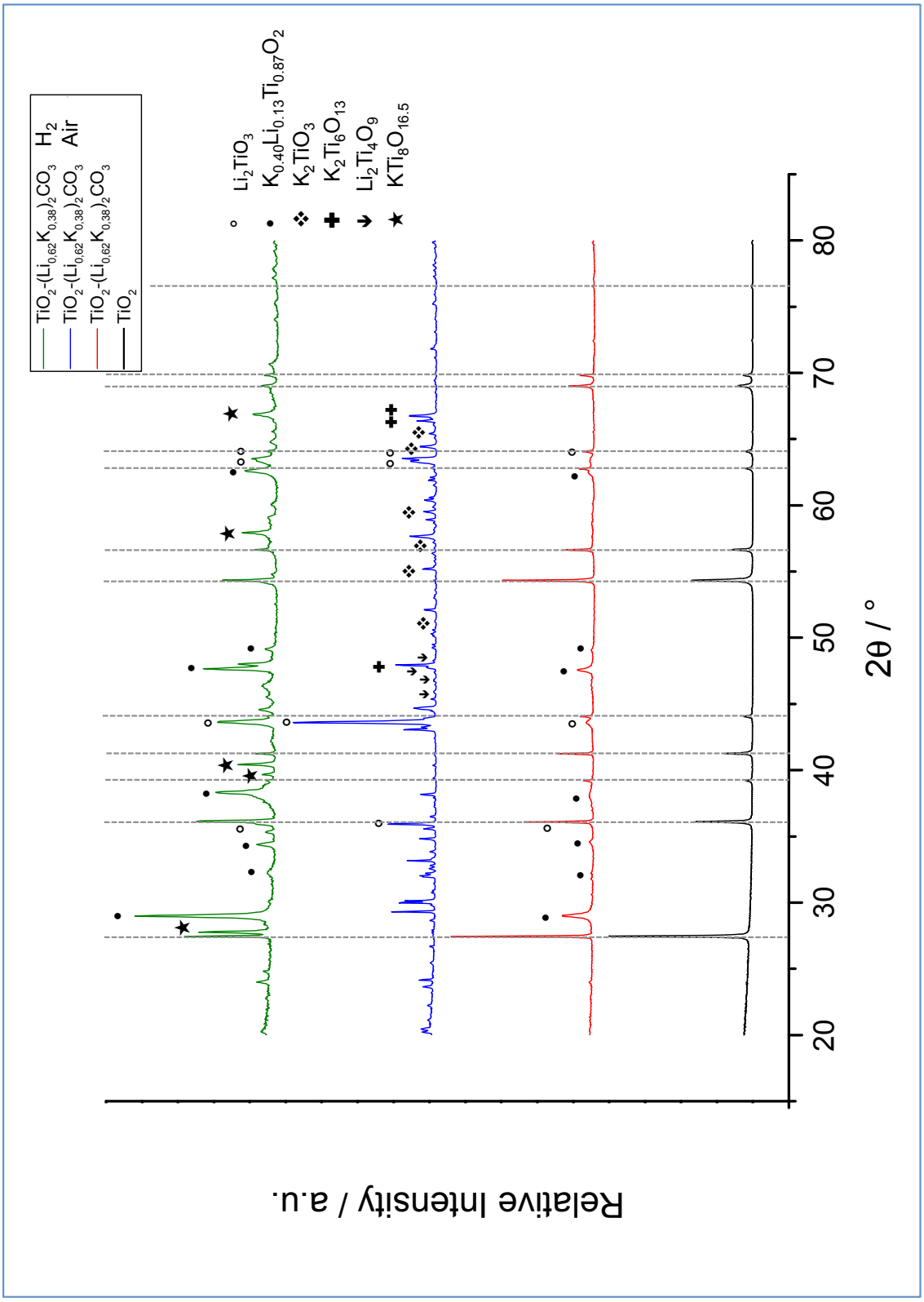

Figure 3.27: XRD patterns for the TiO_2-LiK composite obtained after the synthesis and the treatment in air or hydrogen atmosphere. The XRD pattern of the pure TiO_2 oxide is also reported for comparison.

unequivocally assign because of their small intensity. This confirms the complex composition and microstructure of these materials. Nonetheless, even if incomplete, this preliminary analysis provided some interesting information on the reactivity between YSZ or TiO_2 and the carbonate phase. Further and more accurate XRD measurements as a function of the temperature and in different atmospheres could help in better elucidating the reactivity issues observed during the electrochemical characterisation.

3.6 IR and Raman characterization

So far unfortunately, only few experimental studies on composites reported the IR and/or Raman properties of these materials with CeO_2-based[49,99,223,224] or Y_2O_3, Gd_2O_3, and Dy_2O_3[99] oxides and the $LiNaCO_3$ as the carbonate phase. All these works provided a similar picture: distinctive peaks of the two phases are clearly visible in the expected frequency range, the carbonate contributions being sligthly shifted when considering the composite. However, we were not able to find previous spectroscopic experimental data on TiO_2, YSZ or even ZrO_2-carbonate composites.
In order to complete the structural analysis performed through the XRD analysis, we thus performed IR and Raman measurements on the powders of the YSZ- and TiO_2-based composites just after the synthesis and after the EIS measurements in air or reducing atmospheres. Furthermore, vibrational properties of these materials are among the properties that can be more easily obtained from calculations, thus easily allowing a direct comparison between experimental and theoretical data. As we will see in chapter 6, the spectra obtained from the poweders just after synthesis can be compared with the theoretical ones in order to validate the model built to simulate these materials.

In general, two frequency regions were considered: the low frequencies region (200-800 cm^{-1}), where the vibrations relative to the metal-oxygen (M-O) bonds in the oxide should appear, and the high frequencies one (700-1900 cm^{-1}) where the modes of the carbonate group appear.

3.6.1 Infra-red spectra

3.6.1.1 YSZ-based composite

IR spectra can provide useful information, in particular on the carbonate phase. In the case of YSZ-based materials (figure 3.28 for LiK and figure 3.29 for LiNa), after synthesis two broad bands, at about 1500 and 1420 cm^{-1}, corresponding to the asymmetric stretching of the C-O bonds of the CO_3^{2-} groups and the bands at 860 and 880 cm^{-1} due to the bending of the O-C-O bonds are observed. The contribution of the M-O bonds is instead at frequencies lower than 800 cm^{-1}. In the case of LiK a small peak at 1054 cm^{-1}, associated to the symmetric C-O stretching, is also visible, in agreement with previous experimental reports on the IR properties of the $LiKCO_3$ phase which was found to present in these samples from the XRD analysis.[225] Finally, the weak contribution at 1087 cm^{-1}, also observed in the case of YSZ-LiK, can be attributed to the O-O vibration of oxygen species adsorbed on the oxide surface.[49,226]

When observing the spectra registered from the samples previously treated in air or hydrogen atmosphere, we can note that these contributions due to the carbonate phase become more broad and less intense, in line with the reactivity between YSZ and the carbonates previously described.

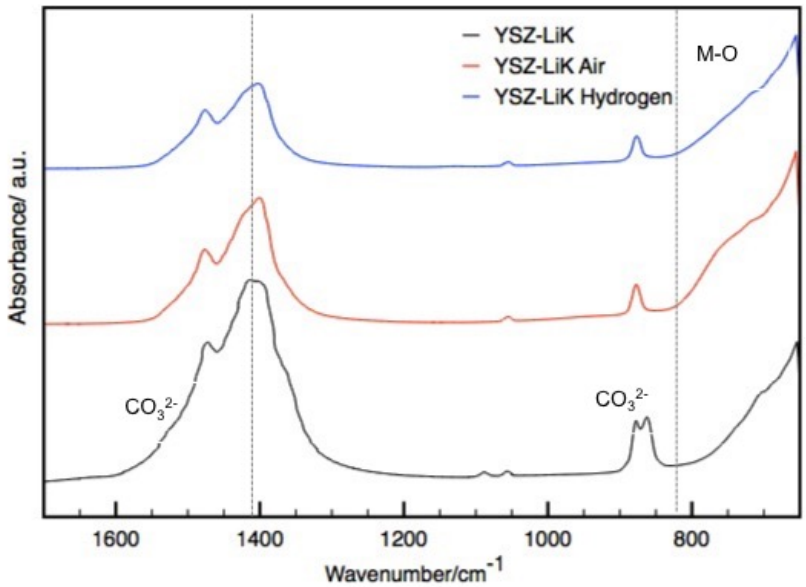

Figure 3.28: FT-IR spectra of the YSZ-$(Li,K)_2CO_3$ composite obtained after the synthesis and the treatment in air or hydrogen atmosphere.

3.6.1.2 TiO_2-$(Li,K)_2CO_3$ composite

The IR spectrum of the TiO_2-based material as obtained after synthesis is represented in black in figure 3.30. Also in this case contributions at 1400-1480, 1050, and 870 cm^{-1} can be attributed to asymmetric, symmetric C-O stretching, and O-C-O bending. However, for these materials, the peaks are less intense. The XRD analysis showed indeed that, after the synthesis some of the carbonate phase had already reacted with the oxide forming some titanates. In the spectra registered for the samples in air (in red in figure 3.30) or hydrogen (in blue in figure 3.30), the most intense peak corresponding to the C-O stretching desappears (air) or shows low intensity (hydrogen). Furthermore, the appearance of the band typical of M-O bonds changes, especially in air. This observation together with the relative intense peaks at 890-870 cm^{-1} and 940 cm^{-1} for samples treated in H_2 and air, respectively, clearly indicates the presence of newly formed species. This point could be however better adressed through the description of the Raman spectra.

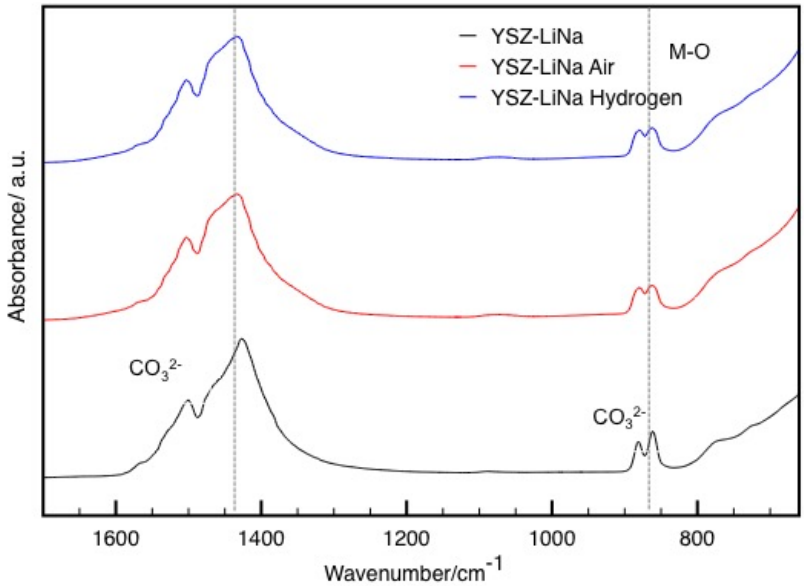

Figure 3.29: FT-IR spectra of the YSZ-$(Li,Na)_2CO_3$ composite obtained after the synthesis and the treatment in air or hydrogen atmosphere.

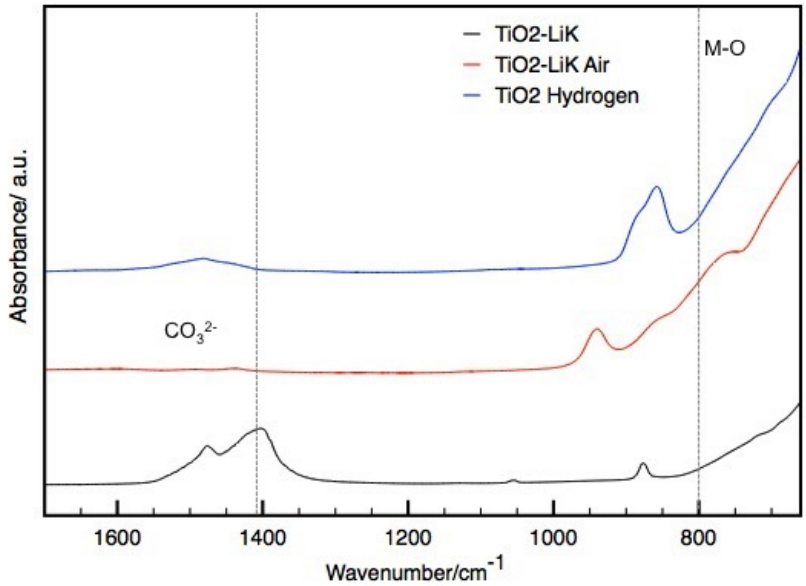

Figure 3.30: FT-IR spectra of the TiO_2-LiK composite obtained after the synthesis and the treatment in air or hydrogen atmosphere.

3.6.2 Raman spectra

3.6.2.1 YSZ-(Li,K)$_2$CO$_3$ composite

Figure 3.31 shows the Raman spectra obtained for the YSZ-LiK samples. After synthesis, the main contribution corresponds to the symmetric stretching of thr C-O bonds with contributions at 1026 and 1080 cm^{-1}. The in-plane O-C-O deformation can also be observed at about 695 cm^{-1}. The peak relative to YSZ at about 150, 470, and 630 cm^{-1} are also present (they are indicated by the vertical dotted lines in figure 3.31). When comparing these results with the ones obtained for the samples treated in air during the EIS measurements, we can observe that even if the peaks typical of the carbonate phase are still present, three intense or relatively intense peaks appears at 578, 250, and 380 cm^{-1}. The first two can be attributed to Zr-O and the last one to Li-O vibrations in Li_2ZrO_3.[227,228] For the samples treated in H_2, the background line appears irregular and enhanced. However, contributions of the carbonates, YSZ, and of Li_2ZrO_3 are clearly present. These results are thus in agreement with the analysis of the XRD patterns previously performed.

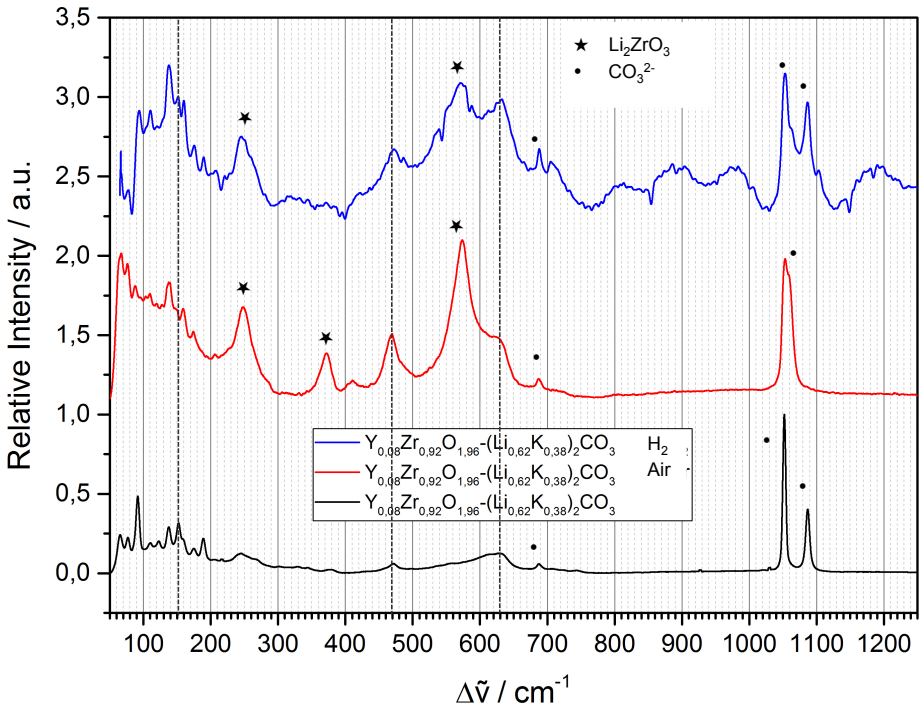

Figure 3.31: Raman spectra of the YSZ-LiK composite obtained after the synthesis and the treatment in air or hydrogen atmosphere.

3.6.2.2 YSZ-(Li,Na)$_2$CO$_3$ composite

Similar results are obtained for YSZ-LiNa materials (see figure 3.32). The contribution of the carbonates at about 1070-1080 and 700 cm^{-1} and of YSZ are clearly visible in particular for the powders obtained after the synthesis, but also for the samples treated in air of hydrogen atmospheres. Li_2ZrO_3 fingerprints, at about 250, 380, and 570 cm^{-1}, are also visible for the samples exposed to oxidising or reducing atmospheres during the electrochemical characterizations. Furthermore, we can see that and in agreement with the XRD analysis, the peaks characteristic of the monoclinic phase of zirconia are present in all the three cases at about 104, 180, 190, 223, 307, 337, 348, 382, 476, 502, 538, 560, 617, and 638 cm^{-1}.[229]

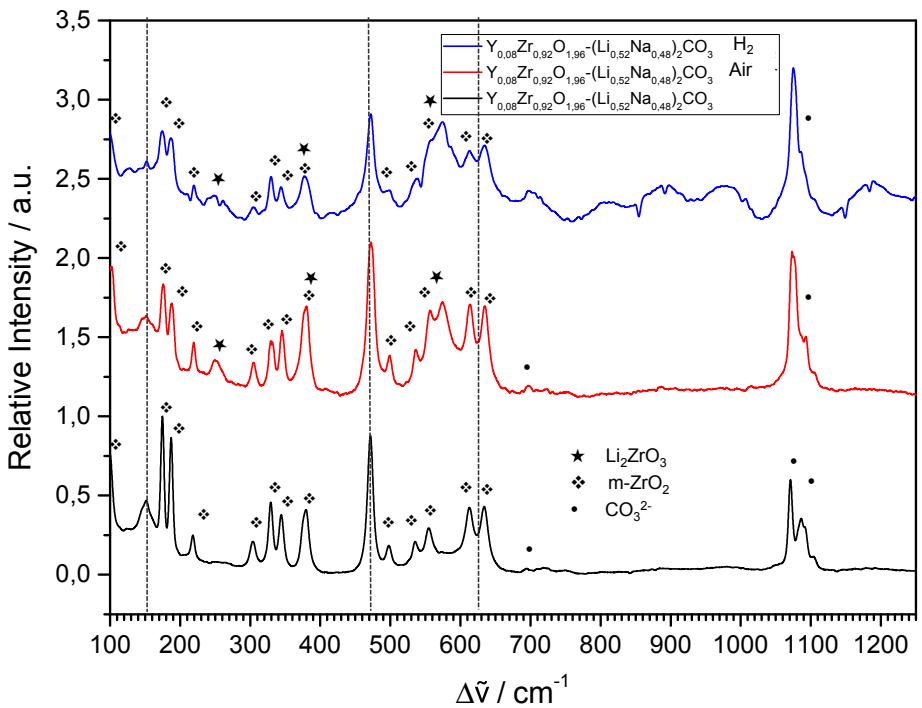

Figure 3.32: Raman spectra of the YSZ-LiNa composite obtained after the synthesis and the treatment in air or hydrogen atmosphere.

3.6.2.3 TiO$_2$-(Li,K)$_2$CO$_3$ composite

Raman spectra of the T-TiO$_2$-LiK powders after synthesis (black line in figure 3.33) show two intense peaks at 450 and 600 cm^{-1} typical of the Ti-O bond vibrations in TiO$_2$, but no contribution of the carbonate phase can be evidenced, even at about 1100 cm^{-1} where the intense peak corresponding to the C-O stretching appeared in the case of YSZ composites. An additional peak at 890 cm^{-1} is instead observed. This signal can be associated to the presence of lithiated titanium dioxide, in line with the XRD analysis. Li insertion causes, indeed, the emergence of bands generally between 848-950^{-1} due to Li-O stretching[230],

observed for example at 865 cm^{-1} in the Raman spectra of $LiTiO_2$[231] that is present in these samples as shown by the XRD characterisation.

The situation is completely different in the case in which the spectra are registered for materials exposed to air (red line in figure 3.30). The bands of TiO_2 are not present in this sample, in line, once again, with the XRD data. Numerous peaks appears instead. By comparison with the Raman spectra of different Li or K titanates[232,233] we can distinguish the contribution of species like Li_2TiO_3 (at about 400, 570 and 658 cm^{-1}) and $K_2Ti_6O_{13}$ (at about 91, 115, 140, 203, 299, 279, and 856 cm^{-1}). These species were also found to be present in the XRD pattern in non negligeable quantities. Similar considerations can be made for the spectra obtained from samples treated in reducing environments. In this case, the signature of the titanium dioxide is visible even if less intense compared to the poweders that did not undergo any treatment. The presence of Li_2TiO_3 is also evident together with an intense peak at about 890 cm^{-1}, characteristic of Li insertion in the TiO_2 lattice. Naturally the spectrum is complex and this complexity makes a definitive assigment of the peaks impossible, but this complexity is consistent with the observed reactivity leading as we said to K or Li titanates, for which, given their complex structures, we can expect several active Raman modes.

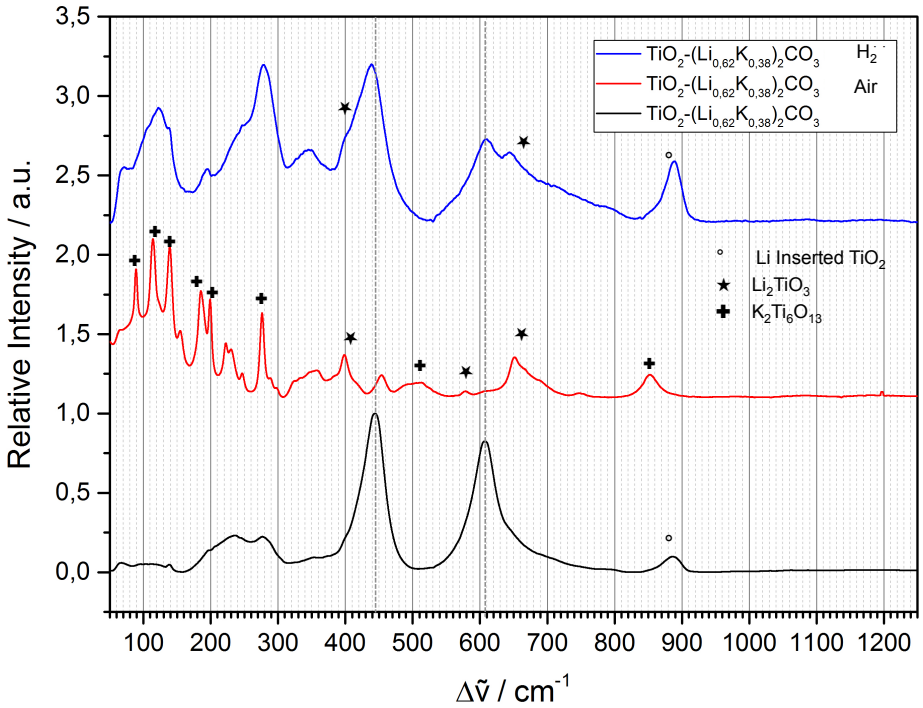

Figure 3.33: Raman spectra of the TiO_2-$(Li,K)_2CO_3$ composite obtained after the synthesis and the treatment in air or hydrogen atmosphere.

3.7 Conclusions

In this chapter, we have shown the peculiar electrochemical behaviour of composite materials made of an oxide phase and a mixture of alkali carbonates. Different parameters were considered in order to complete the experimental data base. The main results can be summarised as follows:

- It clearly appears that carbonate conductivity directly impacts the composite conductivity in a simple way: the higher the conductivity of the pure carbonate phase the higher the conductivity of the final composite material;
- Rationalizing the effect of the oxide phase is much more complex: the unexcpected high conductivity of undoped CeO_2-based materials, almost equal to the one of GDC-based samples, can only be explained considering the role of the oxide-carbonate interface;
- The EIS and TGA-DTA results show that YSZ can react with the carbonate phase at high temperatures of about 560-600°C, as verified through XRD and vibrational spectroscopy, leading to formation of zirconate phases that negatively influence the electrochemical behaviour of these materials;
- In reducing atmospheres unexpected behaviours were observed: the cooling part of the thermal cycle is systematically different from the heating one. GDC-based materials, associated to LiNa or LiK carbonates eutectics, revealed two drops instead of one jump in conductivity; while the first drop can be associated to the carbonate crystallization, the second drop has been assumed to be related to the formation of hydroxide of the alkali cations in the case of GDC. For YSZ-based materials, instead, the reactivity leading to the formation of zirconates seems to be enhanced in this atmosphere;
- TiO_2-based materials shown unfortunately strong reactivity issues: the linear variation of the conductivity as a function of temperature in air atmosphere clearly indicates the presence of reactivity between the oxide and the carbonate, which can lead to the formation of insulating titanate phases, as confirmed by the thermal and structural analysis; furthermore this process seems to clearly enhance the oxide reduction when the measurements are performed in H_2 atmosphere.

All the current experimental results rise several questions on the stability and electrochemical properties of these materials and evidenced the important role of interfaces in provoking such behaviour, thus reflecting the complexity of these materials, which is the direct consequence of their own composite nature. Considering the lack of analytical tools for investigating the interfacial effects directly, modelling at the atomic scale could help getting a better understanding of the properties of the composites and, in particular, the mismatch between expected and unexpected experimental observations. In the following chapters, we will apply the computational strategy explained in chapter 1 to the modeling of the YSZ- (chapter 4, 5, and 6) and TiO_2-based (chapter 7) carbonates, so as to provide information on the electrochemical properties of these materials and on the reactivity issues here observed.

Chapter 4

Modeling of the oxide phase: YSZ

You can't solve a problem on the same level it was created.
You have to rise above it to the next level.
Albert Einstein

Contents

4.1 Introduction **103**
4.2 Computational Details **106**
4.3 ZrO_2 bulk **107**
4.4 ZrO_2 Surfaces **119**
4.5 Reducibility properties of the (111) of *c*-ZrO_2 surface **126**
4.6 Y_2O_3-doped (111) surface **134**
4.7 Conclusions **139**

4.1 Introduction

Zirconium dioxide or zirconia (ZrO_2) exhibits some important properties, like high strength and stability at high temperatures, high fracture toughness and hardness, chemical inertness and resistance to corrosion, large band gap and an excellent oxide ions conduction for the doped material, especially for yttria stabilized zirconia (YSZ)[234–238] These properties make this oxide an appealing material for modern technological applications in various fields: as a gem in substitution of diamonds or in biomedicine such as in hip implants and in dental restoration,[239] as thermal barrier in coatings,[240] in ceramic engineering as a ceramic toughening and strengthen agent,[241] in nuclear industry as a passivating medium for nuclear wastes,[242] in catalysis as a support medium or as an active agent,[243] in microelectronics as a gate dielectric material in substitution of SiO_2, in advanced metal oxide semiconductor devices or in dynamic access memory devices,[244] and last but not least, in oxygen gas sensors[245] and, naturally, as the solid electrolyte in SOFCs.

Zirconia exists in various allotropic forms, such as the monoclinic, tetragonal, and cubic polymorphs, well-characterized at ambient pressure (see figure 4.1). The phase transformations from the cubic to the tetragonal and from the tetragonal to the monoclinic forms occur on cooling from higher temperature. Indeed, at room temperature, zirconia adopts a monoclinic crystal structure ($P2_1/c$) also known as baddeleyite, which is stable up to 1480 K, where it transforms into the tetragonal polymorph ($P4_2/nmc$). Finally, the tetragonal ZrO_2 converts into a cubic fluorite structure (*Fm3m*) at around 2650 K.[236]

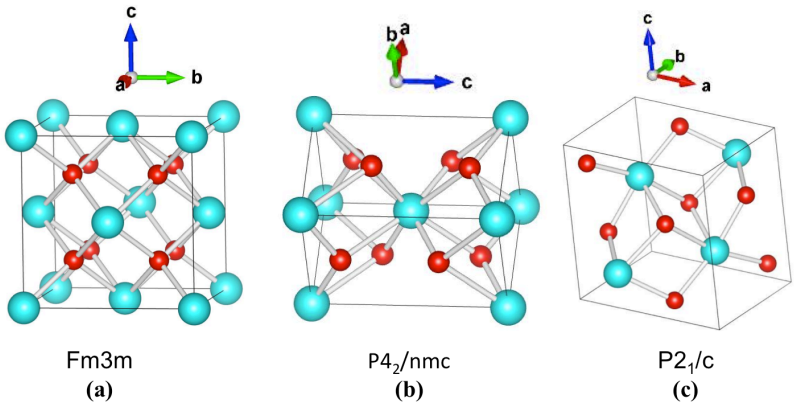

Figure 4.1: Cubic (a), tetragonal (b) and monoclinic (c) ZrO_2 unit cells and relative space groups. Large light blue spheres and small red spheres represent Zr and O atoms, respectively.

It has been observed that Zr^{4+} ions appear to be too large for an efficiently packed rutile structure and at the same time too small to form the eight-fold coordinated fluorite structure.[246,247] For these reasons, during cooling, the high temperature cubic structure is not stable and distorts first into the lower symmetry tetragonal phases (where Zr cations are still eight-fold coordinated) and finally into the lowest symmetry monoclinic phase (which has seven folded Zr cations). Nonetheless, tetragonal and cubic phases can be stabilized at lower temperatures through doping with aliovalent oxides like yttria (Y_2O_3).[236] For each pair of aliovalent Y^{3+} ions that substitutes a pair of Zr^{4+} cations, one oxygen vacancy must be created to ensure the neutrality of the system. The first effect of the doping is the partial or complete structural stabilization, depending on the dopant concentration. At room temperature and for low concentrations (2-6 mol% of yttria), the tetragonal structure is stabilized, but this phase separates into monoclinic or cubic-doped structures as a function of temperature and time and is, therefore, called partially stabilized zirconia (PSZ) as well as tetragonal-stabilized zirconia (TPZ). On the other hand, 8-40 mol% Y_2O_3 is necessary to obtain the fully stabilized cubic structure (YSZ, yttria stabilized zirconia). Over 40 mol%, the system crystallizes as a rhomboedral δ-$Zr_3Y_4O_{12}$ phase.[246,248–250] In addition to the structural stabilization, doping improves the thermo-mechanical properties and determines the high ionic conductivity because of the presence of oxygen vacancies in the doped material.[236] The ionic conductivity, together with the number of vacancies, increases with the dopant concentration reaching a maximum at 8 mol% Y_2O_3 and then significantly decreases for higher dopant

amount, probably because, at higher Y_2O_3 content, vacancies are trapped in defect complexes.[251,252] The mechanism of stabilization in YSZ is not completely understood and it is still subject of debate. A lower of the coordination number of Zr atoms from eight to a value close to seven (like in monoclinic zirconia), as a consequence of the presence of the oxygen vacancies, is the prevailing explanation, in accordance with the observation that the covalent nature of the Zr-O bond favours structures with lower coordination numbers.[253] This rationalization indirectly implies that oxygen vacancies are associated to Zr^{4+} rather than to the Y^{3+} cations, contrarily to the expected electrostatic attraction between the vacancy and the dopant ions.[250,253–255] Unfortunately, experimental studies provide conflicting data that does not give clear indication about the nature of the stabilization mechanism. Indeed, some of them indicate that vacancies prefer to bind to the dopant,[256–260] while more recent works refer to a preferential association between the vacancies and Zr cations.[261,262] Theoretical studies[248,250,253–255,263,264] on the bulk structure of PSZ or YSZ have already supported the latter case in which Y next-nearest neighbour positions (NNN) to the vacancy are energetically favoured with respect to the nearest neighbour (NN) ones. The configuration of Zr, O, Y and oxygen vacancies is however not decisively characterized and the proposed mechanism of stabilization still needs to be better clarified.

Theoretical studies about structural and electronic bulk properties[234,235,237,240,265–275] or about surfaces[238,246,247,249,271,275–287] of pure zirconia polymorphs can also be found in literature. Interatomic potentials (IP),[246,278] as well *as ab initio* calculations, in the framework of the HF approximation,[271,275,288] and of the DFT,[234,235,237,246,247,249,266,268,273,277–279,281–285,287] have already been carried out. The majority of these works are DFT studies, at the LDA level, based on a PAW approach. A moderate number of GGA calculations are also available, and scarce publications using hybrid exchange-correlation functionals[234,266,268] can be found, mostly due to their high computational cost with PAW approaches. In particular, we were not able to found any hybrid DFT calculation on zirconia surfaces. Despite the theoretical works about zirconium dioxide already published, the lack of systematic studies makes difficult to perform a straightforward comparison of the results, which are obtained with different methods and various computational parameters. This becomes particularly evident if one considers that only some works have been devoted to the simultaneous study of the three phases, especially when dealing with surfaces, and even less publications have been based on the simultaneous investigation of bulk and surface properties. In particular, the role of the exchange-correlation functional should then be clarified, with particular attention to the performances of hybrid functionals, which have been rarely employed in the calculations that can be found in literature.

As regards surfaces, their structural characterization is also difficult from an experimental point of view. Despite several experiments[289–291] which have been performed and which suggested the presence in YSZ of a monolayer rich in yttrium on top of a thicker undoped ZrO_2 layer, there is still uncertainty about the location of the oxygen vacancies and Y atoms.[246] Some theoretical studies have been already devoted to the description of the structural properties of YSZ or PSZ surfaces,[246,247,249,285,287,292] but there is not a systematic investigation of dopant and vacancies distribution. This would however be particularly appealing as the knowledge of the geometrical and electronic properties of YSZ surfaces is crucial for the SOFC applications of this material.

In this chapter, we will first report the results of a more comprehensive computational study, investigating simultaneously bulk and surfaces of the three main zirconia phases at ambient pressure (monoclinic, tetragonal and cubic phases). Different hamiltonians and basis set have been tested allowing us to select the protocol that produced the best description of zirconia phases, their structural and electronic properties, in order to use it for the description of the most important surfaces for each phase. The reducibility of the most stable $c(111)$ surface and its doping with Y_2O_3 will subsequently be described in detail, through a systematic study of the stability, geometry and electronic structure of different possible doping configurations.

4.2 Computational Details

All calculations have been carried out using the *ab initio* periodic CRYSTAL09[179] code. For the bulk material, HF and DFT calculations have been performed. At the DFT level, several exchange-correlation functionals have been used: the GGA, PBE[170] functional, and three global hybrid functionals: B3LYP[164,165], B3PW[164,166–169]) and PBE0[172,173]. Furthermore, the PBE0 functional corrected for dispersion according to the Grimme D2[177] scheme has also been considered (and indicated as PBE0-D in the following). All-electron as well as pseudopotential (ECP) basis sets have been used for both Zr and O. In particular we considered three different basis sets, which will be indicated as Zr*-O*, Zr^{ECP}-O* and Zr^{ECP}-O^{ECP}. The subscript * indicates an all-electron basis set for Zr or O atoms, while the subscript ECP indicate that a pseudo-potential is used. Zr*-O* is made up by all-electron basis sets, with a (9s,17sp,9d)→[1s,4sp,3d] contraction scheme for zirconium (indicated as Zr*), and a (8s,6sp,1d)→[1s,3sp,1d] one[293] for oxygen atoms (indicated as O*). This oxygen basis set has already been successfully used in previous calculations on zirconia.[234,266,268] In Zr^{ECP}-O*, the Zr^{ECP} basis set is made up by the small core effective pseudo-potential of Hay and Wadt[294–296] to describe the 28 inner core electrons of the zirconium atom and by a (5sp,4d)→[3sp2d] contraction scheme, previously used by Bredow and Lerch[293], to describe its ($4s^24p^65s^24d^2$) valence electrons. The all-electron basis sets O* is instead used for the oxygen atom. In Zr^{ECP}-O^{ECP}, the all-electron basis set used in Zr^{ECP}-O* for the oxygen atom is substituted by the O^{ECP} basis set, made up by the Durand-Barthelat[297,298] large core ECP to replace the 1s core electrons and by a (4sp)→[2sp] contraction scheme[299] to describe the outer electrons. The Zr^{ECP}-O^{ECP} basis set was also used for the reducibility calculations and for YSZ simulations. In the last case, for the Y atoms, the Hay and Wadt[294–296] small core ECP and the (4sp,2d)→[2sp1d] contraction scheme[299] for the Y ($4s^24p^65s^24d^1$) valence electrons were used.

To investigate the reducibility properties, the clean (111) surface of cubic ZrO_2 was modelled by a (2×2) supercell with a total of 72 atoms ($Zr_{24}O_{48}$), from which two oxygen atoms were removed ($Zr_{24}O_{46}$), but leaving the associated basis set centred in the atomic position of the defect site. Finally, to model the (111) surface of YSZ, in addition to the two vacancies, four Zr atoms of the supercell were replaced by four Y atoms, leading to $Zr_{20}Y_4O_{46}$ and corresponding to the experimental 8 mol% Y_2O_3 doping amount.

For both bulk and surface calculations, a Monkhorst-Pack[300] shrinking factor of six, cor-

responding, respectively, to 80, 40 and 16 points in the irreducible Brillouin zones (IBZ) of the monoclinic, tetragonal and cubic bulk phases and to 20, 16, 20 and 7 points for the *m*(-111), *t*(101), *t*(111) and *c*(111) surfaces have been used. In the case of the calculations on the (111) surface with a (2×2) supercell model, the reciprocal space was sampled using a Monkhorst-Pack grid with shrinking factors $(6 \times 6 \times 1)$, corresponding to 13 points in the IBZ of the supercell.

For the bulk calculations, both the default and extrafine tolerances were considered for the numerical DFT integration, while surface calculations have been all carried out using only extrafine integration values. The default grid of CRYSTAL09 has 55 radial points and a maximum 434 angular points, while the extrafine integration scheme corresponds to 75 radial points and 974 angular points.[179]

For the relative stability investigation of the bulk phases, in some selected cases, we also performed additional frequencies calculations at the Γ point, from which zero-point energy (ZPE) and thermal contributions to the energy have been obtained. Experimental phase transition temperatures have been considered: 1480 K for the monoclinic to tetragonal tran- sition, and 2650 K for the tetragonal to cubic one.[236]

Finally, for the bulk calculations latice parameters and all the atomic positions were allowed to relax during geometry optimization, until the maximum and root-mean square atomic forces and displacements were simultaneously less than $4.5 \times 10^{-4}, 3.0 \times 10^{-4}, 1.8 \times 10^{-3}$ and 1.2×10^{-3} a.u., respectively. In tha case of the study of the YSZ-(111) termination only the atomic positions were instead allowed to relax.

4.3 ZrO_2 bulk

The high temperature cubic phase of ZrO_2 (*c*-ZrO_2, Figure 4.1, (a)) belongs to the space group *Fm3m* and has an *fcc* lattice of zirconium atoms and oxygen atoms in the tetrahedral sites. Therefore, Zr atoms are 8-fold, while O atoms are 4-fold coordinated and there is one ZrO_2 formula unit per unit cell. The structure is completely described by a single parameter: the lattice parameter *a*. The intermediate temperature tetragonal phase (*t*-ZrO_2, Figure 4.1, (b)), which belongs to the space group *P42/nmc*, could be described as a slightly distorted cubic structure, as a result of the alternated displacement of the O atoms upward and inward along the c axis of the tetragonal unit cell, which contains two ZrO_2 formula units. Zirconium atoms are coordinated to 8 oxygen atoms, four organized in a flattened tetrahedron with shorter Zr-O bonds and 4 organized in an elongated tetrahedron with longer Zr-O bonds. The structure is fully described by four parameters: the lattice parameters (*a*, *b*, *c*) and the internal displacement (d_{z0}), defined as the displacement of the oxygen atoms in *t*-ZrO_2 with respect to the position in the ideal cubic phase: d_{z0}=O_z-0.25, where O_z is the fractional *z* coordinate of the oxygen atom in the tetragonal phase and 0.25 is the fractional *z* coordinate in the ideal cubic structure. Also the low temperature monoclinic polymorph (*m*-ZrO_2, Figure 4.1, (c)), belonging to the *P21/c* space group, could be seen as a distortion of the ideal cubic structure with the zirconium atoms 7-fold coordinated or as a further distorted tetragonal structure, in which the lattice vectors are no longer at right angles. In this structure, there are two types of oxygen: one 3-fold coordinated, in an approximately planar configuration, the other 4-

fold coordinated, surrounded by a distorted tetrahedron of Zr atoms. The unit cell contains four ZrO_2 formula units. This structure is fully described by 13 independent parameters, the lattice parameters (a, b, c), the β angle and the x, y, z coordinates of the Zr atom and those of the two types of O atoms in the unit cell.

4.3.1 Structure

Tables 4.1, 4.2 and 4.3 present the structural parameters computed in this study with different methods and basis sets, respectively, for the monoclinic, tetragonal and cubic phases. Our results are compared with both experimental data and results of selected previous theoretical calculations. In the literature, there are plenty of experimental works on the structure of the zirconia polymorphs. Milman et al.[273] have reviewed these data, in particular for the tetragonal polymorph. The experimentally determined structural parameters differ from each other, as consequence, mainly, of the different sample preparation conditions, in particular for the tetragonal and cubic phases, which, in order to be stabilized, are generally doped with various amount of dopants, like Y or Ca. Therefore, as reference data, we decided to use the results obtained on undoped materials by Howard et al.[301] through X-ray powder diffraction, and by Igawa et al.[302] through neutron powder diffraction, respectively for the monoclinic and cubic phases. For the tetragonal polymorph, we chose data from Ingel et al.,[303] measured on Y_2O_3-doped tetragonal zirconia and extrapolated to zero dopant concentration. As already stated, many theoretical calculations have been performed on zirconia polymorphs. Our results are generally in agreement with these calculations. The lowest errors were obtained for the cubic phase, with a maximum mean signed error of -0.94% at the PBE0-D/Zr^{ECP}-O* level (Figure 4.2). All the methods we tested, independently from the basis set, tend to overestimate the lattice parameter a of the cubic phase, except for PBE0 and PBE0-D. The former data are associated with the smallest errors (between -0.02 and -0.37%).

Generally, for the tetragonal phase, the parameter a and c are both overestimated when the all-electron basis sets on Zr and O or the Zr^{ECP}-O* basis set are used, while with the Zr^{ECP}-O^{ECP} basis set, a is overestimated and c underestimated. The parameter d_{z0} is always underestimated with larger errors, especially with the Zr^{ECP}-O^{ECP} basis set. Finally, for the monoclinic phase, all the methods systematically overestimate a, b and c, but underestimate β, except PBE0-D which underestimates a and c and the angle, but overestimates b, independently from the adopted basis set. PBE0 produces results that reproduce best the experimental data, but at the PBE0-D level a significantly reduction of the accuracy is observed, probably because of the addition of the contribution of dispersion forces to the PBE0 structures that are already very close to the experimental ones. In summary, for all the phases, no matter which Hamiltonian is considered, computed errors on lattice vectors with respect to the experiment are small (typically lower than 2.1% for the monoclinic phase, 2.4% for the tetragonal and 0.9% for the cubic one). The PBE functional systematically overestimates the lattice parameters, as generally also HF does. The geometric data are significantly improved at the PBE0 level, with maximal deviations on the lattice vectors with respect to the experiment as low as -0.37% for the cubic phase, -1.59% for the tetragonal polymorph and -0.90% for monoclinic one. PBE0 gives the best results also when compared to the other theoretical methods such as LDA or GGA in the PAW[235,246,265,267,272] or LCAO[268] approach,

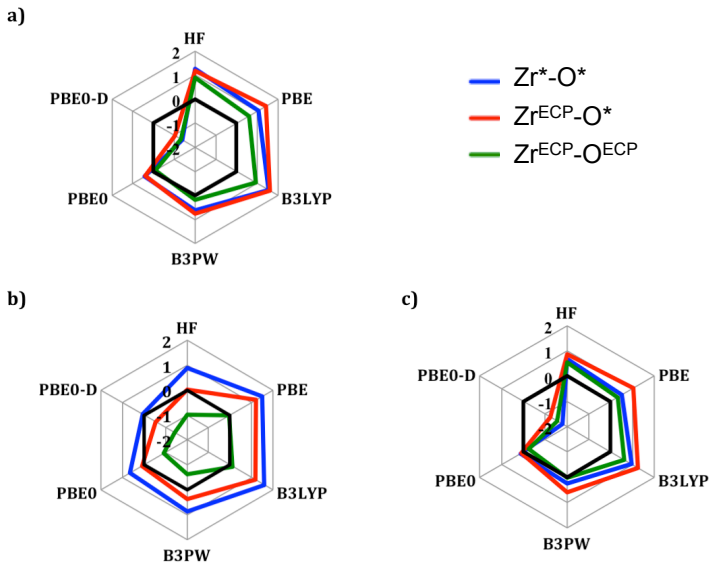

Figure 4.2: Mean Signed Errors (MSE, in %) computed for the lattice vectors of the a) cubic, b) tetragonal and c) monoclinic phases with the three considered basis sets and the six considered Hamiltonians.

or hybrid functionals (PW1PW1,[266] B3LYP[234,268]) in the LCAO approach. Including dispersion however leads to lower accuracy, providing PBE0-D more compact structures, for all the three polymorphs, with respect to experimental data. With this method, the largest errors are obtained on the lattice vector *c* (which is underestimated of 3-4% with the different basis sets) and the β angle of the monoclinic phase (which is underestimated of 2-3% with the different basis sets) and on the internal distortion (d_{z0}) of the tetragonal polymorph (which is underestimated of 14.04%, 28.07% and 56.14% with respectively the basis set Zr*-O*, Zr^{ECP}-O* and Zr^{ECP}-O^{ECP}). Results computed with different basis sets are similar, especially with Zr*-O* and Zr^{ECP}-O*. Without the d polarization functions on O, a decrease in the structural parameters of the three phases is generally obtained: for example, a reduction of 0.030 Å for *a*, 0.013Å for *b*, 0.034Å for *c* and 0.53°for β in the monoclinic phase; of 0.012 Å for *a*, 0.076 Å *c* and 0.015 Å for d_{z0} in *t*-ZrO_2 and of 0.018 Å for a in *c*-ZrO_2 is observed at the PBE0 level. However, these variations are small and more significant when treating non-cubic zirconia phases. In particular, d polarization functions seem important to give a better quantitative description of the β angle of the monoclinic phase and of the d_{z0} internal displacement of the tetragonal one.

4.3.2 Relative Stability

The difference in energy between the monoclinic and tetragonal phases, as well as the one between the tetragonal and cubic polymorphs was computed with the different basis sets and Hamiltonians considered. Results are reported in table 4.4, where these data are compared

Basis set	Method	a	b	c	β	MSE	MUE
Zr*-O*	HF	5.244	**5.214**	5.418	98.21	0.68	1.19
	PBE	5.199	5.301	5.343	98.15	0.51	1.05
	B3LYP	5.243	5.251	5.428	98.47	0.96	1.35
	B3PW	5.192	5.254	5.331	98.38	0.25	0.68
	PBE0	**5.183**	**5.244**	**5.320**	**98.49**	0.14	0.51
	PBE0-D	5.098	5.249	5.113	96.23	-1.79	2.15
Zr^{ECP}-O*	HF	5.244	**5.225**	5.396	99.13	0.86	0.91
	PBE	5.221	5.300	5.382	**99.14**	1.04	1.09
	B3LYP	5.245	5.271	5.416	99.41	1.25	1.25
	B3PW	5.197	5.261	5.342	99.35	0.61	0.61
	PBE0	**5.175**	**5.262**	**5.303**	99.13	0.10	0.61
	PBE0-D	5.089	5.257	5.168	97.43	-1.24	1.67
Zr^{ECP}-O^{ECP}	HF	5.224	**5.227**	5.371	98.66	0.54	0.82
	PBE	5.170	5.293	**5.311**	98.73	0.33	0.63
	B3LYP	5.201	5.268	5.357	**98.93**	0.62	0.77
	B3PW	5.159	5.255	5.294	98.76	0.02	0.47
	PBE0	**5.145**	**5.249**	5.269	98.60	-0.10	0.46
	PBE0-D	5.077	5.250	5.142	97.03	-1.55	1.92
Exp.[a]		5.151	5.212	5.317	99.23		
Other works							
LCAO/LDA[b]	5.091	5.263	5.206	98.39			
LCAO/PW9[b]	5.209	5.304	5.370	99.50			
LCAO/B3LYP[b]	5.232	5.290	5.397	99.42			
LCAO/B3LYP[c]	5.246	5.270	5.405	99.62			
LCAO/PBE0[c]	5.187	5.248	5.326	99.46			
LCAO/PW1PW[d]	5.212	5.238	5.367	99.15			
PAW/LDA[e]	5.108	5.170	5.272	99.21			
PAW/GGA[f]	5.211	5.286	5.388	99.59			

[a] See ref.[301].
[b] See ref.[268].
[c] See ref.[234].
[d] See ref.[266].
[e] See ref.[265].
[f] See ref.[272].

Table 4.1: Equilibrium geometry of *m*-ZrO_2 with different Hamiltonians and basis sets and mean signed error (MSE) and mean unsigned error (MUE) computed for each method. Lattice vectors (*a, b, c*) in Å and β angle in degrees. MSE and MUE in %. Best results for each basis sets in bold face.

Basis set	Method	a	c	c/a	d_{zo}	MSE	MUE
Zr*-O*	HF	3.638	5.263	1.447	0.050	0.89	0.89
	PBE	3.646	5.313	1.457	**0.056**	1.51	1.51
	B3LYP	3.648	5.319	1.458	**0.056**	1.59	1.59
	B3PW	3.625	5.261	1.450	0.053	0.87	0.87
	PBE0	3.617	5.245	1.450	0.052	0.65	0.65
	PBE0-D	**3.596**	**5.199**	**1.446**	0.049	0.06	0.06
Zr^{ECP}-O*	HF	3.628	5.197	1.432	0.037	0.02	0.67
	PBE	3.645	5.289	1.451	**0.051**	1.21	1.21
	B3LYP	3.645	5.287	1.450	**0.051**	1.17	1.17
	B3PW	3.620	5.223	**1.443**	0.046	0.37	0.51
	PBE0	3.612	**5.200**	1.440	0.044	0.08	0.36
	PBE0-D	**3.590**	5.153	1.435	0.041	-0.54	0.54
Zr^{ECP}-O^{ECP}	HF	3.619	5.119	1.414	0.002	-0.97	1.48
	PBE	3.627	**5.192**	1.431	0.038	-0.04	0.69
	B3LYP	3.632	5.203	**1.433**	**0.040**	0.12	0.72
	B3PW	3.609	5.145	1.426	0.033	-0.62	0.94
	PBE0	**3.600**	5.124	1.423	0.029	-0.91	1.06
	PBE0-D	3.580	5.084	1.420	0.025	-1.42	1.42
Exp.[a]		3.592	5.195	1.446	0.057		
Other works							
LCAO/PW1PW[b]		5.107	5.217	1.022	0.048		
LCAO/B3LYP[c]		3.642	5.293	1.453	0.052		
LCAO/PBE0[c]		3.608	5.201	1.441	0.045		
PAW/LDA[c]		3.583	5.140	1.435	0.041		
PAW/GGA[e]		3.642	5.295	1.454	0.024		
PAW/LDA[e]		3.565	5.126	1.438	0.044		
PAW/GGA[f]		3.628	5.250	1.447	0.049		
IP[g]		3.588	5.217	1.454	0.046		

[a] MSE and MUE are computed only for the lattice vectors a and c. See ref. 7
[b] See ref.[266].
[c] See ref.[234].
[c] See ref.[267].
[e] See ref.[235].
[f] See ref.[269].
[g] See ref.[246].

Table 4.2: Equilibrium geometry of t-ZrO_2 and mean signed error (MSE) and mean unsigned error (MUE) computed for each method. Lattice parameters (a, c) and internal distortion d_{z0} in Å. MSE and MUE in %.[a] Best results for each basis sets in bold face.

Basis set	Method	a	MSE	MUE
Zr*-O*	HF	5.135	0.53	0.53
	PBE	5.151	0.84	0.84
	B3LYP	5.118	0.20	0.20
	B3PW	5.154	0.90	0.90
	PBE0	**5.107**	-0.02	0.02
	PBE0-D	5.076	-0.63	0.63
Zr^{ECP}-O*	HF	5.130	0.43	0.43
	PBE	5.155	0.92	0.92
	B3LYP	5.154	0.90	0.90
	B3PW	5.118	0.20	0.20
	PBE0	**5.107**	-0.02	0.02
	PBE0-D	5.075	-0.65	0.65
Zr^{ECP}-O^{ECP}	HF	5.120	0.23	0.23
	PBE	5.129	0.41	0.41
	B3LYP	5.131	0.45	0.45
	B3PW	5.100	-0.16	0.16
	PBE0	**5.089**	-0.37	0.37
	PBE0-D	5.060	-0.94	0.94
Exp.[a]		5.108		
Other works				
LCAO/HF[b]		5.125		
LCAO/PW1PW[c]		5.105		
LCAO/B3LYP[d]		5.150		
LCAO/PBE0[d]		5.103		
PAW/LDAe[e]		5.037		
PAW/GGAf[f]		5.090		
IP[g]		5.076		

[a] Computed from the cubic root of $(\sqrt{2a})^2 \times c$ of *t*-ZrO_2 unit cell in Ref. s24.
[b] See ref.[271].
[c] See ref.[266].
[d] See ref.[234].
[e] See ref.[235].
[f] See ref.[269].
[g] See ref.[246].

Table 4.3: Equilibrium geometry of *c*-ZrO_2 and mean signed error (MSE) and mean unsigned error (MUE) computed for each method. Lattice parameter a in Å. MSE and MUE in %. Best results for each basis sets in bold face.

with the experimental values[304] and with results of previous calculations. At the experimental level, the relative stability is: *c*-ZrO_2 <*t*-ZrO_2 <*m*-ZrO_2. Regarding the difference in energy between the tetragonal and the cubic phases (E_t-E_c), the right order of stability between these two phases is provided independently of the basis set or the method used in the calculations (*i.e.* *t*-ZrO_2 more stable than *c*-ZrO_2). Data are in good agreement with other theoretical results. PBE produces good results, as well as the hybrid functionals B3LYP and B3PW, which generally ensure better accuracy. For instance, considering all the three basis sets taken into account, the minimum and maximum deviations with respect to the experimental value are of -0.014 and 0.024 eV for PBE, 0.003 and 0.039 eV for B3LYP and -0.010 and 0.020 eV for B3PW. Considering the dependence of the basis sets, the main differences in the E_t-E_c values are between the data computed with Zr^{ECP}-O* and the Zr^{ECP}-O^{ECP} basis sets. The cancellation of the d polarization, which had an important effect on the structure of the tetragonal phase, determines a systematic increase of the E_t-E_c value of about 0.03-0.04 eV for all the considered DFT method. The relative stability order of the monoclinic and tetragonal phases is much more basis set and method dependent however. In particular, all-electron basis set Zr*-O* leads to *t*-ZrO_2 more stable than *m*-ZrO_2. In general, PBE0 and PBE0-D fail to identify the monoclinic as the most stable phase. Again the best results are obtained at the PBE and B3PW levels.

When considering ZPE and thermal contributions at the PBE0 level, however, the right order of stability is obtained for the three considered phases, no matter which basis set is considered: *c*-ZrO_2 <*t*-ZrO_2 <*m*-ZrO_2. In particular, the energy difference between the monoclinic and tetragonal phases is notably improved compared to the electronic energy difference case, now comparing nicely with the experimental data. This is, however, associated to a significant overestimation of the energy difference of the tetragonal and cubic phases. We note here, however, that the thermal contribution has been obtained from frequencies calculations performed at the Γ point only, although a more realistic picture would be obtained by considering expensive phonon dispersion calculations

4.3.3 Electronic properties

4.3.3.1 Band gap

Experimental works, investigating the electronic properties of zirconia polymorphs, have been summarily reviewed and discussed by Jiang et al.[237] and by Dash et al.[235]. Reported data on the band gap of this material are spread between 4 and 6 eV. In this regard, it should be noted that in certain cases the sample is analysed as thin amorphous or polycrystalline films. Moreover, results refer to samples of different purity, especially for the cubic and tetragonal phases, which are analysed in the form of doped materials. For example, electron energy loss spectroscopy (EELS) results of McComb[305] report a gap value of about 4 eV for zirconia polymorphs, while vacuum ultraviolet spectroscopy (VUV) data of French et al.[269] report values that are about 1.6 eV higher. Although it is believed that VUV data tend to overestimate the magnitude of the band gap,[269] Dash et al.[235] explained this discrepancy attributing the low energy part of the EELS states to electronic excitations from defect states or oxygen vacancy states in the yttria-stabilized zirconia samples. Theoretical investigation of the electronic structure of zirconia phases has also been a subject of numerous publications:

Basis set	Method	E_m - E_t	E_t - E_c
Zr*-O*	HF	0.017	-0.041
	PBE	0.031	-0.073
	B3LYP	0.066	-0.048
	B3PW	0.065	**-0.067**
	PBE0	0.062	-0.025
		0.079*	0.004*
		-0.004**	-0.741**
	PBE0-D	0.084	-0.022
Zr^{ECP}-O*	HF	-0.043	-0.016
	PBE	**-0.049**	-0.071
	B3LYP	-0.020	**-0.054**
	B3PW	-0.028	-0.077
	PBE0	-0.010	-0.045
		0.011*	0.021*
		-0.054**	-0.828**
	PBE0-D	0.026	-0.038
Zr^{ECP}-O^{ECP}	HF	0.048	-0.001
	PBE	-0.052	-0.033
	B3LYP	-0.011	-0.018
	B3PW	-0.052	-0.037
	PBE0	0.012	-0.013
		0.036*	0.011*
		-0.026**	-0.769**
	PBE0-D	0.050	-0.008
	Exp.[a]	-0.061	-0.057
Other works			
LCAO/B3LYP[b]		-0.031	-0.074
LCAO/PBE0[b]		0.019	-0.049
LCAO/PW1PW[c]		-0.030	-0.058
PAW/LDA[d]		-0.064	-0.049
PAW/GGA[e]		-0.100	-0.070

[a] See ref.[304].
[b] See ref.[234].
[c] See ref.[266].
[d] See ref.[235].
[e] See ref.[269].
Starred and double-starred values refer to the electronic energy plus the ZPE contribution and Gibbs free energy, respectively, obtained from frequency calculations at the Γ point only, considering experimental phase transitions.

Table 4.4: Calculated energy difference between the monoclinic and the tetragonal polymorphs (E_m - E_t) and between the tetragonal and the cubic ones (E_t - E_c). Values in eV. Best results for each basis sets in bold face.

HF,[271,275,288] DFT (mainly with LDA, GGA[55][247] or hybrids[234,266]) as well as calculations carried out with Green's function approach in the GW approximation[235,237,263,269,270,274] are available in literature. However, we performed a more detailed and systematic investigation, computing band gaps for the three polymorphs with different Hamiltonians and basis sets and comparing the results obtained with the various protocols. All the methods identify an insulating feature for zirconia polymorphs, in agreement with the experimental evidence. The analysis of the data, reported in table 4.5, shows that our results are also in line with previous calculations. First, we can notice that, while all the considered methods give accurate results for the structural parameters, the electronic properties, in particular the band gaps, are more sensitive to the choice of the method. For all the three phases, HF calculations show the well-known tendency to overestimate largely band gaps, while PBE produces the lowest values, in agreement with the familiar trend of GGA functionals to underestimate band gaps.

Finally, independently from the basis set, the three hybrid functionals considered (B3LYP, B3PW and PBE0) give comparable results, which improve the accuracy of the data with respect to the other methods (hybrid functional data are about 2 eV higher than the PBE one). In particular, results obtained with the Zr^{ECP}-O* and Zr^{ECP}-O^{ECP} are very similar and about 0.7-1 eV lower than the corresponding results obtained with the all-electron basis set. Band gaps computed with these methods have values that generally lie between the set of experimental data reported in table 4.5. PBE0 results are systematically about 0.5 eV higher than the B3LYP or B3PW ones, as already pointed out by Gallino et al.,[234] in line with the largest amount of Hartree-Fock exchange in PBE0 (25%) than in the two other global hybrids (20%). From the data reported in table 4.5, it is also evident that the differences in the band gaps between the three phases are smaller than 1 eV and the tetragonal phase has the largest band gap, in accordance with previous DFT works, but in disagreement with the experimental results, which assign the largest value to the cubic phase. In particular, the band gap becomes smaller upon going from the tetragonal to the monoclinic and finally to the cubic phase. Only the values at the PBE0-D level, which are generally higher than PBE0 ones and than the experimental data, do not follow this order, providing the largest band gap for the monoclinic phase, followed by the tetragonal and finally by the cubic polymorphs. This might be related to the significant contraction of the monoclinic structure along the a and *c* lattice vectors when the *a* posteriori correction for dispersion is taken into account (see Table 4.1), that is to a volume effect which is much more pronounced in the monoclinic case than in the tetragonal one.

4.3.3.2 Valence and Conduction States

Figure 4.3 presents the band structures and the density of states (DOS), computed for the cubic, tetragonal and monoclinic zirconia phases at the PBE0/Zr^{ECP}-O^{ECP} level.

The band structures of the three polymorphs look similar. In particular, the same sets of bands could be observed for all the phases between -30 and 15 eV: Zr-4p states around -28 eV, O-2s states around -18 eV, and O-2p and Zr-4d states, respectively, below and above the Fermi level. The top of the valence band (VB) is located at the X point in *c*-ZrO_2, the M point in the *t*-ZrO_2 and at the Γ point in the *m*-ZrO_2, while the bottom of the conduction band (CB) is at Γ for *c*-ZrO_2 or *t*-ZrO_2 and at Y in *m*-ZrO_2. The similar topology of the plots suggests

Basis set	Method	Monoclinic	Tetragonal	Cubic
Zr*-O*	HF	14.59	14.72	14.04
	PBE	4.22	4.52	3.81
	B3LYP	6.04	6.34	5.59
	B3PW	6.04	6.32	5.62
	PBE0	6.56	6.86	6.09
	PBE0-D	6.93	6.86	6.12
Zr^{ECP}-O*	HF	14.53	13.67	13.14
	PBE	3.40	3.80	3.13
	B3LYP	5.20	5.55	4.91
	B3PW	5.23	5.58	4.90
	PBE0	5.71	5.93	5.37
	PBE0-D	6.19	6.00	5.43
Zr^{ECP}-O^{ECP}	HF	13.48	13.23	13.23
	PBE	3.47	3.61	3.07
	B3LYP	5.24	5.35	4.89
	B3PW	5.17	5.41	4.86
	PBE0	5.75	5.77	5.37
	PBE0-D	6.22	5.75	5.43
	VUV[a]	5.83	5.78	6.10
Exp.	EELS[b]	4.2	4.2	4.6
	EELS[c]	5.3	5.0	-
Other works				
LCAO/HF[d]	-	13.3	12.3	
LCAO/LDA[a]	4.46	4.28	4.93	
LCAO/PW1PW[e]	5.49	5.83	5.01	
LCAO/B3LYP[f]	5.61	5.70	5.50	
LCAO/PBE0[f]	6.09	6.20	6.03	
PAW/LDA[g]	3.12	4.10	3.10	
PAW/LDA+GW[g]	5.55	6.40	5.42	
PAW/GGA[h]	3.43	3.94	3.22	

[a] See ref.[269]. Pure monoclinic ZrO_2, Y_2O_3 stabilized teragonal-ZrO_2 (4.5 mol%), Y_2O_3 doped cubic-ZrO_2 (9.5 mol%).
[b] See ref.[305]. Pure monoclinic ZrO_2, Y_2O_3 stabilized teragonal-ZrO_2 (4.5 mol%), Y_2O_3 doped cubic-ZrO_2 (9.5 mol%).
[c] See ref.[235]. Pure monoclinic and tetragonal ZrO_2.
[d] See ref.[275].
[e] See ref.[266].
[f] See ref.[234].
[g] See ref.[263].
[h] See ref.[247].

Table 4.5: Computed band gaps (given in eV) of the monoclinic, tetragonal and cubic ZrO_2 phases, calculated with different Hamiltonians and basis sets.

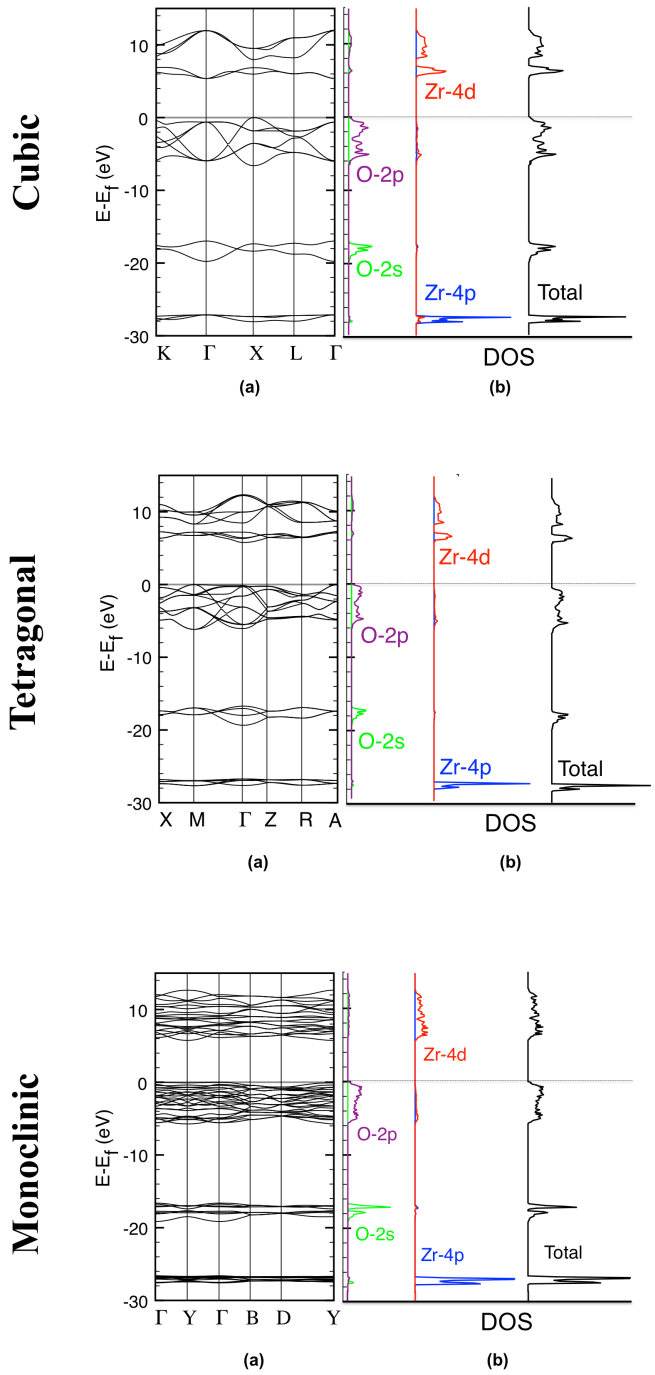

Figure 4.3: Calculated PBE0/Zr^{ECP}-O^{ECP} (a) band structure, and (b) total and Zr-4d, Zr-4p, O-2s, O-2p projected DOS of I) cubic, II) tetragonal and III) monoclinic ZrO_2.The Fermi level has been set as origin of the energy scale. For clarity, DOS for the cubic and tetragonal phases are multiplied by a factor of 5 and 2 respectively.

that the three materials have the same qualitative features of the Zr-O bonding. In particular, the band structures and the density of states for the valence bands of the three polymorphs show very similar features: two low-energy narrow bands and a wider band at higher energy. The wider band, which lies between 0 and about -6 eV, corresponding to the O-2p states, constitutes the top of the VB and is similar for all the polymorphs. A small contribution of the Zr-4d states to this band could be seen from the density of states. The following band at around -18 eV is narrow band, corresponding to the O-2s states. In the density of states, the corresponding peak appears as a doublet, which is sensitive to the oxygen coordination: in *c*-ZrO_2 and *t*-ZrO_2 where O atoms are 4-fold coordinated this double structure is less evident, whereas in the *m*-ZrO_2, the 3-fold oxygen atoms contribute to the higher energy peak, while the 4-fold coordinated contribute to the lower energy of the two peaks. The lowest observed band is another narrow band, which could be associated to the sharp peak in the total and projected DOS due to the Zr-4p states. In agreement with published XPS spectra,[235,269] this peak appears like a doublet independently from the symmetry of the studied phase. The CB bands show instead some differences due the different crystal symmetry of the three phases. The bottom of this band is constituted by the Zr-4d states, but the shape of the correspondent peak in the DOS is different among the three polymorphs. The different features of this structure could be explained through the crystal field theory: in the cubic phase, Zr atoms are exposed to the crystal field of the surrounding oxygen ions, disposed in a cubic environment (O_h point group symmetry). As a consequence of this field and of their symmetry, the zirconium d orbitals are split into two groups, one of lower energy (e_g), constituted by the $d_{x^2\text{-}y^2}$ and the d_{z^2} orbitals, which, pointing between the O anions, experience less the electron-electron interactions than the d_{xy}, d_{xz}, d_{yz}, which, on the contrary, are directed towards the oxygen atoms, and therefore constitute a triply degenerate group (t_{2g}) at higher energy. The same e_g-t_{2g} splitting of the d orbitals is expected in the tetragonal phase, where the zirconium atoms are also 8-fold coordinated, even if there is some distortion from the ideal cubic crystal field. Finally, in the monoclinic phase, which consists of ZrO_7 polyhedra without centre of symmetry, the situation is much more complex, because the d orbitals could potentially interact with the crystal field at different extent.[235,269,305] These features could be easily derived from the band structure and density of states. For *c*-ZrO_2, two distinct conduction bands are evidenced and there is a small gap between these two groups. For *t*-ZrO_2, the situation is similar and two discrete bands with a small gap are still evident. Lastly, for *m*-ZrO_2, where the symmetry lowering is also responsible for the appearance of many energy bands in comparison to the other two phases, a complete different structure, consisting of a single band, appears. Mulliken atomic charges and overlap populations are also reported in Table 4.6 for the three polymorphs. Despite the tendency of Mulliken analysis to overestimate covalency of chemical bonds, some general considerations can be derived from this data. Charge analysis show similar results for the three polymorphs with a value of about +2 and -1 for respectively Zr and O atoms. These values decrease slightly going from the cubic to the tetragonal to the monoclinic phase. Moreover, the bond population of the Zr-O bond increases going from the more (cubic) to the least (monoclinic) symmetrical phase. This data evidences the stronger covalency of the metal-oxygen bond in lower symmetry ZrO_2 structure, which can be explained through symmetry consideration (O-2p and Zr-4d mixing is partially forbidden in *t*-ZrO_2 and especially in *c*-ZrO_2) and considering the well-known

	Monoclinic	Tetragonal	Cubic
q_{Zr}	+2.153	+2.196	+2.210
q_O	-1.045	-1.098	-1.105
b_{Zr-O}	+0.202	+0.168	+0.142

Table 4.6: Mulliken atomic charges (q, in *e*) and overlap population (b, in *e*) computed for monoclinic, tetragonal and cubic zirconia at the PBE0/Zr^{ECP}-O^{ECP} level.

tendency of smaller ionicity to favour structures with lower coordination numbers (7 for Zr atoms in *m*-ZrO_2 and 8 in *c*-ZrO_2).[253]

In summary, there are some similarities in the electronic properties of the three polymorphs (in particular the electronic structures of the cubic and tetragonal phases have some common features), with the differences due to the lower symmetry and to the highest covalency of Zr-O bonds in *t*-ZrO_2 and *m*-ZrO_2. Indeed, the main dissimilarity among the phases is in the hybridization of the Zr-4d, which determines the appearance of a fingerprint in the electronic structure, that is the existence of a gap in the CB between the e_g and t_{2g} states, which is evident in the cubic zirconia, less marked in the tetragonal ZrO_2 and absent in the monoclinic phase.

4.4 ZrO_2 Surfaces

The excellent results obtained for the description of the bulk properties of the three zirconia phases gave us the confidence to move to the study of zirconia surfaces. In particular, as these results showed that the PBE0/Zr^{ECP}-O^{ECP} level is suitable to investigate the properties of ZrO_2 with good accuracy at low computational cost, this protocol was selected for surface calculations. At the experimental level, ZrO_2 surfaces have been already studied.[290,306] In particular, Morterra et al.,[290] studying Y_2O_3 stabilized *t*-ZrO_2 revealed that the surface features of this material depend on the preparation conditions; in particular for tetragonal samples fired at low temperatures the termination corresponding to the (111) plane is favoured, whereas, in samples fired at higher temperatures, terminations corresponding to the (101) plane are more abundant. They also identified the (-111) termination as the prevalent one in *m*-ZrO_2. Surface tension has been measured for polycrystalline zirconia doped with CaO_2[307] and for yttria stabilized zirconia.[308] Values of, respectively, 1.428 J/m^2 and 1.927 J/m^2 have been obtained. Previous theoretical calculations are in agreement with experimental data. Christensen and Carter,[277] systematically studied different surfaces for all the three zirconia polymorphs at the DFT level, identifying the (111), (101) and (-111) as the most stable termination for cubic, tetragonal and monoclinic zirconia, respectively. The cubic (111) surface has been found to be the most stable also by the HF calculations of Gennard et al.,[271] by the interatomic potential (IP) calculations of Xia et al.[246] and Balducci et al.,[278] and by other DFT calculations, like the one of Alfredsson et al.[284] Eichler and Kresse[249] investigated different possible surface terminations for tetragonal (001) and (101) planes with DFT calculations at the GGA level and established that oxygen terminated surfaces are most stable than the zirconium terminated ones, confirming what Christensen

and Carter[277] already suggested. The adsorption of different molecules like sulphuric acid[282] or hydrogen[280] on the most stable tetragonal (101) surface or of water[276,281], and hydrogen on the clean[286] and reduced[283] monoclinic (-111) has also been widely investigated. From these data, we focused our attention on the thermodynamically most stable surface of each phase, namely the cubic (111), the monoclinic (-111) and the tetragonal (101) surfaces, as well as the tetragonal (111) surface, this latter being the predominant termination in *t*-ZrO_2 sintered at high temperature. In the following paragraph, we explore the energetic, electronic and geometrical properties of these surfaces.

4.4.1 Surface Energetics

The first property for which we checked convergence with respect to the number *n* of layers of the slab is the surface energy ($E_s(n)$). For sufficiently thick slab, $E_s(n)$ is expected to converge to the energy of the semi-infinite system. The surface energy for a slab model composed by *n* layers has been computed according to the following equation:

$$E_s(n) = \frac{E_n - nE_{bulk}}{2A} \tag{4.1}$$

where E_n is the total energy of a slab of *n* layers, E_{bulk} is the energy of the bulk system per unit cell and A is the area of the slab unit cell. Before proceeding, it is important to add some remarks on the structure of the four surfaces taken into account. The first thing to note is that we considered only oxygen terminated surfaces, which were found to be most stable in respect to zirconium terminated surfaces by Eichler and Kresse[249] and Christensen and Carter.[277] The simplest system is the cubic surface (111), which is of 'type 2', according to Tasker's classification of crystal surfaces.[309] Indeed, along the normal to the surface there is a sequence of charged planes: the first plane is constituted by oxygen anions, the second by zirconium cations and the third again by oxygen ions. Thus, the repeating unit is constituted by neutral O-Zr-O platelet and this implies that each of the *n* layers of the slab will be composed of three atomic layers and will contain one ZrO_2 formula unit. In tetragonal (101), a slab layer is constituted by five atomic layers (O-O-Zr_2-O-O motif), whereas six atomic layers (O-Zr-O-O-Zr-O motif) form the repetitive unit in tetragonal (111). In both cases, there are two ZrO_2 formula units for one slab layer. Finally, the most complex case is the monoclinic (-111), with twelve atomic layers (O-O-O-Zr-O-Zr-Zr-O-Zr-O-O-O motif) and four ZrO_2 formula units per slab layer. The labelling scheme adopted is reported in Figure 4.4.

Plots of the computed surface energies as a function of the slab thickness, reported in figure 4.5, show that, as expected, $E_s(n)$ strongly depends on the number of layers in the slab model. Moreover, from figure 4.5, (c), it is evident that for *t*(111) an oscillating trend could be observed: the surface energy of even layer slabs converge from below to the energy of the infinite system, while the surface energy of odd layer slabs converge from above. A similar trend has been observed in other systems, such as in the calculations of Labat et al.[86] on the rutile-TiO_2 (110) surface. In our case, however, this behaviour cannot be related to different symmetry properties of the even or odd layer slabs, since they both have the same symmetry operators.

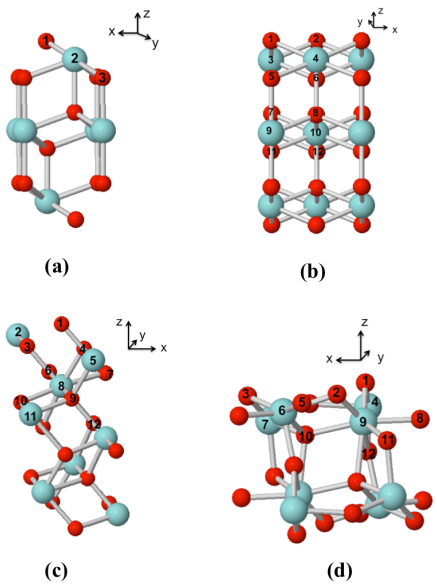

Figure 4.4: Slab models and labeling of the a) *c*(111) surface, composed by three O-Zr-O trilayers, b) *t*(101) surface, composed by three layers (O-O-Zr_2-O-O motif), c) *t*(111) surface, composed by four layers (O-Zr-O-O-Zr-O motif), d) *m*(-111) surface, composed by two layers (O-O-O-Zr-O-Zr-Zr-O-Zr-O-O-O motif). Large light blue spheres represent Zr atoms, while the small red ones stand for oxygen atoms.

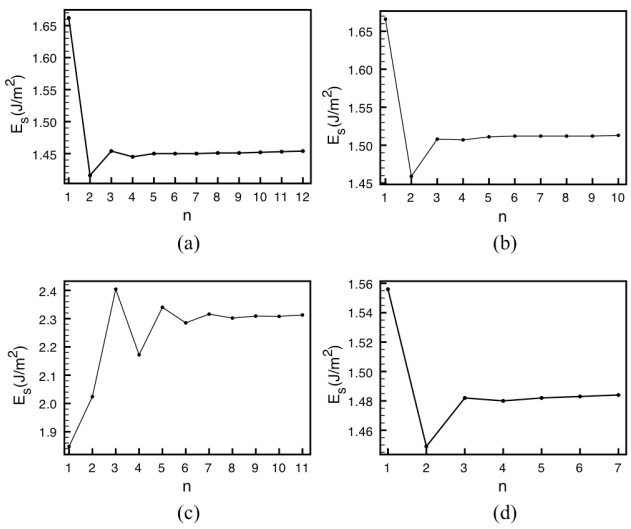

Figure 4.5: Surface energy E_s(in J/m^2) of a) *c*-ZrO_2 (111). b) *t*-ZrO_2 (101). c) *t*-ZrO_2 (111) and d) *m*-ZrO_2 (-111) surfaces as a function of the number n of layers in the slab model.

Comparing the data for all the different surfaces, it could also be noted that the number of slab layers necessary to reach convergence depends both on the symmetry of the system and on the orientation of the surface. For the simplest cubic (111) surface, a slab of 5 layers, with each layer split in three atomic layers and a total number of 15 atoms in the unit cell, could be considered fully converged with a surface energy of 1.450 J/m^2. The tetragonal (101) orientation is equivalent to the cubic (111). For this surface, the fully converged slab contains six layers, for a total of 30 atomic planes and of 36 atoms in the unit cell. In fact, because of the tetragonal distortion, the repetitive unit contains not one, as in the cubic phase, but two ZrO_2 units, increasing in that way the complexity of the system and thus making it more demanding from a computational point of view. For the *t*(111), 8 layers are needed in order to reach convergence, for a total of 48 atoms in the unit cell.

The value of the converged energies are of 1.512 J/m^2 and 2.309 J/m^2 for respectively the *t*(101) and the *t*(111). Finally, for the monoclinic (-111), convergence of the surface energy to the value of 1.482 J/m^2 with increasing slab thickness is reasonably fast considering the symmetry properties of this system. 5 layers, which correspond to 60 atomic layers and 60 atoms in the unit cell, are sufficient to give an adequate description. The values of the converged surface energies for the studied systems are reported in Table 4.7, along with results of previous theoretical works and with experimental data. As already pointed out,[277] care must be taken in comparing the results with the experimental data, which are generally affected by large errors because of the difficulties of the experiments. However, we can notice that our surface energies values are in line with them.

The surface energies of the relaxed surfaces increase in the following order: *c*(111) < *m*(-111) <*t*(101) <<*t*(111). The cubic one is found to be the most stable surface, in accordance with other calculations.[277] Indeed, the first three surfaces are very close in surface energy, especially the monoclinic (-111) and the tetragonal (101), as already observed by Christensen and Carter,[277] who, for these surfaces, obtained values that could be considered nearly the same within the calculation accuracy. Finally, the tetragonal (111) is by far the least stable not only among the tetragonal but also among all surfaces taken into account. The greater stability of *c*(111) and the lower stability of the *t*(111) can be understood by taking into account the coordination of the surface sites, which will be analysed in detail in the following section.

4.4.2 Surface Geometries

In this section, we first give a detailed description of surface sites and then we discuss the computed atomic relaxations, for each of the considered surfaces.

- **Cubic (111)** Oxygen anions exposed on the (111) surface of *c*-ZrO_2 (O_1, see Figure 4.4, (a)) are three fold coordinated, while the outermost Zr atoms (Zr_2) are seven fold coordinated. It is interesting to note that Zr and O atoms on that surface have the same coordination found in monoclinic zirconia. This type of coordination could explain the highest stability of *c*(111) surface with respect to the others. Relaxation of atoms of these surface occurs only perpendicular to the surface and the displacements decay very rapidly with depth of the slab. Small relaxations are observed, with the outermost

	m(-111)-5L	*t*(101)-6L	*t*(111)-8L	*c*(111)-5L
PBE0/Zr^{ECP}-O^{ECP}	1.482	1.512	2.309	1.450
Other works				
LDA/PAW[a]	1.246	1.239	1.649	1.119
HF/LCAO[b]				1.488
PBE/PAW[c]	1.224[d]	1.090	2.091	
PW91/PAW[e]	1.340	1.107[f]		
LDA/PW[g]		1.316		
Exp.[h]			1.428	
Exp.[i]			1.927	

[a] See ref.[277]. For *c*(111), the reported value corresponds to the non relaxed surface.
[b] See ref.[271].
[c] See ref.[282].
[d] See ref.[281].
[e] See ref.[238].
[f] See ref.[280].
[g] See ref.[279].
[h] See ref.[308]. High temperature measurement on polycrystalline zirconia with CaO 6% extrapolated to 0 K
[i] See ref.[307]. High temperature measurement on polycrystalline yttria (8%) stabilized zirconia extrapolated to 0 K.

Table 4.7: Surface energies (in J/m^2), computed at the PBE0/Zr^{ECP}-O^{ECP} level, for the monoclinic (-111), tetragonal (101) and (111) and cubic (111) zirconia surfaces. *x*-L indicates a slab built with *x* layers.

oxygen that relaxes outward and the outermost Zr that relaxes inward. In particular, O_1 relaxation is found to be almost negligible, while Zr_2 is relaxed by ca. 0.03 Å, in excellent agreement with the relaxation calculated for this atom through plane wave calculations by Alfredsson et al.,[284] but contrarily to what observed by Gennard et al.[271] at the HF level, who, studying a three layers slab, found notable displacements only for the outermost oxygen ions (-0.044 Å) and much smaller relaxations for the Zr surface cations (-0.004 Å). As we will see, the atomic relaxations associated to $c(111)$ are the smallest if compared to atomic relaxations of atoms of the other studied surfaces. This not only suggests that its structure is compact, but it is consistent with its greater stability. In fact, Christensen and Carter[277] observed that there is a strong correlation between stability and atom relaxations: the most stable unrelaxed surfaces are those with the lowest relaxations.

- **Tetragonal (101)** The exposed oxygen ions on the $t(101)$ surface (O_1 and O_2, see Figure 4.4, (b)) are all 3-fold coordinated and the exposed zirconium atoms (Zr_3 and Zr_4) are all 7-fold coordinated. The two Zr surface sites present however one important difference. As said before, 8 oxygen atoms surround Zr atoms in bulk t-ZrO_2, four of them disposed with tetrahedral geometry and with shorter Zr-O bonds and the other 4 constitute a tetrahedron with longer Zr-O bonds. When t-ZrO_2 crystals are cut along (101), both long and short Zr-O bonds are cleaved and surface sites missing long (Zr_3) or short (Zr_4) metal-oxygen bond are formed. Oxygen atom O_1 is displaced outward by 0.062 Å and laterally by 0.082 Å, O_2 is displaced inward by 0.017 Å and laterally by 0.030 Å. Zirconium atoms Zr_3 and Zr_4 are both relaxed inward by 0.030 and 0.065 Å respectively and laterally by 0.042 Å and 0.015 Å respectively. Hence, generally, zirconium positions undergo minor changes, as opposite to oxygen atoms that move largely. However, even if these deviations are larger than the displacements observed for the $c(111)$, they are still small and also $t(101)$ could be considered as a compact surface.

- **Tetragonal (111)** The unrelaxed surface exposes three types of Zr atoms, 5-fold, 7-fold and 8-fold coordinated (Zr_2, Zr_5 and Zr_8 respectively, see Figure 4.4, (c)), as well as one 2-fold (O_1), two types of 3-fold (O_3, O_4) and two 4-fold coordinated oxygen atoms (O_6 and O_7). The outermost oxygen is the two-folded O1, which is bonded to the five-folded Zr_2 atom in the second atomic layer, which is in turn bonded to O_3, the third atomic layer. The main displacements occur laterally along both x and the y directions, while are much more limited in the direction perpendicular to the surface, where the outermost Zr relax inwards (by 0.139 Å) and the outermost oxygen and the Zr_5 relax outwards (respectively by 0.063 and 0.150 Å). These relaxations change the features of the surface, in particular the displacement of the oxygen atoms bounded to the 5-folded Zr atom; especially the one of O_1, which is the largest (by 0.364 along x and by 0.519 along y), lead to the tightening of the bond between the O atom and Zr_2, which is important for the stabilization of the surface considering the low coordination of this site. In order to achieve this stabilization of Zr_2, the displacement of the O_7 atom determine the lowering of the coordination number of Zr_8 from 8 to 7 and, of course, of its coordination number from 4 to 3. Therefore, the complexity of this surface and

the presence of lower coordinated cations and anions with respect to the *t*(101) could explain the higher surface formation energy of *t*(111), which is also the one associated with the largest atomic relaxations.

- **Monoclinic (-111)** Monoclinic (-111) plane is characterized by four different types of zirconium cations: two 6-folded (Zr_4, the outermost zirconium atom, and Zr_6, see Figure 4.4, (d)) and a 7-folded atom Zr_9, which has the same coordination number of zirconium atoms in the bulk. Among the surface oxygen atoms, four (O_2, O_3, O_5, O_8) are three-folded, while the outermost O_1 has a 2-fold surrounding. The major displacements occur in the first slab layer, the values become negligible beneath this depth. These values show that even if the monoclinic surface is more complex than *c*(111) and *t*(101), relaxations are not only smaller than the one observed for the least stable *t*(111), but their amplitude is generally comparable to the one observed for the *t*(101), which is very close in energy to this surface. The largest displacements are associated to oxygen O_1 (by 0.112 Å along *x*) and O_3 (by 0.116 Å along *x* and by -0.101 Å along *y*) and are directed toward the under coordinated zirconium atoms.

4.4.3 Surface Electronic Properties

The convergence of the surface electronic properties, in particular of band gaps, with the slab thickness has then been checked for all the considered surfaces. In Figure 4.6 the computed band gaps are reported as a function of the slab thickness for *c*(111), *t*(101), *t*(111) and *m*(-111). Converged band gaps (5.51, 5.46, 5,70 and 5.39 eV, respectively) are in line with the corresponding bulk gap values (5.37, 5.77 and 5.75 eV respectively). An oscillating trend is observed only for the *t*(111) surface with the values of the odd layers slabs that converge from below and the ones of the even layers slab converging from above. This trend is opposite to the one observed for the same system for the surface energy.

Finally, in Figure 4.7, the density of states (DOS) for the studied systems are reported. The same features observed for the corresponding bulk can be noticed for the surfaces: the bottom of the CB is made by the Zr-4d states, while the top of the VB is composed by the O-2p states, constituting a wider band with respect to the lower and narrower valence bands associated to the O-2s or Zr-4p states. The fingerprint feature, being the split of the t_{2g} and e_g states, is still observable in the *c*(111) DOS and it is also present in the DOS of the tetragonal surfaces, especially for the most complex *t*(111). Again this split is not observed for *m*(-111).

For the *c*(111), O-2s and O-2p (three-folded) states of the uncoordinated O atoms (3-fold, O1) are shifted to higher energies with respect to coordinated oxygen atoms, while the projected DOS on uncoordinated and coordinated Zr atoms appears to be essentially the same. This same behaviour could be observed also for the 3-fold coordinated O_1 and O_2 atoms of *t*(101) and for the 2-fold (O1) and 3-fold coordinated exposed oxygen atoms of the *t*(111) surface, which are at higher energy with respect to the states associated to the fully coordinated oxygen atoms. A similar trend is observed also for the monoclinic surface, where the 2-folded O_1 contributes essentially to the higher energy O-2s and O-2p states. They are followed, in order, first by 3-folded and then the four-folded oxygen states, as already observed in the bulk system. Again, for the Zr-4d states of the CB, no

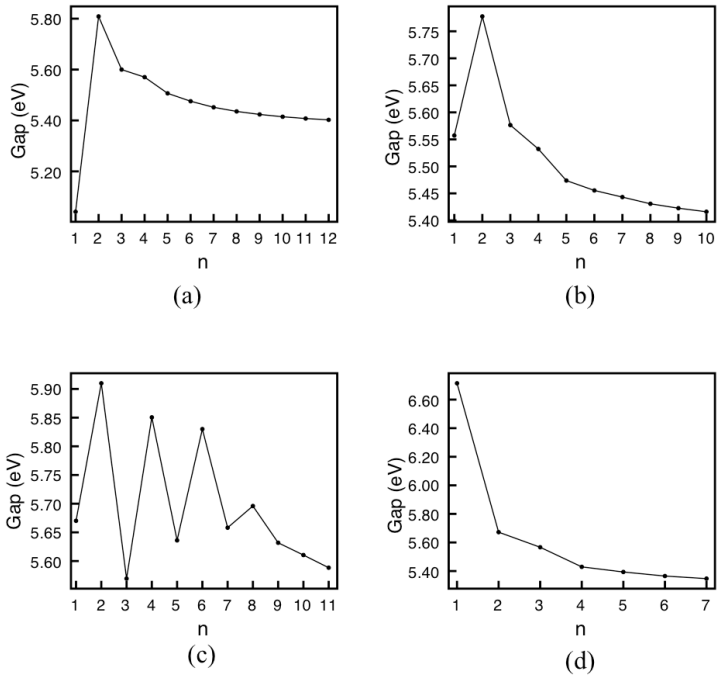

Figure 4.6: Computed band gap as a function of the number n of layers in the slab model of the a) c-ZrO_2 (111), b) t-ZrO_2 (101), c) t-ZrO_2 (111) and d) m-ZrO_2 (-111) surfaces.

remarkable differences in the behaviour of the uncoordinated Zr atoms with respect to the fully coordinated ones could be observed.

4.5 Reducibility properties of the (111) of c-ZrO_2 surface

As a preliminary step toward the study of YSZ, the stability, the structural and electronic properties of the zirconia (111) surface containing only isolated oxygen vacancies were investigated. The formation of colour centres in zirconia has been extensively described for monoclinic ZrO_2 bulk[254,310] and surfaces[283], for tetragonal ZrO_2 bulk[248,283] and surfaces[249], for cubic zirconia bulk,[250,255,263] while only little information can be found on cubic surfaces.[292] When a neutral oxygen atom is removed, two electrons associated to an oxygen anion are left behind in the lattice and a neutral oxygen vacancy (V_O) is formed, with two possible spin states for the resulting system.

The formation of oxygen defects on the clean surface was studied removing two oxygen atoms from a (2×2) supercell of the c(001)surface, resulting in a $Zr_{24}O_{46}$ stoichiometry. Bogicevic et al.[250] observed that as a consequence of the repulsion between the vacancies, oxygen defects in zirconia tend to align along the [111] direction as third nearest neighbours for high (15-40 mol %) Y_2O_3 concentrations. They also observed that for more dilute composition the vacancies could space themselves at greater distances. The two vacancies were then placed along the [111] direction in a symmetrical way at the top and bottom of the supercell. This ensures to leave enough space between the two vacancies (about 13 Å)

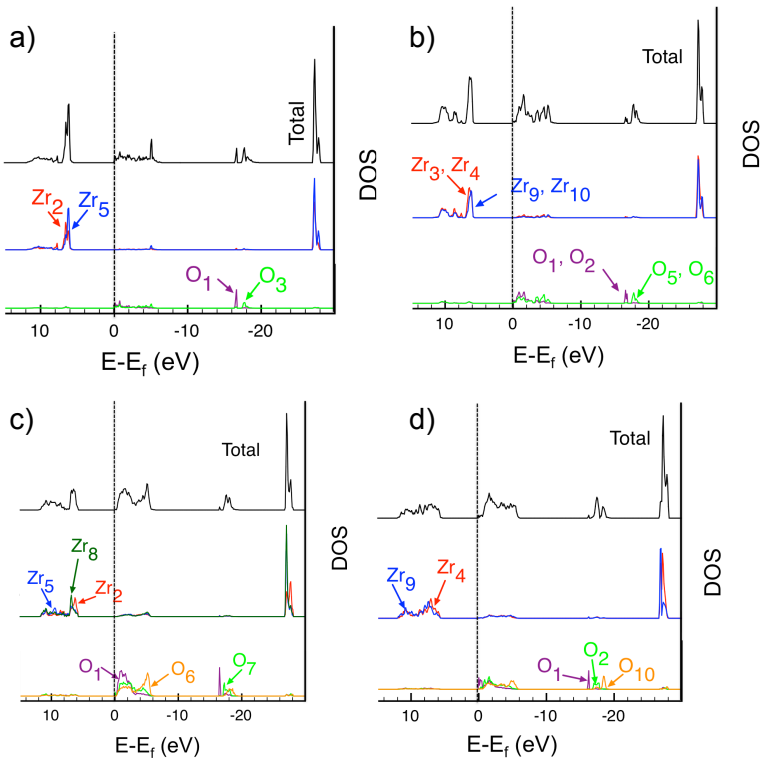

Figure 4.7: Computed total and projected DOS for a) *c*-ZrO_2 (111)-5L. O_1 is 3-folded, O_3 4-folded, Zr_2 7-folded and Zr_5 8-fold coordinated; b) *t*-ZrO_2 (101)-6L, O_1 and O_2 are 3-folded, while O_5 and O_6 are 6-folded. Zr_3 and Zr_4 are 7-folded and Zr_9 and Zr_{10} are 8-fold coordinated; c) *t*-ZrO_2 (111)-8L. O_1 is 2-folded, O_7 is 3-folded and O_6 is 4-folded. Zr_2 is 5-folded, Zr_5 is 7-folded, while Zr_8 is fully coordinated; d) *m*-ZrO_2 (-111)-5L. O_1 is 2-folded, O_2 is 3-folded, while O_{10} is fully coordinated. Zr_4 is 6-folded and Zr_9 is 7-fold coordinated. In every case, the Fermi level has been set as origin of the energy scale. Projected DOS are multiplied by a factor of 3. Labels refer to Figure 4.4.

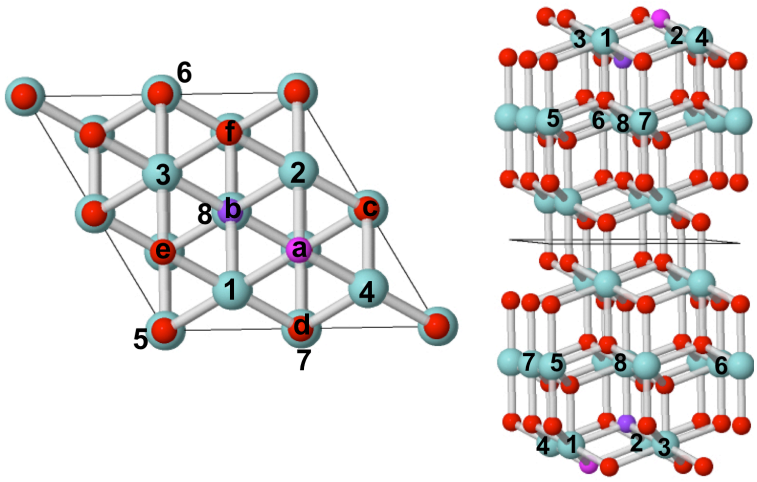

Figure 4.8: Top (left) and lateral (right) views of the (2 × 2) supercell of the (111) ZrO_2 surface. Oxygen atoms are in red, while zirconium atoms are in light blue. Pink for surface vacancies positions, violet for subsurface vacancies positions. Numbers refer to Zr atoms, letters to oxygen atoms. Zirconium atoms numbered 1, 2, 3, and 4 belong to the outermost Zr plane, while 5, 6, 7, and 8 belong to the plane under the subsurface vacancy.

to avoid any spurious interactions between defects. Two possible positions for an oxygen vacancy on the (111) surface were tested. From figure 4.8, it is evident that one corresponds to a three-folded surface oxygen site (indicated as surface vacancy in the following), while the other corresponds to a four-folded bulk-like site (indicated as subsurface vacancy in the following).

4.5.1 Formation Energy and Structural Rearrangements

The energy of formation (E_f) of one surface or subsurface oxygen vacancy on the (111) surface was computed and reported in table 4.8. The energy of formation of n vacancies (E_f^n on the cubic (111) surface was computed with respect to molecular (O_2) or atomic (O) oxygen as, respectively in equations 4.2 and 4.3:

$$E_f^n(\frac{1}{2}O_2) = E(\text{surface with } n \text{ vacancies}) + \frac{n}{2}E(\text{O}_2) - E(\text{surface}) \tag{4.2}$$

$$E_f^n(O) = E(\text{surface with } n \text{ vacancies}) + nE(\text{O}) - E(\text{surface}) \tag{4.3}$$

where $E(\text{surface with } n \text{ vacancies})$ is the energy of the system with n vacancies, either in a singlet or triplet spin state, $E(\frac{1}{2}\text{O}_2)$ is the energy for the O_2 molecule in its ground state of triplet, $E(\text{O})$ is the energy for the O atom and $E(\text{surface})$ is the energy for the clean

	Vacancy	Spin State	$E_f(\frac{1}{2}O_2)$	$E_f(O)$
This work	surface	S	8.4	10.2
		T	8.5	10.3
	subsurface	S	7.0	8.7
		T	7.3	9.1
Other works				
GTO/B3LYP			7.2[a]	-
PAW/PBE			5.9[b]	8.9[b]
PAW/GGA-II			-	8.9[c]
PAW/PBE			-	8.8[d]

[a] See ref.[311] Computed for bulk *t*-ZrO_2.
[b] See ref.[283] Computed for bulk *m*-ZrO_2.
[c] See ref.[310] Computed for bulk *m*-ZrO_2.
[d] See ref.[292] Computed for *c*-(111).

Table 4.8: Formation energy (E_f, in eV) of one surface or subsurface oxygen vacancy (with respect to $\frac{1}{2}O_2$ or to O) on the cubic ZrO_2 (111) surface, as a function of the spin state considered (T for triplet; S for singlet).

surface. The energy of formation for one vacancy was then obtained by simply dividing for the number of vacancies *n*.

Molecular oxygen is generally preferred as reference in more recent works, because it is used in some oxidation techniques providing the right reference for the chemical potential and because the degeneracy of the ground state of triplet for the O atom is poorly described in DFT.[310] The obtained values (see table 4.8) are in agreement with the ones reported in previous theoretical works, which, however, refer to the bulk structure of the tetragonal and monoclinic zirconia phases or to the cubic (111) surface[292], even if in this latter case the role of different oxygen sites was not taken into account. The singlet state is always found to be the most stable independently of the type of vacancy: it is more stable than the triplet one by 0.3 eV and 0.1 eV for a 3-fold subsurface and for the 2-fold surface vacancy, respectively. Considering the difference in stability, the following discussion is based only on the most stable singlet state. Subsurface vacancies resulted to be the most stable, with formation energies of 1.4 and 1.5 eV (with respect to O_2 and O, respectively) lower than the corresponding energies for the surface one. Indeed, Syzgantzeva et al.[283] already reported that even if surfaces are more reducible than bulk, due to the decrease in coordination of surface atoms, the most stable vacancy does not always correspond to those created from under-coordinated oxygen site. The formation energy of the oxygen vacancy can be considered as a measure of the reducibility of the material. These values show that the reduction behaviour of ZrO_2 surfaces from the point of view of energetics is closer to the one of irreducible oxides like MgO ($E_f(O)$ 10.6 eV and 9.8 eV for surfaces[283]) rather than to the one of a reducible oxide such as TiO_2 ($E_f(O)$ 7 eV for the bulk and 5.5-6 eV for surfaces).[283] The irreducible nature of ZrO_2 is thus confirmed.

Optimized geometries for the system with a surface or subsurface vacancy are reported in figure 4.9. Structural rearrangements are generally restricted to atoms in NN positions to the vacancy for both a surface and subsurface defect, in particular to NN oxygen atoms. Again,

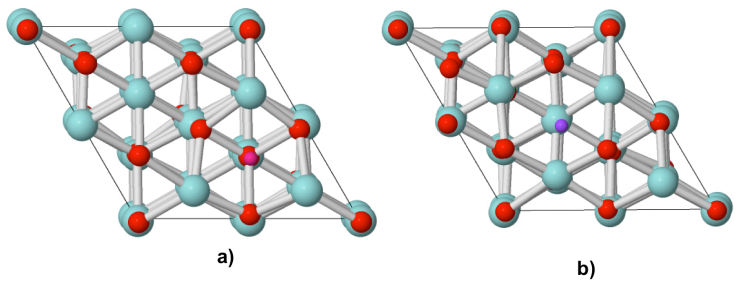

Figure 4.9: Top view of the supercell for the optimized geometry of the (111) surface with a) surface or b) subsurface vacancies. Same color code as in figure 4.8

Vacancy	Label	x	y	z
Surface	O_c(NN)	0.21	0.12	0.00
	O_d(NN)	0.00	-0.24	0.00
	O_b(NN)	-0.21	0.12	0.00
	O_e(NNN)	0.00	-0.10	-0.02
	Zr_1(NN)	0.03	0.02	-0.05
	Zr_2(NN)	0.00	-0.04	-0.05
	Zr_3(NNN)	0.00	0.00	0.11
	Zr_4(NN)	-0.03	0.02	-0.05
Subsurface	O_e(NN)	-0.09	-0.10	-0.07
	O_f(NN)	0.04	-0.13	-0.08
	O_a(NN)	0.09	-0.06	0.02
	O_c(NNN)	0.05	0.07	-0.03
	Zr_1(NN)	0.00	-0.09	-0.02
	Zr_2(NN)	0.06	0.03	-0.02
	Zr_3(NN)	0.07	-0.04	0.04
	Zr_4(NNN)	0.00	0.00	-0.08

Table 4.9: Displacements (in Å, from ideal positions) for the (111) surface with surface or subsurface oxygen vacancies. Atom labels refer to Figure 4.8

Label	Clean	Oxygen Vacancy	
		surface	subsurface
O_e	-1.06	-1.06	-1.06
O_f	-1.06	-1.06	-1.06
O_a	-1.06	-0.35	-1.06
O_c	-1.12	-1.11	-1.12
O_d	-1.12	-1.11	-1.12
O_b	-1.12	-1.11	-0.46
Zr_1	2.17	1.97	2.01
Zr_2	2.17	1.97	2.01
Zr_3	2.17	2.06	2.01
Zr_4	2.17	1.97	2.17
Zr_8	2.21	2.21	2.04

Table 4.10: Mulliken atomic charges (in *e*) of selected Zr and O atoms of the clean (111) surface and of system with surface or subsurface vacancies. Atom labels refer to Figure 4.8

this is similar to a metal oxide like MgO, where F centres are stable and their formation is accompanied by small relaxation of the O atom NN to the defect, indicating electron trapping in the vacancies.[255,283] The surface vacancy is associated to the largest displacements, which cause the NN O atoms to move toward the vacancy and NN Zr atoms to move radially away from it at a distance of 2.39 Å (the distance of NN Zr atoms from the vacancy for the unrelaxed system is 2.22 Å). Smaller relaxations are observed for the most stable system with subsurface vacancies (See Table 4.9).

There could be a relationship between relaxation and charge redistribution: the lower stability of the surface vacancies is accompanied by greater relaxation, which is in turn accompanied by a greater redistribution of charge density. Table 4.10 shows that, on the NN Zr atoms, the atomic charge decreases from +2.17 for the clean surface to +1.97 and +2.01 for a surface and a subsurface vacancy, respectively. Smaller decreases are observed for Zr atoms NNN to the vacancy.

4.5.2 Electronic structure of oxygen vacancy

Reduction via surface or subsurface vacancy formation leads to the creation of a defect state in the gap, (see Figure 4.10). The two left electrons, which filled the O-sp states, now occupy a newly created vacancy state. Therefore, a new doubly occupied defect energy level appears in the band gap. As we can see from the DOS, it is mostly made by Zr-4d states, so we can imagine that after the removal, these two electrons are moving back from O to Zr, occupying a linear combination of the d orbitals of neighbouring Zr atoms.[263] A small contribution of O-2p states could also be observed in figure 4.10. This defect state is localized in the vacancy region. It resembles a neutral V_O^X center in alkaline-earth oxides and has the typical structure of an F-center.[255,283,311]

The main difference in the electronic structure of a surface or subsurface vacancy, except for the slightly more flat band structure of the latter system, is in the position of the defect

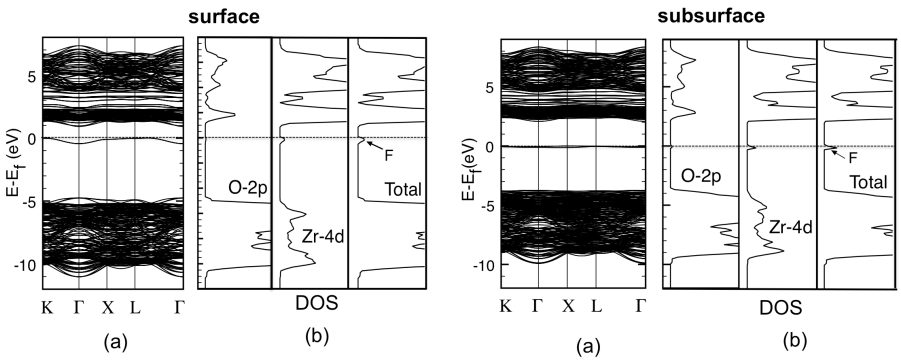

Figure 4.10: Band structure (a) and total and projected density of states (b) for the system with surface (left) or subsurface (right) oxygen vacancies.

Vacancy	Relative to VB	Relative to CB	E_g
surface	4.30	0.92	5.66
subsurface	3.58	2.07	5.79

Table 4.11: Band gap values (E_g) and positions of the defect level with respect to the valence band (VB) and the conduction band (CB) for surface and subsurface vacancies. All data in eV.

state, which depends on the coordination of the site from which the oxygen atom is removed. For a surface vacancy, the defect level is 4.30 eV above the top of the VB and only 0.92 eV under the bottom of the CB. For the most stable subsurface vacancy, instead, the defect level is 3.58 eV above the top of VB and 2.07 eV under the bottom of the CB (see Table 4.11). Therefore, the presence of the vacancy state in the gap decreases the effective band gap, which results to be higher in the case of the most stable type of defect, compared to the other surface case.

Finally, from figure 4.11, it is interesting to note that the defect state is clearly observed both in the DOS of the unrelaxed system, *i.e.* the structure in which the atoms are in the centro-symmetric fluorite positions, and in that of the relaxed one, *i.e.* the structure obtained after the geometry optimization.

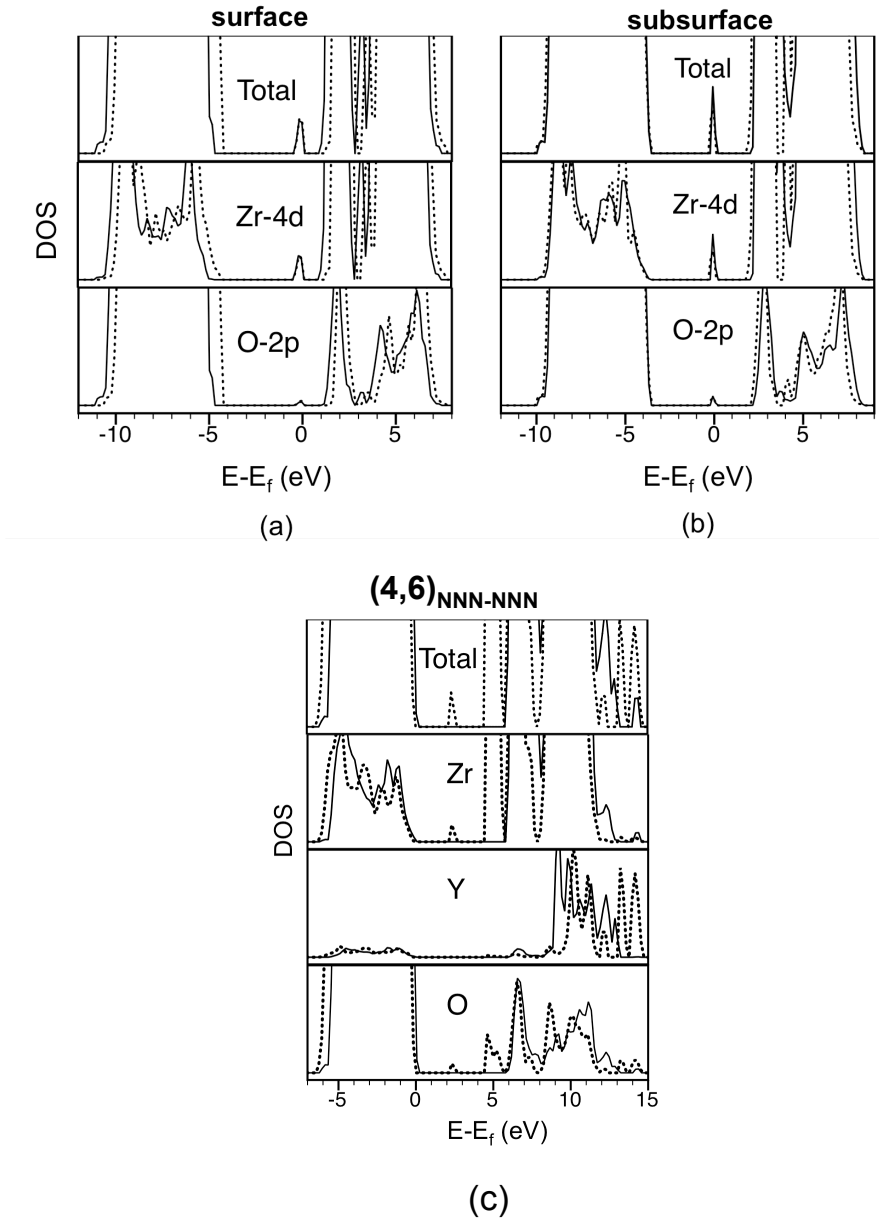

Figure 4.11: Total and projected DOS for the relaxed (plain line) and unrelaxed (dotted line) (111) supercell with a surface (a) or subsurface (b) oxygen vacancy or for the (4,6$_{NNN-NNN}$ configuration of YSZ (c).

4.6 Y_2O_3-doped (111) surface

When ZrO_2 is doped with Y_2O_3, for each pair of aliovalent Y^{3+} ions that substitutes a pair of Zr^{4+} cations, one oxygen vacancy must be created. Hence, since Y has one d-electron less than Zr, this corresponds to remove one oxygen atom together with two electrons (O^{2-}). For this reason, the corresponding vacancy should be a doubly positively charged vacancy ($V_O^{\bullet\bullet}$) also called F^{2+} centre. In order to obtain a representative model for YSZ we created, as before, two oxygen vacancies, one at the top and the other at the bottom of the ZrO_2 supercell and, at the same time, we substituted four Zr with four Y atoms ($Zr_{20}Y_4O_{46}$). This allows mimicking the experimental percentage of 8 mol % Y_2O_3. One pair of Y atoms was positioned at the top and the other at the bottom of the supercell in a symmetrical way, each one in correspondence with one oxygen vacancy. Two and five different configurations of the two Y^{3+} cations with respect to a surface or subsurface vacancy were taken into account, similarly to the work of Ganduglia-Pirovano et al.,[312] who studied the formation of oxygen vacancies and the localization of the excess electrons on different pair of sites on the (111) surface of the cubic fluorite structure of CeO_2. There are four Zr atoms in the outermost Zr plane, three of them (1, 2, and 4 in fig. 4.8) are in nearest-neighbour position (NN) to a surface vacancy, while the fourth one (3 in fig. 4.8) is in a next nearest-neighbour (NNN) position with respect to it. For a subsurface vacancy, instead, Zr atoms 1, 2, and 3 of the outermost Zr layer and Zr atom 8 which belong to the plane below this defect are in NN positions, while Zr atom 4 on the plane above and Zr atoms 5, 6, and 7 in the plane below it are in NNN positions. If we consider the bulk truncated surface, NN and NNN Zr atoms are at a distance of respectively 2.22 Å and 4.20 Å away from the vacancy. Hence for a surface vacancy, the two Y atoms can be introduced both NN to the defect or one can be NN and the other NNN to it, for a total of two possible configurations ($(1,2)_{NN-NN}$ and $(2,3)_{NN-NNN}$). For a subsurface vacancy, the two Y atoms could be placed both NN to the defect, or one in NN and the other in NNN positions or they can be both in NNN sites, for a total of five different configurations ($(1,2)_{NN-NN}$, $(2,8)_{NN-NN}$, $(1,4)_{NN-NNN}$, $(4,8)_{NNN-NN}$, and $(4,6)_{NNN-NNN}$).

4.6.1 Stability and Structural Rearrangements in YSZ-(111) surface

In Table 4.12, the energy due to the creation of the oxygen vacancies and to the simultaneously substitution of Zr with Y atoms (E_{s-f}) was reported for all the considered configurations of the four Y^{3+} cations with respect to a surface or subsurface vacancy (figure 4.12 I). It was computed with respect to O_2) or O, as indicated by the following equations:

$$E_{s-f}(\frac{1}{2}O_2) = E(\text{doped surface}) + 2nE(\text{Zr}) + \frac{n}{2}E(\text{O}_2) - E(\text{surface}) - 2nE(\text{Y}) \tag{4.4}$$

$$E_{s-f}(O) = E(\text{doped surface}) + 2nE(\text{Zr}) + nE(\text{O}) - E(\text{surface}) - 2nE(\text{Y}) \tag{4.5}$$

where *n* is the number of vacancies,E(doped surface) is the energy of the surface containing *n* vacancies and *2n* Y atoms, E(Zr) and E(Y) are the energies of the Zr and Y atoms, respectively.

According to equations 4.4 and 4.5, the negative sign of the computed E_{s-f} values indicate that the doping with Y_2O_3 stabilizes the surface. In particular the preferred configuration for the surface vacancy is $(2,3)_{NN-NNN}$. Indeed, for this kind of vacancy there is only one possible NNN position for the Y ions in the outermost zirconium plane and the $(2,3)_{NN-NNN}$ configuration results to be the most stabilized one. For a subsurface vacancy, we found the following stabilization order: $(1,2)_{NN-NN}$ <$(2,8)_{NN-NN}$ <$(4,8)_{NNN-NN}$ <$(1,4)_{NN-NNN}$ < $(4,6)_{NNN-NNN}$. Again, the preferred configuration is when the Y^{3+} ions are both NNN to the vacancy and, thus, the vacancy is likely to be bound to Zr^{4+} ions rather than to the dopant. Moreover, the most stable subsurface configuration ($(4,6)_{NNN-NNN}$), with two Y in NNN position, is 0.91 eV more stable than the most stable surface one. In summary, subsurface vacancies are favoured and Y^{3+} ions occupy preferentially positions NNN to the defect, in agreement with experimental observations[256–260] and with previous YSZ bulk calculations.[250,263] The observed stability order can be rationalized considering two different aspects related to the doping of zirconia with aliovalent Y_2O_3. On one hand, relatively to the host lattice ions Zr^{4+} and O^{2-}, the dopant ion Y^{3+} and the vacancy $V_O^{\bullet\bullet}$ can be seen as point defect charge -1 and +2, respectively, so that electrostatic interactions should be predominant. Coulomb considerations thus suggest that Y should most likely be NN to the vacancy. On the other hand, it was observed that the covalent nature of Zr-O bonds favours structure with lower Zr coordination, explaining in this way the higher stability at room temperature of the monoclinic ZrO_2 phase (where Zr atoms are 7-fold coordinated) over the tetragonal and cubic zirconia phases (where Zr atoms are 8-fold coordinated). Thus, if in presence of the vacancies, Zr atoms prefer to be NN to the defects while the Y ions prefer NNN positions, in YSZ there will be a reduction of the average zirconium coordination from 8 to a value closer to 7, similar to the value of monoclinic zirconia. This lowering of the Zr coordination is then at the base of the mechanism of stabilization of cubic zirconia through Y_2O_3-doping. Moreover, in a very simple view, Y^{3+} has a larger radius than Zr^{4+} and could thus prefer the eight-fold coordination, whereas the smaller Zr^{4+} can better accommodate the contraction of the lattice in the neighbourhood of the vacancy that accompanies its formation. We can then conclude that the stabilization and the preference for defect sites in YSZ is a consequence of a delicate compromise between size effects and electrostatic interactions. Larger relaxations (between 0.3 and 1 Å) of the oxygen atoms NN to the vacancy with respect to the ones observed for the formation of oxygen vacancies on the pure (111) surface are observed. After the NN O atoms, the Zr atoms NN to the vacancies have the greatest displacements, while the Y atoms are associated to the smallest relaxations. Consequently, Zr atoms NN to the vacancy move away from it, while NN O atoms move toward the defect determining compression regions in the lattice near the defects. Generally, less stable configurations relax more. For Y^{3+} ions that are NN to defect sites, the average Y-O bond length is about 2.0 Å, while for dopant ions NNN to the vacancy it is of about 2.3 Å, very close to the value of the Y-O bond in Y_2O_3.[313] Considering that Y^{3+} ions are larger than Zr^{4+} ions, this confirms that Y^{3+} in NN position are compressed.

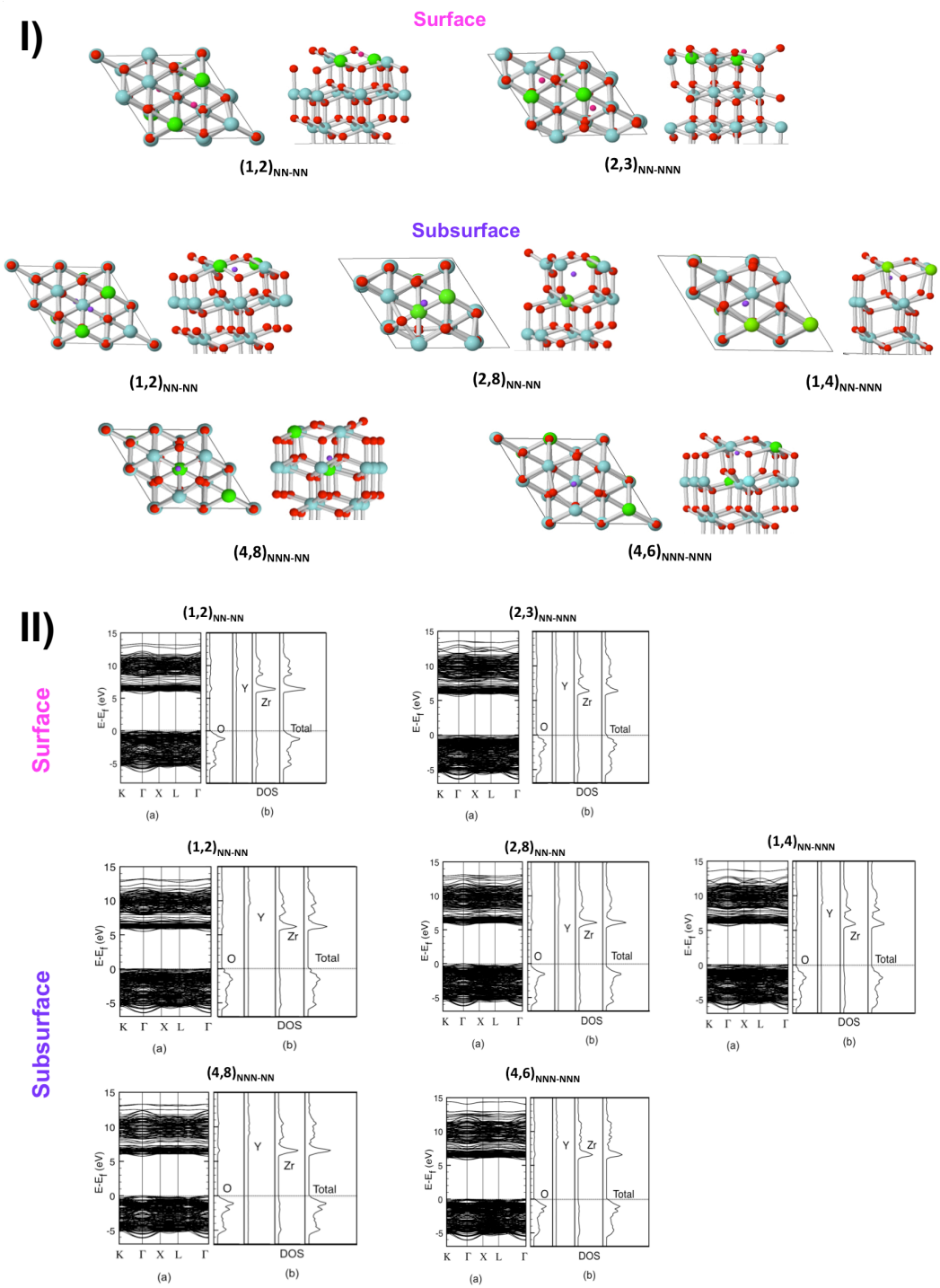

Figure 4.12: (I) Top (left) and top half lateral view (right) of optimized structure of the (2×2) supercell for the seven configurations taken into account for $Zr_{20}Y_4O_{46}$. Oxygen atoms are in red, zirconium atoms in light blue, and yttrium atoms in green. Pink for surface vacancies positions, violet for subsurface vacancies positions. (II) Band structure (a), total and atom projected DOS (b) of the different configurations of the YSZ (111) surface.

Vacancy	Configuration	$E_{s-f}(\frac{1}{2}O_2)$	$E_{s-f}(O)$
surface	(1,2)$_{NN-NN}$	-28.52	-24.98
	(2,3)$_{NN-NNN}$	-31.14	-27.59
subsurface	(1,2)$_{NN-NN}$	-29.43	-25.89
	(2,8)$_{NN-NN}$	-29.98	-26.43
	(1,4)$_{NN-NNN}$	-31.08	-27.53
	(4,8)$_{NNN-NN}$	-30.94	-27.40
	(4,6)$_{NNN-NNN}$	-32.05	-28.50

Table 4.12: Energy of substitution and of the formation of oxygen vacancies (with respect to $\frac{1}{2}O_2$, $E_f(\frac{1}{2}O_2)$, or with respect to O, $E_f(O)$) for different configurations of two Y dopant atoms with respect to a surface or subsurface oxygen vacancy on the cubic ZrO_2 (111) surface. All data in eV.

Vacancy	Configuration	E_g
surface	(1,2)$_{NN-NN}$	5.71
	(2,3)$_{NN-NNN}$	5.65
subsurface	(1,2)$_{NN-NN}$	5.49
	(2,8)$_{NN-NN}$	5.67
	(1,4)$_{NN-NNN}$	5.61
	(4,8)$_{NNN-NN}$	5.74
	(4,6)$_{NNN-NNN}$	5.80

Table 4.13: Computed band gaps (E_g, in eV) for the different configurations of Y atoms with respect to a surface or subsurface vacancy on the (111) surface of YSZ.

4.6.2 Electronic structure of YSZ-(111) surface

The band gap values for the different configurations are reported in table 4.13. These data can be compared with the band gap value obtained for the clean ZrO_2 (111) (2×2)supercell (5.48 eV) and range between 5.49 and 5.80 eV. Even if the highest value is obtained for the most stable system, no simple correlation between the band gap and the stability or the position of the dopant atoms appears.

Band structure and DOS of the different configurations (figure 4.12II) are alike and show similar properties to the ones of the pure system: the VB is constituted by O-2p states, while the bottom of the CB is associated mainly to Zr-4d. However, there are two main differences. The first one is that Y-4d states also contribute to the bottom of the CB, but they lie at higher energies with respect to the corresponding Zr states. Moreover, it can be observed that when the Y atoms are in NNN position with respect to the vacancy, these Y-4d states are at even higher energies. This means that a stronger interaction with the vacancy determines a higher stabilization of Y-4d orbitals. The second difference is that the e_g-t_{2g} splitting of the Zr-4d states is present, especially in the least stable configuration (1,2)$_{NN-NN}$, but a broadening can be observed as a consequence of the doping and the disorder that it determines in the structure. It is to note that despite the fact $V_O^{\bullet\bullet}$ are present in YSZ, no empty electronic state is observed in the gap of any optimized configuration. However, an isolated peak,

corresponding to an empty colour centre, is present in the gap of the unrelaxed structure for each configuration (see for example the DOS for the unrelaxed and relaxed $(4,6)_{NNN-NNN}$ configuration in Figure 4.11c). This result can be explained considering the perturbation in the periodic electrostatic Madelung potential due to the presence of $V_O^{\bullet\bullet}$, which increases the potential on the NN sites lowering the energy of the d states of the ions in that position with respect to the energy of the d states of cations far from the defect. This is why a mid-gap empty state is observed in the band structure and DOS of the unrelaxed system. The large relaxations of oxygen atoms NN to the vacancies generate a Madelung field that prevents the formation of the empty electronic state in the gap, compensating the perturbation of the potential in the neighbourhood of the vacancy and thus pushing the d states back in the CB (figure 4.13).[255,310] The deviation from the ideal cubic symmetry is then crucial for the understanding of the electronic properties of YSZ.

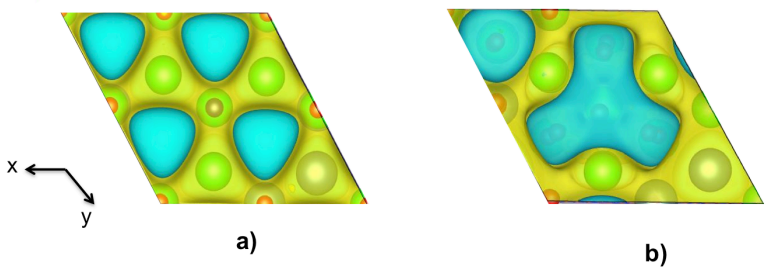

Figure 4.13: Electrostatic potential plots for the (4,6)NNN-NNN configuration, before (a) and after (b) the relaxation of the system. Yellow for positive and light blue for negative values. Isosurface values of 0.005 a.u.

In summary, we first obtained important information on zirconia surface chemistry and reactivity. Indeed, the investigation of the oxygen vacancy formation on the clean (111) surface not only constituted a preliminary step toward the characterization of the YSZ (111) surface, but also the computed vacancy formation energies confirm the irreducible nature of the oxide. This result evidence the different intrinsic conduction properties of zirconia, an ionic conductor, with respect to other oxides, that can be used in composites electrolytes for LT-SOFC applications, as CeO_2. This is even more important since CeO_2 can suffer, in SOFC operating conditions, of partial reduction of Ce^{4+} ions into Ce^{3+} cations, becoming a mixed electron/ion conductor. Naturally, these differences should be taken into account when comparing the properties and performances of different composite in order to elucidate the conduction properties of these materials. Secondly, the results of the systematic investigation of the dopant and vacancies arrangement on the (111) surface allowed us to clarify the effect of the doping on the structural properties of the YSZ (111) surface, to elucidate the proposed mechanism of stabilization, and to explain the electronic features of YSZ where oxygen vacancies, that determine the ionic conductivity of the material, are present but mid-gap states are not observed. Finally, this work allowed to find a model of the YSZ (111) surface (*i.e.* the most stable arrangement with Y atoms and oxygen in $(4,6)_{NNN-NNN}$

configuration) that is realistic (it reproduces the experimental 8 mol% Y_2O_3 amount) and reliable (it is derived from a detailed comparison of the structural and electronic features of different configurations). This model could be used to simulate the oxide-carbonate interface of composite electrolytes.

4.7 Conclusions

In this chapter, periodic DFT calculations were used to study the bulk and the most important surfaces for each of the three ambient pressure zirconia polymorphs (*m*-,*t*-,*c*-ZrO_2), before addressing the formation of oxygen defects on the most stable (111) surface of cubic zirconia as well as the stabilization of this surface through doping with the aliovalent Y_2O_3 oxide. The most important results can be summed up as follows:

- For bulk calculations, the performances of six Hamiltonians (HF, PBE, B3LYP, B3PW, PBE0 and PBE0-D) and of three different basis sets (all electron on both Zr and O (Zr*-O*), pseudopotential for Zr atoms and all-electron on oxygen (Zr^{ECP}-O*) and pseudo-potential on both Zr and O (Zr^{ECP}-O^{ECP})) in predicting the equilibrium geometries, relative stability and the band gaps of the three phases have been investigated in details. The examination of the obtained results shows that all methods were able to reproduce the experimental structural data with good accuracy, but the best results are achieved at the PBE0 level, which improves also the description given by the other hybrid functionals. Geometrical data produced with the same methods but with different basis sets are comparable. Even if fhe use of the d-polarization appears to be slightly more important when dealing with especially the tetragonal and monoclinic phases, that show higher covalency of Zr-O bonds with respect to the cubic polymorph, the smallest basis set, Zr^{ECP}-O^{ECP}, already produces good results and seems suitable for the modelling of zirconia, especially of its surfaces, allowing an accurate description of the system at low computational costs. Concerning the relative stability, no matter which Hamiltonian and basis set is used, hybrid functionals, in particular B3LYP and especially B3PW, outperformed PBE0 and gave the best results, both qualitatively and quantitatively. Furthermore, as expected, band gaps showed a much more strong dependence from the adopted method: HF considerably overestimates and PBE widely underestimates them, while hybrid functionals produce the best results, with PBE0 data being generally a little higher than the B3LYP or the B3PW ones.

- The most aboundant zirconia surfaces have then been considered at the PBE0/Zr^{ECP}-O^{ECP}. For each surface, we investigated the surface energy, the relaxed geometry and the electronic properties, taking care to check the convergence of these properties with respect to the slab thickness before to proceed to examine them in detail. We found that the surface energies follow the order: $c(111) < m(-111) < t(101) << t(111)$. Atomic relaxations showed, indeed, that the most stable *c*(111) is also the most compact surface, with the smallest displacements, confined only to the outermost atomic planes.

- This $c(111)$ surface was consequently used to investigate ZrO_2 reducibility and doping with Y_2O_3. Concerning neutral oxygen vacancy (V_O^X) formed after the removal of O atoms from the clean surface, very large oxygen vacancy formation energies were obtained, with $E_f(O)$ which ranges between 8 and 10 eV, values close to the ones of irreducible oxide like MgO. Moreover, large vacancy formation energy, small relaxation and the presence of a highly localized state in the gap characterized the formation of oxygen defects on this surface.

- As regards the doping with yttria, the computed values for the energy due to the creation of the oxygen vacancies ($V_O^{\bullet\bullet}$) and simultaneously to the substitution of Zr with Y atoms ($E_{(s-f)}$) confirm, as expected, that doping of the (111) zirconia surface with Y_2O_3 is accompanied by the stabilization of the system. Among all the tested configurations, the $(4,6)_{NNN-NNN}$, with a subsurface vacancy and two Y atoms both in NNN position to the defect, is found to be by far the most stable. Consequently, Zr^{4+} ions should prefer to be NN to the vacancies, with the consequent reduction of their coordination number, which supports the idea that the stabilization mechanism is related to the lowering of the coordination of Zr atoms. Large relaxations are observed, in all the studied configurations, for the O atoms NN to the vacancies, which, moving toward the vacancy, determine the contraction of the lattice in the defect region. This deviation from the ideal cubic geometry is fundamental to explain the electronic properties of the system and can be rationalized by electrostatic potential arguments.

In summary, the PBE0/Zr^{ECP}-O^{ECP} level appeared to be a good compromise between accuracy results and computational cost to predict and describe both the structural and electronic properties of zirconia. This computational protocol was used here to characterize the properties of the (111) surface of ZrO_2 and YSZ, in order to identify a suitable model of this surface that will be used in chapter 6 to build a first model of the YSZ-carbonate interface. Before doing that, it is however necessary to characterize likewise the carbonate phase. In the next chapter, we will describe the identification of a reliable computational protocol and of a suitble surface model also for $LiNaCO_3$ and $LiKCO_3$.

Chapter 5

Modeling of the carbonate phase

Here and elsewhere we shall not obtain the best insight into things, until we actually see them growing from the beginning.
Aristotele

Contents

5.1 Introduction **141**
5.2 Computational Details **144**
5.3 $LiNaCO_3$ and $LiKCO_3$ bulk **147**
5.4 $LiNaCO_3$ and $LiKCO_3$ Surfaces **157**
5.5 Li transport at the $LiKCO_3$-(001) surface **163**
5.6 Conclusions **177**

5.1 Introduction

After having characterized the oxide phase, namely YSZ, in the previous chapter, the same procedure should be applied to the carbonate phase. Despite alkali carbonates are extensively used in a lot of different applications[65,314–316] and despite previous works devoted to the study of the electrochemical properties of molten carbonates[67,207,317–322], their fundamental structural, electronic and physico-chemical characteristics are still poorly understood. For this reason, we studied lithium and sodium ($LiNaCO_3$, 50-50mol%) and lithium and potassium ($LiKCO_3$, 50-50 mol%) carbonates using first principles methods. The study of the crystalline structure is a first step toward the construction of a model of the carbonate-oxide interface, but it can nevertheless provide useful information, since the XRD of the composites showed that the crystal phase of the carbonate is present together with the main amorphous carbonate shell that covers the oxide particles.

Very little is known about the structure of $LiNaCO_3$. From an experimental point of view, early works of Eitle and Skaliks[323] and of Christman et al.[324] should be mentioned, but it is through the X-ray diffraction studies of Yatsenko et al.[325–327] that the structure, *cf.* the main

phases of $LiNaCO_3$ present at standard conditions, has been clarified. From a theoretical point of view, to our knowledge, no previous quantum-mechanical calculations of the bulk and surface structures of $LiNaCO_3$ have been performed. $LiNaCO_3$ has two different phase transitions: the first one at 448 K, where α phase transforms to the β one, and at 633 K where the β-$LiNaCO_3$ converts into the γ phase.[327] The first studies[324] suggested amonoclinic *C2* or *C2/m* symmetry for the room temperature α-phase, but the more recent X-ray powder diffraction refinement of Yatsenko et al.[325,326] demonstrated that the primitive cell of this phase is triclinic, belonging to the *P1* space group, with unit cell parameters a = 14.265 Å, b = 14.261 Å, c =3.305 Å, α = 88.41°, β =91.70°, γ = 119.95°. The β-phase is instead a hexagonal phase, with cell parameters a=14.355 Å, c=3.341 Å and space group *P-6*. Finally, for the γ-phase the unit cell parameters a=8.311, c=3.386 together with the space group *P-6* were reported by Zhukov et al.[327]. The structures of the three phases (see Fig. 5.1a-d) are similar and built up of alternating closed-packed layers stacked along the c-axis: one of them contains the Na^+ ions and one third of the carbonate ions, and the other contains the Li^+ cations with the remaining carbonate groups. All the CO_3^{2-} groups are parallel to the (001) plane. Li and Na atoms are located inside different coordination polyhedra: Li atoms occupy tetrahedral sites as in Li_2CO_3, while Na atoms have five first neighbours oxygen atoms disposed in a distorted square pyramid. The low symmetry α phase can be described as a distorted hexagonal β-phase, with a uniform shift of neighbouring layers. Zhukov et al.[327] observed that the β unit-cell contains contains hexagonal sub-cells with a_γ=$a_\beta/\sqrt{3}$ and c_γ=c_β, as for the unit cell of the γ-phase. These sub-cells differ by the orientation of one CO_3^{2-} group. The authors not only studied the γ-phase through X-ray diffraction, but they also performed computer simulations based on the ionic model of the crystal consisting of rigid carbonate ions and Li, or Na, cations. They suggested two possible models of this phase (A and B in Fig. 5.1c and d), which differ just for the orientation of one carbonate group and which are found very close in energy. They concluded that the β-γ transition should be associated to the disordering of the CO_3 groups over the two sets of orientations because of the thermal activation associated to the temperature increase.

As regards $LiKCO_3$, Idemoto et al.[328] studied the crystal structure of Li-K eutectics from neutron diffraction measurements and observed that they crystallise into a mixture of two phases: $LiKCO_3$ (50-50 mol%, melting point 504°C, space group *P21/c*) and the pure Li_2CO_3 (space group *C2/c*)or K_2CO_3 (space group *P21/c*), according to which of the two cations is inexcess inthe eutectic. $LiKCO_3$ structure was previously studied also by Christman et al.[324] through X-ray diffraction and by Idemoto et al.[329] through time-of-flight (TOF) neutron powder diffraction and it was subsequently refined through single-crystal X-ray analysis by Kirfel et al.[330]. All the authors agree on a monoclinic structure with a layered nature, in which layers of Li and K coordination polyhedra are oriented parallel to the (10-1) direction and are connected by carbonate groups which are arranged perpendicularly to the c axis (Fig. 5.1e). The reported cell parameters are very close (a=7.23 Å, b=7.08 Å, c=7.60 Å, β=127.42°[328]). However, Kirfel et al.[330] reconsidered the notation of Idemoto et al.[328] of four- and seven-fold coordinated Li and K cations, observing the presence of LiO_5 distorted orthorhombic pyramids and KO_9 polyhedra of irregular shape. This structure is very similar to the structure of K_2CO_3,which belong to the same space group and is characterized by a layered arrangement of CO_3 groups normal to the [001] direction and interconnected by five-

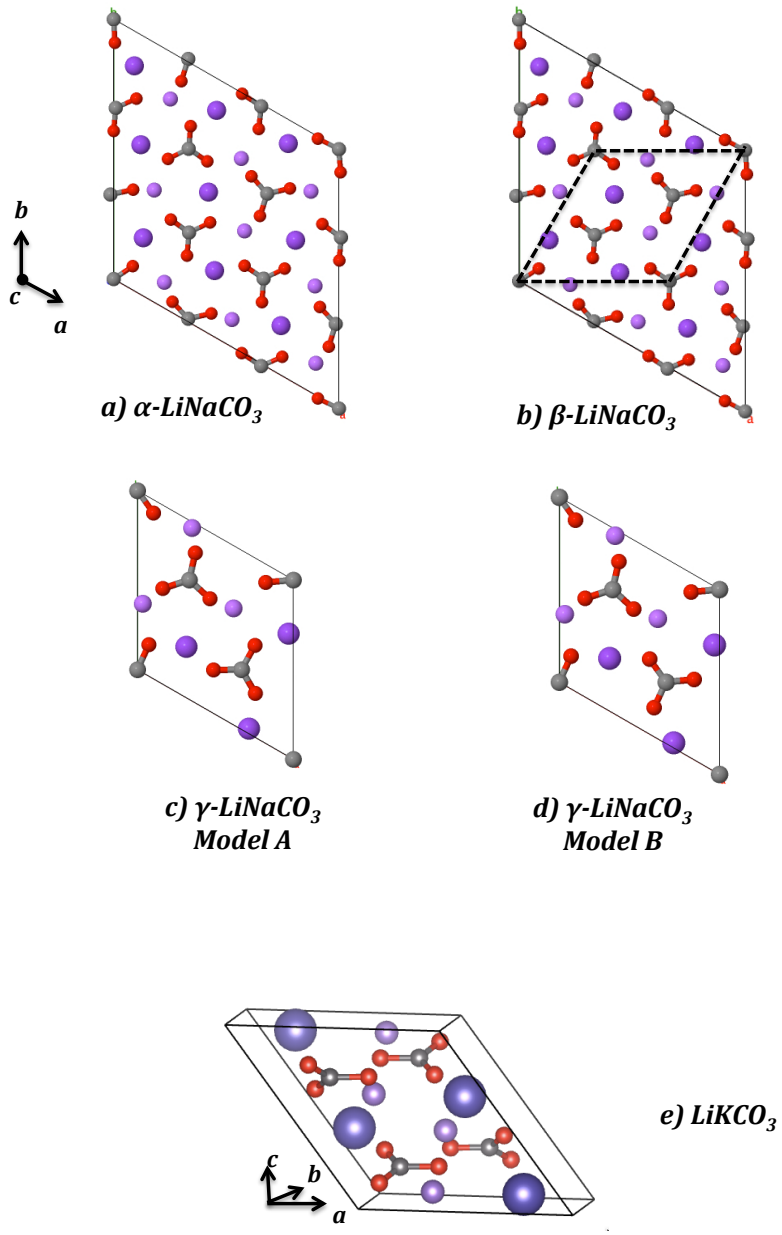

Figure 5.1: Unit cells of the α, β and γ (model A and B) phases of $LiNaCO_3$ and of $LiKCO_3$. Red, grey, violet, light violet spheres represent O, C, Na or K, and Li atoms, respectively. The dotted lines in the β unit cell show one of the possible γ-sub-cells.

or nine-fold coordinated K^+. $LiKCO_3$ lattice is slightly rotated about the *b*-axis relative to that of K_2CO_3.[328]

Although experimental structural investigations of these systems have been numerous, we were not able to find any information about the electronic and surface properties of these mixed carbonates, neither from an experimental or a theoretical point of view. However, the knowledge of these features can be very important for the understanding of the properties of the composites, where the phenomena at the interface between the oxide and carbonate phases are considered to be crucial for the enhanced conductivity of these materials. The only information on surface properties in carbonates are the work of Bruno and Prencipe[331] and of Gao et al.[332]. Bruno and Prencipe[331] modelled the most important terminations of Li_2CO_3 (the (001), (-101), and (110) surfaces). This data can be useful to treat $LiNaCO_3$, since its structure shows similarity to the one in Li_2CO_3: like $LiNaCO_3$, the Li_2CO_3 crystal structure viewed from the *c*-axis is made up by alternating layers. Each layer contains cations and carbonate groups placed normal to the *c*-axis and Li atoms have a tetrahedral coordination. Analogously, Gao studied the stability of various low index surfaces of K_2CO_3, whose structure, as already pointed out, presents some similarities with the one of $LiKCO_3$. The (001) and (110) surfaces were found to be among the most stable terminations.

Finally, the knowledge of the transport properties of the pure carbonates can be usefull in order to understand the effect of the oxide phase on the transport properties of the carbonate at the interfaces. However, previous works in this field have been limited to the study of Li transport in pure crystalline bulk Li_2CO_3, used in Li batteries.[333–336] The $Li_i^\bullet$ interstitial defect was generally found to be the most stable one with low migration barriers (between 0.1 and 0.6 eV in the various works).[333–336] However, similar works on $LiKCO_3$ and on transport in surfaces are completely lacking, even if they are key components when investigating the carbonate-oxide interface.

This chapter is organized into three main sections. In the first one, we report the performances of different exchange and correlation functionals on the structural properties of the bulk carbonate phases in order to select an adequate protocol that provides the best description of these materials, of their structural and electronic properties. In the second part, we examine the results of the investigation of the (001) and the (110) surfaces of $LiKCO_3$ and $LiNaCO_3$, using the the aforementioned protocol. In particular, different types of surface reconstruction (the octopolar reconstruction and reconstruction through the introduction of vacancies for both for Li and Na terminated surfaces) have been taken into account to describe the dipolar (001) direction of $LiNaCO_3$. Finally, in the last one, we investigated Li defects formation and migration through $LiKCO_3$ most stable (001) surface.

5.2 Computational Details

5.2.1 DFT Calculations

All calculations have been performed in the frame of DFT, using the periodic CRYSTAL14[180] code. For the bulk calculations, three exchange-correlation functionals have been used: PBE[170], B3LYP[164,165], and PBE0[172,173] Surface calculations have only been performed at the PBE0 level. As regards the basis sets, Na atoms have been described with a 8-511G[337] ba-

sis set, while the basis sets 5-11G*,[338] 6-21G*,[339,340] and 8-411G*[339,341] have been selected respectively for Li, C and O, using for the uncontracted shells the exponents re-optimized variationally by Bruno and Prencipe[331] in their work on Li_2CO_3. For K atoms, both all-electron (86-511G[337]) and pseudopotential (Hay and Wadt[294–296] small core pseudopotential to describe the 10 inner core electrons together with a 31[299] contraction scheme for the ($3s^2 3p^6 4s^1$) valence electrons, HAYWSC-31) basis sets have been used for bulk calculations. To reduce the computational cost, the HAYWSC-31 base has been used for the study of surface properties. Surface calculations have been carried out using the slab model (a slice of material composed of several atomic layers and delimited by two free surfaces) and imposing 2D periodic boundary conditions. Slabs builtwith a different number of layers have been relaxed, investigating the convergence of the computed structure, surface energy and electronic properties with respect to the number of layers, in order to identify a sufficiently thick slab model that corresponds to a good surface model. Reconstruction of the $LiNaCO_3$-(001) surface was investigated by considering a (2×2) supercell with a *P-6* symmetry in the case of the octopolar reconstructions and of the reconstruction through the formation of vacancies for the Li-terminated (001) surface. In the case of Na-terminated one, the highest possible symmetry was *P11m*.

Defect formation on $LiKCO_3$-(001) surface was simulated by a 2D periodic slab model, consisting of a sequence of 3 slab layers, for a total of 36 atoms with $Li_6K_6(CO_3)_6$ stoichiometry. This model not only ensured the convergence of the structural and electronic properties, but it was also found to be sufficient to avoid spurious interactions between the defect and its periodic image. Neutral, negatively and positively charged Li defects were taken into account. Neutral (V_{Li}) and negatively charged (V'_{Li}) Li vacancies were created by removing, respectively, one lattice Li atom or Li^+ cation from the slab model, for a final $Li_5K_6(CO_3)_6$ stoichiometry. Li atoms or Li^+ ions were removed from both 4-fold coordinated Li surface sites and 5-fold coordinated bulk-like positions. The neutral (Li_i^X) and positive ($Li_i^\bullet$) interstitial Li defects are instead obtained by adding, respectively, one Li atom or one Li^+ ion to the slab stoichiometry, resulting in 37 atoms in the unit cell ($Li_{6+1}K_6(CO_3)_6$). Several different initial positions of the interstitial Li were taken into account in both cases. For charged defects, a background charge that ensures the neutrality of the unit cell was applied as required by calculations under periodic boundary conditions to avoid divergence of the electrostatic potential.[342] Diffusion barriers for Li-related defects were qualitatively estimated performing a relaxed scan of the geometry of the defective system. A (1×2) supercell model of the $LiKCO_3$-(001) surface with one Li vacancy or one interstitial Li defect was used for these calculations.

For $LiNaCO_3$-bulk calculations, we used a Monkhorst-Pack[300] shrinking factor of eight, corresponding, respectively, to 260, 60 and 60 points in the IBZ of the α, β and γ bulk phases, respectively. For the $LiNaCO_3$-(110) surface calculations, the reciprocal space has been sampled using a Monkhorst-Pack grid with shrinking factors $(8\times8\times1)$ corresponding to 25 points in the IBZ of the slab model. In the case of the $LiNaCO_3$-(001) surface, instead, we employed a $(4 \times 4 \times 1)$ grid corresponding to 4 and 10 points in the IBZ of the reconstructed models with *P-6* and *P11m* symmetry, respectively. As regards $LiKCO_3$, a shrinkingfactor of 6 and 4, correspondingto 80 and 30 points in the IBZ of the bulk structure have been used for calculations with the all-electron and pseudopotentials basis sets, respectively. A shrinking

factor of 4 corresponding to 10 points in the IBZ of the $LiKCO_3$-(001) and (110) has been instead used for all the surface calculations.

An extrafine integration scheme, which corresponds to 75 radialpoints and 974 angular points,[180] was considered for the numerical DFT integration. The Coulomb and exchange series were truncated with default threshold values of 10^{-7}, 10^{-7}, 10^{-7}, 10^{-7} and 10^{-14}. A tolerance of 10^{-7} a.u. has been used for the convergence of the self-consistent field procedure. In addition, for systems with an odd number of electrons, a spin-polarized approach was used to perform the calculations. For bulk and surface calculations, all the atomic positions were allowed to relax during slab geometry optimization,until the maximum and root-mean square atomic forces and displacements were simultaneously less than $4.5 \times 10^{-4}, 3.0 \times 10^{-4}, 1.8 \times 10^{-3}$ and 1.210^{-3} a.u., respectively. In the case of defect formation and diffusion on the $LiKCO_3$-(001) surface, optimization was restricted to the atomic positions of the nearest neighbors of the defect, in order to lower the computational cost. For the relative stability investigation of the bulk phases of $LiNaCO_3$ and for the calculations of the IR and Raman spectra of both materials, we also performed additional frequencies calculations at the Γ point, from which zero-point energy (ZPE) and thermal contributions to the energy have been obtained. Experimental phase transition temperatures for $LiNaCO_3$ have been considered: 448 K for the α to β transition, and 633 K for the β to the γ one.[327]

5.2.2 Calculation of the dielectric constant

The dielectric constant (ϵ_r) is necessary for the calculation of the formation energy of charged defect. It was evaluated through the Coupled Perturbed Kohn and Sham (CPKS)[343–345] scheme, a highly accurate and analytical scheme for the calculation of optical properties available in the CRYSTAL package. Tighter thresholds for the truncation of Coulomb and exchange integrals, were used in this case, setting the values to 10^{-8}, 10^{-8}, 10^{-8}, 10^{-8}, and 10^{-16}. A tighter tolerance of 10^{-10} au has also been used for the convergence of the self-consistent field procedure. The dielectric tensor was computed for the $LiKCO_3$-(001) surface using the slab model previously described, with two additional layers of ghost atoms (one above and one below), so as to allow the electron density to polarize despite the non-periodicity along the normal to the slab. The dielectric tensor components (ϵ_{ij}) were then calculated from the corresponding values of the computed polarizability (α_{ij}), according to the following equation:

$$\epsilon_{ij} = \delta_{ij} + \alpha_{ij}/(\epsilon_0 V) \tag{5.1}$$

where δ_{ij} is the Kronecker delta, $\epsilon_0 = 1/4\pi$ is the vacuum permittivity in the Gaussian unit system, and V is the volume of the unit cell which was taken as the area of the slab times its thickness (390.05 Å^3). We calculated the dielectric tensor components to be ϵ_{xx}=2.24, ϵ_{yy}=2.25, ϵ_{zz}=1.60 and given the relatively modest anisotropy we used the average value of about 2.02 for ϵ_r to compute the formation energy of charged defects. We note that, since only atomic positions of the nearest neighbors of the inserted Li were allowed to relax during geometry optimization, we can reasonably expect interaction of the charged defect and its images to be only electronically screened, justifying the use of a high-frequency

static dielectric constant in the Makov-Payne equation, rather than the total low-frequency dielectric constant accounting for both electronic and ionic components.

5.2.3 Calculations in presence of an external electric field

In order to take into account the effect of the voltage applied to the electrolyte in SOFC operating conditions onto the diffusion process of Li defects, we performed single point energy calculations applying an external field to selected structures. We selected the range of potentials generally tested in experiments which goes from 0 to 1.5 V, paying particular attention to the 0.7 V value which is generally used to compare the behaviour of different SOFC cells.[346]

We consequently applied an external electric field corresponding to these voltage values through the Finite Field perturbation (FF) method[347] implemented in CRYSTAL. This method uses a triangular (saw-tooth) potential, corresponding to a square wave electric field, together with a supercell scheme. Since we wanted to evaluate the effect on the diffusion along channels observable on the (001) surface, we applied the electric field along the *b*-axis of the slab model of the surface, *i.e.* the direction along which the channels are oriented. In order to apply the field along this periodic direction at the optimized geometry of the 2D slab structures, a multislab approach was chosen: a (1×2) supercell model of the $LiKCO_3$-(001) surface was replicated not only in two dimensions, but also in the direction perpendicular to the surface with a vacuum layer of at least 30 Å separating subsequent slabs. The difference in the total energy per unit cell between the slab and the multislab models of the considered surface was found below 10^{-5} a.u., validating the multislab model. Electric fields ranging between 0 and 0.002 a.u. (1 a.u.=5.14×10^{11} V/m) were then applied.

To get a deeper insight into the effect of the external electric field, we also applied it to the (1×2) supercell model in the direction perpendicular to the surface. Considering a thickness of 7.42 Å for a 3 layers slab model of the surface, electric fields ranging between 0 and 0.004 a.u. were then applied in this case.

5.3 $LiNaCO_3$ and $LiKCO_3$ bulk

The room temperature triclinic α-phase of $LiNaCO_3$ belongs to the space group *P1* and has 9 $LiNaCO_3$ formula units per unit cell. The structure is defined by six parameters: the three lattice vectors (*a*, *b*, *c*) and the corresponding three angles (α, β, γ). The β and γ phases, which belong to the space group *P-6*, are both described by two parameters (the lattice vectors *a* and *c*). However, while the hexagonal β unit cell contains 9 $LiNaCO_3$ formula units, the hexagonal γ unit cell has just 3. For all the three phases, Li atoms are tetrahedrally coordinated, Na atoms are 5-fold coordinated, and O atoms are four-fold coordinated. $LiKCO_3$ structure belongs to the *P21/c* space group and has 4 formula units per unit cell. It is defined by four parameters: the three lattice vectors (*a*, *b*, *c*) and the β angle. Li and K are five and nine-fold coordinated, while O atoms are fourfold coordinated.

5.3.1 Structure optimization and relative stability

5.3.1.1 $LiNaCO_3$

Tables 5.1, 5.2, and 5.3 contain the cell parameters calculated at the PBE, PBE0 and B3LYP levels for the optimization of the bulk structure of the α, β, and γ $LiNaCO_3$ phases. For the last polymorph, we considered the two models (indicated as Model A and B) proposed by Zhukov et al.[327] in their work. Generally, obtained results are in good agreement with the experimental data, which are also reported for comparison.

For the α phase, all the tested functionals overestimate the lattice vectors *a*, *b*, *c* and the α angle, while they all underestimate the β angle. Finally, PBE and B3LYP tend to overestimate the γ angle, while PBE0 slightly underestimates it. The computed cell volume is always higher than the experimental one, of 5.0%, 3.4%, and 1.6% for PBE, B3LYP, and PBE0 respectively. This latter functional definitely outperforms the others, since its data are associated to the smallest deviation from the experimental data (between -0.4% and 0.6% for the lattice parameters and of 1.6% on the cell volume). This can also be easily derived from figure 5.2a, where the mean unsigned error (MUE) on all the lattice parameters computed with the three functionals is reported for each phase.

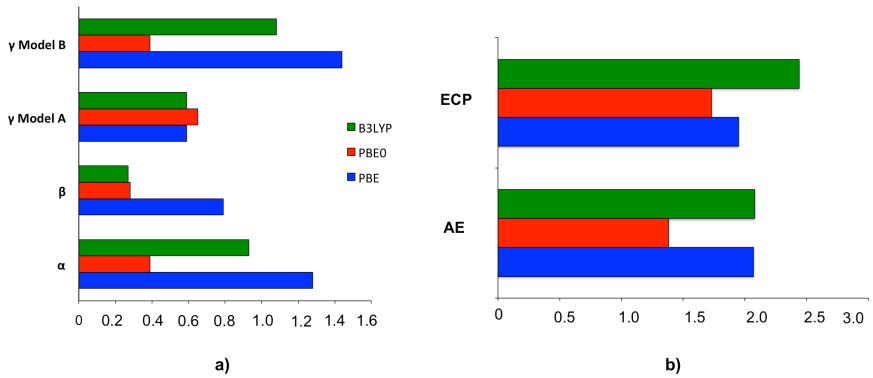

Figure 5.2: Mean Unsigned Errors (MUE, in %) computed for the lattice vectors of a) the three $LiNaCO_3$ polymorphs and b) $LiKCO_3$ with the six considered Hamiltonians and the two basis sets (all-electron (AE) and pseudopotential (ECP)) in the case of $LiKCO_3$.

For the β polymorph, PBE and B3LYP overestimate both the lattice vectors *a* and *c*, while PBE0 overestimates *a* and underestimates *c*. PBE provides the highest errors, with deviation from the experimental data of 1.07% on *a* and 0.52% on *c*. As can be seen from figure 5.2a, PBE0 (MUE of 0.28%) and B3LYP (MUE of 0.27%) performances are, instead, almost comparable: the differences between calculated and experimental cell parameters are of 0.02% or 0.49% on *a* and of 0.54% or 0.06% on *c* for the first and the latter functional, respectively.

Overall, the optimization of the Model A for the γ phase led to very similar results for all the functionals. Indeed, the *a* parameter is always overestimated, with the higher differences from the experimental data obtained at the PBE level (1.10%), followed by B3LYP (0.54%) and PBE0 (0.08%) ones. The *c* parameter is, instead, always underestimated, but

Method	a	b	c	α	β	γ	V	MSE	MUE
PBE	14.491	14.486	3.364	89.20	90.09	120.01	611.46	0.69	1.28
PBE0	14.336	14.327	3.325	88.72	91.32	119.95	591.54	0.25	0.39
B3LYP	14.412	14.410	3.347	89.29	90.61	119.98	602.11	0.53	0.93
Exp.[a]	14.265	14.261	3.305	88.41	91.70	119.95	582.23		

See ref.[326]

Table 5.1: Equilibrium geometry of α-phase of $LiNaCO_3$ with different Hamiltonians and mean signed error (MSE) and mean unsigned error (MUE) computed for each method. Lattice vectors (a, b, c) in Å, angles (α, β, γ) in degrees and volume (V) in Å^3. MSE and MUE in %.

Method	a	c	MSE	MUE
PBE	14.508	3.358	0.79	0.79
PBE0	14.359	3.323	-0.26	0.28
B3LYP	14.425	3.343	0.27	0.27
Exp.[a]	14.355	3.341		

See ref.[325]

Table 5.2: Equilibrium geometry of β-phase of $LiNaCO_3$ with different Hamiltonians and mean signed error (MSE) and mean unsigned error (MUE) computed for each method. Lattice vectors (a, c) in Å. MSE and MUE in %.

	Model A				Model B			
Method	a	c	MSE	MUE	a	c	MSE	MUE
PBE	8.379	3.338	0.51	0.59	8.368	3.405	1.44	1.44
PBE0	8.295	3.300	-0.58	0.65	8.286	3.367	0.37	0.39
B3LYP	8.333	3.320	-0.05	0.59	8.340	3.392	1.08	1.08
Exp.[a]	8.288	3.341			8.288	3.341		

See ref.[327]

Table 5.3: Equilibrium geometry of Model A and Model B of the γ-phase of $LiNaCO_3$ with different Hamiltonians and mean signed error (MSE) and mean unsigned error (MUE) computed for each method. Lattice vectors (a, c) in Å. MSE and MUE in %.

Method	E_α - E_β	E_α - E_β	$E_{\gamma A}$ - $E_{\gamma B}$
PBE	0.014	0.018	-1.381
PBE0	-0.003	0.018	-1.515
	-0.090*	0.174*	-1.384*
	-4.590**	5.983**	-0.529**
B3LYP	0.032	-0.022	-1.558

[a] Starred and double-starred values refer to the electronic energy plus the ZPE contribution and Gibbs free energy, respectively, obtained from frequency calculations at the Γ point only, considering experimental phase transitions.

Table 5.4: Computed energy differences (kcal/mol) between: i) the α and the β polymorphs (E_α - E_β), ii) the β and Model A of the γ phase (E_α - E_β), iii) model A and B of the γ phase ($E_{\gamma A}$ - $E_{\gamma B}$) of $LiNaCO_3$.[a]

the magnitude of the deviation from the reference data follows a completely opposite order of 1.22%, 0.64%, and 0.08% for PBE0, B3LYP, and PBE, respectively. Finally, for Model B of the γ phase, PBE and B3LYP provide overestimated values for the *a* (of 0.96% and 0.62% respectively) and *c* (of 1.92% and 1.53% respectively) lattice parameters, and once again PBE0 largely outperforms the other functionals by underestimating the *a* parameter of 0.02% and overestimating *c* of only 0.76%.

In summary, no matter which functional is considered, the errors on the lattice parameters with respect to the experimental data are very small (MUE, lower than 1% and 1.5% for the β or γ-Model A, and α or γ-Model B phases, see Figure 2a). However, not only the geometrical description of the α-phase and of the Model B of the γ polymorph is greatly improved at the PBE0 level, but, when the results of all the considered phases are taken into account, this functional provides a much more homogeneous global description with respect to PBE and B3LYP, with MUE values always lower than 1%, also for the least accurately described phase (0.38% for the α-phase, 0.28% for the β-phase, 0.65% for Model A and 0.39% for Model B).

From experiments, it is known that the order of stability of the three phases is $\alpha > \beta > \gamma$, but a quantitative evaluation of the relative stability is not available, neither from an experimental or theoretical point of view. Zhukov et al.[327] computer simulation employing the ionic model of the crystal, only reported a difference in packing energy between the A and B models of the γ phase of -15 kcal/mol. From the optimized structures, we evaluated the differences in the electronic energy between Models A and B of the γ phases ($E_{\gamma A} - E_{\gamma B}$), between the α and β phases ($E_\alpha - E_\beta$) as well as the difference between the β and the most stable of the two models of the γ polymorph ($E_\beta - E_{\gamma A}$). Results are collected in Table 5.4. Concerning the two models for the γ-phase, a small energy difference is obtained (between -1.4 and -1.6 kcal/mol with the various functionals), but Model A is always found to be the most stable regardless the choice of the functional. As concerns the other phases, PBE completely fails in predicting the right stability order, PBE0 is the only functional predicting α-$LiNaCO_3$ to be more stable than β-$LiNaCO_3$, while the opposite is true for B3LYP. How-

	a		*b*		*c*		β		V		MSE		MUE	
Method	AE	ECP	AE	ECP	AE	ECP	AE	ECP	AE	ECP	AE	ECP	AE	ECP
PBE	7.299	7.381	7.280	7.289	7.849	7.735	125.88	126.17	337.94	335.97	1.46	1.46	2.07	1.95
PBE0	7.230	7.289	7.210	7.254	7.779	7.767	125.72	125.58	329.25	333.99	0.72	1.00	1.38	1.73
B3LYP	7.285	7.340	7.230	7.287	7.901	7.887	125.56	125.43	338.56	343.72	1.35	1.66	2.08	2.44
Exp.[a]	7.228		7.082		7.600		127.42		308.27					

See ref.[328]

Table 5.5: Equilibrium geometry of $LiKCO_3$ with different Hamiltonians and the all electron (AE) and pseudopotential (ECP) basis sets, together with mean signed error (MSE) and mean unsigned error (MUE) computed for each method. Lattice vectors (*a*, *c*) in Å, angles in degrees (°) and volume in $Å^3$. MSE and MUE in %.

ever, it should be noted that all the computed energy differences are very small (lower than 0.04 kcal/mol). In fact, the three polymorphs have similar structures, since, as already mentioned, the α structure can be seen as a slightly distorted β one and the β unit cell contains as sub-cell the unit cell of the γ phase. When considering ZPE and thermal contributions at the PBE0 level, however, $E_\alpha - E_\beta$ and $E_\beta - E_{\gamma A}$ become slightly larger, while the difference in stability between the two γ phases decreases. Nonetheless, the stability order is not changed and all the previous conclusions still hold.

5.3.1.2 $LiKCO_3$

As regards $LiKCO_3$, we tested the same functionals as in the case of $LiNaCO_3$, but we also took into account the effect of different (all-electron and pseudo-potential) basis sets on the K atoms. All the functionals, independently from the type of basis set utilized, overestimate the lattice vectors *a*, *b*, *c* while they all underestimate the β angle, (see table 5.5). Values obtained with the pseudo-potential are comparable to the ones obtained with the larger basis set and even if associated to slightly higher errors, the MUE with this basis set is lower than 2.5%. In particular, PBE0, which outperforms again PBE and B3LYP, has a MUE of 1.38% and 1.73% for the all-electron and pseudo-potential basis set respectively (figure 5.2b). Accordingly to what observed by Kirfel et al.[330], in $LiKCO_3$ bulk-structure we observed four short Li-O distances between 1.954 and 2.070 Å and a fifth larger one of 2.178 Å, together with nine K-O distances between 2.79 and 4.01 Å. The structure of the CO_3 group is planar but distorted from the D_{3h} symmetry as in K_2CO_3, with one short (1.270 Å), one intermediate (1.289 Å) and one larger (1.297 Å) C-O bond. This can be directly related to the different attractive forces exerted on the O atoms by elements with different electronegativities, O being more strongly attracted by Li^+ than by K^+.[328,330]

5.3.2 IR and Raman Spectra

The Raman spectrum of $LiKCO_3$ was published by Kohara et al.,[225] but no experimental IR data is available for this material. Instead, Zehnder reported the some qualitatively results

in his investigation of structure, anion disorder and structural phase transitions in $LiNaCO_3$ through IR, FT-IR, and Raman spectroscopy in ref.[348] Figures 5.3 and 5.4 show, respectively, the IR and Raman spectra of these compounds computed at the PBE0 level. We devoted our attention to the region between 600 and 1900 cm^{-1}, where the four internal modes of the carbonate group should appear. The free CO_3^{2-} ion has D_{3h} symmetry and four different internal vibrations: the symmetric stretching ($\nu_1(A1')$) at about 1090 cm^{-1}, Raman active; the out-of-plane deformation ($\nu_2(A2'')$) at about 860 cm^{-1}, IR active; and the doubly degenerate asymmetric stretching ($\nu_3(E')$) and in-plane deformation ($\nu_4(E')$) at about 1400 and 700 cm^{-1}, respectively, both IR and Raman active.[349] The computed spectra show that the D_{3h} is broken in these compounds, as a consequence of the coordination of the cations to the CO_3 groups.

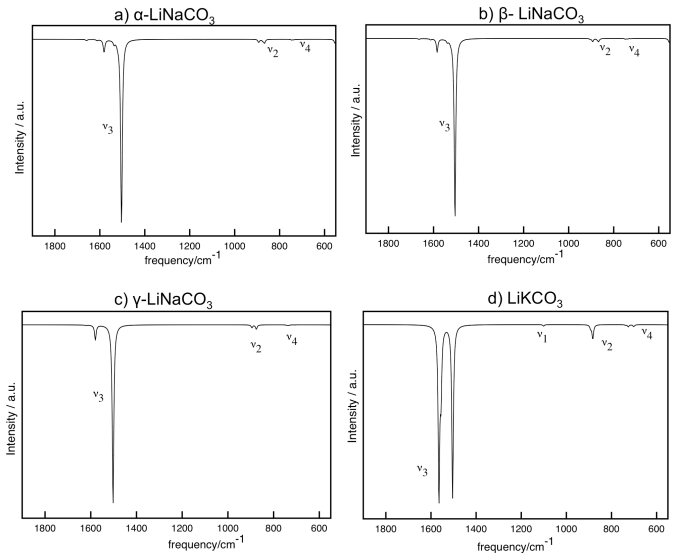

Figure 5.3: IR spectra of $LiNaCO_3$ (a-c) and $LiKCO_3$ (d) computed at the PBE0 level. $LiNaCO_3$ are referred to Model A. Results for Model B are equivalent.

Starting from $LiKCO_3$, the IR spectra shows a fine structure for ν_4 (701.9, 725.6, 737.3 cm^{-1}) and a weak peak at 882.3 cm^{-1} corresponding to ν_2. One of the main results of the change in the environment around the CO_3 groups is given by the appearance in the IR spectra of the ν_1 at about 1100 cm^{-1} with a very weak intensity. For the free carbonate this mode is, in fact, IR inactive. The other main effect is the splitting of the ν_3 into two peaks with contributions at 1499.2, 1504.2, 1555.5 and 1564.7 cm^{-1}. In the case of the IR spectra of γ-$LiNaCO_3$ (figure 5.3.c), instead, the ν_4 band (707.8, 733.0, 740.6 cm^{-1}) is present, but with a very low intensity peak, while the ν_2 presents now a fine structure (875.0, 876.9, 894.8 cm^{-1}) in agreement with the description of Zehnder that explained the splitting through an intermolecular vibrational coupling of the out-of-plane vibration of two types of planar carbonate ions that are superimposed to form linear chains.[348] Moreover, the asymmetric stretching vibration ν_3 is also split into different peaks at 1502.5, 1579.8, and 1620.6 cm^{-1}, showing in this case very different intensities. Finally the ν_1 band is not observed, in agreement with what reported by Zehnder[348], who attributed the absence of this

vibration to a site symmetry of nearly D_3 for the carbonate groups. IR spectra for the α- and β-phases show the same features of the γ-$LiNaCO_3$ spectrum.

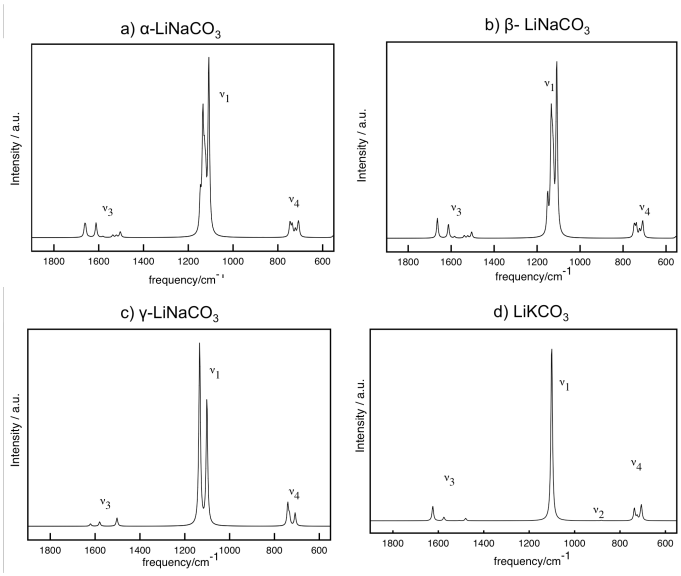

Figure 5.4: Raman spectra of $LiNaCO_3$ (a-c) and $LiKCO_3$ (d) computed at the PBE0 level. $LiNaCO_3$ are referred to Model A. Results for Model B are equivalent

The computed Raman spectrum of $LiKCO_3$ presents a ν_4 band with two main contribution at 705 and 736 cm^{-1} (exp. 695 and 729 cm^{-1})[225] and the ν_3 vibration is also split into four contributions at 1479, 1508, 1575, and 1624 cm^{-1} (exp. 1388. 1418, 1483, and 1517 cm^{-1})[225], again because of the coordination of CO_3 groups to Li and K ions. The most intense peak corresponds to the symmetric stretching ν_1 at 110 cm^{-1} (exp. 1050 cm^{-1})[225], while the least intense is the ν_2 vibration, Raman inactive in the free carbonate group, but visible in $LiKCO_3$, because of the carbonate symmetry distortion in the solid phase. The band at 1753 cm^{-1} is not observed in the theoretical spectra, obtained in the harmonic approximation, confirming the overtone nature assumed by Kohara.[225] We can conclude that there is an overall good agreement between the computed and the experimental data. The main difference when observing the Raman spectra for $LiKCO_3$ and $LiNaCO_3$ is that in the latter case the ν_2 band is completely absent, independently from the bulk phase symmetry. Moreover, the bands associated to ν_1, ν_3, and ν_4 are all split and observed between 1100 and 1150, 1500 and 1660, 700 and 740 cm^{-1}, respectively. In line, with what reported by Zehnder, we can observe that the complexity of the fine structure of these bands increases with decreasing the symmetry of $LiNaCO_3$ bulk phase

5.3.3 Electronic Properties

Very little is known about the electronic structure of pure carbonate materials (M_2CO_3), like Li_2CO_3, Na_2CO_3 or K_2CO_3, even if they have been the subject of various experimental and theoretical studies.[225,350–360] In particular, we were not able to find any experimental data,

but just few theoretical calculations about band gaps and band structure of these latter materials.[358–361] These studies were all performed in the framework of DFT (generally at the GGA level) and provide relatively large band gap and highly localized covalent C-O and ionic M-O bonds, suggesting a strong insulating nature for M_2CO_3. Information on the electronic properties of $LiNaCO_3$ and $LiKCO_3$ is not currently available. Here, we investigated the electronic properties of the various $LiNaCO_3$ polymorphs and of $LiKCO_3$ using different exchange-correlation functionals. Table 5.6 presents band gaps values obtained with the three chosen DFT methods, while in figure 5.5 we only report band structures and density of states (DOS) computed at the PBE0 level, since they were all qualitatively similar.

5.3.3.1 Band Gaps

Previously reported band gaps (E_g), computed at the GGA level, for α-Li_2CO_3 (space group *C2/c*), β-Li_2CO_3 (space group *P6$_3$/mcm*), Na_2CO_3 (space group *C2/m*) and K_2CO_3 (space group *P2$_1$/c*) were of about 5.0[358,361], 3.6,[358,361] 3.9,[360] and 3.7[360] eV, respectively. Considering the characteristics of the C-O and M-O bonding and the well-known tendency of GGA functionals of underestimating band gaps, it is easy to understand why these compounds have been considered as large band gap insulators. A value of 8.8 eV was also recently reported for α-Li_2CO_3 using DFT (at the PBE level) combined to the GW approximation.[362] In the absence of experimental or previous theoretical band gap data for comparison, we can just notice that the computed values (between 4.9 and 5.1 eV for the various $LiNaCO_3$ polymorphs and of 5.69 eV for $LiKCO_3$) obtained at the PBE level follow the same trend observed for the pure carbonates in the previous works using GGA functionals. However, since PBE values are generally underestimated,[363] we expect hybrid functionals to provide more rigorous quantitative results. In fact, B3LYP and PBE0 values are about 2-3 eV higher than PBE ones and closer to the value obtained from GW calculations for Li_2CO_3, showing a strong insulating nature also for $LiNaCO_3$ and $LiKCO_3$. In particular, PBE0 results are systematically about 0.6-0.7 eV higher than the B3LYP data, in line with the largest amount of Hartree-Fock exchange in PBE0 (25%) compared to B3LYP (20%). For all the functionals, band gaps increase in the following order: Model A $\gamma-$ $LiNaCO_3$ $<$ $\alpha-$$LiNaCO_3$ $\sim$ $\beta-$ $LiNaCO_3$ $\ll$ Model B $\gamma-$ $LiNaCO_3$ $<$ $LiKCO_3$. In particular, α, β, and Model Aγ-$LiNaCO_3$ have very close E_g values, while Model Bγ-$LiNaCO_3$ is the only one having a substantially higher value. The differences in the band gaps between the various phases are, however, very small (especially at the B3LYP level) and lower than 0.3 eV, also when γ-Model B $LiNaCO_3$ is taken into account. This observation is in line with the similar structures of the polymorphs and the small energy differences discussed in Section 5.3.1 .

5.3.3.2 Valence and Conduction States and Mulliken Population Analysis

The three $LiNaCO_3$ polymorphs show similar band structures, with the same topology of bands between -25 and 15 eV and with a very flat valence band (VB) as a consequence of the triangular planar CO_3 units, in analogy to what observed for the borate crystals where BO_3 units are present.[269] The main feature of the electronic structure of $LiNaCO_3$ is the presence of five different sets of bands between -25 eV and the Fermi level. At about -23 eV, there is a first narrow band (band I in figure 5.5a-d) mainly associated to the Na-2p states and with a

	PBE	PBE0	B3LYP
α-$LiNaCO_3$	4.90	7.91	7.30
β-$LiNaCO_3$	4.90	7.89	7.30
γ-$LiNaCO_3$ (Model A)	4.87	7.87	7.27
γ-$LiNaCO_3$ (Model B)	5.10	8.12	7.43
$LiKCO_3^a$	5.69 (5.69)	8.68 (8.76)	8.08 (8.16)

[a] Entries for $LiKCO_3$ are computed with the all electron basis set, while values in parenthesis refer to the pseudopotential basis set.

Table 5.6: Band gaps (eV) of the α, β and γ (Model A and B) phases of $LiNaCO_3$ and of $LiKCO_3$ calculated with different Hamiltonians.

smaller contribution of the C-2s and O-2s orbitals. It is followed by band II, at about -20 eV. It is another narrow band corresponding mainly to O-2s and C-2p states. Band III at about -8 eV is instead associated to O-2s and C-2s states. A wider band (band IV) with O-2p, C-2p and smaller O-2s contributions is instead observed between -5 and -7 eV. Finally, the top of the VB is exclusively associated to O-2p states that dominate band V, going from about -3 eV to the Fermi level. These are O-2p non bonding states, which have negligible overlap with other electronic states and directly determine the band gap.[364] The bottom of the conduction band (CB) is, instead, made up by C-2p states between about 8 and 10 eV, while O-2p states contribute to this band at slightly higher energies.

Overall, the overlap between the C and O states in the VB region indicates a very strong covalent bonding within the carbonate group, while an ionic behaviour is observed between Na or Li and the CO_3 units. This conclusion can also be derived from the analysis of the Mulliken atomic charges and overlap populations reported in Table 5.7. In fact, computed bond overlap population is almost zero for Na-O and Li-O bonds (indicating that there is no overlap between Na or Li and O atoms), but it is of about +0.7 for the C-O bonds of the three polymorphs (suggesting a strong overlap between C and O atoms). Charge analysis show again very similar results for the three polymorphs with a value of about +1.0, +0.9, +0.7 and -0.9 for Na and Li, C and O atoms, respectively. Although qualitative, this Mulliken analysis nicely confirms the different bonding types found in these compounds. Similar considerations can be made about band structure (see figure 5.5e) and the Mulliken population of $LiKCO_3$ (see Table 5.7). The main difference is the presence of six different groups of bands instead of five between -25 eV and the Fermi level. The lower energy band (band I figure 5.5e) corresponds to O-2s and C-2s states, while band II is associated to O-2s and C-2p states, and band III is mainly associated to the K-2p states. Band IV has the contribution of C-2s, O-2s and O-2p energy levels, while band V is due to the superimposition of C-2p and O-2p contributions. Also for this carbonate, the top of the VB (band VI) is related to O-2p non-bonding state with almost no overlap with other electronic levels and the bottom of the CB is made up by C-2p states. In summary, the large band gap values and the highly localized covalent C-O bonds and the ionic nature of Li-O and Na-O or K-O bonds suggest that $LiNaCO_3$ and $LiKCO_3$ are electronically insulating.

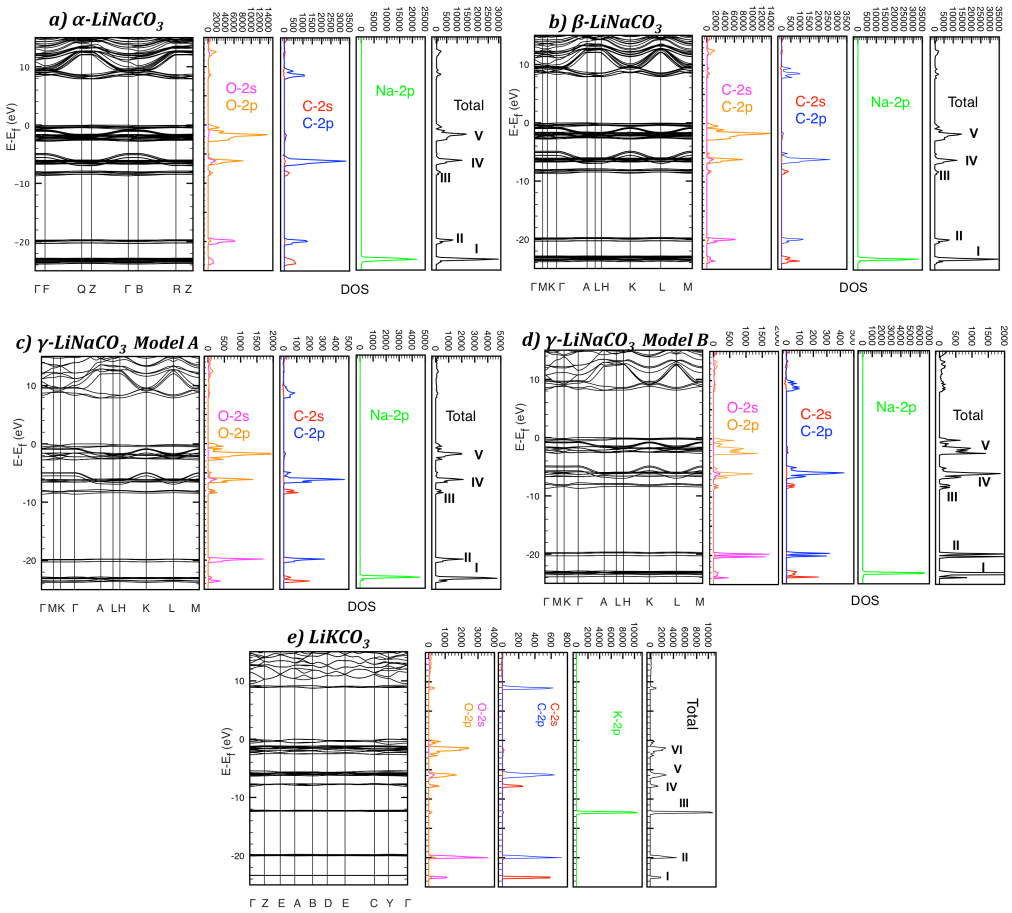

Figure 5.5: Band structure and total and orbital projected density of states (DOS) for the a) α, b) β, c) γ-Model A, d) γ-Model B of $LiNaCO_3$, and e) $LiKCO_3$.

		α-$LiNaCO_3$	β-$LiNaCO_3$	Model A γ-$LiNaCO_3$	Model B γ-$LiNaCO_3$	$LiKCO_3$
Charges	$q_{Na/K}$	+0.985	+0.986	+0.986	+0.983	+1.035
	q_{Li}	+0.940	+0.938	+0.939	+0.939	+0.928
	q_C	+0.665	+0.665	+0.662	+0.666	+0.602
	q_O	-0.863	-0.859	-0.861	-0.861	-0.862
Bond population	$b_{Na/K-O}$	-0.014	-0.016	-0.018	-0.010	-0.008
	b_{Li-O}	-0.006	-0.006	-0.006	-0.008	-0.008
	b_{C-O}	+0.706	+0.694	+0.702	+0.706	+0.682

Table 5.7: Average Mulliken atomic charges (q, in *e*) and overlap population (b, in *e*) computed for the three $LiNaCO_3$ polymorphs and for $LiKCO_3$ at the PBE0 level. $LiKCO_3$ results refer to the HAYWSC-31 basis set.

5.4 $LiNaCO_3$ and $LiKCO_3$ Surfaces

Unfortunately, no experimental or previous theoretical surface studies on $LiNaCO_3$ or $LiKCO_3$ surfaces are available. We started from the papers of Bruno and Prencipe[331] and of Gao et al.[332], who studied the most important terminations of Li_2CO_3 and K_2CO_3, which have a structure similar to $LiNaCO_3$ and $LiKCO_3$, respectively. In order to reduce the time and cost of the calculations, we investigated the surfaces of the γ phase, using the most stable Model A only. Indeed, the γ-phase has a higher symmetry than the α one and at the same time it has fewer atoms in the asymmetric unit cell in comparison to the β phase that belongs to the same space group as γ-$LiNaCO_3$. For sake of simplicity, we selected the (001) and the (110) surfaces and we took into account cation terminated surfaces as Bruno and Prencipe[331] did for Li_2CO_3.

Surface energy ($E_s(n)$) for a slab model of each surface with n layers has beencomputed according to equation 4.1 discussed in the previous chapter for ZrO_2 surfaces.

5.4.1 Reconstruction of the dipolar (001) $LiNaCO_3$ surface

According to Tasker's classification,[309] there are three possible types of surfaces when a ionic or partially ionic crystal is cut along one direction. Type 1 surfaces are made up by neutral planes with the same number of cations and anions in each plane. Surface belonging to type 2 are built up by a series of charged planes organised in a symmetrical way, so that there is no dipole moment perpendicularly to the surface. Finally, type 3 surfaces are constituted by alternating positive and negative charged planes and have a dipole moment perpendicularly to the surface. Directions with a microscopic dipole moment are often called dipolar directions.[365] While non polar surfaces of type 1 and 2 can be stable with moderate surface energies (E_s) and small relaxations with respect to the bulk terminated positions, in the case of dipolar surfaces the surface energy diverges as a consequence of the proportional increase of the dipole moment with the number of layers. In fact, Bruno[365] showed that E_s is proportional to the electrostatic potential V, which for a surface constituted by n polar slices, each built by two parallel planes at a distance l and bearing opposite charge density σ, can be approximated by:

$$V = n2\pi\sigma l \tag{5.2}$$

Equation 5.2 shows that the potential energy near the surface, and consequently the surface energy, diverges ($V \rightarrow \infty$) with the thickness of an infinite slab ($n \rightarrow \infty$). These surfaces are thus not stable without reconstruction or adsorption of additional charged species. It is possible, for example, to quench the dipole modifying the density of ions in the n outermost plane of the surface following the relation:[365]

$$\sum_{i=1}^{n} \sigma_i = \frac{-\sigma_{n+1}}{2} \tag{5.3}$$

where σ_i is the charge density of the i-th plane.

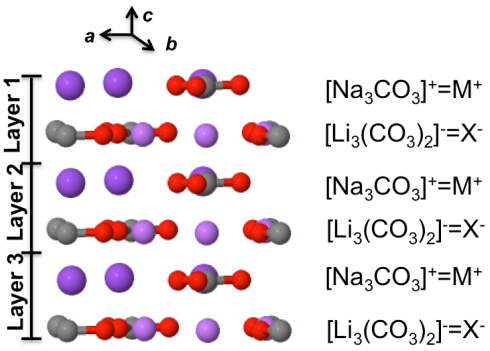

Figure 5.6: Slab model of the (001) surface of γ-LiNaCO3 (Model A), composed by three slab layers (three $[Na_3CO_3]^+$-$[Li_3(CO_3)_2]^-$ platelets). The stoichiometry and total charge of each atomic layer is indicated to evidence the presence of a dipole moment perpendicular to the surface.

Figure 5.6 shows that $LiNaCO_3$-(001) surface can be described as being built up of alternating equally spaced $[Na_3CO_3]^+$-$[Li_3(CO_3)_2]^-$ planes for Na-terminated surfaces (or $[Li_3(CO_3)_2]^-$-$[Na_3CO_3]^+$ planes for Li terminated ones). There is thus a dipole moment perpendicular to the surface that requires reconstruction in order for the dipolar surface to be stabilized. In order to apply the two chosen reconstruction types to this surface, we created a (2×2) supercell of the slab model, with each supercell layer constituted by $[Na_3CO_3]_4^{4+}$-$[Li_3(CO_3)_2]_4^{4-}$ platelet for a total of 12 $LiNaCO_3$ formula units. Some atoms were then moved or eliminated if in excess, in order to perform the two types of reconstruction that can be derived by applying equation 5.3.[365–368] The first one is performed by moving one half of the $[Na_3CO_3]^+$ units in the outermost plane of the Na-terminated supercell into a new plane at the bottom in order to obtain a surface model that is symmetrical about a central plane. The same modification can be applied to the case of the Li-terminated surface, by displacing half of the $[Li_3(CO_3)_2]^-$ units. In both cases, after the reconstruction, the charge of the outermost plane equals half of the charge density in the second plane ($\sigma_1 = -\sigma_2/2$), so that equation 5.3 holds. We will indicate this type of reconstruction as R_1. There can be different ways in which one half of the outermost ions is removed and relocated in a centre-symmetrical plane at the bottom of the slab. The R_1 type reconstruction provides quenching of the dipole moment regardless of the topology obtained, but each topology will correspond to a different value of E_s. However, as demonstrated by Bruno and co-workers[365–368], the symmetry of the bulk structure of a crystal is a major parameter to take into account. We then tried to maximise the symmetry while performing the reconstruction. For Li-terminated surface, it was possible to perform such a R_1 reconstruction preserving the *P-6* symmetry of the bulk system. However, this was not possible for Na-terminated R_1 surfaces, for which the highest possible symmetry corresponds to the *P11m* layer group. The second type of reconstruction is an octopolar reconstruction, performed by removing 75% of $[Na_3CO_3]^+$ (or $[Li_3(CO_3)_2]^-$) units of the outermost plane and 25% of $[Li_3(CO_3)_2]^-$ (or $[Na_3CO_3]^+$) units in the underneath one at the top and bottom of the slab. Consequently, the charge in the first and second surface planes are equal, respectively, to $3/4$ and $-1/4$ of the charge density in

the third plane ($\sigma_1 = \sigma_3/4$ and $\sigma_2 = -3\sigma_3/4$). In the following, such a reconstruction is referred to as R_2, and was performed maintaining the *P-6* symmetry intrinsic to the (001) surface.
We can then introduce the notation $(001)^B_A$ where A stands for the type of reconstruction (R_1 or R_2) and B stands for the exposed cation (Na or Li). For example, $(001)^{Na}_{R2}$ then stands for an octopolar reconstruction of the Na-terminated (001) surface. For each possible reconstruction of the (001) surface we evaluated the convergence of the surface energy and of the electronic properties increasing the number of supercell layers.

5.4.1.1 $(001)^{Na}_{R1}$ surface (layer group *P11m*) and $(001)^{Li}_{R1}$ surface (layer group *P-6*)

The largest relaxations for $(001)^{Na}_{R1}$ (see figure 5.7a) are associated to the first slab layer, while they are almost negligible for the underneath ones. In particular the carbonate groups of the second atomic layer with under-coordinated O atoms (3-fold coordinated) undergo consistent rotation around the *c* and *b*-axis. However, no significant variations are observed for the C-O distances (of about 1.28 Å), indicating that the carbonate groups behave like a rigid unit, as observed for Li_2CO_3[331] or $CaCO_3$.[367,368] On the contrary, Na-O and Li-O distances in the outermost slab layers, where 4-fold Na and 3-fold Li coordinated surface sites reside, shrink of about 0.1 Å. As a consequence of these atomic displacements, the distance between the two atomic layers of the first slab layer (1.5 Å) is lower that the corresponding distance for the underneath layers (1.6 Å).

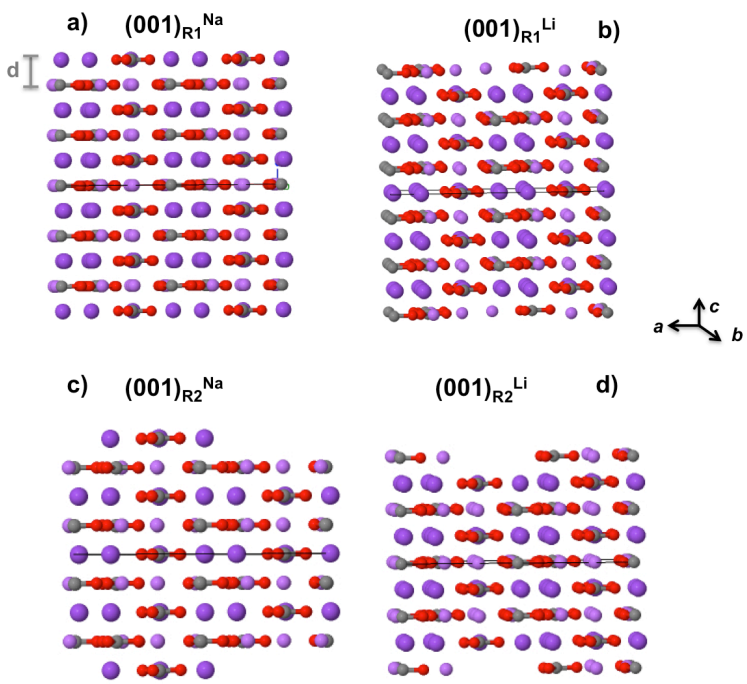

Figure 5.7: Schematic representation of the (2×2) supercell for the a) $(001)^{Na}_{R1}$, b) $(001)^{Li}_{R1}$, c) $(001)^{Na}_{R2}$, and d) $(001)^{Na}_{R2}$ reconstructions. d is the distance between the two atomic planes that constitute each slab layer.

Carbonate	Surface	n	$E_s(n)$	E_g
$LiNaCO_3$	(110)	4	0.50	7.57
	$(001)^{Na}_{R1}$	5	0.41	7.77
	$(001)^{Li}_{R1}$	5	0.52	6.74
	$(001)^{Na}_{R2}$	4	0.58	7.49
	$(001)^{Li}_{R2}$	5	0.58	6.76
$LiKCO_3$	(110)	4	0.46	8.37
	(001)	3	0.21	8.73

Table 5.8: Converged surface energy (E_s in J/m^2), converged band gap (E_g in eV) and number of layers necessary for the convergence (n) for the all the possible reconstructions of the (001) surface, for the non polar (110) surface of γ-$LiNaCO_3$ and for $LiNaCO_3$ surfaces.

Similarly for $(001)^{Li}_{R1}$ (see figure 5.7b), strong relaxations are only observed for the outermost slab layers. The strongest rotation around the *c*-axis is limited to the CO_3 groups of the first atomic layer, followed by the carbonate groups of the second one. The CO_3 units of the second slab layer are just slightly rotated. Again C-O distances do not show significant changes through the entire slab, indicating that the carbonates move like a rigid unit. These atomic movements are caused by under-coordination of the Na, Li and O surface atoms, with 2-fold coordinated Li, 4-fold coordinated Na and 3-fold coordinated O sites at the surface. In fact, a decrease of the Li-O (between 0.08 and 0.18 Å) and Na-O (between 0.10 and 0.53 Å) bond lengths of the first slab layer can be observed to compensate for the presence of dangling bonds. In particular, the rearrangement of the outermost carbonate is such that the coordination number of the Li surface sites increases of one unit after the optimization. Moreover, as a consequence of the reconstruction and relaxation, the distance between the two atomic layers of the first slab layer (1.6 Å) is lower that the corresponding distance for the underneath layers (1.9 Å). For $(001)^{Na}_{R1}$, 5 slab layers are necessary to get convergence of surface energy and band gap to values of 0.41 J/m^2 and 7.77 eV, respectively. Despite a higher symmetry, $(001)^{Li}_{R1}$ appears to be less stable than $(001)^{Na}_{R1}$, since the surface energy for a fully converged surface model made by 5 slab layers is 0.52 J/m2, with a band gap of 6.74 eV (*cf.* Table 5.8 and figure 5.8I). In both case however, the R_1-type reconstruction appears as very stable.

5.4.1.2 $(001)^{Na}_{R2}$ surface and $(001)^{Li}_{R2}$ surface (layer group *P-6*)

The $(001)^{Na}_{R2}$ surface exposes 4-fold coordinated Na and 3-fold coordinated Li sites in the first and second atomic layers, respectively. Atomic relaxations are mainly constrained to the first slab layer. In particular, CO_3 groups of the second atomic layer and those close to the Li surface sites undergo important rotation around the *c*-axis. C-O distances in these groups are subject to negligible variations, evidencing that the carbonates again behave essentially as rigid units during rotation. Also the carbonate groups in the third atomic layers are slightly displaced from their bulk like position, with a consequent reduction of the Li-O distances for the 3-fold coordinated Li sites (of about 0.2 Å). Similarly, Na-O distances for the surface Na sites undergo reduction (decrease go from 0.04 to 0.60 Å) after the optimization of the geometry (see figure 5.7c). The reorganisation of the surface to compensate the

effect of the under-coordination of surface sites determines also a more compact structure for the outermost layers: the distance between the two atomic layers of the first slab layer (1.5 Å) is lower that the corresponding distance for the underneath layers (1.7 Å and 1.8 Å for the second and third slab layers, respectively). Observations similar to the one made for the $(001)^{Na}_{R2}$ surface can also be made for the other octopolar reconstruction $(001)^{Li}_{R2}$ in figure 5.7d. Strong relaxations are observed only for the first three atomic layers; in particular, CO_3 groups in the first atomic layer are rotated about the c-axis, while the ones in the second atomic layer are strongly tilted toward the three-fold coordinated Li or the four-fold coordinate Na surface sites. Na-O, Li-O and C-O distances show the same trend observed for the other type of octopolar reconstruction. The converged surface energy for both the $(001)^{Na}_{R2}$ and $(001)^{Li}_{R2}$ is of 0.58 J/m^2, obtained in the first case for a 4 layers thick surface model with a band gap of 7.49 eV, and for a 5 slab layer model with a gap of 6.76 eV in the latter case (*cf.* Table 5.8 and figure 5.8I). Both the octopolar reconstructions are then less stable than the $(001)^{Li}_{R1}$ and especially than the $(001)^{Na}_{R1}$ reconstructions.

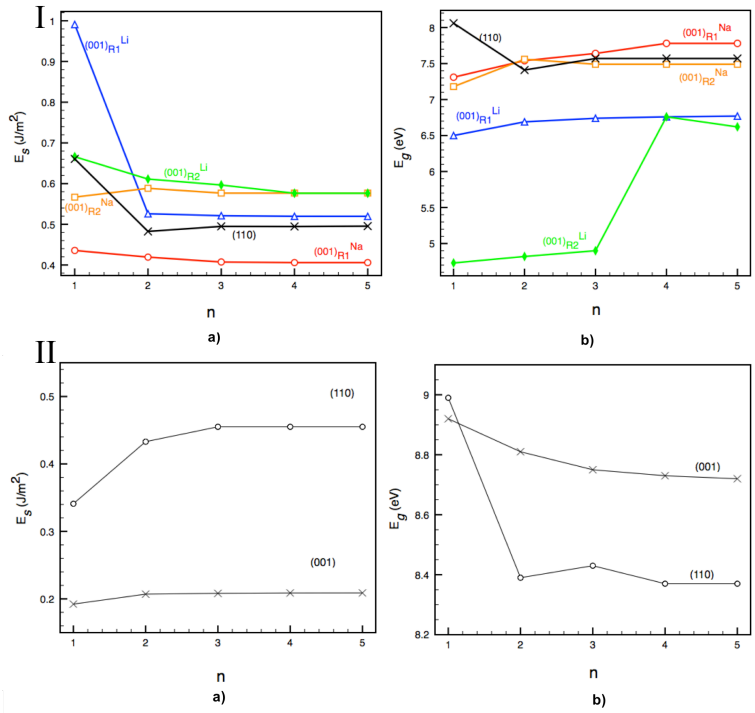

Figure 5.8: a) Surface energy (E_s) and b) band gap (E_g) for I) the reconstructed $LiNaCO_3$-(001) and $LiNaCO_3$-(110) surfaces, as well as for II) $LiKCO_3$ (001) and (110) as a function of the number n of layers in the slab model

To sum up, we find some general trends for all investigated reconstructions of the $LiNaCO_3$-(001) surface:

- Rigid CO_3 moieties rotating mainly around the c axis;
- Shrinking of Li-O and Na-O distances at the surface;

- Shrinking of the distance between the two atomic planes of the first slab layer.

In addition, from the computed surface energies, the following stability order is obtained: $(001)^{Na}_{R1} \gg (001)^{Li}_{R1} > (001)^{Na}_{R2} \approx (001)^{Li}_{R2}$. This clearly differs from the expected stability order based on the symmetry arguments proposed by Bruno[366] and Bruno et al.,[365,367,368] according to which the most stable surface should be the one respecting the bulk symmetry of the crystal.

5.4.2 Non polar (110) $LiNaCO_3$ surface

The $LiNaCO_3$-(110) surface is constituted by a sequence of charged Na^+-CO_3^{2-}-Li^+ planes. It, therefore, belongs to a surface of type 2 and is expected to be stable. Since this surface is not polar, the convergence of the surface energy and of band gap was evaluated by simply considering slab models derived from the bulk structure with an increasing number of slab layers. For this surface, each slab layer is made up by a Na^+-CO_3^{2-}-Li^+ platelet and contains 3 $LiNaCO_3$ formula units. In this case, CO_3 groups are placed perpendicularly to the normal to the plane of the surface (figure 5.9a). Li-terminated (110) surface was not taken into account because, being made by Li^+-Na^+-CO_3^{2-} layers, it has a dipole moment perpendicular to the surface and is then likely to be less stable than the non polar Na-terminated (110). This surface presents two different types of Na and O surfaces sites: in figure 5.9a, Na_1 and Na_2 are 3-fold while Na_3 is 4-fold coordinated; O surface sites are 3-fold coordinated. Surface energies and electronic properties converge easily with increasing slab thickness: a 4-layers slab with a surface energy of 0.68 J/m^2 and a band gap of 7.57 eV (*cf.* Table 5.8 and figure 5.8I) can be already considered converged. This surface is then less stable than the reconstructed (001) one. Surface relaxations are restricted to the very first layer with CO_3 groups slightly rotated around the *a*-axis and the outermost Na^+ ions displaced inward (about -0.3 Å along *c*) in order to compensate the under coordination of the surface O and Na atoms.

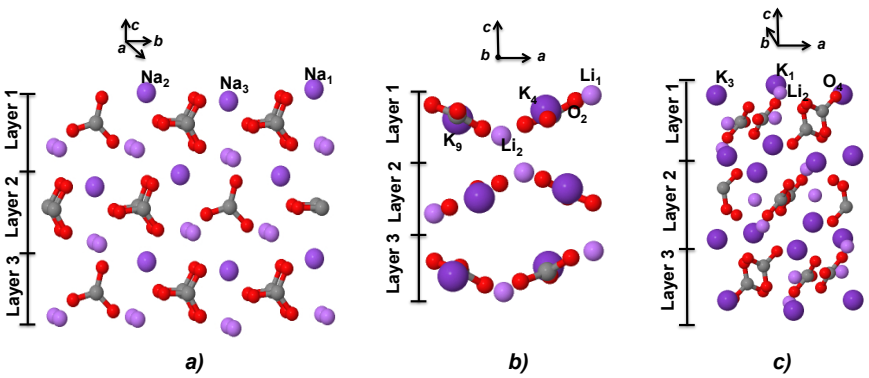

Figure 5.9: Slab models of a) $LiNaCO_3$-(110), b) $LiKCO_3$-(001), and c) $LiKCO_3$-(110).

5.4.3 (001) and (110) $LiKCO_3$ surfaces

The Li-terminated (001) $LiKCO_3$ surface is another type 2 surface, built up by a sequence of charged layers with no dipole moment perpendicular to the [001] direction. It is not possible to have non polar K-terminated surfaces. Each slab layer is made up by 12 atomic layers, with a Li-O-K-O-C-O-O-C-O-K-O-Li motif (figure 5.9b) for a total of 2 formula units. K and Li cations exposed on this surface are 5 or 6-fold (K_4 and K_9, figure 5.9b) and 4- or 5-fold coordinated (Li_1 and Li_2, respectively, in figure 5.9b) , respectively. Also a 3-fold coordinated surface oxygen atom O_2 can be identified. Surface properties converge very quickly: the fully converged slab has just 3 layers, a surface energy of 0.21 J/m^2 and a band gap of 8.73 eV (*cf.* Table 5.8 and figure 5.8II). This surface appears then to be very stable, with almost negligible atomic displacement also in the outermost layer, except for the under-coordinated Li_1 surface atom, which move inward along *c* of about 0.26 Å toward the surface oxygen atom O_2. The $LiKCO_3$-(110) surface presents instead a more complex structure. Each slab layer is neutral if we consider K-terminated surfaces with 24 atomic layers for a total of 4 formula units per slab layer (K-Li-K-O_5-C-Li-C-O_2-C-Li-O_5-K-Li-K motif). Two different K surface sites can be identified on this surface, one characterized by 6 K-O bonds (K_3, figure 5.9c) and the other with a lower coordination number (4 for K_1, figure 5.9c). Finally, Li_2 and O_4 surface atoms are just 3-fold coordinated. This termination is less stable compared to the (001) since the computed surface energy for a converged 4-layer slab (band gap 8.37 eV) is 0.46 J/m^2 (*cf.* Table 5.8 and figure 5.8II). This observation is in line with results obtained on K_2CO_3. The greatest relaxations are observed for the outermost layers of Li atoms and CO_3 groups that rotate around the *b*-axis, concerning particularly the Li_2 and O_4 surface atoms (1.47 Å and 1.23 Å respectively). It is the under-coordination of these surface sites that causes the large displacements on the top layer, whose magnitude is such that consistent atomic movements are needed also for atoms of deeper slab layers. The greater instability and the more important relaxations observed for this surface compared to the (001) can then be explained in terms of the major complexity and of the number and types of under-coordinated surface sites observed.

5.5 Li transport at the $LiKCO_3$-(001) surface

In the previous section, we succesfully identified a suitable model of $LiNaCO_3$ and $LiKCO_3$ most stable surfaces in order to build the oxide-carbonate interface. In this one, we will, instead, discuss Li transport in the carbonate phase. Starting from considerations about the size of the different species, we only took into account the formation of Li-related defects with different charge states, since: i) K ions are indeed bigger than Li ones, and should then move more slowly; ii) the covalently bonded carbonate groups not only are much larger than Li^+ cations, but the creation of anion vacancies through the removal of these groups or their occupation of interstitial sites is also energetically highly demanding.[333,334] Moreover, as discussed in chapter 1 (section 1.3.3), the cations of the carbonate can be involved in defect reactions at the interface with the oxide, that leading to the formation of a space charge layer, can be explain the enhanced performances of the composite observed already at temperature lower than the carbonate melting point, especially when air is the working

atmosphere. Characterising Li transport in the pure carbonate phase can help in the comprehension of the effect of the interface in the composites. For this reason, we studied the diffusion along the most stable $LiKCO_3$ surface and not into the bulk structure of the carbonate. $LiKCO_3$-(001) termination was selected because of its minor complexity with respect to the other studied surfaces, so as to reduce the computational cost.

5.5.1 Defect Formation

5.5.1.1 Structural and Electronic Properties

The neutral V_{Li} vacancy is created through the removal of a neutral Li lattice atom. As can be seen from figure 5.10a for a V_{Li} defect created in a 4-fold coordinated Li surface site, the shape of the band structure of the defective system is similar to that of the pristine system, but the creation of V_{Li} determines the appearance of a new state in the gap at 1.6 eV above the top of the valence band. The analysis of the band through the projected density of states shows that it is associated to the states of the oxygen atoms nearest neighbour (NN) to the defect, which move up crossing the Fermi level.

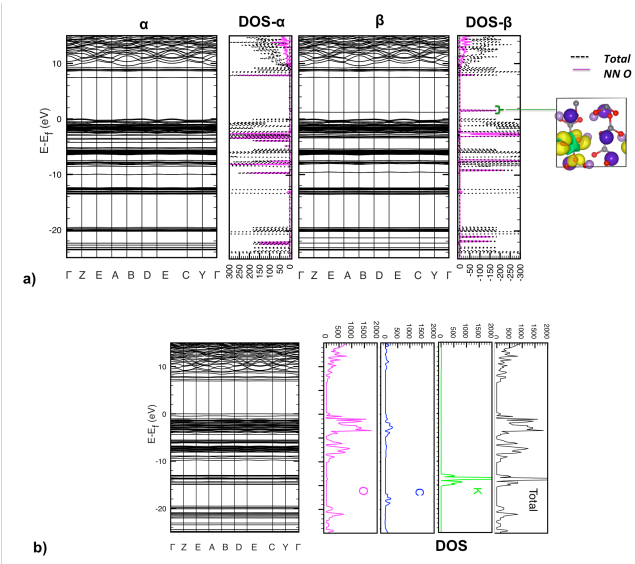

Figure 5.10: a) Band structure and DOS of the (001) surface of $LiKCO_3$ with a V_{Li} vacancy created in a 4-fold coordinated site. The black dotted line is the total density of state (DOS) while the pink line is the DOS projected of the oxygen atoms in nearest-neighbour (NN) positions to the defect. Positive or negative values of the DOS stand for spin-up or spin-down spin states, respectively. Inset: spin density plot with isovalue of 0.001 and yellow for positive and green for negative values; b) Band structure and total and atom projected DOS of the (001) surface of $LiKCO_3$ with a V_{Li}' vacancy created in a 4-fold coordinated site.

The contribution of the other O atoms is not affected by the formation of this type of defect (hole). The inset in figure 5.10a, presenting the spin density plot of the system, shows indeed that the holes are highly localised to the NN O atoms, which are slightly oxidised with

a Mulliken charge of about -0.50*e* compared to the charge of -0.86*e* for the O atoms in the pristine system. These O atoms are also associated to the carbonate groups subject to the largest relaxation after the vacancy creation, with strong rotations around the *b*-axis. Analogous results can be derived for the 5-fold V_{Li} vacancy, which appears to be slightly less stable than the one created in the under-coordinated 4-fold site, as will be explained in Sec. 5.5.1.2.

Negatively charged V'_{Li} defects can also be created in 4 or 5-fold coordinated Li lattice sites through the removal of a Li^+ ion. In this case, their formation is not associated with the appearance of new electronic states in the gap, but from the band structure: in figure 5.10b, we can observe a shift of the CB (in particular of the states associated to the O atoms) to lower energies, with a consequent decrease of the band gap to up to a value of 6.9 (8.0 eV) in the case of the 4(5)-fold coordinated site.

Excess interstitial neutral Li atoms (Li_i^X) were instead added in the large open channels that the $LiKCO_3$-(001) shows along the *b*-axis. There could be a large number of sites where the Li_i^X can be positioned along the channel.

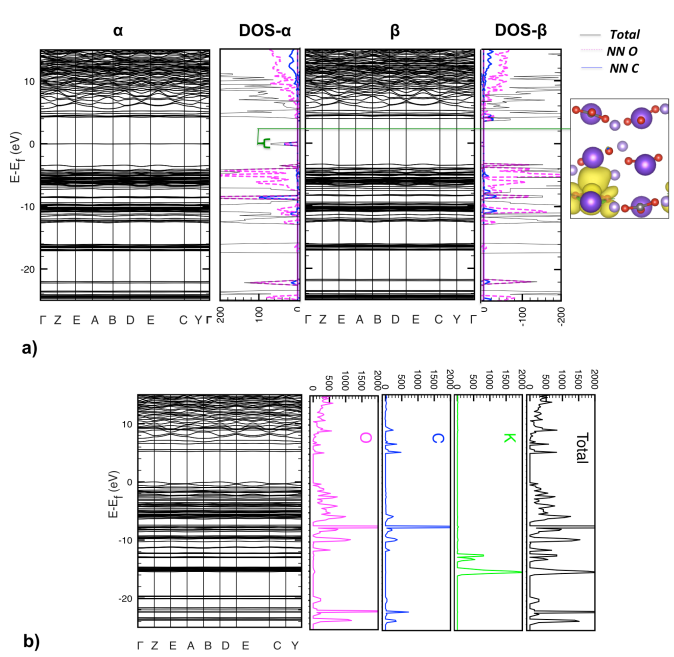

Figure 5.11: a) Band structure and DOS of the (001) surface of $LiKCO_3$ with a Li interstitial atom (Li_i^X). The black line is the total density of state (DOS) while the pink dotted and the blue lines are the DOS projected, respectively, on the oxygen and carbon atoms in nearest-neighbour (NN) positions to the defect. Positive or negative values of the DOS stand for spin-up or spin-down spin states, respectively. Inset: spin density plot with isovalue of 0.001 and yellow for positive and green for negative values; b) Band structure and total and atom projected DOS of the (001) surface of $LiKCO_3$ with a Li^+ interstitial defect ($Li_i^\bullet$) in configuration I_1.

We consequently positioned the defect in different possible initial configurations. However, the majority of the considered initial position for the excess Li atom are found to be unstable,

especially when Li_i^X is positioned close to the side of the channels, and at the end of the optimization process it is always found close to the centre of the channel in a configuration that ensures the highest O coordination (4 Li_i^X-O bonds).

Concerning the electronic properties, band structures reported in figure 5.11a show that a new defect level appears in the band gap at about 3.7 eV above the VB of the clean surface. DOS plots (fig 5.11a) evidence that this state is associated to the C atom and to the O atoms of the CO_3 group closest to the defect. This means that when Li_i^X is introduced in the material it becomes Li^+ donating the excess electron to the lattice. The inset in figure 5.11a, presenting the spin density plot of the system, shows indeed that the excess electron density is highly localised to one CO_3 in the neighbouring of Li_i^X, whose structure appears also to be slightly distorted from the usual planar geometry of the carbonate groups. The Mulliken charge analysis is also in agreement with this picture, because the Li defect shows a charge of about +0.91*e* very close to the average charge for Li in the $LiKCO_3$ lattice (+0.93e)12, while the C and the O atoms of the neighbouring CO_3 is slightly reduced with a charge of about +0.33*e* and -1.03*e* that should be compared to the charge of +0.60*e* and -0.86*e* for the C and O atoms in the clean system.

Finally, we also considered the excess interstitial $Li_i^\bullet$. Again, there could be a lot of possible sites for $Li_i^\bullet$ defects and we started trying to identify the most energetically stable configurations in the open channels oriented along the *b*-axis of the (001) surface. Some of the obtained minima structures are shown in table 5.9. The stability order of the various configurations can be explained through a combination of the level of O-coordination of the $Li_i^\bullet$ defect in each site and of the electrostatic interactions between the positively charged $Li_i^\bullet$ and the K and C atoms in the $LiKCO_3$ lattice that are positively charged. In general, the higher the O-coordination number and at the same time the longer the distances of the interstitial atom from the cations in the lattice of the carbonate, the lower the formation energy for $Li_i^\bullet$. Configurations I_1 and I_3 in table 5.9 present the Li defect near the centre of the channel, where the electrostatic interactions are less important compared to configurations I_2 and I_4 where $Li_i^\bullet$ is close to the side of the channels. I_1 and I_3 are indeed more stable than configurations I_2 and I_4, independently of the O-coordination number. In the most stable configuration I_1, $Li_i^\bullet$ ion is close to the centre of the channel, but still preserves a relative high O-coordination number (3). In this case, $Li_i^\bullet$-C distances are all longer than Li-C distances in the defect-free system, while the shortest $Li_i^\bullet$-K distance is of about 2.71 Å. Since long $Li_i^\bullet$-C and $Li_i^\bullet$-K distances are observed also for I_3, electrostatic effects should not play an important role in determining the greater instability of this configuration compared to I_1, that can be instead explained considering the lower O-coordination number of 2. Configuration I_2 is instead less stable than I_1, despite being 4-fold O coordinated. In fact, for this configuration shorter $Li_i^\bullet$-C and $Li_i^\bullet$-K distances are observed, being $Li_i^\bullet$ close to the lattice atoms at the side of the channels. Finally, configuration I_4 is just slightly more unstable than configuration I_2, even if it has a very low O-coordination number of 2, because it is characterized by an almost symmetrical disposition of $Li_i^\bullet$ with respect to the two O atoms to which it is linked and to the two neighbour K, that are at a distance of 2.31 and 2.46 Å. From the point of view of the electronic properties, the band structure, reported in figure 5.11b for the most stable of the considered $Li_i^\bullet$ configuration, shows a considerable broadening and a lowering of the energies of the CB states associated to the neighbouring C and O atoms, with a decrease of

Site	Relative E_f	O-coordination number	Shortest d($Li_i^\bullet - M$)	Atomic configuration
I_1	0	3	2.71 (M=K) 2.10 (M=C)	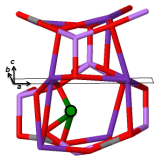
I_2	0.60	4	2.60 (M=K) 2.05 (M=C)	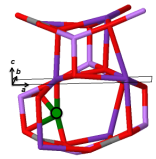
I_3	0.14	2	2.65 (M=K) 2.51 (M=C)	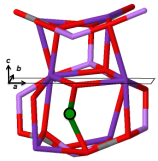
I_4	0.63	2	2.31 (M=K) 2.40 (M=C)	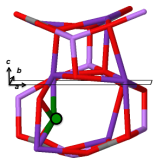

Table 5.9: Parameters of selected $Li_i^\bullet$ configurations: formation energy (E_f, in eV) relative to the most stable configuration, O-coordination number of the defect, value of the shortest distance (d($Li_i^\bullet$-M), in Å) between $Li_i^\bullet$ and the positively charged species (M) in the $LiKCO_3$ lattice, and stick representation of the corresponding atomic configuration evidencing the position of the inserted specie (in green) in the channel and its O-coordination.

the band gap to a value of 5.2 eV. On the contrary, the electronic states associated to the K atoms next to the defects are shifted towards higher energies. Analogous considerations are applied to all the different configurations for the interstitial Li^+ ions. The Mulliken charge analysis shows that the supercell positive +1 charge comes from the carbon and oxygen atoms near the $Li_i^\bullet$: these C atoms have a charge of +0.5*e* compared to the +0.6*e* value of the other C atoms and the NN O atoms have a charge of about -0.7*e* compared to a value of -0.8*e* of other O atoms, while Li and K essentially conserve their charge as in the neutral calculation. The carbonate groups have hence an effective total charge that is less negative compared to the case of the clean surface, determining a weaker ionic contribution to the $Li_i^\bullet$-O bonding.

5.5.1.2 Formation Energy

The formation energy ($E_f(D)$) for a defect D in a charge state q_D is given by equation 5.4:[369–374]

$$E_f(D) = E_t(D) - E_t(X) + \sum_i n_i \mu_i + q_D E_F \tag{5.4}$$

where $E_t(D)$ is the total energy of the defective system, $E_t(X)$ is the total energy of the system without defects, n_i is the number of atoms of element i removed to create the defect (n_i is negative when atoms are added instead), μ_i is the chemical potential of the element i removed (or added), $E_F = E_V + \Delta E_F$ is the Fermi energy of the defective system relative to the value of the band maximum (E_V) of the defect free system, with ΔE_F indicating the position of the Fermi level within the band gap ($0 < \Delta E_F < E_g$). However, when dealing with non-neutral defects, some corrections should be added to this $E_f(D)$ as a consequence of the long-range nature of the Coulomb potential and of the periodic boundary conditions (PBC) imposed in the calculation.[342,375] The formation of the defect determines a constant shift of the potential, which affects the band structure and is not directly evaluable from the calculations, since no absolute reference exists for the electrostatic potential in periodic structures.[375] Van der Walle and Neugebauer[375] suggested to compute this constant offset (ΔV) by inspecting the potential in the system far from the defect and aligning it with the potential in the defect free system. In order to obtain this ΔV, we measured the shift in the energy of the low energy states of the O atoms in the uncharged clean $LiKCO_3$-(001) surface when a charged defect is created in the system, taking into account just O atoms far from the defect. The obtained offset (ΔV) should then be multiplied by the net charge of the system and added to $E_f(D)$. To do that, we analysed the orbital-projected density of states (DOS) for the two systems, as reported in figure 5.12, from which ΔV was estimated to be 7.8 eV.

Moreover, in a periodic charged system to which a background charge is added in order to avoid the divergence of the electrostatic potential, Coulomb interactions contributions (ΔE) to the total energy of the system should be subtracted to $E_t(D)$.[342] In fact, the total energy of the charged defective system treated under the periodic conditions contains defect-defect, defect-background and background-background Coulomb interactions. Although more advanced corrections have been recently proposed for the calculation of formation energies of

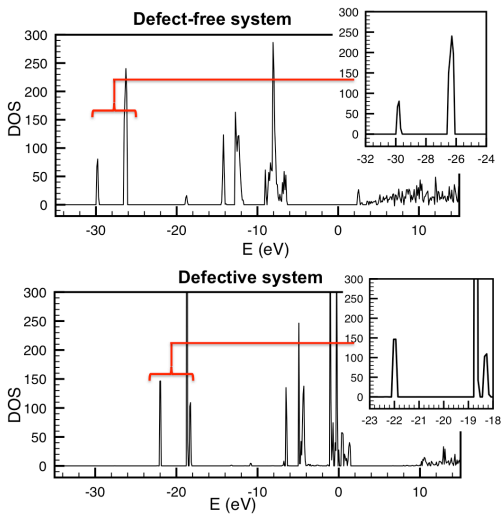

Figure 5.12: DOS projected on one O atom for the defect-free (001) surface (top) and for the same surface with a charged defect (bottom). The selected atom corresponds to an O atom far from the defect. The insets show the enlargement of the plot in the region of the low energy O-2s states.

charged defects in periodic system,[376–380] here we are only interested in a qualitative comparison of various defects formation energies. We then considered the ΔE term to be approximated by the simple Makov-Payne multi-pole correction:[342,380]

$$\Delta E = \frac{q_D^2 \alpha_M}{2\epsilon_r V^{1/3}} + \frac{2\pi q_D Q_D}{3\epsilon_r V} + \mathcal{O}(V^{-5/3}) \tag{5.5}$$

where q_D is the charge of the defect, ϵ_r is the high-frequency dielectric constant of the medium, Q_D is the quadrupole moment of the defect, and α_M is the lattice dependent Madelung constant. Following Bailey et al.[370], the first term in equation 5.5 gives the defect-defect interaction and can be calculated as the nuclear-nuclear interaction in a periodic system made just by H atoms at the positions of the defect multiplied by $(q_D^2)/\epsilon_r$, the second term gives the defect-background interaction which in our case appeared to be negligible, while the last term $(\mathcal{O}(V^{-5/3}))$ is the background-background contribution that was not taken into account, since, as stated in ref.[370], it is almost always very small. A 5-11G* contraction scheme was adopted for H atoms in these calculations. The final corrected defect formation energy $(E'_f(D))$ is then given by the following formula:

$$E'_f(D) = E_f(D) + q\Delta V - \Delta E \tag{5.6}$$

Using this procedure and equation 5.6, we computed the formation energy (indicated simply as E_f in the following) of the four selected Li-related point defects. The relative stability was analysed as a function of the Fermi level, that describes the energy of the reservoir

for the electrons, and of the oxygen chemical potential, which determines if the system is in an oxidising or reducing environment. For Li-associated defects, the chemical potential of the Li atom (μ_{Li}) appears in equation 5.4 in order to compute the corresponding formation energy:

$$\mu_{Li} = \mu_{Li}(\text{metal}) + \Delta\mu_{Li} \tag{5.7}$$

Chemical potentials determine the baseline for the formation energies and consequently need to be well defined. Unfortunately, these atomic chemical potentials are not easily derived, and the common approach is to determine their physically possible range of variation ($\Delta\mu_{Li}$) by taking into account their reference state and the formation energy of the crystal.[371] In particular, here we outline a thermodynamically consistent method to determine the μ_{Li} stability range as a function of the oxygen chemical potential, similarly to the procedure proposed by Gallino and Di Valentin[374] for Cu impurities in ZnO. Mixed carbonates for fuel cells applications are synthetized in air/CO_2 environment.[19] The oxygen chemical potential μ_O characterizes the oxygen environment during synthesis. We can reasonably assume that oxygen poor environments, characterized by low μ_O values, correspond to CO_2 rich conditions that can favour carbonate formation. Conversely, oxygen rich environments, characterized by high μ_O values, correspond to CO_2 poor conditions that can favour lithium oxides (Li_2O, $\Delta H_f(Li_2O)$=-6.21 eV, and Li_2O_2, $\Delta H_f(Li_2O_2)$=-6.56 eV) formation.[381] Naturally high μ_O values correspond also to conditions that favour oxidation, while low μ_O values correspond to conditions that favour reduction. We used for the oxygen chemical potential the oxygen molecule as a reference, $\mu_O = 1/2\mu(O_2) + \Delta\mu_O$, where $\Delta\mu_O$ can vary between 0 (oxygen rich limit) and the $LiKCO_3$ formation energy (oxygen poor limit). We computed the $LiKCO_3$ formation energy ($\Delta H_f(\text{LiKCO}_3)$) to be -12.65 eV. For the lithium chemical potential, we computed μ_{Li}(metal) from the total energy of bulk Li metal (space group *Im-3m*, *a*=3.51 Å)[382] and we derived $\Delta\mu_{Li}$ as a function of $\Delta\mu_O$ imposing the stability of the system against decomposition in elemental Li and against Li_2O and Li_2O_2 formation:

$$\begin{cases} \Delta H_f(\text{LiKCO}_3) \leq \Delta\mu_O \leq 0 \\ \Delta\mu_{Li} \leq 0 \\ 2\Delta\mu_{Li} + \Delta\mu_O \leq \Delta H_f(Li_2O) \\ 2\Delta\mu_{Li} + 2\Delta\mu_O \leq \Delta H_f(Li_2O_2) \end{cases} \tag{5.8}$$

Through the resolution of this system of equations, we obtained the following values for $\Delta\mu_{Li}$ as a function of $\Delta\mu_O$:

$$\Delta\mu_{Li} = 0 \quad \text{for} \quad -12.65 \leq \Delta\mu_O \leq -6.21 \tag{5.9}$$

$$\Delta\mu_{Li} = (-6.21 - \Delta\mu_O)/2 \quad \text{for} \quad -6.21 \leq \Delta\mu_O \leq -0.35 \tag{5.10}$$

$$\Delta\mu_{Li} = -3.28 - \Delta\mu_O \quad \text{for} \quad -0.35 \leq \Delta\mu_O \leq 0 \tag{5.11}$$

Figures 5.13a and b show the dependence of the formation energy from the Fermi level. The slope of the obtained curve corresponds to the defect charge state: positive for a charge of +1, zero for neutral defects, and negative for a charge of -1. In both reducing (fig. 5.13a) and oxidizing atmospheres (fig. 5.13b), V'_{Li} is found to be the most stable defect type over the whole band gap range. Moreover, at the oxygen poor limit, Li_i^X is the second most stable one over the whole band gap. The situation is completely different at the oxygen rich limit, where V_{Li} is the second most stable species after V'_{Li}, independently of the Fermi energy value, while the interstitial Li defects appear to be destabilized compared to the case of reducing environments.

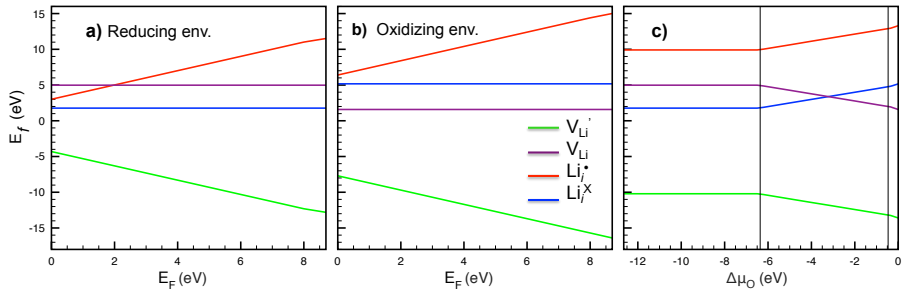

Figure 5.13: Computed formation energy (E_f) of Li-related defect on the $LiKCO_3$-(001) surface as a function of the Fermi level (E_F) a) at the oxygen poor limit ($\Delta\mu_O$=-12.65 eV and $\Delta\mu_{Li}$=0 eV) or b) at the oxygen rich limit ($\Delta\mu_O$=0 eV and $\Delta\mu_{Li}$=-3.28 eV) and c) as a function of the oxygen chemical potential ($\Delta\mu_O$) at the zero Fermi level (E_F=0). The three zones in picture c are referred to the different stability domain of $\Delta\mu_{Li}$ (see text). For the Li vacancies, values are always referred to the more stable 4-fold coordinated surface site.

Figure 5.13c reports instead the dependence of the formation energy from the oxygen chemical potential at the zero Fermi level. We can observe that the plot is clearly divided into three regions, where every defect shows a different slope of the energy formation curve. These regions correspond indeed to the three different stability domains for the Li chemical potential (equations 5.9, 5.10,5.11), obtained after the resolution of the system of equations 5.8 describing the ranges for $\Delta\mu_{Li}$ consistent with the stability of $LiKCO_3$ against decomposition in Li metal or in Li oxides. V'_{Li} is found again to be the thermodynamically most stable defect over the whole $\Delta\mu_O$ range, while $Li_i^\bullet$ is definitively the least stable one. For oxygen poor conditions, Li_i^X is the second more stable defect, but going toward the oxygen rich limit, *i.e.* for increasing $\Delta\mu_O$ values, V_{Li} is progressively stabilized. For sake of simplicity, plots in figure 5.13 only report data relative to the most stable sites for V'_{Li}, V_{Li}, and $Li_i^\bullet$. In the case of V'_{Li} and V_{Li}, vacancies created at the surface (4-fold coordinated sites), where there is more flexibility for the neighbouring atoms to accommodate the creation of the defect, are slightly more stable than the one created in bulk-like positions, but in both cases the differences in the formation energies are, respectively, of the order of about 0.1 and 0.4 eV, respectively, in the same order of magnitude as the difference in formation energies

for the various $Li_i^{\bullet}$ configurations reported in table 5.9. Bearing this in mind, despite the possible different sites for all the defects, conclusions outlined above still holds.

5.5.2 Diffusion mechanism

5.5.2.1 Li vacancies

Since V_{Li}' defects appeared to be the most thermodynamically stable ones, we first investigated their diffusion into the (001) surface. In the case of Li vacancies, Li diffusion corresponds to the repetitively position exchange of one lattice Li^+ and the vacancy.

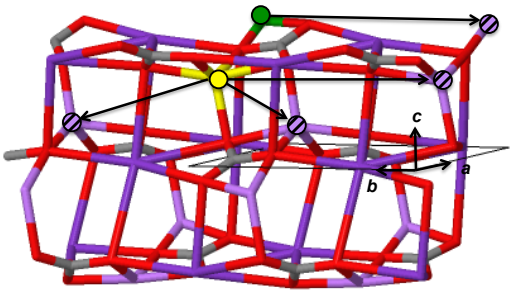

Figure 5.14: Schematic representation of the possible diffusion pathways for V_{Li} or V_{Li}' defects when created in 4-fold (green) or 5-fold (yellow) coordinated sites in (1×2) supercell of the (001) surface. The green and yellow sphere represent the initial vacancy position while the hashed violet spheres stand for the final sites through which the vacancy diffuses.

Figure 5.14 shows the possible diffusion paths for vacancies created in both 5 or 4-fold coordinated defect sites on a (1×2) supercell of the $LiKCO_3$-(001) surface. We consequently performed relaxed scan calculations for one Li diffusing from its lattice position to the corresponding vacant site for each identified path. However, each time one Li is displaced from its original position, all the remaining atoms of the lattice relaxed to restore the starting configuration. We also performed rigid scans in order to gain a better understanding of the process, but barriers of about 30 eV were obtained. Consequently, these results indicate that Li vacancies are not the defects determining the diffusion in the material. This is in agreement with the results of experimental conductivity measurement of Li_2CO_3, indicating that Li transport is essentially due to interstitial Li atoms and not to Li vacancies.[383]

5.5.2.2 Interstitial Li

The diffusion mechanisms for Li_i^X and $Li_i^{\bullet}$ on the $LiKCO_3$-(001) surface were then investigated. Identifying the possible diffusion pathways is a key step in understanding the microscopic diffusion mechanism. Naturally there will be different possible paths for Li_i to migrate through lattice interstices to a crystallographic equivalent position. Moreover, we expect diffusion on the surface to be anisotropic due to the crystalline structure of the system: for example, diffusion though the direction perpendicular to the surface would imply penetrating the electron cloud of the CO_3^{2-} anions and should then be unfavoured, while direct

hopping along the *a*-axis of the surface would involve passing through intermediate interstitial positions with very short Li_i-K and Li_i-C distances, that are energetically not favoured based on the previous discussion in section 5.5.1.1. On the other hand, large open channels exist parallel to the *b*-axis of the surface, and one can then expect a quite straightforward migration of Li_i along this direction. In order to compute the diffusion mechanism of the interstitial Li ion or atom that migrates from one stable initial configuration to a crystallographic equivalent site through lattice interstices (*i.e.* through a direct hopping or interstitial mechanism), we have computed the energy profile associated to the displacement of the defect along the diffusion coordinate. Each point of the energy profile was obtained by keeping fixed the Li defect at different subsequent position along the *b*-axis, while allowing all the remaining atoms to relax. In particular, in the case of the interstitial Li ion, we started from the most stable configurations previously identified for a $Li_i^\bullet$ defect close to the channel centre or side (*i.e.* configurations I_1 and I_2 in table 5.9). In each scan calculation, the interstitial Li was kept fixed at different contiguous positions along the *b*-axis, starting from its initial position and ending up to its corresponding periodic image one, through subsequent steps of 0.39 Å. This method is not as accurate as the costly point-by-point calculation of the potential energy surface, but it nevertheless allows to estimate the energy changes and barriers encountered by the Li_i ion or atom during its migration along the channels, providing a qualitative picture of the conduction properties on the $LiKCO_3$ most stable surface in reasonable timings.

The energy profile computed starting from configuration I_2 is reported in figure 5.15. It shows some new minima and maxima along the pathway that connects the initial position D_i with its equivalent final position D_i'. As we can observe, two main barriers can be observed but the profile is not symmetrical. The first one of 2.08 eV is the highest barrier and separates the 4-fold O-coordinated initial minimum position with a metastable 2-fold O-coordinated configuration S_{1s}, coinciding to configuration I_4 and characterized by the symmetrical orientation of the $Li_i^\bullet$ ion with respect to the two coordinated O and to the two nearest K ions. The corresponding maximum is also 2-fold O-coordinated, but it has a very short $Li_i^\bullet$-K distance of 1.89 Å (tyical Li-K distances are longer than 3.40 Å). The second barrier of 1.28 eV interconnects S_{1s} with another metastable position S_{2s}. S_{2s} results to be less stable than S_{1s} even if it has a higher O-coordination number of 3, because it is destabilised by the interaction with a C atom of one carbonate group at a distance of only 1.84 Å (Li-C distances are generally longer than 2.10 Å). The maximum for the migration from S_{1s} to S_{2s} is just 1-fold O-coordinated, but the electrostatic repulsions are less significant in this case, since the shortest $Li_i^\bullet$-K is of about 2.30 Å, while $Li_i^\bullet$-C distances in the range normally observed for the clean $LiKCO_3$-(001) surface. Finally, migration from this position to the final one D_i' is associated to a negligible barrier. The corresponding maximum is 3-fold O-coordinated like S_{2s}, and the small increase in the energy can be explained considering the further reduction of the $Li_i^\bullet$-C distance observed at the maxima compared to S_{2s}. Throughout the entire diffusion pathway no significant relaxations are observed, except for small atomic displacements of the atoms in the defect neighbourhood. The barriers associated to this path in which $Li_i^\bullet$ diffuses near the channel edge are however quite high (2.08 eV).

Considerably smaller barriers are associated to the second tested pathway, also shown in figure 5.15, which starts from the initial position in configuration I_1, in which $Li_i^\bullet$ is closer to the centre of the channel. In this case, the highest barrier of 0.80 eV is associated to the

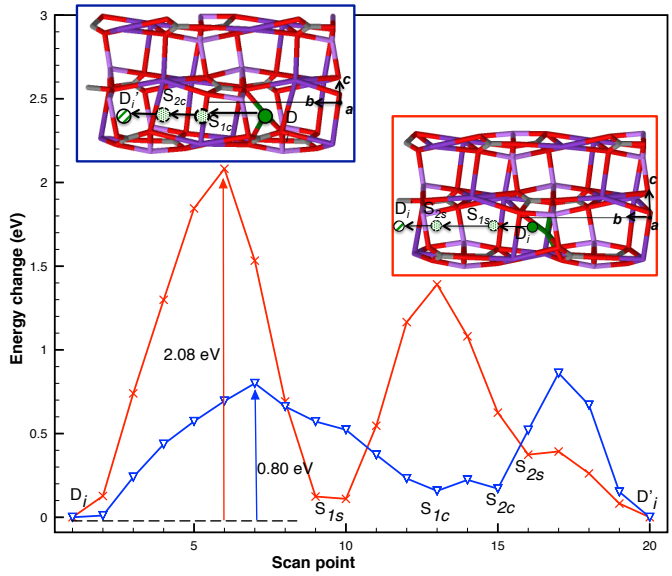

Figure 5.15: Variation of the energy as a function of the $Li_i^\bullet$ defect position along the channels and relative to the energy value of the system with a defect in the initial position of configuration I_1 (blue) or I_2 (red). Insets: schematic representation of the diffusion pathway. $Li_i^\bullet$ diffuses from the initial position Di (green sphere) to the final equivalent one D_i' (hashed green sphere) passing through the intermediate interstitial sites S_{1s} and S_{2s} (dotted spheres) in case of configuration I_2 (red) or S_{1c} and S_{2c} for I_1 (blue).

migration of the $Li_i^\bullet$ defect from the 3-fold O-coordinated D_i initial position to an intermediate configuration S_{1c}, corresponding to configuration I_3, in which it is 2-fold O-coordinated. The corresponding maximum is also 2-fold O-coordinated like S_{1c}, but it is characterized by stronger repulsive interaction between $Li_i^\bullet$ and the closest K and C ions at a distance of 2.40 Å and 1.97 Å, respectively. Another intermediate metastable configuration S_{2c}, very similar to S_{1c}, can also be identified, but the barrier for the corresponding migration is extremely low (0.07 eV), in line with the fact that it is not associated to any change in the O-coordination. Finally, $Li_i^\bullet$ can migrate from S_{2c} to the final D_i' configuration, passing through a 1-fold coordinated maxima associated to a barrier of 0.69 eV. In this case, the interactions with surrounding cations are less important than for the first maxima because the shortest $Li_i^\bullet$-K is of about 2.44 Å, while all $Li_i^\bullet$-C distances are considerably longer than 2.10 Å. $Li_i^\bullet$ diffuses with almost negligible distortion of the surface structure, but just very small relaxations of the carbonate groups and K^+ ions nearby the interstitial Li^+ ion.

In summary, the driving force of $Li_i^\bullet$ diffusion in the channels of the $LiKCO_3$-(001) surface is the attractive interaction between $Li_i^\bullet$ defect and the O atoms of the carbonate groups encountered along the migration path. In fact, the migration path is characterized by the continuous breaking and making of $Li_i^\bullet$-O bonds, while trying to maintain high O-coordination and to minimize the repulsive electrostatic interactions with the surrounding K^+ ions and positively charged C atoms at the same time. These two aspects (*i.e.* the O-coordination and the electrostatic repulsion) should be indeed taken into account together in order to explain the diffusion mechanism. Coordination plays for sure a dominant role, since the energy pro-

file for both pathways follows the variation of the O-coordination along the path. All the observed maxima correspond to the location where $Li_i^{\bullet}$ has either a very small O-coordination number or a relatively low O-coordination number but high repulsive interactions with the surrounding cations. However, this is not sufficient alone to explain the observed barriers: the profile obtained starting from configuration I_2 is characterized by very high barriers (0.41 and 1.28 eV higher than the highest value of the second profile), because in this case $Li_i^{\bullet}$ diffuses close to the channel sides, where it is possible to have higher O-coordination to stabilise the defect but where it is also more easy to have stronger repulsive interactions with the lattice cations. Finally, from the performed scan calculations, maintaining a high $Li_i^{\bullet}$-O coordination number while minimising at the same time the repulsive electrostatic interactions during diffusion results in lower energy barriers. The highest barrier observed for the second considered pathway is however small (0.80 eV), indicating that $Li_i^{\bullet}$ should be able to migrate efficiently through the $LiKCO_3$-(001) surface. Here we should note that this value is slightly higher than the 0.54 eV value computed for direct hopping mechanism by Shi et al.[333] in bulk Li_2CO_3, which is characterised by a layered structure, like in $LiKCO_3$, with LiO_4 polyhedra connected by carbonate groups arranged almost perpendicularly to the *c*-axis. It should be however noticed that this value was however calculated for the bulk structure of the carbonate, using LDA functionals. Furthermore, the substitution of Li with the larger K atoms can strongly affect migration, considering the important role of the electrostatic interaction between the interstitial $Li_i^{\bullet}$ and lattice K^+ ions.

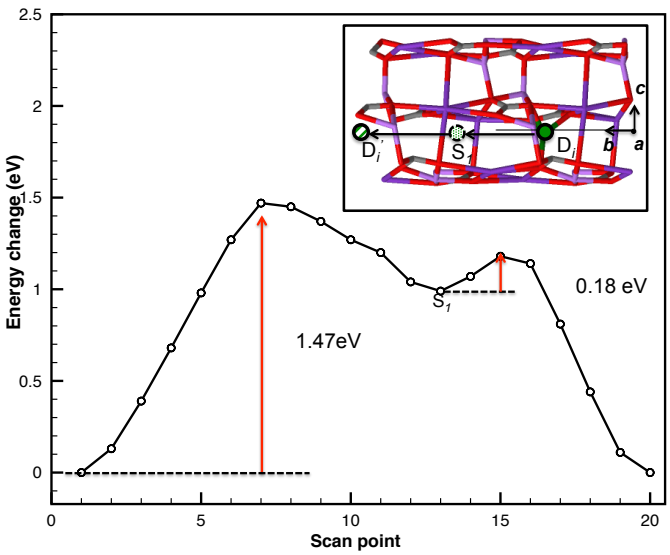

Figure 5.16: Variation of the energy as a function of the Li_i^X defect position along the channels and relative to the energy value of the system with a defect in the initial position. Inset: schematic representation of the diffusion pathway. Li_i^X diffuses from the initial position D_i (green sphere) to the final equivalent one D_i' (hashed green sphere) passing through the intermediate interstitial site S_1 (dotted spheres).

Moving to the Li_i^X, one would expect that the diffusion barrier should be higher compared to $Li_i^{\bullet}$ because of the different defect charge state. Figure 5.16 shows the energy profile

associated to the diffusion along the *b*-axis of one Li_i^X from its most stable positions at the centre of the channel to an equivalent site. Results indicate that the barrier is indeed higher in this case, because a value of 1.47 eV is obtained when Li_i^X is in the configuration associated to the first maximum encountered along the energy profile. As discussed in section 5.5.1.1, the effective total average charge of the CO_3 groups after the Li_i^X formation is indeed more negative than in the case of a $Li_i^\bullet$ defect, because the excess electron is donated from the defect to the lattice. As a consequence, even if the diffusing Li is still positively charged, the contribution to the ionic bonding between Li and the carbonates to the total energy of the system is higher than for the $Li_i^\bullet$ case, making Li_i^X diffusion more difficult, as suggested by the higher barrier. In conclusion, the values obtained for the barrier associated to interstitial Li diffusion indicate that $Li_i^\bullet$ should be the effective diffusion carriers in $LiKCO_3$ and the value of 0.80 eV obtained for its least energetically demanding diffusion pathway can also be compared with the experimental activation (E_{act}) derived from electrical conductivity measurements. Indeed, when the charge carrier is unique, it is possible to connect directly the conduction process with the diffusion one by the use of the Nernst-Einstein relation:

$$D(T) = \frac{kT}{ne^2}\sigma(T) \tag{5.12}$$

where k is the Boltzmann's constant, T the temperature, n is the density of the mobile lithium ions, σ is the conductivity, and e the usual elemental electron charge. From Ref.[384] and Ref.[385], we fitted the experimental diffusion and conduction data on an Arrhenius' plot, obtaining respectively E_{act}=1.1(5) and E_{act}=0.9(2) eV. The range of experimental values for the mobile lithium ions in the solid carbonate is then in a good agreement with the theoretically calculated barrier of 0.80 eV.

5.5.2.3 Effect of the applied voltage on the energy profile

We finally took into account the effect of the voltage applied in SOFC devices on the computed diffusion profiles, through the application of an external electric field that corresponds to selected voltages of 0.7 V and 1.5 V. Bearing in mind the anisotropy of the structure of the $LiKCO_3$-(001) surface, we applied a uniform static electric field in the direction perpendicular to the surface (*c*-axis) as well as a square wave electric field parallel to the periodic direction along which the large open channels are oriented (*b*-axis).

In the case of the perpendicular field to the surface (*c*-axis), as expected, no variation of any of the barriers was obtained for both the computed profiles. Different conclusions can be derived instead when the field is applied along the *b*-axis. In this case, in fact, the field is applied along the same direction as the $Li_i^\bullet$ diffusion pathway. Figures 5.17a and 5.17b show respectively the energy changes during the diffusion for the profile computed when $Li_i^\bullet$ is closer to the side (configuration I_2, 5.17a) or to the centre (configuration I_1, 5.17b) of the channel. In the latter case, where, as already pointed out in the previous section, the electrostatic effects on the migration energies are less important, no significant variation of the profile can be evidenced upon field application. On the other hand, from figure 5.17a it is clear that the other diffusion path is much more affected by the external field. Independently of the intensity of the applied field, a change of the rate-determining step is observed: the

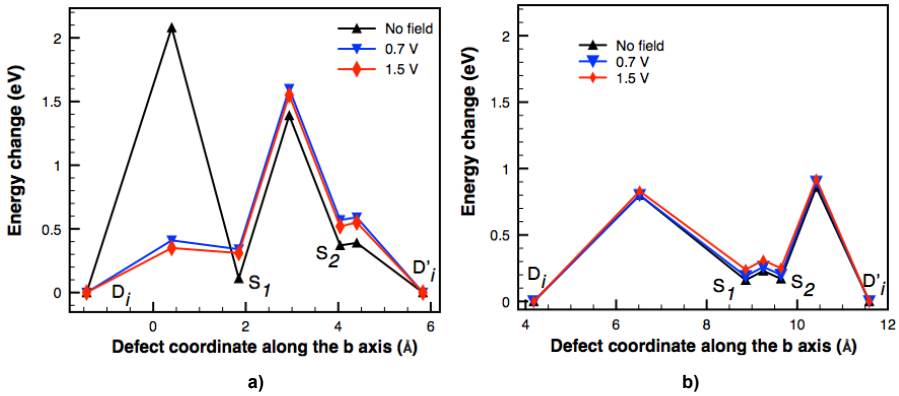

Figure 5.17: Variation of the energy as a function of the $Li_i^\bullet$ defect position along the channels for a defect in the initial position of configuration a) I_2 or b) I_1, in the absence or presence of an electric field applied parallel to the direction of the channels.

highest barrier of 2.08 eV is now dropped to a very small value and the higher the applied voltage is, the higher the decrease observed. The computed barrier heights are now 0.35 eV at 1.5 V and 0.41 eV at 0.7 V, while the value of the energy change associated to the second maximum of the path is not strongly affected. This observation might be explained taking into account the importance of electrostatic interactions found for the two maxima: as stated before, the maxima associated with a strong decrease of the barrier is indeed exposed to strong repulsive interactions of the $Li_i^\bullet$ defect with the surrounding K^+ ions, at very short distances (1.89 Å against the typical Li-K distance that are greater 3.40 Å), while the other is less concerned with the electrostatic effects, since it has longer $Li_i^\bullet$-K and $Li_i^\bullet$-C distances. We also note that the first maximum in the profile of 5.17a corresponds to the structure with the highest z component of the dipole moment along the scan (-6.27 Debye, against for example a value of -3.11 Debye for the other maximum) and with its slightly higher polarizability compared to the other maximum structure (the value of the α_{XY} component of the polarizability tensor in the *ab* plane, *i.e.* the plane were the migration takes place, is of -2.51 in the first case and of -1.44 in the latter), suggesting a stronger effect of the applied electric field on the first maxima than on the second.

5.6 Conclusions

In this chapter, we reported for the first time a comprehensive theoretical study of the geometry, electronic properties and surfaces of mixed carbonates ($LiNaCO_3$ and $LiKCO_3$), taking into account both polar and non-polar orientations. Li transport properties on the most stable and less complex $LiKCO_3$-(001) were subsequently investigated in view of better clarifying the effect of the carbonate phase on the conduction properties of the oxide-carbonate composites. The main conclusions can be summarized as follows:

- Among the three DFT models tested, the hybrid functional PBE0 was found to be the best functional to describe the geometrical features of bulk $LiNaCO_3$ and $LiKCO_3$

allowing at the same time a reliable description of the electronic properties of these materials, which are, at the solid state, strong insulators characterized by covalent interactions within the CO_3 groups and ionic interactions between the O atoms and the metal cations.

- The two (001) and (110) low index surfaces were also taken into account for each carbonate phase. In the case of $LiKCO_3$, the stability order resulted to be $(001) > (110)$, which can be related to the type and to the higher number of under-coordinated. For $LiNaCO_3$, the (001) termination shows a dipolar moment perpendicular to the surface, which may be cancelled out by reconstruction. Both introduction of vacancies (R_1) and octopolar terminations (R_2) of (001), exposing Li ($(001)^{Li}$) and Na ($(001)^{Na}$) were described in detail. The computed stability order for the reconstructed surfaces was: $(001)^{Na}_{R1} \gg (001)^{Li}_{R1} > (001)^{Na}_{R2} > (001)^{Li}_{R2}$, with the reconstructed $(001)^{Na}_{R1}$ surface more stable even than the non polar (110) termination.

- The dominant Li-related diffusion carriers and their diffusion pathways on the most stable and less complex $LiKCO_3$-(001) surface were then studied. Four different defect types were considered: the neutral (V_{Li}) or negative (V'_{Li}) Li vacancy and the interstitial Li atom (Li_i^X) or ion ($Li_i^\bullet$). V'_{Li} was found to be definitely the thermodynamically most stable defects in $LiKCO_3$-(001), while the relative order of stability for Li_i^X, $Li_i^\bullet$, and V_{Li} is more influenced by the oxidizing or reducing environments or by the energy of the reservoir of electrons.

- The high barriers associated to the diffussion of the Li vacancies indicate, however, that it cannot be the defect determining the diffusion in the material. $Li_i^\bullet$ mobility on the (001) surface should be instead quite high since this defect can diffuse via direct-hopping along the large open channels oriented parallel to the *b*-axis of the surface, considering that low barrier (0.80 eV), whose origin could be related to high O-coordination and low electrostatic repulsion arguments, were obtained. The importance of the electrostatic interaction on $Li_i^\bullet$ migration is also evidenced by the application of an external field in the direction parallel to the channels, which resulted in a dramatic reduction of the barrier associated to the maximum exposed to the major electrostatic effects.

In summary, as for the oxide phase, PBE0 was found to provide an accurate and reliable description of $LiNaCO_3$ and $LiKCO_3$. PBE0 was used to investigate the surface properties of these materials, allowing fisrt to identify a suitable model of the most stable $LiNaCO_3$-$(001)^{Na}_{R1}$ and $LiKCO_3$-(001) surfaces and then to characterize Li transport on $LiKCO_3$-(001). In the next chapter, we will se how this functional and the so-identified carbonate model can be used, together with the model of the YSZ-(111) termination found in the previous chapter, to build the YSZ-$LiKCO_3$ interface, to characterize it in terms of stability, structure, and electronic properties, as well as to investigate transport mechanism in these material using the results here obtained on Li transport as a reference to understand interface effects.

Chapter 6

DFT simulation of YSZ-$LiKCO_3$ composite

Not everything that can be counted counts,
and not everything that counts can be counted.
William Bruce Cameron

Contents

6.1 Introduction **179**
6.2 Computational Details **181**
6.3 DFT investigation of the stability and electronic properties of YSZ-$LiKCO_3$ **183**
6.4 DFT Study of Conduction Mechanisms **196**
6.5 Preliminary Results of the MD Simulations **222**
6.6 Conclusions **224**

6.1 Introduction

In chapter 3 we have seen how the performance of YSZ-carbonate electrolytes raised several questions on the stability and electrochemical properties of these composites and, at the same time, highlighted the important role of the interfaces in determining such behaviour. Consequently, even if their electrochemical performances were not found to be better than those of GDC- or SDC-based composites, a better understanding of the YSZ-based ones would, however, help in rationalizing the effect of the oxide phase on the properties of these materials. Considering the lack of experimental analytical tools that can directly investigate the interface effect,[149] modelling at the atomic scale is key to get a better picture of the features of the composites, in order to better explain the conductivity enhancement experimentally observed even at temperatures lower than the melting point of the carbonate phase,[103] but also to directly interpret the effect of the interfaces on the conduction properties. However,

to the best of our knowledge, theoretical works fully addressing the carbonate oxide interface and its properties are completely lacking. Like in experiments, where getting a direct picture of the interface phenomena is difficult, from a modelling viewpoint, obtaining an accurate and reliable description of these two-phase systems requires a careful choice of the methodology and of the models used for each phase. Nevertheless, difficulties can be alleviated by relying on a combined theoretical and experimental approach, using a strategy based on the strict analogy existing between the steps found in the experimental synthesis procedure and those required in the computational protocol proposed in chapter 1. The first step of this building-on approach has required a DFT study of the bulk structure of the oxide and carbonate phases, which, through the comparison with the available experimental data, was used to identify a suitable computational protocol to describe each phase. In the previous chapters, we investigated in details the bulk ZrO_2 (cf. Chapter 4) and carbonate (cf. Chapter 5) phases. Relative to the carbonates, we studied the $LiNaCO_3$ and $LiKCO_3$ (both 50-50 mol%) phases that are formed upon cristallization of $(Li,Na)_2CO_3$ and $(Li,K)_2CO_3$ eutectic mixtures. Even if the cations composition is slightly different from the eutectic one, these phases can nevertheless constitute a first simple approximation of the carbonate material. These studies allowed us to identify the hybrid PBE0 functional as the one providing the most accurate description of both the oxide and carbonate phases structural and electronic properties. Subsequently, always in chapters 4 and 5, the most stable surface structures of each system, their properties, and the doping of the ZrO_2 one with Y_2O_3 so as to obtain YSZ, have been described, allowing to obtain information of the clean surfaces that can be used as reference to understand the effect of the interface formation. But more importantly, through these steps, we were able to identify an adequate model of YSZ-(111) and for instance $LiKCO_3$-(001) most stable surfaces, that will be used in this chapter to build the oxide-carbonate interface model.

Building a suitable model of the oxide-carbonate interface is a key point in the investigation of the transport mechanisms, which is important not only to explain the conductivity enhancement, but especially to directly interpret the effect of the interfaces on the conduction properties. In Chapter 1, the different conduction mechanisms in oxide-carbonate materials proposed by different groups throughout the years have been shortly reviewed. The discussion clearly evidenced that the origin of the elevated performances of these materials is not yet fully understood. In particular, it would be important to identify the species that determine the transport in the device: the oxygen ions, the cations of the salt, the carbonate ions, the protons or several species at the same time? Although the role of oxide and carbonate ions in the electrolyte performances is clear, it has also been supposed that a space-charge layer can be formed at the interface of the composite due to the interfacial interaction: oxygen ions could accumulate at the interface, where there could also be an enrichment of the cations of the carbonate. The higher concentrations of the defects/ions near the phase boundaries compared to the bulk phase may constitute 'superionic highways' at the boundary between the two phases. Moreover, great emphasis has been given on the supposed multi-ionic nature of these materials, which were claimed to be dual or hybrid H^+/O^{2-} or even ternary $H^+/O^{2-}/CO_3^{2-}$ conductors when operating in O_2/CO_2 atmosphere at the cathode side. The multi-ionic conduction can help in rationalizing the conductivity enhancement, but how does the transport take place?[89,92–95]

Static DFT calculation investigating the energetics of Li-, O-, and proton-related defects formation and migration at the interface in the composite model adequately built can thus help elucidating the conductions properties of the oxide-carbonate composites. Here, we stress that even if in these simulations the carbonate is in the solid state, the behaviour of solid alkali carbonates could still be meaningful. In terms of ionic transport, there is indeed an analogy between liquid and solid carbonates for two reasons: i) like ionic solids, ionic melts are envisaged to be crystalline, actually quasi-crystalline with a comparatively much higher degree of disorder but with defects similar to those existing in solids; ii) the results of electrical conductivity measurements on solid and molten carbonates match each other.[126] Futhermore, it should be noted that the interface model thus obtained could also be used as a starting geometry for molecular dynamics (MD) simulations, providing a deeper understanding of the transport properties and conduction mechanisms at higher temperatures when the carbonate is in the molten state.

This chapter is organized into three main sections. In the first one, we describe the strategy used to build a reliable YSZ-$LiKCO_3$ interface model that allows obtaining an accurate description of the material within a reasonable computational time, we validate it by comparing computed and experimental IR and Raman spectra and we analyse in detail the structural rearrangements consequent to the interaction at the interface, the relative stability and the electronic properties of the material. In the second part, we use the interface model previously identified to investigate the formation and the transport properties of Li-, O- and proton-related defects in the oxide-carbonate composite. Finally, in the last section, we discuss the preliminary results obtained through the *ab initio* MD simulations of the YSZ-$LiKCO_3$ interface.

6.2 Computational Details

6.2.1 DFT calculations

All the calculations were performed in the DFT framework using the periodic CRYSTAL14 code.[180] Based on the accurate and reliable description of the structural and electronic properties of both the oxide and the carbonate phases previously obtained, respectively, in chapter 4 and 5, the hybrid PBE0[172,173] functional was selected to describe the exchange and correlation energies.

All the basis sets used to describe Zr, Y, O atoms in YSZ and Li, K, C and O atoms in $LiKCO_3$ are the same of the ones used to study YSZ and $LiKCO_3$ bulk and surface properties in chapters 4 and 5. Li and O-related species were described through the same all-electron basis sets used for the Li and O atoms of the carbonate phase, while protons were described through a 5-11G* contraction scheme.

The YSZ-$LiKCO_3$ interface was built starting from models of the oxide and carbonate most stable surfaces that were previously found to ensure convergence of the structure, surface energy and of the electronic properties of each phase. As regards the oxide phase the building block is a (2x2)-supercell model of the YSZ-(111) surface with a depth of six layers (O-Zr/Y-O trilayers) for a total of 70 atoms, with $Zr_{20}Y_4O_{46}$ stoichiometry, corresponding to the experimental doping amount of 8 mol%. For the carbonate phase, a slab model of the

$LiKCO_3$-(001) termination with a depth of 3 slab layers (three Li-O-K-O-C-O_2-C-O-K-O-Li layers) for a total of 36 atoms and a $Li_6K_6(CO_3)_6$ stoichiometry was considered. The final unit cell has *P1* symmetry. The system obtained combining these building blocks will be indicated as YSZ^{6L}-$LiKCO_3^{3L}$ and has been used for the calculations of the vibrational properties, as well as for the investigation of the transport mechanisms. Auxiliary calculations to investigate the effect of the thickness of the carbonate phase recurring to a model made by a 5 slab layers model of the $LiKCO_3$-(001) surface ($Li_{10}K_{10}(CO_3)_{10}$, 60 atoms) and a 3 oxide slab layers model for YSZ ($Zr_{10}Y_2O_{23}$, 35 atoms) have also been performed. This alternative interface model, with *P1* symmetry, will be indicated as YSZ^{3L}-$LiKCO_3^{5L}$.

Li defects, proton and O-related species were introduced in the optimized unit cell describing the oxide-carbonate interface, which was found to be sufficient to avoid spurious interactions between the defects and their periodic image. Neutral interstitial Li (Li_i^X) or neutral O defects were created by adding one Li/O atom in the unit cell, while the Li and O Frenkel pairs (Li_{FP} and O_{FP}) were obtained by displacing a lattice Li^+ or O^{2-} ion into an interstitial position ($Li_i^\bullet$ or O_i^{2-}) and leaving behind a negatively charged Li vacancy (V'_{Li}) or a doubly positive charged O vacancy($V_O^{\bullet\bullet}$). To study oxide ion or proton transport, one O^{2-} anion together with two interstitial Li cations ($Li_i^\bullet$), in the first case, or two H^+ together with one O^{2-} ion, in the second, were introduced in the system, allowing to ensure the neutrality of the unit cell.

Several different initial positions of the defects were taken into account in all cases. Diffusion barriers for Li-related, O-related and H^+ species were qualitatively estimated performing relaxed scan calculations of the geometry of the defective system along a selected diffusion path in the YSZ-$LiKCO_3$ unit cell.

A Monkhorst-Pack[300] shrinking factor of 4, corresponding to 10 points in the irreducible Brillouin zone (IBZ) of the interface model was used. An extrafine integration scheme[180] corresponding to 75 radial points and 974 angular points was considered. In the case of the geometry optimization of the YSZ-$LiKCO_3$ structure, the lattice parameters and all the atomic positions were allowed to relax, until the maximum and root-mean square atomic forces and displacements were simultaneously less than $4.5 \times 10^{-4}, 3.0 \times 10^{-4}, 1.8 \times 10^{-3}$ and 1.2×10^{-3} a.u., respectively. For the study of the transport mechanism at the composite interface, instead, we just relaxed the atomic position of the atoms belonging to the first coordination sphere around the defects. For the calculations of the IR and Raman spectra of the material, we also performed additional frequencies calculations at the Γ point. IR and Raman intensities were evaluated using the Coupled Perturbed Kohn and Sham (CPKS) scheme.[343–345] The spectra were simulated considering a temperature of 298 K and a wavelength for the incident beam of 632.81 nm in the case of the Raman spectra, in order to take into account the experimental settings (cf. chapter 3). For these calculations, the Coulomb and exchange series were truncated with tighter threshold values of 10^{-8}, 10^{-8}, 10^{-8}, 10^{-8} and 10^{-16} and a tighter tolerance of 10^{-10} a.u. (default 10^{-10} a.u.) has also been applied for the convergence of the self-consistent field procedure.

6.2.2 MD calculations

MD calculations were performed with the Vienna Ab-initio Simulation Package VASP.[188–191] The PBE[170] functional was employed to solve the Kohn-Sham equations. Projector Augmented Wave (PAW)[187,386] generated pseudopotentials were used to describe core electrons; the number of valence electrons for Zr, Y, O, Li, K and C was, respectively, 12, 11, 6, 3, 9, and 4: Zr [$4s^2 4p^6 5s^2 4d^2$], Y [$4s^2 4p^6 5s^2 4d^1$], O [$2s^2 2p^4$], Li [$1s^2 2s^1 2p$], K [$3s^2 3p^6 3p^1$] and C [$2s^2 2p^2$]. A plane-wave energy cutoff of 400 eV was used.

Being interested to the properties of the composite when the carbonate is in the molten state, we decided to use the YSZ^{3L}-$LiKCO_3^{5L}$ model, with a thicker carbonate phase. A vacuum of 25 Å prevented the interaction between successive slabs. All the simulations were performed keeping the lattice vectors fixed and using single k-point sampling at the Γ point of the Brillouin zone. A tolerance of 10^{-5} eV was applied for the convergence of the self-consistent field procedure.

For every state point, we first run a NVT ensemble with a Nosè-Hoover barostat[202–204] for 2ps at the selected temperature. The production run, in the NVE ensamble, was subsequently performed for 2ps. Simulations were carried out at 1000, 1150, and 1250K, corresponding to temperatures higher than the melting point of $LiKCO_3$ ($\sim$ 800 K).

6.3 DFT investigation of the stability and electronic properties of YSZ-$LiKCO_3$

6.3.1 Building the YSZ-$LiKCO_3$ interface model

6.3.1.1 A simple YSZ-$LiKCO_3$ interface model

Before presenting results obtained on the composite system, we detail the strategy followed to build a model of the YSZ-$LiKCO_3$ interface, considering the available experimental data and previously reported theoretical characterization of the isolated phases. Building the interface between chemically and structurally complex phases is a hard task, because different parameters, like the coincidence of the lattice parameters and the initial surface configuration and orientation, should be taken into account. In this case, we decided to start from the most stable surface of each phase we identified on the oxide and carbonate phases in the previous chapters, whose characteristics are briefly summarised in the following discussion.

As described in chapter 5, starting from experimental and theoretical evidences outlining that (111) is the most stable YSZ termination,[123,248,277,287] the oxide model was built by cleaving the clean (111) surface of cubic ZrO_2 from the optimized bulk structure, considering only the most stable O terminated surfaces.[248] Here we just recall that, in order to respect the neutrality of the system and to reproduce the experimental 8 mol% Y_2O_3 doping amount which provides stability and the highest experimental oxygen conductivity, a (2×2) supercell with a thickness of six slab layers (O-Zr-O) for a total of 72 atoms ($Zr_{24}O_{48}$), in which two oxygen vacancies were created and four Zr^{4+} ions of the supercell were replaced by four Y^{3+} cations has been considered. Moreover, in agreement with the observation of oxygen vacancy alignment along the [111] direction[250], the two vacancies were placed along

this direction, one at the top and one at the bottom of the supercell, with a distance of 13 Å, hence avoiding spurious interaction between defects. Two Y atoms were then placed near each vacancy, both in next-nearest neighbour (NNN) positions to the vacancies (one Y on the outermost layer and the other underneath), which was found to be the most stable configuration. The optimized YSZ-(111) model, with a $Zr_{20}Y_4O_{46}$ stoichiometry and indicated as YSZ^{6L}, has cell parameters *a*=*b*=7.196 Å, and γ=120°.

As discussed, instead, in chapter 5, $LiKCO_3$ has a monoclinic structure belonging to the P_{21}/c space group and has a layered nature, in which layers of LiO_5 distorted pyramids and KO_9 polyhedra of irregular shape are oriented parallel to the (10-1) direction and connected by distorted but planar carbonate groups which are arranged perpendicularly to the *c*-axis. The most stable (001) surface was cut from the optimized $LiKCO_3$ bulk structure parallel to the (001) plane, obtaining a converged slab model with cell parameters *a*=7.254 Å, *b*=7.289 Å, γ= 90°and 3 slab layers for a total of 36 atoms and a $Li_6K_6(CO_3)_6$ stoichiometry. This surface model will be indicated in the following as $LiKCO_3^{3L}$.

The epitaxial constraints require a good coincidence of the lattice parameters of the two interacting surfaces, resulting in a strain free system. Unfortunately, while for the lattice parameters *a* and *b* of the aforementioned YSZ and $LiKCO_3$ models there is a moderate mismatch (δ_a=0.8%, δ_b=1.3%), a bigger discrepancy is, instead, observed for the γ angle (δ_γ=33.3%). This would imply the necessity to consider larger unit cells together with the study of all resulting possible lattice coincidences that can be found at the interface between the two phases. Moreover, the YSZ supercell is an oblique one and, as observed by Bruno et al.[387], in these cases, already with small angular mismatch, it is difficult to have a good coincidence between the areas of the two surface lattices, because of the divergence of the lattice parameters when increasing the size of the supercell.

Here, to reduce computational cost, instead of considering larger supercell to reduce lattice mismatch, we cut very large supercell models of the two surfaces ((4×4) for both the $LiKCO_3$-(001) surface and the (2×2) supercell representing YSZ-(111)), and we rotated the carbonate slab of about 30°around the normal to the oxide surface plane (see Figures 6.1a and b), so as to orient the CO_3 groups toward the Zr or Y surface sites. We then tried to identify a new unit cell for the interface (see Figure 6.1c), containing a number of atoms in line with the stoichiometry of each phase, thus ensuring the neutrality of the unit cell. The final unit cell has *P1* symmetry and contains 106 atoms, 36 ($Li_6K_6(CO_3)_6$) belonging to the 3 layers of the carbonate phase and 72 ($Zr_{20}Y_4O_{46}$) organized in 6 O-Zr/Y-O layers along *c* for YSZ. We refer to this model as YSZ^{6L}-$LiKCO_3^{3L}$ in the following. Cell parameters and atomic positions were allowed to relax during geometry optimization.

6.3.1.2 Alternative interface model

In order to verify the convergence of the interface properties with respect to the thickness of the carbonate layer, we performed auxiliary calculations on a model of the carbonate (001) surface made of 5 slab layers, corresponding to a $Li_{10}K_{10}(CO_3)_{10}$ stoichiometry for a total of 60 atoms (indicated as $LiKCO_3^{5L}$). The strategy used to build the interface was the same as the one described above for the other model. However, in order to reduce the computational cost of the calculation, we combined this $LiKCO_3^{5L}$ surface model with a model of YSZ-

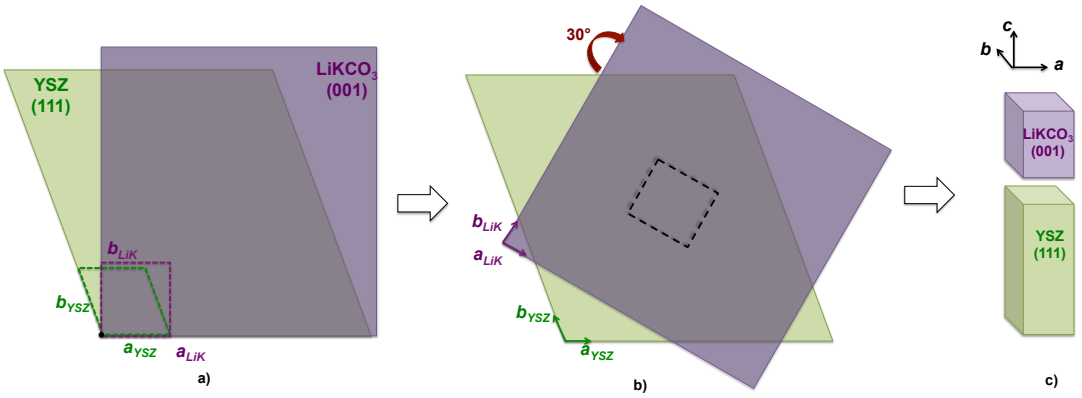

Figure 6.1: Schematization of the building process of the model of the YSZ-$LiKCO_3$ interface considered for all DFT calculations: a) superposition of a (4×4) supercell of the $LiKCO_3$-(001) (in violet) and YSZ-(111) (in green) models previously identified; b) rotation of the $LiKCO_3$-(001) supercell of 30°around the normal to the YSZ-(111) surface plane and identification of a new unit cell for the interface (black dotted line); c) final interface model.

(001) with just three slab layers (YSZ^{3L}) obtained cutting in half the optimized structure of the oxide in the YSZ^{6L}- $LiKCO_3^{3L}$ interface. The geometry of the as-prepared YSZ^{3L}-$LiKCO_3^{5L}$ model was consequently optimized, allowing to relax the cell parameters and the positions of all the atoms in the carbonate phase, but just the outermost O and Zr/Y atoms of the oxide surface that are directly involved in the interfacial interaction, so as to avoid too large deviations from the bulk-like structure of YSZ that can take place considering the reduced thickness of the oxide phase in this model.

6.3.2 YSZ-$LiKCO_3$ structure and stability

Figure 6.2 shows the (a) starting and (b) final optimized geometry obtained for the YSZ^{6L}-$LiKCO_3^{3L}$ interface model built with the aforementioned procedure. Table 6.1 reports the optimized cell parameters of the *P1* supercell describing the interface.

It is evident that, in the optimized model, the oxide phase maintains its crystalline structure with very small deviation from the geometry of the clean systems: the average displacements are of 0.73 Å along *a*, 0.27 Å along *b*, and 0.04 Å along *c*, with the highest deviations normally observed for O atoms in the outermost layers in contact with the carbonate phase. On the other hand, large structural modifications at the carbonate/oxide interface are, instead, observed for the carbonate phase. Strong ion-ion interactions between the two phases can be represented as a process of chemical adsorption of ions of the $LiKCO_3$ slab to the YSZ surface. As a consequence of this interaction at the interphase, in figure 6.2b, the formation of O-Zr or O-Y bonds between the oxygen atom of the carbonate groups and the cations on the YSZ surface can be observed, leading to monodentate and bidentate (bridged) CO_3, if we just consider the coordination to the oxide. The bidentate carbonate shows one O-Y bond of 2.43 Å and a O-Zr one of 2.56 Å, while for the monodentate the O-Zr distance is of about 2.45 Å. These two CO_3 groups belonging to the carbonate layer in contact with the oxide are strongly tilted toward the YSZ surface, in order to allow the interaction with the

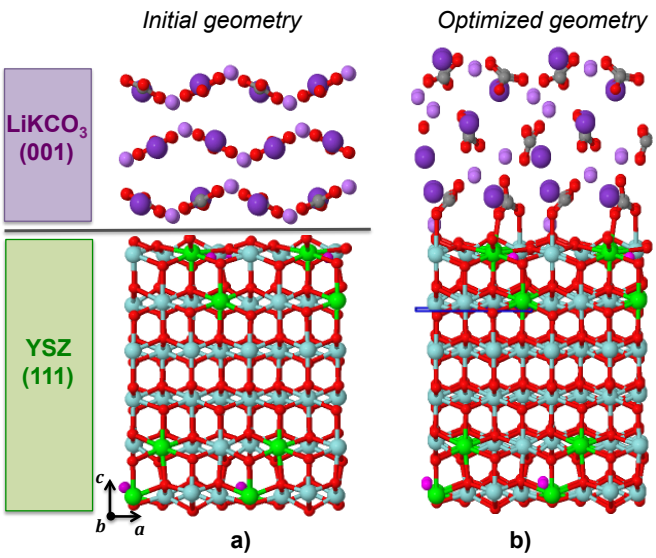

Figure 6.2: a) Initial and b) optimized geometry of the YSZ^{6L}-$LiKCO_3^{3L}$ model of the composite, shown as a (2×2) supercell of the interface model for clarity. Solid blue line indicates the unit cell. Zr, Y, and O atoms are in light blue, green and red, while C, Li and K are in grey, light violet and purple, respectively.

oxide surface sites. Strong variations of the orientation of the CO_3 units belonging to the second carbonate layer, and to a less extent also to the groups in the third and farthest layer from the interface, are also observed. However, only a slight shortening of the C-O bond distances can be evidenced, suggesting that the carbonate groups behave like rigid units. Indeed, when compared to the C-O distance of the unbound O atom (1.32 Å), bound O atoms involved in the monodentate and bidentate coordination with the oxide show C-O bond distances ranging between 1.27 and 1.29 Å. The carbonate/oxide interaction can also lead to the adsorption of the cations of the salt on YSZ. For example, the Li atom closest to the oxide surface is at only ∼0.73 Å from the plane in which the outermost O atoms of the oxide phase lie, where it is stabilized by the interaction with three of these oxygen atoms at distances of 2.16, 1.93 and 2.01 Å, these values being in line with Li-O bonds in the pure carbonate phase (cf. Chapter 5). Finally, although the clean $LiKCO_3$-(001) surface (top half figure 6.2a) shows a very organized structure with large open channels oriented along the *b*-axis, it is much more distorted at the interface, with a strong disordered character typical of amorphous phases. This result is in agreement with the experimental findings: XRD spectra of carbonate-oxide composites are dominated by the high intensity oxide peaks, suggesting that the oxide maintains its crystalline structure, while the carbonate is mostly in the amorphous state,[49,103] with just small contributions of the crystalline carbonate phase[19,98,99]. High resolution transmission electron microscopy (HRTEM)[104,105] and scanning electron microscopy (SEM)[19,98,106,107] images confirm this picture, showing an homogeneous distribution of both phases with a core structure constituted by the crystalline oxide surrounded by an amorphous carbonate shell.

This can be related to the interfacial interaction between the carbonate and the oxide,

	YSZ^{6L}-$LiKCO_3^{3L}$	YSZ^{3L}-$LiKCO_3^{5L}$
a	7.17	7.13
c	6.27	6.25
γ	90.10	90.09
S	45.01	44.49
$E_{ads}^{YSZ/LiKCO_3}$	3.19	3.08
$\beta^{YSZ/LiKCO_3}$	0.07	0.07
E_g	5.78	5.72

Table 6.1: Optimized lattice vectors (a, b, c in Å), angle (γ, in degrees) and surface area (S in Å^2) of the YSZ-$LiKCO_3$ interface models together with the adhesion energy ($E_{ads}^{YSZ/LiKCO_3}$ in eV), specific adhesion energy ($\beta^{YSZ/LiKCO_3}$in eV/Å^2), and band gap (E_g in eV).

which includes two principal terms. The first one corresponds to the contribution of interatomic interactions between ions or atoms of adjacent phases that we have just described; the second one to the elastic energy of mechanical strains emerging inside the crystal lattice of the ionic salt at the interface. This last term generally originates from the misfit in lattice parameters of the two phases: if the lattices of the two phases do not match one another, the contribution of the elastic energy becomes substantial and structural relaxation can occur by spontaneous amorphization of the ionic salt.[69] As described in the previous section, a relatively large mismatch is observed for the lattice parameters of the $LiKCO_3$-(001) and YSZ-(111) surfaces, and even if the YSZ-$LiKCO_3$ model is built to minimize elastic strain, the crystalline carbonate phase spreads over the more rigid oxide one upon relaxation, resulting in a more stable amorphous-like one.

From a thermodynamic point of view, the main property relevant for the description of composite formation and interface stabilization is the adhesion energy. Adhesion energy ($E_{ads}^{YSZ/LiKCO_3}$), the energy gained with the formation of the interface, was computed by the following equation:

$$E_{ads}^{YSZ/LiKCO_3} = E(YSZ) + E(LiKCO_3) - E(YSZ + LiKCO_3) \tag{6.1}$$

where $E(YSZ)$ and $E(LiKCO_3)$ are respectively the total energy of the YSZ or $LiKCO_3$ slab models and $E(YSZ + LiKCO_3)$ is the total energy of the YSZ/$LiKCO_3$ interface. Specific adhesion energy, *i.e.* adhesion energy per unit surface area, was also calculated as

$$\beta^{YSZ/LiKCO_3} = \frac{E_{ads}^{YSZ/LiKCO_3}}{S} \tag{6.2}$$

where S is the surface area of the YSZ/$LiKCO_3$ interface model. $E_{ads}^{YSZ/LiKCO_3}$ and $\beta^{YSZ/LiKCO_3}$ values were corrected for the basis set superimposition error (BSSE) using the standard counterpoise method.[388]

The relative high adhesion energies ($E_{ads}^{YSZ/LiKCO_3}$ of 3.19 eV and $\beta^{YSZ/LiKCO_3}$ of 0.07 eV/Å^2, see table 6.1) obtained indicate that a strong and favorable interaction takes place between the two phases with the carbonate spreading along the oxide surface.

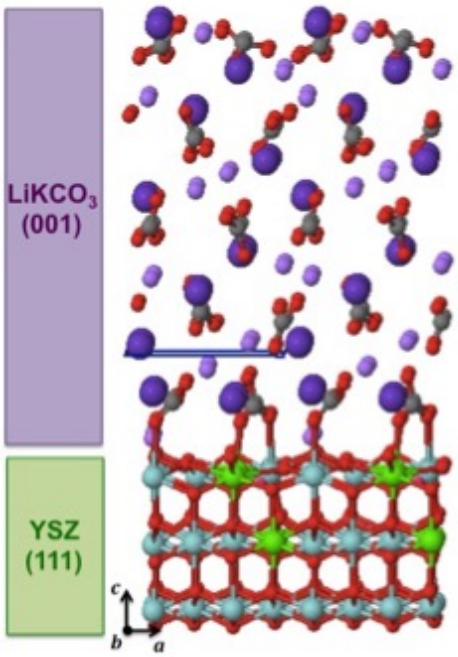

Figure 6.3: Optimized geometry of the YSZ^{3L}-LiKCO$_3^{5L}$ model of the composite, shown as a (2×2) supercell of the interface model for clarity. Solid blue line indicates the unit cell. Zr, Y, and O atoms are in light blue, green and red, while C, Li and K are in grey, light violet and purple, respectively.

We note that that the $\beta^{YSZ/LiKCO_3}$ value obtained is in line with typical values previously obtained by Bruno et al.[387] for various interfaces, like diamond/fosterite ($\beta^{YSZ/LiKCO_3}$=0.07 eV/Å^2) or aragonite/zabuyelite ($\beta^{YSZ/LiKCO_3}$=0.04 eV/Å^2). Furthermore, computed relaxation energies of both phases (0.27 eV/Å^2 for $LiKCO_3$ and 0.07 eV/Å^{2}for YSZ) are in line with the description given above, where a large relaxation of the carbonate phase was evidenced.

Finally, due to the strong disordered structure found for the 3 layer $LiKCO_3$-(001) slab model, we performed auxiliary calculations on the YSZ^{3L}-LiKCO$_3^{5L}$ model with a thicker carbonate phase, whose optimized structure is shown in figure 6.3. We note that very similar results are obtained. In particular, the strongly disordered carbonate phase when combined to the oxide can also be clearly evidenced. Also in this case, Li atoms and monodentate and bridged CO_3 are adsorbed on the oxide surface. In order to release the strain due to the lattice mismatch, the carbonate phase shows again a disordered amorphous-like structure, with the carbonate units that change their orientation compared to the initial ordered structure in $LiKCO_3$-(001) by rigidly rotating mainly about the *b* axis. This perturbation is more important for the atoms closer to YSZ surface and gradually decreases while moving away from it. Values in table 6.1 confirm this picture, with the unit cell parameters (*a*=7.11 Å,

c=6.25 Å,γ =90.09°, and S=44.45 Å^2), adhesion energy (E_{ads}=3.08 eV/Å^2 and β_{ads}=0.07 eV/Å^2) and also the band gap (E_g) obtained for this model perfectly in line with the ones of the YSZ^{6L}-$LiKCO_3^{3L}$ model, confirming the strong oxide-carbonate interaction and the convergence of the latter model with respect to the thickness of the carbonate phase.

In summary, the high adhesion energy computed for the YSZ-$LiKCO_3$ interface indicates that a very strong interaction can take place between the carbonate $LiKCO_3$-(001) and the YSZ-(111) surfaces in the composite material. The adhesion results from both: i) specific adsorption of the cations and anions of the salt on the crystalline oxide surface; ii) minimization of the elastic strain arising from the spread of the carbonate over the oxide, resulting in a more stable amorphous-like structure for the carbonate phase when combined to the oxide to form the composite.

6.3.3 IR and Raman Spectra

To better validate the interface model built, we performed a spectroscopic characterization by considering IR and Raman spectroscopy, which can complement the structural description of the interface in YSZ-$LiKCO_3$, especially when experimental data is available. In chapter 3, we have reported the IR and Raman spectra of YSZ-based composites and this data will be used here to verify the validity of the interface model we built.

Figure 6.4 shows the computed PBE0 IR (a) and Raman (b) spectra of the YSZ^{6L}-$LiKCO_3^{3L}$ composite model, selected IR and Raman frequencies being collected in Tables 6.2 and 6.3, respectively, along with corresponding assignment. The experimental IR and Raman spectra measured for the YSZ-$LiKCO_3$ materials already discussed in chapter 3 are reported here again in figures 6.4c and 6.4d just for ease of comparison. Two frequency regions were especially considered: the low frequencies region (200-800 cm^{-1}), where the vibrations relative to the metal-oxygen (M-O) bonds in the oxide should appear, and to the high frequencies one (700-1900 cm^{-1}) where the four internal modes of the carbonate group appear. In this regard, it is important to remember that the free CO_3 group has D_{3h} symmetry and shows the symmetric stretching ($\nu_1(A_1')$, Raman active) at about 1090 cm^{-1}, the out-of-plane deformation ($\nu_2(A_2'')$, IR active) at about 860 cm^{-1}, and the doubly degenerated asymmetric stretching ($\nu_3(E')$, IR and Raman active) and in-plane deformation ($\nu_4(E')$, IR and Raman active) at about 1400 and 700 cm^{-1}, respectively.[349] However, the lowering of the symmetry as a consequence of the coordination causes the splitting of the doubly degenerated vibrations and the activation of ν_1 and ν_2 in the IR or Raman spectrum, respectively. We already discussed how the coordination to the Li^+ and K^+ cations affects the apperance of these peaks in the spectra of $LiKCO_3$ bulk phase.[389] In that regard, we stress how the splitting of the asymmetric stretching peaks ($\Delta\nu_3$), as a consequence of the coordination, can be used to distinguish the type of coordination when carbonate species are adsorbed on metal oxide surfaces: $\Delta\nu_3$ =0 for symmetrical, $\Delta\nu_3$ =100 for monodentate, $\Delta\nu_3$ =300 for bidentate, $\Delta\nu_3$ =400 for bridged (bidentate) CO_3 groups, and values smaller than 300 for polydentate carbonates in which every oxygen is bonded to metal ions.[390]

We first start with a detailed analysis of the computed IR data, reported in figure 6.4c and in table 6.2. We can observe that the oxide main contribution appears at about 350, 490, and 680 cm^{-1}, in good agreement with experimental data reporting a wide band in the IR

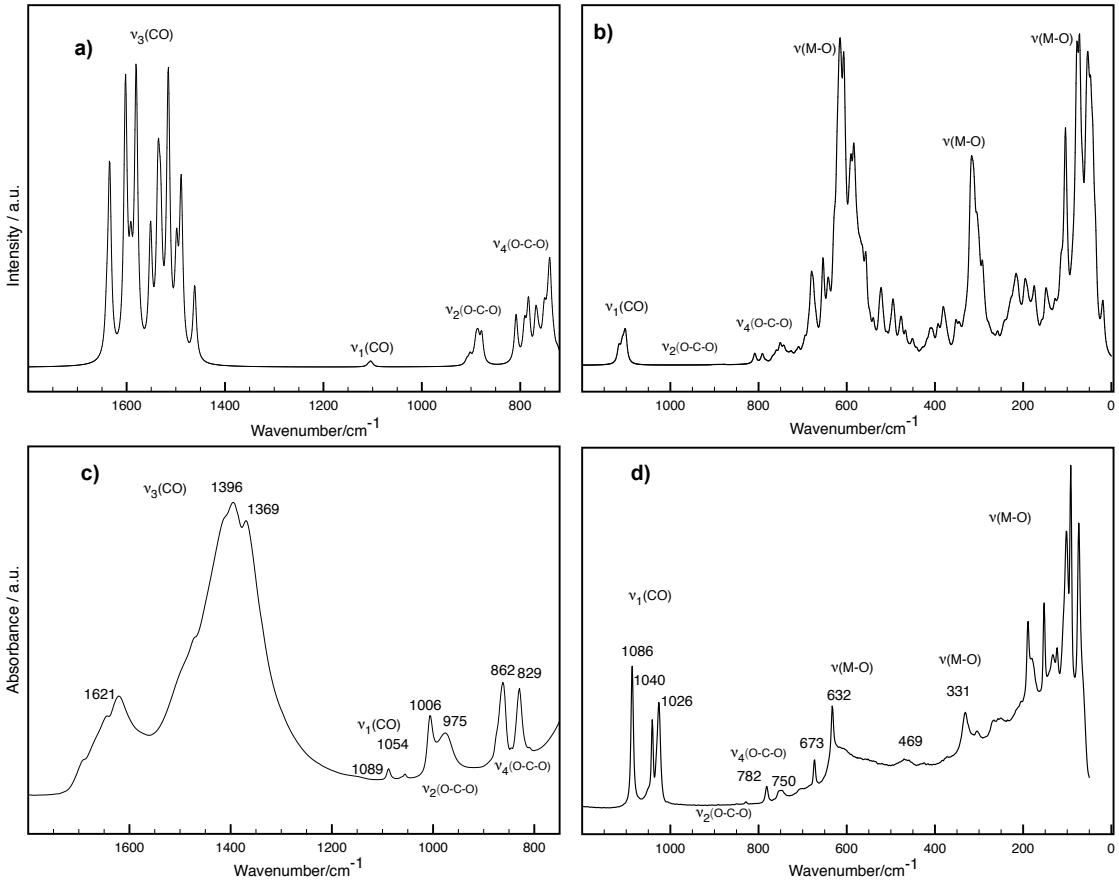

Figure 6.4: Computed (top) and experimental (bottom) IR (a and c) and Raman (b and d) spectra of the YSZ-LiKCO$_3$ composite.

Assignment	Computed	Experimental
ν_3(m-CO)	1591, 1536	
ν_3(b-CO)	1461, 1602	
ν_3(CO)	1489, 1498, 1515, 1534, 1551, 1581, 1635	1369,1396 1622
ν_1(CO)	1105-1115	1054
ν_2(O-C-O)	879, 887, 907	975, 1006
ν(MO)	742-809	-
ν_4(O-C-O)	708, 720, 726, 746, 753	829, 862
ν(MO)	680	700
ν(MO)	$\sim$490	-
ν(MO)	$\sim$350	-

Table 6.2: Comparison between selected computed and experimental IR frequencies (cm^{-1}) for the YSZ-LiKCO$_3$ composite and relative assignment.

spectra of YSZ at around 480 cm^{-1} with contributions at 350 and 615 cm^{-1}.[229] Smaller peaks relative to the M-O bonds in YSZ can also be observed at higher frequencies (742-809 cm^{-1}), where they superimpose with the ν_4 of the carbonate, which shows different contributions (797, 720, 726, 746, 753 cm^{-1}) reflecting not only the coordination to the cation of the carbonate phase, but also to the oxide surface. Also the ν_2 band shows a fine structure with peaks at 879, 887, 903, and 907 cm^{-1}, slightly more complex than the one observed for the weak ν_2 band at 882 cm^{-1} previously obtained for the $LiKCO_3$ bulk in chapter 5. Like in this latter case, the ν_1 is also visible as a very weak broad band at 1105-1115 cm^{-1}, because of the IR activation of this vibration as a consequence of the coordination of the carbonate groups. However, the most important observation concerns the ν_3 contribution between 1450-1640 cm^{-1} showing a very complex fine structure. In bulk $LiKCO_3$, this frequency is split into just two main peaks, with contributions at 1499-1504 and 1555-1564 cm^{-1}. In the composite, instead, several contributions can clearly be observed at 1536 and 1591 cm^{-1} for the CO_3 group linked as monodentate to the YSZ surface (ν_3(m-CO) in table 6.2), at 1461 and 1601 cm^{-1} for the other carbonate coordinated as a bridged CO_3 to the oxide (ν_3(b-CO) in table 6.2), and at 1489, 1498, 1515, 1534, 1551, 1581, and 1635 cm^{-1} for the carbonates not directly linked to YSZ. In addition, as concerns the use of $\Delta\nu_3$ to distinguish between different types of coordination, we can observe that the $\Delta\nu_3$(m-CO) is only 55cm^{-1}, while $\Delta\nu_3$(b-CO) is higher (141 cm^{-1}). These values are however smaller than the typical ones generally reported for $\Delta\nu_3$ of mono- or bridged carbonates, but we should recall that this classification was made to rationalize the CO_2 adsorption on metal surfaces and that here, due to the presence of the alkali metal cations of $LiKCO_3$, even the CO_3 directly linked to YSZ are more appropriately described as polydentate species. The picture obtained is thus in line with previous work describing the adsorption of carbonate species in ZrO_2 samples exposed to CO_2 or CO[391–396] and experimental IR spectra of other oxide-carbonate composite reported in literature.[49,99,223,224]

Additionally, we performed the experimental measurements of the IR spectra of the actual YSZ-$LiKCO_3$ material, reported in chapter 3 and here infigure 6.4c. Table 6.2 reports the experimental frequencies of the most important carbonate or oxide bands observed between 600 and 1800 cm^{-1}, where the computed values are also reported. Since we did not consider surface passivation by water molecules, the wavenumber region between 2000 and 3600 cm^{-1} characteristic of hydrogenated species was not taken into account. If we except the peak at 1087 cm^{-1}[49,226] which can be attributed to the O-O vibration of oxygen species adsorbed on the oxide and the shoulder at 1640 cm^{-1}[397] which can be attributed to the adsorbed water visible in figure 6.4c and could thus not be seen in the spectrum computed for the interface model, all bands discussed can be observed in the experimental spectrum: the oxide bands at around 700 cm^{-1}, followed by the ν_4 and ν_2 vibrations of the carbonate groups and a very weak band corresponding to the ν_1 frequency. Moreover, the most intense peak corresponds also in the experimental spectra to the ν_3 asymmetric stretching of the CO_3 groups. Compared to the fine structure observed in the computational data, in the experimental spectrum this vibration appears however as a large broad band with two main contributions at 1396 and 1621 cm^{-1} and a $\Delta\nu_3$ of $\sim$ 250 cm^{-1}, still in line with the presence of polydentate carbonates. This difference should be attributed to the fact the model is a simple approximation of the interface with only six carbonate groups, two of which are

Assignment	Computed	Experimental
	1102	1026
ν_1(CO)	1108	1040
	1116	1086
ν_2(O-C-O)	894-908	829
ν(MO)	807	782
ν(MO)	742, 751, 759	750
ν_4(O-C-O)	710, 726, 753	705
ν(MO)	680	673
ν(MO)	615	632
ν(MO)	480	469
ν(MO)	317	331

Table 6.3: Comparison between selected computed and experimental Raman frequencies (cm^{-1}) for the YSZ-$LiKCO_3$ composite and relative assignment.

directly involved at the interface. Their effect on the the splitting of ν_3 is then much more pronounced when compared to the experimental samples where an higher number of carbonate groups non directly linked to the oxide can be reasonably expected. Nonetheless, experimental values in table 6.2 are in overall good qualitative agreement with the computed ones, differences being in line with the one obtained for the treatment of the pure bulk carbonate phase in chapter 5.

Moving to the Raman data in figure 6.4b and table 6.3, the oxide peaks dominate the computed spectra at 317, 480, 615 and 680 cm^{-1}, in line with experimental data on pure YSZ reporting a major contribution at 620 cm^{-1} with additional peaks at 259, 369, and 690 cm^{-1} attributed to the disorder created by Y_2O_3 doping in the cubic ZrO_2 structure.[229,398] Minor contributions of this phase can be observed also at 807 and around 750 cm^{-1}, where again they are superimposed with the contribution of the ν_4 vibration of the CO_3 groups (710, 726, 753 cm^{-1}). A very small contribution of the ν_2 frequency, not Raman active for isolated carbonate groups, can also be observed at about 894-908 cm^{-1}, as for the bulk $LiKCO_3$. Also the ν_3 mode showed an extremely low intensity and for this reason was not reported. As for pure $LiKCO_3$, the most intense peak corresponds to the symmetric stretching ν_1. However, while in the bulk this vibration corresponds to one narrow peak around 1100 cm^{-1},[225,389] in the composite three main contributions can be evidenced at 1102, 1108, and 1116 cm^{-1}, consequently describing the effect of the coordination on the YSZ surface. The highest and lowest energy peaks can be attributed, respectively, to the monodentate and bridged CO_3 groups directly linked to YSZ, while the shoulder at 1108 cm^{-1} is the contribution of the remaining carbonates.

In Table 6.3, we also report selected vibrations obtained from the experimentally measured Raman spectrum. From the comparison of figures 6.4b and 6.4d we can observe also in this case an overall qualitative agreement: oxide and carbonate phases contribute in the same frequency range and the fine structure of the ν_1 previously described is confirmed and even more evident in the experimental spectrum. Values in table 6.3 confirm this picture, with deviation of the computed frequencies from the experimental ones that are in line with the

errors previously obtained computing the Raman spectra of pure $LiKCO_3$ at the same level of theory. Differences, especially in the intensities of the ν_1 peak, should again be related to the simplicity of the model we used, which was built by taking into account the slab model of the oxide and carbonate surfaces containing the minimum number of layers necessary to ensure convergence of the properties (6 for the oxide and just 3 for the carbonate) and to lower the computational cost of the calculation.

In summary, comparison of the experimental and computed IR and Raman data therefore confirms the validity of the model of the YSZ-$LiKCO_3$ interface model built, with an overall good qualitative agreement between computed and measured data.

6.3.4 YSZ-$LiKCO_3$ electronic properties

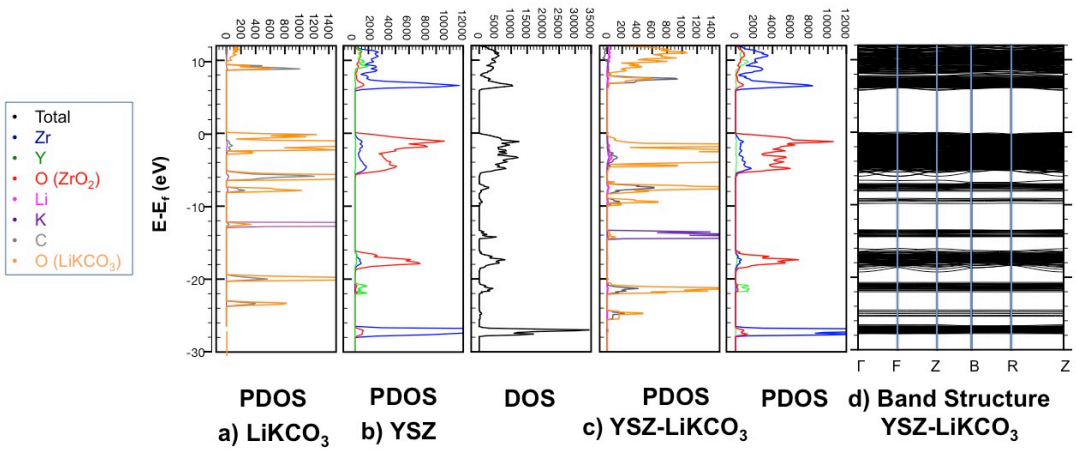

Figure 6.5: Atom projected density of states (DOS) of the clean a) $LiKCO_3$-(001) and b) YSZ-(111) surfaces. c) Total and atom projected density of states (DOS, right) and d) band structure of the composite. The Fermi level has been set as the zero of the energy scale. The Brillouin zone path used for the band structure calculation is Γ-F-Z-B-R-Z, where in terms of the reciprocal basis vectors, Γ corresponds to the point (0,0,0), F to (0,1/2, 0), Z to (0, 0, 1/2), B to (1/2, 0, 0), and R to (1/2, 1/2, 1/2).

Figure 6.5 shows computed PBE0 density of states (DOS, figure 6.5c) and band structure (figure 6.5d) of the YSZ-$LiKCO_3$ composite, along with DOS of the pure YSZ-(111)(figure 6.5b) and $LiKCO_3$-(001) surfaces (figure 6.5a). The E_g value of 5.78 eV of the composite (Table 6.1) is thus extremely close to the one of the pure YSZ-(111) surface (5.80 eV). Unfortunately, we were not able to find neither experimental band gap for this composite nor other theoretical data, since this is the first time this composite is studied. Figure 6.5d shows that between -30 and 12 eV, the electronic structure of the composite shows the same electronic states observed in the pure oxide and carbonate phases. In particular, if we consider the contribution of YSZ, we can observe that the exact same bands of pure YSZ can be found in the band structure of the composite at approximately the same energy values and with the same features: there is a very narrow band at around -28 eV due to the Zr-4p states

and corresponding to a sharp doublet peak in the DOS. It is followed by other two narrow bands at around -22 and -18 eV, corresponding to the Y-2p and O-2s states. Between 0 and -6 eV, the O-2p states with a small contribution of the Zr-4d ones create a wide band constituting, as in pure YSZ, the top of the VB of the YSZ-$LiKCO_3$ composite. Finally, between 5.78 and 12 eV the main contribution to the bottom of the CB is due to the Zr-4d levels. Also the splitting of this contribution in two peaks is still evident from the plot. Finally, compared to the Zr-4d levels, the corresponding Y-4d levels contribute to the VB at slightly higher energies of about 10 eV. As regards the carbonate phase, again the exact same set of six bands observed for the pure $LiKCO_3$ is obtained also in the composite, but this time the levels are slightly shifted (of about 1-2 eV) to lower energies after the stabilizing interaction with YSZ. Between -30 eV and the Fermi level there are six bands: the lower energy band at about -25 eV corresponds to O-2s and C-2s states, while the following band (around -21 eV) is associated to O-2s and C-2p states, and the band at around -14 eV is mainly associated to the K-2p states. At around -9.5 eV the contribution of C-2s, O-2s and O-2p energy levels to a very narrow band can be observed, while the superimposition of C-2p and O-2p levels determine the contribution observed at -7 eV. Under the Fermi level, up to -4 eV, the O-2p non bonding states of the carbonate groups contribute together with the O-2p states of YSZ to the top of the VB. Finally, C-2p states that normally determine the bottom of the CB in pure $LiKCO_3$ at around 8.7 eV are stabilized at lower energies of around 7 eV.

From figure 6.5c, the interaction between the two materials can be further analyzed. Overall, the covalent nature of the C-O bonds in the CO_3 group is confirmed by the strong overlap between the C and O states of the carbonate, as well as the small covalent contribution to the bonding already observed within the oxide phase. An ionic behaviour characterizes, instead, not only the interaction of the cations of the carbonate and the CO_3 units, but also their interaction with the oxygen atoms of YSZ, as suggested by the fact that no superimposition between the levels relative to K or Li and the O levels of the carbonate and of the oxide phases are obtained. On the other hand, a slightly stronger covalent nature is observed for the interaction between the carbonate units and the cations of the oxide phase, as indicated by the overlap between their O and C levels and the Zr or Y states visible in both the CB and VB, and also at around -22 eV.

Mulliken charges and bond populations reported in table 6.4 confirm this picture. The average values are in good agreement with the ones reported in chapters 4 and 5 for the pure oxide and carbonate phases, respectively. They indeed clearly indicate a strong ionic character for the interaction between the cations of the carbonate and the O of the CO_3 units, together with strong covalent behaviour within the carbonate groups. As regards YSZ, a major ionic character with a smaller covalent contribution characterize the Zr/Y-O bonds in this oxide phase even in the composite.

Table 6.4 also shows the average values when considering the atoms directly involved in the formation of the interface layer, that is to say the first O or Zr/Y atomic layer of the YSZ surface and the two CO_3 groups directly linked to the oxide together with the Li atom which is stabilized by interaction with YSZ as we previously described. Charges in this layer are in line with those obtained for the full system, especially for the Li, K, and the oxide O atoms. Interfacial Zr are generally slightly reduced compared to the others (+2.068, +2.088, and +1.986*e* compared to the average +2.346*e*), while the interfacial Y is slightly oxidised

		Full system	Interfacial Layer
Charges	q_{Li}	+0.912	+0.910
	q_K	+1.026	+1.022
	q_C	+0.624	+0.600^m, +0.702^b
	$q_{O_{carb}}$	-0.861	-0.829^m,-0.871^m,0.861^m -0.880^b,-0.840^b,0.984^b
	q_{Zr}	+2.219	+2.068, +2.088, +1.986
	q_Y	+2.346	+2.401
	$q_{O_{ox}}$	-1.133	-1.126,-1.134,-1.094,-1.130
Bond population	$b_{Li-O_{carb}}$	+0.009	+0.007
	$b_{Li-O_{ox}}$	+0.016	+0.016
	b_{K-O}	-0.019	-
	b_{C-O}	+0.674	+0.638
	$b_{Zr-O_{ox}}$	+0.160	+0.177
	$b_{Zr-O_{carb}}$	+0.030	+0.030
	$b_{Y-O_{ox}}$	+0.039	+0.016
	$b_{Y-O_{carb}}$	-0.016	-0.016

Table 6.4: Mulliken charges (q, in *e*) and overlap bond populations (b, in *e*) averaged over all the atoms in the YSZ-$LiKCO_3$ composite model or just over the ones directly involved in the formation of the interfacial layer (first O and Zr/Y atomic layers for YSZ, the two CO_3 groups directly linked on the oxide surface and the Li atom closest to YSZ surface for $LiKCO_3$). m and p exponents are referred to the monodentate and bidentate carbonate group, respectively.

(+2.401e compared to the average +2.346e). Regarding the two carbonates, the charge of the carbon atom involved in the monodentate bonding (+0.600e) is in line with the average value for CO_3 units in $LiKCO_3$ (+0.624e), while the one of C atom involved in the bidentate group is higher (+0.702e). Also the O atoms of these two carbonate groups directly linked to the oxide show charges in line with the average data (-0.829e for the monodentate and -0.880e and -0.840e for the bidentate), but lower than the values for the remaining O of these groups that interact only with the Li^+ and K^+ cations (-0.871e and -0.861e for the monodentate CO_3 and -0.984e for the bidentate one). Computed bond overlap populations confirm these trends: the interaction between the interfacial Li and the O appears to be mainly ionic, even if the bond population is slightly higher (+0.016e) than the average value for Li-O bonds in the carbonate phase(+0.009e). In agreement with the aforementioned charge values for interfacial Zr and Y atoms, the bond population for Zr and the O atoms of YSZ in the interfacial layer is somewhat higher (+0.177e) than the value for bulk-like Zr-O bond(+0.160e), while the opposite is true for Y-O bonds, for which the effect is also more emphasised (+0.016e at the interfacial layer at +0.039e for bulk-like Y-O bonds in YSZ). Compared to these bonds, the interaction between both Zr and Y and the O of the carbonate units show a more important ionic contribution as indicated by the lower overlap population values in table 6.4, but an higher covalent character compared to the Li or K interaction with the O atoms of YSZ.

In summary, in YSZ-$LiKCO_3$, the main electronic properties of the two phases are not altered. The computed band gap of 5.78 eV is mainly determined by the YSZ phase (5.80 eV), with a stabilization toward lower energies of the CB states of the carbonate phase, because of the carbonate-oxide interaction. Both the cations and the anions of the salt are adsorbed on the surface of the oxide through an interaction showing a strong ionic character, with a small covalent behaviour in the case of the bond between the CO_3 groups and the cation surface site of YSZ.

6.4 DFT Study of Conduction Mechanisms

Now that we identified and validated a suitable model of the YSZ-$LiKCO_3$ interface, we can use it to investigate the role of the interface in influencing the conduction mechanisms in carbonate-oxide composite electrolytes. In the following, the transport properties of different possible species (cations of the carbonate, O^{2-} anions, and H^+) will be investigated in detail through periodic DFT calculations, taking into account the conduction mechanisms that have been proprosed over the years to explain the peculiar electrochemical properties of the composites and that we have revised in chapter 1.

First of all, different type of Li-, O-, and proton-related defects have been introduced at the YSZ-$LiKCO_3$ interface in different configurations and the corresponding formation energy (E_f(D)) has been computed to evaluate the relative thermodynamical stability. Since we just considered neutral defects, E_f has been simply computed as:

$$E_f(D) = E_t(D) - E_t(X) + \sum_i n_i \mu_i \tag{6.3}$$

where $E_t(D)$ is the total energy of the defective system, $E_t(X)$ is the total energy of the system without defects, n_i is the number of atoms of element i removed to create the defect (n_i is negative when atoms are added instead), μ_i is the chemical potential of the element i removed (or added). For the oxygen chemical potential, we used the oxygen molecule in its triplet state as a reference.

After having studied the stability, we investigated Li, O and proton transport by performing relaxed scan calculations positioning each time the selected specie at different contiguous positions along a selected conduction path, through subsequent steps of 0.39 Å, as already done for the study of Li transport on the clean $LiKCO_3$ surface. As in chapter 5, we should stress again that this method is not as accurate as the costly point-by-point calculation of the potential energy surface, but it nevertheless allows to estimate the energy changes encountered in each case and the order of magnitude of the energy barrier associated to the different transport phenomena taken into account, so as to provide qualitative information on the peculiar properties of the composites electrolytes.

6.4.1 Li transport

The conductivity enhancement in carbonate-oxide composites is already observed in air atmospheres at certain temperatures lower than the melting point of the carbonate eutectic mixture.[103] In order to explain this observation, it is necessary to take into account the intrinsic transport species in the electrolyte, that is to say the CO_3^{2-} groups, the cations M^+ of the carbonate phase, and the O^{2-} anions of the oxide. In this section, we will concentrate on the role of the species provided by the carbonate phase, while O^{2-} anions will be treated separately. In particular, we will just discuss Li transport. First of all, we should remind that the carbonate phase in these conditions is still in the solid state and that consequently the covalently bonded carbonate groups cannot be the specie determining the transport, since, in these conditions, being much larger than M^+ cations, the creation of anion vacancies through the removal of these groups or their occupation of interstitial sites is energetically highly demanding. Furthermore, if we consider the different cationic species present in the $LiKCO_3$, K ions are bigger than Li ones and should then move slower.[333,334]

The cations of the carbonate phase play an important role when Maier's 'space charge layer theory'[78–84] of heterogeneous ionic conductors is applied to these composites.[95,108,146] Here, we briefly remind that this theory is based on the idea that the interaction at the interface influences the defect chemistry in the boundary layers through surface reactions between the two phases: charge carriers can move toward preferential sites at the interfaces, where they are trapped as a result of their chemical affinity to the second phase. In order to compensate the accumulation of charges at the boundaries, a 'space charge layer', where the counter species of the trapped defects are accumulated, should be formed near the interfaces, thus resulting in high ionic conductivity. In the case of the carbonate phase, the cations (*i.e.* Li^+ in the case of our simulations) can be stabilized by adsorption on the oxide surface, thus increasing cation vacancies in the bulk carbonate phase near the boundaries, which can be responsible for the observed conductivity enhancement in air atmosphere at low temperatures, for example:

$$Li_{Li} + V_A \longrightarrow Li_A^{\bullet} + V_{Li}^{'} \tag{6.4}$$

where the subscripts A and Li indicate an interface and a regular cation lattice site, respectively.

In order to discuss the influence of the interfaces on Li transport in the composites we took into account two different Li-related defects, the neutral interstitial Li atom (Li_i^X) and the neutral Li Frenkel Pair (Li_{FP}).

6.4.1.1 Interstitial Li atom

The first lithium defect we took into account is the neutral interstitial Li atom (Li_i^X). This is relevant to the case where an interstitial Li^+ ion captures an electron in an electrochemical system and can be used to obtain information on the reactivity between YSZ and the carbonate phase by studying Li intercalation in to the oxide lattice. We tested several possible initial configurations for a Li atom added in the model of the YSZ-$LiKCO_3$ interface we previously built. Table 6.5 reports some selected properties computed for the most stable configurations identified when the Li atom is added at the interface in the boundary layer ($Li_i^X(1)$), in carbonate phase at a distance of about 8 Å ($Li_i^X(2)$) or of about 15 Å ($Li_i^X(3)$) from the oxide surface, and in the YSZ lattice ($Li_i^X(4)$). The $Li_i^X(3)$ configuration was studied in order to better describe the effect of the distance from the YSZ-$LiKCO_3$ interface on the defect formation and diffusion and it was obtained recurring to the alternative YSZ^{3L}-$LiKCO_3^{5L}$ model of the oxide-carbonate interface, while the YSZ^{6L}-$LiKCO_3^{3L}$ model was used in all the other cases.

As we can see from the formation energy and the structural parameters reported in table 6.5, the distance from the oxide-carbonate interface does influence the formation of Li_i^X: defects at the interface ($Li_i^X(1)$, E_f of 1.75 eV) and especially the ones in the YSZ lattice ($Li_i^X(4)$, E_f of 1.68 eV) are stabilized by the interaction with the oxide that ensures higher O-coordination compared to defects created in the carbonate phase further away from the oxide surface ($Li_i^X(2)$, E_f of 4.18 eV) and also with respect to Li_i^X in the clean $LiKCO_3$-(001) surface (E_f of 1.77 eV). The most stable $Li_i^X(4)$ defect in the oxide lattice shows six Li_i^X-O bonds with the surrounding O atoms of the YSZ phase, while the second most stable one, $Li_i^X(1)$, forms three Li_i^X-O with O atoms of the surrounding CO_3 groups and another one with one of the outermost YSZ O atoms for a final 4-fold O-coordination, as observed for a Li_i^X defect in the clean $LiKCO_3$-(001). These observations can explain the close values of the formation energy observed in these two cases. $Li_i^X(2)$ and $Li_i^X(3)$ are instead just three fold coordinated and show higher formation energies of 4.18 and 1.99 eV, respectively. To rationalize these data we have to consider both O-coordination and electrostatic interactions between the defect and the positively charged K and C atoms in the $LiKCO_3$ structure, as well as the structural changements observed in the carbonate structure upon YSZ-$LiKCO_3$ interface formation. As discussed in chapter 5, in the clean $LiKCO_3$-(001), Li_i^X defects are always found close to the center of the large open channels that this surface shows along the *b*-axis, in a configuration that ensures the highest O coordination. However, we also showed that the interaction of the oxide and the carbonate phase determines a strongly disordered, amorphous-like, structure for the carbonate phase in the YSZ-$LiKCO_3$ composite,

Configuration	O-coordination number	Shortest d($Li_i^X - M$)	Atomic configuration	Spin density plot	Charge	Spin density	E_f	E_{barr}	Mechanism type
$Li_i^X(1)$	4	2.59 (M=Zr) 2.37 (M=C)	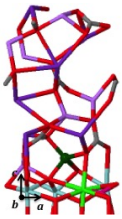	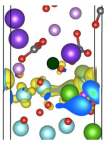	$q_{Li_i^X}$=+0.894 q_{Zr}=+1.776	$b_{Li_i^X}$=+0.000 b_{Zr}=+0.753	1.75	1.00 2.61	Direct Hopping along *b* Knock-off along *a*
$Li_i^X(2)$	3	2.81 (M=K) 1.84 (M=C)	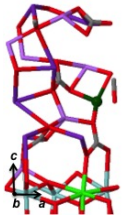	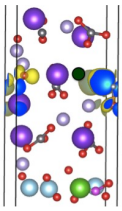	$q_{Li_i^X}$=+0.879 q_C=+0.342 q_O=+0.971 q_O=+0.939	$b_{Li_i^X}$=+0.028 b_C=+0.640 b_O=+0.129 b_O=+0.109	4.18	0.59	Direct Hopping along *b*
$Li_i^X(3)$	3	3.23 (M=K) 2.20 (M=C)	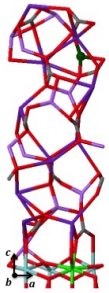	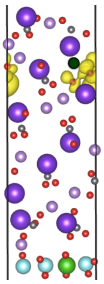	$q_{Li_i^X}$=+0.911 q_C=+0.434 q_O=-1.008 q_O=-1.101 q_O=-1.152	$b_{Li_i^X}$=-0.001 b_C=+0.704 b_O=+0.116 b_C=+0.084 b_C=+0.074	1.99	0.77	Direct Hopping along *b*
$Li_i^X(4)$	6	2.59 (M=Zr) 2.64 (M=C)	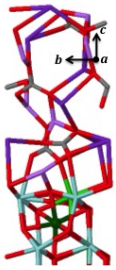	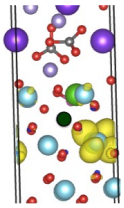	$q_{Li_i^X}$=+0.885 q_{Zr}=+1.824	$b_{Li_i^X}$=+0.001 b_{Zr}=+0.748	1.68	~30 2.06	Linear Direct Hopping Mixed Direct Hopping /Knock-off along *a*

Table 6.5: Parameters of selected Li_i^X configurations: O-coordination number of the defect, value of the shortest distance (d(Li_i^X-M), in Å) between Li_i^X and the positively charged species (M) in the YSZ-$LiKCO_3$ structure, Mulliken charges (q in *e*) and spin density (b in *e*) of Li_i^X and of the neighbouring atoms where the majority of the excess electron is localized, formation energy (E_f, in eV), highest energy barrier associated to Li_i^X diffusion (E_{barr}, in eV) and relative mechanism type, together with the spin density plot (0.002 a.u.) and the ball and stick representation of the corresponding atomic configuration evidencing the position and O-coordination of the interstitial Li atom (in green). Formation energies are computed using for the chemical potential the value obtained for Li bulk metal with $\Delta\mu_{Li} = 0$ (oxygen poor limit, see the text).

with the consequence that the large open channels are now much smaller. This would naturally affect the formation of the interstitial Li defects and the effect can be expected to be enhanced for configuration $\mathrm{Li}_i^X(2)$, where the Li atom is added in the bulk of the carbonate phase compared to configuration $\mathrm{Li}_i^X(3)$ with the interstitial Li closer to the outermost carbonate surface layer, where there is more flexibility for the neighboring atoms to accommodate the creation of the defect. Consequently, even if $\mathrm{Li}_i^X(2)$ and $\mathrm{Li}_i^X(3)$ have the same O-coordination, $\mathrm{Li}_i^X(3)$ also shows longer distances of the interstitial Li from the K and C cations in the carbonate phase, with a behaviour that is much closer to the one of the clean $LiKCO_3$-(001) surface, when compared to $\mathrm{Li}_i^X(2)$ where the electrostatic interactions with the cations of $LiKCO_3$ lattice are much more important.

The importance of the electrostatic effects on the formation of Li_i^X can be better understood if we look at the Mulliken charges reported in table 6.5. As already observed for Li_i^X defects in the clean $LiKCO_3$ surface, when Li_i^X is introduced in the material it becomes Li^+ (with an average charge for the different configurations of +0.892*e* close to the average charge for Li in the YSZ-$LiKCO_3$ lattice (+0.91*e*, see table 6.4), which can thus explain the destabilizing effect of the interaction between the defect and the cations in the composite lattice. The spin density values and plots, reported aways in table 6.5, show the excess electron is donated to the lattice, and, in particular, that it is highly localized to the neighboring atoms of Li_i^X. In the case of $\mathrm{Li}_i^X(1)$ and $\mathrm{Li}_i^X(4)$, where Li_i^X is close to YSZ, the excess electron density is localized on the Zr atoms closest to the defect, showing a charge of +1.776*e* and +1.824*e*, respectively, that should be compared to the average charge value of +2.21*e* for Zr atoms in the composite (see table 6.4). In the case of $\mathrm{Li}_i^X(2)$ and $\mathrm{Li}_i^X(3)$, where the defect is created further away from the oxide surface, the excess charge is localised on the closest CO_3 group, whose structure appears also to be slightly distorted from the usual planar geometry of the carbonate groups, as in the case of Li_i^X in $LiKCO_3$-(001). The C and the O atoms of these CO_3 units are indeed slightly reduced with charges of about +0.3422 and -0.955*e* for $\mathrm{Li}_i^X(2)$ and +0.434*e* and -1.087*e* for $\mathrm{Li}_i^X(3)$, that should be compared to the charge of +0.624*e* and -0.861*e* for the C and O atoms in the defect free YSZ-$LiKCO_3$ system (see table 6.4).

After having described the formation of the Li_i^X defects, their diffusion mechanisms at the YSZ-$LiKCO_3$ interface were then investigated. In particular, two different processes have been taken into account: i) in the first case, for configurations $\mathrm{Li}_i^X(1)$, $\mathrm{Li}_i^X(2)$, and $\mathrm{Li}_i^X(3)$ we studied the defect diffusion from the initial postion to a crystallographic equivalent site in order to obtain information on Li transport in the composite as a function of the defect distance from the interface; ii) in the second case, we investigated the intercalation of a Li defect from the most stable configuration at the interface, $\mathrm{Li}_i^X(1)$, to the most stable configuration found in the YSZ lattice, $\mathrm{Li}_i^X(4)$, which can provide information on the reactivity between YSZ and the carbonate.

Starting from the Li transport in the composite, figures 6.6 a-d show the conduction paths we studied for $\mathrm{Li}_i^X(1)$, $\mathrm{Li}_i^X(2)$, and $\mathrm{Li}_i^X(3)$. In the case of $\mathrm{Li}_i^X(1)$, we studied two different possible types of mechanism, a direct-hopping or 'interstitial mechanism' along the *b*-axis, where the interstitial atom diffuses through lattice interstices at the interface, without displacing lattice atoms (figure 6.6a) and a knock-off mechanism along the *a*-axis, where the interstitial atom diffuses into a host Li lattice site by displacing a neighboring lattice atom

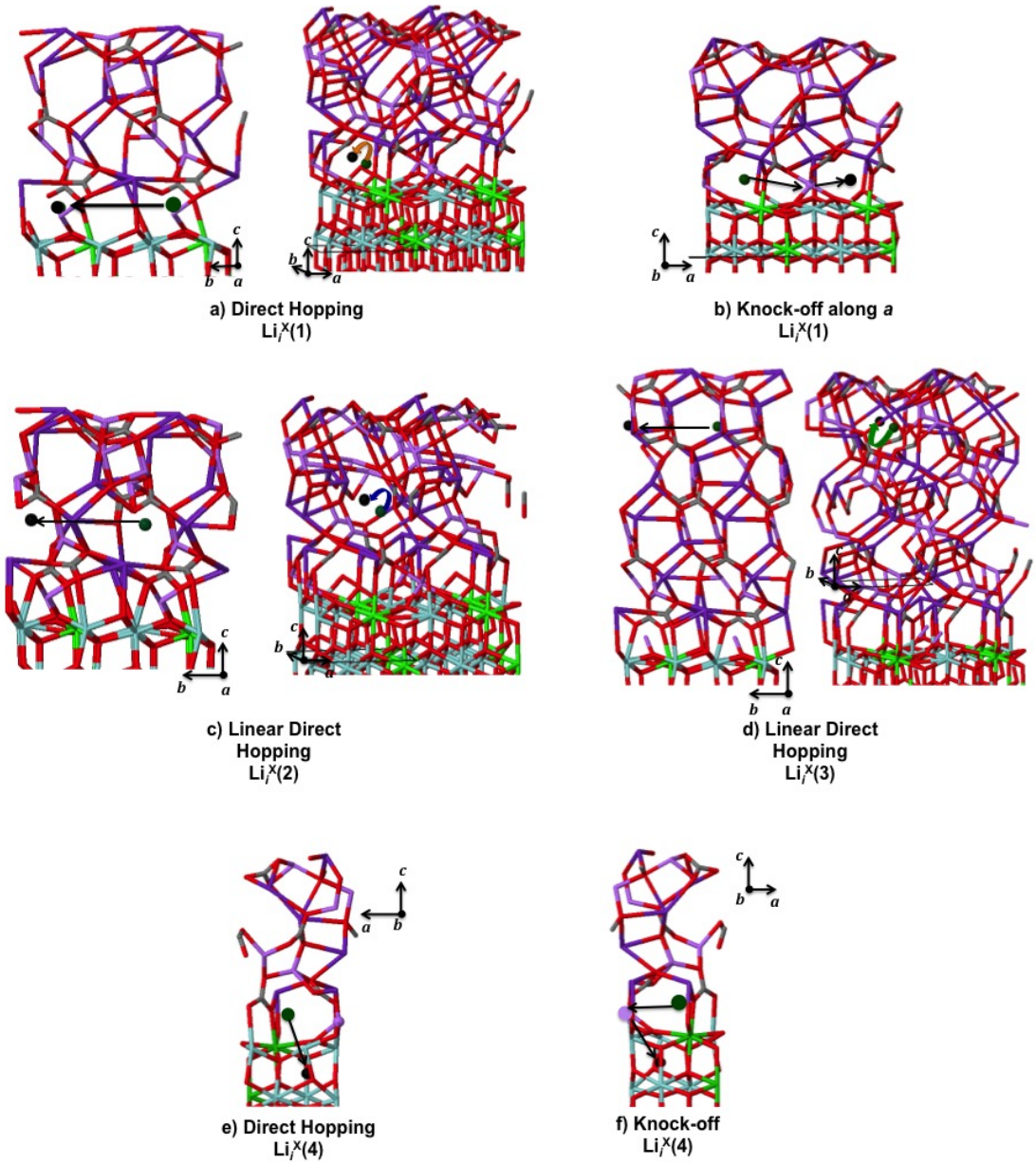

Figure 6.6: Schematic representation of the path for the a) direct hopping and b) knock-off of a Li defect in configuration $Li_i^X(1)$, c) direct hopping of of a Li defect in configuration $Li_i^X(2)$, d) direct hopping of a Li defect in configuration $Li_i^X(3)$, e) direct hopping from $Li_i^X(1)$ to $Li_i^X(4)$, and f) knock-off from $Li_i^X(1)$ to $Li_i^X(4)$. In a, b, c, and d the defect migrates from the initial position indicated by the green sphere to the final equivalent position, the black sphere. For the intercalation mechanisms (e and f), the insertion from the interface configuration $Li_i^X(1)$, in green, to the position in the oxide lattice $Li_i^X(4)$, in black, is considered. For the knock-off mechanisms in b and f, the lattice Li involved in the mechanism is indicated by a light purple sphere.

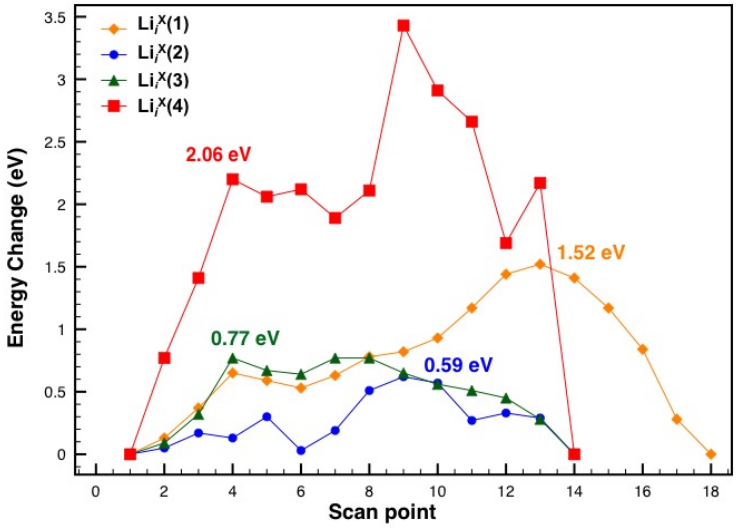

Figure 6.7: Variation of the energy as a function of the Li_i^X defect position along the paths showed in figure 6.6. The direct hopping mechanism path is shown in orange for $Li_i^X(1)$, blue for $Li_i^X(2)$, and in green for $Li_i^X(3)$. The knock-off for Li intercalation from configuration for $Li_i^X(1)$ at the interface into the oxide lattice in position $Li_i^X(4)$ is instead represented in red. For simplicity, among the possible paths in figure 6.6, in the case of the $Li_i^X(1)$ and $Li_i^X(4)$ configurations, only the path associated to the lowest barrier is showed.

into an adjacent interstitial site (figure 6.6b). For $Li_i^X(2)$ (figure 6.6c) and $Li_i^X(3)$ (figure 6.6c), we considered only diffusion through a direct-hopping mechanism in the small channels along the *b*-axis where these defects have been created. Figure 6.7 shows the computed energy profile associated with the displacement of the defect along the diffusion coordinate for the studied mechanisms, while table 6.5 summarizes the value of the highest barrier (E_{barr}) obtained in each case. In each of the three cases, the energy profile is quite flat and all the barriers are quite low, but more importantly lower than the value of 1.47 eV obtained for the diffusion of a Li_i^X defect in the channels of the defect-free $LiKCO_3$-(001) in chapter 5. The highest barrier of 1.00 eV is found when $Li_i^X(1)$ migrates in the YSZ-$LiKCO_3$ boundary layers. In this case, the interstitial Li atom has the highest O-coordination and we should underline that the migration is characterized by the continuous breaking and making of Li_i^X-O bonds, while trying to maintain high O-coordination and to minimize the repulsive electrostatic interactions with the surrounding cations of the YSZ-$LiKCO_3$ lattice. The migration at the interface implies a greater variation of the O-coordination along the path and especially the breaking of the Li_i^X-O bonds seems to greatly affect the energy change along the path. Minor variations in the O-coordination are instead observed in the case $Li_i^X(2)$ and $Li_i^X(3)$, where the defect migrates in the small channels in the disordered carbonate phase, in line with the very flat energy profiles showed in figure 6.7 for these configurations. The value of 0.59 eV obtained for $Li_i^X(2)$ diffusing in the 'bulk' carbonate is 0.88 eV lower than the one for a Li_i^X diffusing in the defect-free $LiKCO_3$-(001), while a sligthly higher barrier of 0.77 eV is obtained for $Li_i^X(3)$. This indicates that in the outermost carbonate layer, as expected, the behaviour is less influenced by the interaction with the oxide and bears more similarity

to the case of pure $LiKCO_3$, in agreement with the minor distortion in the structure observed at these distances from the YSZ surface when describing the structure of the YSZ-$LiKCO_3$ in section 6.3.2 and in agreement also with the analysis of the Li_i^X stability as a function of the distance from the interface previously made.

In summary, we have seen how the interface influences Li_i^X formation and diffusion. In particular, the defect formation can be favored through the chemical affinity of the O atoms of the oxide for the interstitial Li atom. The structural distortion of the carbonate phase as a consequence of the interaction with the oxide strongly affects the transport properties with a reduction of the barrier for Li diffusion when compared to the pure $LiKCO_3$ surface. The distance from the interface is another important parameter, since we saw how the breaking and reformation of the bonds Li_i^X-O with the O atoms of the oxide phase greatly influences the diffusion barrier, while the properties of the outermost carbonate layers tend toward the features of the pure $LiKCO_3$ surface. Finally, it is important to underline that not only interstitial Li are more favourably formed at the YSZ-$LiKCO_3$ interface, but also that, when this happen, the interstitial Li becomes positively charged and the electron is localised on the oxide side. Moreover, $Li_i^X(1)$ at the interface shows higher barriers when compared to analogous defects created farther away from the oxide surface in the carbonate phase. This indicates that Li^+ are trapped on the oxide surface and that a charge separation takes places. These observations suggest that the formation of a 'space charge layer' in the composite is indeed possible. This point will be, however, more properly discussed through the analysis of the Li Frenkel pair formation in section 6.4.1.2.

Moving to the Li intercalation, we studied different paths for a Li_i^X defect that diffuses from the most stable Li configuration at the interface ($Li_i^X(1)$) into the oxide lattice in configuration $Li_i^X(4)$ as shown in figures 6.6e-f. This process can provide information on the known reactivity issues between YSZ and the carbonate. In chapter 3, we discussed how YSZ-carbonate composites show instability issues in both H_2 and air atmospheres. In particular, we saw how, even if YSZ is well-known to be stable in such H_2 rich atmospheres, its composites behave strangely at high temperature, losing performances showing a sudden decrease of conductivity at about 530°C before following a quasi-linear decrease of the conductivity during the temperature decrease corresponding to a behaviour quite similar to YSZ without carbonates. The system appeared to be sligthly more stable under O_2, where the reactivity seems to start at higher temperatures. In both cases, the XRD of the samples registered on the YSZ-carbonate pellets after their exposure to H_2 or air showed the presence of the monoclinic phase of ZrO_2, and of zirconates, like Li_2ZrO_3. ZrO_2 and YSZ can react with Li, Na, or K carbonates at high temperatures ($>$ 600°C) forming zirconates.[219–221] For example, in the case of Li_2CO_3, we have:

$$ZrO_2 + Li_2CO_3 \longrightarrow Li_2ZrO_3 + CO_2 \tag{6.5}$$

Some authors already reported that, zirconates were observed for TZP-(Li,Na)CO_3 (3mol% yttria-doped tetragonal polycrystalline zirconia) after being exposed to oxidant atmosphere[98] or for YSZ composites.[399] However, studies on the stability of YSZ in molten carbonate environments are controversial, because Suski et al.[216] found that YSZ could resist corrosion in molten Li/Na eutectics for approximately 1000h, while, differently from what we observed,

Jiang et al.[217], after investigating YSZ corrosion in air, Ar and H_2 atmsphere, reported that a thin YSZ electrolyte is only able to resist the corrosion in the molten carbonate Li/K under reducing conditions, and Xu et al.[218] found that corrosion effects seem to be retarded with increasing reducing conditions.
The diffusion of the Li species from the carbonate phase into the oxide can be considered as the first step toward the formation of lithium zirconates.[400] The study of the stability of the Li defects at the interface and in the YSZ lattice of the YSZ-$LiKCO_3$ composite as a function of the reducing/oxidising atmosphere and the investigation of the intercalation process from a theoretical point of view can thus help in clarifying the controversial results on the reactivity in these systems. In order to compute the formation energy of Li_i^X defects, the chemical potential of the Li atom (μ_{Li}) is used in equation 6.3:

$$\mu_{Li} = \mu_{Li}(metal) + \Delta\mu_{Li} \tag{6.6}$$

With a strategy similar to the one used in the case of Li defect in $LiKCO_3$, we can determine the physically possible range of variation of this chemical potential ($\Delta\mu_{Li}$) as a function of the oxygen chemical potential. The composites are synthetized in air/CO_2 environment.[19] The oxygen chemical potential μ_O characterizes the oxygen environment and oxygen poor environments are characterized by low μ_O values, while oxygen rich environments are characterized by high μ_O values. Naturally high μ_O values correspond also to conditions that favour oxidation, while low μ_O values correspond to conditions that favour reduction. We used for the oxygen chemical potential the oxygen molecule as a reference, $\mu_O = 1/2\mu(O_2) + \Delta\mu_O$. For the lithium chemical potential, we computed $\mu_{Li}(metal)$ from the total energy of bulk Li metal (space group *Im-3m*, *a*=3.51 Å)[382] and we derived $\Delta\mu_{Li}$ as a function of $\Delta\mu_O$ imposing the stability of the system against decomposition in elemental Li, Zr and against Li_2O ($\Delta H_f(Li_2O)$=-6.21 eV)[381] and Li_2O_2 ($\Delta H_f(Li_2O_2)$=-6.56 eV)[381], Li_2ZrO_3 ($\Delta H_f(Li_2O_2)$=-18.06 eV)[401] and the monoclinic ZrO_2 ($\Delta H_f(Li_2O_2)$=-11.41 eV)[402] formation:

$$\begin{cases} \Delta\mu_{Li} \leq 0 \\ \Delta\mu_{Zr} \leq 0 \\ 2\Delta\mu_{Li} + \Delta\mu_O \leq \Delta H_f(Li_2O) \\ 2\Delta\mu_{Li} + 2\Delta\mu_O \leq \Delta H_f(Li_2O_2) \\ 2\Delta\mu_{Li} + \Delta\mu_{Zr} + 3\Delta\mu_O \leq \Delta H_f(Li_2ZrO_3) \\ \Delta\mu_{Zr} + 2\Delta\mu_O \leq \Delta H_f(ZrO_2) \end{cases} \tag{6.7}$$

Through the resolution of this system of equations, it is possible to obtain the dependence of $\Delta\mu_{Li}$ from $\Delta\mu_O$. For simplicity and with the aim to qualitatively understand how the E_f varies as a function of the atmosphere, here, we can just note that, considering the solution for $\Delta\mu_{Zr} = 0$, at the oxygen rich limit ($\Delta\mu_O = 0$), $\Delta\mu_{Li}$ is -0.47 eV and the E_f is 2.15 eV for $Li_i^X(4)$, while at the oxygen poor limit ($\Delta\mu_O = -2.4eV$), $\Delta\mu_{Li}$ is zero and the corresponding formation energy is 1.68 eV for $Li_i^X(4)$. We stress here that we considered as oxygen poor limit the value of $\Delta\mu_O$ which corresponds at 700 K (close to the temperature

at which we observed the drop of conductivity in YSZ-based samples in reducing environments) to an O_2 partial pressure of 10^{-2} atm; lower $\Delta\mu_O$ values correspond to oxygen partial pressures that cannot be reached experimentally.[403] Similar results are obtained for the other configurations, indicating that the formation energy for a Li_i^X increases when going from a reducing toward an oxidising environment. For sake of simplicity we just considered how $\Delta\mu_{Li}$ varies as a function of $\Delta\mu_O$ for $\Delta\mu_{Zr} = 0$. Independently from the actual type of dependency of $\Delta\mu_{Li}$ from $\Delta\mu_O$ in the other possible domain of variation for $\Delta\mu_{Zr}$, this result does not change.

Finally, we estimated the barrier for Li intercalation into the oxide lattice, studying different possible mechanisms. A schematic path for the linear direct-hopping mechanism for the intercalation of the Li defect from configuration $Li_i^X(1)$ to $Li_i^X(4)$ is showed in figure 6.6e. However, the barriers associated to this process were found to be extremely high (> 10 eV). A non linear direct-hopping path, in which Li_i^X first diffuses on the oxide surface from $Li_i^X(1)$ to a position near the one of the oxygen vacancy of the YSZ surface, was also investigated but it was found to be associated to high barriers ($\sim$ 3-4 eV). Finally, we investigated also a knock-off mechanism (figure 6.6f), in which $Li_i^X(1)$ diffuses toward the position of a Li atom of the carbonate lattice adsorbed on the YSZ surface, which is in turn displaced toward the interstitial position $Li_i^X(4)$ in the oxide lattice. A barrier of 2.06 eV is obtained in this case, as shown in the energy profile of figure 6.7.

In summary, if we assume the intercalation as a first step toward reactivity between YSZ and the carbonate, we can conclude that the high barrier of about 2 eV found for Li intercalation into YSZ is in agreement with the experimetal observation that the reaction takes places at high temperature. Moreover, considering that no products other than ZrO_2 and the zirconates are observed in the XRD, the reduction of the formation energy for the Li defect at the YSZ-carbonate interface and in the YSZ lattice can indeed provide an explanation of the higher instability of the YSZ-based composites in reducing atmosphere we observed in chapter 3, where the reaction seems to start at lower temperatures compared to experiments performed in oxidizing conditions.

6.4.1.2 Li Frenkel pair

A Li Frenkel pair (Li_{FP}) is formed when a Li^+ is displaced from its lattice position to a nearby interstitial site (becoming$Li_i^\bullet$) and creates a vacancy ($V_{Li}^{'}$) at its original site. This type of defect can be hence very helpful in trying to investigate the 'space charge model' when applied to the composite carbonate-oxide electrolytes.

In order to simulate the space charge layer formation, we displaced one of the Li^+ cations from its position to an interstitial site at the YSZ-$LiKCO_3$ interface, where it can be stabilized by the interaction with the oxide. In this way, the remaining $V_{Li}^{'}$ can contribute to the formation of the 'space charge layer' in the bulk carbonate phase near the boundaries. In particular, we tested three possible configurations, displacing Li^+ cations lying at different distances from the interface, so as to create $Li_i^\bullet$-$V_{Li}^{'}$ pairs with increasing separation distance along the *c*-axis (about 2.7 Å for $Li_{FP}^{(1)}$, 4.3 Å for $Li_{FP}^{(2)}$, and 6.7 Å for $Li_{FP}^{(3)}$). In every case, the Li^+ was displaced from its original site to the same position at the interface and then it was allowed to relax. Table 6.6 shows the atomic configuration, the most important structure

Configuration	O-coordination number	Shortest d($Li_i^\bullet - M$)	Atomic configuration	E_f	E_{barr}	Mechanism type
$Li_{FP}^{(1)}$	4	2.66 (M=Li) 2.07 (M=C)	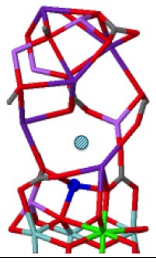	1.15	-	-
$Li_{FP}^{(2)}$	4	2.58 (M=Li) 2.02 (M=C)	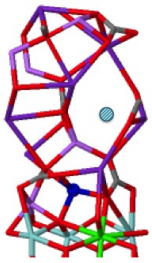	1.07	0.21	Direct hopping
$Li_{FP}^{(3)}$	3	2.47 (M=Li) 2.28 (M=C)	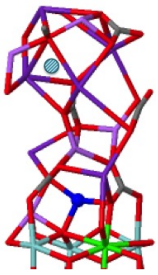	1.26	-	-

Table 6.6: Parameters of selected Li_{FP} configurations: O-coordination number of the defect, value of the shortest distance (d($Li_i^\bullet$-M), in Å) between $Li_i^\bullet$ and the positively charged species (M) in the YSZ-$LiKCO_3$ lattice, formation energy (E_f, in eV), energy barrier associated to the vacancy diffusion (E_{barr}, in eV) and relative mechanism type, together with the stick representation of the corresponding atomic configuration, evidencing the position and O-coordination of the interstitial Li at the interface (in blue) and the Li vacancy left in the bulk carbonate phase (hashed light blue sphere).

parameters and the formation energy (E_f) for the three cases taken into account. As we can see, the E_f values (between 1.07 and 1.26 eV) are all lower than the computed formation energy for a Li_{FP} created in the clean $LiKCO_3$-(001) surface (1.79 eV), indicating that the formation of the interface can indeed modify the defect chemistry of the carbonate phase, because of the stabilizing interaction taking place in the boundary region between the two phases. If we compare the three configurations, we can observe that the greatest rearrangements are observed for the least stable $Li_{FP}^{(3)}$: in order to compensate the creation of $V_{Li}^{'}$ in the site that is very close to the outermost $LiKCO_3$ surface layer, strong variation in the position of the cations (K^+ in particular) in the neighborhood of the vacancy are observed, and, as a result of all these rearrangements, $Li_i^{\bullet}$ is just 3-fold O-coordinated. For $Li_{FP}^{(1)}$ and $Li_{FP}^{(2)}$, the $V_{Li}^{'}$ is created in the layer just above the boundary one and $Li_i^{\bullet}$ is found to be 4-fold O-coordinated in both cases. These configurations show a formation energy lower than the one of $Li_{FP}^{(3)}$, with a relative energy difference that can hence be explained in terms of electrostatic effects if we consider the distances between $Li_i^{\bullet}$ and the M cationic species in the bulk carbonate structure reported in table 6.6.

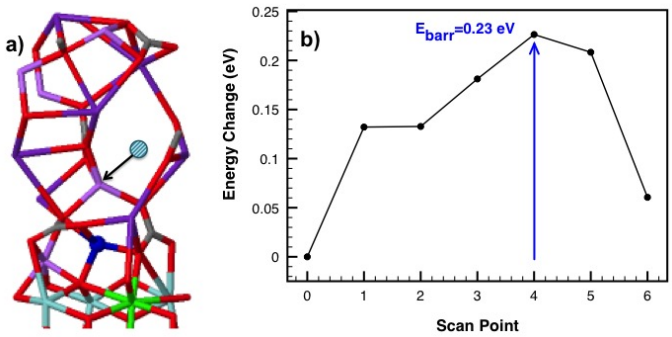

Figure 6.8: a) Schematic representation of the path for the direct hopping diffusion of a $V_{Li}^{'}$ in the bulk carbonate phase when its counter specie ($Li_i^{\bullet}$) is trapped at the interface after the Li_{FP} formation in YSZ-$LiKCO_3$. b)Variation of the energy as a function of the $V_{Li}^{'}$ position along the selected path.

Maier's model is based on the the assumption that the $Li_i^{\bullet}$ species are stabilized and segregated at the interfaces, while the conductivity enhancement is due to vacancy diffusion in the space charge layer. We hence studied the $V_{Li}^{'}$ diffusion considering the most stable $Li_{FP}^{(2)}$ configuration. In the case of Li vacancies, Li diffusion corresponds to the repetitively position exchange of one lattice Li^+ and the vacancy. $Li_i^{\bullet}$ was then kept fixed at the interface, while we performed relaxed scan calculations for one lattice Li diffusing from its original position to the vacant site in $Li_{FP}^{(2)}$ along a selected path according to a simple direct hopping mechanism (see figure 6.8a). As we can see from results in table 6.6 and from the energy profile of figure 6.8b, the vacancy diffusion is associated to a very small barrier of 0.23 eV. Therefore, in the composite, Li transport can easily take place through a vacancy hopping mechanism. In chapter 5, studying Li transport at the clean $LiKCO_3$ surface, we showed that in the pure material, $Li_i^{\bullet}$ can diffuse via direct-hopping along the large open channels characterizing the structure of the surface with low barriers of 0.80 eV, while Li vacancies cannot

be the effective diffusion carriers since the barrier they are associated with is too high. We can consequently conclude that the interface formation in oxide-carbonate materials not only determine a reduction of the defect formation energy associated to Li_{FP} and of the diffusion barrier, but the interaction between the two phases is also responsable for the change in the Li transport mechanism, since vacancy hopping was forbidden in the pure carbonate material, but in agreement with Maier's theory, in the composite $Li_i^{\bullet}$ can be trapped by interaction with YSZ, while V'_{Li} can easily diffuse in the so formed space charge layer.

6.4.2 Oxygen transport

It is well known that oxide ion conduction can take place in the oxide phase via an oxygen vacancy mechanism. However, as we discussed in chapter 1, different explanations on the oxide ion enhancement mechanism in composites have been proposed in literature.
For example, Huang et al.[103] using defect chemistry proposed that in the presence of the carbonate phase, the oxygen ion already conducting in the oxide phase via an oxygen vacancy mechanism, may also accumulate on the surface of the oxide particle, resulting in higher oxygen vacancy concentration in the bulk due to interfacial interaction:

$$O_O^X + V_S \longrightarrow V_O^{\bullet\bullet} + O_S'' \tag{6.8}$$

where the subscripts S and O indicate a surface and a regular lattice site, respectively.
Nevertheless, the most common explanation[95,108,146] for the conductivity enhancement is based on Maier's 'space charge' layer theory. The carbonate-oxide interface is mainly considered to be responsible for the enhanced electrochemical properties, because a space-charge layer can be formed at the phase boundaries due to the interfacial interaction: different negatively charged oxygen species (O_2^-, O^-, and O^{2-}) can cover the surface of the oxide at the interface, where there is also, as we previously described, an enrichment of the cations M^+ (Li^+, Na^+, or K^+) of the carbonate. The higher concentrations of the defects/ions near the phase boundaries compared with the bulk phase may essentially constitute 'high conductivity pathways' at the boundary between the two phases.

Finally, it is worth considering also the properties of O atom migration at the oxide-carbonate interface. Qin and Huang[404–407] observed how the presence of the carbonate at the triple phase boundary (TPB) region (the region where the feeding gas, the electrolyte and the cathode overlap) can enhance the oxygen reduction process (ORR) in SOFC, through a particular mechanism for O migration in the carbonate phase. Through DFT calculations, Qin and Gladney[404] identified CO_5^{2-} and CO_4^{2-} as relevant species to the oxygen reduction in molten carbonates for MCFC applications. Qin and Huang also proposed a new ORR charge-transfer model involving the carbonate phase, in which CO_5^{2-} is the absorber of the oxygen molecule and CO_4^{2-} acts as a transporter of O atom. The migration mechanism for CO_4^{2-} ions in the TPB region can be achieved through a cooperative 'cogwheel' (or 'paddle-wheel') mechanism, involving the breaking and reforming of O-CO_3^{2-} bonds, as described by the equation:

$$CO_4^{2-} + CO_3^{2-} \longrightarrow CO_3^{2-} - - - O - - - CO_3^{2-} \longrightarrow CO_3^{2-} + CO_4^{2-} \tag{6.9}$$

The authors also suggested that this process can be relevant in the case of SOFC with composite carbonate-oxide electrolytes.[406] Even if it is not directly related to the conduction properties of the composite, understanding the effect of the interfaces on the oxygen migration at the TPB region when composite electrolytes are used can be very interesting, especially when considering the case of SOFC-single component fuel cell (SCFC) based on the mixture of oxide-carbonate composites and electronic conductors, like LiNuCuZn oxide.[408–410] These devices are a novel kind of fuel cell that, in contrast to standard fuel cells, does not have a well defined electrolyte layer. Instead, the SCFC has only one, more or less, uniform layer composed of a mixture of electrode and electrolyte materials, but its power density is still comparable to that of three-component fuel cells. The theoretical basis of SCFC is not yet fully understood and more research still needs to be done.[51,96]

6.4.2.1 Oxygen anion related species

In order to verify the enhancement mechanism proposed by Huang et al.[103], we created neutral O Frenkel pair (O_{FP}) in the oxide-carbonate composite, by displacing one O^{2-} from its lattice position in the oxide, where a positively charged O vacancy is thus formed ($V_O^{\bullet\bullet}$), toward an interstitial position at the YSZ-carbonate interface ($O_S^{''}$). Different configurations, considering oxygen ions from different lattice sites, have been tested and the results for the most stable configurations are reported in table 6.7. The oxide lattice slightly rearranges after the vacancy formation and the oxygen anion interacts at the interface with both the Zr cations of YSZ and the Li^+ or K^+ species of the carbonate. However, the value of the formation energy of 4.59 eV is too high to allow explaining the conductivity enhancement in terms of higher oxygen vacancy concentration in the bulk oxide due to interfacial interaction with the carbonate.

The second enhancement mechanism we considered is the one based on the higher concentrations of the defects/ions near the phase boundaries compared with the bulk carbonate or oxide phases. The simultaneous adsorption at the interface of both negatively charged species and of the cations of the carbonate, which is at the base of this mechanism, has been simulated by introducing at the interface one O^{2-} and two interstitial $Li_i^{\bullet}$ (indicated in the following as $2Li_i^{\bullet}$-O^{2-}), which also allowed us to guarantee the neutrality of the unit cell during the calculations. Selected parameters for the most stable configurations we were able to identify are also reported in table 6.7. As we can see, formation energies ranging between -4.20 and -3.05 eV are obtained for the various cases, suggesting that the accumulation of these species at the oxide-carbonate composite interface can indeed favourably take place. In all the three cases of table 6.7, the oxide ion (in orange in the atomic configuration picture) is adsorbed on one of the Zr lattice sites of YSZ at a distance (about 2 Å) slightly shorter than the average Zr-O bonds in YSZ.[411] In the various configurations, O^{2-} interacts at different extent with the interstitial $Li_i^{\bullet}$: in the most stable $2Li_i^{\bullet}$-$O^{2-}(1)$ it is close to both $Li_i^{\bullet}$ (at a distance of about 1.7 Å); in the second most stable ($2Li_i^{\bullet}$-$O^{2-}(2)$), it interacts with just one of the two, while when the O^{2-} is farther away (around 3-4 Å) from the Li ions the least stable $2Li_i^{\bullet}$-$O^{2-}(3)$ configuration is obtained.

We consequently studied the diffusion of the oxide ion at the interfaces considering the most stable configuration. Different type of mechanisms along both the *a* and *b*, involving

Specie	d(O*-M)	Atomic configuration	E_f	E_{barr}	Mechanism type
O_{FP}	-	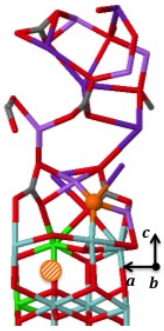	4.59	-	-
$2Li_i^{\bullet}$-$O^{2-}(1)$	2.08 (M=Zr) 1.76 (M=$Li_i^{\bullet}$) 1.74 (M=$Li_i^{\bullet}$)	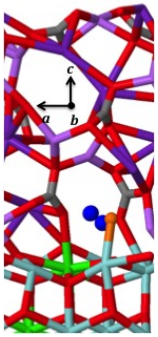	-4.20	2.19	Direct hopping along *a*
$2Li_i^{\bullet}$-$O^{2-}(2)$	2.02 (M=Zr) 1.80 (M=$Li_i^{\bullet}$) 2.94 (M=$Li_i^{\bullet}$)	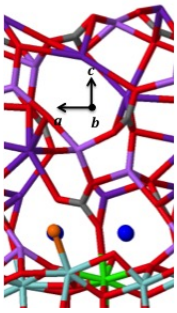	-3.42	-	-
$2Li_i^{\bullet}$-$O^{2-}(3)$	1.95 (M=Zr) 3.93 (M=$Li_i^{\bullet}$) 2.84 (M=$Li_i^{\bullet}$)	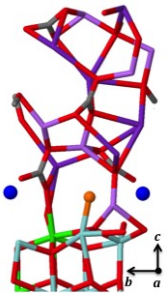	-3.05	-	-

Table 6.7: Parameters for O^{2-}-related species at the YSZ-$LiKCO_3$ interface, namely the oxygen Frenkel pair (O_{FP}) and the O^{2-} anion introduced together with the two interstitial Li cations ($2Li_i^{\bullet}$-O^{2-}): distance (d(O^*-M, in Å) between the O^{2-} anion (O^*) and the closest cations (M), formation energy (E_f, in eV), energy barrier associated to the vacancy diffusion (E_{barr}, in eV) and relative mechanism type, together with stick representation of the corresponding atomic configuration evidencing the position of the O^{2-} anion (in orange), $V_O^{\bullet\bullet}$ (hashed orange sphere), and of the interstitial Li cations (in blue).

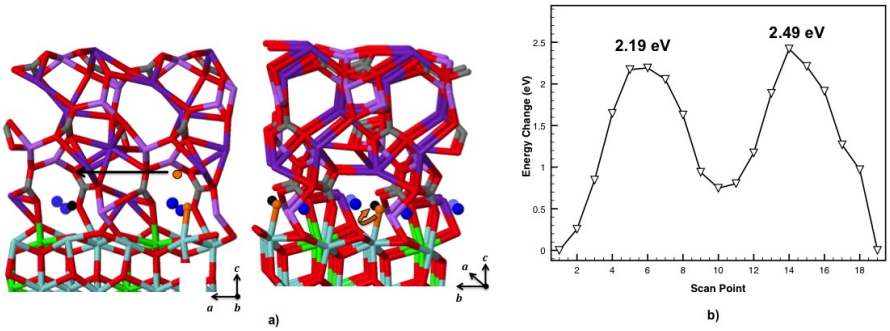

Figure 6.9: a)Views along the *a*- (left) or *b*-axis (right) of a schematic representation of the path for a O^{2-} anion that diffuses at the interface of the YSZ-$LiKCO_3$ composite from the initial configuration $2Li_i^{\bullet}$-$O^{2-}(1)$ (in orange) to a final equivalent position (in black), according to a direct hopping mechanism along the *a*-axis. The interstitial Li cations are represented in blue. b) Variation of the energy as a function of the O^{2-} position along the selected path.

the migration just of the oxide ion or the simultaneous migration of oxygen and Li species at ones. Figure 6.9 only shows the path and the corresponding energy profile that was found to be associated with the lowest barrier, which corresponds to a direct hopping mechanism for the diffusion of the O ion along the *a*-axis of the composite unit cell (see figure 6.9a). The other mechanisms and the results on the other configurations have not been reported since they were found to be associated with barriers higher than 2-4 eV. The energy profile of figure 6.9b shows that the direct hopping along the *a*-axis is associated to a lower barrier of 2.19 eV. On one hand, in this simulation, the carbonate phase is in an amorphous-like yet solid state and the conductivity measurements through EIS experiments in chapter 3 showed that at low temperatures the activation energy for the oxide-carbonate composites is higher that the values typical for the oxide ion conductors (1.6 eV in the case of YSZ-$LiKCO_3$ composites). The barrier of 2.19 eV obtained in the case of $2Li_i^{\bullet}$-$O^{2-}(2)$ can be thus party explained considering the physical state of the carbonate phase and thus supports the assumption that the low temperature activation energy of the composites represents the behaviour of oxide ions partially inhibited by the presence of solid carbonates.[22] On the other hand, the higher value compared to experiments can be explained also considering that we estimated the barrier by simply performing relaxed scan calculations along a path that implies the breaking and reformation of the bonds between the oxide ion and the interstitial Li cations introduced together with it at the interface. If we consider that we previously described how strongly the oxide ion interacts with them, the high barrier could thus also be a consequence of the model we chose.

In conclusion, we showed that the formation of O Frenkel pair in which the oxide ion is adsorbed at the composite interface is associated to high formation energies, while the formation of negatively charged oxygen species associated with cations of the carbonate phase is indeed a favourable process. However, further investigations are needed in order to understand if and how this higher defect concentration at the boundary layers can effectively constitute high conduction pathways for the oxide ion, for instance through molecular

dynamics simulations, allowing to study the behaviour of the material when the carbonate phase is in the molten state.

6.4.2.2 Oxygen atom migration

For the study of the O atom migration, we first considered the adsorption of an oxygen atom in different configurations at the boundary layer (see table 6.8) or in the bulk carbonate phase (see table 6.9) of the composite.

At the boundary layer, we considered the adsorption of the O atom on the bidentate CO_3 ($O_{int}^{(1)}$), on the monodentate carbonate ($O_{int}^{(2)}$), on a Zr site of the YSZ surface ($O_{int}^{(3)}$), and in the YSZ lattice in a correspondence of an oxygen vacancy site ($O_{int}^{(4)}$). As we can see from the formation energies in table 6.8, at the interface the adsorption on the carbonate groups is favoured compared to the adsorption on the oxide. In the case of $O_{int}^{(3)}$, the O atom was initially placed on the free Zr site of the oxide surface, but at the end of the geometry optimization it ended up to be bonded to the closest monodentate carbonate group at a distance of 2.93 Å from the initial Zr site. From a structural point of view, there are no remarkable differences in configurations $O_{int}^{(1)}$, $O_{int}^{(2)}$, and $O_{int}^{(3)}$ since the distance between the O atom we introduced (indicated as O^* in the tables) and the O group of the carbonate group on which it is adsorbed (d(O^*-O_O)) are very close in all the three cases. Furthermore, in every case, the C-O bond for the O atom the the carbonate directly linked to O^* sligthly longer (1.35-1.38 Å) than the remaining C-O distances (1.24-1.27 Å). For configuration $O_{int}^{(4)}$, the O^*-Zr distances are of the same order of magnitude as the Zr-O bonds in zirconium dioxide. Furthermore, in more stable configurations $O_{int}^{(1)}$ and $O_{int}^{(2)}$, O^* is stabilized also by the interaction with the cations of the carbonate phase. $O_{int}^{(1)}$ is the most stable configuration, with a formation energy of 0.96 eV. In this case, O^* is on the O atom of the bidentate group not directly linked to the oxide, which already showed a larger C-O distance (1.32 Å) compared to the other two C-O bonds of this CO_3 group as a consequence of the bidentate type of coordination of this group to the YSZ surface (1.27 and 1.29 Å). As we can see from the value of the Mulliken charges for O^* and of the atoms of the group to which it is bounded, these atoms are slightly oxidised after the adsorption. When O^* is linked to the monodentate group in configuration $O_{int}^{(2)}$, it shows a charge of about -0.80*e*, while a greater oxidation is observed for the O atom of the CO_3 bond to O^*, showing a charge of -0.29*e*, followed by the other atoms of the carbonate with charge values ranging between -0.73 and -0.79*e* (O atoms of CO_3 have an average charge of -0.86*e* in the pure YSZ-$LiKCO_3$ composite, see table 6.4). However, in the case of the bidentate carbonate, the main oxidation take place on the Zr sites of YSZ to which this carbonate is bounded that have charges of +2.07 and +2.09*e* to be compared with the average value of +2.22*e* in the pure YSZ-$LiKCO_3$ composite.
Different configurations for the O^* atom on the CO_3 groups of the carbonate phase lying at about 8 Å from the oxide surface have also been tested and the two most stable are shown in table 6.9. These configurations show similar structural properties and charge values with $O_{int}^{(2)}$ or $O_{int}^{(3)}$ and are found to have similar E_f (1.27 eV for $O_{carb}^{(1)}$) or slightly lower (1.87 eV for $O_{carb}^{(1)}$) stability compared to them.

Migration of the O atom from the most stable configuration $O_{int}^{(1)}$ to $O_{int}^{(2)}$ at the interface

Configuration	d(O*-O$_O$)	d(C-O)	Charge	Atomic configuration	E_{ads}	E_{barr}	Mechanism type
$O_{int}^{(1)}$	1.44	1.38 1.25 1.25	q_{O^*}=-0.81 $q_{O_{O^*}}$=-0.76 q_O=-0.88 q_O=-0.85 q_C=+0.70 q_{Zr}=+2.00 q_{Zr}=+1.99	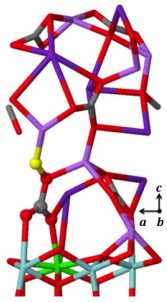	0.96	0.74	Cogwheel
$O_{int}^{(2)}$	1.44	1.34 1.25 1.26	q_{O^*}=-0.78 $q_{O_{O^*}}$=-0.29 q_O=-0.79 q_O=-0.77 q_C=+0.62	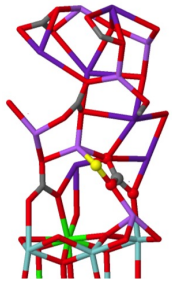	1.29	0.74	Cogwheel
$O_{int}^{(3)}$	1.44	1.35 1.27 1.24	q_{O^*}=-0.82 $q_{O_{O^*}}$=-0.29 q_O=-0.73 q_O=-0.77 q_C=+0.60	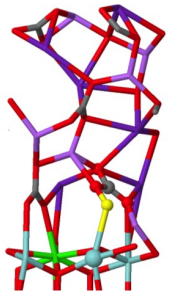	1.57	-	-
$O_{int}^{(4)}$	-		q_{O^*}=-0.69 q_{Zr}=+2.04 q_{Zr}=+2.20	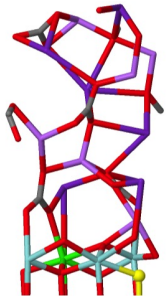	1.58	-	-

Table 6.8: Parameters of selected configurations for an O atom (O*) at the interface of the YSZ-LiKCO$_3$ composite (O$_{int}$): distance (d(O*-O$_O$), in Å) between the O* and the oxygen atom of the CO$_3$ group on which it is adsorbed (O$_O$), distances between the C atom and the O atoms of this carbonate group, Mulliken charges on selected atoms, stick representation of the corresponding atomic configuration evidencing the position of the O* atom (in yellow), formation energy (E$_f$, in eV), energy barrier associated to the O atom diffusion (E_{barr}, in eV) and relative mechanism type.

Configuration	d(O*-O_O)	d(C-O)	Charge	Atomic configuration	E_{ads}	E_{barr}	Mechanism type
$O^{(1)}_{carb}$	1.46	1.38 1.25 1.26	q_{O^*}=-0.81 $q_{O_{O^*}}$=-0.34 q_O=-0.76 q_O=-0.72 q_C=+0.64	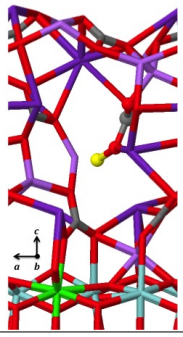	1.27	0.95	Cogwheel
$O^{(2)}_{carb}$	-	1.35 1.25 1.26	q_{O^*}=-0.75 $q_{O_{O^*}}$=-0.29 q_O=-0.81 q_O=-0.74 q_C=+0.61	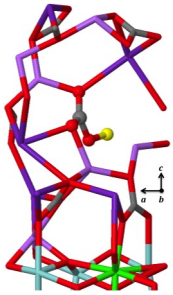	1.87	0.95	Cogwheel

Table 6.9: Parameters of selected configurations for an O atom (O^*) in the carbonate bulk phase of the YSZ-$LiKCO_3$ composite (O_{carb}): distance (d(O^*-O_O), in Å) between the O^* and the oxygen atom of the CO_3 group on which it is adsorbed (O_O), distances between the C atom and the O atoms of this carbonate group, Mulliken charges on selected atoms, stick representation of the corresponding atomic configuration evidencing the position of the O^* atom (in yellow), formation energy (E_f, in eV), energy barrier associated to the O atom diffusion (E_{barr}, in eV) and relative mechanism type.

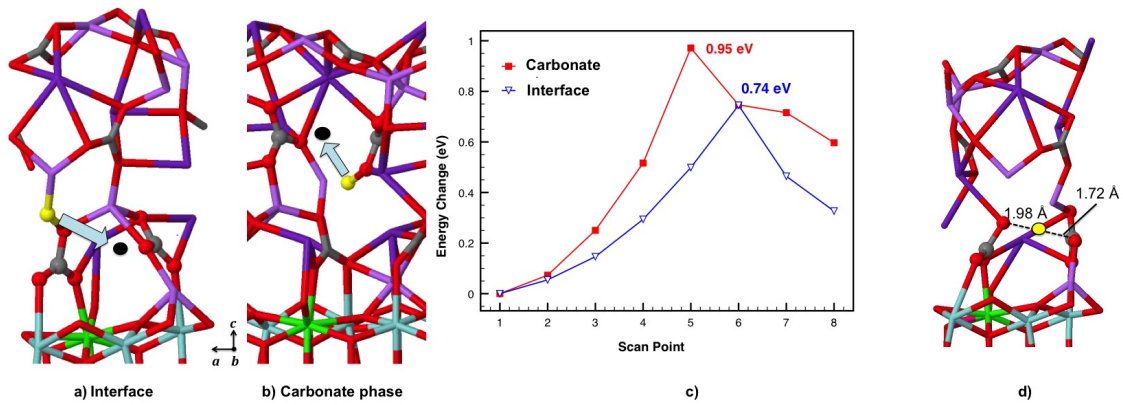

Figure 6.10: Schematic representation of the path for the cogwheel mechanism for the O atom migration at the a) interface from configuration $O_{int}^{(1)}$ (in yellow) to configuration $O_{int}^{(2)}$ (in black) or b) in the carbonate bulk phase in YSZ-$LiKCO_3$ from configuration $O_{carb}^{(1)}$ (in yellow) to $O_{carb}^{(2)}$ (in black). c) Variation of the energy as a function of the O atom position along the path. d) Structure of the configuration associated at the maximum along the path for the migration at the interface.

or from configuration $O_{carb}^{(1)}$ to $O_{carb}^{(2)}$ in the bulk carbonate phase according to the cooperative cogwheel mechanism of equation 6.9 has been subsequently studied. Figures 6.10a-b show a schematic path for this mechanism, while figure 6.10c reports the corresponding energy profile. For instance, at the interface, the oxygen transfer starts with the stretching of the O^*-O bond in configuration $O_{int}^{(1)}$ between the adsorbed oxygen and the oxygen atom of the bidentate CO_3 group to which O^* is bound. This distance is elongated, while the distance between O^* and one of the oxygen of the monodentate carbonate present in the boundary layer of the composite starts to be shortened, showing a concerted bond breaking and forming process. In correspondence of the maximum encountered along the energy profile (see figure 6.10c) a O-O-O linkage is formed, as shown in figure 6.10d. The same description holds for the case of oxygen transfer in the carbonate phase. Migration in the carbonate phase is associated to a slightly higher barrier of 0.95 eV, while at the interface the maximum along the profile corresponds to an energy value of 0.74 eV. DFT calculations on the oxygen migration in molten Li_2CO_3, Na_2CO_3, and K_2CO_3 carbonates according to this cogwheel mechanism have been already performed by Lei et al.[407]. Molten carbonates were simulated through clusters models and the barriers were calculated to be 1.06, 1.36, and 1.33 eV for Li_2CO_3, Na_2CO_3, and K_2CO_3, respectively, at B3LYP level. Our simulations, performed through a periodic approach on a mixed carbonate phase ($LiKCO_3$) in a solid amorphous-like state with the hybrid PBE0 functional, provided barriers that are close to the ones obtained by Lei in the case in which the migration takes place in the pure bulk carbonate phase and are even lower in the case in which the migration takes directly place at the interface.

In conclusion, we have seen how the interface in the YSZ-$LiKCO_3$ composites can influence the migration of the O atom. The adsorption at the interface on the bidentate CO_3 group on the YSZ surface is much more favorable than all the other configurations identified

both at the interface and in the carbonate bulk phase. Furthermore O transfer at the interface was also found to be associated to a low barrier of 0.74 eV, that is 0.21 eV lower than the one for the migration in the carbonate phase, indicating that this process in the composite is fairly easy, but that can also be boosted when taking place in the boundary layers between the two phases.

6.4.3 Proton transport

As we already discussed in more details in chapter 1, in order to explain the enhanced conductivity at lower temperature, oxide-carbonate composite electrolytes were claimed to be multi-ionic conductors made by both intrinsic (M^+, CO_3^{2-}, and O^{2-}) and extrinsic (H^+) species.[89,92–95] In particular, since these materials are considered to be dual or hybrid H^+/O^{2-} conductors, a lot of efforts have been devoted to the investigation of proton transport mechanism in these materials, despite the fact that there are many contradictory results regarding the actual contribution of H^+ to the overall conduction and more importantly despite the huge debate around the the origin of the protonic conduction.[22,93,126]

The first proposed mechanism for hybrid conduction was suggested by Zhu and Mellander[88] and is based on oxide ion conduction in the oxide phase and proton conduction in the carbonate phase through temporal bonding H^+-CO_3^{2-} (HCO_3^-) mechanism. Using defect chemistry this process can be described by the following equation[103]:

$$H_i^\bullet + X_X^X \longrightarrow HX_X^\bullet \tag{6.10}$$

where X indicates a carbonate ion site in the carbonate lattice.
However, the possibility of proton being transported by forming bicarbonate ions (HCO_3^-) is not widely accepted, since there is no such evidence for molten carbonate fuel cells.[94]
For example, Huang et al.[103] believed that at low temperature with low carbonate mobility, it is more reasonable that proton is first formed on the surface of the oxygen site in the oxide lattice and then it becomes an interstitial specie in the interfacial regions, where the transport should take place.
Finally, Zhu and Mat[89] suggested that the interfaces can constitute conduction routes for the hybrid H^+/O^{2-} conduction, where a conduction chain H—O-H, H-O-H, and O-H—O atoms/ions involving the hydrogen and the oxygen species adsorbed on the surface of the oxide can take place introducing an interfacial conducting path/mechanism that can play a key role in the large conductivity enhancement. Going even further, Wang et al.[147] proposed an empirical 'Swing Model' to interpret the proton conduction in composites, suggesting that a proton can form metastable hydrogen bonds with O atoms from both the oxide phase and the carbonate anions. This phenomenon can result in a process of continuous hydrogen bond breaking and formation taking place at the oxide-carbonate interface, in which the carbonate groups serve as a bridge for the proton to move from one hydrogen bond to the other. This process is believed to be even more important when the operating temperature is above the transition temperature of the carbonate phase, where the bending and stretching vibration of C-O bonds are enhanced as well as mobility and rotation of the CO_3^{2-} groups.

Configuration	Atomic configuration	E_f	E_{barr}	Mechanism type
$H_{int}(1)$	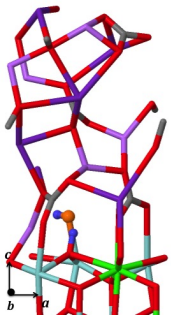	-2.52	2.19 1.06	Linear Direct Hopping Non Linear Direct Hopping
$H_{int}(2)$	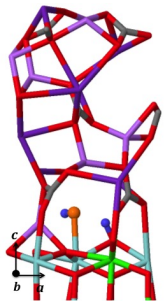	-2.35	2.19 1.06	Linear Direct Hopping Non Linear Direct Hopping
$H_{carb}(1)$	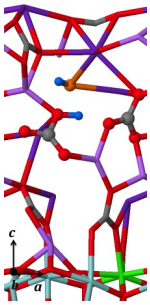	-1.76	0.16 0.35	Intermolecular H transfer Rotation
$H_{carb}(2)$	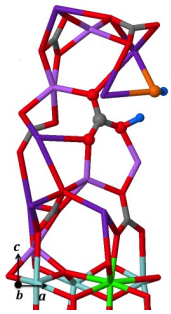	-1.61	0.16 0.35	Intermolecular H transfer Rotation

Table 6.10: Parameters of selected configurations for two protons (H^+) and one oxide ion (O^{2-}) in the YSZ-$LiKCO_3$ composite: stick representation of the corresponding atomic configuration evidencing the position of the O^{2-} ion (orange ball) and protons (light blue balls), formation energy (E_f, in eV), energy barrier associated to the proton atom diffusion (E_{barr}, in eV) and relative mechanism type.

In order to investigate the energetics of proton transport in these composite materials, we introduced proton species in the YSZ-$LiKCO_3$ model. In every case, two H^+ and one O^{2-}, so as to guarantee the neutrality of the unit cell, were randomly added in the unit cell, at the interface or in the bulk carbonate phase, before performing the geometry optimization. The most stable configurations we were able to identify are reported in table 6.10 together with the corresponding formation energy. All the configurations are associated to negative values of the formation energies indicating that this process is a favourable one, even if not as much as the simultaneous formation of $2Li_i^{\bullet}$-O^{2-} species described in the previous section. When the two protons and the oxide ion are introduced at the interface, one H^+ and the O^{2-} form an OH group which is adsorbed on one of the cation surface sites of the oxide, while the remaining proton preferably interacts with the oxygen atoms on the YSZ surface. In none of the configurations obtained by randomly introducing the three ions at the interface, the remaining proton was found to interact with one of the oxygen atoms of the carbonate groups at the interface. The two most stable configurations we were able to found, $H_{int}(1)$ and $H_{int}(2)$, in which the proton adsorbed on the oxide is closer to a carbonate group compared to the first one, are however close in energy, with formation energy values of -2.52 and -2.35 eV. When the protons and the oxide ions are added instead in the bulk carbonate phase, the OH group is formed again and stabilized by the interaction with the cations of the carbonate, while the remaining proton interacts with one carbonate group forming a bicarbonate ion HCO_3^-. Formation energies indicate that also in this case the process is favourable, but the most stable configurations $H_{carb}(1)$ and $H_{carb}(2)$ are about 0.6 and 0.9 eV less stable than $H_{int}(1)$ or $H_{int}(2)$.

As we just reminded, the first proton conduction mechanism proposed by Zhu and Mellander[88] takes place in the carbonate phase through temporal bonding H^+-CO_3^{2-}. We consequently started studying the proton transfer in the carbonate phase according to the path described in figure 6.11a: in the first step the proton is transferred from the most stable $H_{carb}(1)$ configuration to the second most stable $H_{carb}(2)$, one through an inter-carbonate ion transfer, subsequently it rotates around the oxygen atom of the carbonate in configuration $H_{carb}(2)$ while still remaining bonded to it and at this point it can be again transferred to another carbonate through intermolecular proton transfer (step 3). We can thus imagine that the H^+ transport in the carbonate phase requires a continuous sequence of intermolcular proton transfer and rotation steps. From figure 6.11b, showing the energy change along the selected path, we can observe that the inter-carbonate H^+ transfer is associated to a small barrier of 0.18 eV, while the rotation requires an higher barrier of 0.35 eV. In correspondence to the maximum associated to the first intermolecular transfer, a O-H-O linkage is formed (cf. inset M_1 in figure 6.11b): the distance of the H^+ from the O atom to which it was originally bonded is stretched to a value of 1.33Å and the proton is starting to interact also with the O atom of the carbonate group toward which it is migrating, at a distance of 1.15 Å.

Proton transfer in alkali carbonates was previously studied by Lei et al.[412] through DFT calculations. The authors considered both the crystal structure of Li_2CO_3 and the molten state, which was simulated through a cluster approach. The results they obtained (rotation barriers between 0.20 and 1.14 eV and intermolacular proton transfer barriers ranging between 0.02 and 1.12 eV along different directions in the crystalline lithium carbonate and a barrier of 0.08 eV for the intermolecular process in the cluster system) indicate that a fast proton can be

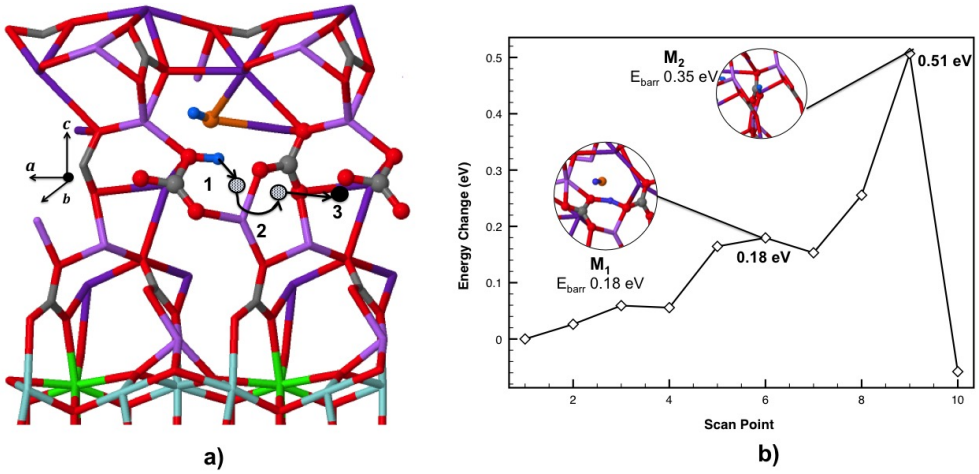

Figure 6.11: a) Schematic representation of the suggested conduction path for proton species in the bulk carbonate phase of the YSZ-LiKCO$_3$ composite. The step 1 represents an intermolecular proton transfer between two carbonate groups (from configuration $H_{carb}(1)$ to configuration $H_{carb}(2)$). In step 2, the proton rotates around the C-O bonds of the CO$_3$ group to which it is bound, so as to assume the right orientation to be easily trasferred to another carbonate group through a second intermolecular H$^+$ trasnfer (step 3). b) Corresponding variation of the energy as a function of the proton position along the path. The initial and final position of the proton is indicated by the light blue and black spheres, respectively, while the white spheres represent intermediate positions.

feasible in the carbonate phase. Our data are in good agreement with these results, especially if we consider that in our simulations we are dealing with a mixed (Li, K) carbonate phase in an amorphous-like solid state.

However, proton conduction in the carbonate phase is not widely accepted since the carbonates, extensively used as electrolytes in MCFC, are not known to be good proton conductors. There should then be an important effect of the oxide-carbonate interface. We already saw that the formation of proton-related species is indeed much more favourable from a thermodynamic point of view when the protons are introduced close to the interfaces, where H$^+$ can interact with the oxygen atoms of the oxide. We consequently investigated also the energetic of proton transfer at the YSZ-LiKCO$_3$ interface. The first mechanism we took into account is a simple linear direct-hopping mechanism according to which the proton adsorbed in the oxygen site of the YSZ lattice, as suggested by Huang et al.[103], becomes an interstitial specie at the interface and diffuses from the initial position in the most stable configuration $H_{int}(1)$ to a final equivalent one (see figure 6.12a). We just considered the transport along the *a*-axis because of the presence of the OH group along the *b* direction. However, the energy profile obtained for this mechanism shows very high barriers (about 3 eV for the highest one, cf. figure 6.12b). We consequently wanted to investigate if the interaction with the carbonates or with the oxygen species that can be present on the surface of the oxide can influence the energetic of the proton transport at the interface. We then studied the path represented in figure 6.13a: in the first step, the proton migrates from its initial position on the oxide sur-

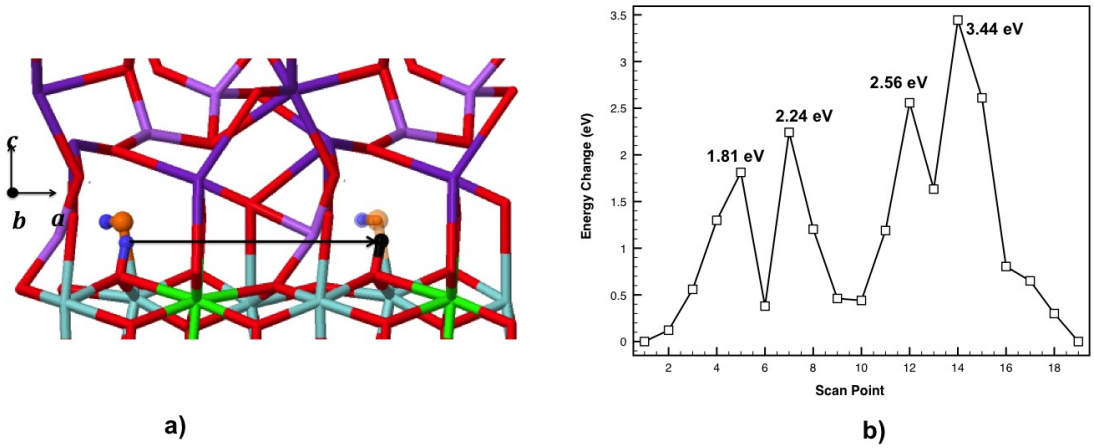

Figure 6.12: a) Schematic representation of the linear direct-hopping path through which the proton adsorbed on the YSZ surface site migrates from its initial configuration ($H_{int}(1)$) to final equivalent one through several intermediate interstitial positions. b) Corresponding variation of the energy as a function of the proton position along the path. The initial and final positions of the proton are indicated by the light blue and black spheres, respectively.

face in configuration $H_{int}(1)$ to an interstitial position at the interface where it interacts with the OH group which was introduced at the interface together with it, while in the following step, it is transferred from this interstitial position to another oxygen surface site. In these first two steps a conduction chain H—O-H, H-O-H, and O-H—O atoms/ions involving the hydrogen and the oxygen species adsorbed on the surface of the oxide, according to the interfacial conducting mechanism that according to Zhu and Mat[89] is established. In the third step, H^+ migrates toward the bidentate carbonate on the YSZ surface, in the fourth it rotates around the oxygen atom of this CO_3 group, while in step 5 it is transferred again toward an oxygen surface site of YSZ. Finally, in the sixth and last step, it migrates toward a final position equivalent to the initial one by interacting with the monodentate CO_3 group adsorbed on YSZ. In this second part of the selected path (steps 3 to 6), there is process of continuos hydrogen bond breaking and formation taking place at the oxide-carbonate interface, in which the carbonate groups serves as a bridge for the proton to move from one hydrogen bond to the other, as in the 'Swing Model' suggested by Wang et al.[147].

As we can see in figure 6.13b, the maxima of the first migration step (inset M_1) is associated to a barrier of 0.23 eV and a structure in which the proton is at a distance of 1.45 Å from the initial YSZ oxygen surface site in configuration $H_{int}(1)$, 1.52 Å from the O of the OH group added at the interface, and 2.02 from one of the O atom of the closest carbonate group. In step 2, a barrier of 0.33 eV corresponds to a maximum in which the proton interacts again with the OH group (at 1.11 Å) and with another O atom of the YSZ surface (at a distance of 1.68 Å, see inset M_2). The extremely low barriers obtained for these steps thus suggest that the presence of the oxygen species adsorbed on the surface of the oxide at the composite interface can introduce an interfacial conducting path through a chain of hydrogen bond breaking and formation between the conducting proton and the adsorbed oxygens.

Moving to the second part of the path, in the third step a maximum of 0.21 eV in which

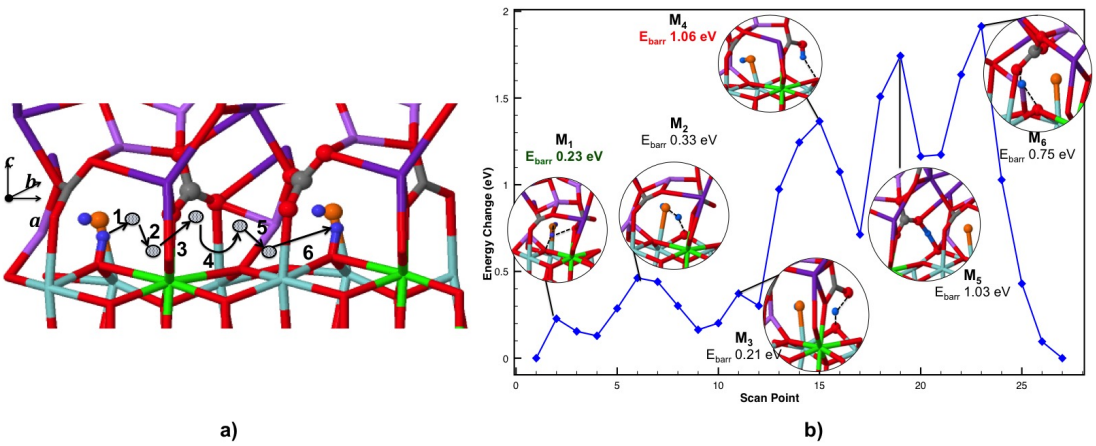

Figure 6.13: a) Schematic representation of the path of the non linear direct hopping mechanism for a proton migrating at the interface of the YSZ-$LiKCO_3$ composite: in step 1 the proton (light blue sphere) migrates from YSZ surface site on which it is adsorbed (configuration $H_{int}(1)$) to an interstitial position interacting with the oxide ion (orange sphere) that was also introduced at the composisite interface; in step 2, the proton migrates from this interstitial position to another oxygen atom of the YSZ suface, from which, in step 3, migrates toward the nearest bidentate carbonate group; step 4 requires the rotation of the proton around the C-O bond, before it migrats toward the surface position indicated as 5. In the final step 6, H^+ directly diffuses to a position equivalent to the starting configuration. b) Corresponding variation of the energy as a function of the proton position along the path. The insets show the structure of the maxima encountered along the path. The initial and final position of the proton is indicated by the light blue and black spheres, respectively, while the white spheres represent intermediate positions.

the proton still interacts with the oxygen of YSZ and also with the O of a CO_3 group (at a distance of 1.11 Å and 1.61 Å, respectively, see inset M_3) is encountered. The rotation step 4 is instead associated to the highest barrier of 1.06 eV. In the corresponding maximum, the proton is still linked to the O atom of the carbonate around which is rotating and is at a distance of 2.12 Å from the oxygen atom of the oxide to which it will be transferred in the next step. The inset M_5 shows the highest energy structure associated to this step: the proton clearly interacts with both the carbonate group (at 1.25 Å) and the YSZ oxygen atom (at 1.36 Å), while the computed barrier is 1.03 eV. A slightly lower barrier of 0.75 eV, in which again the proton is in between a CO_3 group and the final O surface site (at distances of 1.04 and 1.61 Å respectively, cf. inset M_6). The energy barrier encountered along the second part of the interface path we investigated are higher than the ones found in the first part, but still definitely lower than the ones obtained in figure 6.12b for the linear interestitial mechanism at the interface. These results suggest that the continuous hydrogen bond breaking and formation process involving the oxygen of the oxide ion or of the carbonate groups can indeed influence the energetic of the proton transport at the interface. The value of 1.06 eV is low, yet still quite high to explain the conductivity enhancement. Anyhow, we have to remember that in this interface model the carbonate phase is in an amorphous but solid state and when proposing the 'Swing Model' Wang et al.[147] suggested that this phenomenon is particularly important when the carbonate is in the molten state, where the bending and stretching vibration of C-O bonds are enhanced as well as mobility and rotation of the CO_3^{2-} groups, thus enhancing even more the proton transport.

In conclusion, we described the effect of the oxide-carbonate interface on the energetic of proton transport. H^+ migration in the bulk carbonate through temporal bonding H^+-CO_3^{2-} is associated to very low barriers. However, the formation of proton species is way more favourable at the interface where the proton can interact with the oxygen atoms on the oxide surface. At the interface, the presence of oxygen species adsorbed on the oxide seems to definitely help lowering the proton migration barriers already at low temperature. Also the interaction with the carbonates, acting as a bridge for proton between different oxygen surface sites, can decrease the migration energy, but it is reasonable that this effect becomes more important at higher temperature where the enhanced movements of the carbonate group in the melted state can favour the transfer. Here, we should stress that unfortunately this study does not provide information on the origin of the proton species, yet it provides important information on the energetic associated to the H^+ transport in the material.

6.5 Preliminary Results of the MD Simulations

So far we illustrated how static DFT calcultions can be used to provide a suitable interface model and we have seen how, already at low temperatures, these interfaces strongly influence the conduction properties. We can consequently imagine that this influence on the transport properties could be even greater at higher temperatures, where the carbonate phase is melted. As shown when explaining the research strategy in chapter 1, the next step will thus require some calculations where dynamics is taken into account. Starting from the interface model we simulate the behaviour of the system after the melting of the carbonate phase. Never-

	This work	Exp.[413]
T	1000	1100
D_{Li}	1.01	-
D_K	1.20	$3.81 \cdot 10^{-3}$
D_C	0.83	$3.53 \cdot 10^{-3}$
D_{O_C}	0.90	

Table 6.11: Comparison between the computed and experimental values of the diffusion coefficients (D_X, in units of 10^{-2} cm^2/s for the different species of the carbonate phase. Temperature (T) in K.

	This work	Exp.[413]
$E_a^{(D_{Li})}$	0.27	-
$E_a^{(D_K)}$	0.41	0.50
$E_a^{(D_C)}$	0.42	0.51
$E_a^{(D_{O_C})}$	0.26	

Table 6.12: Comparison between the computed and experimental values of the activivation energy for the diffusion coefficients ($E_a^{(D_X)}$, in eV) for the different species of the carbonate phase.

theless, this step is a very challenging problem. Classical MD can be an interesting choice considering the size of the interface model we previously described. However, it could require a slow process to identify and validate an adequate force field. For this reason, we started investigating the oxide-carbonate interface through *ab-initio* MD simulations, using as interface model the one with a thicker carbonate layer (YSZ^{3L}-$LiKCO_3^{5L}$). In this section we will briefly discuss some very preliminary results obtained from these AIMD calculations at 1000, 1150, and 1250 K, mainly with the aim of showing the complexity and the challenge associated to the work that is currently undergoing.

Tables 6.11 and 6.12 report the diffusion coefficients (D_X) and the related activation energies ($E_a^{(D_X)}$) for Li, K, C, and the O atoms of the carbonate groups.

Diffusion coefficient of a specie X was calculated from the mean square displacement (Δr_X^2) using the Einstein relation:

$$D_X = \frac{1}{6} \lim_{t \to \infty} \frac{\Delta r_X^2}{\Delta t} \tag{6.11}$$

The activation energy for diffusion was thus determined from a data fit on the Arrhenius's plot using the following equation:

$$D_X = D_X^0 \exp(-E_a^{D_X}/RT) \tag{6.12}$$

The values of the diffusion coefficients we obtained are shown in table 6.12, where they are compared with the experimental values of the coefficients for K^+ and CO_3^{2-} diffusion

in the pure eutectic Li-K mixture, which is the only available information. The qualitative picture that we derive from this data shows that Li^+ seems to diffuse more easily than K^+, which can be related to the smaller weight and size of the former compared to the latter. The diffusion coefficients for the C and O atoms, covalently hold together to form the carbonate groups, are instead smaller than the ones of the two cationic species in the melt. A similar conclusion can be drawn from a qualitative analysis of the activation energies in table 6.12. It is worth to note that, from a quantitative point of view, the computed values are definitely higher than the experimental data, while the activation energies in table 6.12 are, instead, in overall good agreement with the experimental ones. In order to explain this result, we must remember that the value of diffusion coefficient strongly depends on the density of the model used to simulate the material. On the other side, the activation energy just describes the temperature dependence for the diffusion and this can explain why this is overall in line with the experimental data. First of all, in VASP surfaces are simulated through a 3D slab scheme that requires the presence of an adequate vacuum layer along the direction perpendicular to the surface plane, in order to prevent interaction between succesive slabs. In the presence of this vacuum layer, the volume of the liquid carbonate phase can increase during the simulation determining a reduction of the density which can lead to higher mobilities and consequently to higher diffusion coefficients. This problem was already pointed out by Costa and Ribeiro[414] in their MD study of molten Li_2CO_3-K_2CO_3, where they observed that a 10% decrease in density value causes a significant difference in the diffusion coefficients. We can thus try to apply a scaling factor in order to recover most of the experimental value, as already done in classical MD simulations[318] of Li-Na eutect mixtures. A refinement of the model, by checking the influence of the applied exchange and correlation functional on the structure, or by using larger unit cells with more carbonate layers, can thus be made in future studies trying to identify a more adequate model and computational protocol which will provide more accurate results for the absolute values of the diffusion coefficients, while activation energies are already in relative good agreement.

6.6 Conclusions

In this chapter, we presented the very first DFT investigation of the stability, structural, electronic and vibrational properties of the YSZ-$LiKCO_3$ interface, together with the investigation of the conduction mechanisms in this material. The following conclusions can be drawn from the analysis of the obtained results:

- The large adhesion energy computed (3.19 eV) indicates a strong interaction between the two phases, which has two main origins: adsorption of the ionic species of the salt on the oxide surface and minimization of the elastic strain due to the lattice mismatch between the two surfaces, resulting in a disordered amorphous-like state for the carbonate phase, in agreement with the experimental observations.

- The material shows a band gap of 5.78 eV, very close to the one of pure YSZ and a major ionic character for the ion-ion interactions between YSZ and $LiKCO_3$, with a slightly higher covalent contribution in the case of the adsorption of CO_3^{2-} groups on the oxide surface sites.

- Computed IR and Raman spectra showed an overall very good agreement with measured experimental data, validating the proposed interface model, which is an important first step towards the modelling of transport mechanisms at the interface between oxides and carbonates in composite electrolytes.

- The results obtained for Li transport in the composite are in agreement with the concepts on which Maier's 'space charge layer' model is based: the interfaces in oxide-carbonate composites can reduce the formation energy of Li-related defects because of the chemical affinity of the O atoms of the oxide for these species, but the interstitial Li species are trapped at the interfaces as suggested by the high diffusion barriers. Li transport can, instead, occur through a vacancy hopping mechanism, since the Li vacancy created in bulk carbonate, as a consequence of the interfacial interaction, can easily diffuse, with very low barriers, in the so formed space charge layer.

- The formation of negatively charged oxygen species associated with the cations of the carbonate phase was found to be a favourable process, suggesting again that a space-charge layer can indeed be easily formed at the phase boundaries due to the interfacial interaction. Further investigations, especially at higher temperatures when the carbonate is in the molten state, are however necessary to verify if and how this higher defect concentration at the interfaces can effectively constitute high conduction pathways for the oxide ion. Moreover, we were already able to show how the interface in the YSZ-$LiKCO_3$ can boost the O atom migration, in a process that can be important for the composite-based SCFCs.

- The interface can help also the formation of H-related defects through interaction of H^+ with the oxygen sites of the oxide. Here, the presence of the carbonates and especially of oxygen species adsorbed on the oxide play an important role in the lowering of the barrier associated to proton migration at the interfaces.

In summary, we applied the multi-step strategy designed in the first chapter to model oxide-carbonate composites to the case of YSZ-$LiKCO_3$ materials. We identified and validated a simple model of the YSZ-$LiKCO_3$ interface, providing an overall good agreement with available experimental data. This model was used to provide information on the structural, electronic properties of the material, and more importantly to investigate the conduction mechanisms, which resulted to be extremely influenced by the interfaces. Results reported in this chapter consequently represent an important step toward a deeper understanding of the electrochemical processes determining the performances of these electrolytes and illustrate the applicability of the computational approach suggested to treat these systems, that can also be applied to simulate other composites, as we will show in the next chapter for TiO_2-$LiKCO_3$ materials.

Chapter 7

DFT simulation of TiO_2-$LiKCO_3$ materials

Confusion is a word we have invented
for an order that is not yet understood.
Henry Miller

Contents

7.1 Introduction **227**
7.2 Computational Details and Models **228**
7.3 Structure and Stability of the TiO_2-$LiKCO_3$ interface **230**
7.4 TiO_2-$LiKCO_3$ Electronic Properties **233**
7.5 Li intercalation at the TiO_2-$LiKCO_3$ interface **236**
7.6 Conclusions **242**

7.1 Introduction

In the experimental work illustrated in chapter 3, together with YSZ-based composites, we also studied TiO_2-carbonate materials, trying to understand the effect of oxide phases with different properties on the electrochemical properties of the composites. Unfortunately, results indicated a strong reactivity between this oxide and the carbonates, with formation of titanate phases, probably associated to the partial reduction of the material when working in reducing environments. In order to provide a better understanding of the role of the interfaces in the phenomena taking place in these systems, we performed DFT calculations of the TiO_2-carbonate interface.
Naturally, the computational strategy designed in chapter 1, and illustrated in the previous ones for YSZ-$LiKCO_3$ materials, can also be applied to the modelling of the TiO_2-carbonate interface. For the carbonate phase, the model of the most stable $LiKCO_3$-(001) surface we

described in chapter 5 can be used again as a building block to obtain the interface. As concerns the oxide, we should recall TiO_2 is one of the most investigated solid state systems,[415] because of its versatility and wide range of applications in various field, ranging from paintings, gas-sensing,[416] electronics[417] or optics,[418] homogeneous[419] or heterogeneous catalysis and dye-sensitized solar cells.[420,421] It crystallises most commonly in either the rutile (space group *P4$_2$/mnm*) or anatase phases (space group *I4/amd*). For bulk TiO_2 crystals at ambient conditions, rutile is more stable than anatase, while anatase is the most stable phase for crystals of nanometric dimensions and often shows higher performances.[422–424] The bulk TiO_2 has been extensively studied both theoretically[425–438] and experimentally,[425,430,433,437,439–444]. As regards theoretical investigations, works in the framework of the DFT, either with pure functionals[430,435,445] or with hybrid methods have been widely performed.[446–448] The latters were generally found to provide results in particularly good agreement with the experimental data. Also TiO_2 surfaces have been widely investigated at the experimental and theoretical level. The most stable rutile surfaces, namely (110), (100), and (001), have attracted much attention in recent years. The (110) surface, which is the most stable one, has been extensively studied both experimentally[449–455] and theoretically.[428,432,456–464] Since the anatase polymorph is thermodynamically less stable than the latter and experimental obstacles arise to grow sufficiently large anatase single crystals, the surfaces of this polymorph have been less studied. However, titanium dioxide nanoparticles are commonly of the anatase form and they are often preferred for their superior performances. Experimentally[465,466] and theoretically, the anatase (101) and (100) surfaces have been studied at DFT level, using LDA and GGA[430,467,468] as well as hybrid approaches.[469,470]

Among this large amount of work, we would like to recall that the theoretical investigation previously performed on rutile and anatase bulk[446] and surfaces[470] in our group evidenced that, also for this material, the hybrid PBE0 functional appears as a good compromise to obtain an accurate description of both its structural and electronic properties. Moreover, the study provided a model of the most stable anatase-(101) termination, generally found in TiO_2 nanoparticles for various applications, which will be used in the following to build and study the TiO_2-$LiKCO_3$ interface.

In this chapter, we will investigate the properties and reactivity issues of TiO_2-$LiKCO_3$ composite materials through periodic DFT calculations. We will first describe the structure and stability of the TiO_2-$LiKCO_3$ interface, whose model was built using the same strategy designed for YSZ-$LiKCO_3$ in the previous chapters. Its electronic properties will then be described in detail, before analysing the reactivity issues of these materials by the Li intercalation processes (at the base of titanates formation) in the clean Ti_2-(101) surface and at the oxide-carbonate interface.

7.2 Computational Details and Models

DFT calculations were performed with the CRYSTAL14 code.[180] The PBE0[172,173] functional was employed to solve the Kohn-Sham equations, based on the accurate and reliable description of the structural and electronic properties it provides not only for the carbonate phase, but also for TiO_2, as shown in previous works performed in our group on titanium dioxide

bulk and surfaces.[446,470]

For the Li, K, C and O atoms in $LiKCO_3$, we used the same basis sets already applied for the study of $LiKCO_3$ bulk and surfaces (cf. chapter 5). In order to reduce the cost of the calculations, Durand and Barthelat[297,298] large core pseudopotentials with associated (31/31) and (1/1/41) contractions were, instead, used to describe the O and Ti atoms of the oxide phase, with the exponents re-optimized by Labat and Adamo.[471] These pseudopotentials have been already proven to yield a good description of TiO_2 bulk[472,473] and surfaces.[471]

The TiO_2/$LiKCO_3$ interface was built starting from models of the oxide and carbonate most stable surfaces that were previously found to ensure convergence of the structure, surface energy and of the electronic properties of each phase. As regards, the oxide phase the building block is a (2x2)-supercell model of the anatase TiO_2-(101) surface with a depth of 10 slab layers (ten O-Ti-O trilayres) for a total of 120 atoms with $Ti_{40}O_{80}$ stoichiometry. This supercell has cell parameters a=7.470 Å, b=11.012 Å, γ= 109.827°(see figure 7.1a).[471] For the carbonate phase, a slab model of the $LiKCO_3$-(001) termination with a depth of 5 slab layers (five Li-O-K-O-C-O_2-C-O-K-O-Li layers) for a total of 60 atoms and a $Li_{10}K_{10}(CO_3)_{10}$ stoichiometry was considered. The unit cell for this surface model is characterized by cell parameters a=7.254 Å, b=7.289 Å, γ= 90°(see figure 7.1b). Considering the large mismatch in the cell paramaters of these building blocks (δ_a=3.0%, δ_b=51.0%, and δ_γ=22.0%), in order to build the interface model we applied the same procedure described for the YSZ-$LiKCO_3$ composite: we cut very large supercell models of the two surfaces ((4×4) for both the $LiKCO_3$-(001) surface and the (2×2) supercell representing TiO_2-(101)), we rotated the carbonate slab around the normal to the oxide surface plane so as to orient the CO_3 groups toward the Ti surface sites, and we finally tried to identify a new unit cell for the interface containing a number of atoms in line with the stoichiometry of each phase, thus ensuring the neutrality of the system. The final unit cell has *P1* symmetry and contains 180 atoms, 60 ($Li_{10}K_{10}(CO_3)_{10}$) belonging to the 5 layers of the carbonate phase and 120 ($Ti_{40}O_{80}$) organized in 10 O-Ti-O layers along c for TiO_2. This strategy allows to reduce lattice mismatch without the need to recur to larger unit cells which would require higher computational costs. Auxiliary calculations on the clean TiO_2-(101) surface were performed recurring to a (2x2)-supercell model of this termination.

In order to study Li intercalation, neutral interstial Li atoms (Li_i^X) were introduced in the optimized unit cell describing the oxide-carbonate interface, that, with a minimum distance between periodically repeated images of the defect of $\sim$ 7.5 Å, was found to be sufficient to avoid spurious interactions between each defects and its periodic image.

To study oxide lithium intercalation at the composite interface, diffusion barriers were qualitatively estimated by performing relaxed scan calculations positioning each time the Li at different contiguous positions along the selected migration path, through subsequent steps of 0.39 Å, as already done for the study of Li transport on the clean $LiKCO_3$ surface (cf. chapter 5) or for the study of the conduction mechanisms in chapter 6.

A Monkhorst-Pack[300] shrinking factor of 4, corresponding to 10 points in the irreducible Brillouin zone (IBZ) of the interface model was used. Numerical DFT integration has been performed with 75 radial points and 974 angular points.[180] In the case of the geometry optimization of the TiO_2-$LiKCO_3$ structure, the lattice parameters and all the atomic positions were allowed to relax during the geometry optimization, until the maximum and root-mean

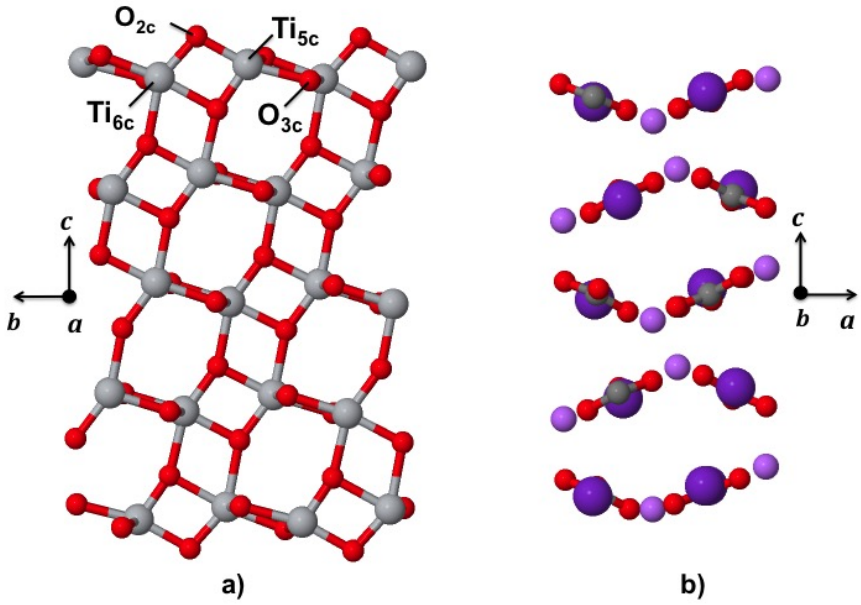

Figure 7.1: Slab models of a) anatase TiO_2-(101) surface ((2 × 2) supercell, with 10 O-Ti-O layers) and b) $LiKCO_3$ (5 slab layers).

square atomic forces and displacements were simultaneously less than $4.5 \times 10^{-4}, 3.0 \times 10^{-4}, 1.8 \times 10^{-3}$ and 1.2×10^{-3} a.u., respectively. For the investigation of Li intercalation, only the the atomic positions of the atoms belonging to the first coordination sphere around the defect were allowed to relax.

7.3 Structure and Stability of the TiO_2-$LiKCO_3$ interface

Before describing the properties of the TiO_2-$LiKCO_3$ interface, we briefly revise the main features of this oxide, whose bulk structure and surfaces have been studied in detail in previous works performed in our group.[446,470] Anatase TiO_2 is a tetragonal phase with space group *I4/amd*. It is built from distorted TiO_6 octahedra, resulting in threefold coordinated oxygen atoms. These octahedra share four adjacent edges, resulting in zigzagging chains running along the *a* and *b* lattice vectors. The slab model of the most stable anatase (101) surface is shown in figure 7.1a and each slab layer is composed by three atomic planes with a O-Ti-O motif. This surface exposes two-fold coordinated oxygen atoms (O_{2c}) bonded to five-fold coordinated titanium atoms (Ti_{5c}) in the second layer. These cations are in turn bonded to three-fold coordinated oxygens (O_{3c}) in the *b* direction, where channels are formed. PBE0 was demonstrated to provide an accurate and reliable description of bulk and surfaces stuctural and electronic properties.

Figure 7.2 shows the optimized geometry of the TiO_2-$LiKCO_3$ interface model we built starting from the most stable TiO_2-(101) and $LiKCO_3$)-(001) surfaces. Table 7.1 reports the optimized cell parameters of the *P1* supercell describing the interface.

As observed in the case of the YSZ-$LiKCO_3$ composite, the oxide phase maintains its

crystalline structure with small deviations from the geometry of the bare surface: the average displacements are of 0.01 Å along *a*, -0.02 Å along *b*, and 0.04 Å along *c*, with the highest deviations normally observed for the Ti and O_{2c} atoms in the outermost layer in contact with the carbonate phase. In particular, the two Ti_{5c} directly interacting with the carbonate groups and the O_{2c} atoms in figure 7.2 are displaced outward, toward the CO_3 units ($\sim$ 0.38 and 0.11 Å, respectively), while the fully coordinated Ti (Ti_{6c}) of the outermost oxide layer are displaced inward ($\sim$ -0.13 Å).

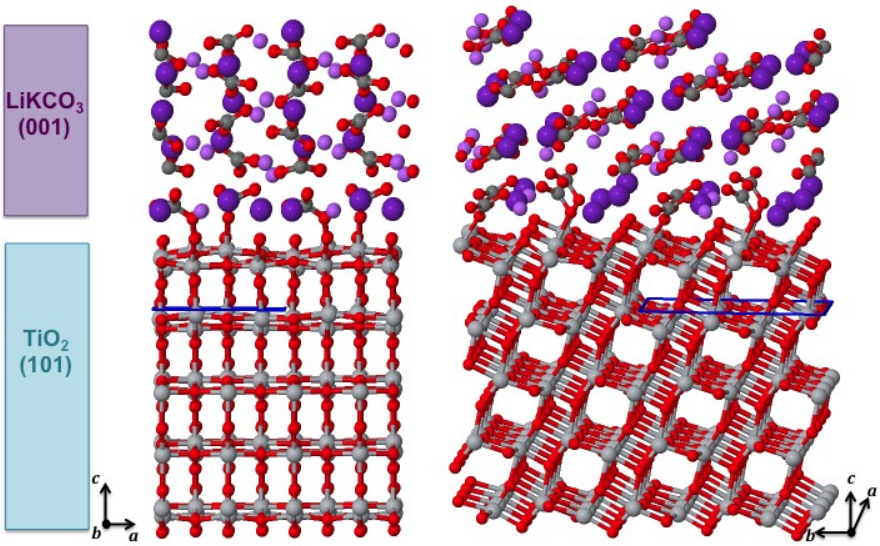

Figure 7.2: Two different views of the optimized geometry of the TiO_2-$LiKCO_3$ interface-model of the composite, shown as a (2×2) supercell of the interface model for clarity. Solid blue line indicate the unit cell. Ti and O atoms are in dark grey, and red, while C, Li and K are in light grey, light violet and purple, respectively.

Again, important changes are, instead, obtained for the structure of carbonate phase. First of all, the interaction between the oxide and the carbonate in the boundary layer implies the adsorption of both the carbonate groups and the cations of the carbonate on the TiO_2 surface, respectively, on the Ti or O surface sites. The creation of Ti-O bonds between the oxygen atom of the carbonate groups leads to two monodentate groups, if we just consider the coordination of these units to the oxide. The lengths of these Ti-O bonds, of about 1.99 and 2.03 Å, are in line with the average length computed for the Ti-O bonds in the oxide lattice (1.95 Å)). The C-O bonds in the two carbonate groups coordinated to TiO_2 (ranging between 1.27 and 1.28 Å) are all very close to the value of the length in the pure carbonate phase (1.28 Å), with the exception of the C-O for the O atom directly linked to a Ti cation, which is sligthly elongated in both cases (1.32 Å). This indicates that, even if these two groups are tilted toward the TiO_2 surface so as to ensure the interaction with the Ti surface sites, the carbonate moities behave as rigid units. As regards the cations, we can observe that both Li and K species in the boundary layer interact with the O surface site of TiO_2 at distances of about 2.07 and 2.69-3.49 Å, respectively, these values being in line with Li-O or K-O bonds in the pure carbonate phase (cf. Chapter 5). Strong rearrangements

	TiO_2-$LiKCO_3$
a	7.46
c	10.45
γ	89.69
S	78.01
$E_{ads}^{TiO_2/LiKCO_3}$	0.75
$\beta^{TiO_2/LiKCO_3}$	0.01
E_g	3.45

Table 7.1: Optimized lattice vectors (a, b, c in Å), angle (γ, in degrees) and surface area (S in Å^2) of the TiO_2-$LiKCO_3$ interface model together with its adhesion energy ($E_{ads}^{YSZ/LiKCO_3}$ in eV), specific adhesion energy ($\beta^{YSZ/LiKCO_3}$in eV/Å^2), and optimized band gap (E_g in eV)

are observed also for the carbonates and the cations belonging to the layers farther away from the oxide surface; figure 7.1b shows an organized structure with large open channels oriented along the *b*-axis and with the five slab layers clearly distinguishable from each other; this is no longer true for the TiO_2-$LiKCO_3$ interface, where as a consequence of the mismatch in the lattice parameters between the two phases, especially along the *b*-axis, upon relaxation, the more flexible carbonate phase spreads over the crystalline oxide structure, so as to release the elastic energy of mechanical strains emerging at the interface.[69] The result is that the carbonate moieties are rotated along the *b*-axis and are all oriented almost parallel to the oxide surface (with the exception only of the ones directly interacting with TiO_2 in the boundary layer), resulting in a more stable amorphous-like carbonate phase. This is in line with the experimental studies reporting a core shell structure for the composites, with a crystalline oxide core covered by an amorphous carbonate layer.[19,49,98,103–107]

In order to evaluate the stability of this interface from a thermodynamic point of view, we computed the adhesion energy ($E_{ads}^{TiO_2/LiKCO_3}$) and the specific adhesion energy ($\beta^{TiO_2/LiKCO_3}$) in a similar manner to what already did for the YSZ/$LiKCO_3$ in the previous chapter (see equations 6.1 and 6.2 in chapter 6).

The positive values of 0.59 eV for $E_{ads}^{TiO_2/LiKCO_3}$ or 0.01 eV/Å^2 for $\beta^{TiO_2/LiKCO_3}$ indicate that the formation of the interface is definitively a favourable process, since it is accompained by a gain in energy. However, these values are lower than the corresponding ones obtained in the case of the YSZ-$LiKCO_3$ material (cf. chapter 6), in agreement with the larger lattice misfit observed in the case of the TiO_2-$LiKCO_3$ interface.

In conclusion, the positive adhesion energy computed for the TiO_2-$LiKCO_3$ interface indicates that a favorable interaction can take place between the carbonate $LiKCO_3$-(001) and the TiO_2-(111) surfaces, with the carbonate spreading along the oxide surface. As already observed in the case YSZ-$LiKCO_3$, the analysis of the interface structure discussed above, this interaction has two main components: i) specific adsorption of the cations and anions of the salt on the crystalline oxide surface; ii) minimization of the elastic strain due to lattice misfit that is realized through the spread of the carbonate over the oxide, resulting in a more stable amorphous-like phase for the carbonate.

7.4 TiO_2-$LiKCO_3$ Electronic Properties

Figure 7.3 reports the PBE0 density of states (DOS, figure 7.3c) and band structure (figure 7.3d) of the TiO_2-$LiKCO_3$ composite, together with DOS of the pure TiO_2-(101)(figure 7.3b) and $LiKCO_3$-(001) surfaces (figure 7.3a) computed with the same computational protocol used for the composite.

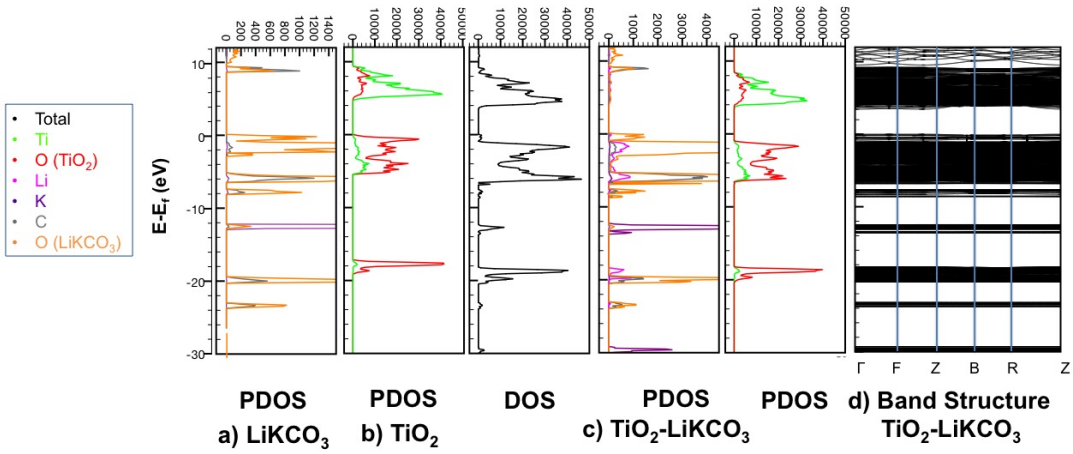

Figure 7.3: Atom projected density of states (DOS) of the clean a) $LiKCO_3$-(001) and b) TiO_2-(101) surfaces. c) Total and atom projected density of states (DOS, left) and d) band structure of the composite. The Fermi level has been set as the zero of the energy scale. The Brillouin zone path used for the band structure calculation is Γ-F-Z-B-R-Z, where in terms of the reciprocal basis vectors, Γ corresponds to the point (0,0,0), F to (0,1/2, 0), Z to (0, 0, 1/2), B to (1/2, 0, 0), and R to (1/2, 1/2, 1/2).

For ease of discussion, here, we briefly revise the electronic properties of the clean TiO_2-(101) surface. The supercell used to model this surface shows a band gap (E_g) of 4.51 eV, in line with previous theoretical calculations at PBE0 level on TiO_2 bulk (4.50 eV)[446] and on the (101) surface (4.63 eV)[470] and overestimated of about 1.00 eV compared to experimental bulk value,[474] due to the significant amount of HF exchange of the PBE0 functional.[446] Several sets of peaks can be observed in the DOS of the TiO_2 in figure 7.3b. They are well separated and correspond to O-2s states around -18 eV, O-2p states below the Fermi level between -6 and 0 eV, and Ti-3d states above the Fermi. The top of the valence band (VB) is associated to the O-2p states with a non-negligible contribution from the Ti-3d states, indicating the partial covalent nature of the bond in the material. Furthermore, a splitting of the O-2p band, due to the separation between bonding and nonbonding O-2p states, is observed. The bottom of the conduction band (CB) is, instead, associated to the Ti-3d states, split into two groups corresponding to the low energy e_g and the high energy t_{2g} states, as a consequence of the octahedral environment of the surrounding oxygen ions.

Figure 7.3c shows that between -30 and 12 eV, the electronic structure the composite has the exact same electronic states observed in the pure oxide and carbonate surfaces. Starting from the oxide contribution, we can observe the O-2s states at around -19 eV, the O-2p states

with a small contribution of the Ti-3d levels between -6 and 0.5 eV, and the Ti-3d states at around 4 eV. All the oxide electronic levels appear to be sligthly shifted (about 0.5 eV) toward lower energies due to the stabilizing interaction with the carbonate. The double-peak feature characteristic of the Ti-3d and O-2p bands in the clean surface is clearly visible even in the composite. Moving to the carbonate phase, the exact same set of six bands observed for the pure $LiKCO_3$ is obtained also in the composite: O-2s states at about -24 eV, O-2s and C-2p states around -20 eV, K-2p at -14 eV, superposition of C-2s, O-2s and O-2p at about -8 eV or of C-2p and O-2p levels around -7 eV, O-2p non bonding states under the Fermi level up to -4 eV, and, finally, C-2p states with small contribution of the O-2p in the CB at around 8.7 eV. If we carefully look at the figure 7.3c, we can note that, while the very bottom of the CB is due to the Ti-3d states as as in the clean TiO_2 surface, the very top of the VB is not associated anymore to the O-2p states of the O atoms of the oxide, but to the non-bonding O-2p states of the carbonate phase. This type of interaction results in a lower band gap of 3.45 eV for the composite (cf. table 7.1) when compared to the pure oxide (4.51 eV).

The analysis of the DOS plot allows us also to characterize the interaction between different species in the composite material. The strong overlap between the C and O states for the carbonate phase confirm again the covalent nature of the C-O bonds in the CO_3 moieties, while the non-negligible contributions of Ti-3d states to the VB or of O-2p level for the O atoms of the oxide to the CB support the deviation from a purely ionic interaction already described for TiO_2 materials. The interaction between the cations of the carbonate and the carbonate units is, instead, mainly ionic as in the pure carbonate, since no superimposition between the levels relative to K or Li and the O levels of the carbonate is obtained. For the same reason, the interaction between K^+ and Li^+ species and the oxide has also an ionic behaviour. As already found for the YSZ-$LiKCO_3$ composite, a slightly stronger covalent character is observed for the interaction between the carbonate units and the Ti cations of the oxide phase, as indicated by the overlap between their O and C levels and the Ti states visible in both the CB and VB.

Mulliken atomic charges and overlap populations are collected in table 7.2. Even if this analysis tends to overestimate the covalent character in chemical bonding, it provides reasonable trends and confirm this picture. The average values are in line with the ones reported in our previous studies on the pure carbonate (cf. chapter 5) and oxide[446] phases.

They indeed clearly indicate a strong ionic character for the interaction between the cations of the carbonate and the O of the CO_3 units, together with strong covalent behaviour within the carbonate groups and a covalent contribution for Ti-O bonds in the oxide phase even in the composite.

Table 7.2 reports also the charge and bond population values averaged only over the atoms directly involved in the formation of the interface layer, that is to say the first O or Ti atomic layer of the oxide surface and the two CO_3 groups directly linked to the oxide together with the Li and K atoms adsorbed on TiO_2. Charges in this layer are in good agreement with the those obtained for the full system. Li and K have always positive charges of about +0.9*e* and +1.0*e* in both the bulk carbonate phase or at the boundary layer of the interface. Also for the two carbonates adsorbed on the oxide, the charge of the carbon atoms of these groups (+0.648 and +0.628*e*) is in line with the average value for CO_3 units in $LiKCO_3$ (+0.624*e*). As regards the O atoms of these two carbonate groups, the ones directly linked to the oxide

		Full system	Interfacial Layer
Charges	q_{Li}	+0.931	+0.935
	q_K	+1.022	+1.008, +0.999, +1.016
	q_C	+0.618	+0.648, +0.628
	$q_{O_{carb}}$	-0.849	-0.867,-0.832,-0.789
			-0.866,-0.829,-0.765
	q_{Ti}	+2.141	+2.103
	$q_{O_{ox}}$	-1.075	-0.984^{2c}, -1.115^{3c}
Bond population	$b_{Li-O_{carb}}$	+0.008	+0.010
	$b_{Li-O_{ox}}$	+0.009	+0.009
	$b_{K-O_{carb}}$	-0.010	-0.010
	$b_{K-O_{ox}}$	-0.002	-0.002
	b_{C-O}	+0.693	+0.670
	$b_{Ti-O_{ox}}$	+0.185	+0.182
	$b_{Ti-O_{carb}}$	+0.149	+0.149

Table 7.2: Mulliken charges (q, in *e*) and overlap bond populations (b, in *e*) averaged over the all atoms in the TiO_2-$LiKCO_3$ composite model or just over the ones directly involved in the formation of the interfacial layer (first O and Ti atomic layers for TiO_2, the two CO_3 groups directly linked on the oxide surface and the Li and K atoms closest to TiO_2 surface for $LiKCO_3$). $2c$ and $3c$ superscripts are referred, respectively, to the surface 2-fold and 3-fold O-coordinated TiO_2 oxygen atoms (see figure 7.1).

show charges in line with the average data (-0.867*e* and -0.866*e*), but sligthly higher than the values for the remaining O of these groups (-0.832*e* and -0.789*e* or -0.829*e* and -0.765*e*). Interfacial Ti are slightly reduced compared to the others (+2.103*e* compared to the average +2.141*e*), with the exception of the two Ti directly linked to the carbonate groups showing a charge of +2.154 and +2.176*e*. Surface O_{2c} are sligthly oxidized (-0.984*e*), while surface O_{3c} are sligthly reduced (-1.115*e*) compared to the average charge for the O atoms of the oxide.

The Mulliken bond overlap populations confirm the trends previously described for the interfaction between the species in the material, with no remarkable differences for Li-O, K-O, or Ti-O bonds in the boundary layer or in the bulk carbonate/oxide phase. Li-O and K-O are mainly ionic in nature, with slightly higher bond overlap populations when the O atoms belong to the carbonate phase ($b_{Li-O_{carb}}$=+0.010*e* vs. $b_{Li-O_{ox}}$=+0.009*e*, $b_{K-O_{carb}}$=-0.010*e* vs. $b_{K-O_{ox}}$=-0.002*e*), while Ti-O bonds show a greater covalent contribution, which is larger when the O atoms belong to the oxide phase ($b_{Ti-O_{ox}}$=+0.182*e* vs. $b_{Ti-O_{carb}}$=+0.149*e*)

In summary, in TiO_2-$LiKCO_3$ composites, the band gap is determined by the O-2p non-bonding states of the carbonate at the top of the VB and by the Ti-3d levels at the bottom of the CB. The results is a band gap of 3.45 eV, even lower than the one of the pure TiO_2 phase (4.51 eV). The interaction between the cations and the anions of the salts and the oxide on whose surface they are adsorbed, is mainly ionic, with a greater covalent character in the case of the bond between the CO_3 moieties and the Ti surface site of the oxide in the boundary layer.

7.5 Li intercalation at the TiO_2-$LiKCO_3$ interface

As we already reminded, the anatase structure has tetragonal symmetry and the structure is made by TiO_6 octahedra sharing two adjacent edges in order to form infite planar double chains with octahedral vacant interstitial sites that are large enough to accomodate Li^+ cations. Both experimental and theoretical works clearly indicate that Li atoms can indeed intercalate in the distorted octahedral cavities of titanium dioxide and that this process is associated to a charge transfer from the intercalated Li atom to a Ti site.[475–488] As concerns the theoretical studies, it is important to stress that pure DFT approaches fail in reproducing the electrochemical behaviour of these systems (band gap and electron localization properties) because of the self-interaction error inherent to the pure LDA or GGA functionals.[489,490] Previous works have been indeed mainly performed recurring to molecular mechanics,[481] HF[479] and DFT+U[480], and more recently to hybrid DFT[476,491] methods, like in our investigation based on the hybrid PBE0 functional.

The electrochemical insertion process can be schematically described as indicated by the following equation:

$$TiO_2 + x(Li^+ + e^-) \longrightarrow Li_xTiO_2 \tag{7.1}$$

where x is the mole fraction of lithium into TiO_2. It was found that in anatase, this process of intercalation follows a zig zag migration path from one octahedral hole to the next. The barrier associated to the intercalation was found to be of about 0.60 eV for bulk anatase through

	ΔE	
Site	TiO_2-$LiKCO_3$	TiO_2
Li_1	0.15	0.17
Li_2	0.18	0.69
Li_3	0.00	0.00

Table 7.3: Relative formation energy (ΔE_f, in eV) with respect to the most stable configuration for a Li_i^X defect in the TiO_2-$LiKCO_3$ composite or at the TiO_2-(101) surface.

both experimental[479] and theoretical investigations[479,480,491]. Recently, an higher barrier of 1.22 eV was instead obtained for the lithium intercalation in the most stable anatase-(101) surface in the theoretical work of Spreafico et al.[491], in which PBE0 was selected as the exchange-correlation functional of choice.

In order to complement the experimental foundings discussed in chapter 3 that clearly indicate the formation of titanate phases for TiO_2-$LiKCO_3$ samples, trying, in particular, to understand the effect of the oxide-carbonate interface in the Li intercalation process, we studied Li insertion at the TiO_2-$LiKCO_3$ interface and on the clean TiO_2-(101) surface as reference.

Figure 7.4 shows the most stable positions we were able to identify for a neutral interstitial Li atom (Li_i^X) at the TiO_2-$LiKCO_3$ interface: Li_1 corresponds to the most stable top-surface adsorption site, Li_2 and Li_3 are instead two different subsurface configurations. We did not consider Li_i^X positions in cavities in deeper surface layers, since they were find to behave like bulklike layers, where Li intercalation is less favorable.[491] Analogous configurations were also identified for the clean TiO_2-(101) surface. Table 7.3 reports the relative energy of the three configurations normalized with respect to the most stable one (Li_3) at the TiO_2-$LiKCO_3$ interface and at the bare (101) surface. In both cases, the Li_3 position in the subsurface octahedral cavity is the most stable one, followed by the top surface configuration Li_1 where the Li atom is coordinated to four O atom of the oxide,[481,491] while the subsurface Li_2 position is the least stable. The relative higher stability of configuration Li_3 compared to the Li_2 one was already observed in the work of Spreafico et al.[481,491] for the bare (101) surface, where it was explained in terms of surface relaxation effects: normally the O_{3c} of the outermost surface layer are relaxed outward, while in the presence of the interstital Li there is the contrasting attractive interaction between the interstitial specie and these oxygens; in the case of Li_3, instead, the Li specie is close to an oxide ion that normally is relaxed inward and consequently, in this case, the attraction of Li is not competing against surface relaxation. When comparing the effect of the interface, we can note that configuration Li_1 is slightly stabilised in the composite system because the interstitial Li atom, which as we will see later is almost completely ionized, can interact also with the O atoms of the neighbouring CO_3 groups. Even more importantly, Li_2, where the interstitial Li is directly below the adsorbed carbonate group is, instead, 0.51 eV more stable at the TiO_2-$LiKCO_3$ than in the clean TiO_2-(101) surface.

We can imagine that, as in titanium dioxide bulk, Li insertion takes place through a multistep zigzag path, in which the interstitial Li first migrates from position Li_1 to Li_2 and then from Li_2 to Li_3, as shown in figure 7.4. Table 7.4 reports the barrier associated to these

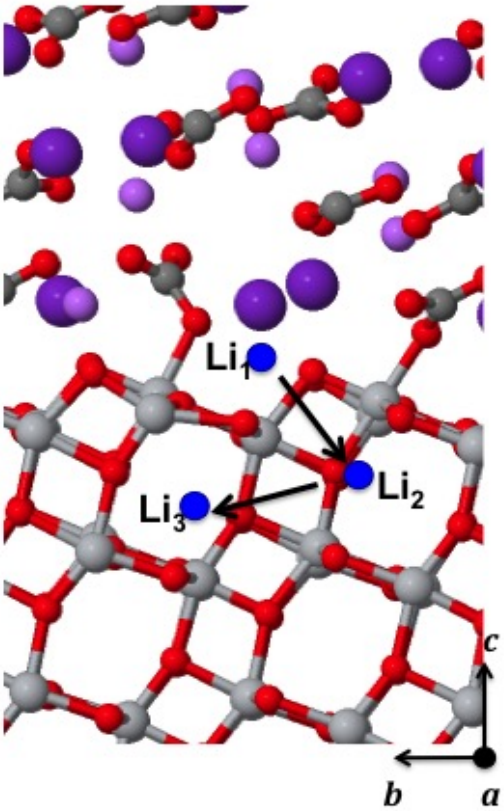

Figure 7.4: Lithium intercalation positions across the TiO_2-$LiKCO_3$ interface, together with the intercalation path. The interstitial Li specie is represented by the blue sphere.

	Path	E_{barr} TiO_2-$LiKCO_3$	TiO_2
This work	Li_1-Li_2	1.04	1.37
	Li_2-Li_3	0.74	0.26
Other work			
PBE0[a]	Li_1-Li_2	-	1.22
	Li_2-Li_3	-	0.21

a See Ref.[491]

Table 7.4: Barrier for the intercalation (E_{barr}, in eV) of Li_i^X in the Ti_2-$LiKCO_3$ interface or in the bare TiO_2-(101) surface.

two steps in TiO_2-$LiKCO_3$ and TiO_2-(101), while figures 7.5 and 7.6 show the corresponding energy profiles. If we start from the TiO_2-(101) case, we can observe that the higher barrier of 1.37 eV is associated to the $Li_1 \rightarrow Li_2$ step, while a smaller barrier of 0.26 eV is obtained for the $Li_2 \rightarrow Li_3$ migration. These values are in excellent agreement with the ones previously obtained by Spreafico et al.[491], especially if we considered that their calculations were carried out via the nudged elastic band (NEB) method, while we simply performed a relaxed scan along a linear path between the initial and final Li_i^X position for each of the two intercalation steps. At the interface, instead, where positions Li_1 and Li_2 are more stable compared to the clean system, the intercalation barrier for the first step is also lowered by 0.33 eV. Even if the barrier for the second intercalation step was found to be higher in the composite, considering both the greater stability of the Li_2 configuration at the interface and the lower barrier for the insertion from the top surface layer to this subsurface position, we can conclude that overall the creation of the TiO_2-$LiKCO_3$ improves the rate of lithium insertion in the subsurface layer of the oxide lattice, thus facilitating Li_xTiO_2 phases formation and accumulation near the oxide surfaces, in line with the experimental observation.[481]

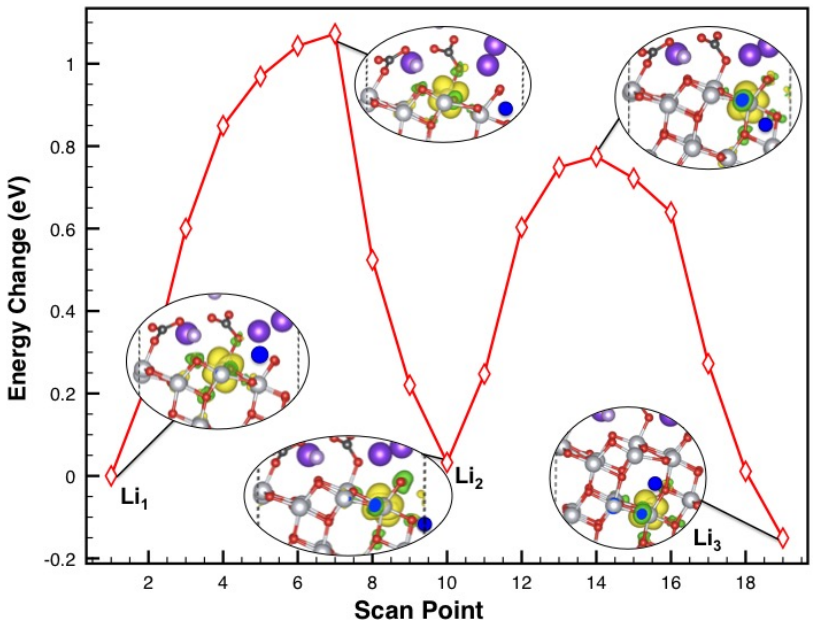

Figure 7.5: Variation of the energy as a function of the Li_i^X position along the intercalation path across the TiO_2-$LiKCO_3$ interface. The insets show the spin density plot associated to the mimima and maxima encountered along the path. Yellow for positive and green for negative values, isosurface 0.001 a.u.

In all the minima identified along the intercalation path in both cases, an almost complete ionization of the interstitial Li has occured. This ionization is slightly more pronounced in the case of the Li_1 top-surface configuration, where the Li atom shows a charge of +0.910e or +0.909e in the case of the TiO_2-$LiKCO_3$ interface or of the pure oxide, respectively. In the surbsurface configurations Li_2 and Li_3, the interstitial Li bears instead an average charge value of +0.891e in the composite and +0.887e for TiO_2-(101). The analysis of the spin

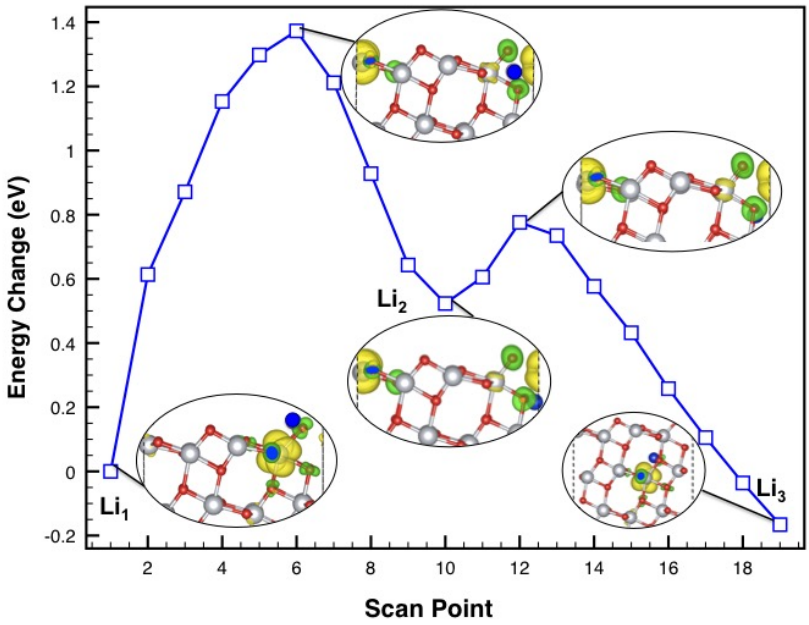

Figure 7.6: Variation of the energy as a function of the Li_i^X position along the intercalation path across the clean TiO_2-(101) surface. The insets show the spin density plot associated the mimima and maxima encountered along the path. Yellow for positive and green for negative values, isosurface 0.001 a.u.

density reveals that an electron transfer has occurred from the alkali metal impurity to one Ti ion, with the unpaired electron occupying one of the empty d-orbitals, determining the reduction of this atom from Ti^{4+} to Ti^{3+}. This is perfectly in line with previous theoretical data[479,480] and with experimental results of synchrotron radiation based electron spectroscopy of lithium doped anatase, which report the growth of a state of mainly Ti-3d character in the band gap and how this Ti-3d level is occupied by 0.85±0.10 electronic charge.[492] It is indeed known that the presence of lithium in the oxide structure can cause a positive shift of its valence band.[493] Furthermore, the electrochemical insertion is accompained by a change in coloration from colorless to dark blue, similarly to what observed in reduced TiO_2 samples exhibiting both intrinsic and extrinsic n-type defects,[480] and in line with what we observed for TiO_2 samples under reducing conditions in chapter 3. In experiments, Li intercalation of anatase is accompanied by the formation of a defect state 1 eV below the CB edge, attributed to localized Ti^{3+} states.[492,494,495] In the inset of figure 7.7 reporting the DOS of the TiO_2-$LiKCO_3$ with a Li_i^X defect, a state at about 1 eV below the minimum of the CB can be clearly seen and this defect is mainly associated to the Ti-3d states of the Ti in the neighborhood of the Li defect on which the excess electron is localized as can be seen by the insets in figure 7.5 showing the spin density plot along the intercalation profile. This result is thus in excellent agreement with the experimental data and also with a previous theoretical work in which the electronic properties of lithium intercalated bulk anatase were studied through GGA+U calculations.[480] This occupied defect state in the band gap can facilitate electron injection in the system and determines a new absorption peak that can explain the

progressive coloration that accompanies Li intercalation.

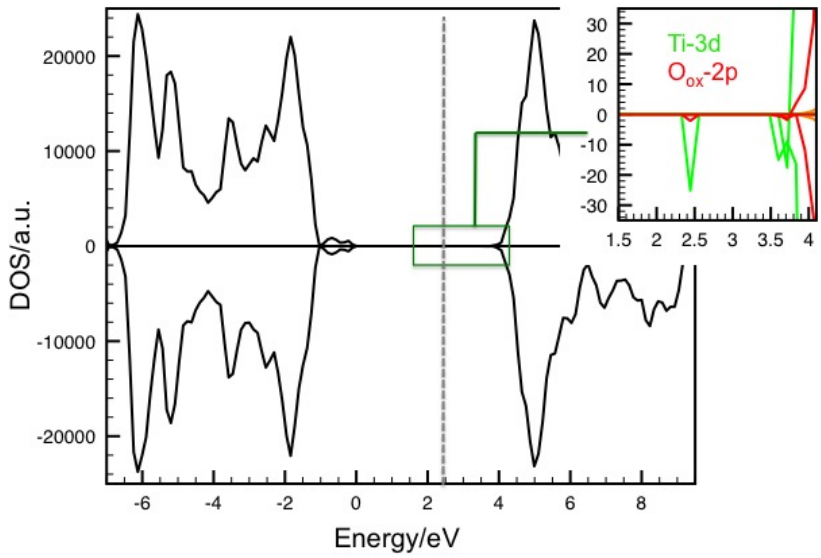

Figure 7.7: DOS for the TiO_2-$LiKCO_3$ interface with a Li_i^X in the Li_1 configuration. Positive or negative values of the DOS stand for spin-up and spin-down states, respectively. The inset shows the Ti-3d (in green) and O-2p (in red, O belonging to the oxide phase) projected-DOS. The grey dotted line indicates the position of the Fermi level.

In correspondence to the maxima encountered along the intercalation path, the charges are similar to the minima and the extra spin is always on a neighbouring Ti atom. However, from the spin plots in the insets of figures 7.5 and 7.6, it is clear that the electron switches its position from one Ti to another during the Li^+ diffusion process. In particular, comparing the two figures, we can observe that when Li_i^X is in configuration Li_1 at the clean TiO_2-(101) surface the excess electron is localized on a neighboring Ti_{6c}, while for the same configuration at the TiO_2-$LiKCO_3$ interface, the reduced Ti is a Ti_{5c} stabilized by the adsorption of a CO_3 group of the carbonate phase. In the following maxima, at the interface the electron is still localized on this Ti center, while for the bare TiO_2 surface it has already been transferred on the following Ti atom, which is a Ti_{5c} surface site, as in the following minima (Li_2) and in the second maxima for the final $Li_2 \rightarrow Li_3$ migration step. In the case of the composite, for the configuration Li_2 and the subsequent maxima, the excess electron is, instead, on a subsurface Ti_{6c} before migrating to a Ti cation of a deeper when Li reaches the Li_3 position. In this last step, that has an higher barrier for the composite compared to the bare TiO_2 surface, the excess electron leaves the top surface layer, where the presence of the second phase can enhance the ion/electron interaction. This picture thus confirms the tentative picture of Li intercalation in TiO_2 given by Lunell et al.[479], according to which '*the electron moves during the diffusion somewhat like a dog an leash tagging along its master, the alkali cation, but happily running to-and-from and sniffing on each titanium lamp post along the way*'. Furthermore, the results indicate that the diffusion barrier heights are anisotropic and depend on the position of the Ti^{3+} center relative to the intercalated Li, in agreement with previous calculations.[480,481]

In summary, the TiO_2-$LiKCO_3$ interface can promote Li insertion in the most favorable subsurface layer, thus helping the possible formation of titanate phases near the oxide surfaces. Li intercalation occurs via a coupled ambipolar process where the motion of Li and the associated electron are correlated to some extent. When Li_i^X enters the oxide lattice is ionized transferring the excess electron to a lattice Ti that is reduced to Ti^{3+} thus influencing the electron injection process in the system. The ion/electron interaction appears enhanced at the interface, where the interstitial Li and the excess electron are located in proximity to adsorbed carbonate, that can thus facilitate charge injection to the oxide.

7.6 Conclusions

In this chapter, in order to complement the experimental observation on titanium dioxide-based materials, we presented a DFT investigation of the stability, structural, electronic properties of the TiO_2-$LiKCO_3$ interface, together with the study of the process of Li intercalation in the oxide lattice, which is at the base of the reactivity between TiO_2 and $LiKCO_3$ experimentally observed. The most important results can be summarized as follows:

- The computed adhesion energy of 0.75 eV indicates that the interaction between the TiO_2-(101) and $LiKCO_3$ surfaces is favourable, even if less strong than in the case of the YSZ-$LiKCO_3$, in line with the larger misfit between the surface unit cells observed in the first case.
- The material shows a band gap of 3.45 eV, lower than the one of pure TiO_2, since it is determined by the O-2p states of the carbonate at the top of the VB and the Ti-3d levels at the bottom of the CB. As for YSZ-$LiKCO_3$, the ion-ion interaction between TiO_2 and $LiKCO_3$ has a major ionic component, with a slightly higher covalent contribution for the adsorption of CO_3^{2-} groups on the titanium dioxide surface .
- The study of Li intercalation in the oxide lattice we performed can help us integrate and better understand the experimental observation about the instabilities of TiO_2-$LiKCO_3$ composites. Li intercalation in the subsurface TiO_2-(101) is indeed favoured from both a thermodynamical and kinetic point of view by the formation of the TiO_2-$LiKCO_3$ interface, which can result in the accumulation of lithium rich Li_xTiO_2 phases near the oxide surface. Furthermore, Li intercalation determines a positive shift of the valence band of the material, facilitating electron injection (reduction). In particular, the lithium ion migrates through a zigzag path connecting octahedral interstitial sites and its motion is correlated to some extent with the migration of the excess electron. This electron is indeed localized on Ti species near the intercalated Li that are reduced from a Ti^{4+} to a Ti^{3+} state. The interface, where these defects are located in proximity to an adsorbed carbonate group, can enhance the Li^+/electron interaction, thus facilitating the oxide reduction.

In conclusion, through the multi-step strategy designed in the first chapter to simulate oxide-carbonate composites, we were able to identify a model the TiO_2-$LiKCO_3$ interface. This model was used to provide information on the structural and electronic properties of

the composite, and more importantly to demonstrate the influence of the oxide-carbonate interface on the mechanisms and phenomena that are at the origin of the instability of these materials. Consequently, results reported in this chapter not only support once again the general validity of the strategy we proposed to model the oxide-carbonate composite systems, but more importantly they integrate and complement the experimental observations about the reactivity issues of these composites, showing the importance of the interplay between theory and experiments when treating such complex materials.

Chapter 8

Conclusions and Perspectives

Nothing in life is to be feared, it is only to be understood.
Now it is time to understand more, so that we may fear less.
Marie Curie

The goal of this work was the study of the ionic conduction in oxide-carbonate composite electrolytes for LT-SOFC applications, in order to provide a better understanding of the origin of their enhanced electrochemical properties. These materials are, indeed, promising candidates for SOFC devices working in the 400-600°C range, where they show conductivity values that are 10-10000 times higher than the ones of solid oxides, like GDC and YSZ traditionally used in SOFCs, in the same temperature range. In order to reach this goal, we proposed for the first time a combined experimental and theoretical approach to investigate such complex systems. The experimental work has been mainly based on a systematic study of the effect of different carbonate and oxide phases on the electrochemical properties of the composite materials, studied through electrochemical impedance spectroscopy measurements. In particular, composites based on Li and Na or Li and K eutectic mixtures and oxides with different properties, namely CeO_2, YSZ and TiO_2, have been studied. A first structural and thermodynamical characterization of these materials, through XRD, IR and Raman spectroscopy and TGA analysis has also been performed. The theoretical study involved, instead, the simulation at the atomic scale of the oxide-carbonate interface that is considered to be responsible for the peculiar properties observed experimentally. In order to reach this goal, we first designed a computational strategy for the modeling of these systems, following the steps used experimentally to synthetize the composites. We consequently started performing periodic DFT calculations on the bulk structure of both the oxide and carbonate phases, already well characterized experimentally, in order to select a reliable computational protocol for their description by the comparison of the theoretical data with the available experimental information. We subsequently used this protocol to identify a suitable model of the most stable surface for each phase, which we then be used to build a model of the oxide-carbonate interface. The third step of this strategy has required the DFT study of this interface, so as to obtain information on the structure, stability, electronic properties and more importantly to investigate different possible conduction mechanisms to elucidate the origin of the enhanced and peculiar features of these systems. Finally, preliminary MD simulations have been also carried out, providing information on the behaviour of these composites at temperatures

higher than the carbonate phase melting point.

In chapter 1, we presented an introduction on the role of solid oxide fuel cells in the current energetic context. We discussed fuel cells operating principles and classifications, and we evidenced the prominsing role of oxide-carbonate composites in the efforts toward the lowering of SOFCs' operating temperature, together with all the challenges and questions still arising from the experimental investigation of these materials. Finally, we presented the combined computational and experimental startegy designed to investigate these systems.

Chapter 2 was devoted to the description of the experimental and theoretical methods used in this work to study the composites. The fundaments of the DFT and MD methods, applied to simulate the materials, and of EIS, used for the electrochemical characterization, have been shortly reviewed.

In chapter 3, we have analysed the peculiar electrochemical behaviour of composite materials made of an oxide phase and a mixture of alkali carbonates. The systematic study demonstrated that the carbonate conductivity directly impacts the composite conductivity in a simple way: the higher the conductivity of the pure carbonate phase, the higher the conductivity of the final composite material. The effect of the oxide phase was found, instead, to be much more difficult to interpret. While the conductivity of YSZ- and GDC- based composites follows the same order of the conductivity levels of the pure oxide phase (*i.e* GDC- based materials are more conductive than the YSZ-ones), undoped CeO_2-based materials showed conductivity values almost equal to the one of GDC-based samples, even if pure CeO_2 is way less conductor than GDC. This result can only be explained considering the role of the oxide-carbonate interface. Furthermore, it was observed that, at high temperatures (560-600°C), YSZ can react with the carbonate phase leading to the formation of zirconate phases that negatively influence the electrochemical behaviour of these materials. Finally, in reducing atmospheres unexpected behaviours were observed: the cooling part of the thermal cycle is systematically different from the heating one. GDC-based materials revealed two drops instead of one jump in conductivity; while the first drop can be associated to the carbonate crystallization, the second drop has been assumed to be related to the formation of hydroxide of the alkali cations in the case of GDC. For YSZ-based materials, instead, the reactivity leading to the formation of zirconates starts even at lower temperatures in this atmosphere compared to oxidising environments. As concerns TiO_2-based materials, strong reactivity issues were observed in this case. Titanate phases are formed already after synthesis and this process seems also to enhance the oxide reduction when the measurements are performed in H_2 atmosphere. All these experimental results rose several questions on the stability and electrochemical properties of these materials and evidenced the important role of interfaces in this behaviour, thus reflecting the complexity of these materials. Considering the lack of analytical tools for investigating the interfacial effects directly, modelling at the atomic scale could help getting a better understanding of the results obtained experimentally.

Chapters 4, 5, 6, and 7 are entirely devoted to the theoretical study of the oxide-carbonate composites. In particular, chapters 4, 5, and 6 illustrate the different steps of the computational strategy proposed in chapter 1 to model these two-phase electrolytes in the case of YSZ-$LiKCO_3$ materials. Chapters 4 and 5 report a detailed study of the pure bulk phases and surfaces for the oxide or carbonate phase, respectively. Chapter 6 provides a description of the strategy used to build the YSZ-$LiKCO_3$ interface model and the characterization of

the structural, electronic, stability, and transport properties of this composite. Chapter 7 extends the application of this same modelling strategy to the simulation of the TiO_2-$LiKCO_3$ interface.

As a first step toward the modelling of the YSZ-$LiKCO_3$ interface, in chapter 4, we first studied the oxide phase. We started considering the most stable ambient pressure zirconia polymorphs (*m*-, *t*-, *c*-ZrO_2) that are very well characterized from the experimental point of view. We then investigated the performances of six Hamiltonians (HF, PBE, B3LYP, B3PW, PBE0 and PBE0-D) and of three different basis sets (all electron on both Zr and O (Zr*-O*), pseudopotential for Zr atoms and all-electron on oxygen (Zr^{ECP}-O*) and pseudopotential on both Zr and O (Zr^{ECP}-O^{ECP})) in predicting the equilibrium geometries, relative stability and the band gaps of the three phases. The PBE0/Zr^{ECP}-O^{ECP} level appeared to be a good compromise between accuracy of the results and computational cost to predict and describe both the structural and electronic properties of zirconia. This computational protocol was used to investigate the properties of the most stable surfaces of each phase and the reducibility of the most stable cubic (111) surface, confirming, in agreement with the experimental observation, the irreducible nature of this oxide. Finally, we investigated the stabilization of this surface through doping with the aliovalent Y_2O_3 oxide, so as to obtain the YSZ-(111) most stable termination. The computed values for the energy due to the creation of the oxygen vacancies ($V_O^{\bullet\bullet}$) and simultaneously to the substitution of Zr with Y atoms ($E_{(s-f)}$) confirmed, as expected, that doping of the (111) zirconia surface with Y_2O_3 is accompanied by the stabilization of the system. Among all the tested configurations, the $(4,6)_{NNN-NNN}$ one, with a subsurface vacancy and two Y atoms both in NNN position to the defect, was found to be by far the most stable and can thus be used as a building-block for the oxide phase when creating a model of the YSZ-$LiKCO_3$ interface.

Before doing that, it was however necessary to study separately also the carbonate phase. In chapter 5, we tested three DFT functionals (PBE, B3LYP, and PBE0) and PBE0 was found to be again the best one to describe the geometrical features of bulk $LiNaCO_3$ and $LiKCO_3$, allowing at the same time a reliable description of the electronic properties of these materials, which are, at the solid state, strong insulators characterized by covalent interactions within the CO_3 groups and ionic interactions between the O atoms and the metal cations. In order to identify the most stable surfaces, the two (001) and (110) low index surfaces were investigated for each carbonate phase. The (001) surface was found to be the most stable surface for both $LiKCO_3$ and $LiNaCO_3$. In the latter case, however, different type of reconstruction had to be taken into account to stabilize this termination that shows a dipolar moment perpendicular to the surface. Finally, in this chapter, we also investigated the Li transport properties for the most stable and less complex $LiKCO_3$-(001) surface, in order to obtain information that can be used as a reference when studying the effect of the interface on cation transport in the composite material. Li vacancies were found to be the most stable type of Li-related defect, but the high barriers associated to their diffussion indicated that they cannot be the defect determining the diffusion in the material. Interstitial Li mobility can instead be quite high, since this type of defect can diffuse via direct-hopping along the large open channels oriented parallel to the *b*-axis of the surface with low barriers (0.80 eV).

Chapter 6 is the logical continuation of the previous two. A model of the YSZ-$LiKCO_3$ interface was build, considering the most stable YSZ (111) and $LiKCO_3$ (001) surfaces men-

tioned above, and investigation was carried out at the PBE0 level, which provided the overall best description of the interface components. This model was validated by comparison of the computed and experimental IR and Raman spectra and thus used to study the stability, structural electronic and transport properties of this material. The large adhesion energy obtained (3.19 eV) indicated that a strong interaction takes place between the two phases, which has two main origins: adsorption of the ionic species of the salt on the oxide surface and minimization of the elastic strain due to the lattice mismatch between the two surfaces, resulting in a disordered amorphous-like state for the carbonate phase in agreement with the experimental observations. In particular, the ion-ion interactions between YSZ and $LiKCO_3$ show a mainly ionic character, with a slightly higher covalent contribution in the case of the adsorption of CO_3^{2-} groups on the oxide surface sites. The different conduction mechanisms investigated for Li, O, and proton species at the interface thus built resulted to be extremely influenced by the interfaces. Li^+ are stabilized at the interface were they are trapped, leaving Li vacancies in the bulk carbonate phase that, contrary to the clean $LiKCO_3$ surface, can diffuse with very low barriers (0.23 eV). The formation of negatively charged oxygen species associated with the cations of the carbonate phase was also found to be a very favourable process. In both cases, the results suggested that a space-charge layer can be formed at the phase boundaries due to the interfacial interaction between the oxide and the carbonate. Futher investigations, especially at higher temperatures when the carbonate is in the molten state, are however necessary to verify if and how this higher defect concentration at the interfaces can effectively constitute high conduction pathways for the oxide ions. Furthermore, we were already able to show how the interface in the YSZ-$LiKCO_3$ can boost the O atom migration, in a process that can be important for the composite-based SCFCs. Finally, the interface can favour also the formation of H-related defects through interaction of H^+ with the oxygen sites of the oxide. Here, the presence of the carbonates and especially of oxygen species adsorbed on the oxide plays an important role in the lowering of the barrier associated to proton migration at the interfaces.

In chapter 7, we further tested the validity of the strategy we proposed to model the oxide-carbonate composite systems by applying it to the case of the TiO_2-$LiKCO_3$ interface. The obtained results complemented the experimental observations about the reactivity issues of these composites exposed in chapter 3, showing the importance of the interplay between theory and experiments when treating such complex materials. The computed adhesion energy of 0.75 eV indicated that the interaction between the TiO_2-(101) and $LiKCO_3$ surfaces is favourable, even if less strong than in the case of the YSZ-$LiKCO_3$, in line with the larger misfit between the surface unit cells observed in the first case. As a consequence of this interaction, the material shows a smaller band gap compared to the one of pure TiO_2. Li intercalation in the subsurface TiO_2-(101) was found to be favoured from both a thermodynamical and kinetic point of view by the formation of the TiO_2-$LiKCO_3$ interface, possibly resulting in the accumulation of lithium rich Li_xTiO_2 phases near the oxide surface. Furthermore, intercalation of Li species in the oxide lattice determines a positive shift of the valence band of the material, facilitating electron injection (reduction) in the material, in line with the experimental findings.

In summary, this work paved the way toward a deeper understanding of the origin of the enhanced electrochemical properties of the oxide-carbonate electrolytes, developped a

combined experimental/theoretical methodology to approach these systems and showed the importance of the interplay between theory (microscopic level) and experiments (macroscopic level) that make the combined approach a very powerful tool for the investigation of the operating principles of LT-SOFCs based on these electrolytes.

Several questions and hypothesis on the role of the interfaces emerged from the experimental results, which have been used to validate the computational protocols and interface models. The theoretical simulations based on this computational strategy provided in turn insights on the role of the interfaces in determining the unexpected experimental observations. Naturally, there is still a lot of work that can be done in order to reach an even deeper comprehension of the conduction properties of the composites. Different research perspectives can be envisaged starting from the results already obtained and from the work that is on-going. Starting from experiments, the first perspective we can identify is a finer analysis of the EIS diagrams through their decompositions in equivalent circuits in order to estimate the possible different contributions. At the same time a finer structural characterization of the composites can be extremely important to obtain informations on the morphology of the interfaces, for example, through transmission electron microscopy (TEM). Furthermore, in-situ XRD measurements as a function of temperature and of the oxidizing/reducing atmosphere and more accurate thermo-gravimetric analysis-differential thermal analysis (TGA-DTA) coupled with mass spectrometry experiments will integrate the preliminary results we showed, providing a better understanding of the reactivity issues encountered in the case of YSZ- and TiO_2-based composites during the the EIS measurements. Finally, we can envisage the synthesis of composites made with oriented oxide particles. Not only these composites have been recently found to provide higher performances, but the presence of a single oritentation will allow an even better match between the experimental samples and the theoretical models of the interface built starting from the most stable termination for each phase.

From the point of view of the theoretical modelling of these materials, MD simulations starting from the interface models already identified can complete the informations we already provided, by describing the system at higher temperatures when the carbonate phase is in the molten state. These calculations will provide insights on the role of the carbonate ions as conducting species or of their influence on the transport of other species at the interface (*i.e.* the proton according to the Swing Model) or on the behaviour of the interfacial oxide ions at higher temperatures. This work is already on-going. In particular, *ab initio* biased molecular dynamic simulations for the investigation of Li transport in the YSZ-$LiKCO_3$ composite to be compared to the static DFT simulation discussed in chapter 5 are already underway. Finally, the DFT investigation of composites in which the oxide phase is a CeO_2-based material (CeO_2, GDC, or SDC) will complete the theoretical work, providing information on the interfacial interaction even in the third type of composites considered in the experimental work. DFT simulations recurring to the PBE0 functional are undergoing for a model of the pure CeO_2-$LiKCO_3$ interface built starting from the most stable $LiKCO_3$-(001) surface and from a model of the CeO_2-(111) most stable termination, which was identified in a work previously performed in our group.[496] A model of the CeO_2-$LiKCO_3$ interface built through the same procedure used for the other materials with 204 atoms (168 belonging to CeO_2 and 36 belonging to the carbonate phase) for a total of 3812 atomic orbitals with the selected computational protocol has already been built, and is under investigation using the

same computational protocol described above. Once the optimized structure will be found, investigation of the conduction mechanisms even in these materials will be possible. Doping the CeO_2 surface with Gd or Sm, as we already did in the case of YSZ, or using the most stable surface of $LiNaCO_3$ to build other interface models can also be envisaged as a future perspective.

List of Figures

1.1 Regional primary energy demand profiles in the 2°C scenario. OECD indicates the countries that signed the *Convention on the Organisation for Economic Cooperation and Development*.[7] 3
1.2 Energy efficiencies of the principal types of energy conversion systems. The solid bars represent what currently is possible, while the non-solid extensions depict projected improvements.[9,11] 3
1.3 Fuel Cell use by application 2009-2013.[8,14] 4
1.4 Schematic representation of SOFC operating principle. 8
1.5 Schematic representation of a) tubular and b) planar SOFC geometries.[32] . 9
1.6 Oxide ion conductivity of selected electrolyte materials for SOFC application from[58] 13
1.7 Schematic representation of MCFC operating principle. 15
1.8 Temperature dependence of the conductivity of various ceria-salt composites compared to the conventional SOFC electrolytes, like YSZ and GDC.[18] . . 20
1.9 (a) TEM image and (b) HRTEM image of a SDC-carbonate composite.[104] . 22
1.10 Schematic Arrhenius plot for a carbonate-oxide composite material. Adapted from[95] 23
1.11 Two interpenetrated percolative phases with an oxide ion conducting oxide and a proton conducting carbonate salt according to Zhu et al.[18] 28
1.12 Interfacial conduction pathway according to the space charge layer theory according to Zhu et al.[146] 29
1.13 A schematic picture of the hybrid H^+/O^{2-} model proposed by Zhu[89] at the interface of the oxide-carbonate materials. Small blue dots represent H^+, while the larger green balls stand for O^{2-}. 30
1.14 A schematic picture of the 'Swing Model' pathway for proton conduction in oxide-carbonate composite according to Wang et al.[147] 31
1.15 A schematic picture of the ternary $H^+/O^{2-}/CO_3^{2-}$ conduction mechanism when CO_2/O_2 is used as the oxidant gases, as proposed by Li's group.[148] . . 32
1.16 Comparison between the experimental protocol for the synthesis of carbonate/oxide composite electrolytes and the proposed computational DFT/MD approach for the modeling of the carbonate/oxide interface at the atomic scale.[150] 33

2.1 Schematic representation of a Bode (a) or Nyquist (b) plot. 60

2.2 Schematic representation of the Nyquist plot of a typical electrolyte-electrode system. 61
2.3 Equivalent cicuit corresponding to the Nyquist plot in figure 2.2 61

3.1 Scheme of the temperature program followed to anneal the gold electrodes on the pellets before electrical characterisation. 65
3.2 a) Photograph of the set-up used for impedance spectroscopy measurements at high temperature in controlled atmosphere. Illustration in the case of the more complete, *i.e.* 'Hydrogen', set-up. b) Photograph of the set-up in which is placed the sample, before being introduced in the furnace. c) Schematic representation of the symmetric configuration used for the EIS measurements. 67
3.3 Nyquist impedance diagrams measured at 385 °C under ambient air with different signal amplitudes (from 50 to 300 mV) on a YSZ-LiK composite. 68
3.4 Typical impedance diagrams measured at low temperatures for a YSZ-LiK composite. 69
3.5 Typical impedance diagrams measured at high temperatures for a YSZ-LiK composite. 69
3.6 GDC-LiNa composite conductivity under oxidising conditions (dry air) during heating. 72
3.7 YSZ-LiNa composite conductivity under oxidising conditions (dry air) . . . 73
3.8 Arrehenius plot of the YSZ-LiK composite conductivity measured under oxidising conditions (dry air). 75
3.9 Arrehenius plot of the YSZ-LiK composite conductivity measured under oxidising conditions using an automated setup. The inset shows the variation of the conductivity over time when the sample is left in air atmosphere at 620°C. 75
3.10 Evolution of the conductivity of TiO_2-$(Li,K)_2CO_3$ composite as a function of temperature in dry air. 76
3.11 Arrhenius plot of pellets made of the YSZ-LiNa composite compared to the one of the pure oxide phase. Measurements performed in air. 77
3.12 Arrhenius plots showing the impact of different carbonate phases on the YSZ-based composite conductivity. Measurements performed in air. 78
3.13 Conductivity measurements of GDC-LiK composites, modified by Li, Rb, Cs or La carbonate addition (5 mol%), as a function of temperature. Ambient air is used as gas operating atmosphere. a) Variation reported in Arrhenius coordinates and b) variation reported in linear coordinates. 79
3.14 Arrhenius plot of oxide-LiNa composites as a function of the oxide phase (YSZ, GDC, CeO_2). Measurements performed in air. The behaviour of the composites is compared to the conductivity level of the pure oxide phases at 600°C indicated by the orizontal lines.[61,209,210] 80
3.15 a) GDC-LiNa or b) GDC-LiK composite conductivity under reducing conditions (23%H_2 in N_2) during one heating/cooling cycle. 81
3.16 Electrical conductivity variations of GDC-LiK during cycling, as a function of the H_2 amount (x) in N_2: x=23%, 50%, and 100%. 82

3.17 Conductivity measurements of YSZ-LiNa composite, during cycling in 23% H_2/N_2. 84
3.18 Conductivity measurements of YSZ-LiK composite, during cycling in 23% H_2/N_2. 84
3.19 Evolution of the conductivity of TiO_2-$(Li,K)_2CO_3$ composite as a function of temperature under reducing (H_2) atmosphere. 85
3.20 Comparison of the Arrhenius plots of TiO_2-$(Li,K)_2CO_3$ materials obtained in air or reducing atmosphere. 86
3.21 TGA and DTA spectra of the YSZ-LiK composite obtained during heating (a and c) or cooling (b and d) in air (a and b) or hydrogen atmosphere (c and d). 87
3.22 DTA and MS spectra of the YSZ-LiK composite obtained during heating. . 87
3.23 TGA and DTA spectra of the YSZ-LiNa composite obtained during heating (a and c) or cooling (b and d) in air (a and b) or hydrogen atmosphere (c and d). 89
3.24 TGA and DTA spectra of the TiO_2-LiK composite obtained during heating (a and c) or cooling (b and d) in air (a and b) or hydrogen atmosphere (c and d). 90
3.25 XRD patterns for the YSZ-$(Li,K)_2CO_3$ composite obtained after the synthesis and the treatment in air or hydrogen atmosphere. The XRD pattern of the pure YSZ oxide is also reported for comparison. 92
3.26 XRD patterns for the YSZ-LiNa composite obtained after the synthesis and the treatment in air or hydrogen atmosphere. The XRD pattern of the pure YSZ oxide is also reported for comparison. 94
3.27 XRD patterns for the TiO_2-LiK composite obtained after the synthesis and the treatment in air or hydrogen atmosphere. The XRD pattern of the pure TiO_2 oxide is also reported for comparison. 95
3.28 FT-IR spectra of the YSZ-$(Li,K)_2CO_3$ composite obtained after the synthesis and the treatment in air or hydrogen atmosphere. 97
3.29 FT-IR spectra of the YSZ-$(Li,Na)_2CO_3$ composite obtained after the synthesis and the treatment in air or hydrogen atmosphere. 98
3.30 FT-IR spectra of the TiO_2-LiK composite obtained after the synthesis and the treatment in air or hydrogen atmosphere. 98
3.31 Raman spectra of the YSZ-LiK composite obtained after the synthesis and the treatment in air or hydrogen atmosphere. 99
3.32 Raman spectra of the YSZ-LiNa composite obtained after the synthesis and the treatment in air or hydrogen atmosphere. 100
3.33 Raman spectra of the TiO_2-$(Li,K)_2CO_3$ composite obtained after the synthesis and the treatment in air or hydrogen atmosphere. 101

4.1 Cubic (a), tetragonal (b) and monoclinic (c) ZrO_2 unit cells and relative space groups. Large light blue spheres and small red spheres represent Zr and O atoms, respectively. 104

4.2 Mean Signed Errors (MSE, in %) computed for the lattice vectors of the a) cubic, b) tetragonal and c) monoclinic phases with the three considered basis sets and the six considered Hamiltonians. 109

4.3 Calculated PBE0/Zr^{ECP}-O^{ECP} (a) band structure, and (b) total and Zr-4d, Zr-4p, O-2s, O-2p projected DOS of I) cubic, II) tetragonal and III) monoclinic ZrO_2.The Fermi level has been set as origin of the energy scale. For clarity, DOS for the cubic and tetragonal phases are multiplied by a factor of 5 and 2 respectively. 117

4.4 Slab models and labeling of the a) *c*(111) surface, composed by three O-Zr-O trilayers, b) *t*(101) surface, composed by three layers (O-O-Zr_2-O-O motif), c) *t*(111) surface, composed by four layers (O-Zr-O-O-Zr-O motif), d) *m*(-111) surface, composed by two layers (O-O-O-Zr-O-Zr-Zr-O-Zr-O-O-O motif). Large light blue spheres represent Zr atoms, while the small red ones stand for oxygen atoms. 121

4.5 Surface energy E_s(in J/m^2) of a) *c*-ZrO_2 (111). b) *t*-ZrO_2 (101). c) *t*-ZrO_2 (111) and d) *m*-ZrO_2 (-111) surfaces as a function of the number n of layers in the slab model. 121

4.6 Computed band gap as a function of the number *n* of layers in the slab model of the a) *c*-ZrO_2 (111), b) *t*-ZrO_2 (101), c) *t*-ZrO_2 (111) and d) *m*-ZrO_2 (-111) surfaces. 126

4.7 Computed total and projected DOS for a) *c*-ZrO_2 (111)-5L. O_1 is 3-folded, O_3 4-folded, Zr_2 7-folded and Zr_5 8-fold coordinated; b) *t*-ZrO_2 (101)-6L, O_1 and O_2 are 3-folded, while O_5 and O_6 are 6-folded. Zr_3 and Zr_4 are 7-folded and Zr_9 and Zr_{10} are 8-fold coordinated; c) *t*-ZrO_2 (111)-8L. O_1 is 2-folded, O_7 is 3-folded and O_6 is 4-folded. Zr_2 is 5-folded, Zr_5 is 7-folded, while Zr_8 is fully coordinated; d) *m*-ZrO_2 (-111)-5L. O_1 is 2-folded, O_2 is 3-folded, while O_{10} is fully coordinated. Zr_4 is 6-folded and Zr_9 is 7-fold coordinated. In every case, the Fermi level has been set as origin of the energy scale. Projected DOS are multiplied by a factor of 3. Labels refer to Figure 4.4. 127

4.8 Top (left) and lateral (right) views of the (2×2) supercell of the (111) ZrO_2 surface. Oxygen atoms are in red, while zirconium atoms are in light blue. Pink for surface vacancies positions, violet for subsurface vacancies positions. Numbers refer to Zr atoms, letters to oxygen atoms. Zirconium atoms numbered 1, 2, 3, and 4 belong to the outermost Zr plane, while 5, 6, 7, and 8 belong to the plane under the subsurface vacancy. 128

4.9 Top view of the supercell for the optimized geometry of the (111) surface with a) surface or b) subsurface vacancies. Same color code as in figure 4.8 130

4.10 Band structure (a) and total and projected density of states (b) for the system with surface (left) or subsurface (right) oxygen vacancies. 132

4.11 Total and projected DOS for the relaxed (plain line) and unrelaxed (dotted line) (111) supercell with a surface (a) or subsurface (b) oxygen vacancy or for the (4,6$_{NNN-NNN}$ configuration of YSZ (c). 133

4.12 (I) Top (left) and top half lateral view (right) of optimized structure of the (2×2) supercell for the seven configurations taken into account for $Zr_{20}Y_4O_{46}$. Oxygen atoms are in red, zirconium atoms in light blue, and yttrium atoms in green. Pink for surface vacancies positions, violet for subsurface vacancies positions. (II) Band structure (a), total and atom projected DOS (b) of the different configurations of the YSZ (111) surface. 136
4.13 Electrostatic potential plots for the (4,6)NNN-NNN configuration, before (a) and after (b) the relaxation of the system. Yellow for positive and light blue for negative values. Isosurface values of 0.005 a.u. 138

5.1 Unit cells of the α, β and γ (model A and B) phases of $LiNaCO_3$ and of $LiKCO_3$. Red, grey, violet, light violet spheres represent O, C, Na or K, and Li atoms, respectively. The dotted lines in the β unit cell show one of the possible γ-sub-cells. 143
5.2 Mean Unsigned Errors (MUE, in %) computed for the lattice vectors of a) the three $LiNaCO_3$ polymorphs and b) $LiKCO_3$ with the six considered Hamiltonians and the two basis sets (all-electron (AE) and pseudopotential (ECP)) in the case of $LiKCO_3$. 148
5.3 IR spectra of $LiNaCO_3$ (a-c) and $LiKCO_3$ (d) computed at the PBE0 level. $LiNaCO_3$ are referred to Model A. Results for Model B are equivalent. . . . 152
5.4 Raman spectra of $LiNaCO_3$ (a-c) and $LiKCO_3$ (d) computed at the PBE0 level. $LiNaCO_3$ are referred to Model A. Results for Model B are equivalent 153
5.5 Band structure and total and orbital projected density of states (DOS) for the a) α, b) β, c) γ-Model A, d) γ-Model B of $LiNaCO_3$, and e) $LiKCO_3$. . . . 156
5.6 Slab model of the (001) surface of γ-LiNaCO3 (Model A), composed by three slab layers (three $[Na_3CO_3]^+$-$[Li_3(CO_3)_2]^-$ platelets). The stoichiometry and total charge of each atomic layer is indicated to evidence the presence of a dipole moment perpendicular to the surface. 158
5.7 Schematic representation of the (2 × 2) supercell for the a) $(001)^{Na}_{R1}$, b) $(001)^{Li}_{R1}$, c) $(001)^{Na}_{R2}$, and d) $(001)^{Na}_{R2}$ reconstructions. d is the distance between the two atomic planes that constitute each slab layer. 159
5.8 a) Surface energy (E_s) and b) band gap (E_g) for I) the reconstructed $LiNaCO_3$-(001) and $LiNaCO_3$-(110) surfaces, as well as for II) $LiKCO_3$ (001) and (110) as a function of the number n of layers in the slab model 161
5.9 Slab models of a) $LiNaCO_3$-(110), b) $LiKCO_3$-(001), and c) $LiKCO_3$-(110). 162
5.10 a) Band structure and DOS of the (001) surface of $LiKCO_3$ with a V_{Li} vacancy created in a 4-fold coordinated site. The black dotted line is the total density of state (DOS) while the pink line is the DOS projected of the oxygen atoms in nearest-neighbour (NN) positions to the defect. Positive or negative values of the DOS stand for spin-up or spin-down spin states, respectively. Inset: spin density plot with isovalue of 0.001 and yellow for positive and green for negative values; b) Band structure and total and atom projected DOS of the (001) surface of $LiKCO_3$ with a V_{Li}' vacancy created in a 4-fold coordinated site. 164

5.11 a) Band structure and DOS of the (001) surface of $LiKCO_3$ with a Li interstitial atom (Li_i^X). The black line is the total density of state (DOS) while the pink dotted and the blue lines are the DOS projected, respectively, on the oxygen and carbon atoms in nearest-neighbour (NN) positions to the defect. Positive or negative values of the DOS stand for spin-up or spin-down spin states, respectively. Inset: spin density plot with isovalue of 0.001 and yellow for positive and green for negative values; b) Band structure and total and atom projected DOS of the (001) surface of $LiKCO_3$ with a Li^+ interstitial defect ($Li_i^\bullet$) in configuration I_1. 165

5.12 DOS projected on one O atom for the defect-free (001) surface (top) and for the same surface with a charged defect (bottom). The selected atom corresponds to an O atom far from the defect. The insets show the enlargement of the plot in the region of the low energy O-2s states. 169

5.13 Computed formation energy (E_f) of Li-related defect on the $LiKCO_3$-(001) surface as a function of the Fermi level (E_F) a) at the oxygen poor limit ($\Delta\mu_O$=-12.65 eV and $\Delta\mu_{Li}$=0 eV) or b) at the oxygen rich limit ($\Delta\mu_O$=0 eV and $\Delta\mu_{Li}$=-3.28 eV) and c) as a function of the oxygen chemical potential ($\Delta\mu_O$) at the zero Fermi level (E_F=0). The three zones in picture c are referred to the different stability domain of $\Delta\mu_{Li}$ (see text). For the Li vacancies, values are always referred to the more stable 4-fold coordinated surface site. 171

5.14 Schematic representation of the possible diffusion pathways for V_{Li} or V_{Li}' defects when created in 4-fold (green) or 5-fold (yellow) coordinated sites in (1×2) supercell of the (001) surface. The green and yellow sphere represent the initial vacancy position while the hashed violet spheres stand for the final sites through which the vacancy diffuses. 172

5.15 Variation of the energy as a function of the $Li_i^\bullet$ defect position along the channels and relative to the energy value of the system with a defect in the initial position of configuration I_1 (blue) or I_2 (red). Insets: schematic representation of the diffusion pathway. $Li_i^\bullet$ diffuses from the initial position Di (green sphere) to the final equivalent one D_i' (hashed green sphere) passing through the intermediate interstitial sites S_{1s} and S_{2s} (dotted spheres) in case of configuration I_2 (red) or S_{1c} and S_{2c} for I_1 (blue). 174

5.16 Variation of the energy as a function of the Li_i^X defect position along the channels and relative to the energy value of the system with a defect in the initial position. Inset: schematic representation of the diffusion pathway. Li_i^X diffuses from the initial position D_i (green sphere) to the final equivalent one D_i' (hashed green sphere) passing through the intermediate interstitial site S_1 (dotted spheres). 175

5.17 Variation of the energy as a function of the $Li_i^\bullet$ defect position along the channels for a defect in the initial position of configuration a) I_2 or b) I_1, in the absence or presence of an electric field applied parallel to the direction of the channels. 177

6.1 Schematization of the building process of the model of the YSZ-$LiKCO_3$ interface considered for all DFT calculations: a) superposition of a (4×4) supercell of the $LiKCO_3$-(001) (in violet) and YSZ-(111) (in green) models previously identified; b) rotation of the $LiKCO_3$-(001) supercell of 30°around the normal to the YSZ-(111) surface plane and identification of a new unit cell for the interface (black dotted line); c) final interface model. 185

6.2 a) Initial and b) optimized geometry of the YSZ^{6L}-$LiKCO_3^{3L}$ model of the composite, shown as a (2×2) supercell of the interface model for clarity. Solid blue line indicates the unit cell. Zr, Y, and O atoms are in light blue, green and red, while C, Li and K are in grey, light violet and purple, respectively. 186

6.3 Optimized geometry of the YSZ^{3L}-$LiKCO_3^{5L}$ model of the composite, shown as a (2×2) supercell of the interface model for clarity. Solid blue line indicates the unit cell. Zr, Y, and O atoms are in light blue, green and red, while C, Li and K are in grey, light violet and purple, respectively. 188

6.4 Computed (top) and experimental (bottom) IR (a and c) and Raman (b and d) spectra of the YSZ-$LiKCO_3$ composite. 190

6.5 Atom projected density of states (DOS) of the clean a) $LiKCO_3$-(001) and b) YSZ-(111) surfaces. c) Total and atom projected density of states (DOS, right) and d) band structure of the composite. The Fermi level has been set as the zero of the energy scale. The Brillouin zone path used for the band structure calculation is Γ-F-Z-B-R-Z, where in terms of the reciprocal basis vectors, Γ corresponds to the point (0,0,0), F to (0,1/2, 0), Z to (0, 0, 1/2), B to (1/2, 0, 0), and R to (1/2, 1/2, 1/2). 193

6.6 Schematic representation of the path for the a) direct hopping and b) knock-off of a Li defect in configuration $Li_i^X(1)$, c) direct hopping of of a Li defect in configuration $Li_i^X(2)$, d) direct hopping of a Li defect in configuration $Li_i^X(3)$, e) direct hopping from $Li_i^X(1)$ to $Li_i^X(4)$, and f) knock-off from $Li_i^X(1)$ to $Li_i^X(4)$. In a, b, c, and d the defect migrates from the initial position indicated by the green sphere to the final equivalent position, the black sphere. For the intercalation mechanisms (e and f), the insertion from the interface configuration $Li_i^X(1)$, in green, to the position in the oxide lattice $Li_i^X(4)$, in black, is considered. For the knock-off mechanisms in b and f, the lattice Li involved in the mechanism is indicated by a light purple sphere. . 201

6.7 Variation of the energy as a function of the Li_i^X defect position along the paths showed in figure 6.6. The direct hopping mechanism path is shown in orange for $Li_i^X(1)$, blue for $Li_i^X(2)$, and in green for $Li_i^X(3)$. The knock-off for Li intercalation from configuration for $Li_i^X(1)$ at the interface into the oxide lattice in position $Li_i^X(4)$ is instead represented in red. For simplicity, among the possible paths in figure 6.6, in the case of the $Li_i^X(1)$ and $Li_i^X(4)$ configurations, only the path associated to the lowest barrier is showed. . . 202

6.8 a) Schematic representation of the path for the direct hopping diffusion of a V'_{Li} in the bulk carbonate phase when its counter specie ($Li_i^{\bullet}$) is trapped at the interface after the Li_{FP} formation in YSZ-$LiKCO_3$. b)Variation of the energy as a function of the V'_{Li} position along the selected path. 207

6.9 a)Views along the *a*- (left) or *b*-axis (right) of a schematic representation of the path for a O^{2-} anion that diffuses at the interface of the YSZ-$LiKCO_3$ composite from the initial configuration $2Li_i^{\bullet}$-$O^{2-}(1)$ (in orange) to a final equivalent position (in black), according to a direct hopping mechanism along the *a*-axis. The interstitial Li cations are represented in blue. b) Variation of the energy as a function of the O^{2-} position along the selected path. 211

6.10 Schematic representation of the path for the cogwheel mechanism for the O atom migration at the a) interface from configuration $O_{int}^{(1)}$ (in yellow) to configuration $O_{int}^{(2)}$ (in black) or b) in the carbonate bulk phase in YSZ-$LiKCO_3$ from configuration $O_{carb}^{(1)}$ (in yellow) to $O_{carb}^{(2)}$ (in black). c) Variation of the energy as a function of the O atom position along the path. d) Structure of the configuration associated at the maximum along the path for the migration at the interface. 215

6.11 a) Schematic representation of the suggested conduction path for proton species in the bulk carbonate phase of the YSZ-$LiKCO_3$ composite. The step 1 represents an intermolecular proton transfer between two carbonate groups (from configuration $H_{carb}(1)$ to configuration $H_{carb}(2)$). In step 2, the proton rotates around the C-O bonds of the CO_3 group to which it is bound, so as to assume the right orientation to be easily trasferred to another carbonate group through a second intermolecular H^+ trasnfer (step 3). b) Corresponding variation of the energy as a function of the proton position along the path. The initial and final position of the proton is indicated by the light blue and black spheres, respectively, while the white spheres represent intermediate positions. 219

6.12 a) Schematic representation of the linear direct-hopping path through which the proton adsorbed on the YSZ surface site migrates from its initial configuration ($H_{int}(1)$) to final equivalent one through several intermediate interstitial positions. b) Corresponding variation of the energy as a function of the proton position along the path. The initial and final positions of the proton are indicated by the light blue and black spheres, respectively. 220

6.13 a) Schematic representation of the path of the non linear direct hopping mechanism for a proton migrating at the interface of the YSZ-$LiKCO_3$ composite: in step 1 the proton (light blue sphere) migrates from YSZ surface site on which it is adsorbed (configuration $H_{int}(1)$) to an interstitial position interacting with the oxide ion (orange sphere) that was also introduced at the composisite interface; in step 2, the proton migrates from this interstitial position to another oxygen atom of the YSZ suface, from which, in step 3, migrates toward the nearest bidentate carbonate group; step 4 requires the rotation of the proton around the C-O bond, before it migrats toward the surface position indicated as 5. In the final step 6, H^+ directly diffuses to a position equivalent to the starting configuration. b) Corresponding variation of the energy as a function of the proton position along the path. The insets show the structure of the maxima encountered along the path. The initial and final position of the proton is indicated by the light blue and black spheres, respectively, while the white spheres represent intermediate positions. . . . 221

7.1 Slab models of a) anatase TiO_2-(101) surface ((2 × 2) supercell, with 10 O-Ti-O layers) and b) $LiKCO_3$ (5 slab layers). 230

7.2 Two different views of the optimized geometry of the TiO_2-$LiKCO_3$ interfacemodel of the composite, shown as a (2 × 2) supercell of the interface model for clarity. Solid blue line indicate the unit cell. Ti and O atoms are in dark grey, and red, while C, Li and K are in light grey, light violet and purple, respectively. 231

7.3 Atom projected density of states (DOS) of the clean a) $LiKCO_3$-(001) and b) TiO_2-(101) surfaces. c) Total and atom projected density of states (DOS, left) and d) band structure of the composite. The Fermi level has been set as the zero of the energy scale. The Brillouin zone path used for the band structure calculation is Γ-F-Z-B-R-Z, where in terms of the reciprocal basis vectors, Γ corresponds to the point (0,0,0), F to (0,1/2, 0), Z to (0, 0, 1/2), B to (1/2, 0, 0), and R to (1/2, 1/2, 1/2). 233

7.4 Lithium intercalation positions across the TiO_2-$LiKCO_3$ interface, together with the intercalation path. The interstitial Li specie is represented by the blue sphere. 238

7.5 Variation of the energy as a function of the Li_i^X position along the intercalation path across the TiO_2-$LiKCO_3$ interface. The insets show the spin density plot associated to the mimima and maxima encountered along the path. Yellow for positive and green for negative values, isosurface 0.001 a.u. 239

7.6 Variation of the energy as a function of the Li_i^X position along the intercalation path across the clean TiO_2-(101) surface. The insets show the spin density plot associated the mimima and maxima encountered along the path. Yellow for positive and green for negative values, isosurface 0.001 a.u. . . . 240

7.7 DOS for the TiO_2-$LiKCO_3$ interface with a Li_i^X in the Li_1 configuration. Positive or negative values of the DOS stand for spin-up and spin-down states, respectively. The inset shows the Ti-3d (in green) and O-2p (in red, O belonging to the oxide phase) projected-DOS. The grey dotted line indicates the position of the Fermi level. 241

List of Tables

1.1 Types of fuel cells and their characteristics. Adapted from[29] and completed. 7
1.2 Melting points of lithium, sodium, and potassium carbonates and of their eutectic mixtures. 21
1.3 Performances of fuel cells based on carbonate-oxide composites together woth the electrolyte conductivity. 24

3.1 Selected characteristic features of different oxide-carbonate composite electrolytes measured either in oxidising (air) or reducing (H_2) atmosphere during heating (H) or cooling (C) cycles: low (E_{act}^{LT}, in eV) and high (E_{act}^{HT}, in eV) temperature activation energies, transition temperature observed in the Arrhenius diagram (T_t, in °C), compared with the melting (T_m, in °C) or recrystallization (T_c, in °C) temperatures of the carbonate phase as measured through TGA-DTA experiments performed on the composites. Italic values for YSZ-LiK are referred to the measures made on the automated setup (see the text for details). 71

4.1 Equilibrium geometry of *m*-ZrO_2 with different Hamiltonians and basis sets and mean signed error (MSE) and mean unsigned error (MUE) computed for each method. Lattice vectors (*a, b, c*) in Å and β angle in degrees. MSE and MUE in %. Best results for each basis sets in bold face. 110
4.2 Equilibrium geometry of *t*-ZrO_2 and mean signed error (MSE) and mean unsigned error (MUE) computed for each method. Lattice parameters (*a, c*) and internal distortion d_{z0} in Å. MSE and MUE in %.[a] Best results for each basis sets in bold face. 111
4.3 Equilibrium geometry of *c*-ZrO_2 and mean signed error (MSE) and mean unsigned error (MUE) computed for each method. Lattice parameter a in Å. MSE and MUE in %. Best results for each basis sets in bold face. 112
4.4 Calculated energy difference between the monoclinic and the tetragonal polymorphs (E_m - E_t) and between the tetragonal and the cubic ones (E_t - E_c). Values in eV. Best results for each basis sets in bold face. 114
4.5 Computed band gaps (given in eV) of the monoclinic, tetragonal and cubic ZrO_2 phases, calculated with different Hamiltonians and basis sets. 116
4.6 Mulliken atomic charges (q, in *e*) and overlap population (b, in *e*) computed for monoclinic, tetragonal and cubic zirconia at the PBE0/Zr^{ECP}-O^{ECP} level. 119

4.7 Surface energies (in J/m^2), computed at the PBE0/Zr^{ECP}-O^{ECP} level, for the monoclinic (-111), tetragonal (101) and (111) and cubic (111) zirconia surfaces. *x*-L indicates a slab built with *x* layers. 123

4.8 Formation energy (E_f, in eV) of one surface or subsurface oxygen vacancy (with respect to $\frac{1}{2}O_2$ or to O) on the cubic ZrO_2 (111) surface, as a function of the spin state considered (T for triplet; S for singlet). 129

4.9 Displacements (in Å, from ideal positions) for the (111) surface with surface or subsurface oxygen vacancies. Atom labels refer to Figure 4.8 130

4.10 Mulliken atomic charges (in *e*) of selected Zr and O atoms of the clean (111) surface and of system with surface or subsurface vacancies. Atom labels refer to Figure 4.8 131

4.11 Band gap values (E_g) and positions of the defect level with respect to the valence band (VB) and the conduction band (CB) for surface and subsurface vacancies. All data in eV. 132

4.12 Energy of substitution and of the formation of oxygen vacancies (with respect to $\frac{1}{2}O_2$, $E_f(\frac{1}{2}O_2)$, or with respect to O, $E_f(O)$) for different configurations of two Y dopant atoms with respect to a surface or subsurface oxygen vacancy on the cubic ZrO_2 (111) surface. All data in eV. 137

4.13 Computed band gaps (E_g, in eV) for the different configurations of Y atoms with respect to a surface or subsurface vacancy on the (111) surface of YSZ. 137

5.1 Equilibrium geometry of α-phase of $LiNaCO_3$ with different Hamiltonians and mean signed error (MSE) and mean unsigned error (MUE) computed for each method. Lattice vectors (*a*, *b*, *c*) in Å, angles (α, β, γ) in degrees and volume (V) in Å^3. MSE and MUE in %. 149

5.2 Equilibrium geometry of β-phase of $LiNaCO_3$ with different Hamiltonians and mean signed error (MSE) and mean unsigned error (MUE) computed for each method. Lattice vectors (*a*, *c*) in Å. MSE and MUE in %. 149

5.3 Equilibrium geometry of Model A and Model B of the γ-phase of $LiNaCO_3$ with different Hamiltonians and mean signed error (MSE) and mean unsigned error (MUE) computed for each method. Lattice vectors (*a*, *c*) in Å. MSE and MUE in %. 149

5.4 Computed energy differences (kcal/mol) between: i) the α and the β polymorphs (E_α - E_β), ii) the β and Model A of the γ phase (E_α - E_β), iii) model A and B of the γ phase ($E_{\gamma A}$ - $E_{\gamma B}$) of $LiNaCO_3$.[a] 150

5.5 Equilibrium geometry of $LiKCO_3$ with different Hamiltonians and the all electron (AE) and pseudopotential (ECP) basis sets, together with mean signed error (MSE) and mean unsigned error (MUE) computed for each method. Lattice vectors (*a*, *c*) in Å, angles in degrees (°) and volume in Å^3. MSE and MUE in %. 151

5.6 Band gaps (eV) of the α, β and γ (Model A and B) phases of $LiNaCO_3$ and of $LiKCO_3$ calculated with different Hamiltonians. 155

5.7 Average Mulliken atomic charges (q, in *e*) and overlap population (b, in *e*) computed for the three $LiNaCO_3$ polymorphs and for $LiKCO_3$ at the PBE0 level. $LiKCO_3$ results refer to the HAYWSC-31 basis set. 156

5.8 Converged surface energy (E_s in J/m^2), converged band gap (E_g in eV) and number of layers necessary for the convergence (n) for the all the possible reconstructions of the (001) surface, for the non polar (110) surface of γ-$LiNaCO_3$ and for $LiNaCO_3$ surfaces. 160

5.9 Parameters of selected $Li_i^\bullet$ configurations: formation energy (E_f, in eV) relative to the most stable configuration, O-coordination number of the defect, value of the shortest distance (d($Li_i^\bullet$-M), in Å) between $Li_i^\bullet$ and the positively charged species (M) in the $LiKCO_3$ lattice, and stick representation of the corresponding atomic configuration evidencing the position of the inserted specie (in green) in the channel and its O-coordination. 167

6.1 Optimized lattice vectors (*a*, *b*, *c* in Å), angle (γ, in degrees) and surface area (S in Å^2) of the YSZ-$LiKCO_3$ interface models together with the adhesion energy ($E_{ads}^{YSZ/LiKCO_3}$ in eV), specific adhesion energy ($\beta^{YSZ/LiKCO_3}$in eV/Å^2), and band gap (E_g in eV). 187

6.2 Comparison between selected computed and experimental IR frequencies (cm^{-1}) for the YSZ-$LiKCO_3$ composite and relative assignment. 190

6.3 Comparison between selected computed and experimental Raman frequencies (cm^{-1}) for the YSZ-$LiKCO_3$ composite and relative assignment. 192

6.4 Mulliken charges (q, in *e*) and overlap bond populations (b, in *e*) averaged over all the atoms in the YSZ-$LiKCO_3$ composite model or just over the ones directly involved in the formation of the interfacial layer (first O and Zr/Y atomic layers for YSZ, the two CO_3 groups directly linked on the oxide surface and the Li atom closest to YSZ surface for $LiKCO_3$). m and p exponents are referred to the monodentate and bidentate carbonate group, respectively. 195

6.5 Parameters of selected Li_i^X configurations: O-coordination number of the defect, value of the shortest distance (d(Li_i^X-M), in Å) between Li_i^X and the positively charged species (M) in the YSZ-$LiKCO_3$ structure, Mulliken charges (q in *e*) and spin density (b in *e*) of Li_i^X and of the neighbouring atoms where the majority of the excess electron is localized, formation energy (E_f, in eV), highest energy barrier associated to Li_i^X diffusion (E_{barr}, in eV) and relative mechanism type, together with the spin density plot (0.002 a.u.) and the ball and stick representation of the corresponding atomic configuration evidencing the position and O-coordination of the interstitial Li atom (in green). Formation energies are computed using for the chemical potential the value obtained for Li bulk metal with $\Delta\mu_{Li} = 0$ (oxygen poor limit, see the text). 199

6.6 Parameters of selected Li_{FP} configurations: O-coordination number of the defect, value of the shortest distance (d($Li_i^{\bullet}$-M), in Å) between $Li_i^{\bullet}$ and the positively charged species (M) in the YSZ-$LiKCO_3$ lattice, formation energy (E_f, in eV), energy barrier associated to the vacancy diffusion (E_{barr}, in eV) and relative mechanism type, together with the stick representation of the corresponding atomic configuration, evidencing the position and O-coordination of the interstitial Li at the interface (in blue) and the Li vacancy left in the bulk carbonate phase (hashed light blue sphere). 206

6.7 Parameters for O^{2-}-related species at the YSZ-$LiKCO_3$ interface, namely the oxygen Frenkel pair (O_{FP}) and the O^{2-} anion introduced together with the two interstitial Li cations (2$Li_i^{\bullet}$-O^{2-}): distance (d(O^*-M, in Å) between the O^{2-} anion (O^*) and the closest cations (M), formation energy (E_f, in eV), energy barrier associated to the vacancy diffusion (E_{barr}, in eV) and relative mechanism type, together with stick representation of the corresponding atomic configuration evidencing the position of the O^{2-} anion (in orange), $V_O^{\bullet\bullet}$ (hashed orange sphere), and of the interstitial Li cations (in blue). . . . 210

6.8 Parameters of selected configurations for an O atom (O^*) at the interface of the YSZ-$LiKCO_3$ composite (O_{int}): distance (d(O^*-O_O), in Å) between the O^* and the oxygen atom of the CO_3 group on which it is adsorbed (O_O), distances between the C atom and the O atoms of this carbonate group, Mulliken charges on selected atoms, stick representation of the corresponding atomic configuration evidencing the position of the O^* atom (in yellow), formation energy (E_f, in eV), energy barrier associated to the O atom diffusion (E_{barr}, in eV) and relative mechanism type. 213

6.9 Parameters of selected configurations for an O atom (O^*) in the carbonate bulk phase of the YSZ-$LiKCO_3$ composite (O_{carb}): distance (d(O^*-O_O), in Å) between the O^* and the oxygen atom of the CO_3 group on which it is adsorbed (O_O), distances between the C atom and the O atoms of this carbonate group, Mulliken charges on selected atoms, stick representation of the corresponding atomic configuration evidencing the position of the O^* atom (in yellow), formation energy (E_f, in eV), energy barrier associated to the O atom diffusion (E_{barr}, in eV) and relative mechanism type. 214

6.10 Parameters of selected configurations for two protons (H^+) and one oxide ion (O^{2-}) in the YSZ-$LiKCO_3$ composite: stick representation of the corresponding atomic configuration evidencing the position of the O^{2-} ion (orange ball) and protons (light blue balls), formation energy (E_f, in eV), energy barrier associated to the proton atom diffusion (E_{barr}, in eV) and relative mechanism type. 217

6.11 Comparison between the computed and experimental values of the diffusion coefficients (D_X, in units of 10^{-2} cm^2/s for the different species of the carbonate phase. Temperature (T) in K. 223

6.12 Comparison between the computed and experimental values of the activivation energy for the diffusion coefficients ($E_a^{(D_X)}$, in eV) for the different species of the carbonate phase. 223

7.1 Optimized lattice vectors (a, b, c in Å), angle (γ, in degrees) and surface area (S in Å^2) of the TiO_2-$LiKCO_3$ interface model together with its adhesion energy ($E_{ads}^{YSZ/LiKCO_3}$ in eV), specific adhesion energy ($\beta^{YSZ/LiKCO_3}$in eV/Å^2), and optimized band gap (E_g in eV) 232
7.2 Mulliken charges (q, in e) and overlap bond populations (b, in e) averaged over the all atoms in the TiO_2-$LiKCO_3$ composite model or just over the ones directly involved in the formation of the interfacial layer (first O and Ti atomic layers for TiO_2, the two CO_3 groups directly linked on the oxide surface and the Li and K atoms closest to TiO_2 surface for $LiKCO_3$). $2c$ and $3c$ superscripts are referred, respectively, to the surface 2-fold and 3-fold O-coordinated TiO_2 oxygen atoms (see figure 7.1). 235
7.3 Relative formation energy (ΔE_f, in eV) with respect to the most stable configuration for a Li_i^X defect in the TiO_2-$LiKCO_3$ composite or at the TiO_2-(101) surface. 237
7.4 Barrier for the intercalation (E_{barr}, in eV) of Li_i^X in the Ti_2-$LiKCO_3$ interface or in the bare TiO_2-(101) surface. 238

Bibliography

[1] Convention-cadre sur les changements climatiques, Website, **2015**, http://unfccc.int/resource/docs/2015/cop21/fre/l09f.pdf.

[2] Energy Technology Perspectives, International Energy Agency, **2014**.

[3] World Energy Outlook Special briefing for COP21, International Energy Agency, **2015**.

[4] World Energy Outlook 2015 Factsheet1, International Energy Agency, **2015**.

[5] Renewable energy progress report, European Commission, **2015**.

[6] Renewables in global energy supply, International Energy Agency, **2007**.

[7] Energy Technology Perspectives, International Energy Agency, **2015**.

[8] T. Elmer, M. Worall, S. Wu, S. B. Riffat, *Renewable and Sustainable Energy Reviews* **2015**, *42*, 913 – 931, DOI http://dx.doi.org/10.1016/j.rser.2014.10.080.

[9] O. Z. Sharaf, M. F. Orhan, *Renewable and Sustainable Energy Reviews* **2014**, *32*, 810 – 853, DOI http://dx.doi.org/10.1016/j.rser.2014.01.012.

[10] S. C. Singhal, *Wiley Interdisciplinary Reviews: Energy and Environment* **2014**, *3*(2), 179–194, DOI 10.1002/wene.96.

[11] M. von Spakovsky, B. Olsommer, *Energy Conversion and Management* **2002**, *43*(912), 1249 – 1257, DOI http://dx.doi.org/10.1016/S0196-8904(02)00011-0.

[12] E. Fabbri, L. Bi, D. Pergolesi, E. Traversa, *Advanced Materials* **2012**, *24*(2), 195–208, DOI 10.1002/adma.201103102.

[13] E. Wachsman, T. Ishihara, J. Kilner, *MRS Bulletin* **2014**, *39*, 773–779, DOI 10.1557/mrs.2014.192.

[14] FCT. Fuel Cell today: the leading authority on fuel cels: the fuel cell today industry review, Website, **2013**, http://www.fuelcelltoday.com/media/1889744/fct_review_2013.pdf.

[15] Z. Shao, W. Zhou, Z. Zhu, *Progress in Materials Science* **2012**, *57*(4), 804 – 874, DOI http://dx.doi.org/10.1016/j.pmatsci.2011.08.002.

[16] E. D. Wachsman, C. A. Marlowe, K. T. Lee, *Energy Environ. Sci.* **2012**, *5*, 5498–5509, DOI 10.1039/C1EE02445K.

[17] I. Thomas A. Adams, J. Nease, D. Tucker, P. I. Barton, *Industrial & Engineering Chemistry Research* **2013**, *52*(9), 3089–3111, DOI 10.1021/ie300996r.

[18] B. Zhu, *Journal of Power Sources* **2003**, *114*(1), 1 – 9, DOI http://dx.doi.org/10.1016/S0378-7753(02)00592-X.

[19] M. Benamira, A. Ringuedé, V. Albin, R.-N. Vannier, L. Hildebrandt, C. Lagergren, M. Cassir, *J. Power Sources* **2011**, *196*(13), 5546–5554, DOI 10.1016/j.jpowsour.2011.02.004.

[20] X. Wang, Y. Ma, S. Li, A.-H. Kashyout, B. Zhu, M. Muhammed, *Journal of Power Sources* **2011**, *196*(5), 2754 – 2758, DOI http://dx.doi.org/10.1016/j.jpowsour.2010.11.033.

[21] R. Raza, X. Wang, Y. Ma, X. Liu, B. Zhu, *International Journal of Hydrogen Energy* **2010**, *35*(7), 2684 – 2688, 2008 International Hydrogen Forum (HyForum2008)2008 International Hydrogen, DOI http://dx.doi.org/10.1016/j.ijhydene.2009.04.038.

[22] M. Benamira, A. Ringued, L. Hildebrandt, C. Lagergren, R.-N. Vannier, M. Cassir, *International Journal of Hydrogen Energy* **2012**, *37*(24), 19371 – 19379, 2011 International Workshop on Molten Carbonates Related Topics, DOI http://dx.doi.org/10.1016/j.ijhydene.2011.10.062.

[23] U. Lucia, *Renewable and Sustainable Energy Reviews* **2014**, *30*, 164 – 169, DOI http://dx.doi.org/10.1016/j.rser.2013.09.025.

[24] C. F. Schoenbein, *The London and Edinburgh Philosophical Magazine and Journal of Science* **1839**, *14*(3rd Series), 43.

[25] W. R. Grove, *The London and Edinburgh Philosophical Magazine and Journal of Science* **1839**, *14*(3rd Series), 127.

[26] L. Mond, C. Langer, *Proceedings of the Royal Society of London* **1889**, *46*(4), 296.

[27] J. A. A. Ketelaar, *History*, New York Millenium Press, **1993**, 1, DOI 10.1002/9783527635566.ch5.

[28] A. J. Appleby, F. R. Foulkes, Van Nostrand Reinhold, **1989**, 1, DOI 10.1002/9783527635566.ch5.

[29] S. P. Jiang, X. Wang, *Fuel Cells: Advances and Challenges*, Wiley-VCH Verlag GmbH and Co. KGaA, **2011**, 179–264, DOI 10.1002/9783527635566.ch5.

[30] F. Lefebvre-Joud, G. Gauthier, J. Mougin, *Journal of Applied Electrochemistry* **2009**, *39*(4), 535–543, DOI 10.1007/s10800-008-9744-7.

[31] E. Baur, H. Preis, *Zeitung fur Elektrochemie* **1937**, *43*, 727.

[32] S. Kakac, a. Pramuanjaroenkij, X. Zhou, *Int. J. Hydrogen Energy* **2007**, *32*(7), 761–786, DOI 10.1016/j.ijhydene.2006.11.028.

[33] N. Q. Minh, T. Takahashi, in *Science and Technology of Ceramic Fuel Cells*, (Herausgegeben von N. Q. Minh, T. Takahashi), Elsevier Science Ltd, Oxford, **1995**, 117 – 146, DOI http://dx.doi.org/10.1016/B978-044489568-4/50006-2.

[34] Y. Sakaki, Y. Takeda, A. Kato, N. Imanishi, O. Yamamoto, M. Hattori, M. Iio, Y. Esaki, *Solid State Ionics* **1999**, *118*(3?4), 187 – 194, DOI http://dx.doi.org/10.1016/S0167-2738(98)00440-8.

[35] A. Mitterdorfer, L. Gauckler, *Solid State Ionics* **1998**, *111*(3?4), 185 – 218, DOI http://dx.doi.org/10.1016/S0167-2738(98)00195-7.

[36] M. Brant, T. Matencio, L. Dessemond, R. Domingues, *Solid State Ionics* **2006**, *177*(9?10), 915 – 921, DOI http://dx.doi.org/10.1016/j.ssi.2006.02.012.

[37] A. Barbucci, R. Bozzo, G. Cerisola, P. Costamagna, *Electrochimica Acta* **2002**, *47*(13?14), 2183 – 2188, DOI http://dx.doi.org/10.1016/S0013-4686(02)00095-6.

[38] E. M. Perry, S. A. Barnett, *Solid State Ionics* **2001**, *143*(2-4), 265 – 273, DOI http://dx.doi.org/10.1016/S0013-4686(02)00095-6.

[39] Z. Shao, S. Haile, *Nature* **2004**, *431*(7005), 170–173, DOI http://dx.doi.org/10.1016/S0013-4686(02)00095-6.

[40] S. P. Jiang, S. H. Chan, *Journal of Materials Science 39*(14), 4405–4439, DOI 10.1023/B:JMSC.0000034135.52164.6b.

[41] S. Aruna, M. Muthuraman, K. Patil, *Solid State Ionics* **1998**, *111*(1?2), 45 – 51, DOI http://dx.doi.org/10.1016/S0167-2738(98)00187-8.

[42] M. Brown, S. Primdahl, M. Mogensen, *Journal of The Electrochemical Society* **2000**, *147*(2), 475–485, DOI 10.1149/1.1393220.

[43] J.-H. Koh, Y.-S. Yoo, J.-W. Park, H. C. Lim, *Solid State Ionics* **2002**, *149*(3?4), 157 – 166, DOI http://dx.doi.org/10.1016/S0167-2738(02)00243-6.

[44] V. Alzate-Restrepo, J. M. Hill, *Applied Catalysis A: General* **2008**, *342*(1?2), 49 – 55, DOI http://dx.doi.org/10.1016/j.apcata.2007.12.039.

[45] A. Benyoucef, D. Klein, C. Coddet, B. Benyoucef, *Surface and Coatings Technology* **2008**, *202*(10), 2202 – 2207, DOI http://dx.doi.org/10.1016/j.surfcoat.2007.09.009.

[46] D. Fagg, J. Frade, M. Mogensen, J. Irvine, *Journal of Solid State Chemistry* **2007**, *180*(8), 2371 – 2376, DOI http://dx.doi.org/10.1016/j.jssc.2007.06.016.

[47] V. Kharton, F. Marques, A. Atkinson, *Solid State Ionics* **2004**, *174*(1?4), 135 – 149, solid State Ionics Dokiya Memorial Special Issue, DOI http://dx.doi.org/10.1016/j.ssi.2004.06.015.

[48] J. W. Fergus, *Journal of Power Sources* **2006**, *162*(1), 30 – 40, DOI http://dx.doi.org/10.1016/j.jpowsour.2006.06.062.

[49] J. Huang, F. Xie, C. Wang, Z. Mao, *International Journal of Hydrogen Energy* **2012**, *37*(1), 877 – 883, 11th China Hydrogen Energy Conference, DOI http://dx.doi.org/10.1016/j.ijhydene.2011.04.030.

[50] Z. Gao, L. V. Mogni, E. C. Miller, J. G. Railsback, S. A. Barnett, *Energy Environ. Sci.* **2016**, –, DOI 10.1039/C5EE03858H.

[51] Y. Zhao, C. Xia, L. Jia, Z. Wang, H. Li, J. Yu, Y. Li, *International Journal of Hydrogen Energy* **2013**, *38*(36), 16498 – 16517, DOI http://dx.doi.org/10.1016/j.ijhydene.2013.07.077.

[52] E. V. Tsipis, V. V. Kharton, *Journal of Solid State Electrochemistry* **2007**, *12*(9), 1039–1060, DOI 10.1007/s10008-007-0468-0.

[53] E. V. Tsipis, V. V. Kharton, *Journal of Solid State Electrochemistry* **2008**, *12*(11), 1367–1391, DOI 10.1007/s10008-008-0611-6.

[54] P.-C. Su, C.-C. Chao, J. H. Shim, R. Fasching, F. B. Prinz, *Nano Letters* **2008**, *8*(8), 2289–2292, pMID: 18605702, DOI 10.1021/nl800977z.

[55] H. Huang, M. Nakamura, P. Su, R. Fasching, Y. Saito, F. B. Prinz, *Journal of The Electrochemical Society* **2007**, *154*(1), B20–B24, DOI 10.1149/1.2372592.

[56] B. C. H. Steele, A. Heinzel, *Nature* **2001**, *414*, 345–352, DOI http://dx.doi.org/10.1016/j.jpowsour.2006.06.062.

[57] S. R. Hui, J. Roller, S. Yick, X. Zhang, C. Decs-Petit, Y. Xie, R. Maric, D. Ghosh, *Journal of Power Sources* **2007**, *172*(2), 493 – 502, DOI http://dx.doi.org/10.1016/j.jpowsour.2007.07.071.

[58] T. Ishihara, *Bulletin of the Chemical Society of Japan* **2006**, *79*(8), 1155–1166, DOI 10.1246/bcsj.79.1155.

[59] M. Mori, Y. Liu, S. Ma, S. ichi Hashimoto, K. Takei, *Journal of the Korean Ceramic Society* **2008**, *45*(12), 760–765, DOI 10.1149/1.2372592.

[60] A. Weber, E. Ivers-Tiffe, *Journal of Power Sources* **2004**, *127*(1?2), 273 – 283, eighth Ulmer Electrochemische Tage, DOI http://dx.doi.org/10.1016/j.jpowsour.2003.09.024.

[61] B. Steele, *Solid State Ionics* **2000**, *129*(1?4), 95 – 110, DOI http://dx.doi.org/10.1016/S0167-2738(99)00319-7.

[62] M. Mogensen, N. M. Sammes, G. A. Tompsett, *Solid State Ionics* **2000**, *129*(1?4), 63 – 94, DOI http://dx.doi.org/10.1016/S0167-2738(99)00318-5.

[63] N. Sammes, G. Tompsett, H. Nfe, F. Aldinger, *Journal of the European Ceramic Society* **1999**, *19*(10), 1801 – 1826, DOI http://dx.doi.org/10.1016/S0955-2219(99)00009-6.

[64] J. C. Boivin, , G. Mairesse, *Chemistry of Materials* **1998**, *10*(10), 2870–2888, DOI 10.1021/cm980236q.

[65] M. Cassir, C. Belhomme, *Plasmas & Ions* **1999**, *2*(1), 3 – 15, DOI http://dx.doi.org/10.1016/S1288-3255(99)80006-9.

[66] S. J. McPhail, A. Aarva, H. Devianto, R. Bove, A. Moreno, *International Journal of Hydrogen Energy* **2011**, *36*(16), 10337 – 10345, european Fuel Cell 2009, DOI http://dx.doi.org/10.1016/j.ijhydene.2010.09.071.

[67] P. Tomczyk, *Journal of Power Sources* **2006**, *160*(2), 858 – 862, special issue including selected papers presented at the International Workshop on Molten Carbonate Fuel Cells and Related Science and Technology 2005 together with regular papers, DOI http://dx.doi.org/10.1016/j.jpowsour.2006.04.071.

[68] J.-H. Wee, K.-Y. Lee, *Journal of Materials Science* **2006**, *41*(12), 3585–3592, DOI 10.1007/s10853-005-5551-2.

[69] N. F. Uvarov, *J. Solid State Electrochem.* **2011**, *15*(2), 367–389, DOI 10.1007/s10008-008-0739-4.

[70] R. C. Agrawal, R. K. Gupta, *J. Mater. Sci.* **1999**, *4*, 1131–1162.

[71] P. Knauth, *J. Electroceramics* **2000**, *5*(2), 111–125, DOI 10.1023/A:1009906101421.

[72] W. Jander, *Angewandte Chemie* **1929**, *42*(19), 462–467, DOI 10.1002/ange.19290421904.

[73] C. C. Liang, *Journal of The Electrochemical Society* **1973**, *120*(10), 1289–1292, DOI 10.1149/1.2403248.

[74] G. Gouy, *Journal of Physical Chemistry* **1903**, *29*, 145.

[75] K. L. Kliewer, J. S. Koehler, *Phys. Rev.* **1965**, *140*, A1226–A1240, DOI 10.1103/PhysRev.140.A1226.

[76] C. Wagner, *Journal of Physics and Chemistry of Solids* **1972**, *33*(5), 1051 – 1059, DOI http://dx.doi.org/10.1016/S0022-3697(72)80265-8.

[77] T. Jow, J. B. Wagner, *Journal of The Electrochemical Society* **1979**, *126*(11), 1963–1972, DOI 10.1149/1.2128835.

[78] J. Maier, *Berichte der Bunsengesellschaft für Phys. Chemie* **1984**, *88*(11), 1057–1062, DOI 10.1002/bbpc.198400007.

[79] J. Maier, *J. Phys. Chem. Solids* **1985**, *46*(3), 309–320, DOI 10.1016/0022-3697(85)90172-6.

[80] J. Maier, *J. Phys. Chem. Solids* **1985**, *46*(3), 309–320, DOI 10.1016/0022-3697(85)90172-6.

[81] J. Maier, *Mater. Chem. Phys.* **1987**, *7*, 485–498.

[82] J. Maier, *Journal of The Electrochemical Society* **1987**, *134*(6), 1524–1535, DOI 10.1149/1.2100703.

[83] J. Maier, *Solid State Ionics* **1994**, *70-71*, 43–51, DOI 10.1016/0167-2738(94)90285-2.

[84] J. Maier, *Prog. Solid State Chem.* **1995**, *23*(3), 171–263, DOI 10.1016/0079-6786(95)00004-E.

[85] V. V. Belousov, *J. Eur. Ceram. Soc.* **2007**, *27*(12), 3459–3467, DOI 10.1016/j.jeurceramsoc.2007.01.014.

[86] S. Jiang, J. W. Jr, *Journal of Physics and Chemistry of Solids* **1995**, *56*(8), 1101 – 1111, DOI http://dx.doi.org/10.1016/0022-3697(95)00025-9.

[87] V. V. Belousov, *Journal of the American Ceramic Society* **1996**, *79*(6), 1703–1706, DOI 10.1111/j.1151-2916.1996.tb08789.x.

[88] B. Zhu, B. Mellander, in *Systems with Fast Ionic Transport - IV*, Bd. 39 von *Solid State Phenomena*, Trans Tech Publications, Bd. 39 von *Solid State Phenomena*, 19–22, DOI 10.4028/www.scientific.net/SSP.39-40.19.

[89] B. Zhu, M. D. Mat, *Int. J. Electrochem. Sci.* **2006**, *1*, 383–402.

[90] B. Zhu, *Journal of Power Sources* **2001**, *93*(1?2), 82 – 86, DOI http://dx.doi.org/10.1016/S0378-7753(00)00564-4.

[91] J. Huang, Z. Mao, L. Yang, R. Peng, *Electrochemical and Solid-State Letters* **2005**, *8*(9), A437–A440, DOI 10.1149/1.1960139.

[92] X. Wang, Y. Ma, B. Zhu, *Int. J. Hydrogen Energy* **2012**, *37*(24), 19417–19425.

[93] L. Fan, C. Wang, M. Chen, B. Zhu, *Journal of Power Sources* **2013**, *234*, 154 – 174, DOI http://dx.doi.org/10.1016/j.jpowsour.2013.01.138.

[94] S. Rajesh, D. A. Macedo, R. M. Nascimento **2013**, 485–494.

[95] B. Zhu, *International Journal of Energy Research* **2006**, *30*(11), 895–903, DOI 10.1002/er.1195.

[96] J. Patakangas, Y. Ma, Y. Jing, P. Lund, *J. Power Sources* **2014**, *263*, 315–331, DOI 10.1016/j.jpowsour.2014.04.008.

[97] B. Zhu, L. Fan, P. Lund, *Appl. Energy* **2013**, *106*, 163–175, DOI 10.1016/j.apenergy.2013.01.014.

[98] A. S. V. Ferreira, T. Saradha, F. L. Figueiredo, F. M. B. Marques, *International Journal of Energy Research* **2011**, *35*(12), 1090–1099, DOI 10.1002/er.1843.

[99] F. J. a. Loureiro, S. Rajesh, F. M. L. Figueiredo, F. M. B. Marques, *RSC Adv.* **2014**, *4*, 59943–59952, DOI 10.1039/C4RA11446A.

[100] S. Tanase, Y. Miyazaki, M. Yanagida, K. Tanimoto, T. Kodama, *Progress in Batteries and Solar Cells*, **1987**, 6.

[101] M. Sangster, A. D. Pelton, *Special Report to the Phase Equilibria Program*, American Ceramic Society Westerville, Ohio, **1987**, 4–231.

[102] G. J. Janz, M. R. Lorenz, *Chem. Eng. Data* **1961**, *6*(3), 321–323.

[103] J. Huang, Z. Gao, Z. Mao, *Int. J. Hydrogen Energy* **2010**, *35*(9), 4270–4275, DOI 10.1016/j.ijhydene.2010.01.063.

[104] X. Wang, Y. Ma, R. Raza, M. Muhammed, B. Zhu, *Electrochemistry Communications* **2008**, *10*(10), 1617 – 1620, DOI http://dx.doi.org/10.1016/j.elecom.2008.08.023.

[105] R. Raza, X. Wang, Y. Ma, X. Liu, B. Zhu, *Int. J. Hydrogen Energy* **2010**, *35*(7), 2684–2688, DOI 10.1016/j.ijhydene.2009.04.038.

[106] C. Lapa, D. de Souza, F. Figueiredo, F. Marques, *International Journal of Hydrogen Energy* **2010**, *35*(7), 2737 – 2741, 2008 International Hydrogen Forum (HyForum2008)2008 International Hydrogen, DOI http://dx.doi.org/10.1016/j.ijhydene.2009.04.056.

[107] Y. Xia, Y. Bai, X. Wu, D. Zhou, X. Liu, J. Meng, *International Journal of Hydrogen Energy* **2011**, *36*(11), 6840 – 6850, DOI http://dx.doi.org/10.1016/j.ijhydene.2011.02.118.

[108] T. Schober, *Electrochemical and Solid-State Letters* **2005**, *8*(4), A199–A200, DOI 10.1149/1.1865592.

[109] X. Li, N. Xu, L. Zhang, K. Huang, *Electrochemistry Communications* **2011**, *13*(7), 694 – 697, DOI http://dx.doi.org/10.1016/j.elecom.2011.04.012.

[110] C. Xia, Y. Li, Y. Tian, Q. Liu, Z. Wang, L. Jia, Y. Zhao, Y. Li, *J. Power Sources* **2010**, *195*(10), 3149–3154, DOI 10.1016/j.jpowsour.2009.11.104.

[111] J. Huang, Z. Mao, Z. Liu, C. Wang **2007**, *9*, 2601–2605, DOI 10.1016/j.elecom.2007.07.036.

[112] A. Bodn, J. Di, C. Lagergren, G. Lindbergh, C. Y. Wang, *Journal of Power Sources* **2007**, *172*(2), 520 – 529, DOI http://dx.doi.org/10.1016/j.jpowsour.2007.07.065.

[113] B. Zhu, C. Y. Wang, J. Di, M. M. Chen, J. M. Zheng, in *Chinese Ceramics Communications*, Bd. 105 von *Advanced Materials Research*, Trans Tech Publications, Bd. 105 von *Advanced Materials Research*, 687–690, DOI 10.4028/www.scientific.net/AMR.105-106.687.

[114] L. Zhang, R. Lan, X. Xu, S. Tao, Y. Jiang, A. Kraft, *Journal of Power Sources* **2009**, *194*(2), 967 – 971, DOI http://dx.doi.org/10.1016/j.jpowsour.2009.06.062.

[115] S. A. Song, S.-C. Jang, J. Han, S. P. Yoon, S. W. Nam, I.-H. Oh, T.-H. Lim, *Journal of Power Sources* **2011**, *196*(23), 9900 – 9905, DOI http://dx.doi.org/10.1016/j.jpowsour.2011.08.032.

[116] W. Liu, Y. Liu, B. Li, T. D. Sparks, X. Wei, W. Pan, *Composites Science and Technology* **2010**, *70*(1), 181 – 185, DOI http://dx.doi.org/10.1016/j.compscitech.2009.10.006.

[117] R. Raza, H. Qin, L. Fan, K. Takeda, M. Mizuhata, B. Zhu, *J. Power Sources* **2012**, *201*, 121–127, DOI 10.1016/j.jpowsour.2011.10.124.

[118] C. Xia, Y. Li, Y. Tian, Q. Liu, Y. Zhao, L. Jia, Y. Li, *J. Power Sources* **2009**, *188*(1), 156–162, DOI 10.1016/j.jpowsour.2008.11.068.

[119] B. Zhu, I. Albinsson, C. Andersson, K. Borsand, M. Nilsson, B.-E. Mellander, *Electrochem. commun.* **2006**, *8*(3), 495–498, DOI 10.1016/j.elecom.2006.01.011.

[120] J. Huang, L. Yang, R. Gao, Z. Mao, C. Wang, *Electrochemistry Communications* **2006**, *8*(5), 785 – 789, DOI http://dx.doi.org/10.1016/j.elecom.2006.03.016.

[121] J. Huang, Z. Mao, Z. Liu, C. Wang, *Journal of Power Sources* **2008**, *175*(1), 238 – 243, DOI http://dx.doi.org/10.1016/j.jpowsour.2007.09.018.

[122] J. Di, M. Chen, C. Wang, J. Zheng, L. Fan, B. Zhu, *Journal of Power Sources* **2010**, *195*(15), 4695 – 4699, DOI http://dx.doi.org/10.1016/j.jpowsour.2010.02.066.

[123] C. Xia, Y. Li, Y. Tian, Q. Liu, Y. Zhao, L. Jia, Y. Li, *J. Power Sources* **2009**, *188*(1), 156–162, DOI 10.1016/j.jpowsour.2008.11.068.

[124] Y. Li, Z. Rui, C. Xia, M. Anderson, Y. Lin, *Catal. Today* **2009**, *148*(3-4), 303–309, DOI 10.1016/j.cattod.2009.08.009.

[125] S. Li, J. Sun, *Int. J. Hydrogen Energy* **2010**, *35*(7), 2980–2985, DOI 10.1016/j.ijhydene.2009.05.096.

[126] H. Nafe, *ECS J. Solid State Sci. Technol.* **2013**, *3*(2), N7–N14, DOI 10.1149/2.015402jss.

[127] A. S. Ferreira, C. M. Soares, F. M. Figueiredo, F. M. Marques, *International Journal of Hydrogen Energy* **2011**, *36*(5), 3704 – 3711, DOI http://dx.doi.org/10.1016/j.ijhydene.2010.12.025.

[128] Y. Ma, X. Wang, R. Raza, M. Muhammed, B. Zhu, *Int. J. Hydrogen Energy* **2010**, *35*(7), 2580–2585, DOI 10.1016/j.ijhydene.2009.03.052.

[129] B. Zhu, X. Yang, J. Xu, Z. Zhu, S. Ji, M. Sun, J. Sun, *Journal of Power Sources* **2003**, *118*(1?2), 47 – 53, scientific Advances in Fuel Cell Systems, DOI http://dx.doi.org/10.1016/S0378-7753(03)00060-0.

[130] Y. Zhen, A. Tok, S. Jiang, F. Boey, *Journal of Power Sources* **2008**, *178*(1), 69 – 74, DOI http://dx.doi.org/10.1016/j.jpowsour.2007.11.113.

[131] R. Raza, B. Zhu, T. H. Fransson, *J. Fuel Cell Sci. Technol.* **2011**, *8*(3), 31010, DOI 10.1115/1.4002904.

[132] J. Huang, F. Xie, C. Wang, Z. Mao, *International Journal of Hydrogen Energy* **2012**, *37*(1), 877 – 883, 11th China Hydrogen Energy Conference, DOI http://dx.doi.org/10.1016/j.ijhydene.2011.04.030.

[133] Z. Gao, R. Raza, B. Zhu, Z. Mao, *International Journal of Energy Research* **2011**, *35*(8), 690–696, DOI 10.1002/er.1718.

[134] Z. Gao, R. Raza, B. Zhu, Z. Mao, C. Wang, Z. Liu, *International Journal of Hydrogen Energy* **2011**, *36*(6), 3984 – 3988, 3rd International Workshop in Hydrogen Energy, DOI http://dx.doi.org/10.1016/j.ijhydene.2010.12.061.

[135] S. K. Imran, R. Raza, G. Abbas, B. Zhu, *J. Fuel Cell Sci. Technol.* **2011**, *8*(6), 61014, DOI 10.1115/1.4004475.

[136] R. Raza, H. Qin, Q. Liu, M. Samavati, R. B. Lima, B. Zhu, *Advanced Energy Materials* **2011**, *1*(6), 1225–1233, DOI 10.1002/aenm.201100318.

[137] L. Zhang, R. Lan, A. Kraft, S. Tao, *Electrochemistry Communications* **2011**, *13*(6), 582 – 585, DOI http://dx.doi.org/10.1016/j.elecom.2011.03.015.

[138] M. D. Mat, X. Liu, Z. Zhu, B. Zhu, *Int. J. Hydrogen Energy* **2007**, *32*(7), 796–801, DOI 10.1016/j.ijhydene.2006.12.012.

[139] J. Hu, S. Tosto, Z. Guo, Y. Wang, *Journal of Power Sources* **2006**, *154*(1), 106 – 114, DOI http://dx.doi.org/10.1016/j.jpowsour.2005.03.225.

[140] M. Afzal, R. Raza, S. Du, R. B. Lima, B. Zhu, *Electrochimica Acta* **2015**, *178*, 385 – 391, DOI http://dx.doi.org/10.1016/j.electacta.2015.07.183.

[141] J. Pereira, S. Rajesh, F. Figueiredo, F. Marques, *Electrochimica Acta* **2013**, *90*, 71 – 79, DOI http://dx.doi.org/10.1016/j.electacta.2012.12.035.

[142] Y. Zhao, D.-B. Xiong, H. Qin, F. Gao, H. Inui, B. Zhu, *International Journal of Hydrogen Energy* **2012**, *37*(24), 19351 – 19356, 2011 International Workshop on Molten Carbonates and Related Topics, DOI http://dx.doi.org/10.1016/j.ijhydene.2011.11.003.

[143] W. Tan, L. Fan, R. Raza, M. A. Khan, B. Zhu, *International Journal of Hydrogen Energy* **2013**, *38*(1), 370 – 376, european Fuel Cell 2011, DOI http://dx.doi.org/10.1016/j.ijhydene.2012.09.160.

[144] Y. Jing, H. Qin, Q. Liu, M. Singh, B. Zhu, *Journal of Nanoscience and Nanotechnology* **2012**, *12*(6), 5102–5105, DOI doi:10.1166/jnn.2012.4940.

[145] R. Raza, Q. Liu, J. Nisar, X. Wang, Y. Ma, B. Zhu, *Electrochemistry Communications* **2011**, *13*(9), 917 – 920, DOI http://dx.doi.org/10.1016/j.elecom.2011.05.032.

[146] B. Zhu, S. Li, B.-E. Mellander, *Electrochem. commun.* **2008**, *10*(2), 302–305, DOI 10.1016/j.elecom.2007.11.037.

[147] X. Wang, Y. Ma, S. Li, A.-H. Kashyout, B. Zhu, M. Muhammed, *J. Power Sources* **2011**, *196*(5), 2754–2758.

[148] Y. Zhao, C. Xia, Y. Wang, Z. Xu, Y. Li, *Int. J. Hydrogen Energy* **2012**, *37*(10), 8556–8561, DOI 10.1016/j.ijhydene.2012.02.053.

[149] B. Zhu, X. Liu, Z. Zhu, R. Ljungberg, *International Journal of Hydrogen Energy* **2008**, *33*(13), 3385 – 3392, 2nd National and 1st Latin American Congress, Hydrogen and Sustainable Energy Sources, DOI http://dx.doi.org/10.1016/j.ijhydene.2008.03.065.

[150] C. Ricca, B. Medina-Lott, V. Albin, F. Labat, C. Adamo, M. Hinojosa, A. Ringuede, *ECS Transaction* **2015**, *68*(1), 2597–2609, DOI 10.1149/06801.2597ecst.

[151] R. H. F. Chung, S. de Leeuw, *Journal of Electroanalytical Chemistry* **2005**, *584*(1), 44 – 53, international Symposium on Material Processing for Nanostructured Devices 2003MPND 2003, DOI http://dx.doi.org/10.1016/j.jelechem.2004.06.035.

[152] I. I. Gainutdinov, N. F. Uvarov, *Solid State Ionics* **2006**, *177*(19?25), 1631 – 1634, solid State Ionics 15: Proceedings of the 15th International Conference on Solid State Ionics, Part I, DOI http://dx.doi.org/10.1016/j.ssi.2006.05.026.

[153] R. H. F. Chung, S. de Leeuw, *Solid State Ionics* **2004**, *175*(1?4), 851 – 855, fourteenth International Conference on Solid State Ionics, DOI http://dx.doi.org/10.1016/j.ssi.2004.09.047.

[154] K. Nomura, M. Kobayashi, *Ionics 9*(1), 64–66, DOI 10.1007/BF02376538.

[155] X. Lei, K. Huang, C. Qin, *Solid State Ionics* **2016**, *289*, 48 – 54, DOI http://dx.doi.org/10.1016/j.ssi.2016.02.018.

[156] M. Born, R. Oppenheimer, *Ann. Phys* **1927**, *84*(4), 457–484.

[157] D. R. Hartree, in *Mathematical Proceedings of the Cambridge Philosophical Society*, Bd. 24, Cambridge Univ Press, Bd. 24, 89–110.

[158] L. H. Thomas, in *Mathematical Proceedings of the Cambridge Philosophical Society*, Bd. 23, Cambridge Univ Press, Bd. 23, 542–548.

[159] E. Fermi, *Rend. Accad. Naz. Lincei* **1927**, *6*(602-607), 32.

[160] P. A. Dirac, in *Mathematical Proceedings of the Cambridge Philosophical Society*, Bd. 26, Cambridge Univ Press, Bd. 26, 376–385.

[161] P. Hohenberg, W. Kohn, *Kohn W, Sham LJ (1965) Phys Rev* **1964**, *140*, A1133.

[162] W. Kohn, L. J. Sham, *Physical review* **1965**, *140*(4A), A1133.

[163] S. H. Vosko, L. Wilk, M. Nusair, *Canadian Journal of physics* **1980**, *58*(8), 1200–1211.

[164] A. D. Becke, *J. Chem. Phys.* **1993**, *98*(7), 5648–5652.

[165] C. Lee, W. Yang, R. G. Parr, *Phys. Rev. B* **1988**, *37*(2), 785–789.

[166] J. P. Perdew, Y. Wang, *Phys. Rev. B* **1992**, *45*(23), 244–249.

[167] J. P. Perdew, Y. Wang, *Phys. Rev. B* **1989**, *40*(5), 3399.

[168] J. P. Perdew, A. Zunger, *Phys. Rev. B* **1981**, *23*(10), 5048–5079.

[169] J. Perdew, W. Yue, *Phys. Rev. B. Condens. Matter* **1986**, *33*(12), 8800.

[170] J. P. Perdew, K. Burke, M. Ernzerhof, *Phys. Rev. Lett* **1996**, *77*, 3865–3868.

[171] L. A. Curtiss, K. Raghavachari, G. W. Trucks, J. A. Pople, *The Journal of chemical physics* **1991**, *94*(11), 7221–7230.

[172] C. Adamo, V. Barone, *J. Chem. Phys.* **1999**, *110*(13), 6158–6170.

[173] M. Ernzerhof, G. E. Scuseria, *J. Chem. Phys.* **1999**, *110*(11), 5029–5036.

[174] A. V. Krukau, O. A. Vydrov, A. F. Izmaylov, G. E. Scuseria, *The Journal of Chemical Physics* **2006**, *125*(22), 224106, DOI http://dx.doi.org/10.1063/1.2404663.

[175] J. Heyd, G. E. Scuseria, M. Ernzerhof, *The Journal of Chemical Physics* **2003**, *118*(18), 8207–8215.

[176] J. Heyd, G. E. Scuseria, M. Ernzerhof, *The Journal of Chemical Physics* **2006**, *124*(21), 219906.

[177] S. Grimme, *J. Comput. Chem.* **2006**, *16*, 1787–1799.

[178] F. Bloch, *Zeitschrift für physik* **1929**, *52*(7-8), 555–600.

[179] R. Dovesi, V. R. Saunders, C. Roetti, R. Orlando, C. M. Zicovich-Wilson, F. Pascale, B. Civalleri, K. Doll, N. M. Harrison, I. J. Bush, P. D'Arco, M. Llunell, *CRYSTAL09 User's Manual*, University of Torino, Torino, **2009**.

[180] R. Dovesi, V. R. Saunders, C. Roetti, R. Orlando, F. Pascale, B. Civalleri, K. Doll, N. M. Harrison, I. J. Bush, P. D. Arco, M. Llunel, M. Caus, *CRYSTAL14 User's Manual*, University of Torino, Torino, **2014**.

[181] A. Dal Corso, *A Pseudopotential Plane Waves Program (PWSCF) and some Case Studies*, Springer Berlin Heidelberg, Berlin, Heidelberg, **1996**, 155–178, DOI 10.1007/978-3-642-61478-1_10.

[182] X. Gonze, F. Finocchi, *Physica Scripta* **2004**, *2004*(T109), 40.

[183] D. Hamann, M. Schlüter, C. Chiang, *Physical Review Letters* **1979**, *43*(20), 1494.

[184] G. Bachelet, D. Hamann, M. Schlüter, *Physical Review B* **1982**, *26*(8), 4199.

[185] D. Vanderbilt, *Physical Review B* **1990**, *41*(11), 7892.

[186] G. Kresse, J. Hafner, *Journal of Physics: Condensed Matter* **1994**, *6*(40), 8245.

[187] P. E. Blöchl, *Physical Review B* **1994**, *50*(24), 17953.

[188] G. Kresse, J. Furthmüller, *Phys. Rev. B* **1996**, *54*, 11169–11186, DOI 10.1103/PhysRevB.54.11169.

[189] G. Kresse, J. Furthmller, *Computational Materials Science* **1996**, *6*(1), 15 – 50, DOI http://dx.doi.org/10.1016/0927-0256(96)00008-0.

[190] G. Kresse, J. Hafner, *Phys. Rev. B* **1993**, *47*, 558–561, DOI 10.1103/PhysRevB.47.558.

[191] G. Kresse, J. Hafner, *Phys. Rev. B* **1994**, *49*, 14251–14269, DOI 10.1103/PhysRevB.49.14251.

[192] M. P. Allen, D. J. Tildesley, *Computer simulation of liquids*, Oxford university press, **1989**.

[193] M. E. Tuckerman, *Journal of Physics: Condensed Matter* **2002**, *14*(50), R1297.

[194] D. Marx, J. Hutter, *Modern methods and algorithms of quantum chemistry* **2000**, *1*(301-449), 141.

[195] R. Car, M. Parrinello, *Physical review letters* **1985**, *55*(22), 2471.

[196] L. Verlet, *Physical review* **1967**, *159*(1), 98.

[197] R. W. Hockney, Potential calculations and some applications., *Techn. Ber.*, Langley Research Center, Hampton, Va., **1970**.

[198] W. C. Swope, H. C. Andersen, P. H. Berens, K. R. Wilson, *The Journal of Chemical Physics* **1982**, *76*(1), 637–649.

[199] H. J. Berendsen, J. v. Postma, W. F. van Gunsteren, A. DiNola, J. Haak, *The Journal of chemical physics* **1984**, *81*(8), 3684–3690.

[200] H. C. Andersen, *The Journal of chemical physics* **1980**, *72*(4), 2384–2393.

[201] G. S. Grest, K. Kremer, *Physical Review A* **1986**, *33*(5), 3628.

[202] N. Shuichi, *Progress of Theoretical Physics Supplement* **1991**, *103*, 1–46, DOI 10.1143/PTPS.103.1.

[203] S. Nos, *Molecular Physics* **1984**, *52*(2), 255–268, DOI 10.1080/00268978400101201.

[204] W. G. Hoover, *Phys. Rev. A* **1985**, *31*, 1695–1697, DOI 10.1103/PhysRevA.31.1695.

[205] J. R. MacDonald, *Wiley-Interscience, John Wiley and Sons,* **1987**, 1–346.

[206] A. J. Bard, L. Faulkner, *Electrochemical Methods: Principles and Applications* **2001**, 386–428.

[207] T. Kojima, Y. Miyazaki, K. Nomura, K. Tanimoto, *J. Electrochem. Soc.* **2008**, *155*(7), F150–156, DOI 10.1149/1.2917212.

[208] V. Lair, V. Albin, A. Ringuedé, M. Cassir, *international journal of hydrogen energy* **2012**, *37*(24), 19357–19364.

[209] M. Dudek, *Journal of the European Ceramic Society* **2008**, *28*(5), 965–971.

[210] R. Fernández-González, T. Molina, S. Savvin, R. Moreno, A. Makradi, P. Núñez, *Ceramics International* **2014**, *40*(9), 14253–14259.

[211] J. Selman, H. Maru, *Advances in molten salt chemistry* **1981**, *4*, 159.

[212] G. Mamautov, J. Braunstein, *Advances in molten salt chemistry: Vol. 4*, Plenum Press, New York, NY, **1981**.

[213] M. Anwar, Z. S. Khan, K. Mustafa, A. Rana, *International Journal of Modern Physics B* **2015**, *29*(24), 1550179.

[214] J.-T. Kim, T.-H. Lee, K.-Y. Park, Y. Seo, K. B. Kim, S.-J. Song, B. Park, J.-Y. Park, *Journal of Power Sources* **2015**, *275*, 563–572.

[215] A. I. Rondão, S. G. Patrício, F. M. Figueiredo, F. M. Marques, *international journal of hydrogen energy* **2013**, *38*(14), 5497–5506.

[216] L. Suski, J. Ko?acz, G. Mordarski, M. Ruggiero, *Electrochimica Acta* **2005**, *50*(14), 2771 – 2780, DOI http://dx.doi.org/10.1016/j.electacta.2004.11.023.

[217] C. Jiang, J. Ma, A. D. Bonaccorso, J. T. S. Irvine, *Energy Environ. Sci.* **2012**, *5*, 6973–6980, DOI 10.1039/C2EE03510C.

[218] X. Xu, W. Zhou, Z. Zhu, *RSC Adv.* **2014**, *4*, 2398–2403, DOI 10.1039/C3RA46600K.

[219] I. Zaplatynski, *Reactions of yttria-stabilized zirconia with oxides and sulfates of various elements*, July, NASA Tech. Memo. TM-79005, Department of Energy - NASA, **1978**.

[220] G. P. Wyers, E. H. P. Cordfunke, W. Ouweltjes, *J. Chem. Thermodyn.* **1989**, *21*(10), 1095–1100, DOI 10.1016/0021-9614(89)90096-7.

[221] P. Pasierb, R. Gajerski, S. Komornicki, M. Rekas, *J. Therm. Anal. Calorim.* **2004**, *77*, 105–113, DOI 10.1021/acs.jpcc.5b11861.

[222] R. Janes, L. Knightley, *Journal of materials science* **2004**, *39*(7), 2589–2592.

[223] T. Ristoiu, T. Petrisor, M. Gabor, S. Rada, F. Popa, L. Ciontea, T. Petrisor, *J. Alloys Compd.* **2012**, *532*, 109–113, DOI 10.1016/j.jallcom.2012.03.098.

[224] M. Mizuhata, T. Ohashi, A. B. Béléké, *Int. J. Hydrogen Energy* **2012**, *37*(24), 19407–19416, DOI 10.1016/j.ijhydene.2011.09.109.

[225] S. Kohara, N. Koura, Y. Idemoto, S. Takahashi, *J. Phys. Chem Solids* **1998**, *59*(9), 1477–1485.

[226] C. Descorme, Y. Madier, D. Duprez, *J. Catal.* **2000**, *196*(1), 167–173, DOI 10.1006/jcat.2000.3023.

[227] D. Peltzer, J. Múnera, L. Cornaglia, *RSC Advances* **2016**, *6*(10), 8222–8231.

[228] Y. V. Baklanova, T. A. Denisova, L. G. Maksimova, A. P. Tyutyunnik, I. V. Baklanova, I. R. Shein, R. B. Neder, N. V. Tarakina, *Dalton Transactions* **2014**, *43*(7), 2755–2763.

[229] C. M. Phillippi, K. S. Mazdiyasni, *J. Am. Ceram. Soc.* **1971**, *54*(5), 254–258, DOI 10.1111/j.1151-2916.1971.tb12283.x.

[230] M. Smirnov, R. Baddour-Hadjean, *The Journal of chemical physics* **2004**, *121*(5), 2348–2355.

[231] D. R. Zhang, H. L. Liu, R. H. Jin, N. Z. Zhang, Y. X. Liu, Y. S. Kang, *J. Ind. Eng. Chem.* **2007**, *13*(1), 92–96.

[232] C. E. Bamberger, G. M. Begun, C. S. MacDougall, *Applied Spectroscopy* **1990**, *44*(1), 30–37.

[233] R. Ramaraghavulu, S. Buddhudu, G. B. Kumar, *Ceramics International* **2011**, *37*(4), 1245–1249.

[234] F. Gallino, C. D. Valentin, G. Pacchioni, *Phys. Chem. Chem. Phys.* **2011**, *13*, 17667–17675.

[235] L. Dash, N. Vast, P. Baranek, M.-C. Cheynet, L. Reining, *Phys. Rev. B* **2004**, *70*(24), 245116–17.

[236] N. Clausen, M. Ruhle, A. H. Heuer, in *Adv. Ceram.*, Bd. 12, The American Ceramic Society, Columbous, OH, **1984**.

[237] H. Jiang, R. I. Gomez-Abal, P. Rinke, M. Scheffler, *Phys. Rev. B* **2010**, *81*(8), 085119–9.

[238] W. Piskorz, J. Grybo, F. Zasada, S. Cristol, A. Adamski, *J. Phys. Chem. C* **2011**, *115*, 24274–24286.

[239] J. Chevalier, L. Gremillard, A. V. Virkar, D. R. Clarke, *J. Am. Ceram. Soc.* **2009**, *92*(9), 1901–1920.

[240] J. Dewhurst, J. Lowther, *Phys. Rev. B* **1998**, *57*(2), 741–747.

[241] D. R. Clarke, C. G. Levi, *Annu. Rev. Mater. res.* **2003**, *33*(383), 125–133.

[242] G. Cousland, R. Mole, M. Elcombe, X. Cui, A. Smith, C. Stampfl, A. Stampfl, *J. Phys. Chem. Solids* **2014**, *75*(3), 351–357.

[243] E. J. Walter, S. P. Lewis, A. M. Rappe, *Surf. Sci.* **2001**, *495*, 44–50.

[244] V. Fiorentini, G. Gulleri, *Phys. Rev. Lett.* **2002**, *89*, 266101–266104.

[245] K. Tanabe, T. Yamaguchi, *Catal. Today* **1994**, *20*, 185–198.

[246] X. Xia, R. Oldman, R. Catlow, *Chem. Mater.* **2009**, *21*(15), 3576–3585.

[247] X. Xia, R. J. Oldman, C. R. A. Catlow, *J. Mater. Chem.* **2011**, *21*(38), 14549–14558.

[248] A. Eichler, *Phys. Rev. B* **2001**, *64*(17), 174103–8.

[249] A. Eichler, G. Kresse, *Phys. Rev. B* **2004**, *69*(4), 045402–8.

[250] A. Bogicevic, C. Wolverton, G. Crosbie, E. Stechel, *Phys. Rev. B* **2001**, *64*(1), 014106–14, DOI 10.1103/PhysRevB.64.014106.

[251] R. Krishnamurthy, Y.-G. Yoon, D. J. Srolovitz, R. Car, *J. Am. Ceram. Soc.* **2005**, *87*(10), 1821–1830, DOI 10.1111/j.1151-2916.2004.tb06325.x.

[252] R. Devanathan, W. Weber, S. Singhal, J. Gale, *Solid State Ionics* **2006**, *177*(15-16), 1251–1258, DOI 10.1016/j.ssi.2006.06.030.

[253] V. Stefanovich, A. L. Shluger, C. R. Catlow, *Phys. Rev. B* **1994**, *49*(17), 11560–11571.

[254] S. Fabris, A. T. Paxton, M. W. Finnis, *Acta Mater.* **2002**, *50*, 5171–5178.

[255] G. Stapper, M. Bernasconi, N. Nicoloso, M. Parrinello, *Phys. Rev. B* **1999**, *59*(2), 797–810, DOI 10.1103/PhysRevB.59.797.

[256] C. R. A. Catlow, A. V. Chadwick, G. N. Greaves, L. M. Moroney, *J. Am. Ceram. Soc.* **1986**, *69*, 272–277.

[257] B. W. Veal, A. G. McKale, A. P. Paulikas, S. J. Rothman, L. J. Nowicki, *Phys. B* **1988**, *150*, 234–240.

[258] P. Li, I.-w. Chen, J. E. Penner-Hahn, *Phys. Rev. B* **1993**, *48*(14), 10063–73.

[259] P. Li, I.-w. Chen, J. E. Penner-Hahn, *Phys. Rev. B* **1993**, *48*(14), 10074–81.

[260] P. Li, I.-w. Chen, J. E. Penner-Hahn, *Phys. Rev. B* **1993**, *48*(14), 10082–10089.

[261] W. L. Roth, R. Wong, A. I. Goldman, E. Canova, Y. H. Kao, B. Dunn, *Solid State Ionics* **1986**, *18 & 19*, 1115–1119.

[262] D. Steele, B. E. F. Fender, *J. Phys. Chem. Solids* **1974**, *7*, 1–11.

[263] B. Králik, E. Chang, S. Louie, *Phys. Rev. B* **1998**, *57*(12), 7027–7036.

[264] L. Jin, Q. Yu, A. Rauf, C. Zhou, *Solid State Sci.* **2012**, *14*(1), 106–110, DOI 10.1016/j.solidstatesciences.2011.11.003.

[265] X. Zhao, D. Vanderbilt, *Phys. Rev. B* **2002**, *65*(7), 075105–10.

[266] T. Bredow, *Phys. Rev. B* **2007**, *75*(14), 144102–11.

[267] J. Lowther, *Phys. Rev. B* **2006**, *73*(13), 134110–8.

[268] D. A. Daramola, M. Muthuvel, G. G. Botte, *J. Phys. Chem. B* **2010**, *114*(29), 9323–9.

[269] R. French, S. Glass, F. Ohuchi, Y. Xu, W. Ching, *Phys. Rev. B. Condens. Matter* **1994**, *49*(8), 5133–5142.

[270] J. C. Garcia, L. M. R. Scolfaro, a. T. Lino, V. N. Freire, G. a. Farias, C. C. Silva, H. W. L. Alves, S. C. P. Rodrigues, E. F. da Silva, *J. Appl. Phys.* **2006**, *100*(10), 104103–9.

[271] S. Gennard, F. Cora, C. R. A. Catlow, *J. Phys. Chem. B* **1999**, *103*, 10158–10170.

[272] A. Kuwabara, T. Tohei, T. Yamamoto, I. Tanaka, *Phys. Rev. B* **2005**, *71*(6), 064301–6.

[273] V. Milman, A. Perlov, K. Refson, S. J. Clark, J. Gavartin, B. Winkler, *J. Phys. Condens. Matter* **2009**, *21*(48), 485404–12.

[274] J. E. Medvedeva, A. J. Freeman, C. B. Geller, D. M. Rishel, *Phys. Rev. B* **2007**, *76*, 235115–7.

[275] R. Orlando, C. Pisani, C. Roetti, E. Stefanovich, *Phys. Rev. B. Condens. Matter* **1992**, *45*(2), 592–601.

[276] A. Ignatchenko, D. G. Nealon, R. Dushane, K. Humphries, *J. Mol. Catal. A Chem.* **2006**, *256*(1-2), 57–74.

[277] A. Christensen, E. Carter, *Phys. Rev. B* **1998**, *58*(12), 8050–8064.

[278] G. Balducci, J. Kaspar, P. Fornsiero, M. Graziani, M. S. Islam, *J. Phys. Chem. B* **1998**, *102*, 557–561.

[279] I. M. Iskandarova, A. A. Knizhnik, E. A. Rykova, B. V. Potapkin, A. A. Korkin, *Microelectron. Eng.* **2003**, *69*, 587–593.

[280] A. Hofmann, S. J. Clark, M. Oppel, I. Hahndorf, *Phys. Chem. Chem. Phys.* **2002**, *4*(14), 3500–3508.

[281] S. T. Korhonen, M. Calatayud, A. O. I. Krause, *jorunal Phys. Chem. C* **2008**, (111), 6469–6476.

[282] F. Haase, J. Sauer, *J. Am. Chem. Soc.* **1998**, *2*(101), 13503–13512.

[283] O. A. Syzgantseva, M. Calatayud, C. Minot, *J. Phys. Chem. C* **2012**, *116*, 6636–6644.

[284] M. Alfredsson, C. Richard A. Catlow, *Phys. Chem. Chem. Phys.* **2001**, *3*(18), 4129–4140.

[285] X. Xia, R. J. Oldman, C. R. A. Catlow, *J. Mater. Chem.* **2012**, *22*(17), 8594–8612.

[286] O. Syzgantseva, M. Calatayud, C. Minot, *J. Phys. Chem. C* **2010**, *114*, 11918–11923.

[287] G. Ballabio, M. Bernasconi, F. Pietrucci, S. Serra, *Phys. Rev. B* **2004**, *70*, 075417–6.

[288] R. Orlando, C. Pisani, E. Ruiz, P. Sautet, *Surf. Sci.* **1992**, *275*(3), 482–492.

[289] M. D. Ridder, R. G. V. Welzenis, H. H. Brongersma, U. Kreissig, *Solid State Ionics* **2003**, *158*, 67–77.

[290] C. Morterra, G. Cerrato, L. Ferrato, *Mater. Chem. Phys.* **1994**, *37*, 243–251.

[291] A. Bernasik, K. Kowalski, A. Sadowski, *J. Phys. Chem. Solids* **2002**, *63*(2), 233–239, DOI 10.1016/S0022-3697(01)00135-4.

[292] M. Shishkin, T. Ziegler, *J. Phys. Chem. C* **2008**, *112*(Figure 1), 19662–19669.

[293] T. Bredow, M. Lerch, *Zeitschrift für Anorg. und Allg. Chemie* **2004**, *630*(13-14), 2262–2266.

[294] P. J. Hay, W. R. Wadt, *J. Chem. Phys.* **1985**, *82*(1), 299–310.

[295] W. R. Wadt, P. J. Hay, *J. Chem. Phys.* **1985**, *82*(1), 284–298.

[296] P. J. Hay, W. R. Wadt, *J. Chem. Phys.* **1985**, *82*(1), 270–283.

[297] J. C. Barthelat, P. Durand, *Gazz. Chim. Ital.* **1978**, *108*, 225–236.

[298] J. C. Barthelat, P. Durand, A. Serafini, *Mol. Phys.* **1977**, *33*, 159.

[299] Available at the following website:, `http://www.crystal.unito.it/basis-sets.php`.

[300] H. J. Monkhorst, J. D. Pack, *Phys. Rev. B* **1976**, *13*(12), 5188–5192.

[301] C. J. Howard, R. J. Hill, B. E. Reichert, *Acta Crystallogr. Sect. B Struct. Sci.* **1988**, *44*(2), 116–120.

[302] N. Igawa, Y. Ishii, T. Nagasaki, M. Y, S. Funahashi, H. Ohno, *J. Am. Ceram. Soc.* **1993**, *76*, 2673–2676.

[303] R. P. Ingel, D. Lewis III, *J. Am. Ceram. Soc.* **1986**, *69*, 325–332.

[304] R. J. Ackermann, E. G. Raum, A. Alexander, *High Temp. Sci.* **1975**, *7*, 304–316.

[305] D. McComb, *Phys. Rev. B. Condens. Matter* **1996**, *54*(10), 7094–7102.

[306] S. Ostanin, A. J. Craven, D. W. Mccomb, D. Vlachos, A. Alavi, M. W. Finnis, A. T. Paxton, *Phys. Rev. B* **2000**, *62*(22), 728–735.

[307] A. Tsoga, A. Gupta, A. Naoumidis, P. Nikolopoulos, *Acta Mater.* **2000**, *48*(18-19), 4709–4714.

[308] D. Sotiropoulou, P. Nikolopoulos, *J. Mater. Sci.* **1991**, *26*(5), 1395–1400.

[309] P. W. Tasker, *J. Phys. C Solid State Phys.* **1979**, *12*(22), 4977–4984.

[310] A. Foster, V. Sulimov, F. Lopez Gejo, A. Shluger, R. Nieminen, *Phys. Rev. B* **2001**, *64*(22), 224108–10, DOI 10.1103/PhysRevB.64.224108.

[311] C. Gionco, M. C. Paganini, E. Giamello, R. Burgess, C. D. Valentin, G. Pacchioni, *Chem. Mater.* **2013**, *25*, 2243–2253.

[312] M. Ganduglia-Pirovano, J. Da Silva, J. Sauer, *Phys. Rev. Lett.* **2009**, *102*(2), 026101–4, DOI 10.1103/PhysRevLett.102.026101.

[313] N. Thromat, C. Noguerra, M. Gautier, F. Jollet, J. P. Duraud, *Phys. Rev. B* **1991**, *44*(15), 7904–79011.

[314] N. Yamazoe, N. Miura, *Sensors Actuators B Chem.* **1994**, *20*(2-3), 95–102, DOI 10.1016/0925-4005(93)01183-5.

[315] T. Noazki, K. Fujimoto, *J. Chem. Soc. Chem. Commun.* **1992**, *17*, 1248, DOI 10.1039/c39920001248.

[316] V. A. D'yakov, C. A. Ebbers, M. V. Pchelkin, V. I. Pryalkin, *J. Russ. Laser Reasearch* **1996**, *17*(5), 489–494.

[317] G. J. Janz, M. R. Lorenz, *Chem. Eng. Data* **1961**, *6*(3), 321–323.

[318] A. Ottochian, C. Ricca, F. Labat, C. Adamo, *J. Mol. Model.* **2015**.

[319] A. Meléndez-Ceballos, V. Albin, S. M. Fernández-Valverde, A. Ringuedé, *Electrochim. Acta* **2014**, *140*, 174–181, DOI 10.1016/j.electacta.2014.05.025.

[320] M. Cassir, M. Olivry, V. Albin, B. Malinowska, J. Devynck, *J. Electroanal. Chem.* **1998**, *452*(1), 127–137, DOI 10.1016/S0022-0728(98)00118-1.

[321] T. Koishi, S. Kawase, S. Tamaki, T. Ebisuzaki, *J. Phys. Soc. Japan* **2000**, *69*(10), 3291–3296.

[322] L. J. A. Siqueira, S. M. Urahata, M. C. C. Ribeiro, *J. Chem. Phys.* **2003**, *119*(15), 8002, DOI 10.1063/1.1609983.

[323] W. Eitel, W. Skalilks, *Z. anorg. allegem. Chem.* **1929**, *183*, 263.

[324] M. Christmann, N. Sadeghi, G. Papin, *Rev. Chim. Minerag* **1978**, *15*, 312.

[325] A. V. Yatsenko, S. G. Zhukov, V. A. D'yakov, A. Etz, W. Molleman, H. Shenk, *Mater. Res. Bull.* **1995**, *30*(6), 739–744.

[326] A. V. Yatsenko, S. G. Zhukov, V. A. D'yakov, H. Schenk, *Acta Crystallogr. Sect. C Cryst. Struct. Commun.* **1996**, *52*(1), 1–3, DOI 10.1107/S0108270195010584.

[327] S. G. Zhukov, A. V. Yatsenko, V. V. Chernyshev, V. A. D'yakov, R. Le Loux, H. Shenk, *Z. Krist.* **1999**, *214*, 255–258.

[328] Y. Idemoto, J. W. J. Richardson, N. Koura, S. Kohara, C. Loong, *J. Phys. Chem. Solids* **1998**, *59*(3), 363–376.

[329] Y. Idemoto, R. J. W. Richardson, N. Koura, R. S. Kohara, C. Loong, *J. Solid State Chem.* **1997**, *159*(128), 156–159.

[330] A. Kirfel, H. Euler, B. Barbier, E. Hägele, H. Klapper, *Zeitschrift für Krist.* **2000**, *215*, 744, DOI 10.1524/zkri.2000.215.12.744.

[331] M. Bruno, M. Prencipe, *Surf. Sci.* **2007**, *601*(14), 3012–3019, DOI 10.1016/j.susc.2007.05.004.

[332] H. Gao, S. Pishney, M. J. Janik, *Surf. Sci.* **2013**, *609*, 140–146, DOI 10.1016/j.susc.2012.11.014.

[333] S. Shi, P. Lu, Z. Liu, Y. Qi, L. G. Hector, H. Li, S. J. Harris, *J. Am. Chem. Soc.* **2012**, *134*(37), 15476–87, DOI 10.1021/ja305366r.

[334] S. Shi, Y. Qi, H. Li, L. G. Hector, *J. Phys. Chem. C* **2013**, *117*, 8579–8593.

[335] H. Iddir, L. A. Curtiss, *J. Phys. Chem. C* **2010**, *114*, 20903–20906.

[336] Y. C. Chen, C. Y. Ouyang, L. J. Song, Z. L. Sun, *J. Phys. Chem. C* **2011**, *115*(14), 7044–7049, DOI 10.1021/jp112202s.

[337] R. Dovesi, C. Roetti, C. Freyria-Fava, M. Prencipe, V. Saunders, *Chem. Phys.* **1991**, *156*(1), 11–19, DOI 10.1016/0301-0104(91)87032-Q.

[338] M. Mérawa, P. Labeguerie, P. Ugliengo, K. Doll, R. Dovesi, *Chem. Phys. Lett.* **2004**, *387*(4-6), 453–459, DOI 10.1016/j.cplett.2004.01.123.

[339] M. Prencipe, F. Pascale, C. M. Zicovich-Wilson, V. R. Saunders, R. Orlando, R. Dovesi, *Phys. Chem. Miner.* **2004**, *31*(8), 559–564, DOI 10.1007/s00269-004-0418-7.

[340] M. Catti, A. Pavese, R. Dovesi, V. R. Saunders, *Phys. Rev. B* **1993**, *47*(15), 9189–9198.

[341] R. Nada, C. Catlow, R. Dovesi, C. Pisani, *Phys. Chem. Miner.* **1990**, *17*(4), 353–362, DOI 10.1007/BF00200131.

[342] M. Leslie, N. J. Gillan, *J. Phys. C Solid State Phys.* **2000**, *18*(5), 973–982, DOI 10.1088/0022-3719/18/5/005.

[343] M. Ferrero, M. Rerat, B. Kirtman, R. Dovesi, *J. Chem. Phys.* **2008**, *129*(24), 244110, DOI 10.1063/1.3043366.

[344] M. Ferrero, M. Rérat, R. Orlando, R. Dovesi, *J. Comput. Chem.* **2008**, *29*, 1450, DOI 10.1002/jcc.

[345] M. Ferrero, M. Rerat, R. Orlando, R. Dovesi, *J. Chem. Phys.* **2008**, *128*(1), 014110–8, DOI 10.1063/1.2817596.

[346] E. Commission, *SOFC Single Cell Performance and Endurance Test Modules*, **2010**.

[347] C. Darrigan, M. Rérat, G. Mallia, R. Dovesi, *J. Comput. Chem.* **2003**, *24*(11), 1305–1312, DOI 10.1002/jcc.10274.

[348] E.-J. Zehnder, *Acta Crystallogr.* **1983**, *A40*, C468–469.

[349] M. H. Brooker, J. B. Bates, *J. Chem. Phys.* **1971**, *54*(11), 4788, DOI 10.1063/1.1674754.

[350] N. Koura, S. Kohara, K. Takeuchi, S. Takahashi, L. A. Curtiss, M. Grimsditch, M.-l. Saboungi, *J. Mol. Struct.* **1996**, *382*, 163–169.

[351] F. Ramondoa, L. Bencivenni, N. Sanna, S. Nunziante Cesaro, *J. Mol. Struct.* **1992**, *253*, 121–147.

[352] W. R. Carper, P. G. Wahlbeck, T. R. Griffiths, *J. Phys. Chem. B* **2012**, *116*(18), 5559–67, DOI 10.1021/jp3016694.

[353] S. Kohara, Y. S. Badyal, N. Koura, Y. Idemoto, S. Takahashi, L. A. Curtiss, M. L. Saboungi, *J. Physics-Condensed Matter* **1998**, *10*(15), 3301–3308.

[354] G. C. Dubbledam, P. M. de Wolff, *Acta Crystallogr. Sect. B Struct. Crystallogr. Cryst. Chem.* **1969**, *25*(12), 2665–2667, DOI 10.1107/S0567740869006285.

[355] W. van Aalst, J. den Hollander, W. J. A. M. Peterse, P. M. de Wolff, *Acta Crystallogr. Sect. B Struct. Crystallogr. Cryst. Chem.* **1976**, *32*, 47–58.

[356] S. Okazaki, M. Matsumoto, I. Okada, *Mol. Phys.* **1993**, *79*, 611–621, DOI 10.1080/00268979300101491.

[357] S. P. Bates, G. Kresse, M. J. Gillan, *Surf. Sci.* **1998**, *409*, 336–349.

[358] I. A. Fedorov, Y. N. Zhuravlev, D. V. Korabel'nikov, *Russ. Phys. J.* **2006**, *49*(10), 61–65.

[359] Y. N. Zhuravlev, I. A. Fedorov, *J. Struct. Chem.* **2006**, *47*(2), 215–219.

[360] Y. Duan, *J. Renew. Sustain. Energy* **2012**, *4*(2012), 013109, DOI 10.1063/1.3683519.

[361] Y. Duan, D. Sorescu, *Phys. Rev. B* **2009**, *79*(1), 014301, DOI 10.1103/PhysRevB.79.014301.

[362] P. Albertus, G. Girishkumar, B. McCloskey, R. S. Sa?nchez-Carrera, B. Kozinsky, J. Christensen, a. C. Luntz, *J. Electrochem. Soc.* **2011**, *158*(3), A343, DOI 10.1149/1.3527055.

[363] J. Muscat, A. Wander, N. M. Harrison, *Chem. Phys. Lett.* **2001**, *342*(3-4), 397–401, DOI 10.1016/S0009-2614(01)00616-9.

[364] L. Kang, Z. Lin, J. Qin, C. Chen, *Sci. Rep.* **2013**, *3*(i), 1366, DOI 10.1038/srep01366.

[365] M. Bruno, *Cryst. Res. Technol.* **2013**, *818*(10), 811–818, DOI 10.1002/crat.201200707.

[366] M. Bruno, F. R. Massaro, M. Prencipe, D. Aquilano, *Cryst. Eng. Comm.* **2010**, *12*, 3626–3633, DOI 10.1039/c002969f.

[367] M. Bruno, F. R. Massaro, M. Prencipe, *Surf. Sci.* **2008**, *602*, 2774–2782, DOI 10.1016/j.susc.2008.07.002.

[368] M. Bruno, D. Aquilano, L. Pastero, M. Prencipe, *Cryst. Growth Des.* **2008**, *8*(100), 2163–2170.

[369] C. L. Bailey, L. Liborio, G. Mallia, S. Tomić, N. M. Harrison, *Phys. Rev. B - Condens. Matter Mater. Phys.* **2010**, *81*(20), 1–8, DOI 10.1103/PhysRevB.81.205214.

[370] C. L. Bailey, L. Liborio, G. Mallia, S. Tomić, N. M. Harrison, *J. Phys. Conf. Ser.* **2010**, *242*, 012004, DOI 10.1088/1742-6596/242/1/012004.

[371] R. M. Nieminen, *Model. Simul. Mater. Sci. Eng.* **2009**, *17*(8), 084001–13, DOI 10.1088/0965-0393/17/8/084001.

[372] S. K. Nayak, W. a. Adeagbo, H. T. Langhammer, W. Hergert, T. Müller, R. Böttcher, *Phys. Status Solidi - Rapid Res. Lett.* **2014**, *8*(6), 527–531, DOI 10.1002/pssr.201409032.

[373] S. Lany, A. Zunger, *Model. Simul. Mater. Sci. Eng.* **2009**, *17*(8), 084002, DOI 10.1088/0965-0393/17/8/084002.

[374] F. Gallino, C. Di Valentin, *J. Chem. Phys.* **2011**, *134*(14), 1–10, DOI 10.1063/1.3575198.

[375] C. G. Van De Walle, J. Neugebauer, *J. Appl. Phys.* **2004**, *95*(8), 3851–3879, DOI 10.1063/1.1682673.

[376] H.-P. Komsa, N. Berseneva, A. V. Krasheninnikov, R. M. Nieminen, *Phys. Rev. X* **2014**, *4*(3), 1–7, DOI 10.1103/PhysRevX.4.031044.

[377] Y. Kumagai, F. Oba, *Phys. Rev. B - Condens. Matter Mater. Phys.* **2014**, *89*(19), DOI 10.1103/PhysRevB.89.195205.

[378] S. T. Murphy, N. D. M. Hine, *Phys. Rev. B - Condens. Matter Mater. Phys.* **2013**, *87*(9), 1–6, DOI 10.1103/PhysRevB.87.094111.

[379] N. D. M. Hine, K. Frensch, W. M. C. Foulkes, M. W. Finnis, *Phys. Rev. B - Condens. Matter Mater. Phys.* **2009**, *79*(2), 1–13, DOI 10.1103/PhysRevB.79.024112.

[380] G. Makov, M. Payne, *Phys. Rev. B* **1995**, *51*(7), 4014–4022, DOI 10.1103/PhysRevB.51.4014.

[381] I. Barini, F. Sauert, E. Schultze-Rhonhof, W. S. Sheng, *Thermochemical data of pure substances. Weinheim [etc.]: VCH, 1993*, VCH, Weinheim, Germany, **1993**, 1993.

[382] M. R. Nadler, C. P. Kempfer, *Anal. Chem.* **1959**, *31*, 2109.

[383] J. Mizusaki, H. Tagawa, K. Saito, K. Uchida, M. Tezuka, *Solid State Ionics* **1992**, *53-56*(PART 2), 791–797, DOI 10.1016/0167-2738(92)90256-O.

[384] M. Dissanayake, B.-E. Mellander, *Solid State lonics* **1986**, *21*, 279–285, DOI 10.1016/0167-2738(86)90190-6.

[385] R. Shannon, B. Taylor, a.D. English, T. Berzins, *Electrochim. Acta* **1977**, *22*(7), 783–796, DOI 10.1016/0013-4686(77)80035-2.

[386] G. Kresse, D. Joubert, *Phys. Rev. B* **1999**, *59*, 1758–1775, DOI 10.1103/PhysRevB.59.1758.

[387] M. Bruno, M. Rubbo, L. Pastero, F. R. Massaro, D. Aquilano *8*, 3–4.

[388] S. F. Boys, F. Bernardi, *Mol. Phys.* **1970**, *19*(4), 553–566, DOI 10.1080/00268977000101561.

[389] C. Ricca, A. Ringuedé, M. Cassir, C. Adamo, F. Labat, *Surf. Sci.* **2016**, *647*, 66–77, DOI 10.1016/j.susc.2015.12.027.

[390] G. Busca, V. Lorenzelli, *Mater. Chem.* **1982**, *7*, 89–126, DOI 10.1016/0390-6035(82) 90059-1.

[391] E. Guglielminotti, *Langmuir* **1990**, *6*(9), 1455–1460, DOI 10.1021/la00099a005.

[392] K. D. Dobson, A. J. Mcquillan, *Langmuir* **1997**, *7463*(15), 3392–3396.

[393] W. Hertl, *Langmuir* **1989**, 96–100.

[394] K. Pokrovski, K. T. Jung, A. T. Bell, *Langmuir* **2001**, (18), 4297–4303.

[395] B. Bachiller-baeza, I. Rodriguez-Ramos, A. Guerrero-Ruiz, *Langmuir* **1998**, *7463*(14), 3556–3564.

[396] H. Tsuji, A. Okamura-yoshida, T. Shishido, H. Hattori, *Langmuir* **2003**, (9), 8793–8800.

[397] B. L. Mojet, S. D. Ebbesen, L. Lefferts, *Chem. Soc. Rev.* **2010**, *39*(12), 4643, DOI 10.1039/c0cs00014k.

[398] I. Kosacki, V. Petrovsky, H. U. Anderson, P. Colomban, *J. Am. Ceram. Soc.* **2004**, *85*(11), 2646–2650, DOI 10.1111/j.1151-2916.2002.tb00509.x.

[399] J. L. Wade, C. Lee, A. C. West, K. S. Lackner, *J. Memb. Sci.* **2011**, *369*(1-2), 20–29, DOI 10.1016/j.memsci.2010.10.053.

[400] M. Mori, T. Abe, H. Itoh, O. Yamamoto, G. Q. Shen, Y. Takeda, N. Imanishi, *Solid State Ionics* **1999**, *123*(1), 113–119, DOI 10.1016/S0167-2738(99)00115-0.

[401] Y. Kato, M. Asano, T. Harada, Y. Mizutani, *J. Nucl. Mater.* **1993**, *203*(1), 27–35, DOI 10.1016/0022-3115(93)90426-Y.

[402] E. J. H. Jr., E. L. Head, C. E. H. Jr., *The Journal of Physical Chemistry* **1964**, *68*(10), 3040–3042, DOI 10.1021/j100792a052.

[403] C. D. Valentin, G. Pacchioni, A. Selloni, V. R. Cozzi, *Society* **2005**, *17*(November), 6656–6665, DOI 10.1021/cm051921h.

[404] C. Qin, A. Gladney, *Comput. Theor. Chem.* **2012**, *999*, 179–183, DOI 10.1016/j. comptc.2012.08.036.

[405] Y. Gong, X. Li, L. Zhang, W. Tharp, C. Qin, K. Huang, *J. Electrochem. Soc.* **2013**, *160*(9), F958–F964, DOI 10.1149/2.031309jes.

[406] X. Lei, K. Haines, K. Huang, C. Qin, *J. Power Sources* **2016**, *305*, 161–166, DOI 10.1016/j.jpowsour.2015.11.095.

[407] X. Lei, K. Haines, K. Huang, C. Qin, *The Journal of Physical Chemistry A* **2015**, *119*(33), 8806–8812, pMID: 26219024, DOI 10.1021/acs.jpca.5b06527.

[408] B. Zhu, Y. Ma, X. Wang, R. Raza, H. Qin, L. Fan, *Electrochemistry Communications* **2011**, *13*(3), 225 – 227, DOI http://dx.doi.org/10.1016/j.elecom.2010.12.019.

[409] B. Zhu, L. Fan, P. Lund, *Applied Energy* **2013**, *106*, 163 – 175, DOI http://dx.doi.org/10.1016/j.apenergy.2013.01.014.

[410] Q. Liu, H. Qin, R. Raza, L. Fan, Y. Li, B. Zhu, *RSC Adv.* **2012**, *2*, 8036–8040, DOI 10.1039/C2RA20694C.

[411] C. Ricca, A. Ringuedé, M. Cassir, C. Adamo, F. Labat, *J. Comput. Chem.* **2014**, *36*(1), 9–21, DOI 10.1002/jcc.23761.

[412] X. Lei, C. Qin, K. Huang, *RSC Adv.* **2015**, *5*, 56205–56209, DOI 10.1039/C5RA07975F.

[413] G. J. Janz, N. P. Bansal, *J. Phys. Chem. Ref. Data* **1982**, *11*(3), 505–693, DOI 10.1063/1.555665.

[414] M. Costa, *J. Mol. Liq.* **2008**, *138*(1-3), 61–68, DOI 10.1016/j.molliq.2007.08.001.

[415] U. Diebold, *Surface science reports* **2003**, *48*(5), 53–229.

[416] O. K. Varghese, C. A. Grimes, *Journal of Nanoscience and Nanotechnology* **2003**, *3*(4), 277–293.

[417] J.-M. Wu, C.-J. Chen, *Journal of the American Ceramic Society* **1990**, *73*(2), 420–424.

[418] K. Siefering, G. Griffin, *Journal of The Electrochemical Society* **1990**, *137*(4), 1206–1208.

[419] C. Simons, U. Hanefeld, I. W. Arends, R. A. Sheldon, T. Maschmeyer, *Chemistry–A European Journal* **2004**, *10*(22), 5829–5835.

[420] A. Hagfeldt, M. Graetzel, *Chemical Reviews* **1995**, *95*(1), 49–68.

[421] K. Kalyanasundaram, M. Grätzel, *Coordination chemistry reviews* **1998**, *177*(1), 347–414.

[422] L. Forro, O. Chauvet, D. Emin, L. Zuppiroli, H. Berger, F. Levy, *Journal of Applied Physics* **1994**, *75*(1), 633–635.

[423] A. Wold, *Chemistry of Materials* **1993**, *5*(3), 280–283.

[424] L. Kavan, M. Grätzel, S. Gilbert, C. Klemenz, H. Scheel, *Journal of the American Chemical Society* **1996**, *118*(28), 6716–6723.

[425] J. Muscat, V. Swamy, N. M. Harrison, *Physical Review B* **2002**, *65*(22), 224112.

[426] N. Vast, L. Reining, V. Olevano, P. Schattschneider, B. Jouffrey, *Physical review letters* **2002**, *88*(3), 037601.

[427] J. Muscat, N. Harrison, G. Thornton, *Physical Review B* **1999**, *59*(3), 2320.

[428] T. Bredow, L. Giordano, F. Cinquini, G. Pacchioni, *Physical Review B* **2004**, *70*(3), 035419.

[429] J. Scaranto, S. Giorgianni, *Molecular Physics* **2009**, *107*(19), 1997–2003.

[430] M. Lazzeri, A. Vittadini, A. Selloni, *Physical Review B* **2001**, *63*(15), 155409.

[431] K. Rościszewski, K. Doll, B. Paulus, P. Fulde, H. Stoll, *Physical Review B* **1998**, *57*(23), 14667.

[432] J. Goniakowski, J. Holender, L. Kantorovich, M. Gillan, J. White, *Physical Review B* **1996**, *53*(3), 957.

[433] S.-D. Mo, W. Ching, *Physical Review B* **1995**, *51*(19), 13023.

[434] C. Lee, X. Gonze, *Physical Review B* **1994**, *49*(20), 14730.

[435] C. Lee, P. Ghosez, X. Gonze, *Physical Review B* **1994**, *50*(18), 13379.

[436] K. M. Glassford, J. R. Chelikowsky, *Physical Review B* **1992**, *46*(3), 1284.

[437] M.-Y. Kuo, C.-L. Chen, C.-Y. Hua, H.-C. Yang, P. Shen, *The Journal of Physical Chemistry B* **2005**, *109*(18), 8693–8700.

[438] P. Reinhardt, B. Hess, M. Causa, *International journal of quantum chemistry* **1996**, *58*(3), 297–306.

[439] J. K. Burdett, T. Hughbanks, G. J. Miller, J. W. Richardson Jr, J. V. Smith, *Journal of the American Chemical Society* **1987**, *109*(12), 3639–3646.

[440] R. C. Weast, M. J. Astle, W. H. Beyer, et al., *CRC handbook of chemistry and physics*, Bd. 69, CRC press Boca Raton, FL, **1988**.

[441] H. Tang, F. Levy, H. Berger, P. Schmid, *Physical Review B* **1995**, *52*(11), 7771.

[442] S. Kowalczyk, F. McFeely, L. Ley, V. Gritsyna, D. Shirley, *Solid State Communications* **1977**, *23*(3), 161–169.

[443] K. Tsutsumi, O. Aita, K. Ichikawa, *Physical Review B* **1977**, *15*(10), 4638.

[444] M. Knotek, P. J. Feibelman, *Physical Review Letters* **1978**, *40*(14), 964.

[445] G. Cangiani, A. Baldereschi, M. Posternak, H. Krakauer, *Physical Review B* **2004**, *69*(12), 121101.

[446] F. Labat, P. Baranek, C. Domain, C. Minot, C. Adamo, *J. Chem. Phys.* **2007**, *126*(15), 154703–12.

[447] J. Muscat, A. Wander, N. Harrison, *Chemical Physics Letters* **2001**, *342*(3), 397–401.

[448] Y.-f. Zhang, W. Lin, Y. Li, K.-n. Ding, J.-q. Li, *The Journal of Physical Chemistry B* **2005**, *109*(41), 19270–19277.

[449] V. E. Henrich, R. L. Kurtz, *Physical Review B* **1981**, *23*(12), 6280.

[450] P. Murray, N. Condon, G. Thornton, *Physical Review B* **1995**, *51*(16), 10989.

[451] U. Diebold, J. F. Anderson, K.-O. Ng, D. Vanderbilt, *Physical review letters* **1996**, *77*(7), 1322.

[452] G. Charlton, P. Howes, C. Nicklin, P. Steadman, J. Taylor, C. Muryn, S. Harte, J. Mercer, R. McGrath, D. Norman, et al., *Physical Review Letters* **1997**, *78*(3), 495.

[453] B. Hird, R. Armstrong, *Surface science* **1997**, *385*(2), L1023–L1028.

[454] R. Bennett, P. Stone, N. Price, M. Bowker, *Physical review letters* **1999**, *82*(19), 3831.

[455] R. Lindsay, A. Wander, A. Ernst, B. Montanari, G. Thornton, N. Harrison, *Physical review letters* **2005**, *94*(24), 246102.

[456] P. Reinhardt, B. Hess, *Physical Review B* **1994**, *50*(16), 12015.

[457] M. Ramamoorthy, D. Vanderbilt, R. King-Smith, *Physical Review B* **1994**, *49*(23), 16721.

[458] D. Vogtenhuber, R. Podloucky, A. Neckel, S. Steinemann, A. J. Freeman, *Physical Review B* **1994**, *49*(3), 2099.

[459] P. Lindan, N. Harrison, M. Gillan, J. White, *Physical Review B* **1997**, *55*(23), 15919.

[460] S. Bates, G. Kresse, M. Gillan, *Surface Science* **1997**, *385*(2), 386–394.

[461] E. áToby Kelsey, et al., *Journal of Materials Chemistry* **1997**, *7*(3), 563–568.

[462] S. Bates, G. Kresse, M. Gillan, *Surface science* **1998**, *409*(2), 336–349.

[463] V. Swamy, J. Muscat, J. D. Gale, N. M. Harrison, *Surface science* **2002**, *504*, 115–124.

[464] J. Scaranto, G. Mallia, S. Giorgianni, C. Zicovich-Wilson, B. Civalleri, N. Harrison, *Surface science* **2006**, *600*(2), 305–317.

[465] W. Hebenstreit, N. Ruzycki, G. S. Herman, Y. Gao, U. Diebold, *Physical Review B* **2000**, *62*(24), R16334.

[466] R. Hengerer, B. Bolliger, M. Erbudak, M. Grätzel, *Surface Science* **2000**, *460*(1), 162–169.

[467] M. Calatayud, C. Minot, *Surface science* **2004**, *552*(1), 169–179.

[468] C. Arrouvel, M. Digne, M. Breysse, H. Toulhoat, P. Raybaud, *Journal of Catalysis* **2004**, *222*(1), 152–166.

[469] A. Beltran, J. Sambrano, M. Calatayud, F. Sensato, J. Andres, *Surface science* **2001**, *490*(1), 116–124.

[470] F. Labat, P. Baranek, C. Adamo, *J. Chem. Theory Comput.* **2008**, *4*(001), 341–352.

[471] F. Labat*, , C. Adamo, *The Journal of Physical Chemistry C* **2007**, *111*(41), 15034–15042, DOI 10.1021/jp074349l.

[472] A. Fahmi, C. Minot, B. Silvi, M. Causá, *Phys. Rev. B* **1993**, *47*, 11717–11724, DOI 10.1103/PhysRevB.47.11717.

[473] B. Silvi, N. Fourati, R. Nada, C. Catlow, *Journal of Physics and Chemistry of Solids* **1991**, *52*(8), 1005 – 1009, DOI http://dx.doi.org/10.1016/0022-3697(91)90029-Y.

[474] H. Tang, H. Berger, P. Schmid, F. Lvy, G. Burri, *Solid State Communications* **1993**, *87*(9), 847 – 850, DOI http://dx.doi.org/10.1016/0038-1098(93)90427-O.

[475] S. Kerisit, K. M. Rosso, Z. Yang, J. Liu, *Work* **2009**, *113*(49), 20998–21007, DOI 10.1021/jp9064517.

[476] S. Kerisit, K. M. Rosso, Z. Yang, J. Liu, *J. Phys. Chem. C* **2010**, *114*(44), 19096–19107, DOI 10.1021/jp103809s.

[477] L. Kavan, *J. Solid State Electrochem.* **2014**, *18*(8), 2297–2306, DOI 10.1007/s10008-014-2435-x.

[478] M. V. Koudriachova, N. M. Harrison, S. W. De Leeuw, *Phys. Rev. Lett.* **2001**, *86*(7), 1275–1278, DOI 10.1103/PhysRevLett.86.1275.

[479] S. Lunell, A. Stashans, L. Ojam??e, H. Lindstr??m, A. Hagfeldt, *J. Am. Chem. Soc.* **1997**, *119*(31), 7374–7380, DOI 10.1021/ja9708629.

[480] B. J. Morgan, G. W. Watson, *Phys. Rev. B - Condens. Matter Mater. Phys.* **2010**, *82*(14), 1–11, DOI 10.1103/PhysRevB.82.144119.

[481] C. L. Olson, J. Nelsonm, S. Islam, C. L. Olson, J. Nelson **2006**, *110*(20), 9995–10001, DOI 10.1021/jp057261l.

[482] J. H. Richter, A. Henningsson, P. G. Karlsson, M. P. Andersson, P. Uvdal, H. Siegbahn, A. Sandell, *Phys. Rev. B - Condens. Matter Mater. Phys.* **2005**, *71*(23), 1–7, DOI 10.1103/PhysRevB.71.235418.

[483] M. L. Sushko, K. M. Rosso, J. Liu, *J. Phys. Chem. C* **2010**, *114*, 20277–20283, DOI 10.1021/jp107982c.

[484] M. Wagemaker, W. J. H. Borghols, E. R. H. Van Eck, A. P. M. Kentgens, G. J. Kearley, F. M. Mulder, *Chem. - A Eur. J.* **2007**, *13*(7), 2023–2028, DOI 10.1002/chem.200600803.

[485] M. Wagemaker, R. van de Krol, a. P. Kentgens, a. a. van Well, F. M. Mulder, *J. Am. Chem. Soc.* **2001**, *123*(46), 11454–11461, DOI 10.1021/ja0161148.

[486] M. Wagemaker, G. J. Kearley, A. A. Van Well, H. Mutka, F. M. Mulder, *J. Am. Chem. Soc.* **2003**, *125*(3), 840–848, DOI 10.1021/ja028165q.

[487] M. Wagemaker, W. J. H. Borghols, F. M. Mulder, *J.Am.Chem.Soc.* **2007**, *129*(March), 4323–4327, DOI 10.1021/ja067733p.

[488] M. Wagemaker, a. P. M. Kentgens, F. M. Mulder, *Nature* **2002**, *418*(6896), 397–399, DOI 10.1038/nature00901.

[489] P. Mori-Sánchez, A. J. Cohen, W. Yang, *Physical review letters* **2008**, *100*(14), 146401.

[490] A. J. Cohen, P. Mori-Sánchez, W. Yang, *Science* **2008**, *321*(5890), 792–794.

[491] C. Spreafico, J. VandeVondele, *J. Phys. Chem. C* **2015**, *119*(27), 15009–15018, DOI 10.1021/acs.jpcc.5b04103.

[492] J. H. Richter, A. Henningsson, P. G. Karlsson, M. P. Andersson, P. Uvdal, H. Siegbahn, A. Sandell, *Phys. Rev. B* **2005**, *71*, 235418, DOI 10.1103/PhysRevB.71.235418.

[493] D. F. Watson, G. J. Meyer, *Coord. Chem. Rev.* **2004**, *248*(13-14), 1391–1406, DOI 10.1016/j.ccr.2004.02.015.

[494] A. Henningsson, H. Rensmo, A. Sandell, H. Siegbahn, S. Sdergren, H. Lindstrm, A. Hagfeldt, *The Journal of Chemical Physics* **2003**, *118*(12).

[495] A. Augustsson, A. Henningsson, S. M. Butorin, H. Siegbahn, J. Nordgren, J.-H. Guo, *The Journal of Chemical Physics* **2003**, *119*(7).

[496] T. Désaunay, A. Ringuedé, M. Cassir, F. Labat, C. Adamo, *Surf. Sci.* **2012**, *606*(3-4), 305–311, DOI 10.1016/j.susc.2011.10.011.

List of publications

- **C. Ricca**, V. Albin, F. Labat, C. Adamo, M. Cassir, A. Ringuedé, 'A first combined electrochemical and modelling strategy on composite carbonate/oxide electrolytes for hybrid fuel cells', *International Journal of Hydrogen Energy*, *just accepted manuscript*, (2016).

- **C. Ricca**, A. Ringuedé, M. Cassir, A. Ottochian, C. Adamo, and F. Labat, 'Defect Formation and Diffusion on the (001) Surface of $LiKCO_3$ for Fuel Cell Applications: Insight from Hybrid DFT', *J. Phys. Chem. C*, 129, 12924-12951, (2016).

- **C. Ricca**, A. Ringuedé, M. Cassir, C. Adamo, and F. Labat, 'Mixed lithium-sodium ($LiNaCO_3$) and lithium-potassium ($LiKCO_3$) carbonates for low temperature electrochemical applications: Structure, electronic properties and surface reconstruction from ab-initio calculations', *Surf. Sci.*, 647, 66-67 (2016).

- **C. Ricca**, B. Medina-Lott, V. Albin, F. Labat, C. Adamo, M. Hinoijosa, M. Cassir, A. Ringuedé, 'Hybrid Fuel Cells with Carbonate/Oxide Composite Electrolytes: An Electrochemical and Theoretical Insight', *ECS Transactions*, SOFC-XIV, Ed. S.C. Singhal, 68, (2015).

- **C. Ricca**, A. Ringuedé, M. Cassir, C. Adamo, and F. Labat, Revealing the properties of the cubic ZrO_2 (111) surface by periodic DFT calculations: reducibility and stabilization through doping with aliovalent Y_2O_3, *RSC Adv.*, 2, 13941?13951 (2015).

- **C. Ricca**, A. Ringuedé, M. Cassir, C. Adamo, and F. Labat, 'A comprehensive DFT investigation of bulk and low-index surfaces of ZrO_2 polymorphs', *J. Comput. Chem.*, 36, 9-21 (2014).

Submitted publications

- **C. Ricca**, A. Grishin, A. Ringuedé, M. Cassir, C. Adamo, and F. Labat, Modeling composite electrolytes for low-temperature solid oxide fuel cells application: structural, vibrational and electronic features of carbonate-oxide interfaces, *Journal of Material Chemistry A*, *submitted*.

Publications in preparation

- **C. Ricca**, A. Ringuedé, M. Cassir, C. Adamo, and F. Labat, 'Conduction mechanisms in oxide-carbonate composite electrolytes for LT-SOFC applications: insights from DFT calculations.', *manuscript in preparation*

Combined theoretical and experimental study of the ionic conduction in oxide-carbonate composites as electrolytes for solid oxide fuel cells (SOFC)

Abstract

Oxide-carbonate composites are promising electrolyte materials for LT-SOFC (400-600°C), because of their enhanced conductivity, of the order of 0.1-1 S/cm at 600°C, when compared to the pure oxide phase in the same temperature range. Despite the large number of studies realized in this field, a deeper understanding on the origins of their improved performances is still necessary. For this purpose, a combined approach joining theory and experiments was developed. From an experimental point of view, we performed a systematic study of the conductivity of the material, measured through electrochemical impedance spectroscopy (EIS), as a function of different oxide (CeO_2-based oxides, yttria-stabilized YSZ, and TiO_2) or carbonate ($(Li,Na)_2CO_3$ or $(Li,K)_2CO_3$) phases and of the operating (oxidising or reducing) atmosphere. Results on YSZ- and CeO_2-based materials indicate that by only taking into account the role of the interfaces between the two materials it is possible to rationalize some surprising observations, while reactivity issues have been observed for TiO_2-carbonate composites. In order to model these two phase materials, we proposed a computational strategy based on periodic Density Functional Theory (DFT) calculations: we first studied the bulk structure of each phase separately in order to select an adequate computational protocol, which has then been used to identify a suitable model of the most stable surface for each phase. These surface models have thus been combined to obtain a model of the oxide-carbonate interface that through static DFT and molecular dynamic (MD) can provide a deeper insight on the interface at the atomic level. This strategy was applied to provide information on the structure, stability and electronic properties of YSZ-$LiKCO_3$ and TiO_2-$LiKCO_3$ materials. YSZ-$LiKCO_3$ was also used as a case study to investigate the conduction mechanims of different transport species (Li^+, O^{2-} and H^+) and the results showed a strong influence of the interfaces on the transport properties of these materials. The TiO_2-$LiKCO_3$ interface model was, instead, used to investigate the reactivity of these materials. Overall, these results pave the way toward a deeper understanding of the basic operating principles of LT-SOFC based on these composite electrolytes offering possible guidelines for further improvements..

Keywords: oxide-carbonate composite, SOFC, DFT, EIS, interface, electrolyte

Etude combinée théorique et expérimentale de la conduction ionique dans les matériaux composite oxyde-carbonate comme électrolytes pour les piles à combustible à oxyde solide (SOFC)

Résumé

Les matériaux composites oxyde-carbonate pourraient constituer des électrolytes pour les piles à combustible à oxyde solide fonctionnant dans une gamme de températures dites basses, entre 400-600°C (LT-SOFC). En fait, ils peuvent atteindre des niveaux de conductivité (0,1 S/cm à 600°C) beaucoup plus élevés par rapport aux phases oxyde traditionnellement utilisées dans les SOFC. Malgré les nombreuses études réalisées dans ce domaine, une meilleure compréhension de l'origine de leurs performances est à ce jour nécessaire. Pour y parvenir, une approche combinée joignant la théorie et l'expérience a été développée. Du côté expérimental, une étude systématique de la conductivité, mesurée à travers la spectroscopie d'impédance électrochimique (SIE), en fonction de la phase oxyde (oxyde à base de CeO_2, oxyde Zr dopé à l'oxyde de yttrium (YSZ) et TiO_2) ou carbonate ($(Li,Na)_2CO_3$ et $(Li,K)_2CO_3$) et de l'atmosphère de travail (oxydante ou réductrice) a été mise en place. Les résultats pour les matériaux à base de CeO_2 ou YSZ ont montré que seule l'interface peut expliquer certaines observations surprenantes, tandis que de la réactivité a été observée dans le cas des composites à base de TiO_2. Pour modéliser ces matériaux composites, on a proposé une stratégie computationnelle qui utilise des calculs périodiques basés sur la théorie de la fonctionnelle de la densité (DFT): la structure du bulk de chaque phase a d'abord été étudiée séparément afin de trouver un bon protocole computationnel, qui a été ensuite utilisé pour identifier un modèle pour la surface la plus stable des deux phases. Ces modèles de surfaces ont donc été combinés pour obtenir un modèle de l'interface oxyde-carbonate, qui peut être utilisé comme structure de départ pour des calculs DFT et de dynamique moléculaire (DM). Cette stratégie a permis d'obtenir des informations sur la structure, la stabilité et les propriétés électroniques des composites YSZ-$LiKCO_3$ et TiO_2-$LiKCO_3$. YSZ-$LiKCO_3$ a été aussi utilisé comme étude de cas pour mieux comprendre l'effet des interfaces sur le transport de différents espèces (Li^+, O^{2-} et H^+), tandis que le modèle de l'interface entre TiO_2 et $LiKCO_3$ a été utilisé pour étudier la réactivité entre ces deux matériaux. Finalement, ces résultats ouvrent la voie vers une plus grande compréhension des principes de fonctionnement des SOFC basées sur les électrolytes composites oxyde-carbonate.

Mots clés: composite oxyde-carbonate, SOFC, DFT, SIE, interface, électrolyte